Universidade de Lisboa
Faculdade de Ciências

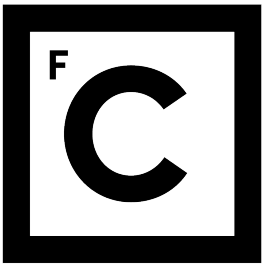

Ciências
ULisboa

Observation and measurement of the Higgs boson in the WW^* decay channel with ATLAS at the LHC

Doutoramento em Física

Joana Machado Miguéns

Tese orientada pela Prof.ª Amélia Maio
e pela Doutora Patricia Conde Muíño

Documento especialmente elaborado para
a obtenção do grau de doutor em Física

2015

Resumo

A medição da produção do bosão de Higgs foi realizada com o detector ATLAS no Grande Colisionador de Hadrões. Foram usados dados de colisões protão-protão, correspondentes a uma luminosidade integrada de 25 fb^{-1}, obtidos a energias de centro-de-mass de 7 e 8 TeV, durante os anos de 2011 e 2012. O canal de decaimento $H \to WW^* \to \ell\nu\ell\nu$ foi analisado, com particular ênfase em eventos com dois electrões ou dois muões no estado final. Desenvolveram-se novas técnicas de análise, que permitiram lidar com a enorme contaminação de processos de fundo de Drell-Yan. Um excesso de eventos foi observado relativamente à previsão para os eventos de fundo, com uma significância de 6.1σ, o que estabelece conclusivamente a observação do bosão de Higgs no canal $H \to WW^* \to \ell\nu\ell\nu$. A taxa de eventos (secção eficaz de produção vezes razão de bifurcação) observada é compatível com a esperada para o bosão de Higgs do Modelo Padrão com uma massa de 125.26 GeV, pelo que o quociente entre as duas taxas é consistente com a unidade: $1.08\ ^{+0.16}_{-0.15}\ \text{(stat.)}\ ^{+0.08}_{-0.07}\ \text{(expt.)}\ ^{+0.13}_{-0.11}\ \text{(theo.)}\ \pm 0.03\ \text{(lumi.)}\ = 1.08\ ^{+0.22}_{-0.20}$.

Palavras-chave:
Modelo Padrão, quebra de simetria electrofraca, bosão de Higgs, LHC, ATLAS

O Modelo Padrão da Física de Partículas descreve e prevê, com grande precisão e exactidão, três das quatro forças fundamentais do Universo, que regem as interacções entre as partículas elementares. Leis matemáticas de simetria definem, com sucesso, a estrutura destas interacções. No entanto as simetrias que estão na base do Modelo Padrão apenas conseguem descrever o comportamento de partículas sem massa, o que não corresponde à realidade. Em 1964, o mecanismo de Higgs foi proposto como uma solução para este problema, designado por "origem da massa". A quebra espontânea da simetria electro-fraca dá-se através deste mecanismo de Higgs, que permite que no Modelo Padrão seja possível descrever partículas com massa. A partícula conhecida hoje como bosão de Higgs aparece como uma manifestação deste mecanismo.

Durante as últimas décadas, as experiências nos colisionadores LEP e Tevatrão realizaram medidas de alta-precisão que, uma e outra vez, provaram a validade do Modelo Padrão. Contudo, o bosão de Higgs conseguiu sempre escapar à detecção, apesar de ser uma peça central da teoria. As experiências do Grande Colisionador de Hadrões (*Large Hadron Collider* ou LHC) no CERN estão presentemente a testar o Modelo Padrão. Desde 2010 que este poderoso instrumento científico colide feixes de protões em condições de energia e luminosidade sem precedente. Um dos grandes objectivos do LHC é perceber a origem da massa das partículas, desvendando qual o mecanismo de quebra de simetria electro-fraca. Este objectivo foi atingido no dia 4 de Julho de 2012, quando as experiências ATLAS e CMS anunciaram a descoberta do bosão de Higgs.

ATLAS é uma das experiências de carácter geral para o LHC. Com um detector de partículas que tem metade do tamanho da Catedral Notre Dame em Paris, e uma colaboração de mais de 3000 cientistas, ATLAS é uma das mais complexas experiências

científicas do Mundo. Durante o Run-I do LHC, que se iniciou a 30 de Março de 2010, e terminou a 17 de Dezembro de 2012, ATLAS recolheu mais de 26 fb^{-1} de dados de colisões protão-protão, a energias de centro-de-massa de 7 e 8 TeV. O trabalho descrito nesta tese foi realizado no seio da colaboração ATLAS. Iniciou-se com estudos de desempenho do trigger de jactos, e progrediu para o tema principal: procura, observação e medições do bosão de Higgs no canal de decaimento $H \to WW^* \to \ell\nu\ell\nu$.

Os jactos hadrónicos são o resultado do processo de hadronização de quarks e gluões, e os objectos produzidos com maior frequência nas colisões do LHC. O trigger de jactos selecciona, em tempo real e com alta eficiência, eventos potencialmente interessantes que contenham jactos, de forma a controlar a esmagadora taxa de produção. Os eventos rejeitados pelo trigger são definitivamente eliminados. Por outro lado, eventos aceites pelo trigger de jactos podem ser usados numa grande variedade de análises de física, como medidas de QCD ou pesquisas do bosão de Higgs ou de Super-simetria. Além disso, o trigger de jactos ainda fornece uma amostra imparcial de eventos com jactos, usada para determinar a incerteza da escala de energia dos jactos, que com grande frequência representa uma fracção da incerteza sistemática dominante em muitas análises, como é o caso da análise $H \to WW^* \to \ell\nu\ell\nu$. Assim, é extremamente importante assegurar o alto desempenho do trigger de jactos. Os primeiros dados do LHC recolhidos por ATLAS foram usados para validar, estudar e melhorar o desempenho deste sistema.

Numa primeira fase dos estudos foram usados dados de colisões protão-protão a uma energia de centro-de-massa de 7 TeV, recolhidos nos primeiros meses de 2010, com o objectivo de examinar, de forma maioritariamente qualitativa, o comportamento do segundo nível (*level-2* ou L2) do trigger de jactos. Em geral os resultados mostraram um desempenho excelente: a reconstrução das características cinemáticas - η, ϕ e E_{T} dos jactos no L2 era muito semelhante ao resultado da reconstrução *offline*; as curvas de eficiência do L2 em função da energia transversa medida *offline* eram bastante verticais, mostrando uma selecção eficiente de jactos por parte do L2; e em geral a simulação descrevia bem as diferentes distribuições. Como consequência destes estudos, o L2 foi declarado como validado, e aceite pela colaboração ATLAS para rejeitar eventos em tempo real.

Em seguida, usaram-se dados colectados a $\sqrt{s} = 7$ TeV em 2010 para estudar diferentes tipos de calibração hadrónica, com o objectivo de calibrar os jactos do L2 do trigger. Os resultados mostraram que, calibrando os jactos do L2 com a mesma calibração usada para os jactos reconstruídos *offline*, era possível uniformizar a razão entre o momento transverso do jacto reconstruído no L2 e reconstruído *offline* (resposta em p_{T}). Esta razão mostrou variações inferiores a $\sim 1-2\%$ em função de p_{T} e η. Para além disso, a calibração de jactos *offline* aplicada no L2 melhorava a eficiência de selecção de jactos no L2, em comparação com a eficiência avaliada à escala electromagnética usada na altura pelo trigger de jactos. Como tal, durante a aquisição de dados em 2012, o L2 do trigger de jactos aplicou a calibração *offline*.

Por fim, a eficiência global do trigger de jactos de ATLAS foi avaliada com dados de colisões protão-protão a $\sqrt{s} = 7$ TeV, recolhidos em 2011. Os resultados mostraram um bom desempenho do trigger de jactos, e que este sistema fazia uma selecção eficaz

dos eventos num largo intervalo de energias transversas dos jactos. Para além disso, a supressão de ruído devido ao empilhamento de eventos permitiu melhorar a eficiência da selecção do trigger. As curvas de eficência de selecção do trigger em função do momento transverso dos jactos reconstruídos *offline* mostraram uma subida mais abrupta após a supressão de ruído. Consequentemente, o ponto de 99% de eficiência, i.e. o valor de p_{T} a partir do qual mais de 99% dos jactos *offline* são aceites pelo trigger, melhorou em cerca de 5 GeV.

O canal $H \to WW^* \to \ell\nu\ell\nu$ é um dos mais sensíveis no LHC. Neste canal identifica-se o bosão de Higgs pelo seu decaimento em dois bosões W, que por sua vez decaem leptonicamente, para um electrão ou muão e o neutrino correspondente. Este canal goza de uma elevada razão de bifurcação de $H \to WW^*$, bem como de uma assinatura experimental relativamente limpa, com dois leptões isolados de cargas opostas e energia transverse em falta (*missing transverse energy* ou $E_{\mathrm{T}}^{\mathrm{miss}}$).

Vários processos constituem fundos para a análise $H \to WW^* \to \ell\nu\ell\nu$, dado que mimetizam a assinatura experimental dos eventos de sinal. Em particular, eventos de WW e outros eventos de di-bosões, processos com quarks top, eventos com multi-jactos, produção de um bosão W em associação com jactos, e processos de Drell-Yan ($q\bar{q} \to Z/\gamma^* \to \ell^+\ell^-$). Neste canal de decaímento não é possível fazer a reconstrução completa da massa do bosão de Higgs, devido à presença dos dois neutrinos no estado final. A massa transversa dos eventos, usada para distinguir o sinal do fundo, está directamente relacionada com massa do bosão de Higgs, mas o sistema apresenta pouca resolução para esta grandeza. Assim, dado que o sinal não se manifesta como um pico de eventos, é fundamental que a contaminação dos diferentes fundos seja determinada com grande exactidão e precisão.

Durante as primeiras tentativas de descoberta do bosão de Higgs, o canal $H \to WW^* \to \ell\nu\ell\nu$ foi responsável pela maior parte do poder de exclusão de ATLAS. Para além disso, este canal contribuiu para a descoberta do bosão do Higgs em 2012. Apesar de não oferecer a melhor sensibilidade à massa do bosão de Higgs, o elevado número de eventos neste canal permite que se façam medições muito precisas das taxa de produção, bem como dos acoplamentos do bosão de Higgs aos fermiões e aos bosões vectoriais. Nesta tese descrevem-se as medidas efectuadas no canal $H \to WW^* \to \ell\nu\ell\nu$, usando 25 fb^{-1} de dados de colisões protão-protão no LHC, a energias de centro de massa de 7 e 8 TeV, recolhidos pelo detector ATLAS em 2011 e 2012.

A actividade gerada no detector ATLAS resultante do empilhamento de eventos causa uma diminuição do desempenho na reconstrução de diferentes objectos. A reconstrução da energia transversa em falta é particularmente afectada. Em ATLAS verificou-se uma degradação na resolução desta quantidade com o aumento do empilhamento de eventos ao longo da tomada de dados. A principal consequência foi o aumento da falsa-$E_{\mathrm{T}}^{\mathrm{miss}}$ no detector, i.e. aquela que não tem origem em partículas que não interagem com o detector. Desta forma, eventos de Drell-Yan podem ser reconstruídos em ATLAS com uma quantidade significativa de energia transversa em falta, apesar de não produzirem neutrinos no detector. Com uma secção eficaz de produção cerca de 10^4 vezes superior ao sinal, este processo constitui, assim, um fundo dominante na análise $H \to WW^* \to \ell\nu\ell\nu$,

principalmente em eventos com leptões do mesmo sabor no estado final - dois electrões ou dois muões.

A degradação da resolução da energia transversa em falta dificulta a supressão da contaminação do fundo de Drell-Yan, sem rejeição substancial de eventos de sinal. Assim, desenvolveu-se uma nova variável cinemática - f_{recoil} - que mede a actividade hadrónica de baixo momento transverso que equilibra o sistema de dois leptões. Uma selecção desta variável suprime o fundo de Drell-Yan por mais de um factor de 7, mantendo cerca de 65% de eficiência para eventos de sinal, mesmo depois de uma selecção de eventos com elevada energia transversa em falta.

Após a aplicação da selecção de eventos, o número de eventos de Drell-Yan é reduzido para aproximadamente o mesmo número de eventos de sinal. No entanto, estimar a contaminação de Drell-Yan nas regiões de sinal com exactidão é particularmente difícil. Em geral, a previsão dada pelas simulações não é fiável, já que depende da descrição do empilhamento de eventos, das caudas das distribuições de falsa-$E_{\mathrm{T}}^{\mathrm{miss}}$ e dos jactos de baixo momento transverso. Assim, o método Pacman foi desenvolvido essencialmente pela autora, com o objectivo de estimar o número de eventos de Drell-Yan com base exclusivamente em dados. Neste método utilizam-se em dados as distribuições de f_{recoil}, e assim, tanto a estimativa da contaminação de Drell-Yan, como as incertezas sistemáticas associadas, são independentes da forma como a simulação descreve estas distribuições. As incertezas sistemáticas do método Pacman foram detalhadamente avaliadas com recurso a simulação de Monte Carlo, e validadas com dados. Com este método, o número de eventos de Drell-Yan nas regiões de sinal é estimado com uma precisão superior a 50%.

Os resultados finais da análise $H \to WW^* \to \ell\nu\ell\nu$ apresentam um excesso de eventos de dados, em relação à previsão de eventos de fundo. O excesso observado tem uma significância estatística de 6.1σ, um resultado que estabelece conclusivamente e pela primeira vez a observação do bosão de Higgs neste canal de decaimento. A taxa de eventos de sinal observada é compatível com a taxa de eventos prevista (secção eficaz de produção do bosão de Higgs vezes a razão de bifurcação $H \to WW^*$) para o bosão de Higgs do Modelo Padrão com uma massa de 125.36 GeV. Por este motivo, o quociente entre as duas taxas, medido com uma precisão de aproximadamente 20%, é consistente com a unidade: $1.08^{+0.22}_{-0.20}$.

Abstract

A measurement of the Higgs boson production has been performed with the ATLAS detector at the Large Hadron Collider. Proton-proton collision data was used, corresponding to an integrated luminosity of 25 fb^{-1}, obtained at center-of-mass energies of 7 and 8 TeV, during 2011 and 2012. The $H \to WW^* \to \ell\nu\ell\nu$ decay channel was analyzed, with particular emphasis on events with two electrons or two muons in the final state. New analysis techniques were developed to deal with the overwhelming contamination from Drell-Yan background processes. An overall excess of events was observed over the predicted background, with a significance of 6.1σ, conclusively establishing the observation of the Higgs boson in the $H \to WW^* \to \ell\nu\ell\nu$ channel. The observed rate of events is compatible with the expectation for a Standard Model Higgs boson with a mass of 125.36 GeV, as shown by the ratio between the observed and expected cross section times branching ratio, measured at $1.08\ ^{+0.16}_{-0.15}$ (stat.) $^{+0.08}_{-0.07}$ (expt.) $^{+0.13}_{-0.11}$ (theo.) ± 0.03 (lumi.) $= 1.08\ ^{+0.22}_{-0.20}$.

Keywords:

Standard Model, electroweak symmetry breaking, Higgs boson, LHC, ATLAS

Acknowledgements

First, I would like to express my gratitude to Prof. Amélia Maio and to Patricia Conde Muíño. They introduced me to the world of experimental particle physics more than six years ago, and they have guided and supervised me through a Masters and a PhD. I am grateful that they allowed me to be at CERN for my entire PhD, and I am particularly thankful for the encouragement they showed in the past months. I would also like to thank LIP and all the colleagues of the Portuguese ATLAS group.

I acknowledge the support from Fundação para a Ciência e a Tecnologia, through the grant SFRH/BD/69173/2010.

I am deeply grateful to Prof. Daniel Froidevaux. He welcomed me and took me in at CERN, and I feel very fortunate to have had the chance to work with him and the members of the CAT team. I thank him for the guidance, support, experience, knowledge and availability he has always showed me. But mostly, I am very thankful that he introduced me to Michael Dührssen. I cannot express how fortunate I feel having had him as a mentor during my PhD. He is an endless source of knowledge and encouragement and I thank him for all he has taught me, for his constant patience and availability, and for his friendship.

I am very grateful for all the people I had the opportunity to meet and work with during my PhD. I thank Cibrán Santamarina Ríos, who taught me how to do physics analyses and motivated me when I was just starting. Big thanks go to the people I had the pleasure of sharing the office with while at CERN - Miguel Fiolhais, João Gentil and Susana Santos. I would like to thank Michael Begel who convened the jet trigger group, where I started doing my first work. I would also like to thank Jianming Qian, Pierre Savard, Biagio Di Micco, Tatsuya Masubuchi, Christian Schmitt and Corrinne Mills, who encouraged my work as they successfully convened the HSG3 group.

I am thankful to a long list of HSG3 friends and colleagues, with whom I have shared work or just plain HSG3 craziness, both crucial in helping me along the way. I thank Olivier Arnaez, from whom I learnt so much. Very special thanks go to João Guimarães da Costa, Hugh Skottowe and Tomo Lazovich, who I had the great pleasure of working with in the same flavor analysis. A special word is also due to Johanna Bronner, for the best collaboration one could wish for. I am very grateful to Magda Chelstowska, for her invaluable friendship. I also wish to thank Joe Kroll and Elliot Lipeles, for their encouragement. Finally, huge thanks go to Aaron Armbruster, Evelyn Schmidt, Joe Taenzer, Jonathan Long, Manuela Venturi, Richard Polifka, Stefan Gadatsch and Valerio Bortolotto.

Last but not least, I want to thank my friends and family. My friends outside the physics world, both in Portugal and Geneva, who keep me sane. My family, for believing in me and being an endless source of support. I thank Gué and Matilde, who are always with me. I thank my Mother for always enduring me. I thank my Father for always being there. And I thank Rudi, for the love and the moon. Obrigada.

Contents

List of Figures

List of Tables

Introduction

The Standard Model of particle physics provides a remarkably predictive and accurate description of three of the four known fundamental forces of the Universe, that govern the interactions between elementary particles. The structure of these interactions is successfully defined by mathematical symmetry laws. However, the underlying symmetries of the Standard Model can only describe the behavior of massless particles, which of course does not correspond to reality. In 1964, the Higgs mechanism was proposed as a solution to the mass problem. Through the Higgs mechanism, electroweak symmetry is spontaneously broken and fundamental particles acquire mass. A direct manifestation of this mechanism is the particle now known as the Higgs boson.

High-precision measurements carried out by collider experiments at LEP and the Tevatron over the past decades have, again and again, proved the validity of the Standard Model. Nonetheless, the Higgs boson kept escaping observation, despite being a key piece of this theory. The Large Hadron Collider at CERN is currently putting the Standard Model to the test. Since 2010, this powerful machine has been colliding beams of protons at unprecedented conditions of energy and luminosity. One of the major goals of the LHC was to understand the mechanism of electroweak symmetry breaking, either by finding the Higgs boson or excluding its existence. This goal was achieved on July 4^{th} 2012, when the ATLAS and CMS experiments announced the discovery of the elusive particle.

The work described in this thesis was carried out within the ATLAS collaboration. It started with performance studies of the jet trigger, and was followed by work on the main topic: Higgs boson searches, observation and measurements, in the $H \to WW^* \to \ell\nu\ell\nu$ channel.

The observation of the $H \to WW^*$ decay is a fundamental test of the Standard Model. The $H \to WW^* \to \ell\nu\ell\nu$ channel is a very sensitive experimental signature at the LHC, that profits from the high $H \to WW^*$ branching fraction, and a clean experimental signature with two isolated charged leptons. It contributed to the discovery of the Higgs boson and currently provides the best measurements of Higgs production rates in ATLAS. The two neutrinos in the final state do not allow for the reconstruction of the Higgs resonance. Therefore, this analysis is particularly challenging, and relies on precise and accurate estimation of the different sources of background. Important contributions were made by the author to the $H \to WW^* \to \ell\nu\ell\nu$ analysis in ATLAS,

particularly on the channels with two leptons of the same flavor in the final state. These include, in chronological order:

- studies of an alternative analysis approach to the $H \to WW^* \to \ell\nu\ell\nu$ channel, with the definition of control regions that allowed the extraction of both the normalization and the transverse mass shape of the main WW background;
- comprehensive evaluation of the systematic uncertainties impacting the Drell-Yan background in the $H \to WW^* \to \ell\nu\ell\nu$ analysis with data collected in 2011;
- co-responsible for the production of skimmed dataset formats for usage of the whole $H \to WW^* \to \ell\nu\ell\nu$ analysis group;
- direct contribution to the discovery of the Higgs boson;
- development of a new kinematic variable and a new data-driven method to suppress and estimate the Drell-Yan background, as well as the associated systematic uncertainties, for the $H \to WW^* \to \ell\nu\ell\nu$ analysis with data collected in 2012;
- optimization of the object definitions and event selections for the $H \to WW^* \to \ell\nu\ell\nu$ analysis with two same flavor leptons, with data collected in 2011 and 2012;
- optimization of the definition and computation of the transverse mass used to extract the Higgs signal in the $H \to WW^* \to \ell\nu\ell\nu$ analysis;
- main analyzer of $H \to WW^* \to \ell\nu\ell\nu$ in the same flavor channels;
- co-editor of the supporting internal documentation for the final LHC Run I $H \to WW^* \to \ell\nu\ell\nu$ analysis paper.

During Run-I, the LHC collided bunches of protons every 50 ns, i.e. at an event rate of 20 MHz, with hadronic jets being the most common outcome of these collisions. The ATLAS jet trigger keeps the overwhelming rate under control, by selecting potentially interesting events containing jets, which can be used in a variety of physics analyses. Events triggered on jets also have an important impact in the $H \to WW^* \to \ell\nu\ell\nu$ analysis, since they are essential to study the jet energy scale and resolution, which represent the dominant sources of experimental systematic uncertainty. Thus, it is important that the jet trigger system performs well. Significant contributions were made to validate, study and improve the performance of the jet trigger, with the first LHC data collected by ATLAS. In particular:

- validation of the level-2 jet trigger through a detailed assessment of its performance using the first data collected in 2010;
- studies of a hadronic calibration of level-2 trigger jets using data collected in 2010;
- evaluation of the performance of the jet trigger with data collected in 2011;
- co-responsible for producing jet trigger efficiency distributions, approved as public results by the ATLAS Collaboration.

The thesis is organized as follows. Chapter 1 introduces the relevant theoretical framework. It describes the mathematical formulation of the Standard Model and discusses some of the phenomenological aspects at the LHC. Chapter 2 presents the ATLAS experiment. The ATLAS detector at the LHC, and its different subsystems, are discussed first, followed by a description of the reconstruction. In Chapter 3, the work developed to assess and improve the performance of the ATLAS jet trigger, using early LHC data, is presented. Finally, in Chapter 4, measurements of the Higgs boson in the $H \to WW^* \to \ell\nu\ell\nu$ channel, using the full Run-I LHC data collected by ATLAS, are discussed.

Natural units are used throughout this document: $\hbar = c = 1$.

Chapter 1

Theory Overview

This chapter introduces the theoretical framework for this thesis. The Standard Model (SM) is a theory that describes the dynamics of the subatomic world, and its mathematical formulation is presented first. Its main components, namely the electromagnetic, weak and strong interactions, are derived using symmetry arguments, and it is shown that the same arguments motivate the existence of an elementary particle, referred to as the Higgs boson. The Higgs boson was first observed at the Large Hadron Collider (LHC), a powerful machine that is testing the SM theory. General features, related to the description of the high energy proton-proton collisions occurring at the LHC, are also discussed in this chapter. Finally, phenomenological aspects of the Higgs boson at the LHC, namely production mechanisms, decay modes, and how it was discovered, are presented here as well.

1.1 Standard Model of Particle Physics

The Standard Model (SM) of particle physics is a theory that provides a unified description of three of the four fundamental forces - strong, electromagnetic (EM) and weak - that govern the dynamics of all known elementary particles. Moreover, the theoretical predictions of the SM show a remarkable agreement with observations and high precision measurements made by different experiments over the years, making it widely accepted and one of the most successful scientific theories to date.

The following sections, which briefly describe the history, phenomenology and mathematical formalism of the SM, were written based on the reviews [1–3] and text books [4, 5] that contain thorough descriptions of this subject.

1.1.1 Historical background

Mathematically, the SM is a non-abelian gauge quantum field theory (QFT) - or a Yang-Mills theory - based on the $SU(3)_C \otimes SU(2)_L \otimes U(1)_Y$ symmetry group. This formulation of the SM was developed throughout the 20^{th} century, motivated by the theoretical work of many different people.

The initial steps to build the SM were taken by Glashow [6] in 1961, who proposed that the EM and weak forces are two aspects of a single electroweak (EW) interaction. Thus, he formulated the EW theory, a unified description of the EM and weak interactions, under the $SU(2)_L \otimes U(1)_Y$ group. In 1964, Brout, Englert [7], Higgs [8], Guralnik, Hagen and Kibble [9], following on the work of Nambu [10], Goldstone, Weinberg and Salam [11, 12], introduced the concept of spontaneous symmetry breaking (SSB) into particle physics, proposing the mechanism by which elementary particles acquire mass. Higgs [13], in particular, noted that there was a new elementary particle associated to this mechanism, that became known as the Higgs boson. Finally, in 1967, Weinberg [14] and Salam [15] incorporated SSB into Glashow's unified $SU(2)_L \otimes U(1)_Y$ model, completing the EW sector of the SM.

The remaining part of the SM, describing strong interactions, was developed in parallel. It started taking shape in 1964, when Gell-Mann [16] and Zweig [17] independently suggested the quark model, and in 1965, when Greenberg, Han and Nambu [18] introduced the quark property of color charge. The first formulation of the strong interactions as a gauge QFT, that became known as Quantum Chromodynamics (QCD), was made in 1973, by Fritzsch and Gell-Mann [19], using the $SU(3)_C$ symmetry group. Finally, in 1973 Gross, Wilczek [20] and Politzer [21], discovered the special property of QCD known as asymptotic freedom.

The final breakthrough in the SM came in 1972, when 't Hooft and Veltman [22] demonstrated that it was a renormalizable theory. This meant that detailed calculations could be made using perturbation theory and predictions could be worked out to be tested experimentally. The mathematical formalism of the SM was, thus, established by 1972. From that date onwards, an impressive list of experimental observations and precision tests gave growing credit to the theory.

After the discovery of neutral weak currents [23] at CERN in 1973, the Glashow-Weinberg-Salam model of EW interactions became widely accepted and the three shared the Physics Nobel Prize in 1979. The $W^{\pm}$ and Z bosons were first observed in 1983 by the UA1 and UA2 collaborations [24, 25] at CERN, further establishing the EW model as pillar of the SM. Rubbia and van der Meer were awarded the Physics Nobel Prize in 1984 for their decisive contribution in this discovery.

On the QCD side of the SM, experiments of scattering of electrons on protons [26, 27] performed at SLAC and MIT in the late 60's, provided evidence for quarks. As a consequence, Friedman, Kendall and Taylor were awarded the Physics Nobel Prize in 1990. Further testimony of the existence of quarks came in 1974, with the discovery of the charm-anticharm bound state known as J/ψ [28, 29]. Richter and Ting were laureated with the Physics Nobel Prize for this discovery in 1976. Evidence of gluons was found in 1979, with the observation of three-jet events at PETRA [30].

In 1976, the discovery of the τ lepton [31] - a third generation lepton - prompted searches for third generation quarks. The bottom and antibottom [32] quarks were discovered in 1977 and in 1995 the top quark was finally observed by the CDF and D$\emptyset$ Collaborations [33, 34] at Fermilab.

The LEP and Tevatron colliders, installed at CERN and Fermilab respectively, performed extensive tests of the SM, that remained unscathed in the accessible high-energy domain. However, one piece of the SM puzzle was still missing, as the Higgs boson kept escaping observation. Only in 2012, after over 20 years of efforts, the ATLAS and CMS Collaborations at CERN announced the observation of a new particle [35, 36] that resembled the elusive Higgs boson, completing the Standard Model of particle physics. Consequently, Higgs and Englert were award the Nobel Prize in Physics in 2013.

1.1.2 Particles and forces

Similar to Mendeleev's Periodic Table of Elements, the substantial particle content of the SM exhibits some structure and can be organized accordingly. Here we refer to elementary particles, i.e. point-like and with no internal structure, each one possessing a unique set of quantum numbers to characterize it. For each particle (for example an electron, e^- or e), there also exists an antiparticle (the positron e^+ or $\bar{e}$), with the same mass and spin, but opposite electrical charge and quantum numbers.

SM particles can be first categorized into two types: fermions and bosons. Fermions are spin-1/2 particles that make up conventional matter. They include leptons, such as the electrons that orbit the nuclei of atoms; and quarks, of which protons and neutrons are made of. Bosons are integer spin particles and they are mediators of the fundamental forces.

The fermionic sector of the SM can be naturally organized into three families/generations of increasing mass, each one being composed of two elements, that form a doublet, as shown in Table 1.1. The reason why Nature chose to replicate one generation of particles into three, or if more generations exist, is unknown. All known stable matter is actually made up of only first generation fermions, in the form of u and d quarks, that constitute protons and neutrons, and electrons. Second and third generation fermions are unstable and decay into lighter particles.

For leptons, each doublet includes an electrically charged particle (ℓ) and the corresponding neutral particle - the neutrino (ν). A lepton number can be assigned to these particles, and it is 1 for leptons and -1 for antileptons. In the SM, the lepton number is conserved, both overall and within generations. This means that when particles interact, the number of leptons of the same family remains the same. It also implies, for example, that leptons can only be created in lepton/antilepton pairs of the same generation.

Quarks (q) carry fractional electric charges and the doublets in each generation are formed by a $+2/3$ e-charged up-type quark and a $-1/3$ e-charged down-type quark. The six different types of quarks that exist are commonly referred to as flavours. Quarks have a property (or quantum number) named color, that can be viewed as a charge that is conserved in the SM, just like the electric charge. In fact, each flavour of quark comes in three different colors - red (R), green (G) and blue (B) - tripling the actual number of quarks in the SM, with respect to what is shown in Table 1.1. Then there are also the antiquarks ($\bar{q}$), which carry anticolors ($\bar{\text{R}}$, $\bar{\text{G}}$, $\bar{\text{B}}$).

	Generation	Name	Symbol	Mass	Charge [e]	Spin
Leptons	1^{st}	electron-neutrino	ν_e	< 2 eV	0	1/2
		electron	e	0.511 MeV	-1	1/2
	2^{nd}	muon-neutrino	ν_μ	< 0.19 MeV	0	1/2
		muon	μ	105.658 MeV	-1	1/2
	3^{rd}	tau-neutrino	ν_τ	< 18.2 MeV	0	1/2
		tau	τ	1776.82 MeV	-1	1/2
Quarks	1^{st}	up	u	2.3 MeV	$+2/3$	1/2
		down	d	4.8 MeV	$-1/3$	1/2
	2^{nd}	charm	c	1.275 GeV	$+2/3$	1/2
		strange	s	95 MeV	$-1/3$	1/2
	3^{rd}	top	t	173.07 GeV	$+2/3$	1/2
		bottom	b	4.18 GeV	$-1/3$	1/2

TABLE 1.1: Fermions in the SM: leptons, quarks and their properties. Particle masses from Ref. [37]. Neutrinos are treated massless in the SM, which is a good approximation, even though current results indicate the masses are very small but non-zero.

It is hypothesized in the SM, and experimental results suggest this is correct, that all naturally occurring particles are color singlets and that no colorful states can be produced. This feature is known as color confinement, and is the reason why, unlike leptons, quarks have not been observed as free particles. In fact, quarks can only exist in colorless bound states - the hadrons. Two types of hadrons exist: mesons are combinations of quark and anti-quark of the same color ($q\bar{q}$); and baryons are bound states of three different colored quarks or antiquarks (qqq or $\bar{q}\bar{q}\bar{q}$). It is useful to define the baryon number, which is conserved in the SM. This quantum number is 1 for baryons and -1 for anti-baryons, and it follows naturally that quarks carry a baryon number of 1/3, while anti-quarks have a baryon number of $-1/3$.

When fermions interact, they do so by exchanging bosons, that are, therefore, referred to as force mediators (or carriers). Four fundamental forces exist in Nature, with strengths spanning several orders of magnitude. The strength of an interaction is determined by its coupling constant. The gravitational force is too weak to play a significant role in elementary particle physics and will not be considered henceforth. The strong force is responsible for binding quarks together to form nucleons. The EM force provides attraction between electrons and atomic nuclei. The weak force accounts for the nuclear β-decay. These forces are described by gauge theories, so the corresponding bosons are often called gauge bosons. The known gauge bosons in the SM are listed in Table 1.2 and will be presented next.

The photon is a massless, neutral, spin-1 boson that mediates EM interactions. Photons only couple to electrically-charged particles. Thus, quarks and charged leptons can interact electromagnetically, but the neutrinos cannot. Because its carrier has no mass, the EM interaction has infinite range and a $1/r^2$ behaviour with distance.

Gluons are also massless, neutral, spin-1 bosons and they carry the strong force. They couple to the color charge and, therefore, mediate the interactions between quarks, but

Name	**Symbol**	**Mass [GeV]**	**Charge [e]**	**Spin**	**Force**	**Relative strength**
gluons (8)	g	0	0	1	strong	1
photon	γ	0	0	1	EM	10^{-2}
W bosons	$W^{\pm}$	80.395	± 1	1	weak	10^{-13}
Z boson	Z^0	91.1876	0	1		

TABLE 1.2: Gauge bosons and fundamental forces in the SM. Particle masses from Ref. [37].

not leptons. Gluons themselves have color and can, unlike photons, interact directly with each other, which has consequences on the long distance behavior of the strong interaction (as discussed in Section 1.1.5). Gluons are bicolored, carrying one unit of color and one unit of a different anticolor. A total of eight gluons exists with different colors.

All fermions carry a "weak charge" and can, therefore, experience weak interactions. Three massive, spin-1 gauge bosons mediate the weak interactions. Charged-current weak interactions are mediated by the $W^{\pm}$ bosons, and are involved in transitions between up-type and down-type quarks, or charged leptons and the corresponding neutrinos. The detailed analysis of the energy and angular distributions of β-decays, such as $\mu^- \rightarrow e^- \bar{\nu}_e \nu_\mu$ or $n \rightarrow p e^- \bar{\nu}_e$, have made clear that only left-handed (right-handed) fermion (antifermion) helicities[1] participate in charged-current interactions, which, therefore, violate parity. Neutral-current weak interactions are mediated by the Z^0 and conserve flavour. Similar to the gluons in the strong interaction, the W and Z bosons also couple to each other. Finally, since the W bosons hold electric charge, they can also couple to the photon and interact via the EM force. The range of the weak interaction is related to the masses of the heavy weak bosons and shows, thus, a sharp cutoff at distances larger than 10^{-18} m.

The description of the particle content of the SM would not be complete without mentioning the Higgs boson. Although it does not mediate any of the fundamental interactions, it is an essential piece of the SM. With a mass of approximately 125 GeV (see Section 1.2.3.4 ahead), no intrinsic spin and no charge, the Higgs boson causes SSB, delivering mass to other elementary particles. Thus, the Higgs boson couples to all particles with mass, including itself.

1.1.3 Symmetries

In a QFT, such as the SM, particles are described as excitations of a local field $\phi(x)$. The properties and interactions of the field are encoded in a Lagrangian density (or simply Lagrangian), usually a function of the field and its first-order space-time derivatives:

$$\mathcal{L}(x) = \mathcal{L}(\phi, \partial_\mu \phi). \tag{1.1}$$

[1] For right-handed particles, the direction of its spin and its motion are the same; for left-handed particles they are opposite.

The action is defined as the integral of the Lagrangian over space-time. The equations of motion can be derived by invoking the principle of least action:

$$\delta S = \delta \int \mathrm{d}^4 x \mathcal{L}(\phi, \partial_\mu \phi) = 0, \tag{1.2}$$

which produces the Euler-Lagrange equation:

$$\partial_\mu \left(\frac{\partial \mathcal{L}}{\partial(\partial_\mu \phi)} \right) - \frac{\partial \mathcal{L}}{\partial \phi} = 0. \tag{1.3}$$

Symmetries play a fundamental role in the SM. A symmetry is a group of transformations one can perform on the fields, that leave the Lagrangian invariant. We differentiate between global symmetries, that allow one to change a field in the same way all over space-time; and local symmetries, where the field can be changed differently in each space-time point.

The power of using of symmetries can be understood from Noether's theorem, which states that for every continuous transformation of a field $\phi(x)$ that leaves the Lagrangian invariant, there is a conserved current. In other words, symmetries in Nature yield conservations laws and, conversely, conservation laws have underlying symmetries. For example, if a system is symmetric under rotations, then the angular momentum is conserved.

Let us assume $\delta\phi(x)$ is transformation of $\phi(x)$:

$$\phi(x) \to \phi(x) + \delta\phi(x) \tag{1.4}$$

Invariance requires the Lagrangian to remain unchanged under this transformation:

$$\begin{aligned} 0 &= \delta\mathcal{L} \\ &= \frac{\partial \mathcal{L}}{\partial \phi}\delta\phi + \frac{\partial \mathcal{L}}{\partial(\partial_\mu \phi)}\delta(\partial_\mu \phi) \\ &= \frac{\partial \mathcal{L}}{\partial \phi}\delta\phi - \partial_\mu\left(\frac{\partial \mathcal{L}}{\partial(\partial_\mu \phi)}\right)\delta\phi + \partial_\mu\left(\frac{\partial \mathcal{L}}{\partial(\partial_\mu \phi)}\delta\phi\right) \\ &= \left[\frac{\partial \mathcal{L}}{\partial \phi} - \partial_\mu\left(\frac{\partial \mathcal{L}}{\partial(\partial_\mu \phi)}\right)\right]\delta\phi + \partial_\mu\left(\frac{\partial \mathcal{L}}{\partial(\partial_\mu \phi)}\delta\phi\right). \end{aligned} \tag{1.5}$$

The term in square brackets is zero according to the Euler Lagrange equation (Equation 1.3), so Equation 1.5 reduces to:

$$\partial_\mu J^\mu = 0, \quad J^\mu = \frac{\partial \mathcal{L}}{\partial(\partial_\mu \phi)}\delta\phi \tag{1.6}$$

where J^μ is the conserved current according to Noether's theorem. Moreover:

$$Q = \int \mathrm{d}^3 x J^0 \tag{1.7}$$

is the corresponding conserved charge.

It will be shown next that the SM is a gauge theory that can be built using symmetry arguments. In fact, all interactions can be derived based on the principle of local gauge invariance or, in other words, on the requirement that the system remains unchanged under local gauge transformations. In particular, the SM is invariant under transformations of the $SU(3)_C \otimes SU(2)_L \otimes U(1)_Y$ symmetry group, where the indices denote the resulting conserved quantities. QCD can be determined by requiring local gauge invariance under the $SU(3)$ group and color charge (C) is conserved. The EW part of the SM is invariant under $SU(2)_L \otimes U(1)_Y$, with the weak hypercharge (Y) and the weak isospin (T) (which acts only on left-handed fields, hence the index L) being the conserved quantities.

1.1.4 Quantum electrodynamics

Let us consider the Dirac Lagrangian, which describes a free fermion of mass m:

$$\mathcal{L}_{\text{Dirac}} = \bar{\psi}(x)(i\gamma^\mu \partial_\mu - m)\psi(x), \tag{1.8}$$

where $\psi(x)$ is the spinor field representing fermions, $\bar{\psi}(x) = \psi(x)^\dagger \gamma^0$ is its adjoint, and γ^μ are the Dirac γ-matrices, which satisfy the anticommutation relation $\{\gamma^\mu, \gamma^\nu\} = \gamma^\mu\gamma^\nu + \gamma^\nu\gamma^\mu = 2g^{\mu\nu}$. Applying the Euler-Lagrange equation (Equation 1.3) to the Dirac Lagrangian yields the Dirac equation of motion for a fermion:

$$(i\gamma^\mu \partial_\mu - m)\psi(x) = 0. \tag{1.9}$$

$\mathcal{L}_{\text{Dirac}}$ is invariant under global gauge transformations of the $U(1)$ group:

$$\psi(x) \to U\psi(x) = e^{i\theta}\psi(x), \tag{1.10}$$

where θ is an arbitrary real constant (the phase of $\psi(x)$ is purely conventional). According to Noether's theorem (see Equations 1.6 and 1.7):

$$J^\mu = \bar{\psi}\gamma^\mu\psi \quad \text{and} \quad Q = \int \mathrm{d}^3x \bar{\psi}\gamma^0\psi = \int \mathrm{d}^3x \psi^\dagger\psi, \tag{1.11}$$

are the conserved electric current and electric charge.

However, if one applies a local gauge transformation, where θ is a function of x^μ:

$$\psi(x) \to U\psi(x) = e^{i\theta(x)}\psi(x), \tag{1.12}$$

the Lagrangian does not remain invariant, since the derivative of ψ adds another term:

$$\partial_\mu\psi(x) \to e^{i\theta(x)}\partial_\mu\psi(x) + ie^{i\theta(x)}\psi(x)\partial_\mu\theta(x). \tag{1.13}$$

The local gauge invariance of the Lagrangian can, nonetheless, be imposed by replacing the derivative ∂_μ by the covariant derivative D_μ, that transforms as:

$$D_\mu \psi(x) \rightarrow e^{i\theta(x)} D_\mu \psi(x). \tag{1.14}$$

For that, a gauge vector field $A_\mu(x)$ must be introduced, that when transformed cancels the offending term in Equation 1.13. The covariant derivative is, thus, defined as:

$$D_\mu \equiv \partial_\mu + iqA_\mu(x), \tag{1.15}$$

where q is an arbitrary real constant and $A_\mu(x)$ transforms as:

$$A_\mu(x) \rightarrow A_\mu(x) - \frac{1}{q}\partial_\mu \theta(x). \tag{1.16}$$

Local invariance of the Lagrangian is, thus, achieved simply by replacing ∂_μ by D_μ in Equation 1.8:

$$\begin{aligned} \mathcal{L} &= \bar{\psi}(x)(i\gamma^\mu D_\mu - m)\psi(x) \\ &= \mathcal{L}_{\text{Dirac}} - q\bar{\psi}(x)\gamma^\mu A_\mu(x)\psi(x). \end{aligned} \tag{1.17}$$

Requiring the Dirac Lagrangian to be invariant under local gauge transformations has generated a new term:

$$-q\bar{\psi}(x)\gamma^\mu A_\mu(x)\psi(x), \tag{1.18}$$

that represents the well known QED interaction between a fermion with charge q and an external electromagnetic potential $A_\mu(x)$. This interaction is illustrated in the Feynman diagram of Figure 1.1. Instead of being an external potential, $A_\mu(x)$ can be turned into a true propagating field, by considering the Proca Lagrangian:

$$\mathcal{L}_{\text{Kin}} = -\frac{1}{4}F_{\mu\nu}(x)F^{\mu\nu}(x), \tag{1.19}$$

where $F_{\mu\nu} = \partial_\mu A_\nu - \partial_\nu A_\mu$ is the usual electromagnetic field strength tensor. This Lagrangian describes a free photon field. It should be noted that $\mathcal{L}_{\text{Kin}}$ remains invariant under the transformation in Equation 1.16. However, a mass term, such as $\frac{1}{2}m^2 A^\mu A_\mu$, is prohibited, as it would violate local gauge invariance. Thus, the photon field is predicted to be massless.

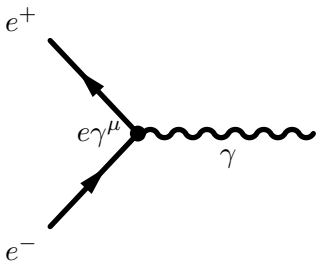

FIGURE 1.1: Feynman diagram for basic QED vertex.

In summary, imposing local gauge invariance on a free fermion Lagrangian has allowed us to generate the full QED Lagrangian:

$$\mathcal{L}_{\text{QED}} = \bar{\psi}(x)(i\gamma^\mu\partial_\mu - m)\psi(x) - q\bar{\psi}(x)\gamma^\mu A_\mu(x)\psi(x) - \frac{1}{4}F_{\mu\nu}(x)F^{\mu\nu}(x), \tag{1.20}$$

with terms describing the kinetic energy and mass of the fermion, the kinetic energy of the photon, and the interaction between the two.

1.1.5 Quantum chromodynamics

We will denote the quark field of color $\alpha = 1, 2, 3$ and flavor $f = 1, ..., 6$ by q_f^α. Quarks are triplets of color under $SU(3)_C$ and we will use the vector notation for simplification:

$$q_f = \begin{pmatrix} q_f^{\text{R}} \\ q_f^{\text{G}} \\ q_f^{\text{B}} \end{pmatrix} \quad \text{and} \quad \bar{q}_f = (\bar{q}_f^{\bar{\text{R}}}, \bar{q}_f^{\bar{\text{G}}}, \bar{q}_f^{\bar{\text{B}}}). \tag{1.21}$$

The Lagrangian for free quarks is similar to the one presented in Equation 1.8:

$$\mathcal{L} = \sum_f \bar{q}_f(i\gamma^\mu\partial_\mu - m_f)q_f. \tag{1.22}$$

The summation over the quark flavour f will be omitted henceforth, but it is implied.

The Lagrangian in Equation 1.22 is invariant under global $SU(3)$ transformations in the color space:

$$q(x) \to Uq(x) = e^{i\frac{\lambda_a}{2}\theta_a}q(x), \tag{1.23}$$

where U are 3×3 matrices, with $UU^\dagger = U^\dagger U = 1$ and $\det U = 1$. The fundamental representation of these matrices under $SU(3)$ is provided by the generators $\frac{\lambda_a}{2}$ ($a = 1, ..., 8$), known as Gell-Mann matrices. θ_a are a set of arbitrary parameters. The Gell-Mann matrices are traceless and satisfy the commutation relation $[\lambda_a, \lambda_b] = if_{abc}\lambda_c$, with f_{abc} providing the $SU(3)$ structure constants, which are real and totally antisymmetric, manifesting the non-abelian nature of this theory.

Similar to what was shown for QED, the structure of QCD can be determined from local gauge invariance, i.e. by replacing θ_a by $\theta_a(x)$ in Equation 1.23. Since now there are 8 parameters, 8 different gauge fields are needed. The gluons $G_\mu^a(x)$ are thus introduced to define the covariant derivative:

$$D_\mu \equiv \partial_\mu + ig_s\frac{\lambda_a}{2}G_\mu^a(x), \tag{1.24}$$

where g_s denotes the strong coupling constant. It should be noted that g_s is a single universal coupling, while for QED one can assign arbitrary charges to different fermions. The gluon fields transform under $SU(3)$ as (only considering an infinitesimal transformation):

$$G_\mu^a \to G_\mu^a - \frac{1}{g_s}\partial_\mu\theta_a - f_{abc}\theta_b G_\mu^c, \tag{1.25}$$

which is more complicated than the transformation introduced for the photon in Equation 1.16, as the non-commutativity of $SU(3)$ gives rise to an additional term involving the gluons themselves.

Replacing the partial derivative by the covariant derivative in Equation 1.22, as well as introducing a gauge-invariant kinetic term for the gluons, based on the gluon tensor field:

$$G^a_{\mu\nu} = \partial_\mu G^a_\nu - \partial_\nu G^a_\mu - g_s f_{abc} G^b_\mu G^c_\mu, \tag{1.26}$$

yields the final Lagrangian for QCD:

$$\mathcal{L}_{\text{QCD}} = \sum_f \bar{q}_f (i\gamma^\mu \partial_\mu - m_f) q_f - g_s \sum_f (\bar{q}_f \gamma^\mu \frac{\lambda_a}{2} q_f) G^a_\mu - \frac{1}{4} G^a_{\mu\nu} G^{\mu\nu}_a. \tag{1.27}$$

The second term in this QCD Lagrangian represents the interaction between color currents of the quarks (shown in parenthesis) and the gluon fields G^a_μ, illustrated in the left-most Feynman diagram of Figure 1.2. Inspection of $G^a_{\mu\nu}$ in Equation 1.26 shows that the $G^a_{\mu\nu} G^{\mu\nu}_a$ is not purely kinetic as it is for photons, but includes an induced self interaction between gluons, responsible for the 3 and 4-gluon QCD vertices shown in Figure 1.2 (middle and right-hand-side). The strength of this self interaction is, again, given by the same unique coupling constant g_s, appearing in the fermionic part of the Lagrangian. Finally, it should be noted that, just as for photons, gauge invariance requires the gluons to be massless.

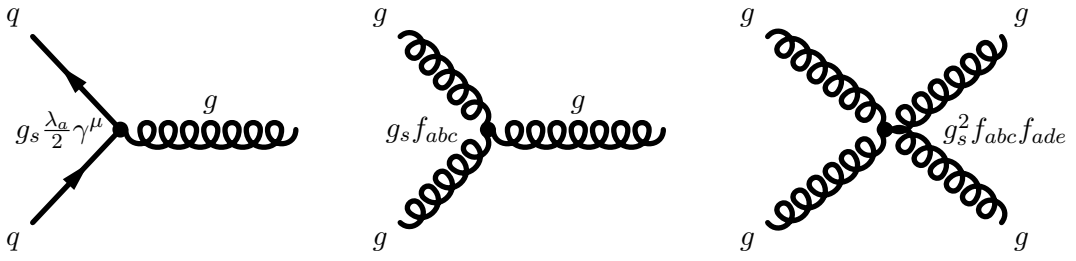

FIGURE 1.2: Feynman diagrams for basic basic QCD vertices.

As just shown, the non-Abelian structure of the $SU(3)_C$ group adds a self-interaction term to QCD, not present in QED. A consequence of this self-coupling is asymptotic freedom, a behavior that can be understood in terms of the running of the strong coupling constant. Despite the name, the SM model coupling constants show a dependence on energy (distance), referred to as running. For the EM interaction, the coupling gets stronger with higher energies, or equivalently shorter distances. However, the coupling of QCD shows the opposite behavior. Here we define the strong coupling constant $\alpha_s = g_s^2/4\pi$, which decreases with the energy scale Q of the physics process, as shown in Figure 1.3. Let us consider two quarks: if the distance between them increases, the strong coupling becomes sizable, pulling the quarks together into a confined state; on the other hand, when the quarks are close together, α_s decreases, and they essentially behave like free particles within the hadron.

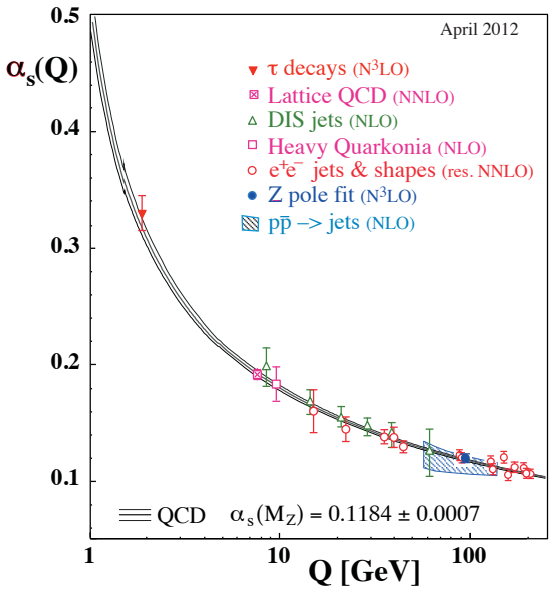

FIGURE 1.3: Running of the strong coupling α_s with the energy scale Q, from Ref. [38].

1.1.6 Weak interactions and electroweak unification

As discussed in Section 1.1.2, low energy experiments have shown that weak interactions violate parity, since only left-handed fermions and right-handed anti-fermions couple to the $W^{\pm}$ bosons. Thus, their description requires that the left- (L) and right-handed (R) components of the spinor fields be separated using projection operators $P_{L,R}$:

$$\psi_{L,R}(x) = P_{L,R}\psi(x) = \frac{1}{2}(1 \mp \gamma^5)\psi(x), \tag{1.28}$$

with $\gamma^5 = i\gamma^0\gamma^1\gamma^2\gamma^3$. To determine the Lagrangian we will consider that the left-handed fermions appear in doublets and the right-handed ones in singlets. The simplest symmetry group with doublet representation is $SU(2)$. We also aim at providing a unified description of the weak and EM interactions, as discussed in Section 1.1.1. We need, therefore, to consider the $U(1)$ group as well, presented in Section 1.1.4. We will, thus, take the $SU(2)_L \otimes U(1)_Y$ symmetry group to describe EW interactions. The L subscript denotes the left-handed fermion fields, although the weak isospin T is the conserved quantum number. The index Y represents the weak hypercharge, which must be used since the naive identification with the electric charge does not work (this will be shown ahead).

Let us start by defining the fermion fields, using only one generation of up- and down-type quarks for simplicity, with spinor fields denotes by $u(x)$ and $d(x)$, respectively:

$$\psi_1(x) = \begin{pmatrix} u_L \\ d_L \end{pmatrix}, \quad \psi_2(x) = u_R, \quad \psi_3(x) = d_R, \tag{1.29}$$

Bear in mind that the discussion remains valid for the lepton sector:

$$\psi_1(x) = \begin{pmatrix} \nu_{\ell L} \\ \ell_L \end{pmatrix}, \quad \psi_2(x) = \nu_{\ell R}, \quad \psi_3(x) = \ell_R. \tag{1.30}$$

The free Lagrangian can be written similar to the QED and QCD cases (Equations 1.8 and 1.22):

$$\begin{aligned} \mathcal{L} &= i\bar{u}(x)\gamma^\mu \partial_\mu u(x) + i\bar{d}(x)\gamma^\mu \partial_\mu d(x) \\ &= \sum_{j=1}^{3} i\bar{\psi}_j(x)\gamma^\mu \partial_\mu \psi_j(x). \end{aligned} \tag{1.31}$$

It should be noted that the mass term for the fermions was removed from the Lagrangian, as it would mix the left- and right-handed fields, spoiling the gauge invariance (this will be fixed later).

The Lagrangian in Equation 1.31 is invariant under global gauge transformations of the $SU(2)_L \otimes U(1)_Y$ symmetry group. $U(1)$ transformations consist of simple phase factors, as already shown in Equation 1.10:

$$\psi(x) \to e^{i\frac{Y}{2}\beta}\psi(x), \tag{1.32}$$

where β denotes an arbitrary parameter and Y is the weak hypercharge. As for $SU(2)$ transformations, they act only on the left-handed doublets and are of the type:

$$U_L = e^{i\frac{\sigma_a}{2}\alpha_a}. \tag{1.33}$$

U_L are 2×2 unitary matrices, with $\det U = 1$. The fundamental representation of these matrices are provided by $\frac{\sigma_a}{2}$, with $a = 1, 2, 3$, which are the generators of $SU(2)$ known as Pauli matrices. α_a are arbitrary parameters. The Pauli matrices are traceless and satisfy $[\sigma_a, \sigma_b] = 2i\epsilon_{abc}\sigma_c$, where ϵ_{abc} is a totally antisymmetric tensor (Levi-Civita symbol), that gives the structure constants of $SU(2)$. Thus, the fermion fields transform as:

$$\begin{aligned} \psi_1(x) &\to e^{i\frac{\sigma_a}{2}\alpha_a + i\frac{Y}{2}\beta}\psi_1(x) \\ \psi_2(x) &\to e^{iY\beta}\psi_2(x) \\ \psi_3(x) &\to e^{iY\beta}\psi_3(x). \end{aligned} \tag{1.34}$$

Further requiring that the invariance of the Lagrangian holds locally, i.e. when $\alpha_a = \alpha_a(x)$ and $\beta = \beta(x)$, requires the usual introduction of the covariant derivative and of four gauge fields (since four parameters exist). The gauge field $B_\mu(x)$ is associated to $U(1)_Y$ and transforms similar to the photon, as shown in Equation 1.16. The three gauge fields $W^a_\mu(x)$ transform similar to the gluon fields in Equation 1.25. The covariant derivative is, thus, defined as:

$$D_\mu \equiv \partial_\mu + ig'\frac{Y}{2}B_\mu(x) + ig\frac{\sigma_a}{2}W^a_\mu(x), \tag{1.35}$$

where g' and g are the coupling constants of $U(1)_Y$ and $SU(2)_L$ respectively. It should be noted that the couplings to B_μ are completely free as in QED, and the hypercharge

can be an arbitrary parameter. This freedom does not exist for $SU(2)$ though, and the coupling g is unique due to the non-abelian nature of this group.

To finalize the Lagrangian, we introduce the strength tensors:

$$B_{\mu\nu} = \partial_\mu B_\nu - \partial_\nu B_\mu \quad \text{and} \quad W^a_{\mu\nu} = \partial_\mu W^a_\nu - \partial_\nu W^a_\mu - g\epsilon_{abc} W^b_\mu W^c_\mu, \tag{1.36}$$

that allow the definition of the usual kinetic terms for the gauge fields. It is important to mention that these kinetic terms are not purely kinetic, due to the non-Abelian structure of the $SU(2)$ group. Similar to what was seen for QCD, they generate the cubic and quartic self-interactions among the gauge bosons, shown in the Feynman diagrams of Figure 1.4. The final Lagrangian for the EW interactions becomes:

$$\mathcal{L}_{\text{EW}} = \sum_{j=1}^{3} i\bar{\psi}_j(x)\gamma^\mu D_\mu \psi_j(x) - \frac{1}{4}B_{\mu\nu}B_{\mu\nu} - \frac{1}{4}W^a_{\mu\nu}W^{\mu\nu}_a. \tag{1.37}$$

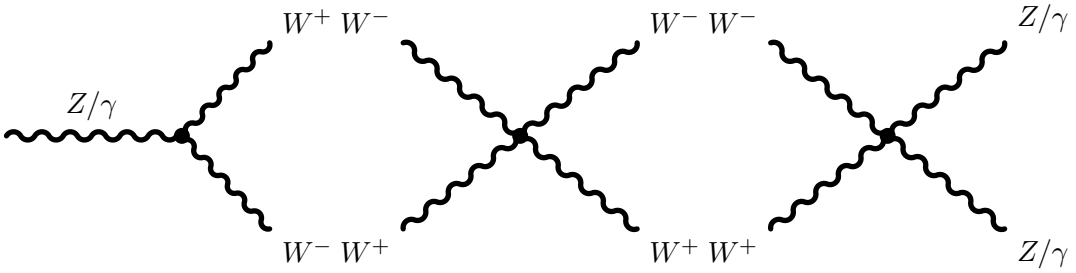

FIGURE 1.4: Feynman diagrams for cubic and quartic gauge bosons self-interactions.

Expanding the covariant derivative in the Lagrangian in Equation 1.37, one obtains terms for the interactions between the fermions and the gauge bosons:

$$\mathcal{L}_{\text{int}} = -g\bar{\psi}_1\gamma_\mu\frac{\sigma_a}{2}W^a_\mu\psi_1 - g'B_\mu\sum_{j=1}^{3}\frac{Y}{2}\bar{\psi}_j\gamma^\mu\psi_j. \tag{1.38}$$

The first term in Equation 1.38 contains the charged-current interactions. Let us define:

$$W_\mu = \frac{W^1_\mu + iW^2_\mu}{\sqrt{2}} \quad \text{and} \quad W^\dagger_\mu = \frac{W^1_\mu - iW^2_\mu}{\sqrt{2}}. \tag{1.39}$$

$W^\dagger_\mu$ and W_μ can, in fact, be directly identified with the $W^\pm$ gauge bosons[2]. Taking into account Equation 1.28, one can write the charged-current interactions between the W bosons and the fermions as:

$$\mathcal{L}_{\text{CC}} = -\frac{g}{2\sqrt{2}}W^\dagger_\mu\sum_f\left(\bar{u}_f\gamma^\mu(1-\gamma^5)d_f + \bar{\nu}_{\ell f}\gamma^\mu(1-\gamma^5)\ell_f\right) + \text{h.c.}, \tag{1.40}$$

where the index f runs over the number of families, u and d are the spinor fields for up- and down-type quarks, the spinor fields for the charged leptons and the corresponding

[2] W_μ annihilates a W^+, or creates a W^-; $W^\dagger_\mu$ annihilates a W^-, or creates a W^+

neutrinos - ℓ and ν_ℓ - have also been added, and "h.c." denotes the hermitian conjugate. These interaction vertices are shown in the Feynman diagrams of Figure 1.5. The $\bar{\psi}\gamma^\mu(1-\gamma^5)\psi$ structure of these charged weak currents, usually referred to as V-A (vector minus axial), is different from the $\bar{\psi}\gamma^\mu\psi$ (purely vector) structure previously seen, for example, in Equation 1.18, and reveals the parity violating nature of the weak interactions.

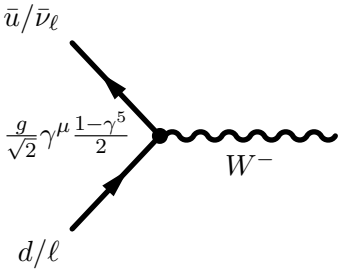

FIGURE 1.5: Feynman diagram for charged-current interaction vertex.

Going back to the interaction Lagrangian in Equation 1.38, after extracting the charged-current interactions, we are left with the $W^3_\mu(x)$ and $B_\mu(x)$ fields. These can be combined as follows:

$$\begin{pmatrix} W^3_\mu \\ B_\mu \end{pmatrix} = \begin{pmatrix} \cos\theta_{\mathrm{W}} & \sin\theta_{\mathrm{W}} \\ -\sin\theta_{\mathrm{W}} & \cos\theta_{\mathrm{W}} \end{pmatrix} \begin{pmatrix} Z_\mu \\ A_\mu \end{pmatrix}, \tag{1.41}$$

where A_μ and Z_μ are the physical photon and the Z^0 boson, respectively, and θ_{W} is the weak mixing angle. The Lagrangian for neutral-current interactions can, thus, be written as:

$$\mathcal{L}_{\mathrm{NC}} = -\sum_j \bar{\psi}_j\gamma^\mu\left[A_\mu\left(g\frac{\sigma_3}{2}\sin\theta_{\mathrm{W}} + g'\frac{Y}{2}\cos\theta_{\mathrm{W}}\right) + Z_\mu\left(g\frac{\sigma_3}{2}\cos\theta_{\mathrm{W}} - g'\frac{Y}{2}\cos\theta_{\mathrm{W}}\right)\right]\psi_j. \tag{1.42}$$

The term associated to A_μ, i.e. to the photon, should match the interaction term for QED seen in Equation 1.18. For that, the following conditions must be imposed:

$$g\sin\theta_{\mathrm{W}} = g'\cos\theta_{\mathrm{W}} = e \quad \text{and} \quad \frac{Y}{2} = Q - T_3, \tag{1.43}$$

where e denotes the elementary charge, Q is the EM charge operator and $T_3 = \frac{\sigma_3}{2}$ is the third component of the weak isospin T. A summary of these quantum numbers for the SM fermions is presented in Table 1.3. Taking the Lagrangian in Equation 1.42, the terms associated to Z_μ can be rewritten to clearly indicate the Z boson vertices in Figure 1.6:

$$\mathcal{L}^Z_{NC} = -\frac{e}{2\sin\theta_{\mathrm{W}}\cos\theta_{\mathrm{W}}}Z_\mu\sum_f \bar{f}\gamma^\mu(v_f - a_f\gamma^5)f, \tag{1.44}$$

where f denotes the fermion spinor field, the sum runs over all SM fermions, $a_f = T_3$ and $v_f = 1 - 4|Q|\sin^2\theta_{\mathrm{W}}$.

	T	T_3	Y	Q [e]
$\nu_{\ell L}$	1/2	1/2	−1	0
ℓ_L	1/2	−1/2	−1	−1
ℓ_R	0	0	−2	−1
u_L	1/2	1/2	1/3	2/3
d_L	1/2	−1/2	1/3	−1/3
u_R	0	0	4/3	2/3
d_R	0	0	−2/3	−1/3

TABLE 1.3: Weak isospin (T), hypercharge (Y) and EM charge (Q) quantum numbers for leptons and quarks. u and d denote the up- and down-type quarks; ℓ denotes the leptons and ν_ℓ the corresponding neutrinos. The subscripts L and R indicate the left- and right-handed components respectively. Right-handed neutrinos (sterile) are omitted as they have all quantum numbers equal to zero.

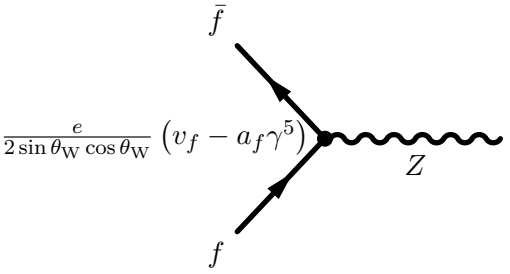

FIGURE 1.6: Feynman diagram for neutral-current interaction vertex (Z boson only).

On a side-note, it follows from Equation 1.43 that:

$$\cos\theta_W = \frac{g}{\sqrt{g^2+g'^2}} \quad \text{and} \quad \sin\theta_W = \frac{g'}{\sqrt{g^2+g'^2}}. \tag{1.45}$$

These relations and Equation 1.41 can be used to express Z_μ as:

$$Z_\mu = \cos\theta_W W_\mu^3 - \sin\theta_W B_\mu = \frac{g' W_\mu^3 - g B_\mu}{\sqrt{g^2+g'^2}}, \tag{1.46}$$

and A_μ as:

$$A_\mu = \sin\theta_W W_\mu^3 + \cos\theta_W B_\mu = \frac{g' W_\mu^3 + g B_\mu}{\sqrt{g^2+g'^2}}, \tag{1.47}$$

a notation which will be useful ahead.

To summarize, the requirement of local gauge invariance has, once again, allowed the construction of a Lagrangian that describes the EM and weak interactions in a unified manner, correctly reproducing the physical interactions between the fermions and the photon, W and Z bosons. However, the same gauge invariance forbids any mass terms for the gauge bosons or the fermions. Although this represents no problem for the photon, experiments have shown that the W and Z bosons, as well as the fermions, are massive (see Table 1.2).

1.1.7 Spontaneous symmetry breaking

The previous sections have introduced a fully symmetric Lagrangian, based on local gauge invariance, that describes the strong and EW interactions of the SM. Gauge symmetry is essential, as it guarantees that the theory is renormalizable and that perturbation theory can be used to make predictions. However, it also prevents the addition of mass terms to the W and Z bosons. In order to generate the masses the gauge symmetry must be broken in some way, while still keeping the Lagrangian symmetric. This can be achieved through spontaneous symmetry breaking (SSB).

Let us consider a complex scalar field $\phi(x)$ with a Lagrangian:

$$\mathcal{L} = \partial_\mu \phi^* \partial^\mu \phi - V(\phi), \tag{1.48}$$

where:

$$V(\phi) = \mu^2 \phi^* \phi + \lambda (\phi^* \phi)^2, \tag{1.49}$$

which is invariant under global phase transformations, such as the ones in Equation 1.10. For the potential to have a ground state it must be bounded from below, which means $\lambda > 0$. If the mass term μ^2 is positive, the potential $V(\phi)$ has a minimum at $\langle 0|\phi|0\rangle = \phi_0 = 0$ In this case, Equation 1.48 is simply the Lagrangian of a spin-zero particle, of mass μ and quartic coupling λ. On the other hand, if $\mu^2 < 0$, the potential has a minimum for:

$$\langle 0|\phi|0\rangle = |\phi_0| = \sqrt{\frac{-\mu^2}{2\lambda}} = \frac{v}{\sqrt{2}}, \tag{1.50}$$

as shown in Figure 1.7. The quantity v ($v^2 = -\mu^2/\lambda$) is called the vacuum expectation value (vev). Due to the $U(1)$ phase invariance of the Lagrangian, there is, in fact, an infinite number of degenerate states of minimum energy, lying around a circle of radius $v/\sqrt{2}$:

$$\phi_0 = \frac{v}{\sqrt{2}} e^{i\theta}. \tag{1.51}$$

The choice of a particular solution, $\theta = 0$ for example, as the ground state, causes the symmetry to get spontaneously broken.

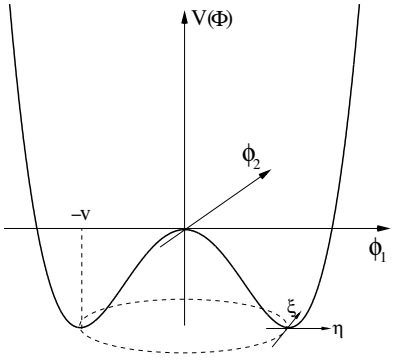

FIGURE 1.7: Potential V of a scalar field ϕ with $\mu^2 < 0$ and $\lambda > 0$, as described in Equation 1.49.

As discussed in Section 1.1.3, particles are excitations of the fields. Thus, to understand the particle content of the Lagrangian in Equation 1.48 with $\mu^2 < 0$, one must parametrize $\phi(x)$ in terms of excitations (perturbations) of the ground state v:

$$\phi(x) = \frac{1}{\sqrt{2}}[v + \eta(x) + i\xi(x)], \tag{1.52}$$

$\eta(x)$ and $\xi(x)$ being real fields. The potential now takes the form:

$$V = -\frac{\mu^2}{2}\eta^2 - \frac{\lambda}{2}\left[(v+\eta)^2 + \xi^2\right]^2 - \mu^2 v\eta - \frac{\mu^2}{2}\xi^2 - \frac{1}{2}\mu^2 v^2, \tag{1.53}$$

which describes a massive state η, with mass $m_\eta^2 = -\mu^2$, and a massless state ξ. ξ is massless because it corresponds to excitations around the flat direction of the potential, i.e. the changes in phase that do not cause the potential energy to change. The appearance of massless excitations associated with a SSB mechanism is a general result, known as Goldstone theorem. The total number of such massless particles, referred to as Nambu-Goldstone bosons, corresponds to the number of field excitations in which the potential is flat.

Let us now consider a local gauge transformation of $\phi(x)$. As shown in Section 1.1.4, this requires ∂_μ to be replaced by D_μ, with the introduction of the gauge field A_μ and tensor field $F_{\mu\nu}$. The Lagrangian in Equation 1.48 becomes:

$$\mathcal{L} = (\partial_\mu - iqA_\mu)\phi^*(\partial_\mu + iqA_\mu)\phi - V(\phi) - \frac{1}{4}F_{\mu\nu}F^{\mu\nu}. \tag{1.54}$$

For $\mu^2 > 0$, this is basically the QED Lagrangian from Equation 1.20, but for a charged scalar particle of mass μ (apart from the quartic self-coupling term mentioned above). For $\mu^2 < 0$, the parametrization of $\phi(x)$ as a perturbation around the ground state, shown in Equation 1.52, leads to the following Lagrangian:

$$\mathcal{L} = \frac{1}{2}\partial_\mu\eta\partial^\mu\eta + \frac{1}{2}\partial_\mu\xi\partial^\mu\xi - \frac{1}{2}\mu^2\eta^2 + \frac{1}{2}q^2v^2A_\mu A^\mu - qvA_\mu\partial^\mu\xi - \frac{1}{4}F_{\mu\nu}F^{\mu\nu} \\ +\text{interaction terms.} \tag{1.55}$$

Again, we find a description of a massive scalar particle η and a massless Nambu-Goldstone boson ξ, in the first three terms of the Lagrangian. But more important is the appearance of a fourth term proportional to $A_\mu A^\mu$, corresponding to a mass for the gauge field proportional to the vev: $m_A = qv$.

The Lagrangian in Equation 1.55, and the new mass term for $A_\mu A^\mu$, seems to have introduced an additional degree of freedom in the theory. Therefore, there must be a field which is not physical. Indeed, the bilinear term $qvA_\mu\partial^\mu\xi$ represents a vertex with one A_μ line and one $\partial^\mu\xi$ line, and must be eliminated if one is to obtain the correct particle content of the theory. The gauge freedom can be used to transform A_μ as:

$$A_\mu(x) \to A_\mu(x) - \frac{1}{qv}\partial_\mu\xi(x), \tag{1.56}$$

and to make a local phase transformation on $\phi(x)$:

$$\phi(x) = \frac{1}{\sqrt{2}}[v + \eta(x) + i\xi(x)] \simeq \frac{1}{\sqrt{2}}[v + \eta(x)]e^{i\frac{\xi(x)}{v}} \rightarrow \frac{v + \eta(x)}{\sqrt{2}}. \tag{1.57}$$

The resulting Lagrangian no longer depends on ξ:

$$\mathcal{L} = \frac{1}{2}\partial_\mu\eta\partial^\mu\eta - \frac{1}{2}\mu^2\eta^2 + \frac{1}{2}q^2v^2A_\mu A^\mu - \frac{1}{4}F_{\mu\nu}F^{\mu\nu} + \text{cubic and quartic terms.} \tag{1.58}$$

This choice of gauge, for which only the physical particles are left in the Lagrangian, is called the unitarity gauge. The Nambu-Goldstone boson has been absorbed ("eaten") by the gauge field, which acquired mass. This mechanism is referred to as the Higgs mechanism. The theory now describes two massive states: the gauge boson A_μ and the scalar η, called a Higgs boson.

1.1.8 EW symmetry breaking and the Higgs boson

The previous section illustrated the Higgs mechanism of SSB, as applied to the symmetry of QED. The consequence was the appearance of a massive photon, which of course does not correspond to reality. However, it will be shown in what follows that the same Higgs mechanism can be used to break EW symmetry, while still keeping QED an exact symmetry. As a consequence, the W and Z bosons will acquire mass, and the photon will remain massless. QCD will be ignored here, since it is already correctly described by the theory presented in Section 1.1.5 (gluons are massless).

Let us, thus, consider an $SU(2)$ doublet of complex scalar fields:

$$\Phi(x) = \begin{pmatrix} \phi^+(x) \\ \phi^0(x) \end{pmatrix}. \tag{1.59}$$

The quantum numbers for these fields are shown in Table 1.4. The Lagrangian:

$$\mathcal{L}_{\text{Higgs}} = (D_\mu\Phi)^\dagger D^\mu\Phi - \mu^2\Phi^\dagger\Phi - \lambda(\Phi^\dagger\Phi)^2, \tag{1.60}$$

with D_μ defined as in Equation 1.35, describes the field $\Phi(x)$ and is invariant under $SU(2)_L \otimes U(1)_Y$ local gauge transformations, as explained in Section 1.1.6. For $\lambda > 0$ and $\mu^2 < 0$, the scalar field Φ will develop a vacuum expectation value. Because the electric charge is a conserved quantity, only the neutral scalar field ϕ^0 can acquire a vev:

$$\langle 0|\Phi|0\rangle = \frac{1}{\sqrt{2}}\begin{pmatrix} 0 \\ v \end{pmatrix} \tag{1.61}$$

Once a particular ground state is chosen, the $SU(2)_L \otimes U(1)_Y$ symmetry gets spontaneously broken into the $U(1)$ symmetry of QED. According to the Goldstone theorem, three massless states should appear in the process.

Similar to what was shown in Equation 1.57, Φ can be parametrized as a perturbation of the ground state. Four real fields are used - $H(x)$ and $\theta_a(x)$ $(a = 1, 2, 3)$ - and local

	T	T_3	Y	Q [e]
ϕ^+	1/2	1/2	1	1
ϕ^0	1/2	−1/2	1	0

TABLE 1.4: Weak isospin (T), hypercharge (Y) and EM charge (Q) quantum numbers for $SU(2)_L$ doublet of complex scalar fields $\phi(x)$.

$SU(2)$ invariance allows the elimination of the dependence on $\theta_a(x)$:

$$\begin{aligned}\Phi(x) = \begin{pmatrix} \theta_1(x) + i\theta_2(x) \\ \frac{1}{\sqrt{2}}\left[v + H(x)\right] - i\theta_3(x) \end{pmatrix} &\simeq e^{i\frac{\sigma_a}{2v}\theta_a(x)} \begin{pmatrix} 0 \\ \frac{1}{\sqrt{2}}\left[v + H(x)\right] \end{pmatrix} \\ &\to \frac{1}{\sqrt{2}} \begin{pmatrix} 0 \\ v + H(x) \end{pmatrix}.\end{aligned} \tag{1.62}$$

The fields $\theta_a(x)$ represent the massless Nambu-Goldstone bosons associated with the SSB mechanism. When choosing the unitary gauge (and taking the parametrization of Φ in Equation 1.62), these fields get "eaten up" by the gauge bosons, which acquire mass. Thus, the Lagrangian will not contain any terms associated to $\theta_a(x)$.

We note that the covariant derivative in Equation 1.35 can be written as:

$$D_\mu = \begin{pmatrix} \partial_\mu - \frac{i}{2}(gW_\mu^3 + g'B_\mu) & -\frac{ig}{2}(W_\mu^1 - iW_\mu^2) \\ -\frac{ig}{2}(W_\mu^1 + iW_\mu^2) & \partial_\mu + \frac{i}{2}(gW_\mu^3 - g'B_\mu) \end{pmatrix}, \tag{1.63}$$

and look only at the kinetic piece of the Lagrangian in Equation 1.60:

$$(D_\mu\Phi)^\dagger D^\mu\Phi = \frac{1}{2}\partial_\mu H\partial^\mu H + \frac{1}{8}g^2(v+H)^2|W_\mu^1 + iW_\mu^2|^2 + \frac{1}{8}(v+H)^2|gW_\mu^3 - g'B_\mu|^2. \tag{1.64}$$

Using the relations in Equations 1.39, 1.46 and 1.47, one is able to identify the quadratic terms related to each gauge boson, and extract the corresponding masses for the $W^\pm$ and Z^0 bosons:

$$m_W = \frac{1}{2}vg \quad \text{and} \quad m_Z = \frac{1}{2}v\sqrt{g^2 + g'^2}, \tag{1.65}$$

while the photon remains massless ($m_A = 0$). We note that the W and Z boson masses can be related to each other, using the weak mixing angle: $m_W = m_Z \cos\theta_{\mathrm{W}}$.

The final form of the Higgs Lagrangian in Equation 1.60 can be written as:

$$\mathcal{L}_{\text{Higgs}} = \frac{1}{2}\partial_\mu H\partial^\mu H + (v+H)^2\left(\frac{g^2}{4}W_\mu^\dagger W^\mu + \frac{g^2}{8\cos^2\theta_{\mathrm{W}}}Z_\mu Z^\mu\right) - \lambda v^2 H^2 - \lambda v H^3 - \frac{\lambda}{4}H^4, \tag{1.66}$$

where all fields are written as physical particles. From this Lagrangian, one can see that the generation of masses for the gauge bosons has the consequence of adding a new particle, H, to the theory - the Higgs boson. The SM Higgs boson is a spin-0 scalar, with no electric charge. It is also its own antiparticle and has a mass:

$$m_H = \sqrt{-2\mu^2} = v\sqrt{2\lambda}. \tag{1.67}$$

Note that although v can be determined by experimental measurements ($v \approx 246$ GeV), the quartic coupling λ is still a free parameter. Therefore, unlike the W and Z masses which are fixed, the Higgs mass is not predicted in the SM. Nonetheless, theoretical arguments of perturbativity, triviality and unitarity can be used to set the Higgs mass well below ~ 1 TeV. Moreover, fits to EW precision data [39] have historically favored a light Higgs, with a mass of ~ 100 GeV.

Other terms in the Lagrangian of Equation 1.66 show the Higgs boson interacts with the massive electroweak bosons, and with itself, in a very particular way. In fact the couplings (denoted g) are always proportional to the masses of the coupled bosons (denoted V):

$$g_{HVV} = \frac{2m_V^2}{v}, \quad g_{HHVV} = \frac{2m_V^2}{v^2}, \quad g_{HHH} = \frac{3m_H^2}{v}, \quad g_{HHHH} = \frac{3m_H^2}{v^2} \tag{1.68}$$

Thus, all Higgs couplings are determined by m_H, m_W, m_Z and the vacuum expectation value v. The corresponding diagrams are shown in Figure 1.8.

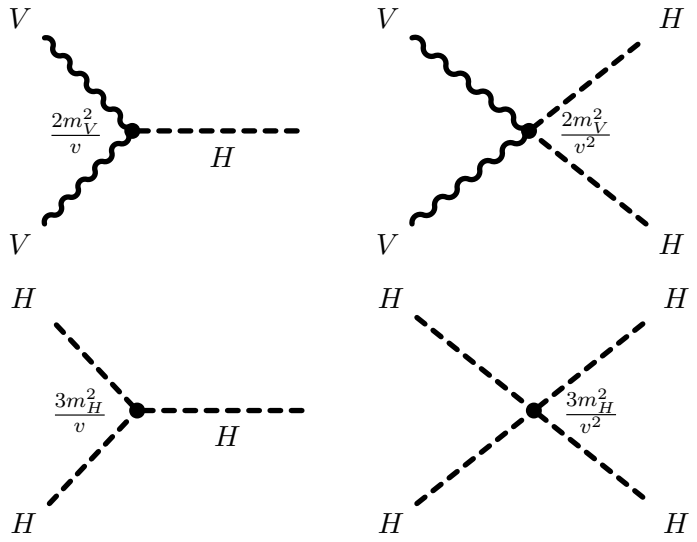

FIGURE 1.8: Feynman diagrams for Higgs interaction vertices.

Spontaneous breaking of EW symmetry has generated masses for the gauge bosons, but the fermions remain massless, as discussed in Section 1.1.6. Fortunately, these masses can be generated by including in the theory interaction terms between the fermions and the newly added scalar. These are referred to as Yukawa couplings, and an $SU(2)_L \otimes U(1)_Y$-invariant Lagrangian for these can be written as (here for the first

fermion generation only):

$$\begin{aligned}\mathcal{L}_{\text{Yukawa}} = &- c_1 \begin{pmatrix} \bar{u}_L & \bar{d}_L \end{pmatrix} \begin{pmatrix} \phi^+ \\ \phi^0 \end{pmatrix} d_R \\ &- c_2 \begin{pmatrix} \bar{u}_L & \bar{d}_L \end{pmatrix} \begin{pmatrix} \phi^{0*} \\ -\phi^- \end{pmatrix} u_R \\ &- c_3 \begin{pmatrix} \bar{\nu}_{eL} & \bar{e}_L \end{pmatrix} \begin{pmatrix} \phi^+ \\ \phi^0 \end{pmatrix} e_R + \text{h.c.}\end{aligned} \tag{1.69}$$

The second term in the Lagrangian involves the charge-conjugate Higgs doublet $\Phi_C = i\sigma_2\Phi^*$, which has quantum numbers opposite do Φ (see Table 1.4). In the unitary gauge, this Lagrangian takes a much simpler form:

$$\mathcal{L}_{\text{Yukawa}} = -\frac{1}{\sqrt{2}}(v+H)\big(c_1\bar{d}d + c_2\bar{u}u + c_3\bar{e}e\big), \tag{1.70}$$

clearly showing mass terms for the fermions:

$$m_d = c_1\frac{v}{\sqrt{2}}, \quad m_u = c_2\frac{v}{\sqrt{2}}, \quad m_e = c_3\frac{v}{\sqrt{2}}. \tag{1.71}$$

We note that since the parameters c_i are unknown, the fermion masses are not predicted by the SM. However, the Yukawa couplings, shown in the Feynman diagram of Figure 1.9, are completely fixed by the fermion masses: $g_{Hff} = m_f/v$.

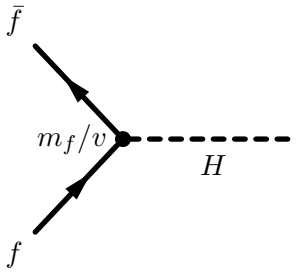

FIGURE 1.9: Feynman diagram for Yukawa couplings between the Higgs boson and the fermions.

To summarize, it is possible to generate masses for the gauge bosons $W^\pm$ and Z, as well as for the fermions, by introducing a isospin doublet of scalar fields in the SM. The $SU(2)_L \otimes U(1)Y$ gauge symmetry gets spontaneously broken (or hidden) as a consequence, and a new particle appears in the theory - the Higgs boson. The $U(1)$ gauge symmetry of QED, as well as the $SU(3)_C$ color symmetry of QCD, remain unbroken in the process. The final SM Lagrangian can be written as a sum of the different pieces in Equations 1.27, 1.37, 1.66 and 1.70 presented throughout these sections:

$$\mathcal{L}_{\text{SM}} = \mathcal{L}_{\text{QCD}} + \mathcal{L}_{\text{EW}} + \mathcal{L}_{\text{Higgs}} + \mathcal{L}_{\text{Yukawa}}. \tag{1.72}$$

1.2 Phenomenology at the LHC

The Large Hadron Collider (LHC) at CERN has been colliding particles at unprecedented conditions of energy and luminosity, putting the SM to the test, like no other scientific instrument before. The experimental features of the LHC will be discussed in Chapter 2. In this section, however, we discuss some phenomenological aspects of the LHC, namely which tools are nowadays used to describe the complicated environment at hadron colliders. We also provide some discussion on the Higgs boson, in the context of the LHC, i.e. how it is produced at the LHC, how it can be searched for experimentally, how it was eventually discovered by the experiments at the LHC, and what is the current status. We conclude by showing the current picture of the SM, by comparing the theory with experiment.

1.2.1 Proton-proton collisions

Figure 1.10 depicts a typical high-energy proton-proton (pp) collision, such as the ones occurring at the LHC at CERN. In what follows, we will provide a brief description of the different aspects involved in such an event. More detailed explanations can be found in Refs. [40–42].

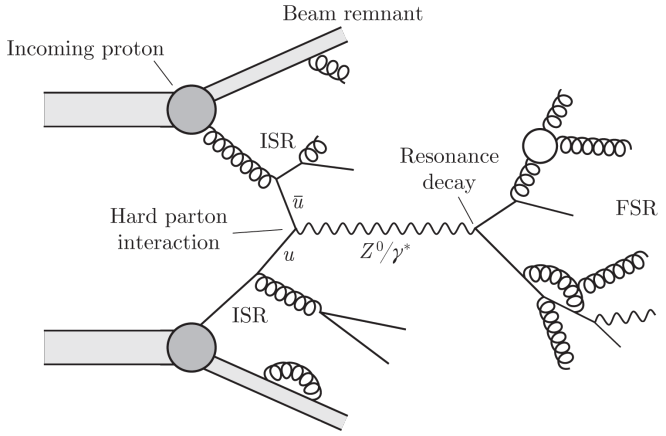

FIGURE 1.10: Schematic diagram of an event in a proton-proton collision.

1.2.1.1 General aspects

Initially, two protons are coming in on a collision course. The protons should be viewed as complex composite particles, with three valence quarks (uud), that continuously interact with each other, exchanging gluons. The gluons can, themselves, interact and generate more gluons, or spontaneously produce $q\bar{q}$ pairs that rapidly annihilate. The result is a sea of quarks and gluons within the proton itself. Any of these constituents of the proton, referred to as partons, can interact in the high energy pp collision.

A collision between two partons, one from each side, with large momentum transfer, gives the hard process of interest. In the case of the production of a heavy resonance,

such as a Higgs boson or a Z boson as shown in Figure 1.10, the decay should be viewed as part of the process, since spin correlations, for example, will be transferred from the production to the decay stages.

The remaining partons in each proton can continue to travel essentially in the original directions, forming the beam remnants, or also interact in the same pp collision. These interactions are usually soft, as they involve low momentum transfer between the partons, and constitute the underlying event (UE). Though with a much smaller probability, more than one hard parton interaction can occur in the same pp collision, and these are referred to as multi-parton interactions (MPI).

A high energy collision involves accelerated color and EM charges, that can radiate gluons and photons (Bremsstrahlung). Emissions associated with the incoming colliding partons are referred to as Initial State Radiation (ISR). Emissions made by final state particles are called Final State Radiation (FSR).

As the distance between outgoing partons increases, so does the strong interaction between them, forcing them to be confined in colorless states. At this point the process of hadronization occurs, by which a collimated bunch of hadrons - a jet - is created from the color fields between the partons. Jets will be discussed in Section 1.2.2.

One final aspect of pp collisions worth mentioning, and not depicted in Figure 1.10, is that the LHC collides bunches of protons, rather than single protons. As a result, several pp collisions can occur in a single event (bunch crossing), a phenomenon referred to as pile-up. In fact two distinct forms of pile-up can occur, but these will be discussed in Section 2.2.2.

1.2.1.2 Cross-sections

The cross-section is a measure of the probability of a specific scattering process, under some given set of initial and final conditions. Cross-sections for some relevant processes at the Tevatron and at the LHC are shown in Figure 1.11. The computation of these cross-sections uses the factorization theorem. Factorization allows for the separation of a cross-section into two parts: the hard scattering and the soft reactions. The scale Q^2 that is assumed to separate these two components is called the factorization scale - μ_{F}.

The strong coupling α_s is small for the hard scattering component of a collision (see Section 1.1.5). The hard processes can, therefore, be described using perturbative QCD (pQCD), which relies on an order-by-order expansion of the observables in α_s. The soft part of a collision, on the other hand, involves low momentum transfers and high α_s. It is, thus, essentially non-perturbative, and precise calculations cannot be done.

Let us assume a pp interaction between protons A and B. The hard scattering occurs between partons a and b, resulting in the final state X: $ab \to X$. The total proton scattering cross-section can be written as:

$$\sigma_{AB} = \int \mathrm{d}x_a \mathrm{d}x_b f_{a/A}(x_a, \mu_{\mathrm{F}}^2) f_{b/B}(x_b, \mu_{\mathrm{F}}^2) \hat{\sigma}_{ab\to X}. \tag{1.73}$$

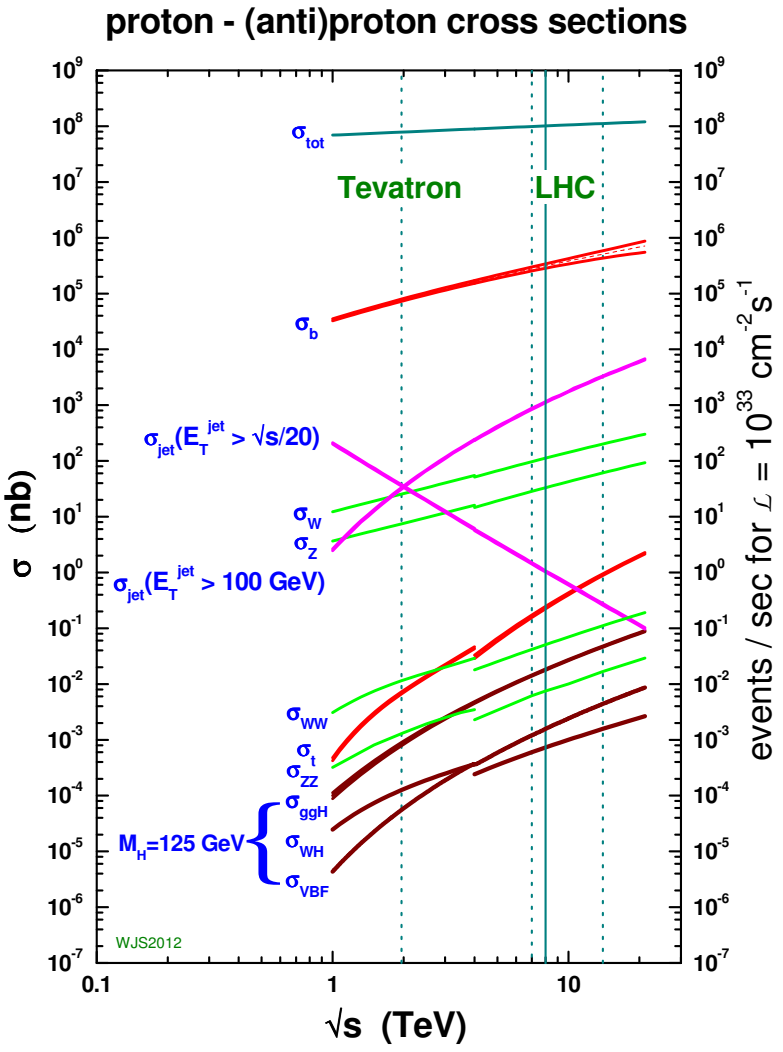

FIGURE 1.11: Cross-sections of some relevant processes, as a function of the center-of-mass energy in $p\bar{p}$ (left) and pp (right) colliders. The vertical lines indicate the center-of-mass energies used at the Tevatron and at the LHC. Taken from Ref. [43].

The terms $f_{a/A}$ and $f_{b/B}$ are parton distribution functions (PDFs), that contain the non-perturbative soft component of the collision. They essentially provide the probability that the proton A has a parton a carrying a fraction x_a of its momentum (similar for B). PDFs depend on the non-physical factorization scale μ_{F}. This dependence is provided by the DGLAP equation [44]. Usually $\mu_{\mathrm{F}} = Q$ is taken, where Q is the momentum transfer of the hard process. PDFs are universal and independent of the hard process. They are measured experimentally, for example from fits to deep inelastic scattering data.

The term $\hat{\sigma}_{ab\to X}$ in Equation 1.73 is the partonic cross-section of the hard-scattering process. In the framework of pQCD, this cross-section is written as an expansion in terms of the renormalized coupling $\alpha_s(\mu_{\mathrm{R}}^2)$:

$$\hat{\sigma}_{ab\to X} = \hat{\sigma}_0 + \alpha_s(\mu_{\mathrm{R}}^2)\hat{\sigma}_1 + \alpha_s^2(\mu_{\mathrm{R}}^2)\hat{\sigma}_2 + \dots . \tag{1.74}$$

$\hat{\sigma}_0$ is the lowest order prediction, and is obtained by calculating the matrix element (ME), or the amplitude, represented by the tree-level Feynman diagrams. The higher order contributions involve more complex Feynman diagrams (radiations of gluons, loops, boxes) and computations, and usually yield infinite results. Renormalization techniques were introduced to deal with these infinities. The renormalization scale μ_{R} is the energy scale for which these divergences are absorbed in the coupling constant.

The expansion in the strong coupling constant has introduced a dependence on yet another unphysical scale. The renormalization scale μ_{R} is the value at which α_s is computed. Again, $\mu_{\mathrm{R}} \sim Q$ is usually taken. A cross-section computed at a fixed order depends on μ_{R} and μ_{F}, and variations of these scales provide handles on the theoretical uncertainties. The dependence becomes weaker with increasing orders of calculation, and would vanish if the cross-section was computed to all order in perturbation theory. Thus, results obtained only at leading order (LO) suffer from large uncertainties and higher-order corrections (next-to-leading order, NLO, or next-to-next-to-leading order, NNLO) can be significant. It is useful to define the K-factor, as the ratio between the NLO and LO cross-sections.

1.2.1.3 Monte Carlo event generators

All the complexity of a high-energy hadron collision is described by programs referred to as Monte Carlo (MC) event generators. MC generators predict observables, such as momentum or angular distributions, that can be compared to data. They work sequentially, to implement the different steps of a collision, as described in Section 1.2.1.1, and are essential to any physics analysis.

First, a Matrix Element Monte Carlo, convoluted with the PDFs described in Section 1.2.1.2, will generate a hard-scatter (HS) $2 \to n$ (generally $n \lesssim 6$) process at a fixed-order, usually LO or NLO. In the case of the production of short-lived resonances, the decays to stable particles are also performed, taking into account the partial decay widths and any other properties, such as spin correlations.

Higher-order effects in perturbation theory are added to the HS event, using a Parton Shower (PS) MC, which simulates the multiple emission of soft radiation. PS methods are non-perturbative and, thus, less precise than the ME. Several methods exist and they are approximate, allowing for some tuning to measurements. The combination of a ME with a PS generator - matching - must be treated carefully, to avoid double counting of diagrams or any gaps in the phase-space. PS shower generators are also used to generate FSR and ISR.

The process of hadronization, by which the outgoing partons end up confined in hadrons, is non-perturbative, as already mentioned. Different phenomenological models exist, such as the Lund string model or the cluster model, and are implemented in MC generators. They are derived from experimental input and can usually be tuned to provide better predictions.

Finally, the simulation of the UE and pile-up is usually handled by overlaying extra $2 \to 2$ scatterings, occurring at a scale of a few GeV, referred to as minimum bias

events. Because these processes are, again, mostly non-perturbative, implementations in MC programs rely heavily on tuning to data.

1.2.2 Jets

As previously mentioned, quarks and gluons have not been observed isolated. Inside the hadrons they essentially behave as free particles - asymptotic freedom - but the strong force keeps them confined in those colorless states. Almost immediately after being produced, a quark or a gluon will shower and hadronize, originating a jet, i.e. a collimated spray of energetic hadrons that emerges approximately in the direction of the original parton. At the LHC, jets are among the most commonly produced objects (see Figure 1.11). Figure 1.12 shows the display of a *pp* collision event collected by ATLAS on October 5^{th} 2010, where a total of eights jets were observed. These jets can be used either as observables, that one can measure and calculate, or as tools, that one can employ to extract specific properties of a particular final state. Understanding jets is, therefore, crucial to almost any physics analysis at the LHC. In this section we summarize the challenges relating to jets, but Refs. [45, 46] provide more detailed descriptions.

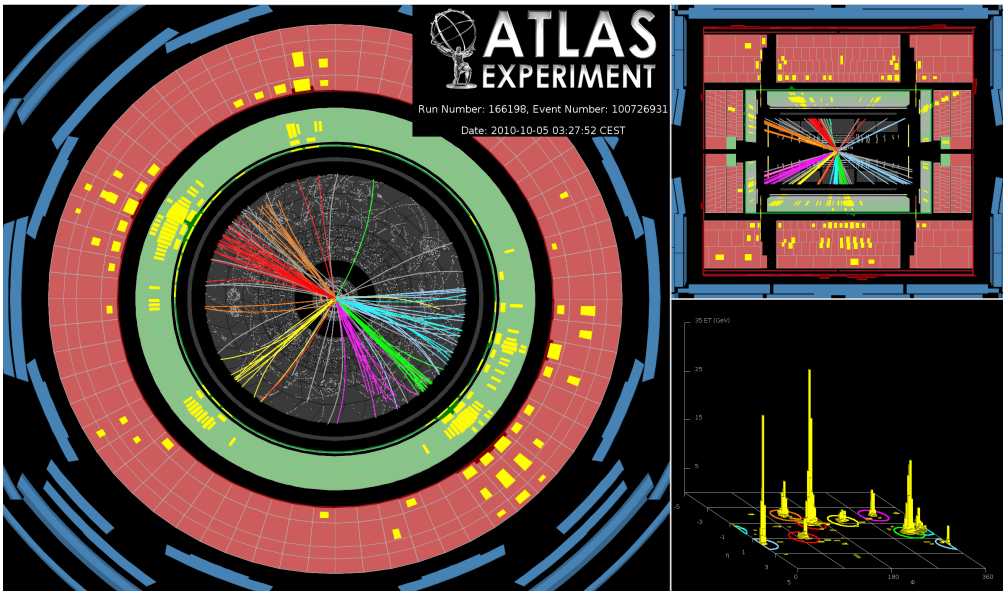

FIGURE 1.12: The highest jet multiplicity event collected in the ATLAS detector by the end of October 2010. The event has eight jets with transverse momentum above 60 GeV.

The main challenge with jets is related to the definition. The underlying physics is governed by the partons, but jets are what is observed in particle detectors. It should be, nonetheless, possible to define jets in such a way that the kinematics of the jets provide a useful measure of the kinematics of the underlying partons, so that measurements in data can be compared to theoretical predictions from Monte Carlo. This is generally achieved through a jet definition, which is basically a consistent set of rules for how to group inputs to form a jet, and assign a momentum to the resulting jet. A good jet

definition can be applied to experimental measurements, such as energy depositions in a calorimeter, to hadrons coming from the hadronization model in a Monte Carlo, to the output of PS Monte Carlo, or to partonic calculations, and the resulting jets should provide a common and stable representation of the fundamental physics process. In particular, the procedure must lead to calculable results and be resilient to - or at least it should be possible to reliably correct for - showering, hadronization, UE and even pile-up effects, as illustrated in Figure 1.13.

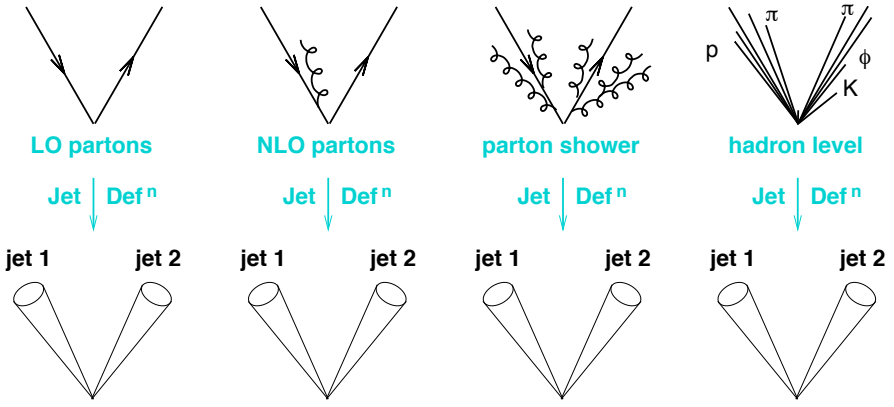

FIGURE 1.13: The application of a jet definition to different inputs should yield stable and identical results. From Ref. [40]

There are two aspects related to jet definitions. The first one is the set of rules used to group, or cluster, the inputs into jets. This is is referred to as a jet algorithm, and it usually has one or more associated parameters, that indicate how close two inputs have to be to belong to the same jet. The second aspect is how to combine the momenta of the inputs into the momentum of the jet. This is handled by the recombination scheme, the simplest and most commonly used one being the full 4-vector sum (or E-scheme).

Jet algorithms are usually classified into two broad categories. Cone algorithms have a "top-down" approach and perform a partition clustering, relying on the collinear nature of QCD showering. On the other hand, sequential recombination algorithms show a "bottom-up" approach and perform a hierarchical clustering, using a metric of distance to combine inputs starting from the closest ones. Historically, many jet algorithms have been defined and used by different experiments. In what follows, two jet algorithms used by the ATLAS experiment, and relevant to the discussion in this thesis, will be presented and compared.

The cone algorithm used in the ATLAS experiment is of the iterative cone type. R is the key parameter of the algorithm, and essentially defines the radius of the cone. It works as follows:

1. A seed input i, usually a parton, a hadron, or a calorimeter cell, for example, with a transverse momentum above some threshold, sets the initial direction;

2. The momenta of all inputs j within a cone of radius R around i are summed, using some recombination scheme. The operation is performed in the azimuthal angle ϕ

and rapidity y (or pseudorapidity η) space, i.e. taking all j constituents for which $\Delta R_{ij} = \sqrt{(y_i - y_j)^2 + (\phi_i - \phi_j)^2} < R$;

3. The direction of the resulting sum is used as a new seed, and the procedure is iterated until the direction of the cone is stable.

Once all stable cones have been found in a event, one must deal with the situation where two cones, obtained by iterating two distinct seeds, overlap and share inputs. Here, a split-merge procedure may be used, where one starts by defining an overlap threshold f. If more than fraction f of the softer cone's transverse momentum is in inputs shared with the harder cone, then the two cones are merged into one. Otherwise, the cones are split by assigning the shared inputs to the closest cone.

One of the most important attributes expected of a jet algorithm is that it is infrared and collinear (IRC) safe. This means that if one modifies the event by a collinear splitting or by adding of a soft emission, the hard jets found in the event should remain the same. IRC safety ensures that jets remain calculable in pQCD. Iterative cone algorithms, although historically used by several experiments, have been shown to be IRC unsafe, as illustrated in Figure 1.14.

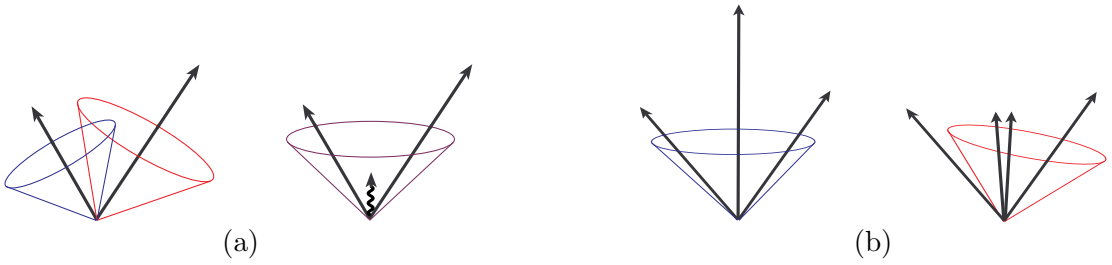

FIGURE 1.14: Illustration of (a) infrared sensitivity in the cone algorithm, where the presence of soft radiation between the two cones may cause merging; and (b) collinear sensitivity in the cone algorithm, where the result is sensitive to the energy ordering of the particles acting as seeds. Adapted from Ref. [47].

Sequential recombination algorithms, on the other hand, generally guarantee IRC safety, and are, therefore, more commonly used nowadays. They are based on a pair-wise recombination scheme, intended to undo the QCD showering. Several recombination algorithms follow this generic definition:

1. Compute the minimum distance $d_{ij} = \min(p_{\mathrm{T}i}^{2a}, p_{\mathrm{T}j}^{2a})\frac{\Delta R_{ij}^2}{R^2}$ between all inputs i and j, where p_{T} is the transverse momentum;

2. If $d_{ij} < d_{iB}, d_{jB}$, with $d_{iB} = p_{\mathrm{T}i}^{2a}$, inputs i and j are combined into a single input and the process is repeated from step 1;

3. If $d_{ij} > d_{iB}$, then i is identified as a jet and removed from the list of inputs;

4. Continue the process until all inputs are clustered or considered as jets.

Here, R is the distance parameter of the algorithm, similar to the cone radius previously defined. The distance ΔR_{ij} is, again, defined in the (y, ϕ) or (η, ϕ) space. For $a = -1, 0, 1$, one will obtain different jet algorithms: anti-k_t [48], Cambridge-Aachen (C/A) [49, 50] and the k_t [51, 52], respectively.

In the k_t algorithm, the parameter R controls the size of the jet. If a given input has no other inputs within a distance R, then it will become a jet, the obvious consequence being that arbitrarily soft particles can become jets. This was solved by the introduction of the anti-k_t algorithm, that favors clustering of hard, rather than soft, inputs. Interestingly, the anti-k_t algorithm gives the most cone-like jets, more so than cone algorithms, which is a desirable feature at the experimental level. The C/A algorithm recombines pairs of inputs solely based on the angular ordering, regardless of their momenta, until the separation is larger than the distance parameter R.

1.2.3 Higgs boson

Despite the tremendous success of the SM, the Higgs boson, that was shown in Section 1.1.8 to be fundamental for the consistency of the theory, escaped detection attempts at LEP and at the Tevatron, for over 20 years. One of the major goals at the LHC was to understand if the Higgs mechanism is truly responsible for EW symmetry breaking, by either finding the Higgs particle, or excluding its existence. In this section we discuss the phenomenology of SM Higgs boson production and decays at the LHC [3].

1.2.3.1 Production

At the LHC, the Higgs boson can be produced mainly through four different mechanisms: gluon fusion (ggF), vector boson fusion (VBF), associated production with a gauge boson, also known as Higgs-stralung (WH and ZH, jointly VH), and associated production with a top quark pair (ttH). The Feynman diagrams for these mechanisms can be seen in Figure 1.15. Figure 1.16a shows the cross-sections for each production process, as a function of the Higgs boson mass m_H (remember the mass is not predicted in the SM) and at a center-of-mass energy of $\sqrt{s} = 8$ TeV. The total SM Higgs boson production cross-section at the LHC, at $\sqrt{s} = 7, 8$ and 14 TeV, is shown in Figure 1.16b, as a function of m_H. An overview is presented in Table 1.5. State-of-the-art information on Higgs production at the LHC can be found in the reports [53–55] by the LHC Higgs Cross Section Working Group [56].

Gluon fusion production of the SM Higgs boson [57], through a heavy quark loop, dominates by far at the LHC, up to masses of 1 TeV. The main contribution to the loop arises from the top quark, due to the large Yukawa coupling. The cross-section for ggF [58] is currently known at NNLO in QCD [59–64], with soft gluon contributions resummed up to NNLL (next-to-next-to-leading logarithm[3]) [65], and also includes NLO EW corrections [66, 67]. The dynamics of the ggF mechanism are controlled by QCD,

[3]The calculation of a cross-section at fixed order (see Section 1.2.1.2) generally displays a class of divergent terms with large logarithms, that can be accounted for using resummation.

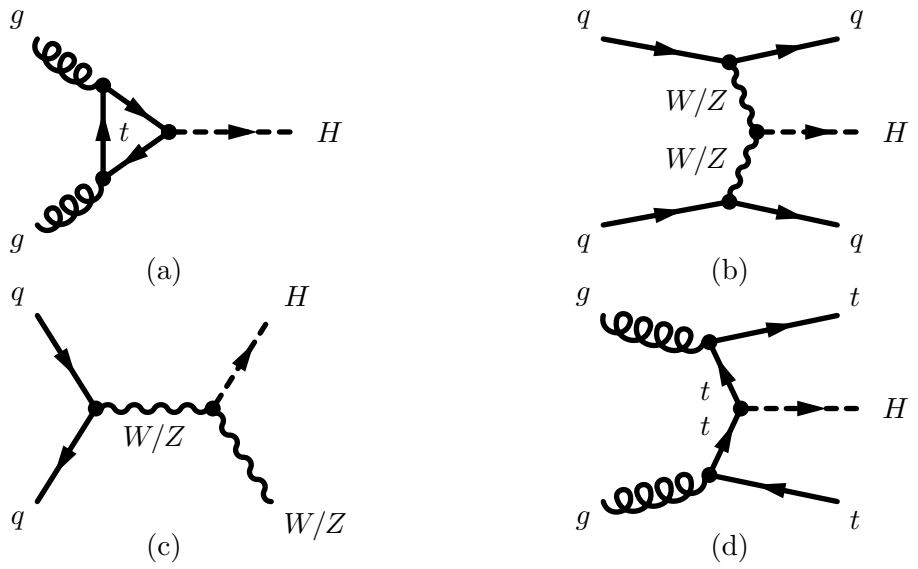

FIGURE 1.15: Feynman diagrams for the dominant SM Higgs boson production mechanisms at the LHC: (a) gluon fusion (ggF); (b) vector boson fusion (VBF); (c) associated production with a gauge boson (VH, including WH and ZH); and (d) associated production with a top quark pair (ttH).

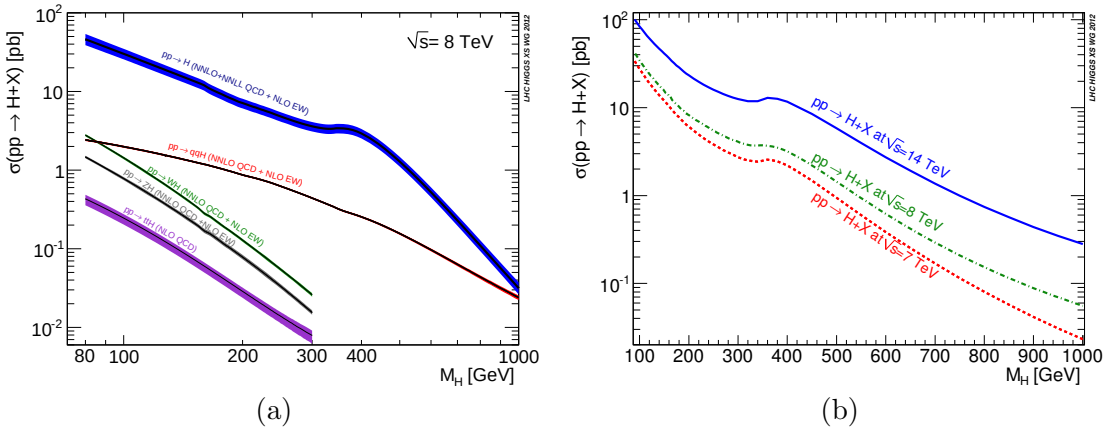

FIGURE 1.16: (a) Cross-sections for the different production mechanisms of the SM Higgs boson at the LHC, as a function of the Higgs mass and at a center-of-mass energy of $\sqrt{s} = 8$ TeV. (b) Total cross-section for SM Higgs boson production at the LHC, as a function of the Higgs mass, and at different center-of-mass energies - $\sqrt{s} = 7, 8$ and 14 TeV. Taken from Ref [56].

and understanding the effects of higher-order corrections is fundamental. NLO corrections increase the LO cross-section by about $80 - 100\%$. These were computed in the limit where the mass of the top quark is assumed to be infinite, as well as maintaining the full dependence on the masses of the top and bottom quarks, with differences of only a few percent. The NNLO corrections have been computed only in the large m_t limit, (an approximation that works better than 1%, for $m_H \lesssim 300$ GeV), increasing the cross-section by an additional 25%. Improvement of the NNLO calculation is obtained by including NNLL resummations, causing yet another increase of $7 - 9\%$ in the cross-section. Two-loop EW effects are known and their impact on the cross-section depends

Production	**Symbol**	**Mechanism**	**Cross-section [pb]**	**Theory Uncertainties [%]**	
			$\sqrt{s}$ = 8 (7) TeV, m_H = 125 GeV	QCD scale	PDFs + α_s
Gluon fusion	ggF	$gg \to H$	19.27 (15.13)	$^{+7.2}_{-7.8}$ ($^{+7.1}_{-7.8}$)	$^{+7.5}_{-6.9}$ ($^{+7.6}_{-7.1}$)
Vector boson fusion	VBF	$qq \to qqH$	1.58 (1.22)	± 0.2 (± 0.3)	$^{+2.6}_{-2.8}$ ($^{+2.5}_{-2.1}$)
Higgs-stralung	WH	$qq \to WH$	0.70 (0.58)	± 1.0 (± 0.9)	± 2.3 (± 2.6)
	ZH	$qq/gg \to ZH$	0.42 (0.34)	± 3.1 (± 2.9)	± 2.4 (± 2.7)
Associated w/ top	ttH	$gg \to t\bar{t}H$	0.13 (0.09)	$^{+3.8}_{-9.3}$ ($^{+3.2}_{-9.3}$)	± 8.1 (± 8.4)

TABLE 1.5: Overview of the dominant SM Higgs boson production mechanisms at the LHC. The cross-sections are shown at a center-of-mass energy of $\sqrt{s} = 8$ TeV, and for a Higgs boson mass of $m_H = 125$ GeV. Theoretical uncertainties on the cross-sections are also included. The numbers for $\sqrt{s} = 7$ TeV (both cross-sections and theory uncertainties) are shown in parenthesis. Taken from Ref. [56].

strongly on the Higgs mass.

The second largest contribution to the Higgs boson production comes from the vector boson fusion mechanism. VBF possesses a very distinct signature, with two hard jets produced in the forward regions, originating from the two outgoing quarks. The Higgs boson appears between the jets, in the central region of the detector. The VBF cross-section, which is an order of magnitude smaller than ggF, is currently computed at approximate NNLO in QCD [68] and full NLO in QCD and EW [69–71]. The process is purely electroweak (at leading order) and the QCD corrections have a smaller impact than for the ggF production mode. As a result, the theoretical uncertainties on VBF are also much smaller (see Table 1.5), of the order of $\sim 3\%$.

Associated production with a vector boson [72], where a W or Z boson will radiate a Higgs boson, comes next in line. These processes are only relevant for $m_H \lesssim 300$ GeV, and the cross-sections are currently computed at NNLO in QCD [73] and NLO in EW [74].

Finally, SM Higgs boson production through ttH is extremely rare, and only relevant for $m_H \lesssim 300$ GeV as well. The cross-section estimation is done at NLO QCD [75–78] and is three orders of magnitude smaller than ggF. It is, nonetheless, important to probe this production mode, as it offers direct access to the couplings of the Higgs boson to the top quark.

Theoretical uncertainties on the cross-sections, indicated in Table 1.5 or by the colored bands in Figure 1.16a, arise from the choice of PDFs, and renormalization and factorization scales (see Section 1.2.1.2). The scale uncertainties are assessed by varying μ_F and μ_R around a central value μ_0, which depends on the process: $\mu_0/2 < \mu_F, \mu_R < 2\mu_0$. As for the PDFs, the MSTW2008 NNLO PDF set [79] is used in the calculations, and the uncertainties are evaluated following the prescription detailed in Ref. [80].

1.2.3.2 Decays

The Higgs boson decay modes depend on its mass, as shown in Figure 1.17. Nonetheless, decays into the heaviest particles kinematically available will be favored, since the

couplings of the Higgs boson are directly proportional to the mass of the particles involved (see Section 1.1.8). Table 1.6 presents an overview of the branching fractions for a SM Higgs boson with $m_H = 125$ GeV. Figure 1.18 shows the Feynman diagrams of the different Higgs decays.

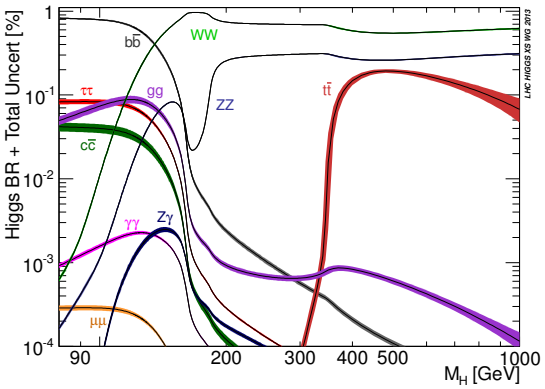

FIGURE 1.17: Branching ratios of the SM Higgs boson as a function of its mass. Taken from Ref [56].

Decay mode	**Branching fraction** $m_H = 125$ **GeV**	**Uncertainty** [%]
$H \to b\bar{b}$	5.77×10^{-1}	$^{+3.21}_{-3.27}$
$H \to WW^*$	2.15×10^{-1}	$^{+4.26}_{-4.20}$
$H \to gg$	8.57×10^{-2}	$^{+10.22}_{-9.98}$
$H \to \tau\tau$	6.32×10^{-2}	$^{+5.71}_{-5.67}$
$H \to c\bar{c}$	2.91×10^{-2}	$^{+12.17}_{-12.21}$
$H \to ZZ^*$	2.64×10^{-2}	$^{+4.28}_{-4.21}$
$H \to \gamma\gamma$	2.28×10^{-3}	$^{+4.98}_{-4.89}$
$H \to Z\gamma$	1.54×10^{-3}	$^{+9.01}_{-8.83}$
$H \to \mu\mu$	2.19×10^{-4}	$^{+6.01}_{-5.86}$
Γ_H^{total} [GeV]	4.07×10^{-3}	$^{+3.97}_{-3.93}$

TABLE 1.6: Branching ratios and total width (Γ_H^{total}) of the SM Higgs boson at $m_H = 125$ GeV. Taken from Ref [56].

At low Higgs mass, the Higgs decays to fermions (Figure 1.18a) are preferred, since a decay to two gauge bosons would require one of them to be too off-shell. Thus, for $m_H \lesssim 130$ GeV, the decay to a pair of b quarks - $H \to b\bar{b}$ - completely dominates the partial width. It is followed by the $H \to \tau\tau$, $H \to c\bar{c}$ and $H \to gg$ decays, the latter being significant as it occurs via a heavy quark loop (Figure 1.18d). We note, however, that the decay into a top quark pair - $H \to t\bar{t}$ - only becomes sizable for high masses of $m_H \gtrsim 2m_t$.

In the intermediate and high mass regions, the mass of the Higgs boson is sufficient to produce a pair of gauge bosons (Figure 1.18b). Therefore, the Higgs partial width

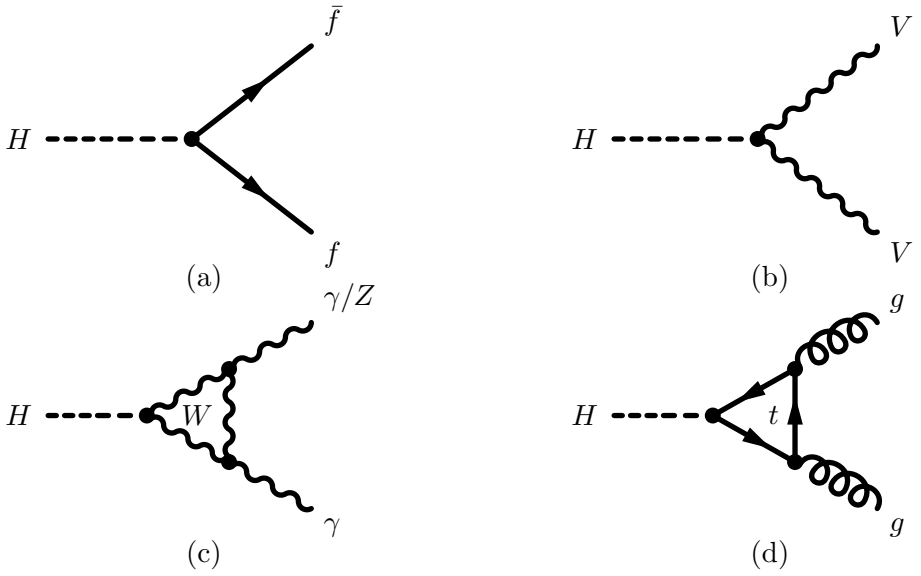

FIGURE 1.18: Feynman diagrams for the decay modes of the SM Higgs boson into: (a) fermions; (b) gauge bosons; (c) two photons or a photon and a Z boson, via a W loop; and (d) gluons.

becomes entirely dominated by the decay into two W bosons - $H \to WW^{(*)}$ -, followed by the decay into two Z bosons - $H \to ZZ^{(*)}$. It should be noted, however, that these decays also contribute significantly in the low mass region. In fact, $H \to WW^*$ has the second largest branching fraction for $m_H = 125$ GeV (see Table 1.6).

The Higgs boson decay into photons - $H \to \gamma\gamma$ - occurs mainly via a W boson and top quark loop (see Figure 1.18c), and though it has a very small branching ratio, it is experimentally important in the low Higgs mass region. The decays $H \to Z\gamma$ (Figure 1.18c) and $H \to \mu\mu$ (Figure 1.18a) are very rare, but also being probed at the experimental level.

Precise calculations of the SM Higgs boson branching ratios (as well as the production cross-sections) are essential for a correct interpretation of the experimental data. The latest computations of the branching ratios can be found in the reports [53–55] by the LHC Higgs Cross Section Working Group [56], and use the programs HDECAY [81–83] and PROPHECY4F [84–86]. In a first step all Higgs partial widths are calculated using HDECAY, which includes all relevant higher-order QCD corrections, as well as EW NLO corrections. Then, the branching ratios are derived from the full set of partial widths. Finally the results are modified to include the $H \to WW/ZZ \to 4f$ (fully leptonic, semi-leptonic and fully hadronic) partial widths, at NLO QCD and EW, from PROPHECY4F, which takes into account signal-background interference effects. The uncertainties on the branching ratios, shown in Table 1.6 or indicated by the colored bands in Figure 1.17, are due to missing higher-order corrections and uncertainties of the input parameters, such as the quark masses.

1.2.3.3 Search channels at the LHC

Searching for the SM Higgs boson was one of the primary goals of the ATLAS and CMS experiments at the LHC. To develop a search strategy one needs to take into account not only the production and decay modes of the Higgs boson, but also the final state signatures, as shown in Figure 1.19. An additional aspect that needs to be considered, and not taken into account in Figure 1.19, are the background processes, that will provide similar or identical signatures as the Higgs boson, at a higher rate. Fully hadronic final states have basically no sensitivity at the LHC, where QCD multijet production dominates the total cross-section by many orders of magnitude. Thus, final states with leptons, though occurring at a smaller rate, will provide better sensitivity. Finally, different approaches should be taken depending on the Higgs boson mass considered. Here, we describe the main analysis channels, used by the experiments at the LHC, to search for and to measure the Higgs boson at $m_H = 125$ GeV.

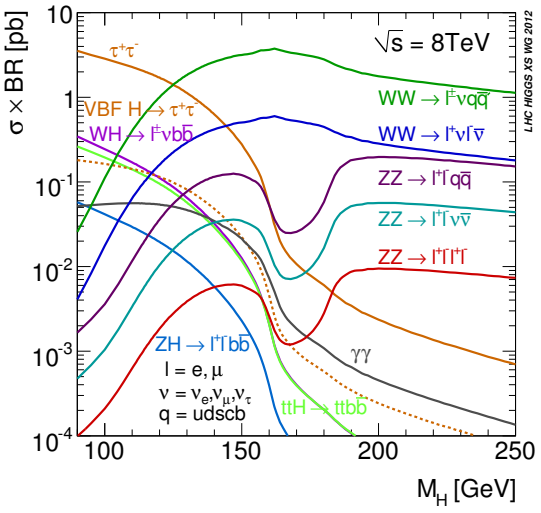

FIGURE 1.19: SM Higgs boson production cross-section times branching ratios, for different final states, at $\sqrt{s} = 8$ TeV. Taken from Ref [56].

The $H \to \gamma\gamma$, $H \to ZZ^* \to 4\ell$ and $H \to WW^* \to \ell\nu\ell\nu$ decays are the most sensitive for a Higgs boson with $m_H = 125$ GeV. In fact, it was through the combined results of searches in these channels that the SM Higgs boson was first observed at the LHC. The final states are very clean and all the production modes can be exploited, although the bulk of the sensitivity in these channels is provided by ggF.

Despite the very low $H \to \gamma\gamma$ branching ratio and signal-to-background ratio, this channel profits from a very distinct signature, of two high energy photons forming a narrow invariant mass peak, thus offering large sensitivity in the low Higgs mass range. Direct $\gamma\gamma$ production, which shows a falling diphoton mass spectrum, constitutes one of the main sources of background.

The $H \to ZZ^* \to 4\ell$ channel also has a very low branching ratio, but the Higgs boson can, again, be fully reconstructed with very good resolution, from the 4-lepton

invariant mass. Moreover, the background contributions, which come mainly from continuum $ZZ^{(*)} \to 4\ell$ production, are small, making it the channel with the best signal-to-background ratio. Due to these features, the $H \to ZZ^* \to 4\ell$ channel is very sensitive, not only for $m_H = 125$ GeV, but over a large mass range.

The $H \to WW^* \to \ell\nu\ell\nu$ channel is one of the most sensitive, over a very large range of Higgs masses. It takes advantage of the large $H \to WW^*$ branching fraction and sizable leptonic decays of the W bosons, providing a clean signature of two oppositely-charged leptons and large missing transverse energy (the neutrinos are not detected by the experiments), at a relatively high rate. On the downside, the escaping neutrinos do not allow for the full reconstruction of the Higgs mass, making the identification of the signal very challenging. The main background contributions arise from leptonic decays of continuum $WW^{(*)}$ and $t\bar{t}$ production. The $H \to WW^* \to \ell\nu\ell\nu$ channel is the main focus of this thesis and more details will, therefore, be provided in Chapter 4.

Out of all the fermionic decays of the Higgs boson, only the $H \to \tau\tau$ and $H \to b\bar{b}$ channels offer experimental sensitivity. However, the identification of the final state products is difficult, and these channels are much less sensitive than the previously described bosonic modes. Probing them is, nonetheless, very important, as they give direct access to the Higgs couplings to fermions.

The $H \to \tau\tau$ decay channel is analyzed in the leptonic, semi-leptonic and hadronic modes, depending on the τ decays. Reconstruction of the τ leptons is challenging and the di-tau invariant mass has very poor resolution. The dominant background source is $Z \to \tau\tau$. Explicit searches for a VBF-produced Higgs, with two very forward jets in the final state, help suppress the backgrounds, providing the largest sensitivity.

Although $H \to b\bar{b}$ has the largest branching fraction, the ggF production mode cannot be probed, due to the overwhelming QCD multijet background. Thus, this channel relies on the VH and ttH production modes, where a leptonic decay of the gauge bosons can help suppress the backgrounds, though largely reducing the rates. Moreover, efficient identification of jets originating from b-quarks is challenging, but fundamental to identify the $H \to b\bar{b}$ decay.

1.2.3.4 Discovery and current status

Early searches for the Higgs boson at the LHC, during 2011 data-taking, did not immediately reveal the elusive particle. However, the combined results of different search channels excluded the existence of the Higgs boson in a large range of masses. For the ATLAS experiment [87], the m_H ranges $111.4 - 116.6$ GeV, $119.4 - 122.1$ GeV and $129.2 - 541$ GeV were excluded at 95% confidence level (CL), while the CMS experiment [88] excluded a SM Higgs boson in the $127 - 600$ GeV mass range, at 95% CL.

On the 4$^{\text{th}}$ of July 2012, using only a fraction of the full dataset provided by the LHC, the ATLAS and CMS collaborations at CERN announced the discovery of a new particle, when searching for the SM Higgs boson [35, 36]. The excess of events observed was compatible with the production and decay of the SM Higgs boson, with a mass of

approximately 125 GeV. The discovery was possible through the combined results of several channels, though $H \to \gamma\gamma$, $H \to ZZ^* \to 4\ell$ and $H \to WW^* \to \ell\nu\ell\nu$ analyses dominated the result.

Figure 1.20a shows the diphoton invariant mass distribution observed by CMS at the time of the discovery, where an excess of events over the fitted background distribution can be clearly seen at $m_{\gamma\gamma} \sim 125$ GeV. As shown in Figure 1.20b, the combined excess observed by ATLAS had a local p-value of $p_0 = 1.7 \times 10^{-9}$. This presents a measure of the probability that, in the absence of a Higgs boson, the background can produce a fluctuation greater than or equal to the excess observed in the data. This probability can be translated in terms of number of standard deviations, and corresponds to an excess with a local significance of $Z_0 = 5.9\sigma$ (CMS measured 5σ), which is above the threshold required to claim a discovery[4].

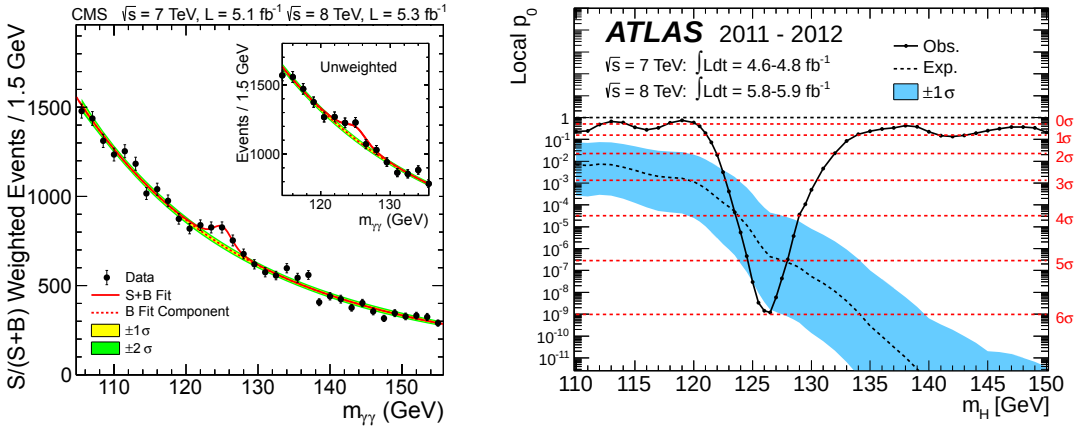

(a) (b)

FIGURE 1.20: (a) Diphoton invariant mass distribution observed by CMS, showing an excess of events over the fitted background [36]. (b) Local p-value observed by ATLAS, as a function of m_H, showing an excess of events with a local significance of 5.9σ [35]. These observations contributed to the announcement of the discovery of a Higgs boson, with $m_H \sim 125$ GeV, on the 4^{th} of July 2012.

After the observation, both experiments have extensively tested the properties of the newly discovered Higgs boson, using the full available dataset:

Overall rate The rates measured in the different channels have been compared to those predicted by the SM [89, 90], as shown in Figure 1.21a. This is done using the signal strength μ, i.e. the ratio between measured and SM-predicted cross-section times branching ratio ($\sigma \times \text{BR}$). Results show compatibility with the SM for both ATLAS and CMS.

Decays The latest measurements in the $H \to \tau\tau$ and $H \to b\bar{b}$ channels provide evidence of the direct decay of the Higgs boson to fermions, at the 3.7σ level for ATLAS [89] and 3.8σ for CMS [91].

[4] An observed signal is generally accepted as a discovery if the p-value is less than 2.9×10^{-7}. This is the one-sided probability for a fluctuation in a Gaussian distribution with width σ to be observed at least 5σ away from the mean. An observation at the 3σ level is considered an evidence

Production modes Specific Higgs production modes have also been probed [89, 90], as indicated in Figure 1.21b. The procedure separates the VBF and VH processes, which involve the Higgs boson coupling to vector bosons, from the ggF and ttH processes, which involve the Higgs boson coupling to fermions. Then, two signal strength parameters are measured - $\mu_{\mathrm{ggF+ttH}}$ and $\mu_{\mathrm{VBF+VH}}$ - which scale the SM-predicted rates to the observed ones. Results show, once again, consistency with the SM expectation. Furthermore, there is 4.1σ evidence from ATLAS [89] that a fraction of the Higgs boson production occurs through VBF.

Mass Precision measurements of the mass of the Higgs boson have been performed by both collaborations, using the $H \to \gamma\gamma$ and $H \to ZZ^* \to 4\ell$ channels, as they provide the best mass resolution. The measured masses are $m_H^{\mathrm{ATLAS}} = 125.36 \pm 0.37\,(\mathrm{stat.}) \pm 0.18\,(\mathrm{syst.})$ GeV [92] and $m_H^{\mathrm{CMS}} = 125.03^{+0.26}_{-0.27}\,(\mathrm{stat.})^{+0.13}_{-0.12}\,(\mathrm{syst.})$ GeV [90].

Couplings The couplings of the Higgs boson to fermions and gauge bosons [89, 90] have been compared to those of the SM as well, using the framework described in Ref. [55]. The procedure defines scale factors κ_j, in such a way that the cross-section σ_j and partial decay width Γ_j, associated to the SM particle j, scale with κ_j^2. The measured coupling scale factors for all fermions - $\kappa_{\mathrm{F}} = \kappa_t = \kappa_b = \kappa_\tau = \kappa_g$ - and for all vector bosons - $\kappa_{\mathrm{V}} = \kappa_W = \kappa_Z$ - are shown in Figure 1.21c. Different channels, as well as the combined result, show couplings compatible with those predicted by the SM.

Spin and parity Finally, the $J^P = 0^-, 1^+, 1^-, 2^+$ spin-parity hypotheses (J and P denote the spin and parity quantum numbers, respectively) are disfavored by both ATLAS [93] and CMS [94, 95], when tested against the 0^+ hypothesis of the SM.

To summarize, the latest measurements of the Higgs boson show remarkable compatibility with the SM expectations, and neither of the collaborations has observed any significant deviations from this theory. The success of the SM is further illustrated in Figure 1.22, where cross-sections measured by the ATLAS experiment are compared to theory expectations, calculated at NLO or higher. The remarkable agreement spans several orders of magnitude in cross-section, and a variety of SM benchmark processes.

Despite the tremendous success of the SM, it is well known that physics beyond the SM (BSM) must exist. For example, phenomena such as dark-matter and dark-energy, which compose 96% of the Universe, or the observed matter-antimatter asymmetry, remain unexplained by the SM. Moreover, the lightness of the discovered Higgs boson has some theoretical consequences, the most important one being the so-called hierarchy problem. One-loop radiative corrections to the Higgs boson mass are quadratically divergent, and tend to make the Higgs boson heavier. In other words, when introducing a cutoff energy scale Λ, above which the SM is no longer valid, the renormalized Higgs mass m_H is expressed as the difference between a "bare mass" and an expression proportional to Λ^2 (the radiative correction). Choosing $\Lambda \approx 10^{16}$ GeV, the scale of grand unification of all forces, an incredible amount of fine-tuning needs to occur for the bare mass to cancel the radiative correction term, generating the observed $m_H \approx 125$ GeV. The

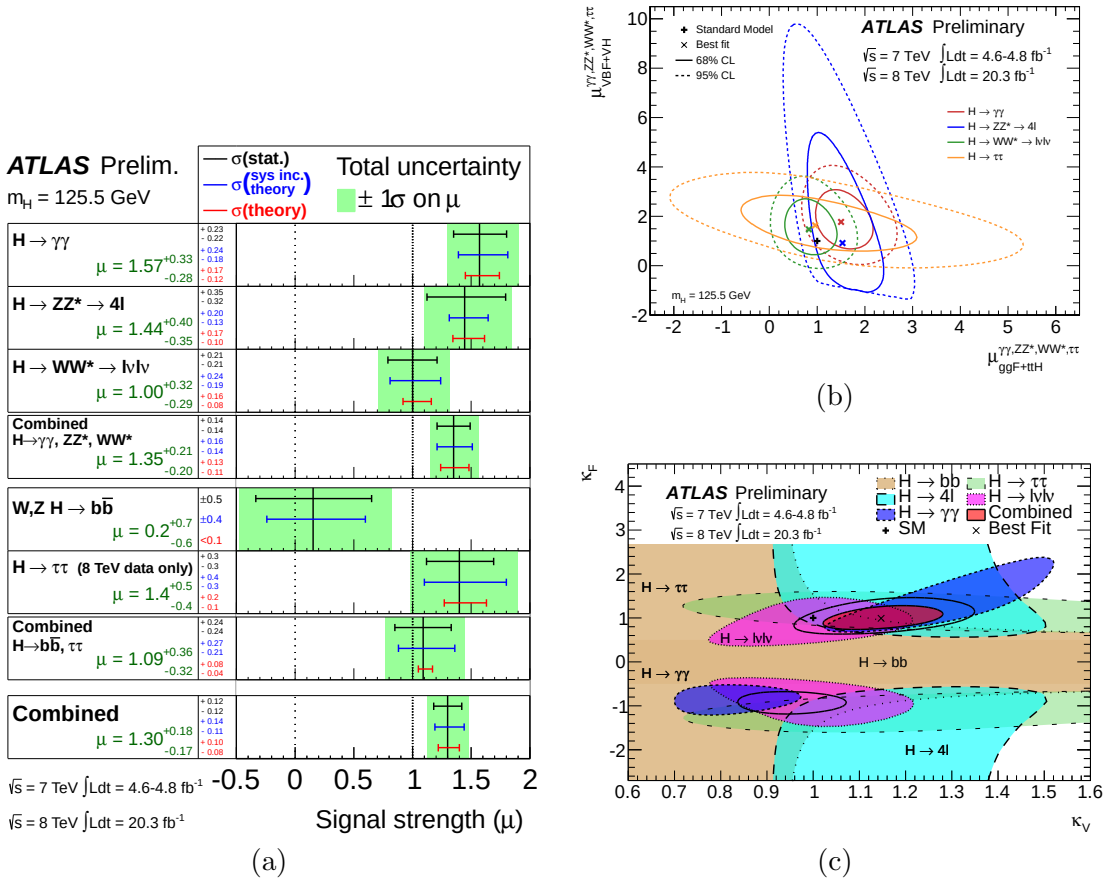

FIGURE 1.21: Results from ATLAS on measurements of the Higgs boson with $m_H = 125.5$ GeV. (a) Measured signal strengths normalized to the SM expectations, for the individual final states and various combinations. (b) Likelihood contours in the ($\mu_{\mathrm{ggF+ttH}}$, $\mu_{\mathrm{VBF+VH}}$) plane for different channels. (c) Results of fits that probe different coupling strength scale factors for fermions and vector bosons, assuming only SM contributions to the total width, for the individual channels and their combination. Figures taken from Ref. [89].

cutoff can, of course, be placed at a lower energy scale, for a more natural cancellation to occur. In this case, BSM physics is expected at the TeV scale. Supersymmetry (SUSY), a theory that introduces a new symmetry relating fermions and bosons at the TeV scale, is presented as an elegant solution to the hierarchy problem, as it cancels out the quadratic divergences. Moreover, SUSY has the advantage of introducing a candidate for dark-matter. The TeV scale is about to be undergo major scrutiny for Run II of the LHC, which will start in the beginning of 2015. Hopefully the experiments will be able to provide solutions to these problems in the very near future.

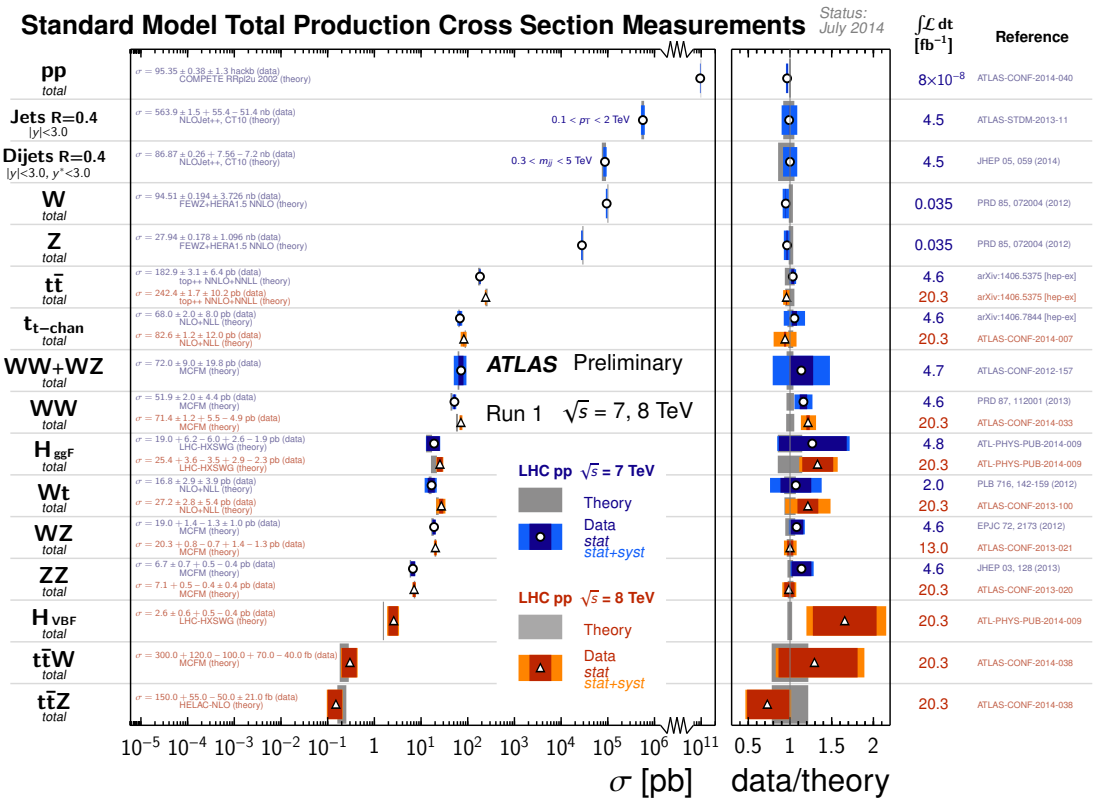

FIGURE 1.22: Detailed summary of several SM total production cross section measurements by ATLAS, compared to the corresponding theoretical expectations. All theoretical expectations were calculated at NLO or higher. The W and Z vector-boson inclusive cross sections were measured with 35 pb^{-1} of integrated luminosity from the 2010 dataset. All other measurements were performed using the 2011 dataset or the 2012 dataset. Extracted from Ref. [96].

Chapter 2

The ATLAS Experiment

This chapter introduces experimental setup used for the development of the work described in this thesis. It starts with a description of the LHC machine, which provided the proton-proton collision data used here. The data was collected by ATLAS, an immense multi-purpose particle detector located in the LHC tunnel at CERN. A description of its components is also provided. Finally, an overview of how physics objects are identified and reconstructed in the ATLAS detector is presented.

2.1 LHC

The Large Hadron Collider (LHC) [97] at CERN (European Organization for Nuclear Research) is the world's most powerful tool for particle physics research. The superconducting, two-ring, hadron accelerator and collider is designed to accelerate and collide protons[1] at unprecedented conditions of energy and luminosity, with the key objectives of exploring the Standard Model in the TeV energy scale, and searching for the Higgs boson and for potential new physics beyond the Standard Model. In what follows, different aspects of the LHC will be discussed, using the information available in Refs. [97–99].

The LHC is installed in a tunnel that had previously housed the LEP (Large Electron-Positron) machine. The tunnel is 26.7 km in circumference, and lies between 45 m (towards Léman lake) and 170 m (under the Jura mountains) below the surface, in the French-Swiss border near Geneva. Being a particle-particle collider (as opposed to particle-antiparticle), the LHC has two rings with counter-rotating beams. To avoid collisions with gas molecules, these beam pipes are kept in a ultrahigh vacuum of 10^{-13} atm. The LHC machine is basically composed of electromagnetic devices, that are used to manipulate the circulating beams. A total of 9593 magnets - dipoles, quadrupoles, sextupoles, etc. - together with radio-frequency cavities, form the LHC. The LHC was designed to operate at a $\sqrt{s} = 14$ TeV, i.e. with a 7 TeV energy per proton beam, which can only be achieved with superconducting technology. Therefore, the LHC also has a cryogenic system, that maintains the 27 km long accelerator at a temperature of 1.9 K, colder than the outer space, using superfluid helium.

[1] The LHC also collides lead ions, but those will not be discussed in this thesis.

The most essential pieces of the LHC are the 1232 super-conducting, 14.3 m long, 35 tons heavy, dipole magnets. Due to size restrictions imposed by the LEP tunnel, the LHC dipoles have a "two-in-one" design, where two sets of coils and beam pipes share the same mechanical structure and cryostat, as illustrated in Figure 2.1. The coils use niobium-titanium (NbTi) cables, which become superconducting at temperatures below 10 K. An electric current of 11850 A flows in these coils, generating a magnetic field of 8.33 T, that bends the beams around the circular trajectory. At the LHC, this bending power is, in fact, the limiting factor for the energy achieved, rather than the acceleration itself. The acceleration is provided by 400 MHz radio-frequency (RF) cavities, that also compensate for energy losses, keeping the beam energy constant.

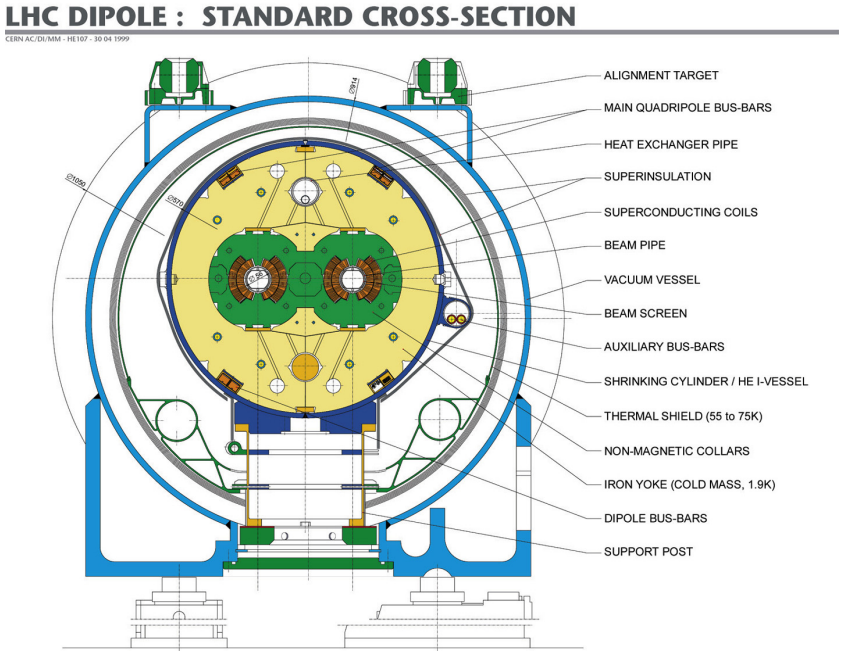

FIGURE 2.1: Diagram showing the cross-section of an LHC dipole magnet.

There are 392 quadrupole magnets at the LHC. The most important ones are the insertion quadrupoles, which are placed near the interaction points (IPs), where the collisions occur. They squeeze the beam down to the smallest size possible, thereby increasing the chance of head-on collisions between the protons. Higher multipole magnets are embedded in the main dipoles and quadrupoles, and are used to make corrections on the beam trajectories.

In four regions around the LHC, the two beam pipes are brought together into a single pipe, forming the IPs. Around these points, particle detectors are built, to capture the outcome of the collisions. The four main experiments at the LHC are: ATLAS (A Toroidal LHC ApparatuS) at IP1, CMS (Compact Muon Solenoid) at IP5, ALICE (A Large Ion Collider Experiment) at IP2, and LHCb (Large Hadron Collider beauty) at IP8. ATLAS and CMS are general-purpose detectors, designed to exploit the full potential of the LHC collision data. ALICE and LHCb are specialized detectors, built to provide dedicated studies on heavy ion physics and b-quark physics, respectively.

It becomes clear from Figure 2.2 that the LHC is, in fact, only the last link in a large chain of accelerators at CERN, that successively increases the energy of the circulating beam. The chain begins with a small hydrogen bottle, from where protons are extracted. They are then injected into LINAC 2, a linear accelerator that brings the beam energy up to 50 MeV. At the circular Booster (PSB) proton beam reaches 1.4 GeV in energy, before it is fed to the PS (Proton Synchrotron) for an acceleration to 26 GeV. Finally, the SPS (Super Proton Synchrotron) increases the beam energy to 450 GeV, and transfers the protons in bunches to both LHC rings (clockwise and anti-clockwise), where they are accelerated for ~ 20 minutes to the nominal energy of 7 TeV per beam.

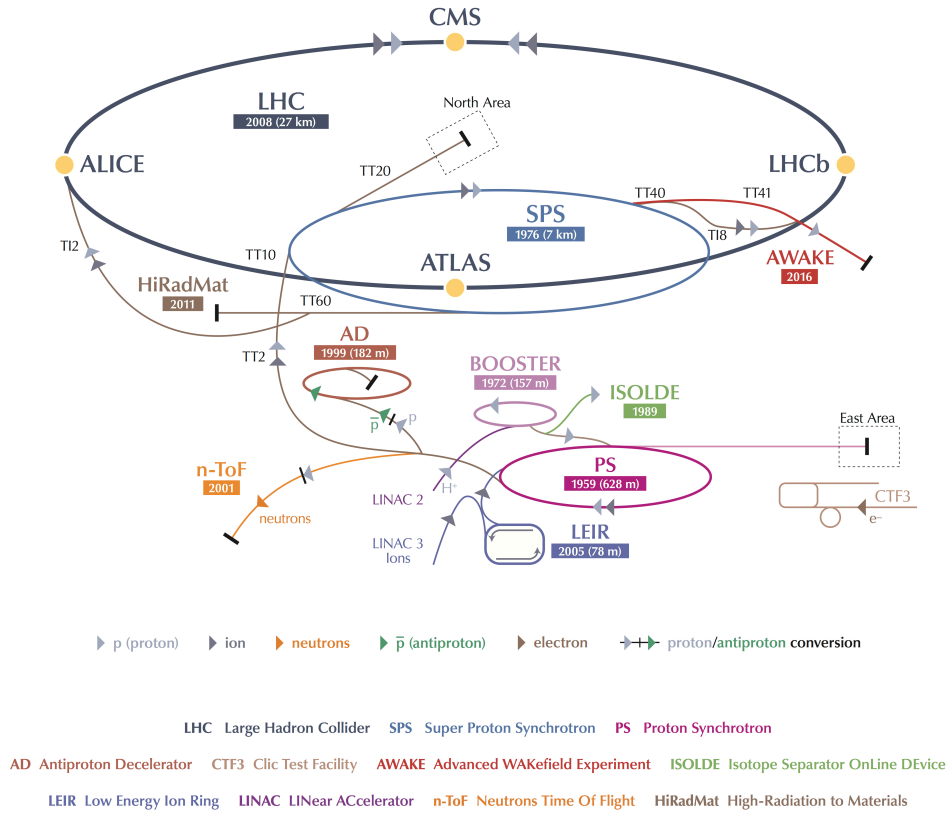

FIGURE 2.2: The accelerator complex at CERN.

The event rate for a given physics process at the LHC is given by:

$$\frac{\mathrm{d}N}{\mathrm{d}t} = L \times \sigma, \tag{2.1}$$

where σ is the cross section for the process in question, and L is the instantaneous luminosity of the machine. The total number of events N produced throughout data-taking is obtained by integrating Equation 2.1 in time:

$$N = \int L \, \mathrm{d}t \times \sigma = \mathscr{L} \times \sigma, \tag{2.2}$$

with $\mathscr{L}$ denoting the integrated luminosity, usually expressed in units of inverse cross-section (barn^{-1}). As already shown in Figure 1.11, the cross-section for interesting

processes, such as production of a Higgs boson, is several orders of magnitude smaller than the total cross-section at the LHC. Thus, high luminosity is fundamental to produce enough events to reach the physics goals of the LHC. Simply put, this is achieved by having the largest number of particles potentially colliding in the smallest possible area, at a given interaction point.

The LHC luminosity can be written as a function of different parameters of the beam:

$$L = \frac{N_b^2 k_b f_{\text{rev}} \gamma_r}{4\pi \epsilon_n \beta^*} F, \tag{2.3}$$

where N_b is the bunch intensity; k_b is the number of bunches per beam; f_{rev} is the revolution frequency; γ_r is the usual relativistic gamma factor; F is the geometric luminosity reduction factor; ϵ_n is the normalized emittance; and β^* is the β-amplitude function at the interaction point.

Some of the parameters in Equation 2.3 cannot be used to increase the luminosity. For example, at the LHC $f_{\text{rev}} = 11245$ Hz, fixed by the LHC perimeter and the speed of the circulating protons. Also, the factor F is related to the fact that collisions do not occur head-on but at a crossing angle to minimize parasitic interactions between the non-colliding bunches.

The remaining parameters in Equation 2.3, however, have been exploited by the LHC during data taking, to obtain high luminosity performance. The bunch intensity, given by the number of protons in each bunch, is especially important since $L \propto N_b^2$. The parameter k_b gives the number of bunches per beam, and associated to this quantity is the bunch spacing, i.e. the separation between them. β^* and ϵ_n basically express the size and shape of the beam. The normalized emittance, ϵ_n, indicates the spread of the beam in the transverse phase space. It can be understood as a measure of the brightness of the beam and it is determined by the injection chain. The squeeze process of the beam at the IPs is parametrized by β^*, the beta function at the interaction point. The beam size at the IP is proportional to $\sqrt{\beta^*}$ and determined by the quadrupole magnets. Thus, high luminosity is achieved by having bright beams (low emittance) with low β^*.

The installation of the LHC in the LEP tunnel began in 2000, and proton beams circulated in the accelerator, for the first time, on September 10^{th} 2008. Unfortunately, on the 19^{th} of September, during powering tests, a faulty electrical connection between two magnets caused mechanical damage to the accelerator and release of helium into the tunnel [100], an incident which significantly delayed the start of data-taking. Proton beams re-circulated in the LHC on the 20^{th} of November 2009, with the first collisions at $\sqrt{s} = 900$ GeV being registered by the detectors 3 days later. On November 30^{th} 2009, the beams were successfully accelerated to 1.18 TeV, and the LHC became the world's highest energy particle accelerator.

The LHC Run I physics program officially began on the 30^{th} of March 2010, when the first collisions at $\sqrt{s} = 7$ TeV were recorded. The beam energy was kept at half the nominal value as a consequence of the incident in 2008, and a total of ~ 5 pb^{-1} of collision data were delivered to ATLAS, in a year devoted to commissioning of the machine. The 2011 run began with $\sqrt{s} = 7$ TeV collisions on the 13^{th} of March 2011.

During this year, the performance limits of the machine were explored, and almost 6 fb^{-1} of data were delivered. 2012 was the peak performance year of the LHC. The beam energy was ramped to 4 TeV, and the first $\sqrt{s} = 8$ TeV collisions were seen on April 5$^{\text{th}}$ 2012. By December 17$^{\text{th}}$ 2012, a total of 23 fb^{-1} of pp collision data had been delivered to the experiments.

Table 2.1 summarizes some of the relevant parameters of the LHC, comparing the values during the different data-taking periods with the nominal LHC design ones. As shown, at peak performance, the number of bunches was kept at half the nominal value, for reasons related to the rapid increase of effects that cause beam instabilities (electron cloud, unidentified falling objects...). Nonetheless, the LHC achieved a very high luminosity performance, by keeping the beam intensity above the design value ($L \propto N_b^2$). Furthermore, the injectors succeeded in delivering beams with lower than nominal emittances and an aggressive squeeze of β^* was pursued.

Parameter	**2010**	**2011**	**2012**	**design value**
Beam energy [TeV]	3.5	3.5	4	7
Stored beam energy [MJ]	~ 28	~ 110	~ 140	362
β^* at IP1 and IP5 [m]	2.0/3.5	1.5/1.0	0.6	0.55
Bunch spacing [ns]	150	75/50	50	25
Max. number of bunches	368	200/1380	1380	2808
Max. bunch intensity [protons per bunch]	1.20×10^{11}	1.45×10^{11}	1.7×10^{11}	1.15×10^{11}
Normalized emittance [mm mrad]	~ 2.0	~ 2.4	~ 2.5	3.75
Peak instantaneous luminosity [cm^{-2} s^{-1}]	2.1×10^{32}	3.7×10^{33}	7.7×10^{33}	1.0×10^{34}
Integrated luminosity to ATLAS [fb^{-1}]	0.05	6	23	~ 100 (per year)

TABLE 2.1: Overview of performance related parameters at the LHC. The design values are compared to the values adopted during different data taking periods. Adapted from Ref. [99].

The LHC is currently undergoing its first long shutdown, with the goal of consolidating the accelerator. Running will resume in 2015, with an increased collision energy of 13 TeV, and an increase in the peak luminosity to 1.7×10^{34} cm^{-2}s^{-1}. It is expected that the LHC will deliver ~ 100 fb^{-1} of pp collision data over the course of 3 years.

2.2 A Toroidal LHC Apparatus

The LHC has extended the frontiers of particle physics, setting new standards on particle physics experiments. ATLAS (A Toroidal LHC ApparatuS) [101, 102] is one of the experiments at the LHC. With a particle detector which has half the size of the Notre Dame cathedral in Paris, and a collaboration of over 3000 scientists (including ~ 1000 students) from 177 institutions in 38 different countries, ATLAS is one of the world's biggest experiments.

2.2.1 General aspects

ATLAS is a 25 m high, 44 m long, 7000 tonnes heavy detector, installed ~ 100 m underground, at the LHC IP1. Figure 2.3 illustrates its overall layout. As shown, ATLAS

basically consists of cylindrical layers of subdetectors built around the beam pipe, with end-caps on each side, to cover the largest possible solid angle around the interaction point. The ATLAS subdetectors are: an inner detector (ID) composed of tracking devices, calorimeters for particle energy measurement, and a muon spectrometer (MS) for muon detection. ATLAS also includes a magnet system, essential for momentum measurement and charge identification, and a trigger and data acquisition (TDAQ) system, fundamental to collect LHC data with high performance. All these elements will be described in detail in the following sections.

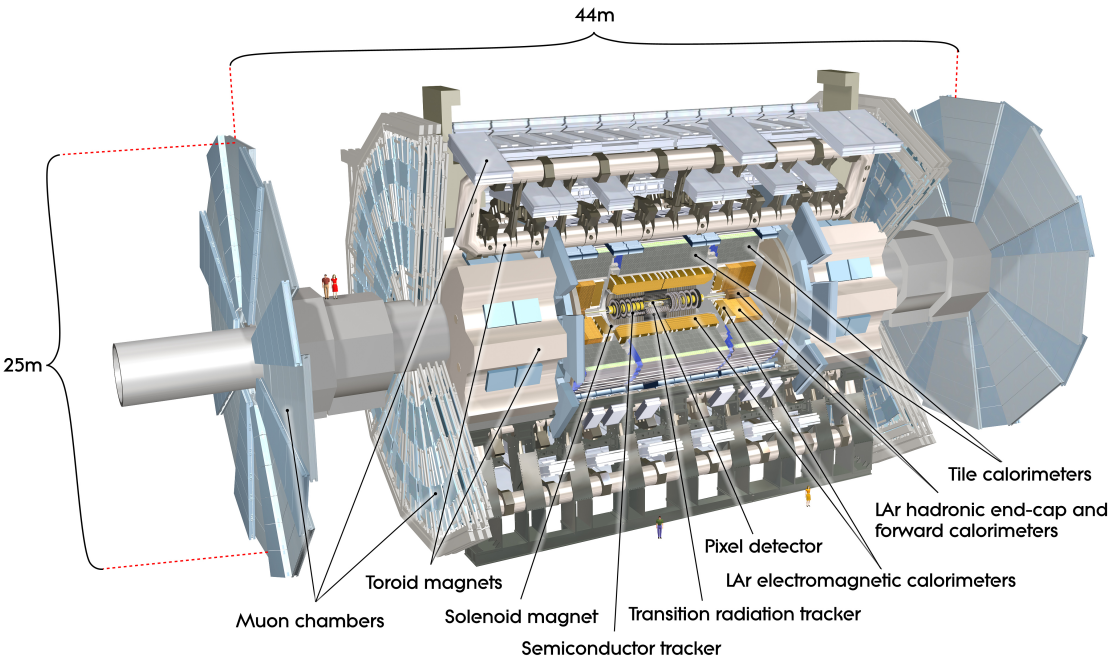

FIGURE 2.3: Cut-away view of the ATLAS detector. From Ref. [103].

ATLAS uses a right-handed coordinate system, with the origin placed at the interaction point. The beam direction defines the z-axis. The A-side (C-side) of the detector is defined as that with positive (negative) z. The positive x axis is defined as pointing to the center of the LHC ring, and the positive y-axis points upwards. The $x-y$ plane is orthogonal to the beam direction and referred to as the transverse plane. Quantities such as transverse momentum, p_{T}, transverse energy, E_{T}, or missing transverse energy, $E_{\mathrm{T}}^{\mathrm{miss}}$, are defined in this transverse plane. The azimuthal angle ϕ is measured around the beam axis and the polar angle θ is the angle from the beam axis. R is the distance to the interaction point. The rapidity, y, and pseudorapidity η are defined as:

$$y = \frac{1}{2}\ln\left(\frac{E+p_z}{E-p_z}\right) \quad \text{and} \quad \eta = -\ln\tan\left(\frac{\theta}{2}\right), \tag{2.4}$$

where E denotes the energy and p_z the component of the momentum along the beam direction. In the limit of massless particles, $y = \eta$, and both are invariant under Lorentz boosts along the beam axis. The $\eta - \phi$ coordinate space, with a distance:

$$\Delta R = \sqrt{\Delta\eta^2 + \Delta\phi^2}, \tag{2.5}$$

is commonly used.

The ATLAS detector is a general-purpose instrument, designed to exploit the full potential of the LHC collision data. The goals of the ATLAS physics program are diverse, and include precision tests of QCD interactions, EW interactions and flavour physics, searches for physics beyond the SM, such as new heavy gauge bosons (W' and Z') or supersymmetric particles, and searches for the SM (or BSM), Higgs boson(s), to elucidate the mechanism for EW symmetry breaking. Accomplishing these physics goals, under the harsh experimental environment created by the high luminosity and high energy conditions of the LHC, poses stringent requirements on the design of the ATLAS detector:

- Fast, radiation-hard electronics and sensor elements, as well as high detector granularity to handle the particle fluxes and to reduce the influence of overlapping events;
- Large acceptance in pseudorapidity, with almost full azimuthal angle coverage;
- Good charged-particle momentum resolution and reconstruction efficiency in the inner tracker;
- Vertex detectors close to the interaction region, to observe secondary vertices needed for tagging of τ-leptons and of b-jets;
- Very good electromagnetic calorimetry for electron and photon identification and measurements;
- Full-coverage hadronic calorimetry, for accurate jet and missing transverse energy measurements;
- Good muon identification and momentum resolution over a wide range of momenta, and the ability to determine unambiguously the charge of high transverse momentum muons;
- Highly efficient triggering on low transverse momentum objects with sufficient background rejection.

The main requirements are quantified in Table 2.2.

2.2.2 Data-taking

So far, ATLAS has recorded over 26 fb^{-1} of pp collision data from the LHC. The integrated luminosity collected in time, for each period of data taking since the start of the Run I, is shown in the distributions of Figure 2.4 [104]. The distribution in Figure 2.4b also illustrates the remarkable efficiency with which the data was collected. Each subsystem has generally operated with efficiencies close to 99%, and $\sim$ 95% of the 2012 dataset was deemed suitable for physics analyses [105].

Detector component	**Required resolution**	**η coverage**	
		Measurement	**Trigger**
Tracking	$\sigma_{p_T}/p_T = 0.5\%\ p_T \oplus 1\%$	± 2.5	
EM calorimetry	$\sigma_E/E = 10\%/\sqrt{E} \oplus 0.7\%$	± 3.2	± 2.5
Hadronic calorimetry (jets)			
barrel and end-cap	$\sigma_E/E = 50\%/\sqrt{E} \oplus 3\%$	± 3.2	
forward	$\sigma_E/E = 100\%/\sqrt{E} \oplus 10\%$	$3.1 < \lvert\eta\rvert < 4.9$	
Muon spectrometer	$\sigma_{p_T}/p_T = 10\%$ at $p_T = 1$ TeV	± 2.7	± 2.4

TABLE 2.2: General performance goals of the ATLAS detector. Units for energy E and transverse momentum p_T are in GeV. From Ref. [101].

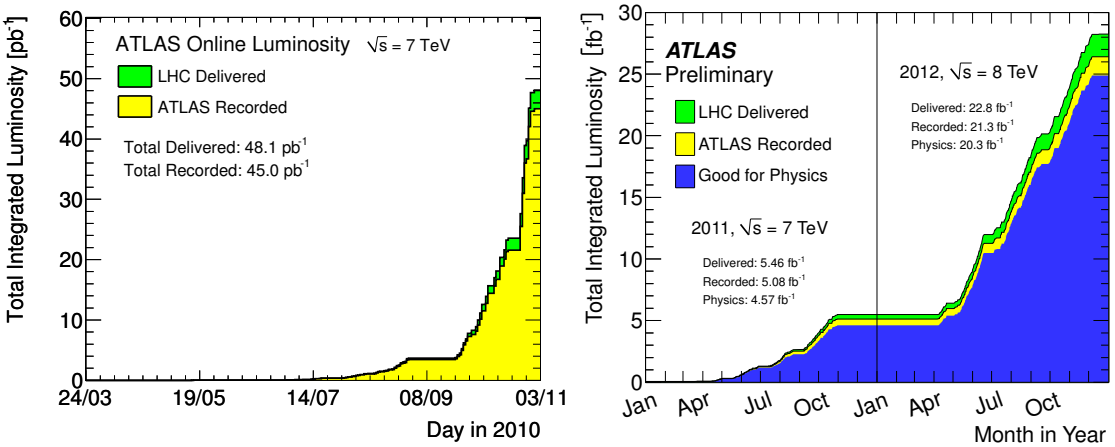

(a) (b)

FIGURE 2.4: Cumulative luminosity versus time delivered to (green) and recorded by ATLAS (yellow), during stable beams and for pp collisions at 7 and 8 TeV centre-of-mass energies. (a) refers to the 2010 dataset. (b) refers to the 2011 and 2012 datasets, and also shows integrated luminosity certified to be of good quality (blue). From Ref. [104].

The high luminosity delivered by the LHC, though needed because of the small cross-sections expected for many of the processes of interest, comes at a cost to the experiments, due to the pile-up. As discussed in Section 1.2.1.1, every candidate event of interest produced at the LHC is accompanied by several inelastic pp interactions in the same bunch crossing, a phenomenon referred to as in-time pile-up. The mean number of interactions per bunch crossing, μ [106], corresponds to the mean of the Poisson distribution of the number of interactions per crossing calculated for each bunch:

$$\mu = \frac{L_{\text{bunch}}\sigma_{\text{inel}}}{f_{\text{rev}}}, \tag{2.6}$$

where L_{bunch} is the instantaneous luminosity per bunch (obtained from Equation 2.3 divided by the number of bunches), σ_{inel} the inelastic cross-section (taken as 71.5 mb for 7 TeV collisions and 73.0 mb for 8 TeV collisions [104]) and f_{rev} the revolution frequency of the LHC, as discussed in Section 2.1.

Figure 2.5 shows the distributions of the mean number of interactions per bunch

crossing in ATLAS [104], for the 2011 and 2012 data-taking periods (there was no pile-up in 2010). In 2011, the average mean number of interactions per crossing was $\langle\mu\rangle = 9.1$, with a clear difference between two periods illustrated in Figure 2.5a, coming from the reduction of β^* (see Table 2.1). In 2012, the larger instantaneous luminosity caused a significant increase in pile-up, with respect to 2011, as shown in Figure 2.5b. The average mean number of interactions per bunch crossing was $\langle\mu\rangle = 20.7$ during 2012 data-taking, with tails up to ~ 40 interactions. These numbers are, in fact, comparable to what was expected for nominal LHC working conditions, due to the smaller number of bunches used (see Table 2.1).

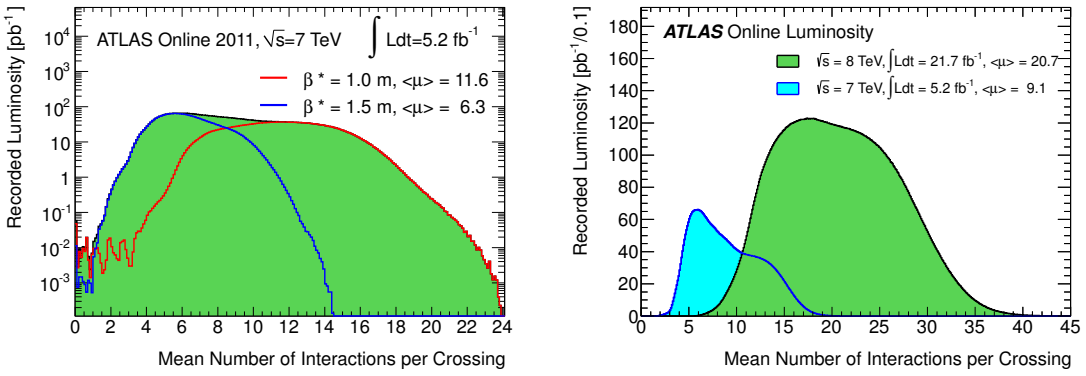

(a) (b)

FIGURE 2.5: Luminosity-weighted distribution of the mean number of interactions per bunch crossing in ATLAS. (a) shows the distributions for the 2011 dataset, before and after a technical stop in September 2011, where β^* was reduced from 1.5 m to 1.0 m. (b) compares the distributions for the 2011 and the 2012 data. From Ref. [104].

Another form of pile-up has occurred in ATLAS, due to certain instrumental features of the detector. The electronic signals generated by some of the components of ATLAS, in response to energy depositions for example, are longer than the spacing between two bunches at the LHC. Thus, during data-taking, contributions from the previous bunch crossing can overlay with the current bunch crossing, in a phenomenon referred to as out-of time pile-up.

2.3 ATLAS detector

In this section, the different subdetectors that form ATLAS are described, namely the inner detector, the calorimeters, and the muon spectrometer. A description of the magnet system is also provided.

2.3.1 Magnet system

As illustrated in Figure 2.6, the ATLAS magnet system [101] is composed of four large superconducting magnets: one solenoid and three toroids (one barrel and two end-caps). The magnetic fields generated by these magnets bend the trajectories of charged

particles in the ID and MS respectively, allowing for the determination their momentum and charge. The solenoid magnet is aligned with the beam axis and surrounds the ID, providing a 2 T axial magnetic field, while minimizing the radiative thickness in front of the calorimeters. The barrel toroid and the two end-caps, consisting of eight coils each, surround the calorimeters, and produce a toroidal magnetic field for the muon detectors, of approximately 0.5 T and 1 T in the central and end-cap regions, respectively.

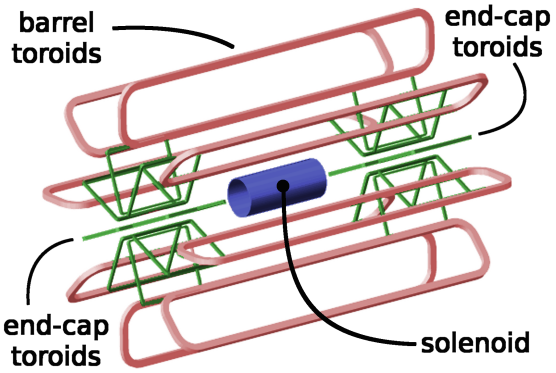

FIGURE 2.6: The magnet system of ATLAS.

2.3.2 Inner detector

The layout of the inner detector [101] is shown in Figure 2.7a. As the name suggests, the ID is the innermost layer of ATLAS, and sits close to the interaction point. Silicon pixel sensors and silicon microstrip sensors in the Pixel detector and in the Semiconductor Tracker (SCT) respectively, used together with the straw tubes of the Transition Radiation Tracker (TRT), offer very fine detector granularity in both $R-\phi$ and z coordinates. This is essential to achieve robust pattern recognition, excellent momentum resolution and primary and secondary vertex measurements of charged tracks above a p_{T} threshold (typically 0.5 GeV), in an environment where approximately 1000 particles will emerge from the IP at every bunch crossing. In the barrel region, the elements of the ID are arranged in concentric cylinders around the beam axis, while in the end-cap region they form disks perpendicular to the beam axis. Figure 2.7b illustrates the different ID subdetectors being traversed by a charged track in the barrel region. They will be described in what follows.

2.3.2.1 Pixel

The Pixel detector is a silicon pixel precision tracking device, and the element of ATLAS that is closest to the IP. With over 80 million readout channels, the pixel provides very high granularity. It consists of three concentric layers in the barrel region (as illustrated in Figure 2.7b) and three additional disks that form each of the two end-caps, providing a coverage of $|\eta| < 2.5$. Located 5 cm away from the beam pipe, the first Pixel layer in the barrel is referred to as the B-layer, since it is fundamental to the identification of secondary vertices originating from b-quarks. A total of 1744 rectangular

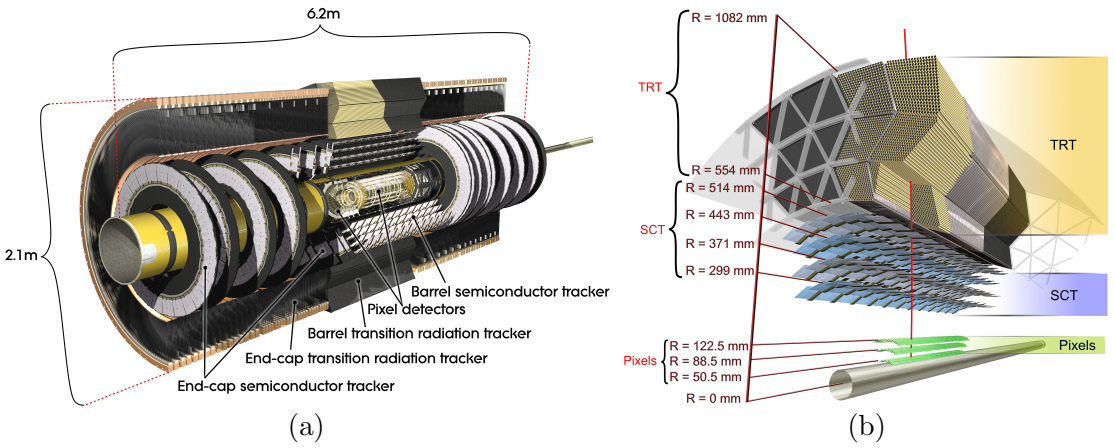

FIGURE 2.7: (a) Cut-away view of the ATLAS inner detector. (b) Illustration of the elements of the inner detector in the barrel region, being traversed by a charged particle in ATLAS. From Ref. [103].

pixel modules, with an area of $\sim$ 10 cm^2, form the Pixel layers and disks, each one containing $\sim$ 47000 pixels, with a minimum size of 50×400 μm^2 in $R-\phi \times z$. The Pixel typically provides at least three measurement points for charged particles originating at the IP. The intrinsic accuracies for Pixel measurements are 10 μm^2 ($R-\phi$) and 115 μm (z for the barrel and R for the end-caps).

2.3.2.2 SCT

With over 6 million readout channels, the SCT forms the second layer of the ATLAS detector and surrounds the Pixel. The detector consists of 4088 two-sided modules of silicon microstrip sensors placed at a small stereo angle of 40 mrad, to provide resolution along the strip length. The modules are arranged in four concentric layers in the barrel, and nine planar disks at each end-cap. The SCT typically provides eight strip measurements, corresponding four space-points, for charged particles originating from the IP. The readout strips are placed every 80 μm on the silicon, allowing for an accuracy of 17 μm ($R-\phi$) and 580 μm (z in the barrel and R in the end-caps).

2.3.2.3 TRT

The TRT is the outermost layer of the ID, and surrounds the silicon trackers. The 4 mm diameter polyimide straw tubes of the TRT (visible in Figure 2.7b) typically provide 36 hits per track, offering a coverage of $|\eta| < 2.0$ and over 350000 readout channels. The straw tubes are filled with a gas mixture of 70% Xe, 27% CO_2 and 3% O_2, to allow for the detection of transition radiation photons, thus enhancing the discrimination power between electrons and pions and offering complementary electron identification to that of the calorimeter. In the barrel region, the 144 cm long straws are placed parallel to the beam axis. In the end-caps, 37 cm long straws are arranged radially in wheels. The TRT only provides $R-\phi$ measurements, with an intrinsic accuracy of 130 μm per straw. This lower accuracy, compared to the Pixel and the SCT, is compensated by the larger

number of measurements and longer measured track. The sensitive volume of the TRT covers large radial distances, from 563 mm to 1066 mm, which allows for significant contributions to the momentum measurement.

2.3.3 Calorimeters

The ATLAS calorimeter system [101] consists of several different electromagnetic and hadronic detectors, with full ϕ symmetry. They are placed around the ID and the solenoid magnet, with a layout shown in Figure 2.8. The innermost layer of the calorimeter system is composed of one EM calorimeter in the barrel (EMB), one EM calorimeter (EMEC) and one hadronic calorimeter (HEC) at each endcap; and a forward calorimeter (FCal), that covers the regions closest to the beam. The TileCal is a hadronic calorimeter, that forms the outer layer of the system, and it is composed of one central barrel and two extended barrels on each side.

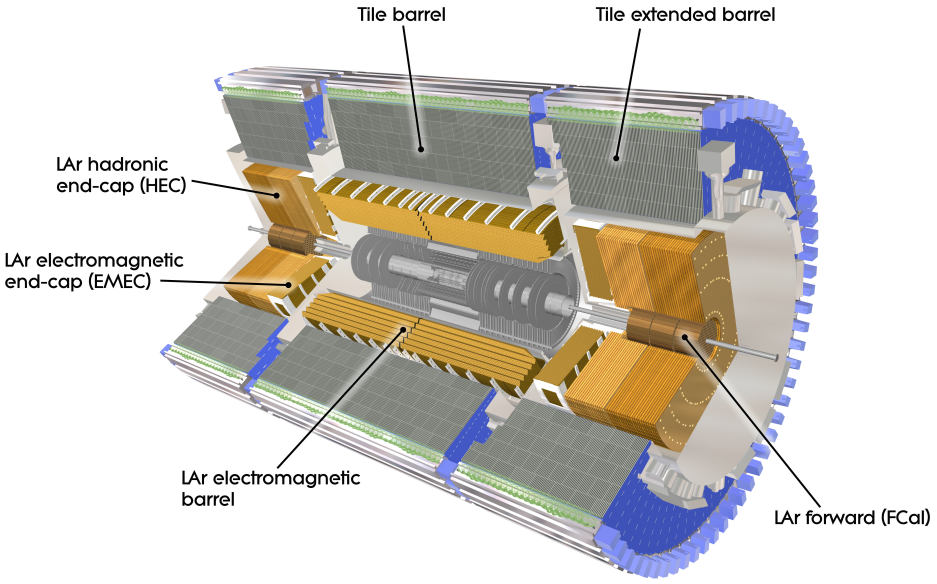

FIGURE 2.8: The ATLAS calorimeters. From Ref. [103].

The ATLAS calorimeters provide energy and topology measurements, over the $|\eta| < 4.9$ range. In the η region that matches the inner detector coverage, the fine granularity of the EM calorimeter provides precision measurements of electrons and photons. The coarser granularity of the rest of the ATLAS calorimeter system is sufficient to satisfy the physics requirements for jet reconstruction and missing transverse energy measurements.

The ATLAS calorimeters are sampling detectors, a term which refers to the design choice, where layers of a sensitive medium alternate with layers of a dense absorber material. Particles crossing the calorimeters will lose energy through interactions with the nuclei of the absorber medium, forming particle showers/cascades. The sensitive medium will generate a signal proportional to this lost energy, either through ionization or scintillation. The inner calorimeters of ATLAS use liquid argon (LAr) as the active medium, whereas the TileCal uses scintillator tiles alternating with steel plates.

The calorimeters of ATLAS are non-compensating, which refers to the response to electrons or photons versus hadrons, i.e. $e/h \neq 1$ ($e/h = 1$ for an ideal calorimeter). While EM showers, initiated by electrons or photons, develop mainly through Bremsstrahlung and pair production, hadronic showers are more complex, and will develop through the strong interaction between the produced hadron and the nuclei in the absorber medium. Hadronic showers have, in fact, a significant purely EM component, arising mostly from neutral pion decays ($\pi^0 \to \gamma\gamma$). Furthermore, some of the energy released during the development of a hadronic shower is either invisible or lost to nuclear recoils and dissociation. Because this energy is not captured in the active material, the ATLAS calorimeters have $e/h > 1$ responses and are, therefore, non-compensating. This non-compensation can be corrected for, by applying a hadronic calibration to hadronic objects, such as jets, as discussed in Section 2.6.4.3 ahead.

2.3.3.1 Electromagnetic calorimeters

The EM calorimeters use liquid argon as the active material and lead plates as the absorber. Liquid argon was chosen for its intrinsic linear behavior, stability of response over time, and radiation-hardness. The lead-LAr layers have an accordion shaped geometry, as shown in Figure 2.9a. This naturally provides a complete ϕ symmetry, without any azimuthal cracks, and allows the calorimeters to have several active layers in depth.

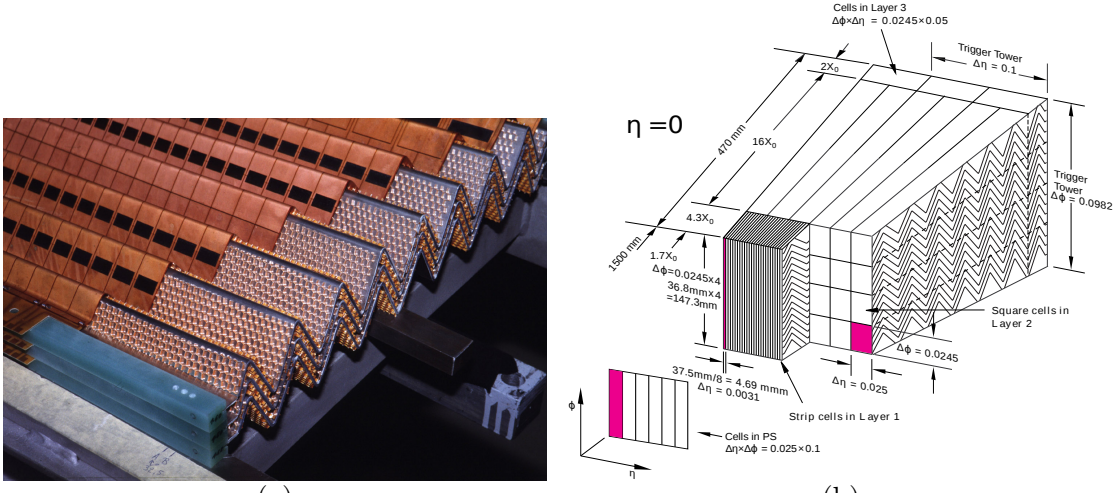

(a) (b)

FIGURE 2.9: (a) Accordion-shaped geometry of the LAr calorimeter. (b) Schematic diagram of the cross-section of the EM barrel calorimeter, including the presampler (labelled "PS"). From Refs. [103, 107].

The EMB calorimeter has a coverage of $|\eta| < 1.475$ and consists of two identical, 3.2 m long, half barrels, separated by a 4 mm gap at $z = 0$. At the end-caps, each EMEC is divided into an outer wheel that covers $1.375 < |\eta| < 2.5$, and an inner wheel covering the region $2.5 < |\eta| < 3.2$. The total thickness of the EM calorimeter is > 22 radiation lengths (X_0) in the barrel and $X_0 > 24$ in the end-caps. In the region $|\eta| < 1.8$, the EM calorimeters are complemented by an instrumented, 11 mm deep, argon layer - the

presampler (see Figure 2.9b) - which provides a measurement of the energy lost in the material in front of the EM calorimeters.

Figure 2.9b illustrates the geometry of the EM calorimeter in the barrel region, showing it is finely segmented, both laterally and longitudinally, into cells (individual read-out elements) of varying sizes. In the region devoted to precision physics ($|\eta| < 2.5$) the EM calorimeter is segmented longitudinally into three layers. The first layer is very finely segmented in η, providing accurate position measurement. The second layer has a segmentation of 0.025×0.025 ($\Delta\eta \times \Delta\phi$), and collects the largest fraction of the energy of the EM shower. The third layer only collects the tail of the electromagnetic shower and is, therefore, less segmented in η. The inner end-cap wheel ($2.5 < |\eta| < 3.2$) is segmented into two sections only, with coarser lateral granularity.

Figure 2.10 displays the shape of a typical ionization pulse produced by a cell in the second layer of the LAr EM calorimeter. As shown, the pulse is much longer than the 25 ns nominal bunch spacing at the LHC. The bipolar shaping of the pulse, with a positive peak and a negative tail of equal integral, is designed so that the out-of-time energy from previous/following bunches is, on average, canceled out over several bunches. However, fluctuations in an event-by-event basis will cause out-of-time pile-up, as discussed in Section 2.2.2.

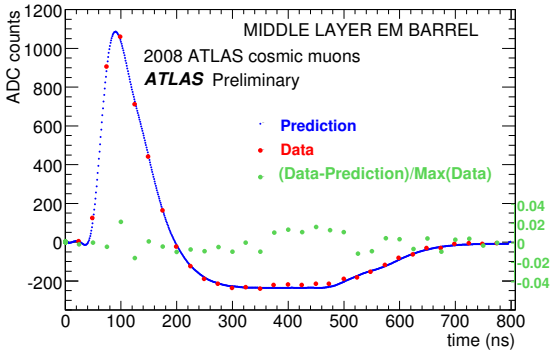

FIGURE 2.10: Predicted and observed pulse shapes in the second layer of the LAr EMB calorimeter. From Ref. [107].

2.3.3.2 Hadronic calorimeters

The TileCal sits around the LAr calorimeters, providing a $|\eta| < 1.7$ coverage in pseudorapidity and full azimuthal coverage. The central barrel of the TileCal covers the $|\eta| < 1.0$ region, while its two extended barrels cover the range $0.8 < |\eta| < 1.7$. The TileCal is divided azimuthally into 64 modules of $\Delta\phi \sim 0.1$, one of which is shown in Figure 2.11a. It is also segmented longitudinally into three layers. Extending from an inner radius of 2.28 m to an outer radius of 4.25 m, the TileCal has a thickness of 9.7 interaction lengths (λ) at $\eta = 0$, providing full containment of the hadronic showers produced in the LHC collisions.

The geometry of a TileCal module is illustrated in Figure 2.11b. It shows the scintillator tiles, which constitute the active material, alternating with the steel plates that serve as the absorber. The wavelength-shifting fibers, which are in contact with the tile edges, and collect the scintillating light onto photomultiplier tubes housed at the edge of each module, are also displayed. The TileCal is also equipped with three calibration systems: charge injection, laser and ^{137}Cs radioactive source.

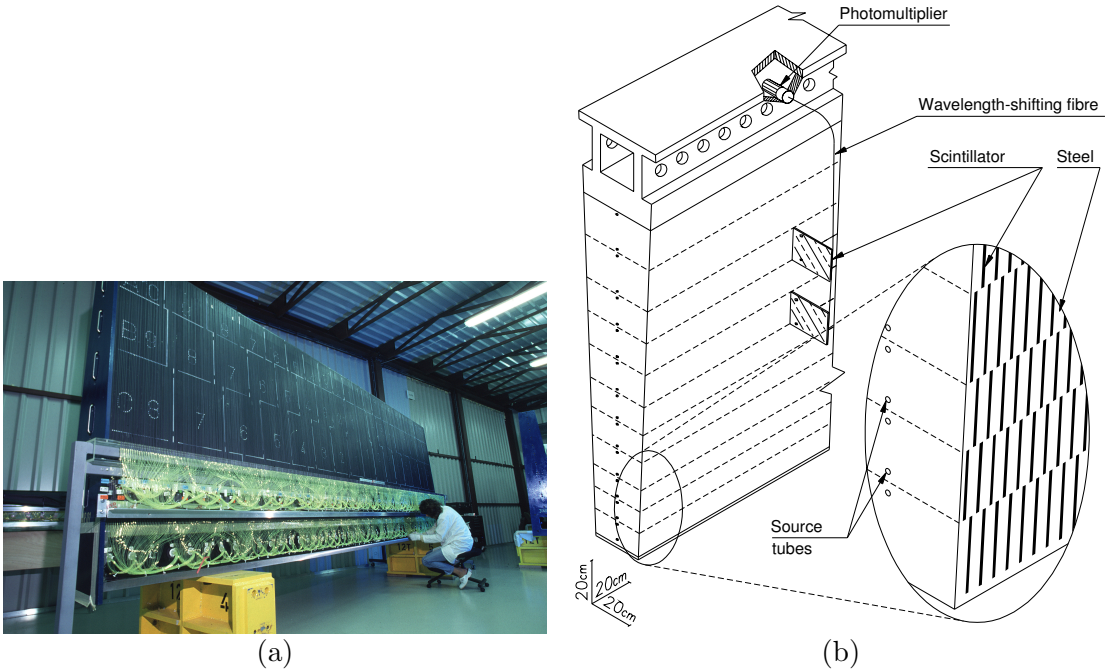

FIGURE 2.11: (a) Picture of a module of the TileCal. (b) Schematic drawing showing the scintillator tiles, the steel plates, the fibers, and photomultipliers in a TileCal module. From Refs. [101, 103].

The TileCal is segmented in a three-dimensional cell structure, creating a projective geometry for trigger and energy reconstruction. It is more granular than the EM calorimeter, with a cell size of 0.1×0.1 in the first two layers and 0.2×0.1 in the last layer ($\Delta\eta \times \Delta\phi$). In this context, it is useful to define the concept of tower as a summation of calorimeter cells in η, that approximately points back to the IP, as shown in Figure 2.12.

The hadronic calorimeter is extended to larger pseudorapidities by the HEC, which provides a coverage of $1.5 < |\eta| < 3.2$, thereby slightly overlapping with the TileCal and the FCal (described next). It consists of two independent wheels per end-cap, placed directly behind the EMEC. Each wheel is composed of 32 identical wedge-shaped modules, and is longitudinally segmented into two layers. The readout cells have a 0.1×0.1 granularity in the $1.5 < |\eta| < 2.5$ region, and 0.2×0.2 for larger η values ($\Delta\eta \times \Delta\phi$). Unlike the TileCal, the HEC calorimeters use copper plates as the absorber medium, interleaved with LAr gaps, serving as the active material, in a flat-plate design.

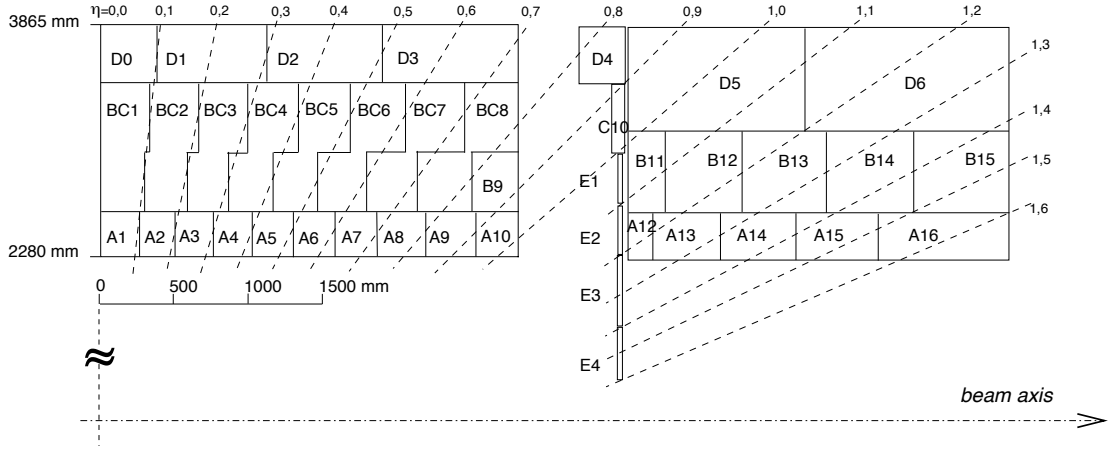

FIGURE 2.12: Segmentation in depth and in η of a TileCal module in the central (left) and extended (right) barrels. From Ref. [101].

2.3.3.3 Forward calorimeters

The FCal is approximately 10 interaction lengths deep, and consists of three 45 cm modules at each side. It extends the coverage of the ATLAS calorimeter system to $3.1 < |\eta| < 4.9$. The first module is made of copper and optimized for electromagnetic measurements. The remaining two, on the other hand, are made of tungsten, and measure predominantly hadronic energy. LAr is the active medium in all modules.

2.3.4 Muon spectrometer

The muon spectrometer [101], whose layout is shown in Figure 2.13, occupies the outermost part of the ATLAS detector. It is designed to detect muons and measure their momentum in the $|\eta| < 2.7$ pseudorapidity range, as well as trigger on them in the $|\eta| < 2.4$ region. The triggering system also performs bunch crossing identification. The MS comprises four subsystems: Monitored Drift Tubes (MDT), Cathode Strip Chambers (CSC), Resistive Plate Chambers (RPC), and Thin Gap Chambers (TGC). In the barrel region, the muons chambers are arranged in three cylindrical layers, around the beam axis and between the eight coils of the toroid magnets. In the end-caps, the chambers are installed also in three layers, this time perpendicular to the beam, in front of and behind the two end-cap toroids.

The ATLAS toroid magnets (see Section 2.3.1) provide a magnetic field for the muon momentum measurements, that is mostly orthogonal to the muon trajectories. In the $|\eta| < 1.4$ range, magnetic bending of the muons is performed by the large barrel toroid, whereas the toroid end-caps bend the muon trajectories in the region with $1.6 < |\eta| < 2.7$. In the transition region with $1.4 < |\eta| < 1.6$, the magnetic deflection is provided by a combination of the barrel and end-cap toroid fields.

The MDT and CSC subsystems are primarily designed for precision measurements of muon track coordinates and momentum. The MDT provides coverage in the more central region of $|\eta| < 2.7$ (except in the innermost end-cap layer, where the coverage is

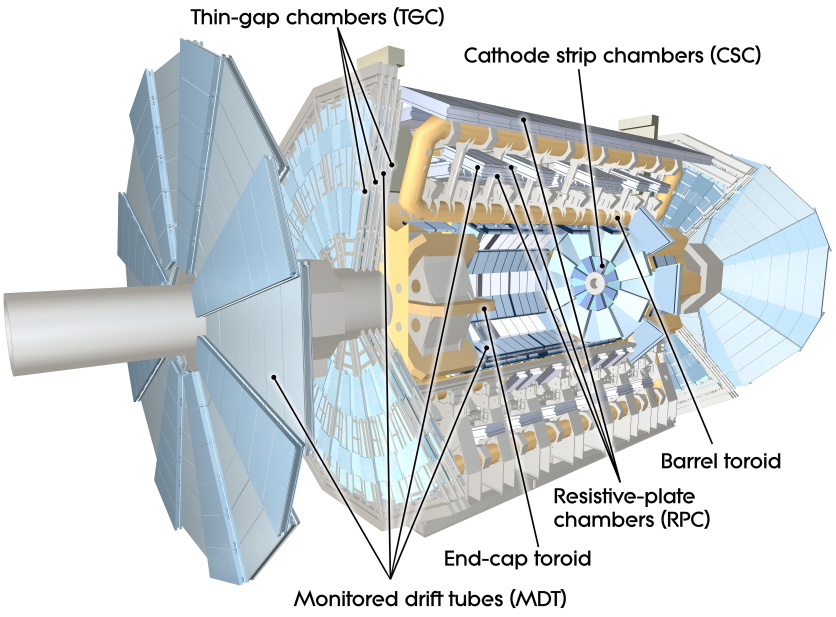

FIGURE 2.13: The ATLAS muon spectrometer. From Ref. [103].

limited to $|\eta| < 2.0$). The CSC, which can cope with higher background rates, is located in the more forward region of $2.0 < |\eta| < 2.7$. The RPC and TGC muon subsystems are designed to provide fast and robust readout, to be used by the trigger system (see Section 2.4 ahead), in the pseudorapidity ranges of $|\eta| < 1.05$ and $1.05 < |\eta| < 2.4$, respectively.

2.4 ATLAS trigger and data acquisition

The LHC has collided bunches of protons every 50 ns, i.e. with an event rate of 20 MHz. The amount of information that the ATLAS detector outputs to describe a full event, including all $\sim$ 20 simultaneous pp interactions, is about 1 MB. The typical rate at which this information can be written to storage is a few 100 MB/s. This means that the event output at the LHC must be reduced by five orders of magnitude before it can be stored by ATLAS. Thus, a very fast and effective trigger and data acquisition system is required, to promptly analyze online all events, and select for storage and offline analysis the few hundred whose properties suggest they might contain interesting signals. The trigger system of ATLAS is described in what follows.

2.4.1 Trigger system overview

The ATLAS TDAQ system is schematically represented in Figure 2.14. The trigger [101, 108] consists of three levels of event selection, designed to efficiently capture the physics of interest. Each level refines the decision made by the previous level and, if necessary, applies additional selection criteria. The first level - L1 - is hardware-based, implemented in costum-made electronics. It uses a limited amount of the total detector information to

take a decision in less than 2.5 μs, reducing the event rate to $\sim 75 - 100$ kHz. The two following levels are implemented in software, using commercially available computers and networking hardware, and are collectively known as the High Level Trigger (HLT). Unlike L1, HLT algorithms use the full granularity and precision of the different ATLAS sub-detectors. The second level - L2 - uses simplified algorithms on reduced information seeded by the L1, to take a decision in 40 ms and reduce the event rate to less than 3.5 kHZ. The third and last level is called the Event Filter - EF - and uses offline-like algorithms on fully-built events, to select $\sim 200 - 300$ Hz of data to storage, with an average event processing time of ~ 4 seconds.

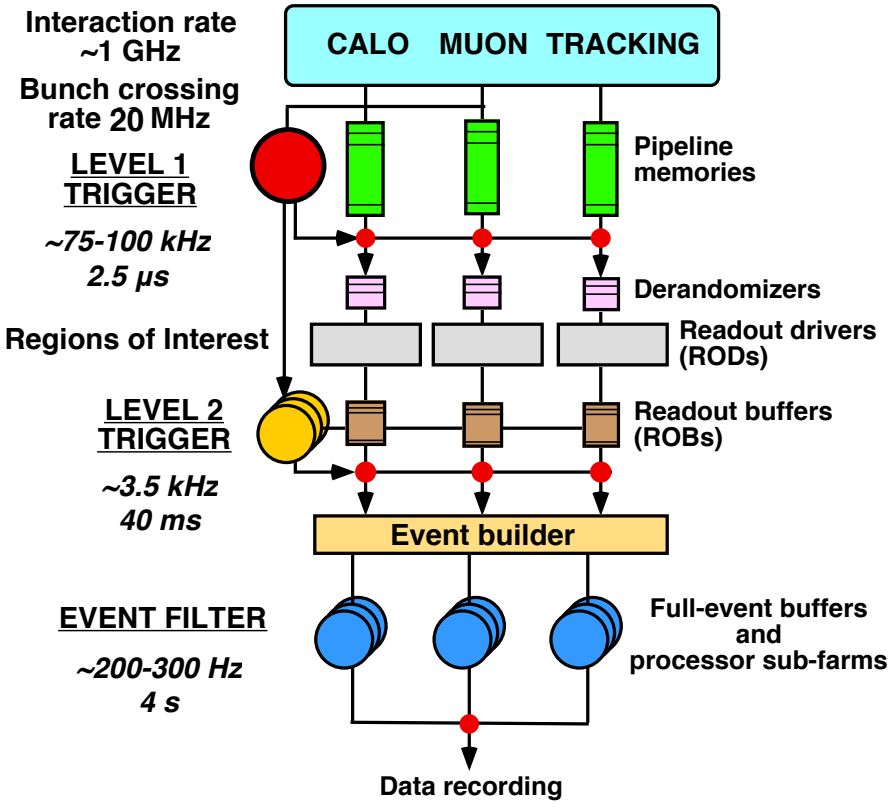

FIGURE 2.14: Schematic diagram of the TDAQ system of ATLAS. Adapted from Ref. [109].

2.4.2 Level 1

The L1 trigger has dedicated access to data from the ATLAS calorimeters and the muon system. The L1 calorimeter trigger (L1Calo) uses reduced-granularity information from all calorimeters, namely E_{T} values in 7200 trigger towers (TT). The trigger towers (sums of cells is along η) are 0.1×0.1 in $\Delta\eta \times \Delta\phi$ over most of the calorimeter, and larger in the forward region, as illustrated in Figure 2.15. Based on this information the L1Calo algorithms identify the following objects: EM clusters, τ-leptons, jets, missing transverse energy, scalar sum E_{T}, and total transverse energy of identified L1 jets. A decision is then made, based on the multiplicities and E_{T} thresholds of these objects. The L1 muon trigger (L1Muon) uses measurements of trajectories in the different stations of the RPC

and TGC trigger chambers, located in the barrel and end-cap regions of the muon spectrometer (see Section 2.3.4). The input to the trigger decision is the multiplicity for various muon p_{T} thresholds.

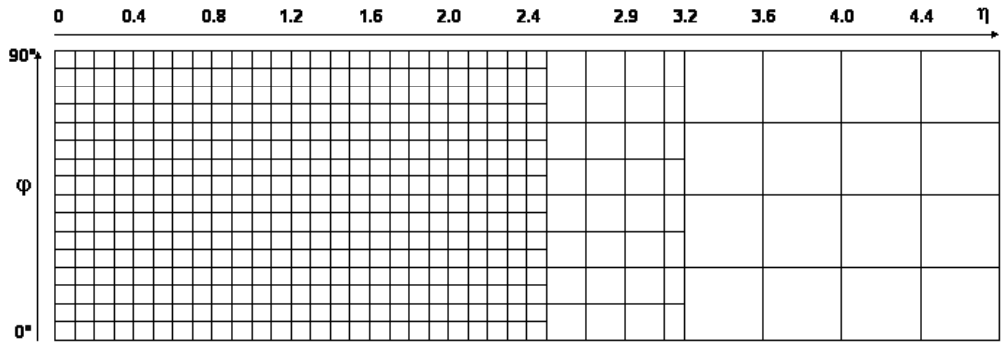

FIGURE 2.15: Trigger tower granularity for $\eta > 0$ and one quadrant in ϕ. From Ref. [110].

Results from the L1Muon and L1Calo triggers are processed by the central trigger processor (CTP), which is responsible for making the overall L1 accept/reject decision. For this, the CTP programs up to 256 configurations. The configurations consist mostly of E_{T} or p_{T} requirements and are, therefore, often referred to as thresholds. Nonetheless, different isolation criteria can be applied for L1 EM cluster and τ-lepton objects, and different sizes can be specified for L1 jet objects, as well. The CTP implements a trigger menu, i.e a list of L1 items. A L1 item is a logical combination of specified multiplicities of one or more of the configured L1 thresholds. For example, the item `L1_2EM25i` refers to events with, at least, two L1 isolated EM objects with $E_{\mathrm{T}} > 25$ GeV. A prescale factor N can also be associated to each of the L1 items in the menu, in which case only 1 in N events identified by that L1 item is passed on to the HLT. To allow for optimal use of the bandwidth with changes in luminosity and/or background conditions, the L1 prescales are adjustable within luminosity block[2] boundaries.

During the 2.5 μs latency of the L1 trigger, the event data, which is composed of different fragments, is held in pipeline memories, located within detector-specific front-end electronics. Once L1 accepts the event, the data is transferred to detector-specific Readout Drivers (RODs), via intermediate buffers - the "derandomizers" in Figure 2.14. Then, the data is passed to the DAQ/HLT system over Readout Links (ROLs). 1574 Readout Buffers (ROBs), contained in Readout System (ROS) units, receive and temporarily store the data fragments (one per ROB), either until the event is rejected by L2, in which case the data is discarded, or until the data has successfully been transferred by the DAQ system to the EF.

Though the L1 trigger decision is based only on the multiplicity of trigger objects, or flags indicating which thresholds were passed, L1 also defines one or more Regions-of-Interest (RoIs) in each identified event, with information that is subsequently used by

[2]During a data-taking run, a time interval in which the conditions do not change and lasting approximately one minute, is referred to as a luminosity block (LB). A LB is, in fact, the smallest granularity available during data-taking.

the HLT. The RoI data includes the $\eta - \phi$ position of the identified objects, information on the type of feature identified and the criteria (threshold) passed. Typically, RoIs are defined for all the objects that contributed to the event being selected - primary RoIs - though secondary RoIs, usually from low p_{T} objects, are also made available. For every selected event, the L1 RoIs are sent to the RoI builder, via eight dedicated ROLs. The RoI builder information can, then, be accessed by the L2.

2.4.3 Level 2

L2 has access to the entire event data, at full detector precision and granularity. However, the L2 trigger accesses data from the ROS selectively, based on the information obtained from the RoI builder. Only the data needed in order to make the L2 decision is moved, typically in regions around the RoI defined by L1. With this RoI approach, only $2 - 6\%$ of the total data volume is accessed by L2. The improved selection of L2, with respect to L1, is obtained by sharpening the E_{T} measurement, or even raising the thresholds of L1, applying further isolation criteria and using the information of the ID.

Once L2 obtains the information from the L1 RoIs, the decisions are applied in a series of steps, each refining the existing information by acquiring additional or more precise data, from increasingly more detectors. This step-wise decision is achieved using a sequence of feature extraction (FEX) algorithms, followed by hypothesis (HYPO) algorithms. FEX algorithms represent the bulk of the L2 trigger processing, as they consume most of the available time. Typically, they request detector data from within the RoIs and search for useful features. HYPO algorithms have very fast execution times, and determine whether the features identified by the FEX algorithms meet some pre-defined criteria. With this step-by-step approach, events can be rejected at an intermediate step, thereby minimizing the amount of data moved.

In a first step at L2, the FEX algorithms confirm the validity of a L1 object, using data from the sub-detector from where it originated, i.e. the muon system or the calorimeters. After this confirmation, the FEX algorithms search for additional features, potentially in other detectors. Muon, EM cluster and τ RoIs, for example, receive additional information from the ID tracking devices at L2. Jet RoIs, on the other hand, are processed in the calorimeters only (with the exception of b-tagging). All the information is, then, combined to form more specialized global L2 trigger objects, which become candidates for muons, electrons, photons, τ-leptons, jets, missing transverse energy and b-physics objects. Based on these objects, a global decision is taken using the trigger menu. The trigger menu includes not only the L1 item mentioned above, but the whole trigger chain, i.e. a full sequence of L1 $\rightarrow$ L2 $\rightarrow$ EF signatures, which is usually denoted by the EF signature name. This comprises the respective prescale factors, as well as possible pass-through factors, used to accept a fraction of the identified events, regardless of the actual decision of the trigger.

2.4.4 Event Filter

Once L2 accepts an event, the data fragments are collected from the ROBs, and the full event is built, in a process referred to as event building. After event building, the complete event is stored in a single memory, accessible by the EF. The EF is a processing farm, that performs the last step of online event selection. The steering of the event selection at the EF is very similar to that described above for the L2. However, due to the larger processing time available, the EF can use standard ATLAS event reconstruction and analysis algorithms (see Section 2.6), adapted to the online environment. The rejection power of the EF, compared to that of the L2, comes from having access the full event data, instead of just a fraction around the L1 RoIs, from using refined algorithms and better calibrations, and from tightening the $E_{\mathrm{T}}/p_{\mathrm{T}}$ thresholds, where necessary. Events that do not fulfill any of the EF selection criteria, established in the trigger menu, are permanently expunged from the system.

The processing of the EF should result in a complete tagging of the events, to allow for a subsequent efficient selection for physics analyses. Thus, in addition to selecting events, the EF also classifies them into a pre-determined set of inclusive event streams, based on the trigger type: `Muons`, `Egamma`, `JetTauEtmiss` and `MinBias` (triggers for inelastic *pp* collisions). Upon acceptance by the EF, each event is recorded locally in one or more files, according to this stream classification. The event files are then transferred to permanent storage at the CERN Computing Center, for later offline processing and analysis.

2.5 ATLAS simulation and computing

The ATLAS experiment has developed a computing model, i.e. a set of software and middleware tools, that allow members of the collaboration all over the world to access ATLAS data. The building blocks of this model are the Athena [111] software framework, which operates on top of a hierarchical model of computing - the GRID.

The ATLAS experiment is one of the most complex ever built, and running ATLAS software is very CPU intensive. Moreover, the amount of data produced by the LHC will simply be too large for individual scientists to have local access to. Thus, the GRID is used to created a distributed computing framework throughout several facilities in remote locations, that are able to communicate with each other and share tasks. Such facilities are referred to as Tiers. Tier-0 is located at CERN, and handles the most unrefined data, referred to as RAW data. Ten worldwide facilities constitute Tier-1, that deals primarily with event reconstruction. Approximately 35 more facilities form Tier-2, that provides the analysis abilities for the ATLAS collaboration.

Athena includes software for event simulation, event trigger, event reconstruction and physics analysis tools. Event simulation [112] is fundamental in an experiment such as ATLAS. It carries the events from generation to output, in a format which is identical to that of the true detector, allowing for a direct comparison (on a statistical

basis) between the real data and the theoretical models. The simulation software chain is generally divided into three steps. The first is the generation of events using a MC program, as described in Section 1.2.1.3. The second step is the simulation of the detector and physics interactions. In ATLAS, the simulation is integrated into ATHENA and uses the GEANT4 [113] simulation toolkit. GEANT4 basically simulates the entire ATLAS detector (material, geometry and subsystems, including trigger) and its response to traversing particles. Digitization is the last step, and consists in converting the energy deposited in the sensitive regions of the detector into voltages and currents, for comparison to the readout of the ATLAS detector. The output of this process is referred to as RAW data, and is identical to the output of the ATLAS TDAQ system during real data-taking (see Section 2.4.1).

The complexity of the full simulation (FullSim) of the ATLAS detector just described, has led to the development of fast simulation strategies. These allow for a faster production of the high simulated event statistics needed for physics analyses. ATLFAST-II [112] is a fast simulation framework developed for the ATLAS experiment. It is made of two components: the Fast ATLAS Tracking system (Fatras), for ID and MS simulation, and the Fast Calorimeter Simulation (FastCaloSim), for calorimeter simulation. Optionally, any of these sub-detectors can be simulated with the nominal GEANT4, providing flexibility to suit the needs of different physics analyses.

To summarize, whether ATLAS data is simulated or real, its most primary form is called RAW data. Once collected, RAW data is transferred to Tier-0, where the offline event reconstruction is performed. The output of these reconstruction algorithms is, typically, ESD (Event Summary Data) or AOD (Analysis Object Data) files, that are exported to the various Tier-1 and Tier-2 locations. From these, DPDs (Derived Physics Data) can be obtained. These are light, n-Tuple-like files, that contain only a small amount of information on the events, to be used for direct analysis by the individual scientists, usually performed using the ROOT [114] framework.

2.6 Event reconstruction in ATLAS

Events accepted by the ATLAS trigger system are stored on tape, for later offline analysis. The term "event reconstruction" refers to the set of methods and algorithms, implemented in ATHENA, employed to transform the output of the ATLAS detector into physically meaningful objects, such as electrons, muons or jets, and complete event kinematics. Event reconstruction software is applied to RAW data, either from real data events or from simulated events. In this section, the reconstruction of different physics objects in ATLAS is described, with focus on those relevant to the analyses presented in Chapters 3 and 4.

2.6.1 Tracks and vertices

The goal of track reconstruction is to accurately determine the trajectories of charged particles in the ATLAS detector. Moreover, reconstruction of common intersection

points of a set of tracks is necessary to identify collision vertices, or decay vertices of unstable particles. These represent fundamental aspects in the reconstruction of electrons, muons, jets, b-jets, primary vertices, among others.

2.6.1.1 ID tracking

Charged particles produced at the IP of ATLAS enter the ID and solenoid field, and follow a circular trajectory in the transverse plane. Their tracks can be fully described by a set of five parameters:

- q/p_{T}, the charged curvature, where q denotes the electric charge and p_{T} the transverse momentum;
- ϕ, the azimuthal angle;
- θ, the polar angle;
- d_0, the transverse impact parameter, i.e. the distance of closest approach of the track to the reference point[3] in the transverse $x-y$ plane;
- z_0, the longitudinal impact parameter, i.e. the z coordinate of the track at the point of closest approach mentioned in the previous bullet point; strictly speaking, the longitudinal impact parameter is $|z_0|\sin\theta$.

In the ATLAS ID, tracks can be measured with $p_{\mathrm{T}} > 100$ MeV and $|\eta| < 2.5$.

ID tracking [115, 116] consists of two sequences of reconstruction algorithms: the main inside-out track reconstruction, and a consecutive outside-in tracking. The first step in the inside-out sequence is the creation of three-dimensional representations of the hits in the silicon detectors, or space-points. Three space-points, which are required to be in different layers of the silicon detectors, form a track seed. Further hits are then added, moving away from the interaction point, and a track candidate is built, using a combinatorial Kalman filter [117]. Seeds can fail to become track candidates, e.g. if the final number of hits does not meet the predetermined requirements. Each seed can become, at most, a single track candidate, and seeds for which all space-points have already been used to build a track candidate will be discarded. Once ambiguities are resolved, the track candidates are extended into the TRT.

In the outside-in approach, the track search starts from segments reconstructed in the TRT, and extends them inwards by adding silicon hits, in a process referred to as back-tracking. Back-tracking is designed to reconstruct tracks from secondary interactions. Tracks with a TRT segment, but no extension into the silicon detector, are referred to as TRT-standalone tracks.

The increasing detector occupancy with pile-up results in a degradation of the track reconstruction, as it increases the combinatorial fake tracks, i.e. reconstructed tracks

[3]The primary vertex (hard scatter collision vertex) is, generally, the reference for track reconstruction but, until it is know, the center of the luminous region (beamspot) is used as a preliminary reference.

which cannot be matched to either a primary vertex or a secondary particle. Robust requirements on the hits (measurement points assigned to a track), holes (non-existing but expected measurement points), and outliers (hits that reduces the quality of the track fit) of the silicon detectors are used to minimize this impact, and improve the quality of the reconstructed track. Moreover, cuts on the d_0 and z_0 impact parameters (or their errors, denoted by σ) are also generally used in analyses, to ensure the track originates from the primary hard-scattering vertex.

The performance of the ID tracking in ATLAS has been studied using $\sqrt{s} = 7$ TeV data [118, 119]. A reasonably good description of the data by the MC simulation was found, and it was shown that the reconstruction algorithms are robust in a high pile-up environment.

2.6.1.2 Primary vertices

For any physics analysis, knowledge of the position of the primary interaction point of the *pp* collision, referred to as the primary vertex (PV), is essential. It allows for an accurate reconstruction of the tracks, which are usually refitted under the constraint that they originate from the reconstructed PV. Furthermore, the number of primary vertices (N_{PV}) in an event provides a direct measurement of the in-time pile-up.

PV reconstruction [120] in ATLAS is organized in two iterative steps: the vertex finding algorithm, which associates reconstructed tracks to the vertex candidates, and the vertex fitting algorithm, dedicated to the reconstruction of the vertex position and corresponding error matrix. First, reconstructed tracks passing some selection criteria are pre-selected. Then, a vertex seed is found, by looking for a global maximum in the distribution of z coordinates of the tracks, here computed with respect to the center of the beamspot. The vertex position is determined using the adaptive vertex fitting algorithm [121], constrained by the beamspot position. It is a robust χ^2-based fitting, that takes the input seed and the tracks around it. Each track carries a weight, which is a measure of its compatibility with the fitted vertex. Tracks incompatible with the vertex by more than $\sim 7\sigma$ are used to seed a new vertex, and the procedure is repeated until no tracks are left.

Reconstructed primary vertices have at least two tracks originating from them. In each event, the PV with the largest $\sum p_{\mathrm{T}}^2$ of associated tracks is identified as the hard scatter PV, while the others are considered to originate from in-time pile-up interactions.

The performance of primary vertex reconstruction in ATLAS has been evaluated with $\sqrt{s} = 7$ TeV data [118, 120]. The increasing density of collisions with pile-up degrades the vertexing performance, especially because of vertices which are too close together to be resolved. However, it was found that this is adequately described by the simulation. Furthermore, the probability to reconstruct fake vertices increases with pile-up, but it can be controlled with robust quality requirements on the tracks.

2.6.2 Muons

Muons produced at the IP of ATLAS will traverse the ID and the calorimeters, and lose a fraction of their energy, mainly through EM processes, before reaching the MS, which is the main instrument used to identify them. ID information is often used in addition to the MS, as it provides an independent measurement of the muon momentum. The calorimeters can also be used, though to a smaller extent.

A general description of tracking in the ID has been provided in Section 2.6.1.1. Tracking in the MS [122] is logically subdivided into four stages. First, the raw data is processed to form drift-circles in the MDT and clusters in the CSC. Track segments, defined as straight lines in a single MDT or CSC station, are then formed from the patterns of drift-circles and clusters. Track candidates are built from these segments, typically starting from the outer stations and extrapolating back through the magnetic field and to the inner stations. The track-fitting procedure takes into account all relevant effects, to obtain the final track candidates.

In what follows, the different aspects related to the reconstruction of muons in ATLAS, including reconstruction at the trigger level, are described.

2.6.2.1 Reconstruction and indentification

Different muon identification strategies exist in ATLAS, and lead to four different types of muons [122, 123]:

Stand-alone (SA) muons are reconstructed using the MS only, with the direction of flight and the impact parameter at the IP determined by extrapolating the MS track back to the point of closest approach in the beam line, taking into account the energy loss in the calorimeters;

Combined (CB) muons are identified from the successful combination of a SA track and an independent ID track;

Segment-tagged (ST) muons are reconstructed from a track in the ID, which is extrapolated to the MS and has at least one track segment in the MDT or CSC;

Calorimeter-tagged (CaloTag) muons are reconstructed from a track in the ID, which is associated to an energy deposit in the calorimeter as expected from a minimum ionizing particle.

CB candidates can be reconstructed up to $|\eta| < 2.5$, and constitute the sample with the highest muon purity. CB muons are used in this thesis and the following descriptions will be focused on them, unless stated otherwise.

The reconstruction of CB muons is performed using two independent and complementary algorithms, referred to as chains: Staco (or Chain-1) and Muid (or Chain-2) [122, 123]. The Chain-1 algorithm performs a statistical combination of the track

parameters of the SA and ID muon tracks, using the covariance matrices of both measurements. Chain-2, on the other hand, performs a global refit of the muon tracks, using both ID and MS measurements. Chain-1, used in this thesis, is typically more robust against background, whilst Chain-2 has a slightly higher efficiency.

Because the track reconstruction in the ID and in the MS are independent, the overall reconstruction efficiency for Chain-1 CB muons can be computed as the product of the reconstruction efficiency in the ID, the reconstruction efficiency in the MS, and the track matching efficiency between the ID and the MS. A tag-and-probe method [122, 123] is employed to determine both the efficiency in the ID, and the combined MS reconstruction times matching efficiency.

The tag-and-probe method uses a sample of $Z \to \mu^+\mu^-$ events, selected by requiring two oppositely charged, isolated tracks, with a dimuon invariant mass near that of the Z boson. This sample has a purity of more than 99.9%, with background contributions from $Z \to \tau\tau$, $W \to \mu\nu$, $W \to \tau\nu$, $b\bar{b}$, $c\bar{c}$ and $t\bar{t}$ processes. One of the tracks, labelled the tag, is required to be a CB muon, and to have triggered the event. If the ID efficiency is to be measured, the other track, referred to as the probe, is required to be a SA or CB muon. On the other hand, if the goal is to determine the MS and matching efficiency, the probe track is required to be an ID track or a CaloTag muon. It has been shown [123] that the latter reduces the $Z \to \mu\mu$ backgrounds, without biasing the efficiency measurement.

Once the tags and probes are selected, the ID reconstruction efficiency is calculated as the fraction of SA or CB probes that have a match to ID tracks. A successful match is evaluated if the probe and the ID track have the same measured charge, and are close-by in the $\eta - \phi$ plane, with $\Delta R < 0.01$. Similarly, the MS and matching efficiency is computed as the fraction of ID or CaloTag probes that have a match to a CB muon, this time using $\Delta R < 0.05$.

The overall reconstruction efficiency for Chain-1 CB muons, evaluated with data collected in 2012 [123], is shown in Figure 2.16 for both data and MC simulation, as a function of η and p_{T} of the muon. The ratio of the efficiencies in data and MC, referred to as the efficiency scale factor (SF), is shown in the bottom part of the plots. The efficiency SFs are used to correct the simulated efficiency to the one observed in data, in bins of ϕ and η, at the analysis level. Since the simulation reproduces well the data, the SFs are, in general, very close to unity (within $2 - 3\%$).

Figure 2.16b indicates that the CB muon reconstruction efficiency has no dependence with p_{T}, in the evaluated range. However, Figure 2.16a shows the efficiency is strongly affected by the acceptance of the MS. This is visible at $\eta \approx 0$, where a gap in the MS exists for ID services, as well as for $|\eta| \approx 1.2$, between the barrel and the end-caps, where some muon chambers, in certain regions in ϕ, had not yet been installed. Nonetheless, the overall Chain-1 CB muon reconstruction efficiency observed in data is above 96%.

Efficiency SFs have different sources of systematic uncertainty [122, 123]. Variations on the dimuon selection cuts induce changes in the scale factors, that are quoted as systematic uncertainties. A 0.2% systematic uncertainty on the SF arises from the

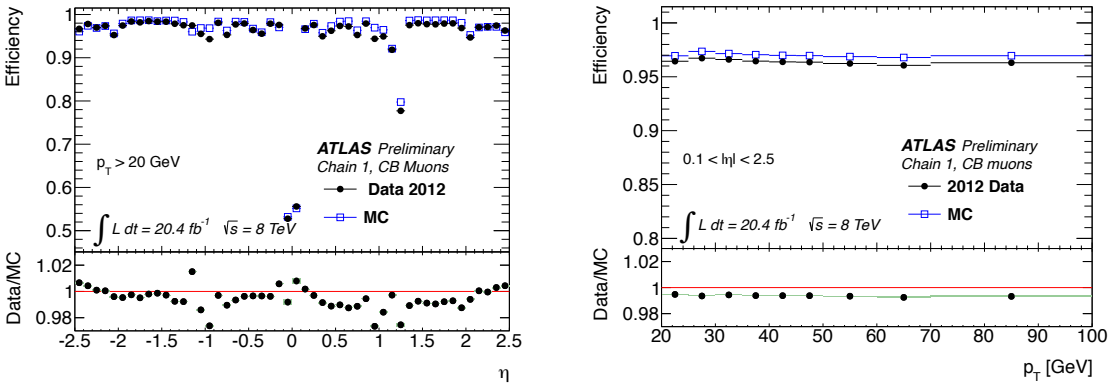

(a) (b)

FIGURE 2.16: Reconstruction efficiency for Chain-1 CB muons, as a function of: (a) η of the muon, for muons with $p_{\mathrm{T}} < 20$ GeV; and (b) p_{T} of the muon, for muons with $0.1 < |\eta| < 2.5$. The panel at the bottom shows the efficiency scale factors, i.e. the ratio between the observed and predicted efficiencies. From Ref. [123].

comparison of using CaloTag muon probes or ID track probes, and from the evaluation of the residual background contamination of the $Z \to \mu\mu$ sample. The comparison of the efficiencies with those measured using the tag-and-probe method on $J/\psi \to \mu\mu$ decays, provides an additional systematic of $1 - 2\%$ for muons with $p_{\mathrm{T}} < 10$ GeV. Finally, for muons with $p_{\mathrm{T}} > 100$ GeV, a systematic uncertainty in the form of $1\% \times p$ (in TeV) is added, based on a 10% variation of the muon energy loss in the calorimeters.

2.6.2.2 Momentum scale and resolution

For CB muons, the combination of an ID and a MS track ensures good momentum resolution over three orders of magnitude, with the ID dominating the momentum resolution at low muon p_{T}, and the MS dominating at high p_{T}. Determination of the muon momentum resolution, as well as the momentum scale [122, 123], is fundamental to understand the muon reconstruction performance of ATLAS. This is done using $Z \to \mu\mu$ events.

Figure 2.17a shows the invariant mass distribution of events with two isolated, opposite charge, Chain-1 CB muons, around the Z mass peak, for both 2012 data and simulation [123]. The dimuon mass resolution observed in data ranges from 1.5 to 3 GeV, depending on the η region, and has a shift and a larger spread with respect to the MC prediction. The mass resolution is translated into muon momentum resolution and scale, by smearing the generated muon momentum until the simulation reproduces the observed dimuon invariant mass. The corrected dimuon mass spectrum is displayed in Figure 2.17b, showing the clear improvement in the data/MC agreement. The muon momentum scale is corrected by approximately 0.1%, and has an uncertainty ranging from 0.1% to 0.2%, validated using $J/\psi \to \mu\mu$ and $\Upsilon \to \mu\mu$ decays. The muon momentum scale corrections and resolution smearing are applied to MC simulation in the studies presented in this thesis.

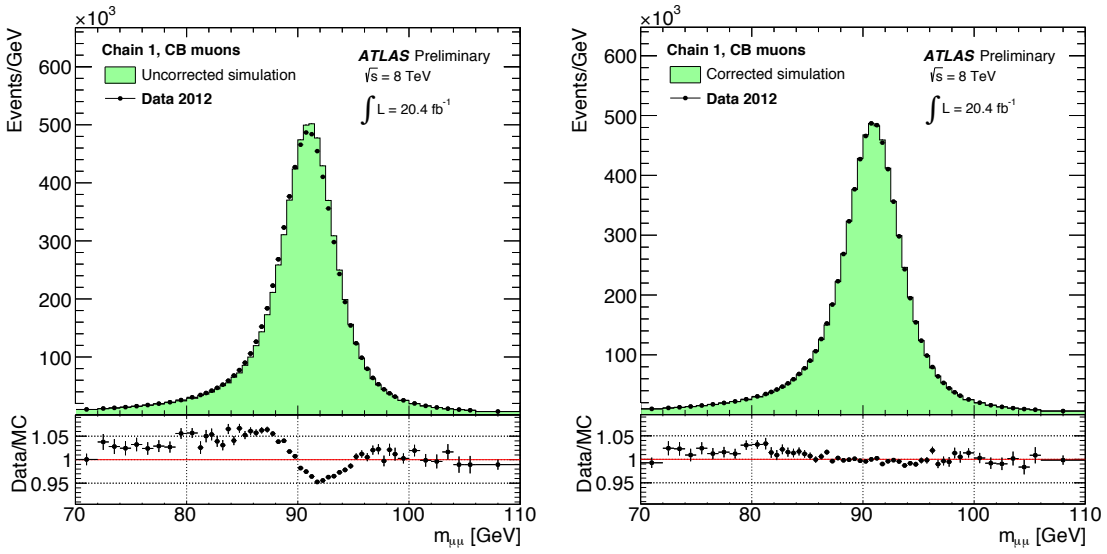

FIGURE 2.17: Dimuon invariant mass of isolated, opposite charge, Chain-1 CB muons, around the Z mass peak, for 2012 data and $Z \to \mu\mu$ simulation: (a) before any corrections; and (b) after smearing and scale corrections. From Ref. [123].

2.6.2.3 Isolation

Lepton isolation is a powerful tool in any physics analysis, as it allows the selection of samples with higher purity. It is generally used to reject QCD backgrounds and select leptons from EW decays. In the case of muons, isolation is particularly useful to suppress muons originating from heavy quark or hadron decays, which are generally accompanied by additional particles close-by.

Two types of isolation [122] varibales are usually defined:

Track isolation - the scalar sum of p_{T} of good quality tracks, in a cone of radius ΔR (usually $\Delta R < 0.3, 0.4$) around the muon, excluding the muon track, divided by the muon p_{T};

Calorimeter isolation - the E_{T} sum of energy depositions in the calorimeters, in a cone of radius ΔR (usually $\Delta R < 0.3, 0.4$) around the muon, excluding the muon energy loss, divided by the muon p_{T}.

Isolation efficiencies are determined using the tag-and-probe method, described in Section 2.6.2.1 above. They are defined as the fraction of probe muons passing a given set of isolation cuts. The dependence of the isolation efficiencies with pile-up was studied using 2011 data [124]. While the track isolation efficiency, shown in Figure 2.18a, shows very little dependence in the primary vertex multiplicity, there is a clear degradation of the efficiency for calorimeter isolation in a high pile-up environment, as illustrated in Figure 2.18b. A quadratic correction is, therefore, applied to the calorimeter isolation, which is able to recover the efficiency at high number of primary vertices.

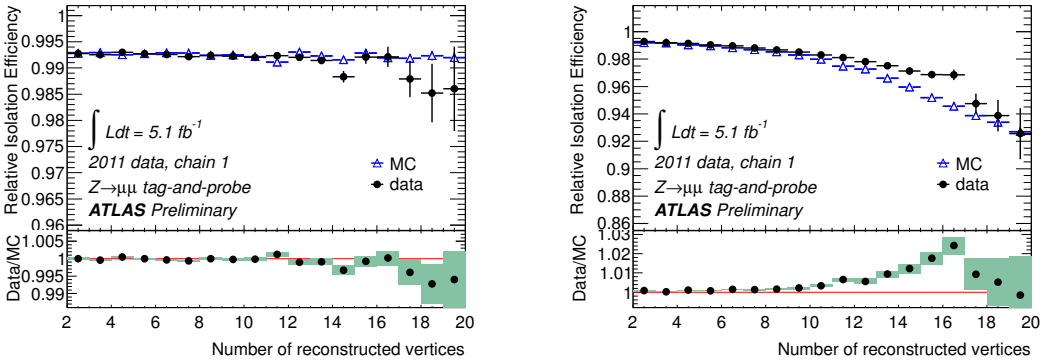

FIGURE 2.18: Muon isolation efficiency in $Z \to \mu\mu$ decays for: (a) a track isolation cut of $\sum p_{\mathrm{T}}(\Delta R < 0.3)/p_{\mathrm{T}}^{\mu} < 0.15$; and (b) a calorimeter isolation cut of $\sum E_{\mathrm{T}}(\Delta R < 0.3)/p_{\mathrm{T}}^{\mu} < 0.13$ (before pile-up correction). From Ref. [124].

Similar to what was described for the reconstruction efficiency scale factors, isolation scale factors are also applied as MC corrections at the analysis level. These are meant to correct the isolation efficiencies predicted by the simulation to match the ones observed in data. Since the MC describes the data well, these scale factors are generally close to unity, as shown in the ratios of Figure 2.18.

2.6.2.4 Muon trigger

Muon identification at the trigger level makes use of three trigger stations at each of the RPC and TGC detectors. The L1Muon [101] trigger algorithm requires a coincidence of hits in these stations, within a road that tracks the path of the muon from the IP through the detector. The coincidence is required in both η and ϕ projections, as well as in time. The width of the road is related to the p_{T} of the muon. The RoIs are defined with a granularity of 0.1×0.1 (0.3×0.3) in $\Delta\eta \times \Delta\phi$ in the RPC (TGC). The geometric coverage of the L1 trigger is of $\sim 99\%$ in the end-caps, and $\sim 80\%$ in the barrel, due to regions of the MS not covered by the RPC.

Three types of muon algorithms are available at L2 [125], which use the information within the L1 RoIs. First, the L2 standalone (SA) algorithm performs a muon track fit, using information from the MDT chambers. Tracks reconstructed in the ID can also be combined with SA tracks, using a fast track combination (CB) algorithm. Isolation algorithms also exist at L2, which discriminate between isolated and non-isolated muons by examining energy depositions in the calorimeter.

The EF [125] processing starts by reconstructing tracks in the MS precision chambers, around the muon candidates identified by the L2. These tracks are extrapolated to the IP, forming a SA EF muon candidate. Similar to L2, SA tracks are generally combined with tracks reconstructed in the ID, forming a CB EF muon. This "outside-in" approach is complemented with an "inside-out" strategy, where the ID tracks are

reconstructed first, and then extrapolated to the muon detectors. The use of complementary strategies improves the overall performance and efficiency during data-taking. Offline-like algorithms are used at the EF, at full detector granularity.

Figure 2.19 shows the combined efficiency of two single muon trigger chains, which ran unprescaled during 2012 data-taking [126], as a function of the offline muon p_{T}. These chains are used in the studies presented in this thesis. The efficiencies are, again, determined using $Z \to \mu\mu$ events and the tag-and-probe method [125], and defined as the fraction of L1, L2 and EF muon objects that match the probe muon and pass the respective trigger requirements. The curves in Figure 2.19 show a sharp turn-on for $p_{\mathrm{T}}^{\mu} > 25$ GeV, where they reach a plateau efficiency of $\sim 70\%$ in the barrel (Figure 2.19a) and $\sim 86\%$ in the end-cap (Figure 2.19b). The efficiencies below 100%, particularly in the barrel region, are caused by the geometric coverage of the L1Muon trigger, which is about $\sim 80\%$ in the barrel, due to the gap at $\eta \approx 0$ for ID services. Similar to what has been described for reconstruction and isolation efficiencies, also trigger scale factors are computed as the ratio between data and MC trigger efficiencies, to correct for the mismodeling of the trigger performance in simulated samples. These scale factors are applied at the analysis level for physics studies

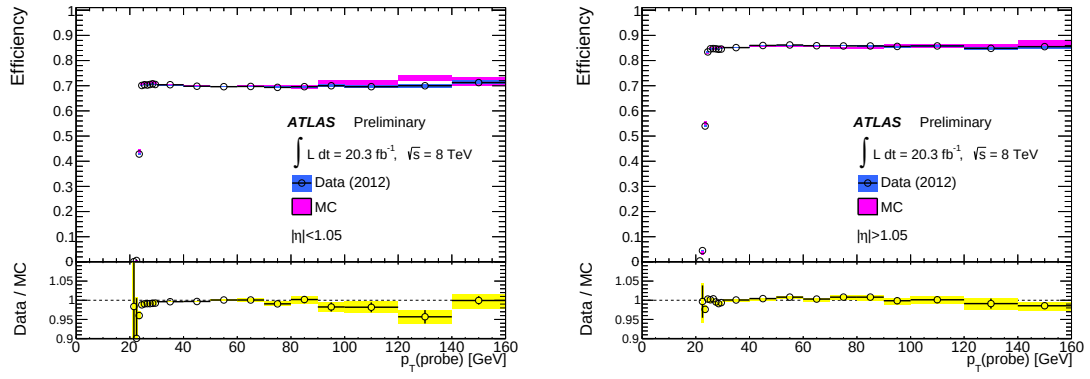

(a) (b)

FIGURE 2.19: Efficiency of two single muon trigger chains (i.e. L1→L2→EF sequence of selections), `mu24i_tight` and `mu36_tight`, convolved as an OR between the two, measured with respected to offline reconstructed muons in the: (a) barrel; and (b) endcap. From Ref. [126].

2.6.3 Electrons

In the ATLAS detector, central electrons are reconstructed up to $|\eta| < 2.47$, from energy deposits in the EM calorimeter, matched to tracks in the ID. They can be distinguished from other particles using different identification criteria. Further suppression of backgrounds is achieved through isolation. The different aspects related to electron objects in ATLAS, including identification at the trigger level, are discussed in the following sections.

2.6.3.1 Reconstruction and identification

The first step of electron reconstruction [127–129] is the reconstruction of the EM cluster. For this purpose, the EM calorimeter of ATLAS (see Section 2.3.3.1) is divided into towers, with a granularity of 0.025×0.025 ($\Delta\eta \times \Delta\phi$). A sliding-window, with a size of 3×5 towers, searches for towers with a total transverse energy above 2.5 GeV. EM clusters are reconstructed from these seed towers. Simulation predicts an efficiency of EM cluster reconstruction of 100%, for true electrons with $E_{\mathrm{T}} > 20$ GeV, originating from W or Z boson decays.

Tracks reconstructed in the ID (see Section 2.6.1.1), with $p_{\mathrm{T}} > 400$ GeV, are extrapolated to the middle layer of the EM calorimeter. The extrapolated coordinates of the tracks are compared to the coordinates of the EM cluster, and the two are loosely matched, using requirements on $\Delta\eta$ and $\Delta\phi$. An electron candidate is reconstructed if at least one track is matched to the seed cluster. In the case of several tracks being matched, preference is given to the one with silicon hits and closest to the cluster in the $\eta - \phi$ space. If no tracks are matched, the cluster is classified as an unconverted photon candidate.

At this point, the parameters of the electron-track candidates are re-estimated using Gaussian Sum Filter (GSF) [130], which improves the result of the Kalman filter (see Section 2.6.1.1) by taking bremsstrahlung effects into account. The track-cluster matching procedure is then repeated, using the GSF refitted tracks and tighter matching requirements.

All seed clusters with matching tracks are considered electron candidates. The clusters of electron candidates are rebuilt in all layers of the EM calorimeter sequentially, now using 3×7 (5×5) cells in the barrel (endcaps). The cluster position is adjusted in each layer, to take into account the distribution of the energy deposition. The electron candidate energy is determined by summing the estimated energy deposited in the material in front of the EM calorimeter, the measured energy deposited in the cluster, the estimated energy deposited outside the cluster (lateral leakage), and the estimated energy deposited beyond the EM calorimeter (longitudinal leakage). The η and ϕ coordinates of the electron candidate are taken from the matching track parameters.

A sample of electrons reconstructed as just described, has significant contributions from background objects such as hadronic jets, and electrons from photon conversions, Dalitz decays and semi-leptonic heavy flavor hadron decays. Electron identification [127–129] uses several discriminating variables to suppress these backgrounds, while keeping high efficiency for signal electrons. A cut-based menu, where electrons are identified by sequential cuts on the variables, as well as a likelihood (LH) menu, where multivariate analysis (MVA) techniques are employed, are available.

Electrons and photons deposit nearly all of their energy in the EM calorimeter, and typically less than 1% of the energy enters the hadronic calorimeter. Moreover, electron and photon showers are generally smaller, in the plane orthogonal to its direction, than hadronic showers. These are some of the features exploited by the electron identification variables. An exhaustive list of these variables can be found in Ref. [129]. They include

leakage of the EM cluster energy into the hadronic calorimeter, amount of energy in the last layer of the EM calorimeter, width and shape of the EM shower, quality of the track (number of hits in the silicon detectors, impact parameters), information of the TRT, quality of the track-cluster matching, and photon conversions.

Three identification categories are available in the cut-based menu [129]: *loose++*, *medium++* (which is a subset of *loose++*), and *tight++* (which is a subset of *medium++*)[4]. Each category adds cuts on more discriminating variables with respect to the previous category, and also tightens the cuts on the variables already used. The result is higher background rejection as one moves to the tighter categories, at the cost of lower electron efficiency. A *multilepton* category also exists, which has a similar signal efficiency to the *loose* operating point, but with better background rejection. The cut-based menu has been changed throughout the different data-taking periods, to cope with the increase in pile-up.

As for the LH menu [129], it contains three identification selections: *loose*, *medium*, and *very tight*. Each of these selections cuts on a different LH discriminant, built with different electron variables. The operating points of the LH menu were designed to match the signal efficiencies of the cut-based *multilepton*, *medium* and *tight* selections, while providing more background rejection. The background rejection, measured in simulation, ranges from $\sim 95 - 99.5\%$ for the cut-based menu, and from $\sim 99 - 99.7\%$ for the LH menu.

Similar to what has been described for muons, electron reconstruction and identification efficiency is measured with the tag-and-probe method, using $Z \to ee$ and $J/\psi \to ee$ decays [127–129]. Samples with two opposite charge electrons and a reconstructed dielectron invariant mass compatible with the masses of Z and J/ψ resonances are selected. Strict selection criteria are applied to one of the electrons in the pairs, which becomes the tag. The remaining electrons in the pairs are referred to as the probes. The efficiency is defined as the fraction of probe electrons passing the selection under testing. The reconstruction efficiency is measured with respect to clusters in the EM calorimeter, whereas the identification efficiency is determined with respect to reconstructed electrons.

The combined identification and reconstruction efficiency was studied using data collected in 2012 [129]. Figure 2.20 shows this efficiency measured in data and MC, for the different identification categories of the LH menu. The shapes of the curves are mostly determined by the identification efficiency, since the reconstruction efficiency is approximately flat, ranging from $95 - 99\%$, depending on E_{T} and η. The data-to-MC ratio of efficiencies, shown in the lower panels of the distributions, are applied as correction scale factors to the MC, in bins of E_{T} and η, at the analysis level. The increase of the efficiency with E_{T}, shown in Figure 2.20a, is expected, since electrons become better separated from background. The dependence of the efficiency with η, displayed in Figure 2.20b, is dominated by features of the ATLAS detector. In particular, the large drop in efficiency observed for $1.37 < |\eta| < 1.52$, corresponds to the transition region

[4]For 2011 data-taking, the working points of the so-called "plus-plus menu" had looser counterparts - *loose*, *medium* and *tight* - but these were abandoned in 2012.

between the barrel and endcap calorimeters. In physics analyses, electrons reconstructed in this so called crack region are generally excluded.

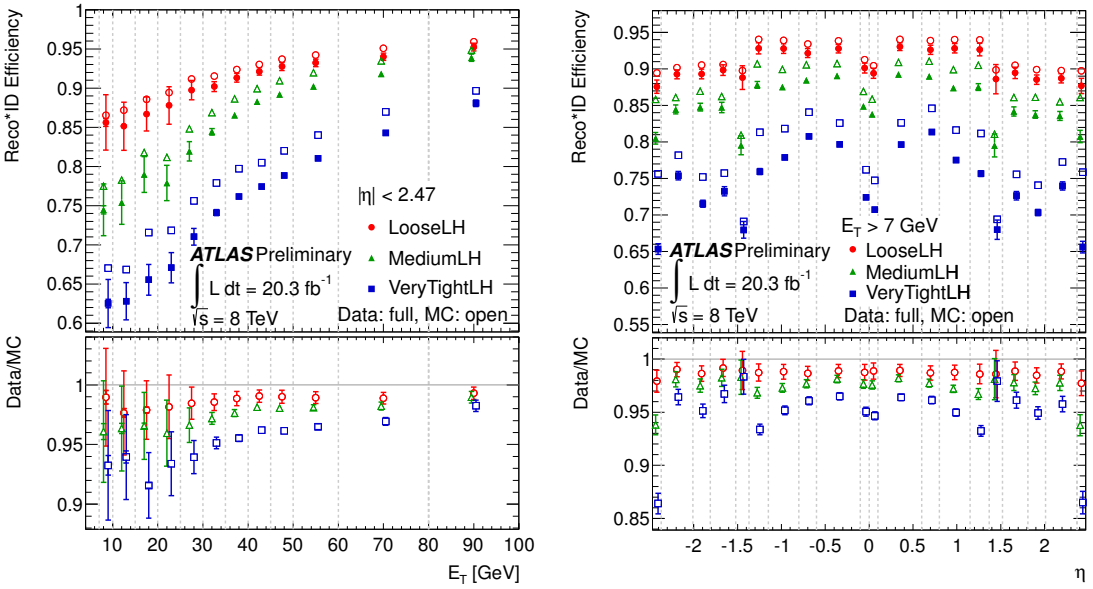

(a) (b)

FIGURE 2.20: Combined reconstruction and identification efficiency for electrons identified with the LH menu, as a function of: (a) electron E_{T}; and (b) electron η. The panel at the bottom shows the efficiency scale factors, i.e. the ratio between the observed and predicted efficiencies. From Ref. [129].

The impact of in-time pile-up was also assessed, by looking at the dependence of the electron efficiencies with the number of primary vertices, and shown to be below 4%.

Systematic uncertainties on the electron efficiencies are estimated by recomputing the efficiency measurements with some modifications, for example on the selection of the tag electrons or the background estimation method. The total uncertainty on the identification efficiency measurements depends on η and E_{T}, and amounts to $\sim 5-6\%$ ($\sim 1-2\%$) for electrons with $E_{\mathrm{T}} < 25$ GeV ($E_{\mathrm{T}} > 25$ GeV).

2.6.3.2 Energy calibration, scale and resolution

The four terms that contribute to the electron energy - estimate of energy in front of the EM calorimeter, energy measured in the cluster, lateral leakage and longitudinal leakage, as described in Section 2.6.3.1 - are parametrized as a function of the cluster energy. The parametrization is based on detailed simulations, that accurately describe the geometry of the ATLAS detector and the interactions of particles with matter. It allows for the application of a MC-based calibration to both data and simulation, at the cluster level [127, 131], that corrects for energy lost in the passive material, in the material upstream and beyond the calorimeter, and for leakage outside the cluster, among others. At this point, the electron energy scale is predicted to be better than 1%. However, as will be shown next, the well-known mass of the Z resonance can be

used to further calibrate the electron energy, and improve the knowledge on the energy scale and resolution.

Mis-calibration of the electron energy induces a shift in the invariant mass distribution of $Z \to ee$ events. Thus, residual calibration corrections [131] for the electron energy scale are determined by a fit, that tests compatibility of the dielectron invariant mass of $Z \to ee$ decays in data, with the Z lineshape predicted in simulation. Because it is found that the electron energy resolution in data is, in fact, slightly worse than that in simulation, a correction for the simulated electron resolution is also computed in the fit. The fit is performed in bins of η. Variations of the fit procedure, changes in the electron identification criteria or event selection, and background estimation procedures, are among the different sources of systematic uncertainty. After the corrections are applied, the dielectron mass distributions in data and simulation agree at the level of $1 - 2\%$, which, as shown in Figure 2.21a, is within the uncertainty on the electron calibration.

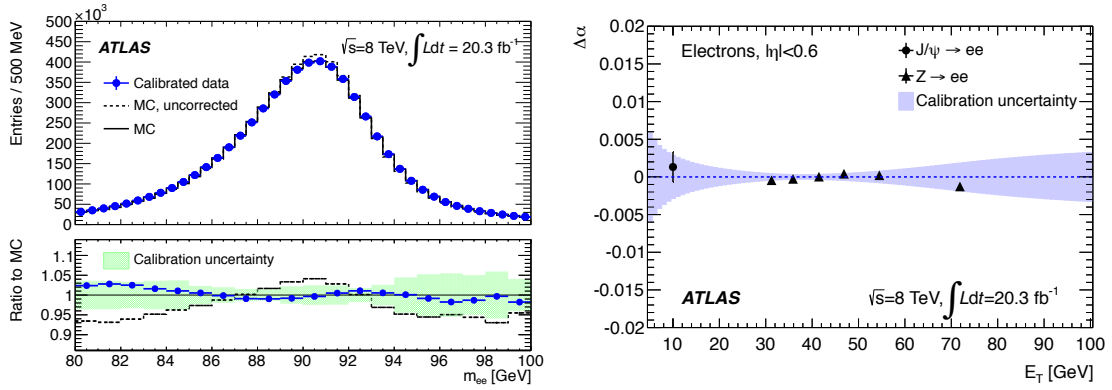

(a) (b)

FIGURE 2.21: (a) Dielectron invariant mass distribution for $Z \to ee$ decays in data and simulation; energy scale corrections are applied to the data; the simulation is shown before and after the energy resolutions corrections; the ratio between data and simulation is shown in the bottom pad, which also displays the uncertainty on the electron calibration. (b) Electron energy scale corrections, computed as a validation in bins of electron E_{T}, using calibrated electrons with $|\eta| < 0.6$ from $Z \to ee$ and J/ψ decays; the uncertainty on the electron energy calibration is shown by the colored band. From Ref. [131].

After the electron energy is fully calibrated, the electron energy scale is validated by recomputing the corrections, this time in bins of E_{T}, over broad η ranges. $J/\psi \to ee$ decays are used together with $Z \to ee$, to provide an additional cross-check [131]. As illustrated in Figure 2.21b for electrons with $|\eta| < 0.6$, the resulting corrections (labelled $\Delta\alpha$) are, as expected, constant and close to zero, within $1 - 2‰$. The calibrated energy scale is accurate within $0.04 - 1.1\%$, depending on E_{T} and η of the electron (accuracy is worse in the crack region). Finally, the electron energy resolution has a relative uncertainty of 10%, that rises to 40% for high E_{T}.

2.6.3.3 Isolation

Also for electrons, further rejection of backgrounds originating from hadronic jets can be achieved by applying isolation requirements, on top of the electron identification selection:

Calorimeter isolation - defined as the sum of transverse energy deposited in calorimeter cells or topological clusters in a cone of ΔR (typically $\Delta R = 0.3, 0.4$) around the electron, excluding cells within 0.125×0.175 ($\Delta\eta \times \Delta\phi$) of the electron cluster; calorimeter isolation is corrected from energy leakage from the electron to the isolation cone, as well as for the effect of pile-up, using a correction parametrized as a function of the number of primary vertices;

Track isolation - defined as the scalar sum of p_{T} of good quality tracks with $p_{\mathrm{T}} >$ 400 MeV, in a cone of radius ΔR (typically $\Delta R = 0.3, 0.4$) around the electron, excluding the electron track.

Isolation cuts are typically applied on these isolation variables divided by the E_{T} of the electron. Studies of isolation in simulated events [132] show that with an optimized selection on isolation variables, it is possible to reject over 60% of hadronic jets in a sample of tight electrons, while maintaining a 95% efficiency for the signal. Isolation efficiencies are, as usual studied using $Z \to ee$ events and the tag-and-probe method. At the analysis level, isolation SFs are applied to simulation, in order to reproduce the efficiency of the isolation cuts observed in data.

2.6.3.4 Electron trigger

The L1Calo system includes the Cluster Processor (CP), which contains the electron/photon trigger algorithm [101] (as well the τ trigger algorithm), used to identify electrons at the first level of the trigger system. As illustrated in Figure 2.22, a sliding-window, of 4×4 trigger towers, identifies 2×2 EM clusters (shown in green), whose center defines the RoI position. The most energetic of two neighboring EM towers in the cluster, out of the four combinations possible, must pass the pre-defined trigger threshold. Isolation thresholds are set, either by using the 12 towers surrounding the EM cluster in the EM and hadronic calorimeters (rings), or by using the four hadronic trigger towers located behind the EM cluster (core). Isolation is set in absolute values, rather than ratios of isolation energy to cluster energy. Overlap of neighboring sliding-windows is prevented by requiring that the transverse energy in the EM cluster is a local E_{T} maximum (more in Section 2.6.4.5 ahead).

L2 [102] receives the L1 RoI and accesses the detector data around it at full granularity. The L2 cluster building algorithm scans the cells in the second layer of the EM calorimeter, searching for the one with the highest E_{T}. Subsequently, a cluster of 0.075×0.175 in $\Delta\eta \times \Delta\phi$, referred to as the pre-seed, is built around this cell. Shower shapes and hadronic leakage computations are exploited at L2 to select a sample of electrons and photons clusters, with low background contamination. The reconstruction

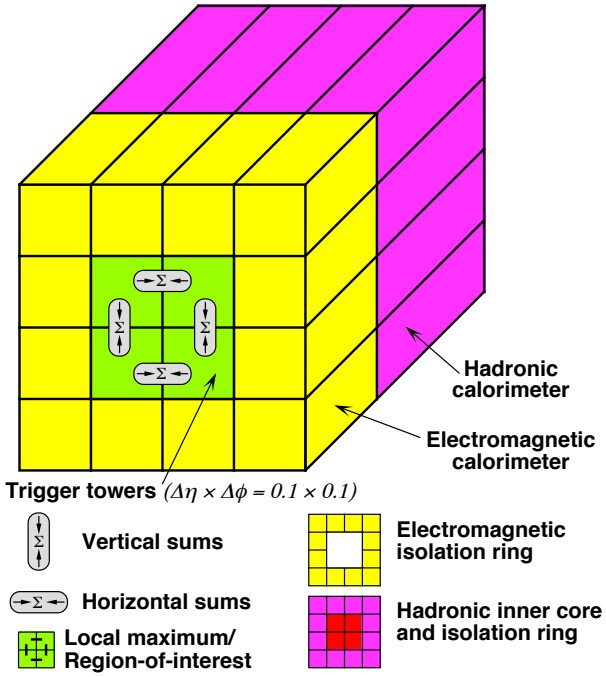

FIGURE 2.22: Schematic diagram of the L1Calo electron trigger algorithm. From Ref. [101].

of L2 electron candidates is, then, performed by searching for tracks in the ID, and matching them to the identified cluster. The online track reconstruction is based on fast pattern recognition algorithms, running in regions centered around the L1 RoIs.

At the EF trigger level [102], offline-like algorithms are used as much as possible, for the reconstruction of calorimeter and tracking quantities. In general, these algorithms do not run over the full event, but rather in regions where the L2 has identified electron candidates, accessing only the corresponding subsample of the detector. The use of more shower shape variables, and improved calibrations and algorithms with respect to L2, results in a further rate reduction at the EF. Typically, the EF algorithms apply loser selections compared to the offline algorithms, to ensure that the trigger remains fully efficient for offline objects.

To determine the efficiency of the electron trigger, the tag-and-probe method is, once again, used. A *tight++* electron is selected as the tag, and an isolated electron is taken as the probe, so that the pair is compatible with a $Z \to ee$ decay. The trigger efficiency is, then, computed as the fraction of probe electrons matching an online electron that passes the trigger selection. An example is shown in Figure 2.23, where the efficiency for three different electron trigger chains, which ran unprescaled during 2011 data-taking, is shown as a function of η and E_{T} of *tight++* offline electrons [133]. Inefficiencies of these triggers arise mainly from the resolution of the reconstruction and identification algorithms at the trigger level, which is poorer when compared to offline algorithms. Trigger efficiencies are computed for simulated events as well, which were shown to reproduce well the results in data. Small differences are, in any case, corrected for by computing trigger scale factors, from the data/MC ratios of efficiencies.

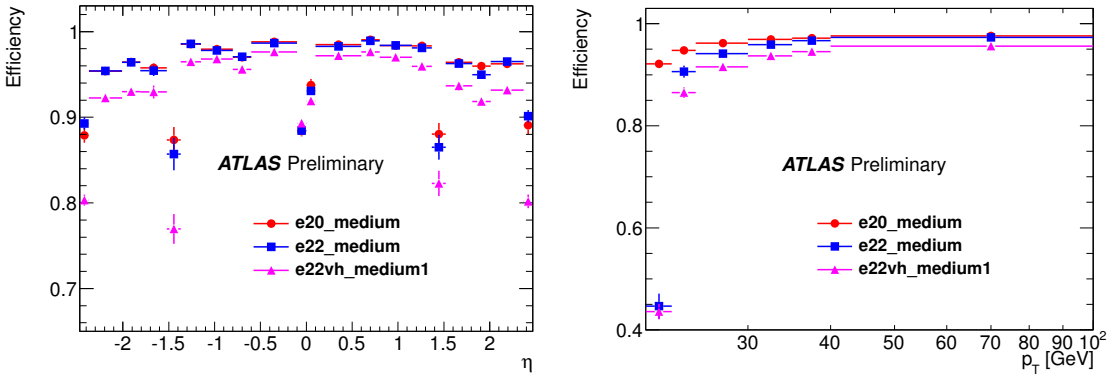

(a) (b)

FIGURE 2.23: Efficiency of three different single electron trigger chains (i.e. L1→L2→EF sequence of selections), `e20_medium`, `e22_medium` and `e22vh_medium1`, measured with respected to: (a) offline reconstructed electron η; and (b) offline reconstructed electron E_{T}. From Ref. [133].

2.6.4 Jets

Hadronic jets are the experimental signatures of quarks and gluons, and they are the most commonly produced objects at the LHC. Jet reconstruction is a key ingredient of the ATLAS physics program. The challenges of defining jets have already been discussed in Section 1.2.2, and these extend directly to jet reconstruction in ATLAS. Moreover, in the non-compensating calorimeters of ATLAS, calibration of jet the energy is crucial, if jets are to serve as proxies of the original partons. Finally, improving the uncertainty on the jet energy is of great important, as this is the dominant source of experimental uncertainty in numerous physics analyses. In summary, reconstruction of hadronic final states is a complex task, particularly under the heavy pile-up conditions of the LHC, and it will be addressed in what follows.

2.6.4.1 Reconstruction

Figure 2.24 presents a schematic overview of jet reconstruction in ATLAS [134]. Standard jet reconstruction uses the anti-k$_t$ jet algorithm [48], as implemented in the FastJet software package [135], with distance parameters of $R = 0.4, 0.6$. The full 4-vector sum is chosen as the recombination scheme. As discussed in Section 1.2.2, this is an IRC-safe jet algorithm, that reconstructs regular, cone-like jets, and allows for comparisons between data and NLO MC simulations.

The jet finding algorithm can be used on different inputs ("jet constituents" in Figure 2.24), from both data and simulation, such as truth-level particles (only available in simulation), detector tracks, or clusters of energy depositions in the calorimeters. Calorimeter jets are the ones used in the work of this thesis, and the discussion that follows will, unless stated otherwise, focus on them.

Topological clusters [136] (topo-clusters) are the most widely used inputs for calorimeter jet finding in ATLAS. Other inputs include calorimeter towers (see Section 2.3.3.2)

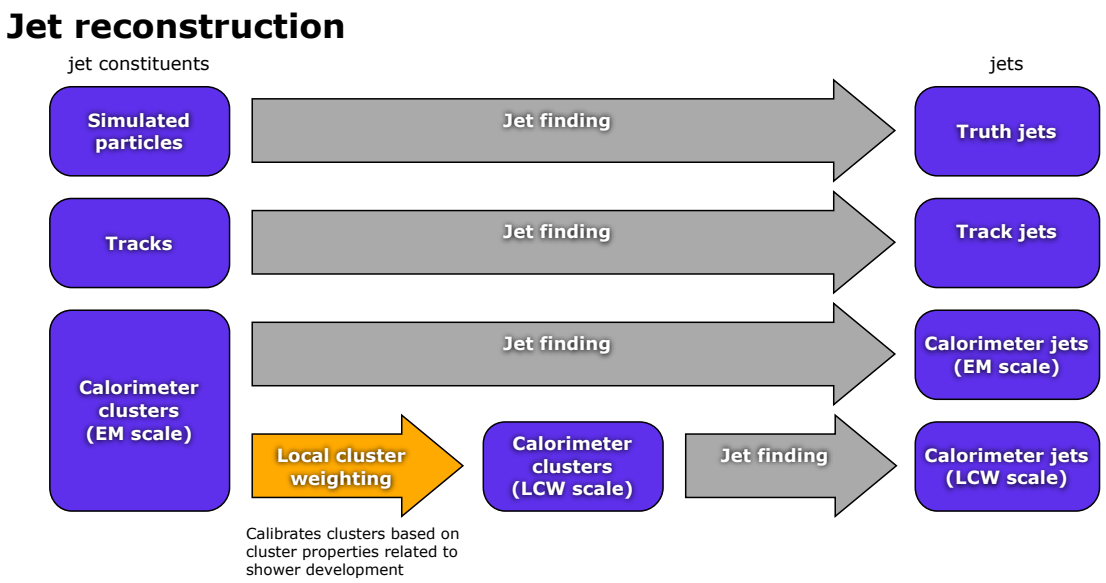

FIGURE 2.24: Schematic overview of jet reconstruction in ATLAS. From Ref. [134].

or topological towers (topo-towers), which are a combination of calorimeter towers and topo-clusters. Topo-clusters are three-dimensional agglomerates of energy depositions in the calorimeters. The formation of topo-clusters follows patterns of signal significance in calorimeter cells, defined as the cell signal-to-noise ratio. The cell noise definition includes both electronic noise and noise introduced by pile-up, making topo-clusters very resilient to these effects.

Topological clustering starts with a seed cell, with signal-to-noise ratio above a certain threshold, typically of 4. Neighboring cells with a signal-to-noise ratio of at least 2 are added to the cluster iteratively, until no neighboring cell has as a signal-to-noise ratio above 2. In a final step, all the nearest neighbors surrounding the cluster are added. Clusters can, then, be merged or split, depending on local energy maxima. The final topo-clusters are defined as massless objects, with an energy computed from the sum of all clustered cells, and a direction provided by the energy-weighted barycenter of the cluster.

The energy of topo-clusters, and resulting jets, is measured at the so-called "EM scale" of the ATLAS calorimeters. This is the correct energy scale for the energy deposited by EM showers, but does not correct for the lower response for hadronic showers, as discussed in Section 2.3.3. For this reason, and as illustrated in Figure 2.24, topo-clusters can also be reconstructed from calibrated calorimeter cells. This calibration is performed using the local cluster weighting method (LCW) [137], that corrects for non-compensation, energy losses in dead material and out-of-cluster energy depositions, improving the response of the ATLAS calorimeters to hadrons.

The LCW scheme relies on the classification of topo-clusters as electromagnetic-like or hadronic-like. The classification is based on cluster shape variables, such as energy density or longitudinal shower depth, that characterize the topology of the energy deposit. Calibration weights are computed according this classification, using MC

simulations for single charged and neutral pions. The weights are derived with respect to the true energy deposited in the detector, and denote the probability for a cluster to originate from a hadronic interaction. The calibration also includes corrections for energy deposited outside the clusters and in the dead material of the detector.

The energy response of calorimeter jets has been evaluated in simulation [134], and shown in Figure 2.25a for jets built from topo-clusters at the EM scale, and in Figure 2.25b for jets at the LCW scale. The response is defined as:

$$\mathfrak{R}^{\mathrm{EM(LCW)}} = \frac{E_{\mathrm{jet}}^{\mathrm{EM(LCW)}}}{E_{\mathrm{jet}}^{\mathrm{truth}}}, \tag{2.7}$$

where $E_{\mathrm{jet}}^{\mathrm{EM(LCW)}}$ is the reconstructed jet energy, and $E_{\mathrm{jet}}^{\mathrm{truth}}$ is the energy of the matching truth jet. The distributions in Figure 2.25 clearly show the lower response of the ATLAS calorimeters to hadronic showers, and the improvement of the response with the application of the LCW calibration.

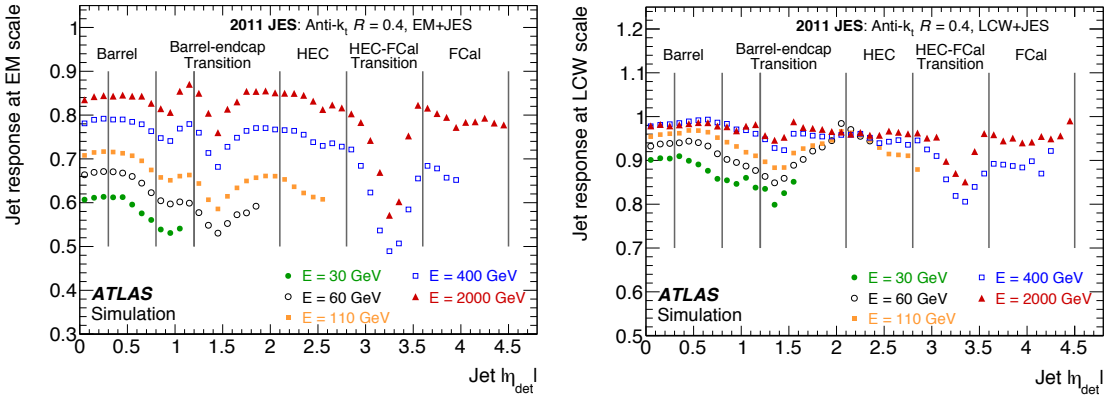

(a) (b)

FIGURE 2.25: Average response of simulated jets formed from topo-clusters: (a) at the EM scale; and (b) at the LCW scale. The response is shown separately for various truth-jet energies, and as a function of the jet pseudorapidity. From Ref. [134].

2.6.4.2 Quality and pile-up

Once a jet has been reconstructed in ATLAS, it must be distinguished from background jet candidates, referred to as fake jets, not originating from the hard scattering. Features such as the quality of the electronic pulse, or the fraction of energy deposited in the HEC and LAr calorimeters, are used to suppress fake jets originating from noise. Furthermore, a good jet will deposit energy in the direction of the shower development, which can be used to discriminate jets originating from cosmic ray muons, or beam-induced backgrounds (the beam collides with residual gas in the beam pipe or with the beam collimators). Finally, the jet time, defined with respect to the event time recorded by the trigger, can also be used to suppress these non-collision backgrounds. *Looser*, *loose*, *medium* and *tight* jet quality selections [138] were designed, to provide different levels of rejection for fake jets and efficiency for good jets. The *looser* selection, in particular,

provides an efficiency above 99.8% for good jets, with a fake jet rejection as high as possible.

Particles associated with a jet extend over a wide area of the detector, which increases the probability of overlap with particles originating from pile-up interactions. Jet reconstruction from calorimeter signals is, therefore, particularly sensitive to pile-up effects. The jet vertex fraction (JVF) [139] can be used to mitigate the impact of pile-up in jet reconstruction. By matching ID tracks to jets, one can obtain a measure of the fraction of the jet energy associated with the PV, as illustrated in Figure 2.26a. JVF is defined as the fraction of $\sum p_{\mathrm{T}}$ of tracks matched to a given jet and originating from the hard-scatter PV, to the $\sum p_{\mathrm{T}}$ for all tracks matched to the jet. The discrimination between hard-scatter jets and pile-up jets provided by JVF is shown in Figure 2.26b. A lower cut on the absolute value of JVF is generally used, since JVF $= -1$ is assigned to calorimeter jets which do not have any associated tracks (outside ID acceptance).

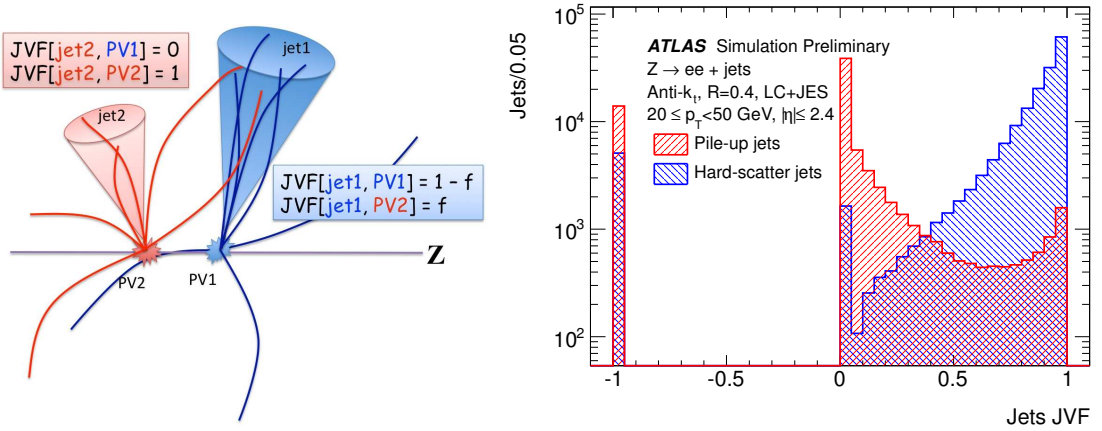

(a) (b)

FIGURE 2.26: (a) Schematic representation of the JVF principle. (b) JVF distribution for simulated hard-scatter and pile-up jets. From Ref. [139].

2.6.4.3 Jet calibration

As already discussed, the ATLAS calorimeters are non-compensating, and have lower responses to hadrons, when compared to electrons or photons. The correct jet energy scale (JES) can be restored through calibration of the jet. The standard jet calibration scheme of ATLAS [134] is presented in Figure 2.27. It is composed of a sequence of calibration steps, that are applied sequentially to calorimeter jets, either at the EM scale or at the LCW scale. After the full calibration procedure, the energy scale of the calibrated calorimeter jets is referred to EM+JES, or LCW+JES. In reality, the jet calibration is designed to correct not only for effects of calorimeter non-compensation, but also for energy losses in inactive regions of the detector (dead material), energy from particles not contained in the calorimeter (leakage), energy deposited by particles belonging to the truth jet that were not included in the reconstructed jet (out-of-cone), and signal losses in the process of creating the topo-clusters or reconstructing the jets.

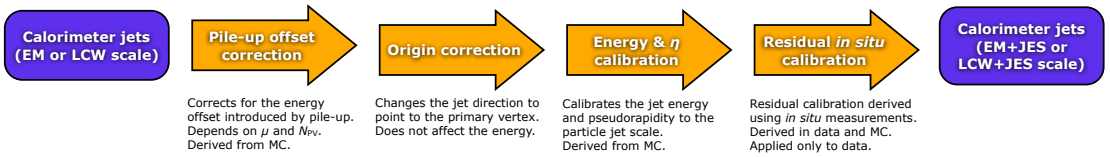

FIGURE 2.27: Schematic overview of the ATLAS jet calibration scheme. From Ref. [134].

The first step in jet calibration consists of a pile-up correction. The soft collisions that accompany the hard-scattering event in a bunch crossing at the LHC, referred to as in-time pile-up, present a background of soft diffuse radiation for jets, that offsets the energy measurement. Also, the overlapping signals from out-of-time pile-up affect the reconstruction of the jet kinematics. During 2011 data-taking, the pile-up correction consisted of an average correction parametrized by N_{PV} and $\langle\mu\rangle$ [134]. For the increased pile-up in 2012 data-taking [139], the pile-up correction was improved, and adopted the jet areas method [140]. This method uses the area of the jet, as a measure of its susceptibility to pile-up, and the median p_{T} density as an estimate of the pile-up in an event. Therefore, it allows for a correction of the 4-momentum of the jet, for event-by-event and jet-by-jet fluctuations with pile-up. The dependence of the reconstructed jet p_{T} with the N_{PV} was shown, in simulation, to be reduced after the pile-up correction, as displayed in Figure 2.28a. The procedure also reduces the pile-up degradation of the jet p_{T} resolution.

The direction of a calorimeter jet is reconstructed with respect to the geometrical center of the ATLAS detector. The origin correction [137] component of the jet calibration makes the jet point back to the hard-scatter primary vertex. The kinematic observables of each topo-cluster are recalculated using the direction determined from the PV, and the jet 4-momentum is redefined thereafter. The jet energy is unaffected, but the angular resolution of the jet is improved after the origin correction, and there is a slight improvement ($< 1\%$) in the p_{T} response as well.

The third calibration step applies energy- and η-dependent corrections [137] to the reconstructed jet, calibrating it to the scale of the matching MC truth particle jet. For each η bin, the jet response (see Equation 2.7) is parametrized as a logarithmic function of the energy of the reconstructed jet. The calibrated jet energy is, then, obtained, by multiplying the reconstructed jet energy by the inverse of the calibrating function. This means that the average jet energy scale correction is simply the inverse of the responses shown in Figure 2.25.

The final step of the JES calibration procedure consists of applying a residual correction, based on *in situ* measurements, that corrects for remaining data-to-MC differences [134]. These *in situ* techniques exploit the transverse momentum balance between the jet and a well-measured reference object. The jet calibration in data is then adjusted using the data-to-MC comparison of $p_{\mathrm{T}}^{\mathrm{jet}}/p_{\mathrm{T}}^{\mathrm{ref}}$, shown in Figure 2.28b. Some of the *in situ* methods are, for example: relative η-intercalibration, where the jet response in a particular region is corrected relative to the jet response in the central region; direct

transverse momentum balance between a photon or a Z boson and a jet, which allows for a correction of the jet response in the central region; and balance between a high p_{T} jet and a recoil system of low p_{T} jets, which have been well calibrated by the previous techniques.

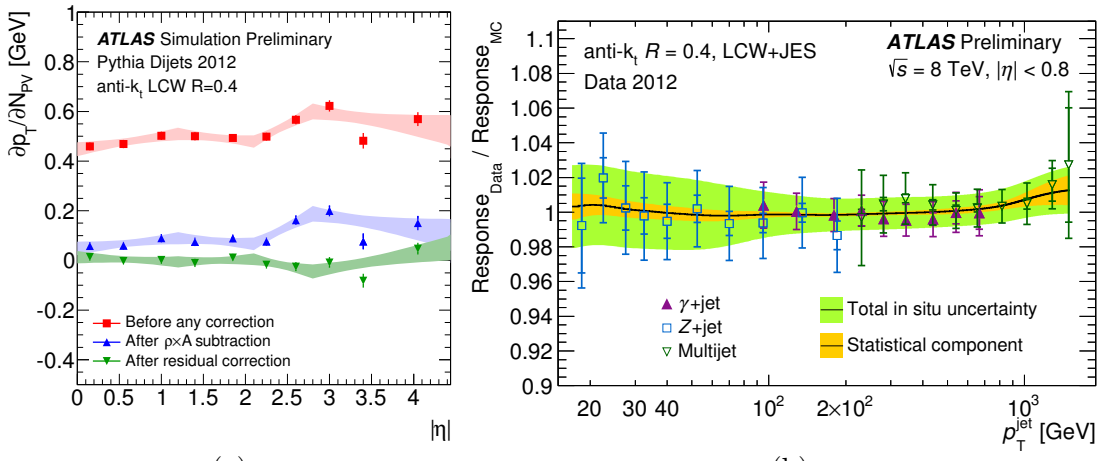

FIGURE 2.28: (a) Dependence of the jet p_{T} with the number of primary vertices, for simulated events, before and after the JES pile-up correction. (b) Data-to-MC ratio of the jet response, as a function of the transverse momentum of the jet, for three *in situ* techniques combined, to determine the *in situ* energy scale correction. From Refs. [139, 141].

2.6.4.4 Jet energy scale and resolution

The steeply falling jet p_{T} spectrum causes jets to easily shift in and out of analyses selections. For this reason, the uncertainty on the JES [141] is frequently the dominant systematic uncertainty in many physics analyses. It arises from a variety of sources. The uncertainties affecting the *in situ* measurements translate into uncertainties on the JES. They usually originate from the assumptions made by the *in situ* techniques, and can be assessed by varying the event selection criteria, as well as from the selection, calibration and modeling of the objects used as reference [134]. Additional JES uncertainties due to specific event topologies, such as selection of samples with different flavour compositions, are also accounted for [134]. Finally, the uncertainties originating from the pile-up correction are evaluated *in situ*, using track-jets and the p_{T} balance between the jet and a Z boson. They range between $2-5.6\%$ [139]. The quadrature sum of these different components is shown in Figure 2.29, as a function of p_{T} and η of the jet, and constitutes the total uncertainty on the JES.

Knowledge of the jet energy resolution (JER) is also important for many physics analysis, as it has a direct impact on the determination of the missing transverse energy (see Section 2.6.6 ahead). The JER has been measured using two different *in situ* methods [142]. The MC describes the jet energy resolution measured in data within $\sim 10\%$, and the two methods show compatible results within the uncertainties, which are dominated by the closure of the methods and the data/MC agreement. The fractional

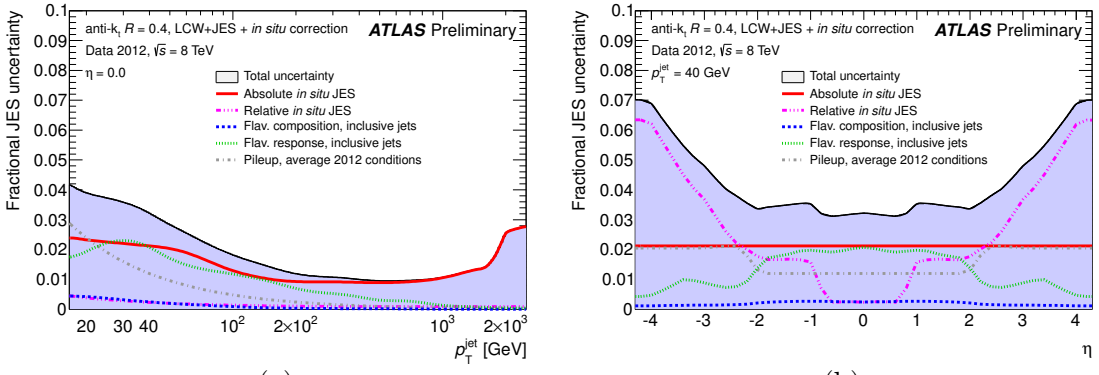

(a) (b)

FIGURE 2.29: Fractional jet energy scale systematic uncertainty components, as a function of (a) p_{T} and (b) η, for anti-k$_t$ jets with $R = 0.4$, calibrated using the LCW+JES scheme. From Ref. [141].

JER measured in data, using one of the methods, is shown in Figure 2.30, for jets calibrated with the two different calibration schemes. For jets with $p_{\mathrm{T}} > 30$ GeV, the LCW+JES calibration improves the JER by $10 - 30\%$, compared to EM+JES jets.

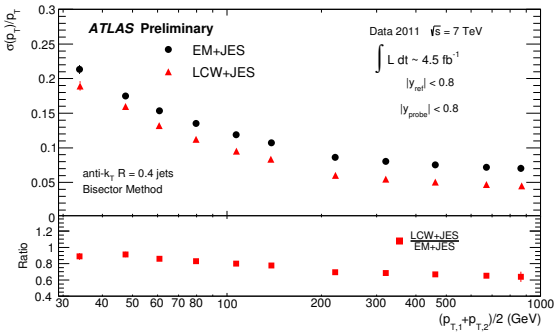

FIGURE 2.30: Fractional jet energy resolution as a function of the average jet transverse momenta measured with the bisector *in situ* technique, using the EM+JES and LCW+JES calibration schemes with 2011 data, in anti-k$_t$ with $R = 0.4$ topo-cluster jets. From Ref. [143].

2.6.4.5 Jet trigger

The Jet/Energy-sum Processor (JEP) of the L1Calo trigger contains the Jet/Energy Module (JEM), that executes the jet selections at L1 [101]. The JEM works with so-called jet-elements, which are 2×2 sums of trigger towers in the EM calorimeters, added to 2×2 trigger towers in the hadronic calorimeters. Jet elements have, therefore, a 0.2×0.2 granularity ($\Delta\eta \times \Delta\phi$ space) in the $|\eta| < 3.2$ range (see Figure 2.15). In the forward region extending to $|\eta| = 4.9$, given the limited granularity of the TTs in the FCal (see Figure 2.15), the jet elements are 0.4 in $\Delta\phi$, with only two (one) η bins in the forward (backward) side, with the coordinates of $\eta = 3.2, 4.05$ ($\eta = -3.9$). The forward jet trigger at L1 was originally designed to be used only for $E_{\mathrm{T}}^{\mathrm{miss}}$ calculation, hence the very limited granularity.

Jet reconstruction at L1 uses a simple sliding-window algorithm. The size of the window is programmable, and sizes of 2×2, 3×3 or 4×4 jet elements can be chosen, as shown in Figure 2.31. A jet is reconstructed if the total transverse energy (EM + hadronic) in the jet elements within the window is above a pre-defined E_{T} threshold. Transverse energy sums in jet elements are expressed in counts, with 1 count ≈ 1 GeV, at the EM-scale.

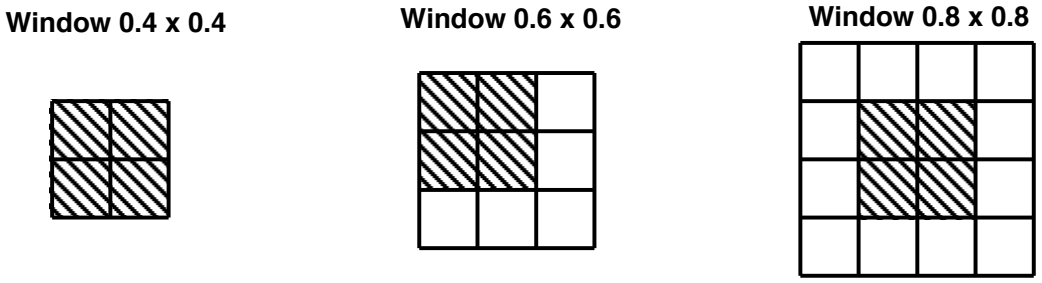

FIGURE 2.31: L1 jet trigger sliding-window algorithm with different sizes, based on jet elements. Each square represents a jet element, with 0.2×0.2 granularity ($\Delta\eta \times \Delta\phi$ space). The shaded squares represent a jet cluster, which defines the RoI coordinates. From Ref. [101].

The L1 sliding window has a step size of 0.2 in $\Delta\eta$ and $\Delta\phi$ (one jet element), which means that significant overlap between neighboring windows can occur. To prevent this overlap, the transverse energy of a jet cluster, i.e. the region spanned by 2×2 jet elements, is required to be a local maximum within ± 0.4 units in $\Delta\eta$ and $\Delta\phi$. This procedure is illustrated in Figure 2.32. The center of this local maximum also defines the coordinates of the L1 jet RoI.

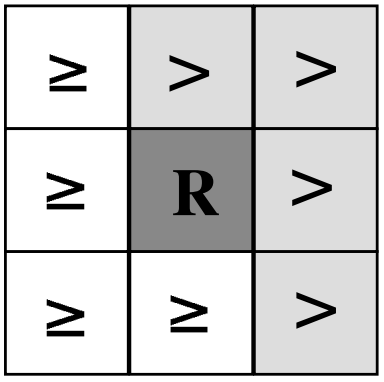

FIGURE 2.32: Local E_{T} maximum test for a jet cluster "R", formed by 2×2 jet elements. The η axis is the horizontal one and the ϕ axis is the vertical one. From Ref. [101].

The L2 jet trigger [102] accesses the calorimeter data, at full granularity, that lies in a rectangular region centered around the L1 jet RoI. This region can be defined to have any size, and typically a window of 1.4×1.4 ($\Delta\eta \times \Delta\phi$) is chosen. The $\eta - \phi$ position and E_{T} of each detector cell that falls in the chosen window is read out by L2. This information is then used as input to the jet reconstruction algorithm.

During Run-I, L2 jets were reconstructed using a simplified version of the cone algorithm, present in Section 1.2.2, with $R = 0.4$. The procedure is illustrated in Figure 2.33, and works as follows:

1. The L1 RoI position is used as the first seed, and sets the initial direction;

2. The energies of all calorimeter cells k, within a cone of radius $R = 0.4$ around the L1 RoI seed, are summed to obtain the energy of the L2 jet j_1 - E_{j_1}; the η and ϕ coordinates of j_1 - η_{j_1} and ϕ_{j_1} - are computed as energy-weighted sums:

$$E_{j_1} = \sum_k E_k, \quad \eta_{j_1} = \frac{\sum_k E_k \eta_k}{E_{j_1}} \quad \text{and} \quad \phi_{j_1} = \frac{\sum_k E_k \phi_k}{E_{j_1}}; \tag{2.8}$$

3. The jet j_1 is used to define a new seed, and the procedure is iterated N times (typically $N = 3$) to create the jet j_N, which constitutes the final reconstructed L2 jet.

At this point, it is important to note that only one L2 jet is reconstructed per L1 RoI.

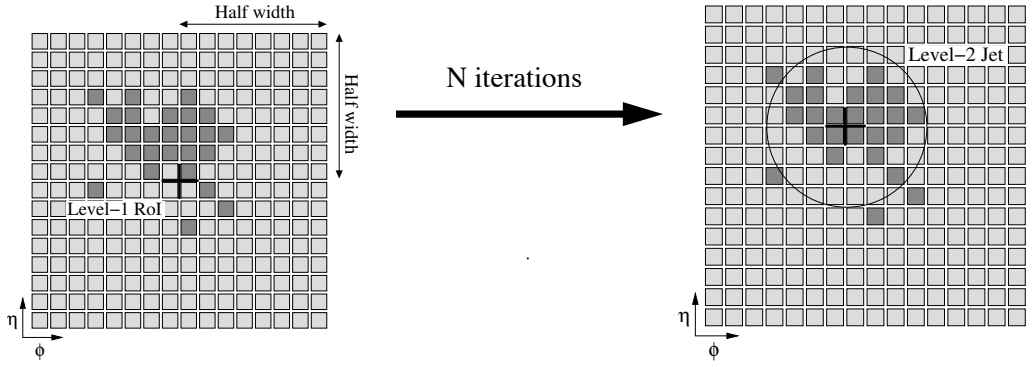

FIGURE 2.33: Schematic diagram of the algorithm of the L2 jet trigger, based on the cone algorithm with $R = 0.4$, seeded by the L1 RoI. Each square represents a calorimeter cell, with the darker colors illustrating large energy depositions. From Ref. [102].

Similar to L1, the energy of the L2 trigger jet is reconstructed at the EM scale. At the trigger level, a hadronic calibration can be applied to L2 jets, to correct for the non-compensation of the ATLAS calorimeters, as discussed in Section 2.3.3. At the start of Run-I, the default calibration procedure of L2 jets was based on the Sampling Method. In a dedicated procedure, the L2 jet was regarded as a sum of energy depositions in the EM and hadronic samplings of the ATLAS calorimeters:

$$E = E^{\mathrm{EM}} + E^{\mathrm{had}}. \tag{2.9}$$

To calibrate the L2 jet - E^{cal} - the energy in each sampling was corrected by a weight w:

$$E^{\mathrm{cal}} = w^{\mathrm{EM}} E^{\mathrm{EM}} + w^{\mathrm{had}} E^{\mathrm{had}}. \tag{2.10}$$

The weights were computed using QCD multijet MC samples, and by minimizing the function:

$$\chi^2 = \sum_i^{N_{\text{jets}}} \left(\frac{E_i^{\text{truth}} - E_i^{\text{cal}}}{\sigma_i} \right)^2 , \tag{2.11}$$

where the sum runs over all jets in the sample, σ denotes the jet resolution, and E^{truth} is the true energy of the jet (obtained by running the jet algorithm directly over the MC truth particles). The weights w^{EM} and w^{had} were computed for different jet η bins, and chosen to have a logarithmic dependence on the jet energy E:

$$w = a + b \log E. \tag{2.12}$$

The calibration constants a and b were determined, for each weight and η bin, using a fit to Equation 2.12.

Finally, the EF [102] accesses the data in calorimeter cells, for events passing the L2 selection. These cells are used to construct 0.1×0.1 calorimeter towers, topo-clusters, and topo-towers. All four options can serve as input to sophisticated jet reconstruction algorithms, such as cone or anti-k$_t$, with different distance parameters, similar to ones used by ATLAS in offline analysis. The offline procedures of hadronic calibration of jets are also available at the EF. Originally, only cells in a window of programable size around the jets identified at L2 were unpacked. This RoI-based approach proved to be inefficient, particularly in busy multijet environments. Thus, for 2011 data-taking, a Full Scan (FS) approach was adopted for the jet trigger at the EF [144]. With the FS procedure, the entire event data is unpacked, and the full calorimeter is scanned for jets in events accepted at L2, which greatly improves the performance.

The efficiency of the jet trigger was studied in detail, using data collected in 2010 and in 2011. These studies are reported in Chapter 3.

2.6.5 *b*-tagging

It is crucial for the ATLAS physics program to be able to identify b-jets, i.e. jets originating from b-quarks. This is achieved by means of a b-tagging algorithm, generally exploiting the relatively long lifetime of B-hadrons, which generate secondary decay vertices in the detector, displaced from the primary vertex. Various b-tagging strategies have been developed in ATLAS, to achieve high b-tagging efficiencies for real b-jets, while keeping the misidentification rates of c- or light-jets (originating from u, d and s quarks, or gluons) to a minimum. They rely on the selection of high quality ID tracks (see Section 2.6.1.1), which are associated to reconstructed jets (see Section 2.6.4), using a ΔR cut. b-tagging in ATLAS is, thus, available for jets with $|\eta| < 2.5$ and $20 < p_{\text{T}} < 300$ GeV.

The impact parameters of the tracks within the jets are combined in the JetProb and IP3D b-tagging algorithms [145]. In fact, the signed impact parameter significances, d_0/σ_{d_0} and z_0/σ_{z_0}, are used. A positive or negative sign is assigned to the impact parameter, based on the assumption that the decay point of the b-hadron lies along

its flight path. Thus, tracks from b-hadron decays tend to have positive-signed impact parameters, indicating they originated in front of the PV, whereas tracks originating from the primary vertex will have the same probability for a negative or positive sign, due to resolution effects. Furthermore, the division of the impact parameter by its error σ, ensures that more weight is given to tracks which are measured more precisely.

b-jets originate from b-quarks, which produce b-hadrons when they hadronize. These b-hadrons decay mainly through EW interaction, causing a $b \to c$ transition at the quark level (favored when compared to the $b \to u$ transition), resulting in the production of c-hadrons, that also undergo weak decays. Thus, the typical topology of particles in a b-jet has a decay chain with two vertices. Another class of b-tagging algorithms - SV0 and SV1 [145] - attempts to reconstruct an inclusive secondary vertex, compatible with a b-hadron decay, from the tracks within the jet. The JetFitter [145] algorithm uses a Kalman filter [117] to exploit the topology of b- and c-hadron decays within the jet, reconstructing a common line on which the PV and the b- and c-vertices lie.

The most commonly used b-tagging algorithm in ATLAS is the so-called MV1 algorithm [146]. MV1 is the result of the combination of the IP3D, SV1 and JetFitter algorithms, through MVA techniques. It employs an artificial neural network, trained on simulation using b-jets as signal and light-jets as background, to compute a tag weight for each jet. Typically, a fixed cut, referred to as the working point, is applied to the tag weight, to select b-jets. Figure 2.34a shows a performance curve for the MV1 algorithm, measured in simulated $t\bar{t}$ events, where the rejection rate of light-jets is shown as a function of the b-jet identification efficiency. The working point is, in general, chosen from this curve, to obtain a certain b-tagging identification efficiency.

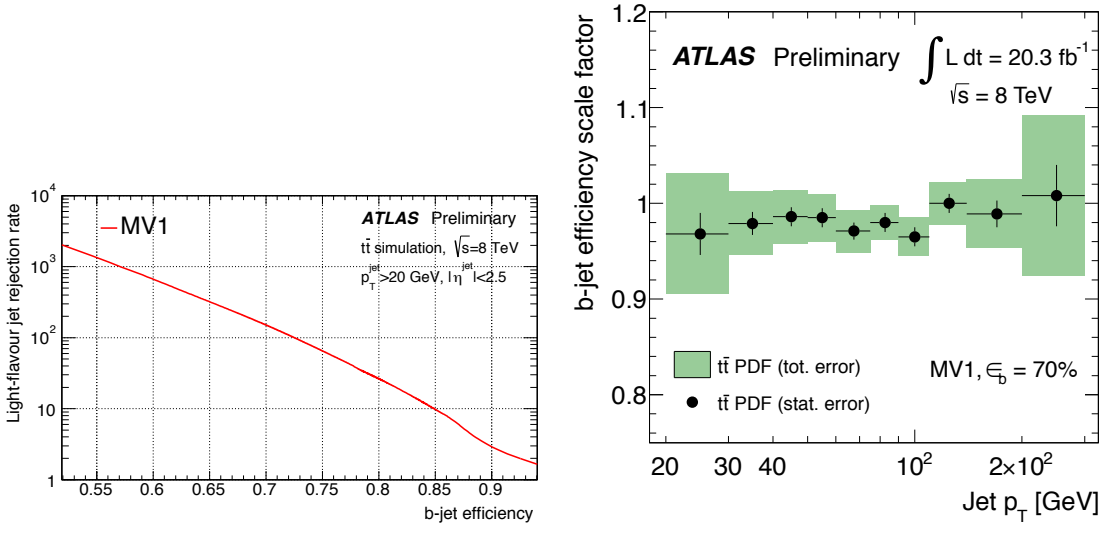

(a) (b)

FIGURE 2.34: Performance and calibration of the MV1 b-tagging algorithm: (a) light-jet rejection, defined as the inverse of the mistag rate, versus b-jet efficiency, evaluated in a simulated sample of $t\bar{t}$ events; and (b) b-jet efficiency scale factors for a 70% b-tagging efficiency working point, evaluated with a combinatorial likelihood approach. From Refs. [146, 147].

Once the working point is defined, the performance of the b-tagging algorithm must be evaluated in data, and differences between simulation and data must be corrected. This process of calibrating the b-tagging algorithm requires measuring the efficiency with which a b-jet is tagged (ϵ_b), as well assessing the c-tag efficiency (ϵ_c) and mistag rate (ϵ_l), i.e the probabilities of mistakenly tagging a c- or light-jet as a b-jet. Results are generally presented in the form of p_{T}-dependent data-to-MC efficiency ratios, referred to as scale factors. The scale factors and their uncertainties depend on the working point of the b-tagging algorithm.

The c-tag efficiency has been measured using in an inclusive sample of jets associated with D^* mesons, with uncertainties ranging, from $8\% - 15\%$ [146]. The negative tag method [146] allows for the measurements of the mistag rate, with uncertainties ranging from $15 - 43\%$. As for the b-tag efficiency, several methods have been developed [148, 149]. A recent one [147] uses a combinatorial likelihood approach, in a data sample of dileptonic $t\bar{t}$ events ($t \to Wb \to \ell\nu b$). The method exploits the correlations between jets in the events, providing a large gain in precision. For a 70% b-jet efficiency working point of the MV1 algorithm, scale factors compatible with one, and with an uncertainty of $\sim 2\%$ are obtained, as shown in Figure 2.34b.

2.6.6 Missing transverse energy

The missing transverse momentum is defined as the imbalance of momentum in the transverse plane, where momentum conservation occurs in the ATLAS detector. Such an imbalance can be an indication that some particles produced in the pp collision, e.g. neutrinos or other weakly-interacting particles, have not been detected. The imbalance is denoted with the symbol $\boldsymbol{E}_{\mathrm{T}}^{\mathrm{miss}}$, whereas the symbol $E_{\mathrm{T}}^{\mathrm{miss}}$ is used for its magnitude, and referred to as missing transverse momentum/energy. It is obtained from the negative vector sum of the momenta of all particles detected in the collision, since the transverse momentum in the initial state is zero:

$$\boldsymbol{E}_{\mathrm{T}}^{\mathrm{miss}} = -\sum \boldsymbol{p}_{\mathrm{T}} \quad \text{and} \quad E_{\mathrm{T}}^{\mathrm{miss}} = |\boldsymbol{E}_{\mathrm{T}}^{\mathrm{miss}}|. \tag{2.13}$$

Because a sum over many objects is involved in its reconstruction, large uncertainties are generally associated with $E_{\mathrm{T}}^{\mathrm{miss}}$.

$E_{\mathrm{T}}^{\mathrm{miss}}$ generated by weakly-interacting particles is generally referred to as true missing transverse energy. This is opposed to fake missing transverse energy, caused by misreconstructed physics objects, effects of finite detector resolution, the presence of dead or noisy regions in the detector, cosmic-rays, among others. Pile-up, in particular, contributes significantly to the increase of fake $E_{\mathrm{T}}^{\mathrm{miss}}$, since the introduction of more signals in the detector degrades the $E_{\mathrm{T}}^{\mathrm{miss}}$ resolution. Different computations of $E_{\mathrm{T}}^{\mathrm{miss}}$ have been developed in ATLAS, with the goal of minimizing fake $E_{\mathrm{T}}^{\mathrm{miss}}$ and improving the $E_{\mathrm{T}}^{\mathrm{miss}}$ resolution under the harsh pile-up conditions of the LHC. These are often referred to as flavors and will be presented in what follows.

2.6.6.1 Calorimeter-based

The large rapidity coverage of the ATLAS calorimeter, as well as the fact that it is sensitive to neutral particles, motivate the calorimeter-based reconstruction of $E_{\mathrm{T}}^{\mathrm{miss}}$, denoted by $E_{\mathrm{T}}^{\mathrm{miss,calo}}$ [150–152]. The computation of $E_{\mathrm{T}}^{\mathrm{miss,calo}}$ starts with the association of energy deposits in the calorimeter to reconstructed high p_{T} objects in the event, which is done in a specific order, starting with electrons, followed by photons, hadronic decays of τ-leptons, and finally jets. This association allows for the use of the dedicated calibrations and corrections of each reconstructed physics object, as described in the previous sections, thereby improving the measurement of the missing transverse momentum. Energy deposits not associated with any object, generally with low p_{T}, are included in the so-called "soft term". Finally, the momentum of muons reconstructed in the ATLAS MS is also used in the reconstruction of this flavour of $E_{\mathrm{T}}^{\mathrm{miss}}$, ensuring that all interacting particles produced in the collisions are, therefore, taken into account.

The calculation of $E_{\mathrm{T}}^{\mathrm{miss,calo}}$ is done as follows:

$$E_{\mathrm{T}}^{\mathrm{miss,calo}} = \sqrt{\left(E_x^{\mathrm{miss,calo}}\right)^2 + \left(E_y^{\mathrm{miss,calo}}\right)^2}, \tag{2.14}$$

with:

$$E_{x(y)}^{\mathrm{miss,calo}} = E_{x(y)}^{\mathrm{miss},e} + E_{x(y)}^{\mathrm{miss},\gamma} + E_{x(y)}^{\mathrm{miss},\tau} + E_{x(y)}^{\mathrm{miss,jets}} + E_{x(y)}^{\mathrm{miss,SoftTerm}} + E_{x(y)}^{\mathrm{miss},\mu}. \tag{2.15}$$

Each term is calculated as the negative sum of the corresponding calibrated hard objects, projected onto the x and y directions. For electrons, the *medium++* energy cluster is calibrated as described in Section 2.6.3. The photon clusters are included at the EM-scale and τ-leptons are reconstructed from LCW topoclusters and include a specific calibration of the energy scale. Jets with $p_{\mathrm{T}} > 20$ GeV are reconstructed from topo-clusters using the anti-k$_t$ algorithm, with $R = 0.4$, at the LCW+JES scale, as described in Section 2.6.4. Finally, the muon term is obtained simply from the negative sum of the momentum of all segment-tagged muons (see Section 2.6.2). As for the soft term, it is calculated from topo-clusters and tracks, not associated to any of the high p_{T} objects. Topo-clusters are calibrated at the LCW-scale, and any overlap with the tracks is removed, to avoid double-counting.

The SoftTerm can be a significant contribution to the global $E_{\mathrm{T}}^{\mathrm{miss,calo}}$ quantity. However, this term suffers from significant fluctuations due to pile-up, which introduces additional soft diffuse radiation in the detector. The effects from pile-up can be suppressed by using the soft term vertex fraction (STVF) [151] which, similar to JVF described in Section 2.6.4.2, is calculated as the fraction of $\sum p_{\mathrm{T}}$ of tracks matched to the soft term (i.e. not associated to reconstructed physics objects) that can be associated to the hard-scattering PV. The $E_{\mathrm{T}}^{\mathrm{miss,SoftTerm}}$ term in Equation 2.15 can be weighted by STVF, and the resulting computation of missing transverse energy is names $E_{\mathrm{T}}^{\mathrm{miss,STVF}}$.

$Z \to \ell\ell$ decays have been used to study the performance of $E_{\mathrm{T}}^{\mathrm{miss}}$ [151]. No true missing transverse momentum is expected for these events. Therefore, the width of the

$E_{x(y)}^{\text{miss}}$ distributions provides a direct measurement of the resolution of $E_{\text{T}}^{\text{miss}}$. This is shown in Figure 2.35, where the resolution of the two $E_{\text{T}}^{\text{miss}}$ components are shown for $Z \to \mu\mu$ and $Z \to ee$ events in data and simulation, for $E_{\text{T}}^{\text{miss,calo}}$ and $E_{\text{T}}^{\text{miss,STVF}}$, as a function of $\sum E_{\text{T}}$. $\sum E_{\text{T}}$ is the total transverse energy in the event, computed as the scalar sum:

$$\sum E_{\text{T}} = \sum E_{\text{T}}^{e} + \sum E_{\text{T}}^{\gamma} + \sum E_{\text{T}}^{\tau} + \sum E_{\text{T}}^{\text{jets}} + \sum E_{\text{T}}^{\text{SoftTerm}} + \sum p_{\text{T}}^{\mu}, \qquad (2.16)$$

where the terms are defined as in the $E_{\text{T}}^{\text{miss}}$ computation. The data is well described by the MC and there is a clear improvement of the resolution with the STVF pile-up suppression.

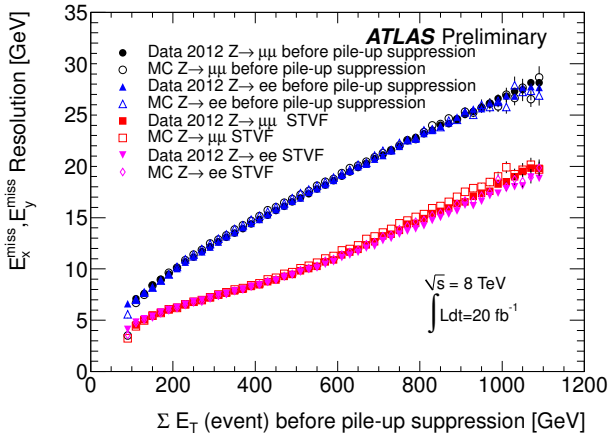

FIGURE 2.35: E_x^{miss} and E_y^{miss} resolution as a function of $\sum E_{\text{T}}$, for $Z \to ee$ and $Z \to \mu\mu$ events in 2012 data and simulation, for $E_{\text{T}}^{\text{miss,calo}}$ and $E_{\text{T}}^{\text{miss,STVF}}$ flavors. From Ref. [151].

Because $E_{\text{T}}^{\text{miss}}$ is a sum of different terms, its overall uncertainty is evaluated by combining the uncertainties on each term, such as the uncertainties on the scale and resolution of charged leptons and the uncertainties on the JES and JER. The relative impact of each depends on the topology of the event. All have already been discussed in the previous sections, apart from the uncertainties on the soft term, which is specific to the $E_{\text{T}}^{\text{miss}}$ computation. The uncertainties on the scale and resolution of $E_{\text{T}}^{\text{miss,SoftTerm}}$ arise both from the MC modeling of the data and effects of pile-up, and have been evaluated using $Z \to \mu\mu$ events [151]. For $E_{\text{T}}^{\text{miss,calo}}$ ($E_{\text{T}}^{\text{miss,STVF}}$), they are of the order of 4% (8%) on the scale, and 2% (5%) on the resolution.

2.6.6.2 Track-based

An independent and complementary measurement of the missing transverse momentum can be achieved using tracks reconstructed in the ID, and will be denoted as $p_{\text{T}}^{\text{miss,track}}$ [153–157]. With respect to calorimeter-based measurements of $E_{\text{T}}^{\text{miss}}$, it has the advantage that tracks can be easily associated to the PV, thus reducing the impact of pile-up. However, a track-based reconstruction of $E_{\text{T}}^{\text{miss}}$ also has limitations, namely due to the smaller coverage of the ATLAS ID when compared to the calorimeters, and the

fact that neutral particles cannot be detected in the ID. Furthermore, the performance of $p_{\mathrm{T}}^{\mathrm{miss,track}}$ tends to degrade when high p_{T} tracks are involved, since the curvature of these tracks in the magnetic field is smaller, and the uncertainty on their momenta is larger.

The computation of $p_{\mathrm{T}}^{\mathrm{miss,track}}$ is done as follows:

$$p_{\mathrm{T}}^{\mathrm{miss,track}} = -\sum p_{\mathrm{T}}^{\mathrm{tracks}}, \tag{2.17}$$

where the sum runs over all tracks reconstructed in the ID, that pass the following quality criteria (see Section 2.6.1.1):

- $p_{\mathrm{T}} > 500$ MeV;
- $|\eta| < 2.5$;
- at least 1 Pixel hit;
- at least 6 SCT hits;
- $|d_0| < 1.5$ mm;
- $|z_0 \sin\theta| < 1.5$ mm.

This selection results in a good track momentum measurement and an efficient rejection of fake tracks. Furthermore, signal leptons are also added to the calculation of $p_{\mathrm{T}}^{\mathrm{miss,track}}$, even if their tracks fail the listed quality cuts. The goal is to ensure that electrons or muons used in the physics study, which carry the majority of the momentum of an event, are included in the computation of $p_{\mathrm{T}}^{\mathrm{miss,track}}$. ID tracks that overlap with the added leptons are removed from the computation. This procedure also entails replacing the momentum of tracks associated to electrons by the calorimeter cluster energy.

For events with jets in the final state, where the resolution of $p_{\mathrm{T}}^{\mathrm{miss,track}}$ is expected to worsen, due to the amount of neutral particles carried by the jets, an improved version of the previous definition can be considered, denoted in what follows by $p_{\mathrm{T}}^{\mathrm{miss,jetCorr}}$ [157]. It simply consists of adding the reconstructed jets to the computation of $p_{\mathrm{T}}^{\mathrm{miss,track}}$, again removing the overlapping ID tracks. This definition, though no longer purely track-based, helps overcome the limitations of $p_{\mathrm{T}}^{\mathrm{miss,track}}$, by increasing the coverage and allowing for the measurement of neutrals.

The performance of the track-based measurements of $E_{\mathrm{T}}^{\mathrm{miss}}$ have been thoroughly studied, as well as compared to the calorimeter-based measurements of $E_{\mathrm{T}}^{\mathrm{miss}}$, in the context of the $H \to WW^* \to \ell\nu\ell\nu$ analysis [157], described in Chapter 4. The distributions in Figure 2.36 illustrate this performance in simulated signal events, produced through the ggF mechanism (see Section 1.2.3.1), with one accompanying jet in the final state, i.e. $gg \to H \to WW^* \to \ell\nu\ell\nu + 1$ jet. The four different flavors of $E_{\mathrm{T}}^{\mathrm{miss}}$ are shown. The bias of the $E_{\mathrm{T}}^{\mathrm{miss}}$ measurements, defined as the mean of the distribution of $\left(E_{\mathrm{T}}^{\mathrm{miss}} - E_{\mathrm{T}}^{\mathrm{miss,true}}\right)/E_{\mathrm{T}}^{\mathrm{miss,true}}$[5], is shown in Figure 2.36a, as a function of $\langle\mu\rangle$. The $E_{\mathrm{T}}^{\mathrm{miss}}$

[5] $E_{\mathrm{T}}^{\mathrm{miss,true}}$ is computed in MC simulated events from all non-interaction particles.

resolution, defined as the RMS of the same distribution, is displayed in Figure 2.36b. Both distributions clearly show the stability of the track-based measurements of $E_{\mathrm{T}}^{\mathrm{miss}}$ with pile-up, compared to the calorimeter-based reconstructions. $p_{\mathrm{T}}^{\mathrm{miss,track}}$ appears to be the most stable flavor of $E_{\mathrm{T}}^{\mathrm{miss}}$, but there is a severe degradation of its resolution in the presence of neutral particles of the jet. This degradation is, however, recovered by $p_{\mathrm{T}}^{\mathrm{miss,jetCorr}}$, which generally shows the best performance out of all four $E_{\mathrm{T}}^{\mathrm{miss}}$ flavors.

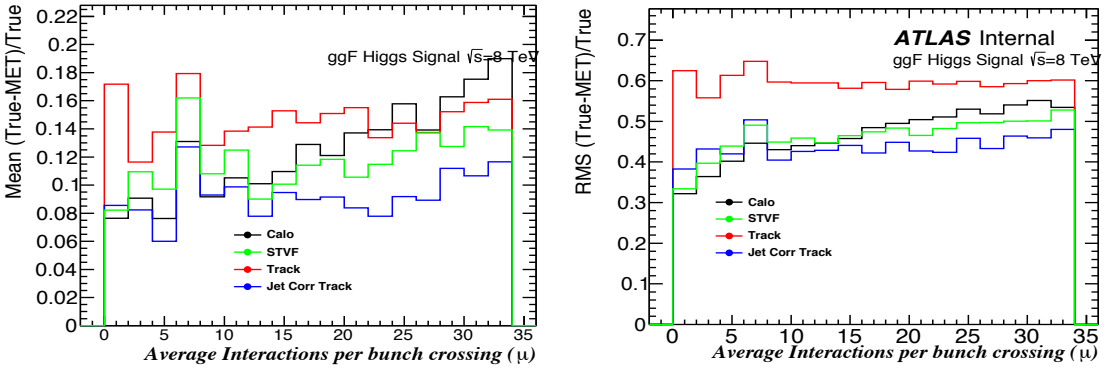

(a) (b)

FIGURE 2.36: Bias (a) and resolution (b) of different $E_{\mathrm{T}}^{\mathrm{miss}}$ flavours, measured in simulated samples of $H \to WW^* \to \ell\nu\ell\nu$ events, produced through the ggF mechanism, with one accompanying reconstructed jet in the final state, as a function of the mean number of interactions per bunch crossing. $E_{\mathrm{T}}^{\mathrm{miss,calo}}$ in black, $E_{\mathrm{T}}^{\mathrm{miss,STVF}}$ in green, $p_{\mathrm{T}}^{\mathrm{miss,track}}$ in red and $p_{\mathrm{T}}^{\mathrm{miss,jetCorr}}$ in blue. From Ref. [157].

Similar to the calorimeter-based flavors of $E_{\mathrm{T}}^{\mathrm{miss}}$, assessing the uncertainties on $p_{\mathrm{T}}^{\mathrm{miss,track}}$ and $p_{\mathrm{T}}^{\mathrm{miss,jetCorr}}$ requires the evaluation of the uncertainties on the soft term only, since the remaining uncertainties originate from the hard objects in the event. The method used to evaluate these uncertainties exploits the balance between the soft term and the term originating from the hard objects, in inclusive $Z \to \mu\mu$ events, for data and simulation [157]. The soft term is decomposed in two projections, with respect to the $\boldsymbol{p}_{\mathrm{T}}^{\mathrm{miss,Hard}}$ vector built from hard objects - one longitudinal and one perpendicular. The first component is sensitive to the scale of $p_{\mathrm{T}}^{\mathrm{miss,track}}$ ($p_{\mathrm{T}}^{\mathrm{miss,jetCorr}}$), while the latter represents a measurement of the resolution. Both the MC modeling of the data and pile-up effects contribute to the systematic uncertainties. Uncertainties on the scale (resolution) of the soft term are of the order of $\sim 5\%$ ($\sim 10\%$).

Chapter 3

ATLAS Jet Trigger Performance with Early LHC Data

Jets are the most commonly produced objects at the LHC. They can either be produced directly in the hard-scatter collision, originate from the decay of a heavy resonance, such as the Higgs boson or a vector boson, be the result of ISR/FSR, or be produced in pile-up interactions and the UE. Jets can serve as observables, that one can directly measure, as well as tools, that can be employed to extract properties of a particular final state, as is the case of the analysis presented in Chapter 4. Jets themselves are the signal in QCD physics studies, and constitute a source of background in nearly every physics analysis at the LHC. For these reasons, understanding jets is fundamental for ATLAS.

In ATLAS, jets are primarily identified through the jet trigger. Its goal is to select potentially interesting physics events containing jets, with a very high efficiency, controlling the overwhelming jet production rate of the LHC. Events rejected by the trigger system are permanently discarded. On the other hand, events accepted by the jet trigger can be used in a variety of physics analysis, ranging from QCD to Higgs and Supersymmetry searches. Having an unbiased sample of events triggered on jets is also fundamental to determine the uncertainty on the jet energy scale (addressed in Section 2.6.4.4), which often dominates the systematic uncertainties in many physics analysis, such as the one presented in Chapter 4. Thus, validating the jet trigger and ensuring it is selecting events as expected is extremely important.

This chapter deals with the validation and performance studies of the jet trigger, done using LHC pp collision data, collected by the ATLAS detector in 2010 and 2011. It is divided in three sections. The first addresses the validation studies done for the L2 jet trigger with the first $\sqrt{s} = 7$ TeV data collected by ATLAS, which are partly included in the public documents [108, 158]. The second section presents studies performed for the possibility of a hadronic calibration for L2, using data collected in 2010. Finally, a detailed study of the efficiency of the jet trigger, with early 2011 data, is shown in the third part, elaborating on the work shown in Refs. [159–161].

3.1 Validation of the jet trigger at L2 with 2010 data

ATLAS began collecting pp collision data, at $\sqrt{s} = 7$ TeV, on March 30^{th} 2010. During this data-taking period, only L1 was used to trigger on jets, while the HLT was running in so-called pass-through mode. This means that the L2 and EF algorithms were running online, but the event was accepted regardless of the trigger decision. This situation presented the perfect opportunity to assess the performance of the jet trigger at L2, before it had a real impact on event selection in ATLAS.

The L2 jet trigger performance was evaluated in a number of different ways, which are described next. First, distributions of basic L2 jet kinematics were used to compare real data and MC simulation. Then, L2 jets were matched to offline reconstructed jets, in both data and MC, in order to evaluate residuals, energy response ratios and trigger efficiencies, of L2 with respect to offline. This work was fundamental to declare the L2 jet trigger validated, after which it was turned-on for online event selection.

We note that the errors presented throughout these studies are purely statistical. The number of simulated events was normalized to the number of events in data, independently for each of the presented distributions. Finally, L2 (L1) jets are often labelled as LVL2 (LVL1).

3.1.1 Samples and event selection

The work was developed using $\sqrt{s} = 7$ TeV pp collision data from the LHC, collected by the ATLAS detector between April 8^{th} and June 5^{th} 2010. This dataset corresponds to an integrated luminosity of approximately $\mathscr{L} = 17$ nb^{-1}, covering the data-taking periods referred to as A2, B and C.

Events from the `MinBias` data stream were used in the analysis. Inelastic pp collision events were primarily selected with the `L1_MBTS_1` trigger. This trigger requires at least one hit on either of the 32 Minimum Bias Trigger Scintillators (MBTS), installed on both sides of the ATLAS detector endcaps (MBTS_A and MBTS_C). For the presented analysis, this represents an orthogonal trigger, meaning that the selected sample was unbiased for the jet trigger. The efficiencies for this trigger selection were determined elsewhere [162].

Data events were further selected using a Good Run List (GRL), meaning that only runs and luminosity blocks with the appropriate data quality flags were used, ensuring the beam, detector, trigger and reconstructed physics objects are deemed suitable for physics analysis [163]. Moreover, LBs where the HLT was not running, or where L1 was prescaled, were excluded from the analysis. The resulting dataset is summarized in Table 3.1.

Data was compared to simulated minimum bias events at $\sqrt{s} = 7$ TeV, which were generated using the Pythia 6.4.21 MC program [164], with the ATLAS MC09 parameter tune [165]. The MC was normalized to the number of events in data, on a

Period	Run	LB range	Notes
A2	152777	81 – 329	*
	152844	195 – 234	
	152845	111 – 349	*
	152878	100 – 214	
	152933	46 – 173	
	152994	294 – 353	*
	153030	120 – 203	
	153134	354 – 362	
	153136	249 – 253	
	153159	88 – 177	*
	153200	145 – 178	
B	153565	258 – 953	
	154810	159 – 220	*
	154813	8 – 17 83 – 187	
	154815	9 – 38	*
	154817	9 – 287	
	155073	88 – 200 202 – 247 249 – 272 274 – 394 397 – 407	*
	155112	137 – 166 186 – 215 217 – 322 324 – 493 495 – 592 594 – 609 612 – 625	
	155116	9 – 26 28 – 44 46 – 93	*
	155160	241 – 503	*
C	155228	133 – 148	*
	155280	360 – 375	
	155569	228 – 467	
	155634	144 – 147 149 – 326 328 – 333	
	155669	264 – 311	
	155678	250 – 308	**
	155697	264 – 266 268 – 334 336 – 352 354 – 506	
	156682	449 – 475 477 – 507 509 – 512	**

TABLE 3.1: Dataset used in the analysis for validation of the L2 jet trigger. The run numbers, luminosity blocks and data-taking periods are shown. The symbols in the column labelled as "Notes" indicate that tighter selections were applied to the LBs, compared to the ones provided by the GRL, either because the HLT was not running online (*), or because the L1 jet trigger was prescaled (**).

case-by-case basis. Thus, the cross-section of the generated process and the luminosity of the data were not used.

Collision candidates, on both data and simulation, were selected by requiring at least one reconstructed primary vertex in each event, situated within $|z| < 10$ cm of the ATLAS detector geometrical centre and having at least 5 tracks pointing to it [163].

The jet trigger chains, with their corresponding L1, L2 and EF thresholds, relevant for this analysis, from the trigger menu used during the considered data-taking period, are detailed in Table 3.2. The analysis focuses on inclusive central jet triggers. Forward jet triggers were not considered in this study and are, therefore, not included in the table.

Trigger chain	**L1 signature**	**L2 signature**	**Thresholds [GeV]**		
			L1	**L2**	**EF**
EF_j10	L1_J5	l2_j7	5	7	10
EF_j20	L1_J10	l2_j15	10	15	20
EF_j40	L1_J15	l2_j30	15	30	40
EF_j80	L1_J30	l2_j60	30	60	80

TABLE 3.2: Inclusive central jet trigger chains relevant for the analysis, running in the trigger menu for early 2010 data taking.

Jets reconstructed at L2 were obtained from the lowest E_{T} signature in the menu, i.e. l2_j7. This signature is seeded the by L1_J5 item, and accepts events with at least one central ($|\eta| < 3.2$) jet passing $E_{\mathrm{T}} > 7$ GeV. Though available, the hadronic calibration of L2 jets (see Section 2.6.4.5) was not running online, and the E_{T} thresholds are, therefore, applied at the EM scale. L2 jets were retrieved using the Trigger Decision Tool [166], with the option alsoDeactivateTEs enabled, ensuring that all jets reconstructed at L2 were recovered, and not just those passing the threshold.

At this point, it is important to note that a completely independent analysis of the L2 jet trigger is not possible. As described in Section 2.6.4.5, L2 reconstruction is seeded by L1. In this case, the considered L2 jets have been reconstructed from L1_J5 RoIs. The bias of L1_J5 cannot be removed and its effect will be seen throughout the analysis. We will, nonetheless, refer to L2 jets as if we were solely analyzing the L2 jet trigger, as this analysis is as unbiased as it can possibly be. The reader should, therefore, bear in mind that the selection of L1, namely from L1_J5, is always present. More details on the performance of the L1 jet trigger can be found in Refs. [158, 167].

Offline jets were used as a reference in this analysis. They were reconstructed from topo-clusters, using the anti-k$_t$ jet algorithm, with a distance parameter of $R = 0.4$, and a minimum p_{T} cut of 4 GeV (see Section 2.6.4.1). The choice of the distance parameter was motivated by the jet algorithm used at L2, i.e. a cone algorithm with a radius of $R = 0.4$. This way, L2 and offline jets are more similar in size, which should provide a fairer comparison. With the goal of further minimizing the differences, no hadronic calibration was considered for the offline reconstructed jets, and the energy measurements are presented at the EM scale.

A selection criteria [163] aimed at improving the quality of the offline reconstructed jets was also applied (see Section 2.6.4.2). An offline jet was considered *bad* if it held at least one of these features:

$n_{90} \leqslant 5$ and $f_{\mathrm{HEC}} > 0.8$ n_{90} is the number of cells accounting for at least 90% of the jet energy. f_{HEC} the jet energy fraction in the hadronic endcap of the ATLAS detector. This selection tags jets reconstructed from sporadic noise bursts in the HEC, where most of the energy is in single calorimeter cells.

$|f_{\mathrm{quality}}| > 0.8$ and $f_{\mathrm{EM}} > 0.95$ f_{quality} is the fraction of jet energy from bad-quality calorimeter cells. f_{EM} is the jet energy fraction in the electromagnetic calorimeter. These requirements select mis-reconstructed jets originating from noise burst in the EM calorimeter

$t_{\mathrm{jet}} > 50\,\mathrm{ns}$ t_{jet} is the jet energy-squared-weighted cell time. This selection selects out-of-time energy depositions such as those originating from cosmic ray muons.

An *ugly* offline jet would have: $f_{\mathrm{cor}} > 0.5$ and $f_{\mathrm{TG3}} > 0.5$, where f_{cor} is the fraction of the electromagnetic scale jet energy from cells within the jet that are considered problematic in the detector data-base, and f_{TG3} is defined as the fraction of jet energy in the TileGap3 layer. A jet that is neither *bad* nor *ugly* is considered *good*. Only *good* jets with $f_{\mathrm{HEC}} < 1 - |f_{\mathrm{quality}}|$ and $|\eta| < 2.8$ were used in this analysis. By using $|\eta| < 2.8$, instead of $|\eta| < 3.2$, we ensure that all of the jet energy is reconstructed in the central calorimeters, and avoid possible biases in the measurements, arising from reconstruction in transition-regions.

3.1.2 L2 jet kinematics in data and simulation

In this section we present distributions for basic kinematic quantities of L2 jets, both in real data, shown by black points, and MC simulation, shown as the full yellow histograms.

Figure 3.1 shows a distribution of the L2 jet multiplicity in each event. As expected, the number of events decreases with increasing jet multiplicity and the distribution shows L2 reconstructed up to seven jets per event. Moreover, an overall excellent agreement is seen between data and simulation. The discrepancies visible in the last three bins are attributed to low statistics of the MC sample.

Figure 3.2a shows the pseudorapidity distribution of the selected L2 jets. The distribution is shaped as expected, and is revealing of the structure of the ATLAS detector. As for the comparison between data and MC, some disagreements are clearly visible, particularly in the negative side around the crack region ($-2.1 < \eta_{\mathrm{L2}} < -1.2$) and in the region of the HEC ($2.1 < |\eta_{\mathrm{L2}}| < 2.8$). These discrepancies will be explained ahead.

The ϕ distribution of L2 jets is presented in Figure 3.2b. It shows the anticipated flat distribution, indicative of the uniformity of the detector along the azimuthal angle. The

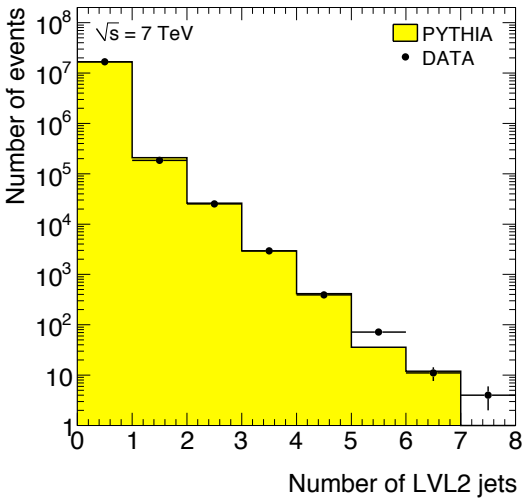

FIGURE 3.1: Multiplicity of L2 jets.

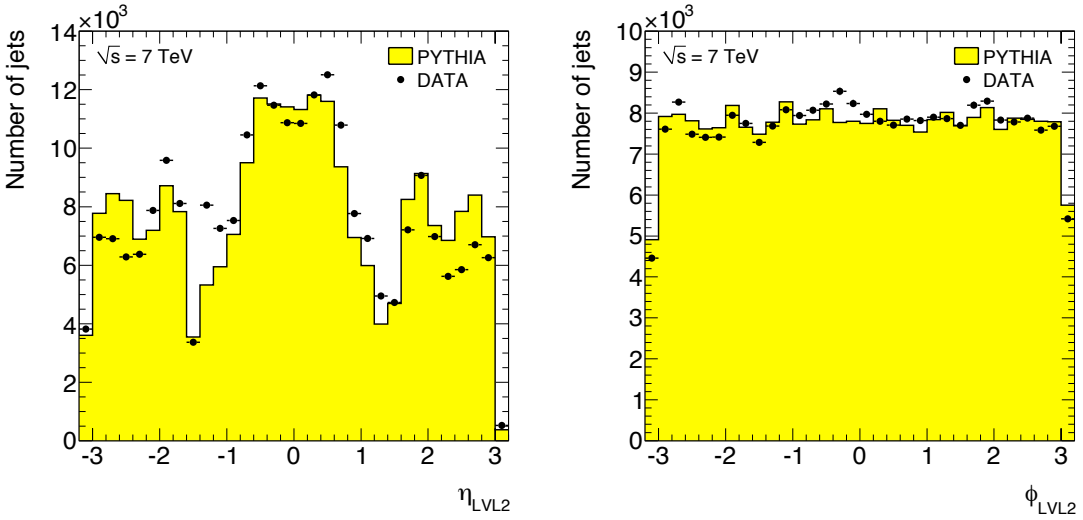

(a) (b)

FIGURE 3.2: Angular distributions of L2 jets: (a) η and (b) ϕ.

agreement between data and simulation is overall reasonable. A small peak structure is observed in the data, causing a discrepancy with the MC for $-0.6 < \phi_{\mathrm{L2}} < 0$.

The differences between data and simulation, seen for the angular distributions of L2 jets in Figure 3.2, were narrowed down to the $1.2 < |\eta| < 2.1$ region, where spikes in data where visible for $-3.0 < \phi < -2.6$, $-0.6 < \phi < 0$ and $1.6 < \phi < 2.2$. The L1 jets that seeded the L2 jets under study were also investigated, to try to understand the origin of the observed discrepancies. Since L2 identifies one jet per L1 RoI, the so-called RoIWord of each jet can be used to provide a unequivocal matching between L1 and L2. The ϕ distribution for L1 jets with $1.2 < |\eta| < 2.1$ is shown in Figure 3.3a. This distribution shows spikes in the same positions reported for L2. This is an indication that the origin of the discrepancies is in fact L1, and not L2.

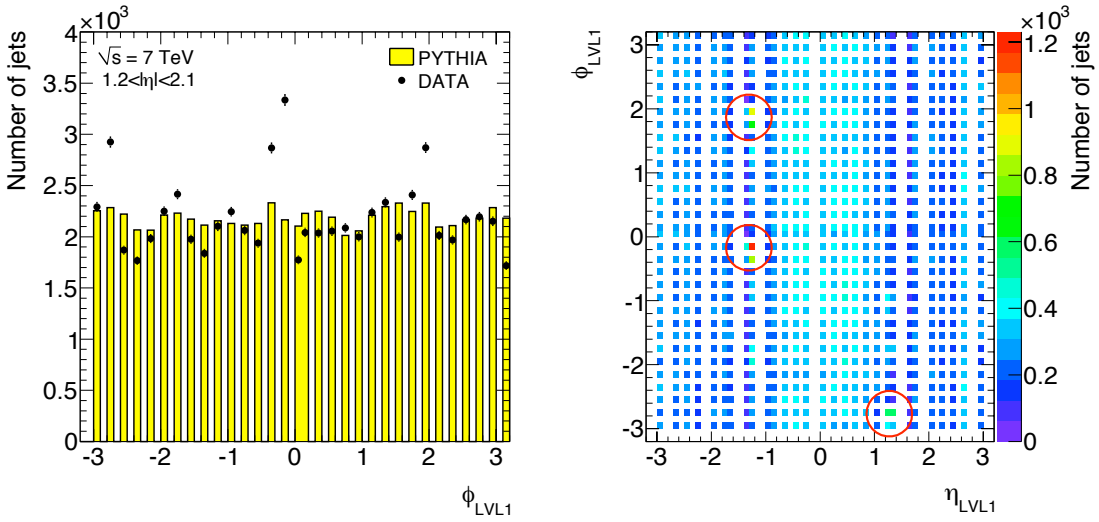

FIGURE 3.3: Angular distributions of L1 jets: (a) ϕ distribution of L1 jets with $1.2 < |\eta_{\mathrm{L1}}| < 2.1$; and (b) (η, ϕ) map of L1 jets in data, with the red circles indicating noisy calorimeter towers.

The (η, ϕ) map for L1 jets in data, displayed in Figure 3.3b, shows three "hot spots", marked by red circles. These "hot spots" are regions where the number of reconstructed L1 jets is much higher than in the closely surrounding calorimeter cells. They are attributed to noisy trigger towers, that caused a large fraction of jets to be reconstructed from noisy calorimeter signals, rather than true energy deposits. These noisy regions are not reproduced by the simulation. The "hot spots" are located in the same η and ϕ regions signaled before, where the data/MC discrepancies were seen for L2 jets. Therefore, the origin of these discrepancies is not the reconstruction at L2 *per se*, but the electronic noise in the trigger towers, which already affects jet reconstruction at L1.

In what follows, we remove trigger jets, from data only, that were reconstructed in the noisy calorimeter regions. The procedure consists in applying rectangular selection cuts, on the (η, ϕ) position of the L1 jets. The corresponding L2 jets are automatically removed by use of the RoIWord. In particular, the following regions were excluded:

- $-1.4 < \eta < -1.1$ and $-0.6 < \phi < 0.0$;
- $-1.4 < \eta < -1.1$ and $1.6 < \phi < 2.2$;
- $1.1 < \eta < 1.6$ and $-3.0 < \phi < -2.6$.

Figure 3.4 shows the E_{T} spectrum of L2 jets in data and MC, after the removal of jets in data that fall in the noisy L1 regions. Both linear and logarithmic scales on the y-axis are presented. As mentioned, no calibration is applied at L2 and this spectrum is presented at EM scale. The steeply falling shape of the distribution with increasing E_{T} is characteristic of jets. The data/MC agreement is good even in the tails, as can be seen in Figure 3.4b.

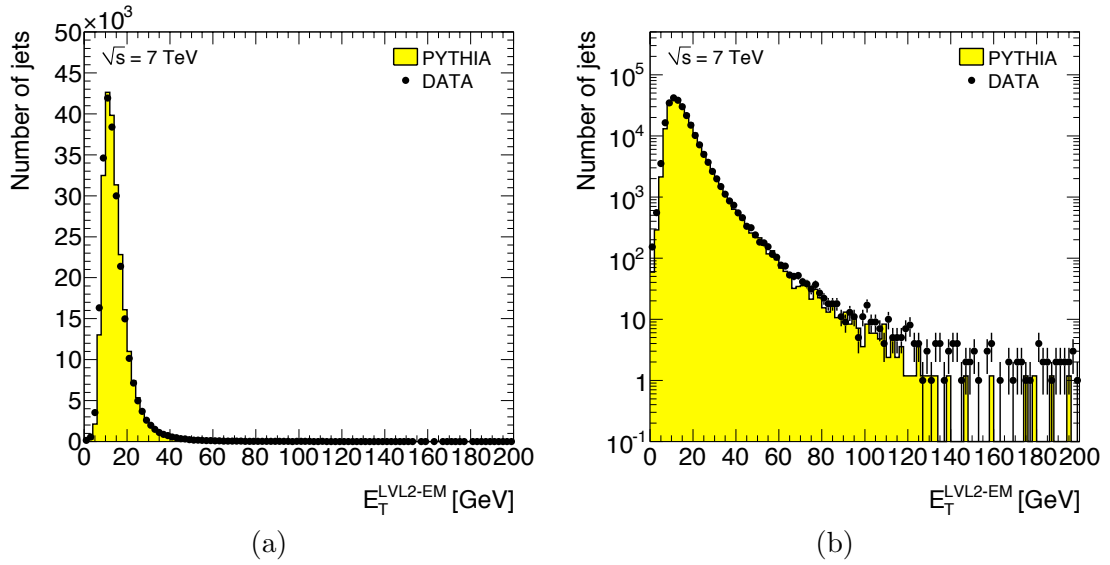

FIGURE 3.4: E_{T} distribution of L2 jets at the EM scale, after removal of jets falling in noisy calorimeter regions, with: (a) linear scale on the y-axis; and (b) logarithmic scale on the y-axis.

Lastly, for completeness, the L2 jet distributions of multiplicity, η and ϕ, after removal of the noisy L1 regions, can be seen in Figure 3.5 and Figure 3.6. The overall data/MC agreement of the distributions clearly improves.

3.1.3 Comparison of L2 and offline jet reconstruction

A comparison between L2 and offline reconstructed jets, in both data and Monte Carlo, is presented in this Section.

Besides the jet selection presented in Section 3.1.1, an extra set of cuts was applied to offline reconstructed jets in data, motivated by the findings described in the previous section. The aim was to remove offline jets that could possibly be associated with trigger jets reconstructed from noise, and not reproduced by simulation. In a similar fashion to what was done to trigger jets, the cuts were applied as a rectangular (η, ϕ) selection, that can be found in Section 3.1.2. Figure 3.7 presents the (η, ϕ) map of the offline reconstructed jets in data, used in the subsequent analysis. The areas where the additional cuts were applied are clearly visible, and they coincide with the problematic regions spotted before.

3.1.3.1 Matching L2 and offline jets

The comparison between L2 and offline reconstructed jets requires matching between the two, to ensure that both are a reconstruction of the same "true jet". The matching procedure is done using the distance ΔR between the jets in the $\eta - \phi$ space:

$$\Delta R = \sqrt{(\eta_{\mathrm{offline}} - \eta_{\mathrm{L2}})^2 + (\phi_{\mathrm{offline}} - \phi_{\mathrm{L2}})^2} \tag{3.1}$$

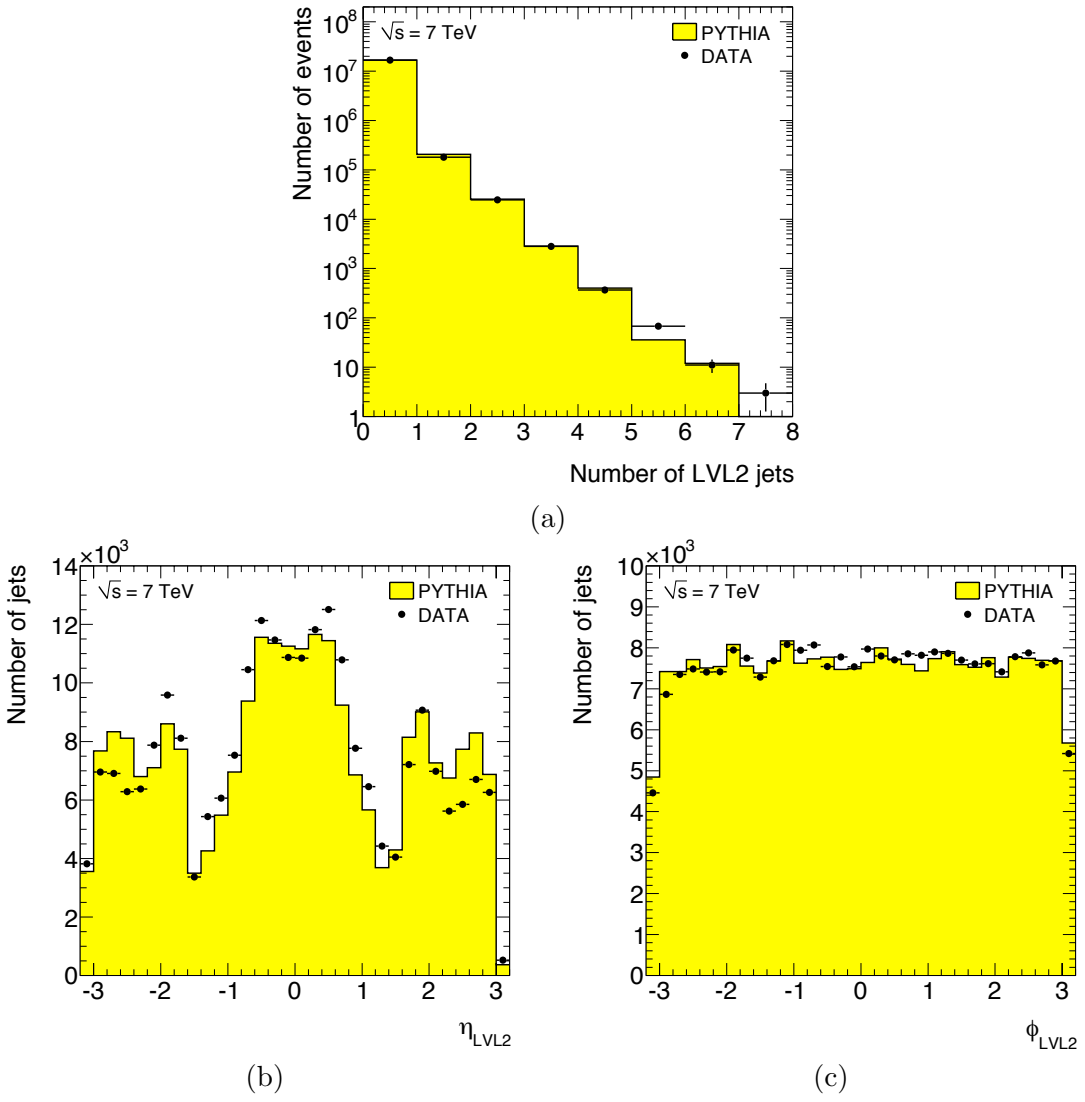

FIGURE 3.5: Distributions of jet multiplicity (a), η (b) and ϕ (c) of L2 jets, after removal of jets falling in noisy calorimeter regions.

The distribution of ΔR between the offline reconstructed jets and the closest L2 jet is presented in Figure 3.8. An excess of events in data, with respect to simulation, is visible in the tails of the ΔR distribution. Still, the MC describes the overall shape of the data distribution reasonably well.

For all L2-offline comparisons that follow, the distance between matched jets was required to be $\Delta R < 0.25$, as indicated in the distribution. This distance approximately corresponds to the local minimum, and selects the peak of the distribution near zero, ensuring one is looking at the same jet object, reconstructed by L2 and offline. Thus, for a given event, a L2 jet is matched to an offline jet if, out of all the L2 jets in the event, it is the closest to that offline jet, within $\Delta R < 0.25$. The rejected tail of the ΔR distribution contains pairs of offline-L2 jets that do not actually correspond to the same jet, but to other jets in the event. This cut is, therefore, essential to make a fair comparison.

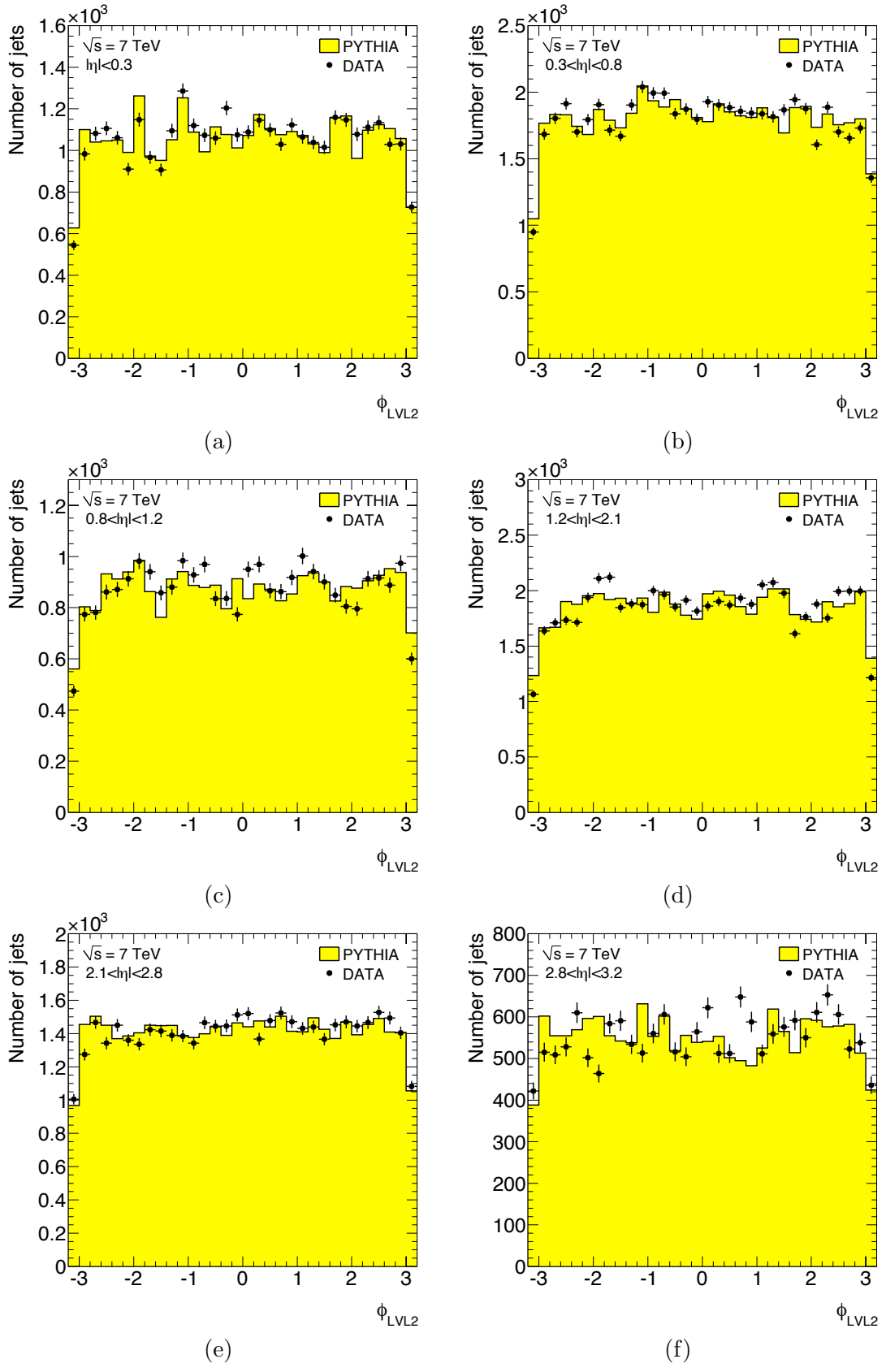

FIGURE 3.6: ϕ distribution of L2 jets, after removal of jets falling in noisy calorimeter regions, in η slices: (a) $|\eta_{L2}| < 0.3$; (b) $0.3 < |\eta_{L2}| < 0.8$; (c) $0.8 < |\eta_{L2}| < 1.2$; (d) $1.2 < |\eta_{L2}| < 2.1$; (e) $2.1 < |\eta_{L2}| < 2.8$; (f) $2.8 < |\eta_{L2}| < 3.2$

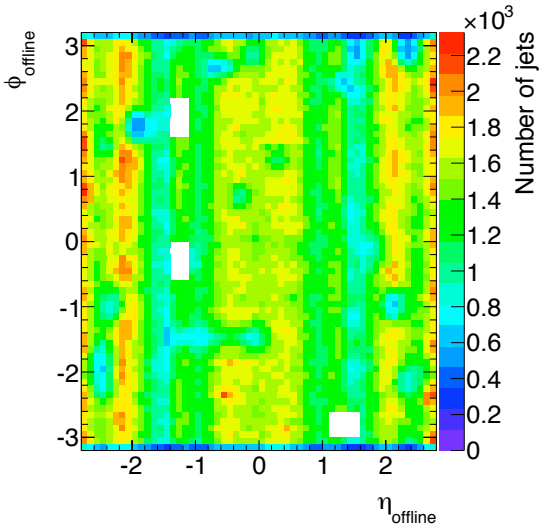

FIGURE 3.7: (η, ϕ) map for offline reconstructed jets in data. The white areas indicate the offline jets removed from the analysis, as they were reconstructed in regions where noisy trigger towers were identified.

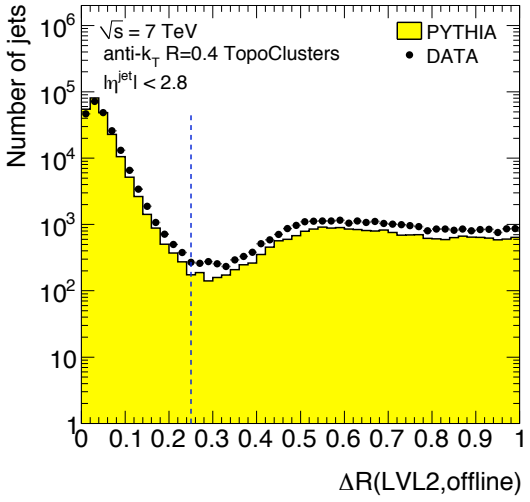

FIGURE 3.8: ΔR distribution for offline jets and the closest L2 jet.

Unmatched L2 jets Out of all the selected L2 jets ($\sim$ 250 k), $\sim$ 780 of them could not be matched to an offline jet within the $\Delta R < 0.25$ cut. All of them were low E_{T} jets, as shown in Figure 3.9, where the transverse energy distribution of the L2 jets (at the EM-scale) is plotted for data and simulation. In fact, there were no L2 jets with $E_{\mathrm{T}} > 35$ GeV without a matching to an offline jet. It will be shown in Section 3.1.3.4 ahead that this E_{T} range is strongly biased by L1, for which the fraction of fakes is relatively high.

Unmatched offline jets Out of $\sim$ 5 M offline jets reconstructed in the analyzed data sample, only 4 jets, with $E_{\mathrm{T}} > 35$ GeV, had no matching to any L2 jets within $\Delta R < 0.25$. Two of those offline jets did, however, have a matching within $0.25 < \Delta R < 0.4$.

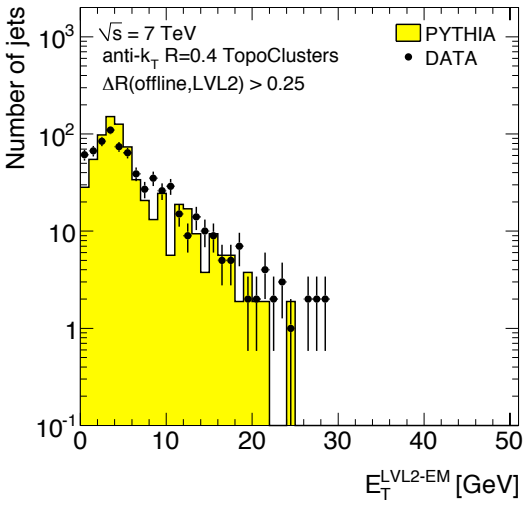

FIGURE 3.9: E_{T} distribution (EM-scale) of LVL2 jets not matched to any offline jet within $\Delta R < 0.25$.

The other two were not seen by L2 or L1. However both of them had $\eta \approx 1.4$, i.e. fell in the crack region of the calorimeters, where the efficiency of the jet trigger is poor, as will be shown Section 3.1.3.4 ahead.

3.1.3.2 L2 residuals with respect to offline

The reconstruction of the kinematics of L2 jets was evaluated with respect to offline, by calculating the η and ϕ residuals between the matched jets. The $\Delta\eta$ and $\Delta\phi$ distributions are presented in Figure 3.10. Both distributions show prominent peaks around zero, revealing the ability of the L2 jet trigger to reconstruct the jet position very similar to the offline reconstruction algorithm. The slight asymmetry of the distributions around zero is a bias related to the granularity of the L1 jet element, and to the overlap removal algorithm applied at L1 (see Figure 2.32). It is, therefore, visible in both data and simulation. Moreover, the distributions show a reasonable data/MC agreement, except for the tails in the positive side of the $\Delta\phi$ distribution (Figure 3.10b).

For completeness, these same $\Delta\eta$ and $\Delta\phi$ distributions are presented in bins of offline jet E_{T}, measured at the EM scale, in Figures 3.11 and 3.12. These distributions show an excellent performance of the L2 jet trigger in reconstructing the jet position in all E_{T} ranges. The data/MC agreement is better in the higher E_{T} bins, compared to the low E_{T} regions, where the MC modeling is dominated by non-perturbative effects of soft QCD. Furthermore, the discrepancy in the tails of the $\Delta\phi$ distribution in Figure 3.10b seem to disappear for $E_{\mathrm{T}} > 20$ GeV.

Figure 3.13 shows the reconstruction of the transverse energy of the jet at L2, with respect to offline, all measured at the EM scale. The distribution of $\Delta E_{\mathrm{T}}/E_{\mathrm{T}}^{\mathrm{offline}}$ peaks at zero, indicating L2 also reconstructs the jet energy very similar to offline. Moreover, the simulation seems to describe the data distribution in the peak reasonably well,

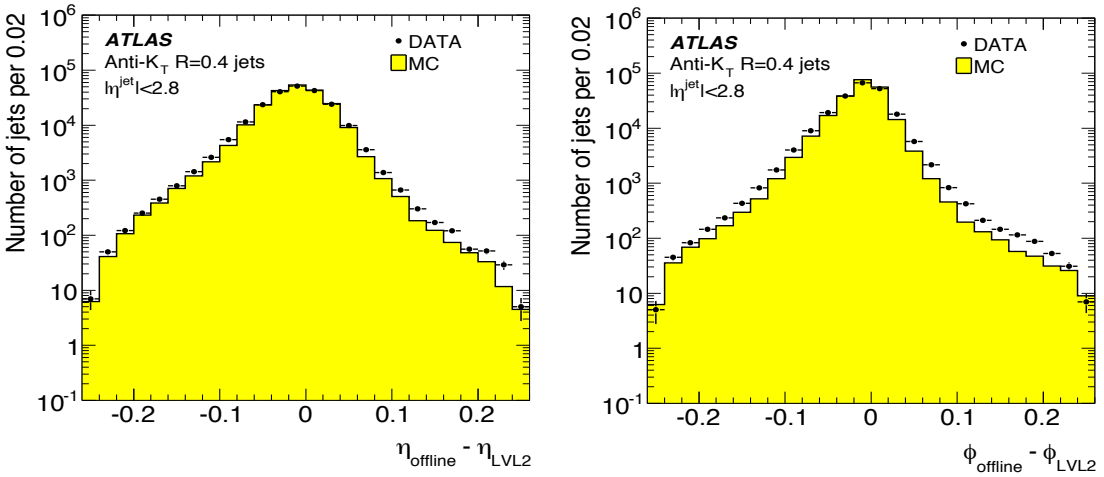

(a) (b)

FIGURE 3.10: Residuals between L2 and offline reconstructed jets: (a) η and (b) ϕ.

with some discrepancies visible in the tails. There is also a large negative tail in the distribution, present in both data and simulation.

L2 jets in this tail, i.e. having $\Delta E_{\mathrm{T}}/E_{\mathrm{T}}^{\mathrm{offline}} < -1$, have low transverse energy, as shown in Figure 3.14a. Moreover, they are poorly matched to offline jets, as they are also in the tails of the ΔR, $\Delta\eta$ and $\Delta\phi$ distributions, as can be seen in Figures 3.14b, 3.14c and 3.14d.

The negative tail in Figure 3.13 is partly caused by a bias from the L1 jet trigger E_{T} selection. As mentioned in Section 3.1.1, the effect of `L1_J5` cannot be removed. This bias should vanish at high E_{T}, when the `L1_J5` selection becomes fully efficient (see Section 3.1.3.4 ahead). Indeed, this is shown in Figure 3.15, where the E_{T} resolution is presented in bins of offline jet E_{T}. The overall data/MC agreement in these distributions is reasonable, particularly in the peaks, improving for higher jet E_{T}.

3.1.3.3 L2 response ratio with respect to offline

Comparisons between the transverse jet energy reconstructed at L2 and offline can also be done by looking at the average E_{T} ratio between the two. This is shown in Figure 3.16a in bins offline jet E_{T}, and in Figure 3.16b in bins of offline jet η. No hadronic calibration is applied, and all energies are measured at the EM scale. The data points are, again, shown in black, while the simulation is now shown by open red markers. The error bars on the points correspond to the RMS of the $E_{\mathrm{T}}^{\mathrm{L2}}/E_{\mathrm{T}}^{\mathrm{offline}}$ distribution in each bin.

Figure 3.16a shows, as observed before, that L2 reconstructs the transverse energy of the jet very similar to offline. The deviation of the ratio from unity at low E_{T}, which corresponds to the negative tail in Figure 3.13, is present in both data and simulation, with roughly the same shape and magnitude. As explained, it is caused by the E_{T} selection of `L1_J5`, which is not fully efficient for low offline E_{T}. Nonetheless, for $E_{\mathrm{T}} >$

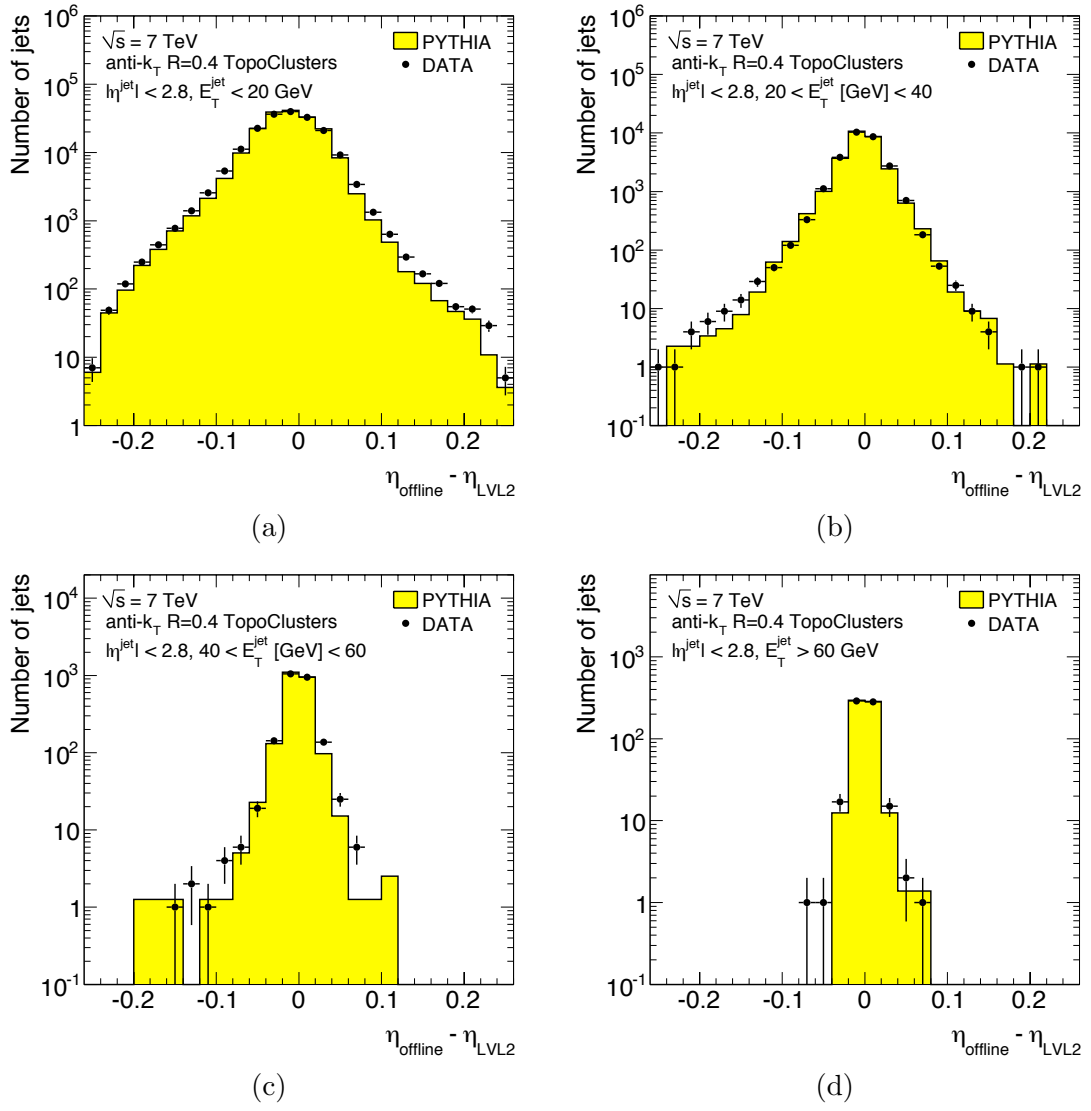

FIGURE 3.11: $\Delta\eta$ distributions between L2 and offline reconstructed jets in bins of E_{T}: (a) $E_{\mathrm{T}}^{\text{offline-EM}} < 20$ GeV; (b) $20 < E_{\mathrm{T}}^{\text{offline-EM}} < 40$ GeV; (c) $40 < E_{\mathrm{T}}^{\text{offline-EM}} < 60$ GeV; (b) $E_{\mathrm{T}}^{\text{offline-EM}} > 60$ GeV

30 GeV, where the bias from L1 is no longer significant, the L2 jet response ratio is within $\pm 1\%$ from unity, with respect to offline. The flatness of the distribution is remarkable, and indicates that the L2 jet reconstruction at the EM scale is very close to the offline reconstruction, despite the different jet algorithms and effects of L1 seeding. Finally, the agreement between data and simulation is also very good, at the level of $1 - 2\%$.

With the goal of reducing the bias from L1, the transverse energy ratio in Figure 3.16b is plotted only for offline jets with $E_{\mathrm{T}} > 30$ GeV, as a function of η. The distribution shows the energy reconstruction at L2 suffers significant variations with η, revealing the structure of the ATLAS detector. The flatness in η of the L2 response ratio with respect to offline is, overall, within $\pm 3 - 5\%$. In the central region of the detector the distributions is very uniform, and L2 tends to overestimate the jet energy by $\sim 2\%$. The agreement between data and simulation is generally good and of about $1 - 2\%$,

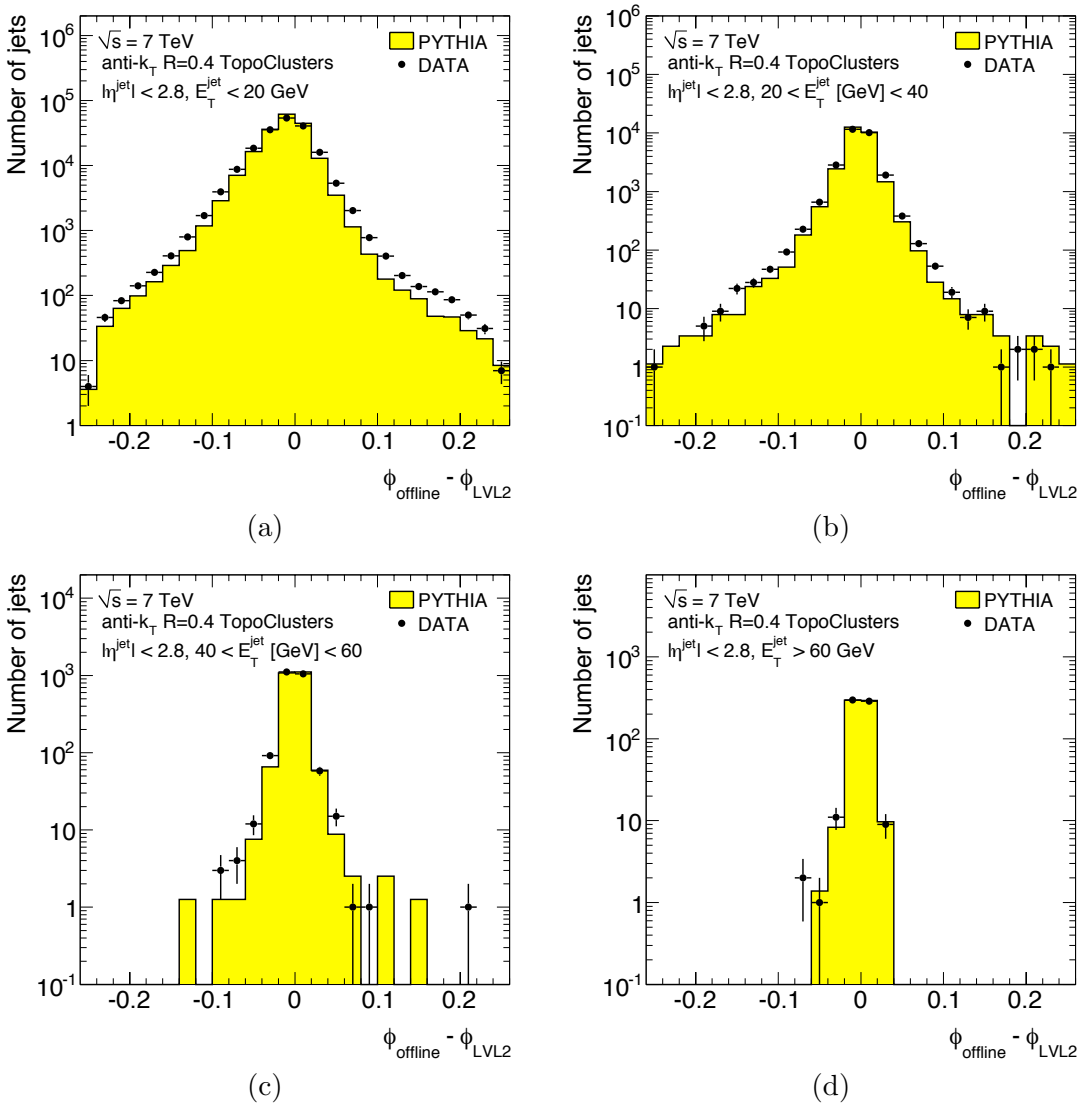

FIGURE 3.12: $\Delta\phi$ distributions between L2 and offline reconstructed jets in bins of E_{T}: (a) $E_{\mathrm{T}}^{\text{offline-EM}} < 20$ GeV; (b) $20 < E_{\mathrm{T}}^{\text{offline-EM}} < 40$ GeV; (c) $40 < E_{\mathrm{T}}^{\text{offline-EM}} < 60$ GeV; (b) $E_{\mathrm{T}}^{\text{offline-EM}} > 60$ GeV

except for a significant $\sim 5\%$ discrepancy in the positive-side HEC. This discrepancy was attributed to high-voltage tests occurring in that part of the ATLAS detector, during the considered data-taking period.

3.1.3.4 L2 efficiency with respect to offline

This section presents the efficiency curves of the different L2 jet trigger signatures, shown in Table 3.2, with respect to the offline jet E_{T} and η. Since the `L1_MBTS_1` trigger is orthogonal with respected to the jet trigger, the efficiencies can be directly determined from the unbiased collected data sample. We will consider the so-called *per*

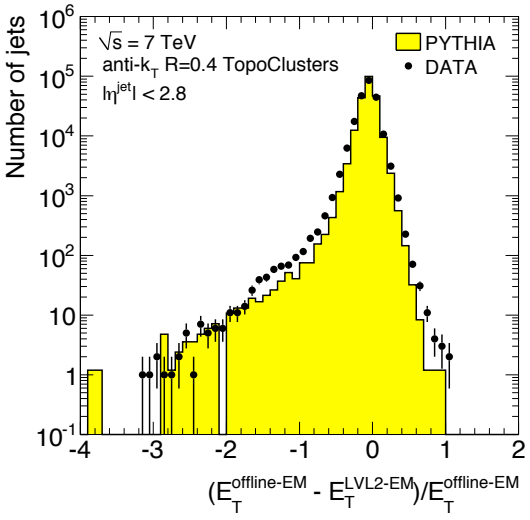

FIGURE 3.13: $\Delta E_{\mathrm{T}}/E_{\mathrm{T}}^{\mathrm{offline}}$ distribution between L2 and offline reconstructed jets, at the EM scale.

jet efficiencies. For a general L2 signature denoted by `l2_jx`, these are defined as:

$$\varepsilon(\texttt{l2\_jx}) = \frac{\text{number of offline jets with a match to a L2 jet passing } \texttt{l2\_jx}}{\text{total number of offline jets}}, \qquad (3.2)$$

where "passing `l2_jx`" means $E_{\mathrm{T}}^{\mathrm{L2}} >$ `x` GeV, at the EM scale. Thus, these efficiencies represent the probability for a certain offline jet to be triggered by the given chain. They will be presented as a function of both E_{T} (EM scale) and η of the offline jet.

Figure 3.17 shows, in red, the efficiencies for the first four L2 jet trigger thresholds (see Table 3.2), as a function of the offline jet E_{T}. Data is shown by the full markers, while simulation is shown by the empty markers. As already discussed, the L2 selection is biased by `L1_J5`. Thus, the efficiency for the `L1_J5` item is also shown in Figure 3.17, in black. The curve was obtained by verifying if the L1 jet that matches the L2 jet under consideration (matching done via RoIWord as explained in Section 3.1.2) passes the `L1_J5` threshold.

Looking first at the `l2_j7` efficiency curve in Figure 3.17a one can see that it is highly biased by L1. In fact, the black and red curves are identical, indicating that the selection of `L1_J5` is much harder than that of `l2_j7`. Therefore, in this case, all the trigger selection is entirely delivered by L1, whereas L2 provides no rejection.

Figure 3.18 shows the `l2_j7` efficiency as a function of the pseudorapidity of the offline jet, in four ranges of offline jet E_{T}. The data is shown in full black markers, whereas the simulation is represented by the red open markers. The transverse energy thresholds were chosen to approximately separate the typical regions in the efficiency curve of Figure 3.17a: the $\sim 50\%$ efficiency point (generally around the trigger threshold); the so-called quadratic region, or turn-on region; and the plateau, where the $\sim 99\%$ efficiency point is reached and the turn-on is maximum and roughly flat.

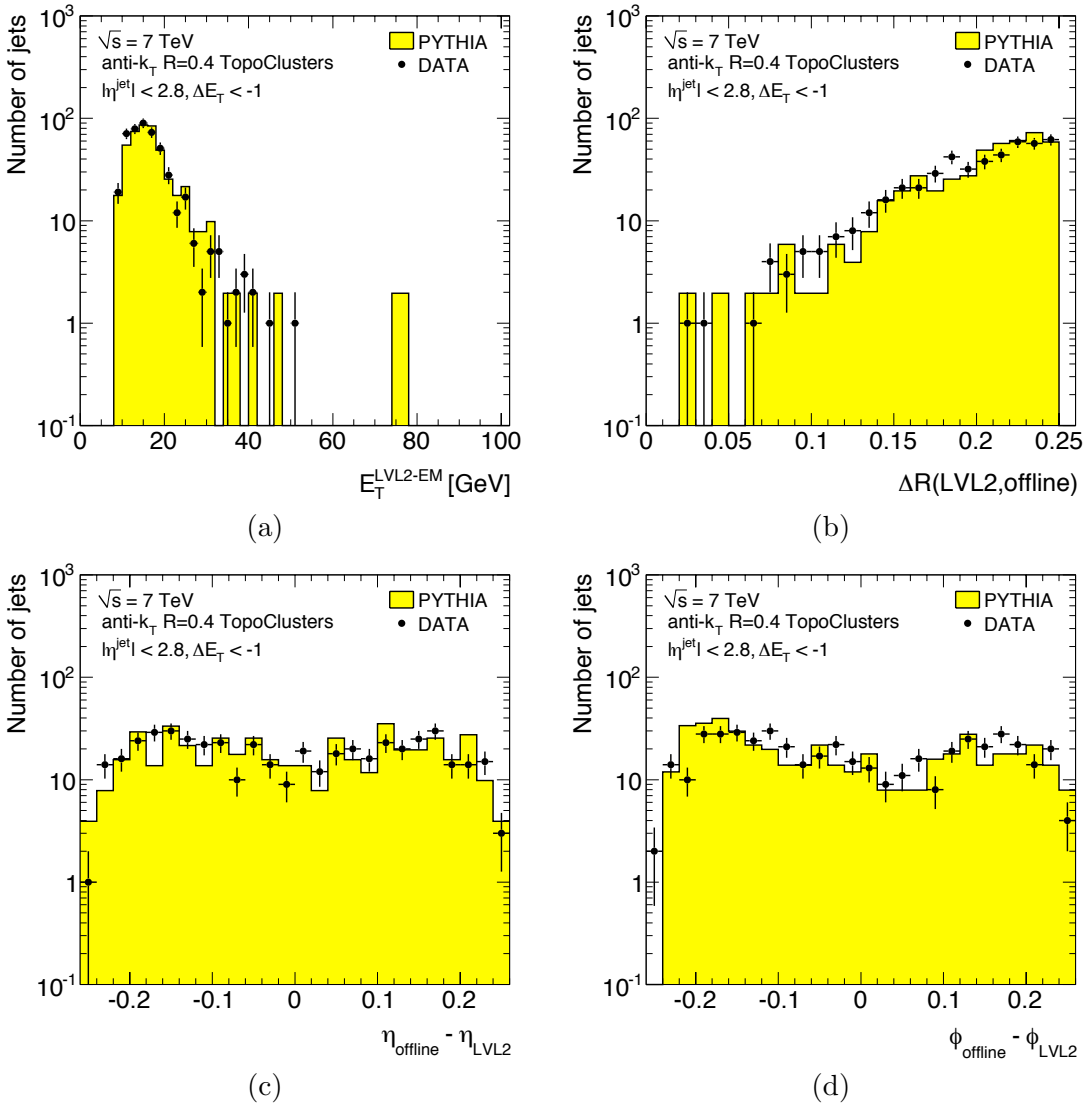

FIGURE 3.14: Distributions for jets with $\Delta E_{\mathrm{T}}/E_{\mathrm{T}}^{\mathrm{offline}} < -1$: (a) E_{T} of L2 jets; and (b) ΔR, (c) $\Delta\eta$ and (d) $\Delta\phi$ between L2 and offline reconstructed jets.

Thus, Figure 3.18b in particular, focuses on the turn-on region of the efficiency curve in Figure 3.17a. There, a large discrepancy is visible between data and simulation, of the order of 5% in the central region, reaching up to 20% in the crack regions. However, as the plateau region is approached, most of the data/MC differences disappear, as shown in Figure 3.18c. Some discrepancies of $\sim 5\%$ are still visible in the crack regions of the detector, but they vanish when looking fully at the plateau, displayed in Figure 3.18d.

Figure 3.17b shows the efficiency curve for the `12_j15` signature. The bias of L1 is smaller here than in the previous case. In fact, it is clear that for $E_{\mathrm{T}}^{\text{offline-EM}} \approx 15$ GeV, L2 is cutting harder than L1, and performing the jet selection. Moreover, in this region one can see an excellent agreement between data and simulation, an indication of the good performance of the L2 jet trigger. However, for $E_{\mathrm{T}}^{\text{offline-EM}} \gtrsim 15$ GeV, the `L1_J5` and `12_j15` efficiency curves superimpose, indicating that in this E_{T} region the rejection is, again, delivered by L1.

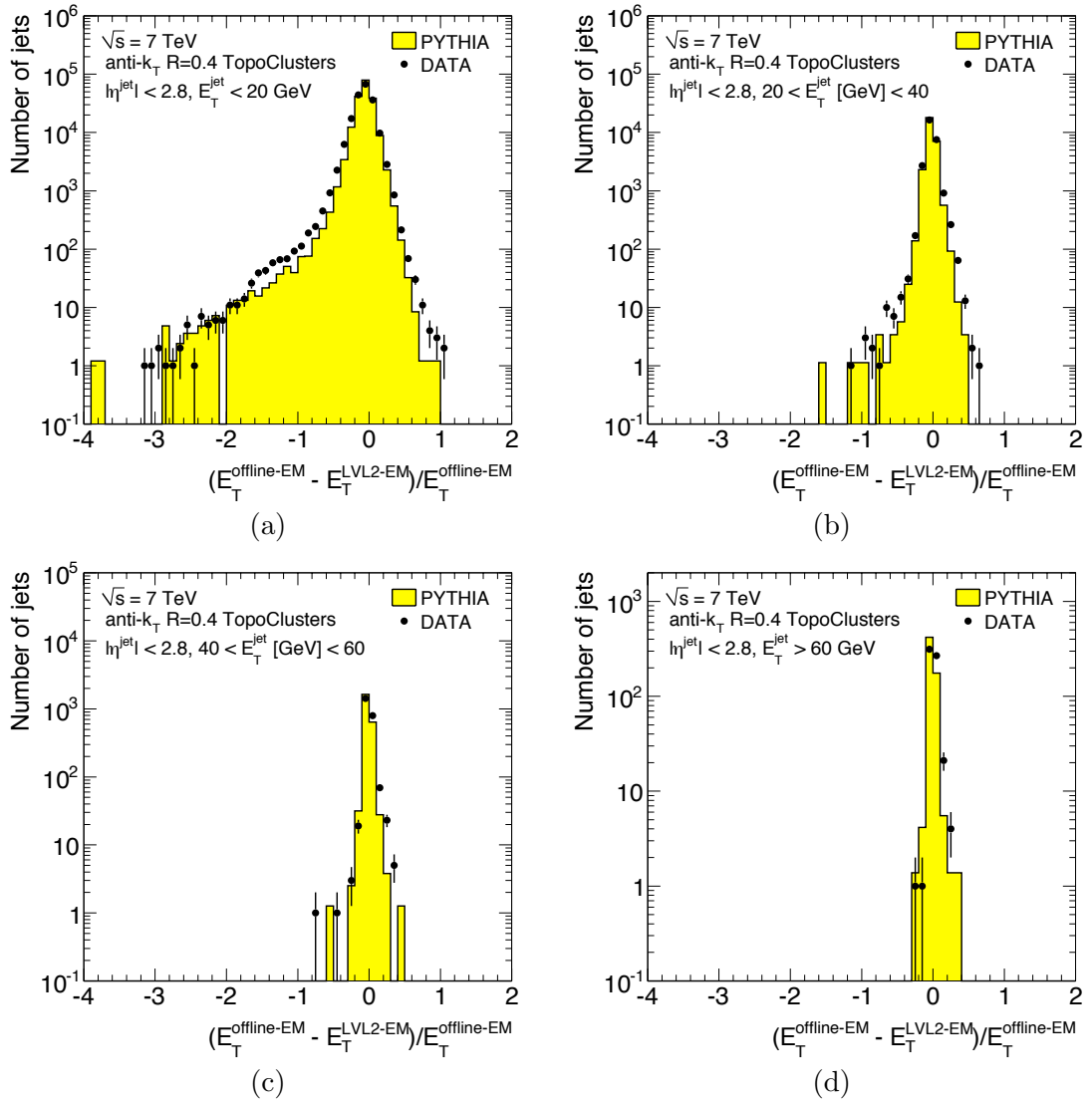

FIGURE 3.15: $\Delta E_{\mathrm{T}}/E_{\mathrm{T}}^{\mathrm{offline}}$ distribution between L2 and offline reconstructed jets, at the EM scale, in bins of E_{T}: (a) $E_{\mathrm{T}}^{\text{offline-EM}} < 20$ GeV; (b) $20 < E_{\mathrm{T}}^{\text{offline-EM}} < 40$ GeV; (c) $40 < E_{\mathrm{T}}^{\text{offline-EM}} < 60$ GeV; (b) $E_{\mathrm{T}}^{\text{offline-EM}} > 60$ GeV

The `l2_j30` efficiency curve is presented in Figure 3.17c. This curve begins accepting jets for $E_{\mathrm{T}}^{\text{offline-EM}} \approx 25$ GeV. At this point, `L1_J5` is practically 100% efficient and we can, therefore, consider `l2_j30` is not biased by L1. The turn-on for `l2_j30` is rather fast, as the efficiency curve is sharp. Plateau is reached for $E_{\mathrm{T}}^{\text{offline-EM}} \approx 40$ GeV. The agreement between data and simulation is very good except, for a small E_{T} range in the turn-on region before plateau.

To get a better understanding of this data/MC difference in the turn-on region, let us look at Figure 3.19. It shows the `l2_j30` efficiency, for data and simulation, as a function of η of the offline jet. The E_{T} range chosen for Figure 3.19b is restricted to that of the problematic region in Figure 3.17c. The curve clearly shows the discrepancy between data and simulation is more significant in the positive side of the HEC, a region

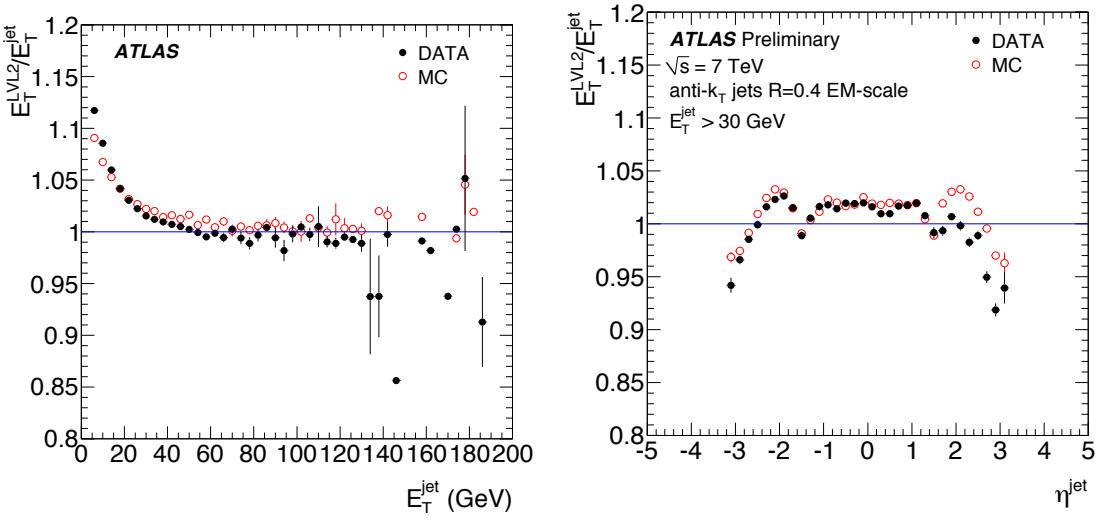

(a) (b)

FIGURE 3.16: Average L2 jet energy response ratio with respect to offline, as a function of the offline jet: (a) E_{T} and (b) η, for jets with $E_{\mathrm{T}} > 30$ GeV.

already flagged as problematic in Section 3.1.3.3. The central region up to $|\eta| < 2.1$, on the other hand, shows only small differences of $\sim 2-3\%$.

Finally, the `l2_j60` efficiency is plotted in Figure 3.17d. Here, the same conclusions drawn for the `l2_j30` efficiency curve, about the L1 bias, apply. `l2_j60` begins to accept jets for $E_{\mathrm{T}}^{\text{offline-EM}} \approx 55$ GeV. As in the previous case, the turn-on is fast and plateau is reached at $E_{\mathrm{T}}^{\text{offline-EM}} \approx 70$ GeV. There is some disagreement between data and MC in the turn-on region, but the statistics are too poor to make a firm conclusion.

3.1.4 Summary and conclusions

The performance of the L2 jet trigger was thoroughly studied using the early *pp* collision data collected by ATLAS in 2010, during a period where the HLT was not actively used for online event rejection.

Data was compared to simulation in distributions of basic kinematic variables of jets reconstructed at L2. The distributions showed the expected shapes, and an overall good agreement between data and MC was seen. Some discrepancies were spotted in localized regions of the detector, and further investigation revealed they were related to noisy trigger towers at L1. Those noisy regions were masked for the subsequent studies.

Then, L2 and offline reconstructed jets were matched in ΔR. All L2 jets with $E_{\mathrm{T}} > 35$ GeV had a match to an offline jet, and only four offline jets were left unmatched.

The η, ϕ and E_{T} residuals of L2 jets with respect to offline were evaluated. It was found that L2 reconstructed jets are, in general, very similar to offline, a remarkable result considering the different jet algorithms used by L1, L2 and offline. Tails and asymmetries in the distributions are present in both data and simulation, and they are

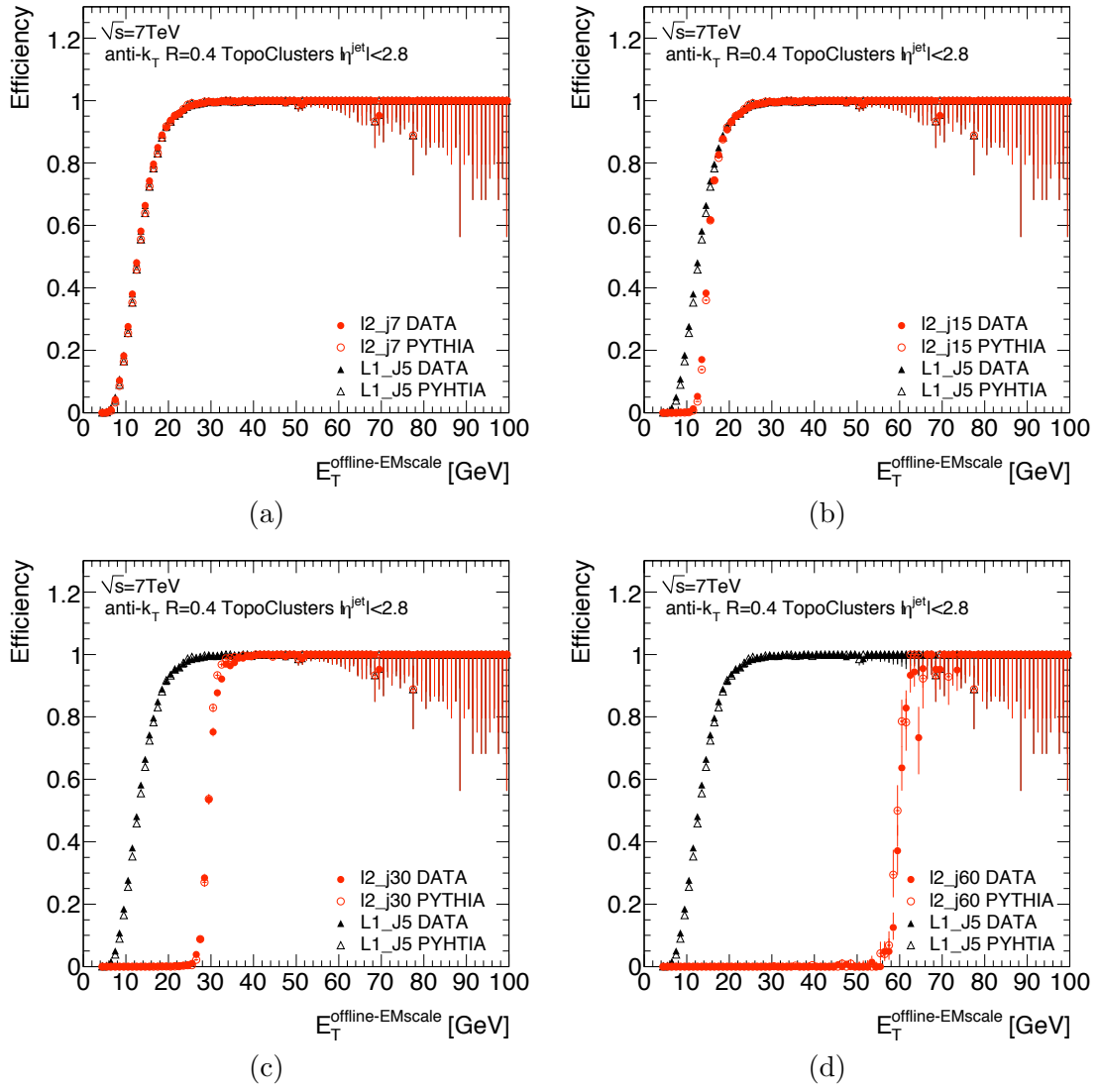

FIGURE 3.17: Efficiencies of the L2 jet trigger, as a function of the offline jet E_{T}, for different signatures: (a) `l2_j7`; (b) `l2_j15`; (c) `l2_j30`; (d) `l2_j60`.

attributed to the bias of L1. The data/MC agreement found was good and improved with the increasing jet E_{T}.

The L2 jet energy response ratio, with respect to offline, was also analyzed. In an E_{T} range unbiased by the L1 selection, the dependence of the L2 response with E_{T} of the offline jet is found to be stable and within 1%. The dependence of the L2 jet energy scale with η of the offline jet is stronger, particularly in the HEC, ranging from $2-5\%$ and reflecting the structure of the detector. The data/MC agreement found was of about $1-2\%$, considered good. The exception is a discrepancy of $\sim 5\%$ in the positive side of the HEC, a behavior which is understood. Again, this is a remarkable result that indicates that L2 introduces very little bias with respect to offline at EM-scale.

Finally, efficiency curves for four L2 jet trigger signatures were analyzed. Although the first two thresholds, `l2_j7` and `l2_j15`, were highly biased by L1, with `L1_J5` providing all the selection, `l2_j30` showed a sharp turn-on and an overall good agreement

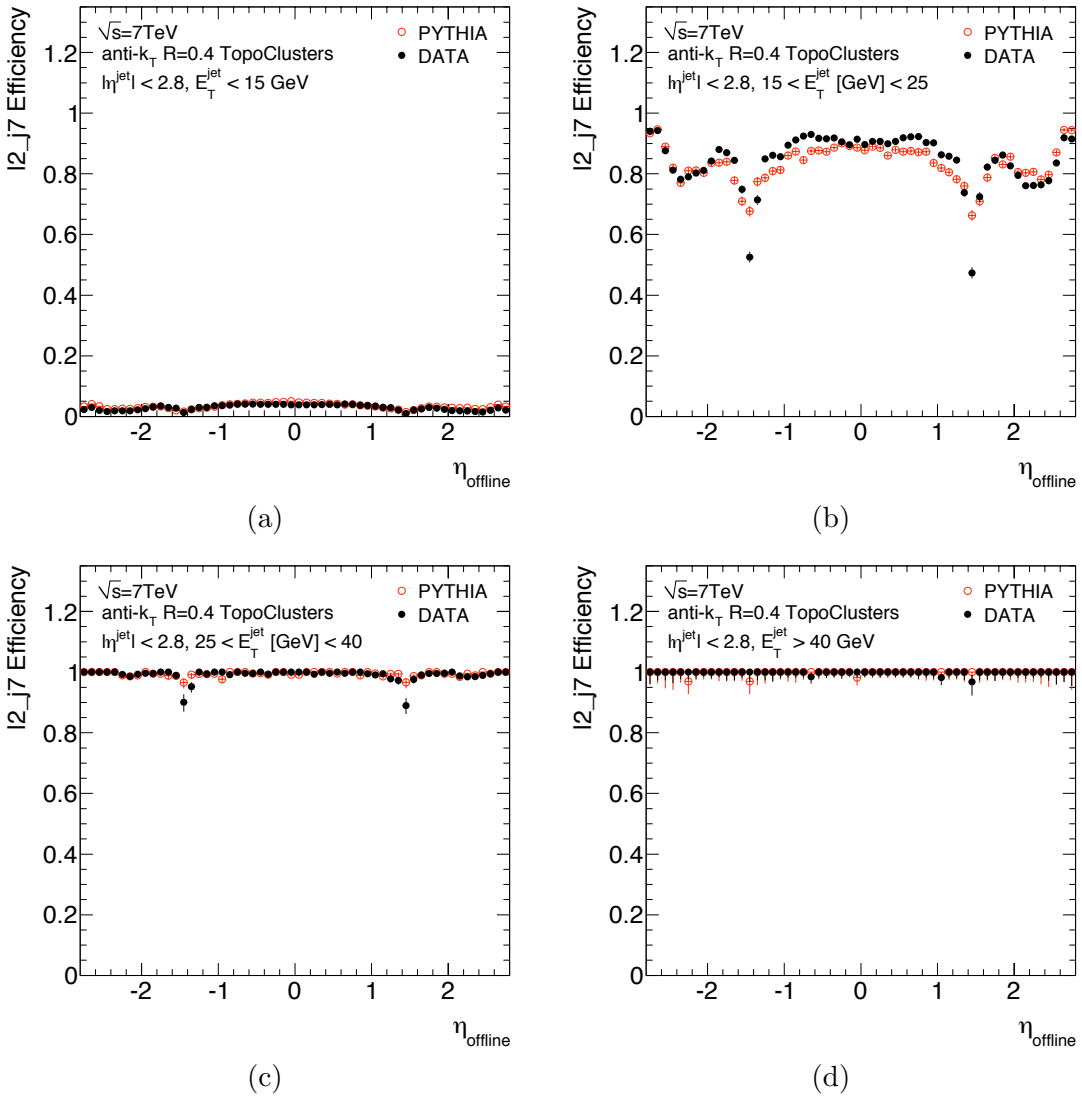

FIGURE 3.18: `l2_j7` efficiency as a function of offline jet η in bins of offline jet E_{T}: (a) $E_{\mathrm{T}}^{\text{offline-EM}} < 15$ GeV; (b) $15 < E_{\mathrm{T}}^{\text{offline-EM}} < 25$ GeV; (c) $25 < E_{\mathrm{T}}^{\text{offline-EM}} < 40$ GeV; (d) $E_{\mathrm{T}}^{\text{offline-EM}} > 40$ GeV;

between data and simulation, at the level of $2-3\%$. Data/MC discrepancies observed in the turn-on region were found, once more, to be more significant in the HEC. The `l2_j60` efficiency curve was dominated by low statistics. However, the data/MC agreement observed for the L2 jet energy response ratio as a function of the offline jet E_{T} seems to indicate that the good behavior of the L2 jet trigger extends at least up to $E_{\mathrm{T}} \approx 120$ GeV.

Altogether, the ATLAS L2 jet trigger showed an excellent performance with the early $\sqrt{s} = 7$ TeV data. The presented studies were fundamental in declaring L2 jet trigger validated, which started running online in rejection mode on the 13^{th} September 2010 (the EF remained in pass-through mode until 2011).

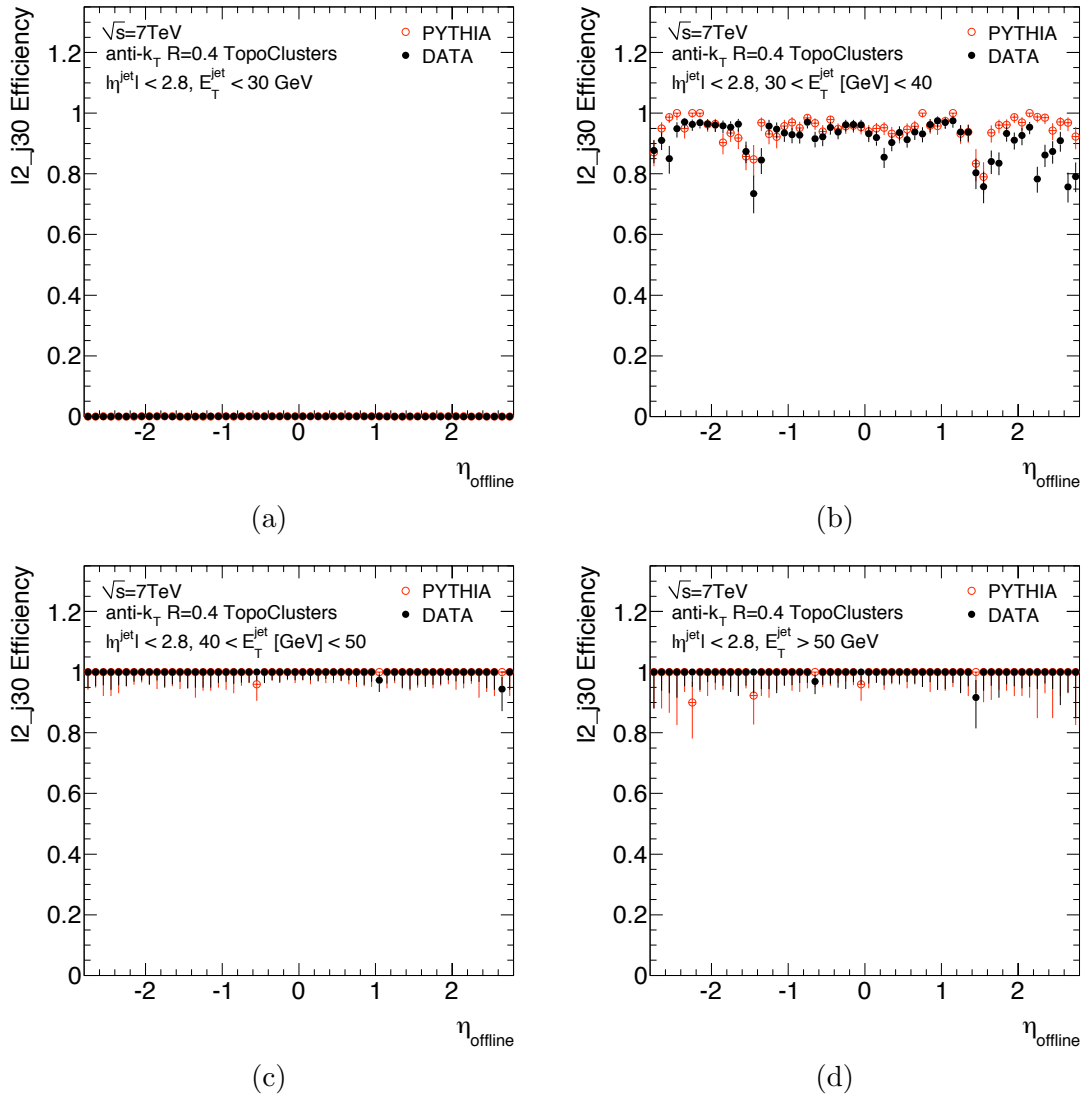

FIGURE 3.19: `l2_j30` efficiency as a function of offline jet η in bins of offline jet E_{T}: (a) $E_{\mathrm{T}}^{\text{offline-EM}} < 30$ GeV; (b) $30 < E_{\mathrm{T}}^{\text{offline-EM}} < 40$ GeV; (c) $40 < E_{\mathrm{T}}^{\text{offline-EM}} < 50$ GeV; (d) $E_{\mathrm{T}}^{\text{offline-EM}} > 50$ GeV;

3.2 Studies of a hadronic calibration for L2 trigger jets

The challenges of measuring and calibrating the jet energy have already been addressed. At the trigger level, a sharp distinction between low and high E_{T} jets around the trigger thresholds is crucial to provide efficient rejection and the most unbiased event selection possible, ensuring the allocated bandwidth is not filled, and important data is not lost. This is particularly challenging, given the rapidly falling p_{T} spectrum of jets.

The efficiency of the jet trigger at L2 was evaluated with respect to offline jets at the EM scale, and results were reported in Section 3.1.3.4. However, calibrated jets are the object of interest in physics analyses. Figure 3.20 shows, in red, the efficiency curve for the `l2_j30` trigger signature, as a function of the offline jet E_{T} at the EM scale, which is identical to the curve in Figure 3.17c. In blue, the `l2_j30` efficiency is shown as a

function of the calibrated jet p_{T}, so at the EM+JES scale (L2 is still at the EM scale). Data is shown by the full markers, while simulation is represented by the open markers. The blue curves show a slower L2 turn-on, when compared to the red curves, which are sharper. Thus, the conclusion is that L2 introduces a stronger bias when considering offline jets at the EM+JES scale.

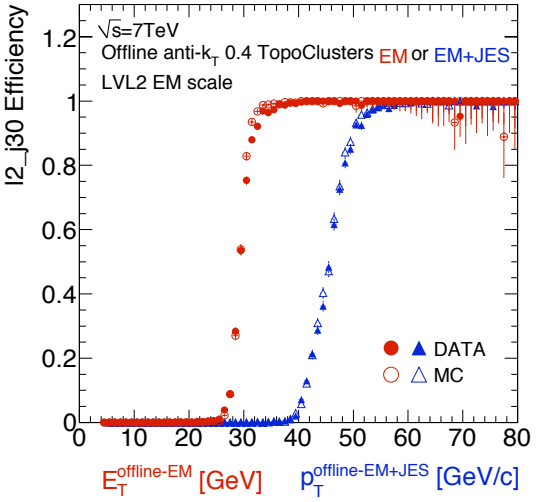

FIGURE 3.20: Efficiency for the `l2_j30` jet trigger signature, as a function of the offline jet E_{T}, at the EM scale in red and at the EM+JES scale in blue. Data is shown by the full markers and simulation by the open markers. The red curves are identical to the ones shown in Figure 3.17c.

The bias introduced by L2 when looking at offline jets at the EM+JES scale can be improved by also applying hadronic calibration to L2 jets, which should sharpen the turn-on of the efficiency curves. As described in Section 2.6.4.5, the L2 jet trigger was prepared to run with a dedicated calibration scheme, based on MC simulation. However, when ATLAS started collecting data in 2010 and 2011, it was decided that the jet trigger would run at the EM scale, because the calibration had not yet been validated with data. The goal of the studies presented in this section was to perform that validation.

The validation studies of L2 described in the previous section also showed that, despite the differences in jet reconstruction between offline and the trigger environment, the L2 and offline EM energy scales were very similar (see Section 3.1.3.4). For this reason, an additional calibration approach was also considered for L2. It simply consisted of applying the offline JES calibration directly to L2 jets. Here, the JES calibration refers only to the energy- and η-dependent weights, derived from simulation, described in Section 2.6.4.3, which calibrate the offline jets to the scale of the truth particle jet. Given the similarity of the L2 and offline reconstructed jets at the EM scale, it was expected that applying the same calibration to both would perform at least as good as the EM scale. Thus, the goal of the studies described in what follows was also to test this procedure, verifying which calibration scheme provided the smallest L2 bias.

The studies of a hadronic calibration for L2 trigger jets were performed in two stages. First, the L2 p_{T} response ratio and relative resolution with respect to offline were evaluated. These two quantities are directly related to the L2 efficiency curves as a function of offline jet p_{T}, which were determined in the second stage. In particular, the response ratio determines approximately where the 50% efficiency point occurs, while the relative resolution impacts the sharpness of the curve.

3.2.1 Samples and event selection

The studies were performed using $\sqrt{s} = 7$ TeV pp collision data from the LHC, collected by the ATLAS detector between April 8$^{\mathrm{th}}$ and August 29$^{\mathrm{th}}$ 2010. During this period only the L1 trigger was used to select events, and the HLT ran in pass-through mode. The datasets used and the event and object selection applied are, for the most part, similar to what was described for the studies in Section 3.1. Therefore, we refer back to Section 3.1.1 for details, while the differences will be clarified in what follows.

In a first stage of these studies, the L2 response ratios and relative p_{T} resolutions were evaluated with respect to offline. The `L1_MBTS_1` trigger, used to select events in the analysis described in Section 3.1, became heavily prescaled throughout 2010 data-taking. Therefore, the jet trigger was used at this stage, to obtain a sample of jets in data with sufficient statistics, and covering a large range in jet p_{T}. As already mentioned, the HLT was not actively running online. Thus, different data samples were obtained from the `JetTauEtmiss` stream[1], and selected using all central inclusive L1 jet triggers available in the menu: `L1_J5`, `L1_J10`, `L1_J15`, `L1_J30`, `L1_J55`, `L1_J75` and `L1_J95`. The data-taking periods referred to as A2, D, E2, E4, E7, F1 and F2 were used and analyzed separately, with the goal of identifying potential effects of changes in the data-taking conditions.

In the second step of the studies presented here, the L2 jet trigger efficiency was evaluated with respect to offline, similar to what was shown in Section 3.1.3.4. The strategy consisted of using an orthogonal trigger and, therefore, inelastic pp collision events were selected using `L1_MBTS_1`, as described in Section 3.1.1. The data used belongs to the A2, B, C and D data-taking periods, which is the same dataset shown in Table 3.1, with the addition of period D. After this, the `L1_MBTS_1` trigger became too prescaled to provide enough events for the efficiency measurements.

Similar to the previous analysis, a GRL was applied to all selected data samples, ensuring the quality of the chosen events. Collision candidates were selected by requiring at least one reconstructed PV in each event, with at least 5 tracks pointing to it.

Offline jets were reconstructed from topo-clusters, using the anti-k_t jet algorithm with $R = 0.4$, $p_{\mathrm{T}} > 4$ GeV and $|\eta| < 3.2$. Only *good* jets were used (see Section 3.1.1) and both the EM and EM+JES energy scales were considered (see Section 2.6.4.3).

L2 jets with $|\eta| < 3.2$ were retrieved from the `l2_j7` signature, using the Trigger Decision Tool, as described in Section 3.1.1. As already discussed, no hadronic calibration

[1] During early data-taking in 2010, the `JetTauEtmiss` stream was called `L1Calo`.

was being applied at the trigger level during data-taking, and the E_{T} thresholds were measured at the EM scale. However, two different sets of calibration constants were retrieved, and applied "offline" to the selected L2 jets. Thus, three different energy scales were considered for L2 jets: the EM scale; the so-called "calibrated" scale, which is the result of applying the dedicated L2 calibration scheme, described in Section 2.6.4.5; and the EM+JES scale, obtained when applying the offline JES calibration scheme, as described in Section 2.6.4.3. It is important to note that while the dedicated L2 calibration constants were computed specifically for L2 jets, the calibration constants of the EM+JES scheme were calculated for offline jets, but applied to L2 jets.

L2 and offline jets were matched following the prescription in Section 3.1.3.1, with the difference that a $\Delta R < 0.4$ cut was used instead. The pairs of L2/offline matched jets were mostly analyzed at comparable energy scales, i.e. EM/EM, or calibrated/EM+JES, or EM+JES/EM+JES. Therefore, we will generally refer to the L2 energy scale only, since the offline jet energy scale is implied.

3.2.2 L2 response ratio and relative resolution with respect to offline

The average p_{T} ratio between L2 and offline jets was evaluated for each of the samples collected with the different L1 triggers. This is shown in Figures 3.21 through 3.27, in bins of offline jet p_{T} on the left, labeled with (a), and in bins of offline jet η on the right, labeled as (b). The data points are obtained from the mean of a Gaussian fit to the distribution of $p_{\mathrm{T}}^{\mathrm{L2}}/p_{\mathrm{T}}^{\mathrm{offline}}$ in each bin. The error bars in each point correspond to the uncertainty on the mean.

These distributions are similar to what was shown in Section 3.1.3.3 and, as discussed there, they are only meaningful when the L1 selection is fully efficient. Thus, Table 3.3 summarizes the offline p_{T} thresholds, both at the EM and EM+JES scales, for which the different L1 triggers used are 100% efficient. These thresholds are indicated by the vertical black and red lines in the distributions versus p_{T}, labeled as (a). The distributions as a function of η, labeled as (b), were plotted using offline jets with p_{T} above the L1 bias only.

L1 trigger	**Offline p_{T} threshold [GeV]**	
	EM scale	**EM+JES**
L1_J5	50	80
L1_J10	60	90
L1_J15	65	110
L1_J30	75	130
L1_J55	120	190
L1_J75	140	210
L1_J95	150	250

TABLE 3.3: Offline p_{T} thresholds, at the EM and EM+JES scales, for which the different L1 triggers are fully efficient.

Each Figure uses a different data sample, selected with a different L1 trigger, as indicated in each distributions individually. For simplicity, only one representative data-taking period is shown in each Figure, as also indicated. The distributions for all data-taking periods can be found in Appendix A. No significant differences were observed between different periods.

The three curves in each Figure show the different L2 jet energy scales: EM in black circles, dedicated L2 calibration in blue squares, and EM+JES in red triangles. It is important to note that since L2 and offline jets are compared in similar footing, i.e. EM with EM, and calibrated or EM+JES with EM+JES, the x-axis of the plots can be either $p_{\mathrm{T}}^{\text{offline-EM}}$ or $p_{\mathrm{T}}^{\text{offline-EM+JES}}$, depending on the curve.

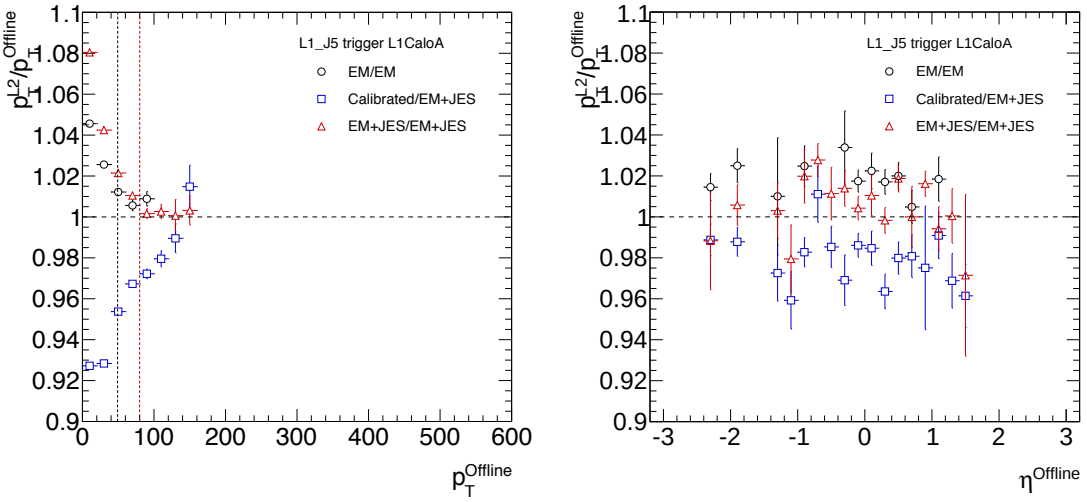

FIGURE 3.21: Average L2 jet transverse momentum response ratio with respect to offline, using a dataset collected with the `L1_J5` trigger in data-taking period A. (a) is plotted as a function of $p_{\mathrm{T}}^{\text{offline-EM}}$ for the black curve, and versus $p_{\mathrm{T}}^{\text{offline-EM+JES}}$ for the remaining curves. Also in (a), the vertical lines indicate the EM (black) and EM+JES (red) offline thresholds for which the `L1_J5` selection is fully efficient (see Table 3.3). (b) is plotted as a function of η, for offline jets above the L1 bias threshold. The black distributions use pairs of L2 and offline matched jets, both at at the EM scale. The blue (red) distributions use L2 jets at the calibrated (EM+JES) scale, and matched offline jets at the EM+JES scale.

The overall impression of the different Figures is that, as anticipated, the distributions for EM (black circles) and EM+JES (red triangles) scales show similarities. This means that the EM+JES energy scale of L2 jets with respect to offline EM+JES is very close to the EM energy scale of L2 with respect to EM offline. As for the dedicated L2 calibration, it generally tends to over-correct the energy of the L2 jet, particularly at low p_{T}.

The L2 EM and EM+JES response ratios are approximately flat with offline p_{T}, within $\pm 1\%$, in the $50 - 400$ GeV range analyzed ($80 - 550$ GeV for EM+JES). There appears to be a slight slope in the distributions of the response ratio versus p_{T}, meaning L2 overestimates the offline jet p_{T} by up to 1% for $p_{\mathrm{T}}^{\text{offline}} \lesssim 110$ GeV, and underestimates it by $\sim 1\%$ for jets with $p_{\mathrm{T}}^{\text{offline}} \gtrsim 110$ GeV.

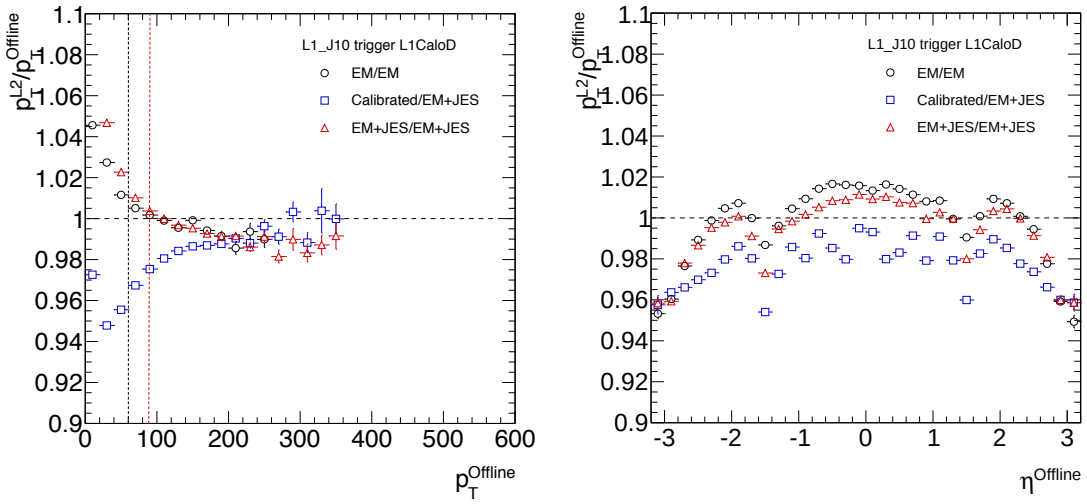

(a) (b)

FIGURE 3.22: Average L2 jet transverse momentum response ratio with respect to offline, using a dataset collected with the L1_J10 trigger in data-taking period D. See the caption of Figure 3.21 for further details.

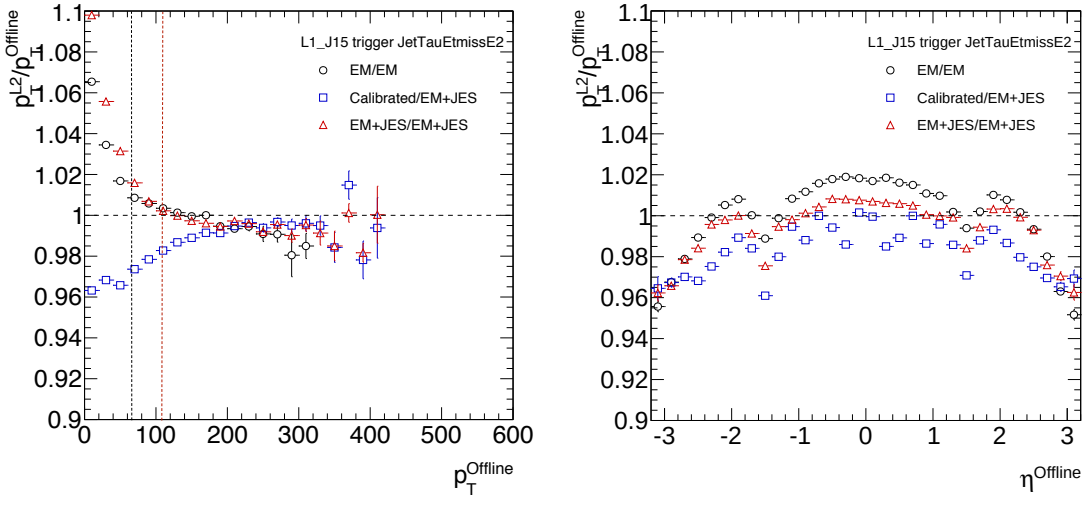

(a) (b)

FIGURE 3.23: Average L2 jet transverse momentum response ratio with respect to offline, using a dataset collected with the L1_J15 trigger in data-taking period E2. See the caption of Figure 3.21 for further details.

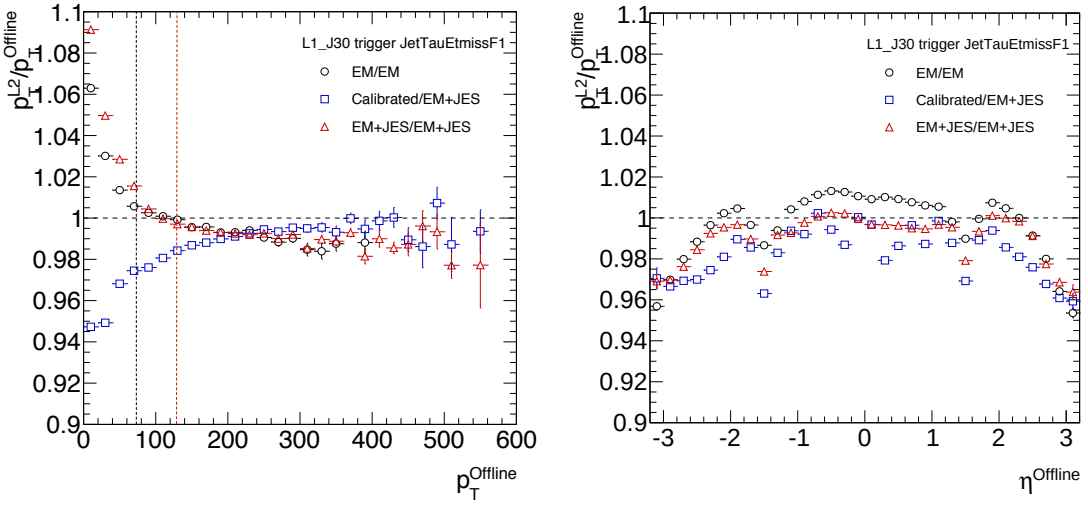

(a) (b)

FIGURE 3.24: Average L2 jet transverse momentum response ratio with respect to offline, using a dataset collected with the L1_J30 trigger in data-taking period F1. See the caption of Figure 3.21 for further details.

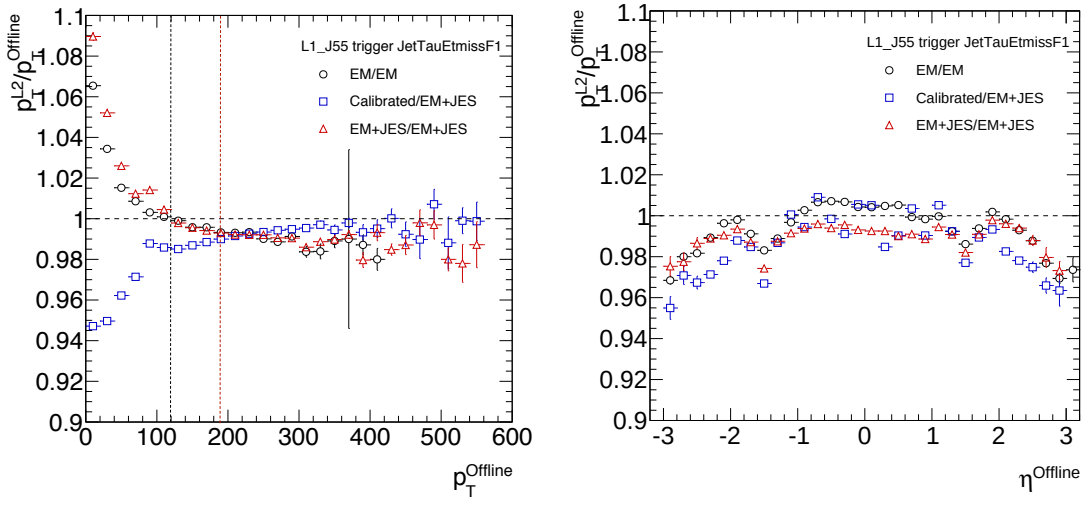

(a) (b)

FIGURE 3.25: Average L2 jet transverse momentum response ratio with respect to offline, using a dataset collected with the L1_J55 trigger in data-taking period F1. See the caption of Figure 3.21 for further details.

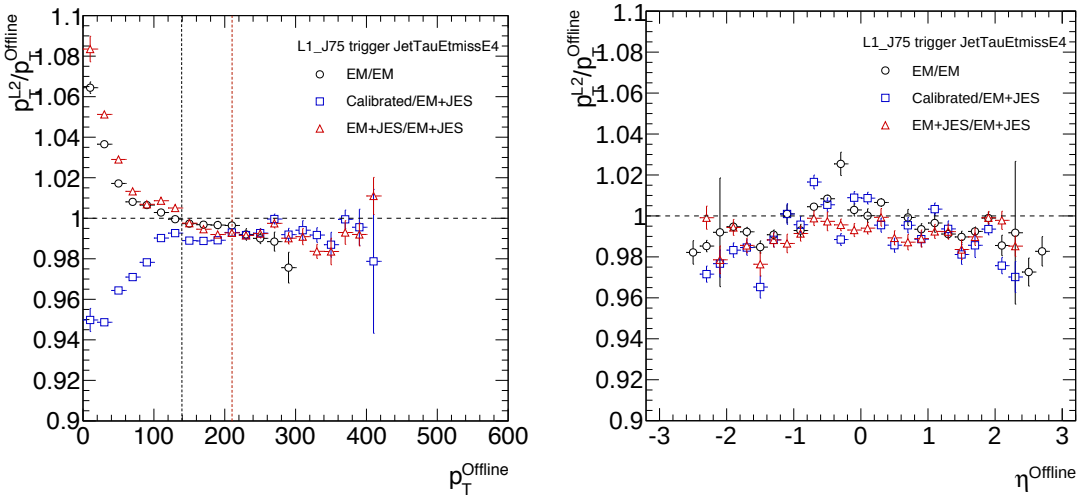

(a) (b)

FIGURE 3.26: Average L2 jet transverse momentum response ratio with respect to offline, using a dataset collected with the L1_J75 trigger in data-taking period E4. See the caption of Figure 3.21 for further details.

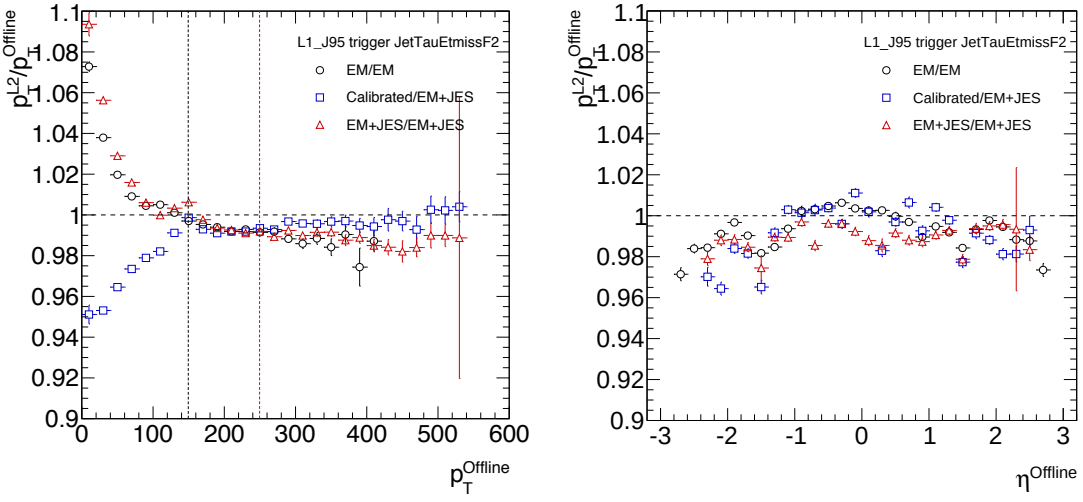

(a) (b)

FIGURE 3.27: Average L2 jet transverse momentum response ratio with respect to offline, using a dataset collected with the L1_J95 trigger in data-taking period F2. See the caption of Figure 3.21 for further details.

The calibrated scale of L2 jets appears to be less stable with offline p_{T}. Up to $p_{\mathrm{T}}^{\text{offline-EM+JES}} \lesssim 160$ GeV, the response ratio with respect to offline shows a strong slope, and L2 underestimates the offline EM+JES p_{T} by up to $\sim 2\%$ (see Figures 3.21a and 3.22a). However, for $p_{\mathrm{T}}^{\text{offline-EM+JES}} \gtrsim 160$ GeV, the response ratio flattens and is within approximately $\pm 0.5\%$ of unity (see Figures 3.25a, 3.26a and 3.27a).

As a function of η, the L2 jet response ratios with respect to offline suffer large variations. In the crack regions of the detector, the L2 reconstruction of the jet p_{T} is consistently lower than the offline p_{T}, for any energy scale, reaching up to -4% deviation from unity. In the endcaps, all distributions show a strong slope. The offline p_{T} is generally underestimated in this region. The deviation from 1 reaches up to -4% in for $|\eta| \approx 3.2$. In the central region of the detector, the EM and EM+JES L2 energy scales are generally uniform with η within 0.5%, whereas the dedicated L2 calibration produces strong variations of up to $\sim 3\%$.

In the central region of the detector, and for $p_{\mathrm{T}}^{\text{offline-EM}}$ in the $50 - 70$ GeV range, L2 EM reconstruction consistently overestimates the offline EM p_{T} by $\sim 2\%$ (see Figures 3.22b and 3.23b). The ratio in the central region approaches unity for higher transverse momenta. For $p_{\mathrm{T}}^{\text{offline-EM}} \gtrsim 110$ GeV, the overestimation in the central region is only $\sim 0.5\%$ (see Figures 3.25b and 3.27b).

As for the EM+JES L2 scale in the central region, it starts by overestimating to offline EM+JES p_{T} by $\sim 1\%$ (see Figure 3.22b). As $p_{\mathrm{T}}^{\text{offline-EM+JES}}$ increases, the ratio gets closer to unity (see Figures 3.23b and 3.24b). For $p_{\mathrm{T}}^{\text{offline-EM+JES}} \gtrsim 150$ GeV, L2 already underestimates the offline p_{T} by $\sim 1\%$ (see Figure 3.25b).

Finally, the L2 calibrated scale in the central region, despite showing large variations with η, generally underestimates the offline EM+JES p_{T}, in the lower p_{T} range, by $1-3\%$ (see Figures 3.21a, 3.22a, 3.23a and 3.24a). For $p_{\mathrm{T}}^{\text{offline-EM+JES}} \gtrsim 200$ GeV, however, the response ratio is within $\pm 1\%$ of unity (see Figures 3.25a, 3.26a and 3.27a).

To summarize, all energy scales considered for L2 provide roughly flat response ratios with offline p_{T}, that improve at higher transverse momenta. As a function of η, the response ratios in the cracks and endcaps suffer large variations. However, for EM and EM+JES scales, they are relatively stable in the central region of the detector.

We now look at the relative p_{T} resolution of L2 jets, with respect to offline jets, in bins of offline p_{T}, as shown in the distributions of Figure 3.28. These distributions are similar to the ones in (a) of Figures 3.22 - 3.27, so we refer to the beginning of this section for details on the distributions (the dataset collected with `L1_J5` is not shown here due to low statistics). The difference is that the width of the gaussian fit to the $p_{\mathrm{T}}^{\mathrm{L2}}/p_{\mathrm{T}}^{\text{offline}}$ distributions, divided by the mean of the fit, is plotted for each bin, instead of the mean.

The relative resolution appears to be approximately stable in the full analyzed p_{T} range. L2 jets at the EM scale show the best relative resolution with respect to offline, overall better than 2.5%. The relative p_{T} resolution of L2 jets with the dedicated calibration is worse than EM jets, but generally better than 4.5%. As for L2 jets at the

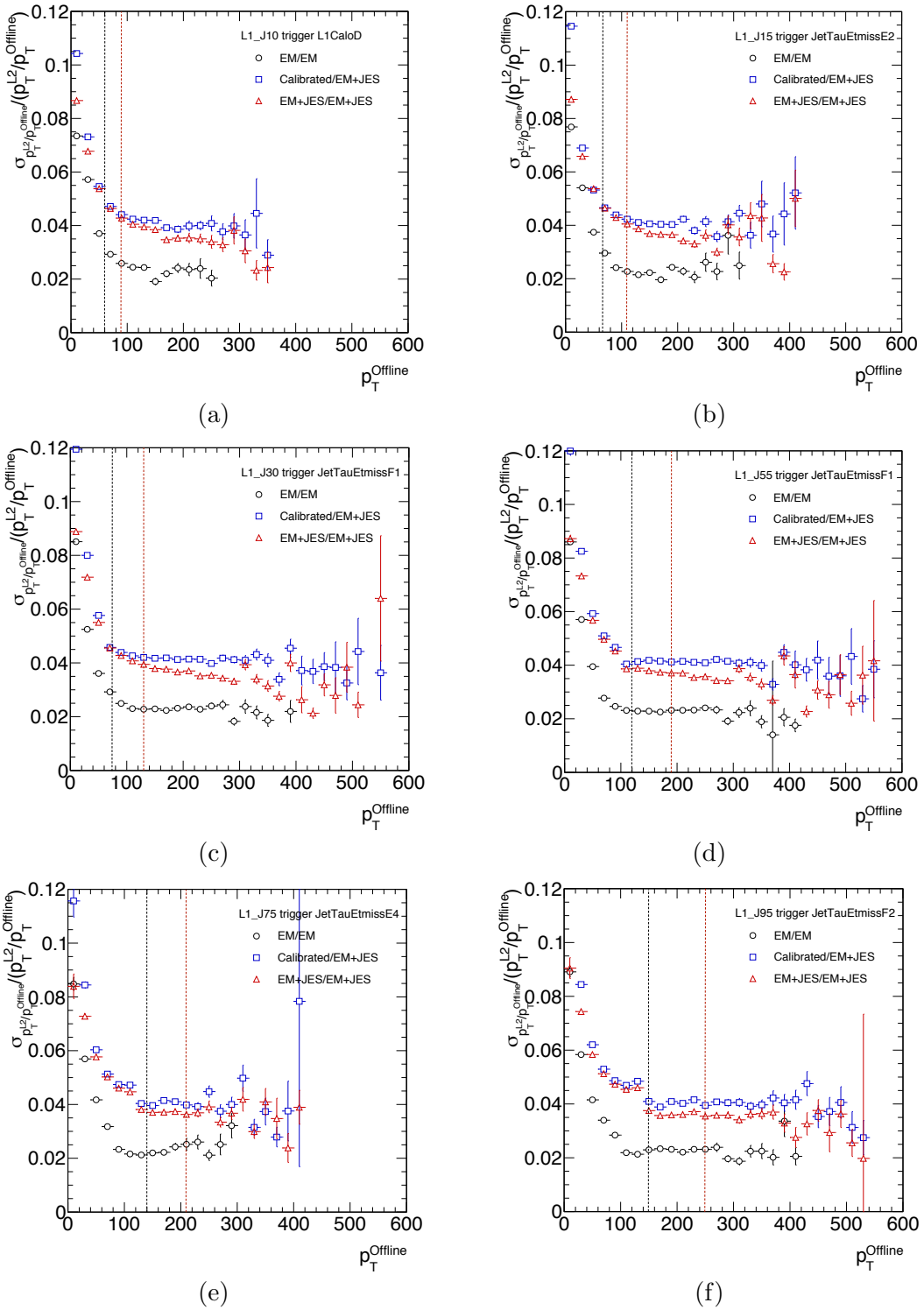

FIGURE 3.28: Relative L2 jet p_T resolution with respect to offline, in bins of $p_T^{\text{offline-EM}}$ for the black curve, and versus $p_T^{\text{offline-EM+JES}}$ for the remaining curves. The vertical lines indicate the EM (black) and EM+JES (red) offline thresholds for which the L1 trigger selection is fully efficient (see Table 3.3). The black distributions use pairs of L2 and offline matched jets, both at the EM scale. The blue (red) distributions use L2 jets at the calibrated (EM+JES) scale, and matched offline jets at the EM+JES scale. Each plot uses a different data sample, namely events triggered by: (a) `L1_J10` in period D; (b) `L1_J15` in period E2; (c) `L1_J30` in period F1; (d) `L1_J55` in period F1; (e) `L1_J75` in period E4; and (f) `L1_J95` in period F2.

EM+JES scale, they have a relative resolution slightly better than the calibrated scale, ranging from $3-4\%$ which appears to somewhat improve with increasing offline p_{T}.

3.2.3 L2 efficiency with respect to offline

Here we present the measurements of the L2 jet trigger efficiency, as a function of p_{T} of the offline jets. The *per jet* efficiencies were considered, and computed as in Equation 3.2. The different energy scales available for L2 were tested, always as a function of p_{T} of the offline jet at the EM+JES scale, as this is the quantity of interest for physics analyses. Since the bias of `L1_J5` cannot be removed, as explained throughout Section 3.1, we focused on two L2 signatures that are mostly unbiased by L1 and present sufficient statistics for the studies: `l2_j45` and `l2_j70`.

The efficiency curve for `l2_j45` is shown in Figure 3.29 as a function of $p_{\mathrm{T}}^{\text{offline-EM+JES}}$. In Figure 3.29a, the full p_{T} range is shown, while Figure 3.29b focuses on the p_{T} range of the turn-on. Figure 3.30 is similar, but the efficiency for the `l2_j70` trigger is displayed.

Five different efficiency curves are shown in each Figure. The `L1_J5` efficiency, which is included for completeness, is represented by the black circular markers. The curves shows some inefficiencies for $p_{\mathrm{T}}^{\text{offline-EM+JES}} \approx 80$ GeV, which had already been observed to a smaller extent in Section 3.1.3.4. These are caused by L1 and will impact the measurements of the L2 efficiencies. The green diamond markers show the efficiency curves for L2 jets at the EM scale. The blue square markers indicate the efficiency measured using L2 jets with the dedicated L2 calibration. The efficiency curves for L2 jets calibrated at the EM+JES scale are shown by the red triangular markers. Finally, the orange crosses are similar to the previous case, but the L2 jets calibrated at the EM+JES scale are restricted to the central part of the detector ($|\eta| < 1.0$ range).

In the orange efficiency curves in Figures 3.29 and 3.30, the pseudorapidity range of the jets was restricted to the central region, since it was previously shown (see Section 3.2.2), that the L2 EM+JES response ratio with respect to offline is very uniform in this region of ATLAS. The goal behind this restriction was to evaluate how sharp the turn-on curve could be, if an improved calibration was derived for L2 jets, that produces a flat response ratio across the entire η range. Such a calibration, which we will refer to as "improved EM+JES" in what follows, should also improve the relative p_{T} resolution of L2 with respect to offline jets, thereby sharpening the efficiency curves. Uniformity of the response ratio with pseudorapidity can be achieved by applying relative η-intercalibration to L2 jets, a *in situ* calibration method which was briefly explained in Section 2.6.4.3, in the context of offline jet calibration. In the context of the jet trigger, this method was thoroughly studied in Ref. [168].

The different calibrated efficiency curves in Figure 3.29 show similar behaviors. They all begin to turn for $p_{\mathrm{T}}^{\text{offline-EM+JES}} \approx 40$ GeV, and reach plateau around $p_{\mathrm{T}}^{\text{offline-EM+JES}} \approx 60$ GeV. The improved EM+JES calibration appears to produce the sharpest curve, followed by EM+JES, and finally the dedicated L2 calibration. The efficiency curve for L2 jets at the EM scale is, as expected, displaced with respect to the calibrated curves,

and it is not as sharp. It starts turning for $p_{\mathrm{T}}^{\text{offline-EM+JES}} \approx 55$ GeV, reaching plateau around 80 GeV.

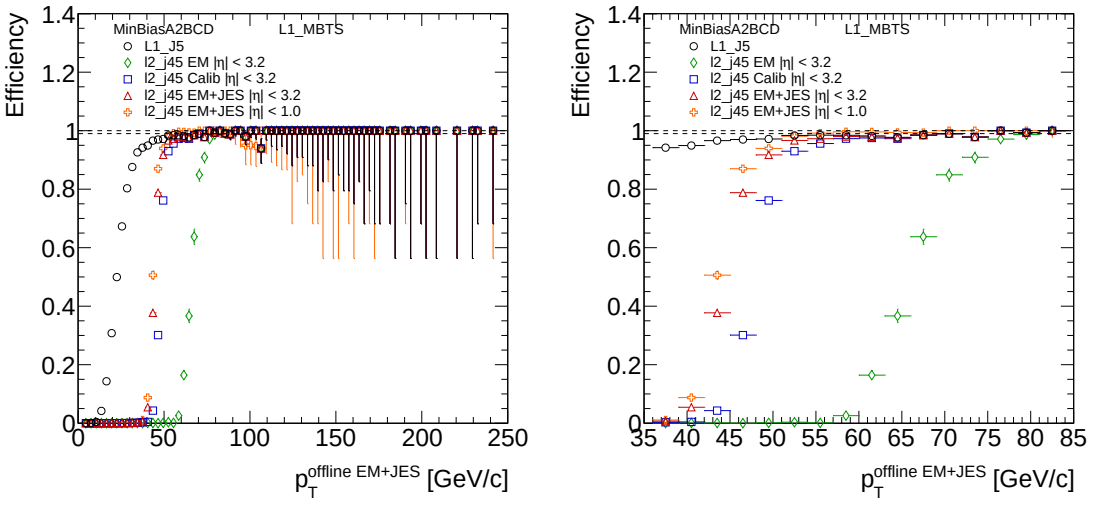

FIGURE 3.29: Efficiency for the `l2_j45` jet trigger signature, for different L2 jet energy scales, as a function of the offline jet p_{T} at the EM+JES scale: (a) for the full p_{T} range; and (b) for a smaller p_{T} range focusing on the turn-on.

Very similar observations can be made from the `l2_j70` efficiency curves in Figure 3.30. The calibrated curves begin to turn for offline jets with $p_{\mathrm{T}} \approx 60$ GeV, and plateau is reached at a threshold of ~ 80 GeV. The EM scale efficiency curve, on the other hand, appears less sharp, as it begins selecting jets with $p_{\mathrm{T}} > 90$ GeV, and reaches plateau at ~ 110 GeV.

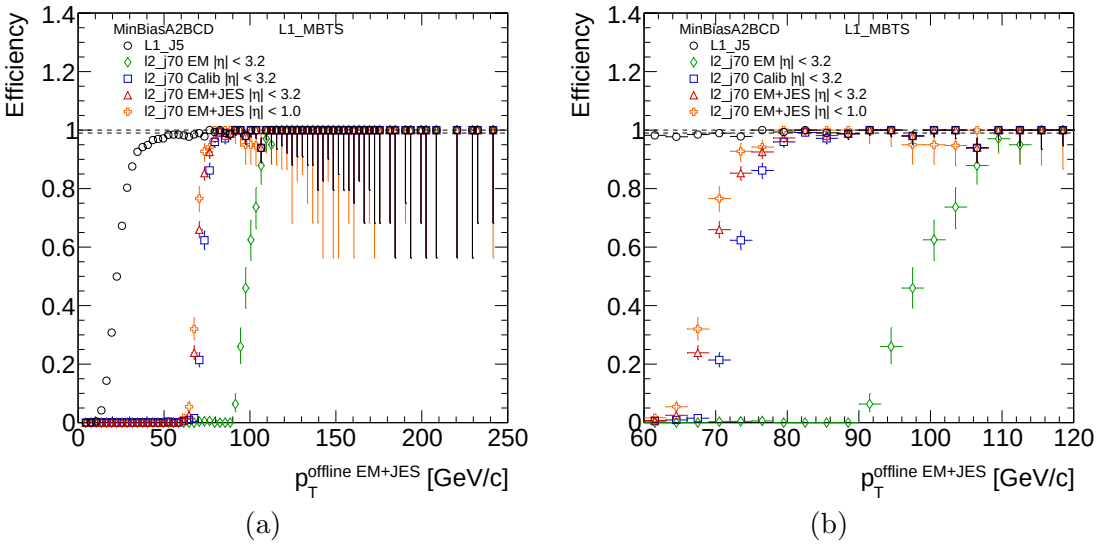

FIGURE 3.30: Efficiency for the `l2_j70` jet trigger signature, for different L2 jet energy scales, as a function of the offline jet p_{T} at the EM+JES scale: (a) for the full p_{T} range; and (b) for a smaller p_{T} range focusing on the turn-on.

A fairer comparison between the calibrated efficiency curves and the displaced efficiency curve at the EM scale can be provided by lowering the EM scale L2 trigger threshold, so that the turn-on occurs approximately at the same $p_{\mathrm{T}}^{\text{offline-EM+JES}}$ of the calibrated curves. This is illustrated in Figure 3.31, with the `l2_j45` efficiency shown in Figure 3.31a, and the `l2_j70` efficiency shown in Figure 3.31b. The calibrated efficiency curves are identical to the ones shown in Figures 3.29b and 3.30b. However, the EM scale curves have been moved by lowering the L2 threshold. Thus, the `l2_j45` efficiency curve was replaced by `l2_j30`, at the EM scale, in Figure 3.31a. Similarly, `l2_j45` at the EM scale was used instead of `l2_j70`, in Figure 3.31b.

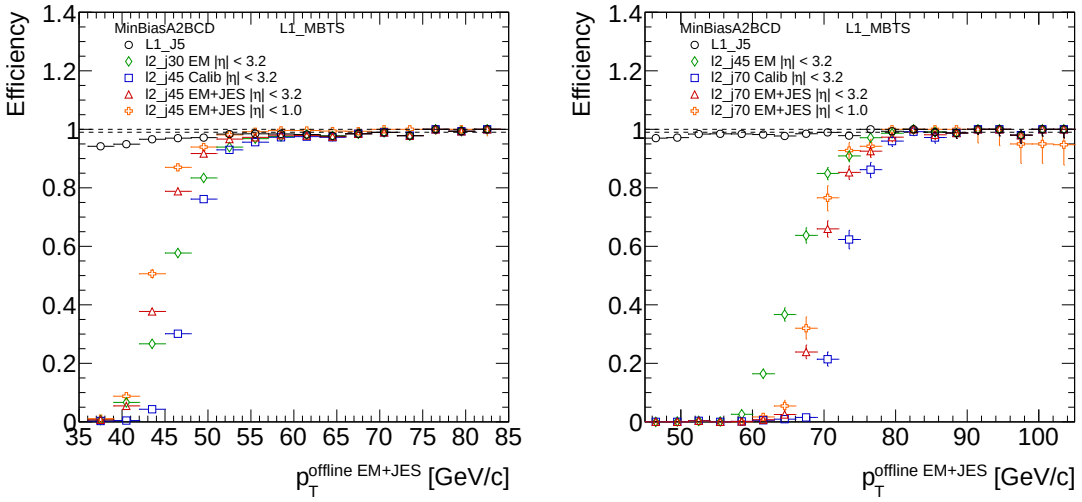

FIGURE 3.31: Efficiency for (a) `l2_j45`, and (b) `l2_j70` jet trigger signatures, for different L2 jet energy scales, as a function of the offline jet p_{T} at the EM+JES scale. The p_{T} range chosen for the x-axis focuses on the turn-on region. The L2 thresholds at the EM scale were lowered to effectively match the calibrated thresholds.

Figure 3.31 shows that once the L2 EM thresholds are lowered, all efficiency curves show very similar behaviors. Thus, it appears adjusting the EM scale L2 trigger thresholds is, in fact, equivalent to applying a hadronic calibration to L2 jets. In other words, all cases considered in Figure 3.31 seem to provide a similar bias with respect to offline jets at the EM+JES scale. This is particularly noticeable in the lower p_{T} region, with the `l2_j45` signature in Figure 3.31a. To quantitatively assess which jet energy scale at L2 performs the best, we will compute the integrated efficiencies and rejection fractions next.

For a given offline p_{T} threshold Y, and a `l2_jx` trigger, the integrated efficiency is defined as:

$$\varepsilon^{\text{int}}(\texttt{l2\_jx}) = \frac{\text{number of offline jets with } p_{\mathrm{T}} > \mathrm{Y} \text{ with a match to a L2 jet passing } \texttt{l2\_jx}}{\text{total number of offline jets with } p_{\mathrm{T}} > \mathrm{Y}}. \tag{3.3}$$

The integrated efficiency curves for the `l2_j45` and `l2_j70` trigger signatures are shown in Figures 3.32a and 3.32b, respectively, as a function of the offline p_{T} threshold. The ranges on the x- and y-axis focus on the regions where the efficiencies reach plateau.

The dips in the curves around $\sim$ 80 GeV are caused by the inefficiencies at L1 and are, therefore, ignored for the purpose of these studies. Furthermore, the inefficiencies vanished for later data-taking periods.

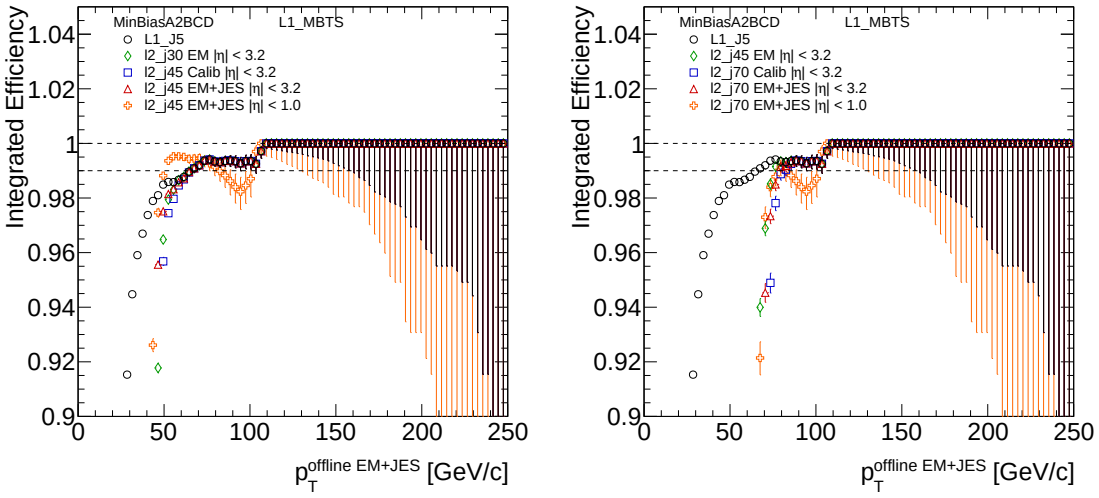

(a) (b)

FIGURE 3.32: Integrated efficiency for (a) `l2_j45`, and (b) `l2_j70` jet trigger signatures, for different L2 jet energy scales, as a function of the offline jet p_{T} at the EM+JES scale. The L2 thresholds at the EM scale were lowered to effectively match the calibrated thresholds.

The integrated efficiency curve for a given trigger is generally used to obtain the 99% efficiency point. This is an important quantity to determine the performance of a given trigger, since, typically, 99% efficiency points close to the trigger thresholds are indicative of sharp turn-on curves. The $p_{\mathrm{T}}^{\text{offline-EM+JES}}$ value for which the curve reaches an integrated efficiency of 0.99, is understood as the minimum p_{T} threshold for which at least 99% of the offline jets with p_{T} above the threshold are accepted by the trigger. These values are summarized in Table 3.4. For the `l2_j45` trigger, the EM, calibrated and EM+JES scales provide the same 99% efficiency point. However, it is clear from Figure 3.32a that the efficiency on plateau is dominated by the `L1_J5` selection. Thus, the 98% efficiency points are also included in Table 3.4.

efficiency points	`l2_j45`		`l2_j70`	
[GeV]	**98%**	**99%**	**98%**	**99%**
EM (lowered)	53	67	72	76
Calibrated	56	67	77	82
EM+JES	52	67	75	79
Improved EM+JES	48	50	73	77

TABLE 3.4: Approximate 98% and 99% efficiency points, for $p_{\mathrm{T}}^{\text{offline-EM+JES}}$ in GeV, extracted from the different curves in Figure 3.32.

For the `l2_j45` signature, the worst 98% efficiency point is provided by the dedicated L2 calibration. The improved EM+JES calibration appears to show a sharper turn-on,

improving this 98% efficiency point by ~ 8 GeV. The EM and EM+JES scales show very similar performances. As for `l2_j70`, the differences between the several L2 jet energy scales are smaller, and the results for the different curves are very similar. The EM scale and the improved EM+JES calibration at L2 provide the earliest turn-on, followed by the EM+JES scale. The dedicated L2 calibration, on the other hand, worsens this result by up to 5 GeV.

At the trigger level, one is interested in obtaining the largest rejection possible against low p_{T} jets. The integrated rejection fraction, for a given offline p_{T} threshold Y, and a `l2_jx` trigger, can be calculated as:

$$1 - \frac{\text{number of offline jets with } p_{\mathrm{T}} < \mathrm{Y} \text{ with a match to a L2 jet passing } \texttt{l2\_jx}}{\text{total number of offline jets with } p_{\mathrm{T}} < \mathrm{Y}}. \quad (3.4)$$

The integrated rejection fraction curves for the `l2_j45` and `l2_j70` trigger signatures are shown in Figures 3.33a and 3.33b, respectively, as a function of the offline p_{T} threshold. If one chooses a particular $p_{\mathrm{T}}^{\text{offline-EM+JES}}$ threshold in the x-axis, the curves will indicate the fraction of offline jets, with p_{T} below that threshold, that gets rejected by the trigger. Thus, all curves start at 100%, since all jets with low p_{T} are rejected. For very high p_{T}, the curves will shown the total fraction of offline jets rejected by the given trigger. Figure 3.33 shows that all L2 trigger jet energy scales provide a similar levels of rejection of low p_{T} offline jets.

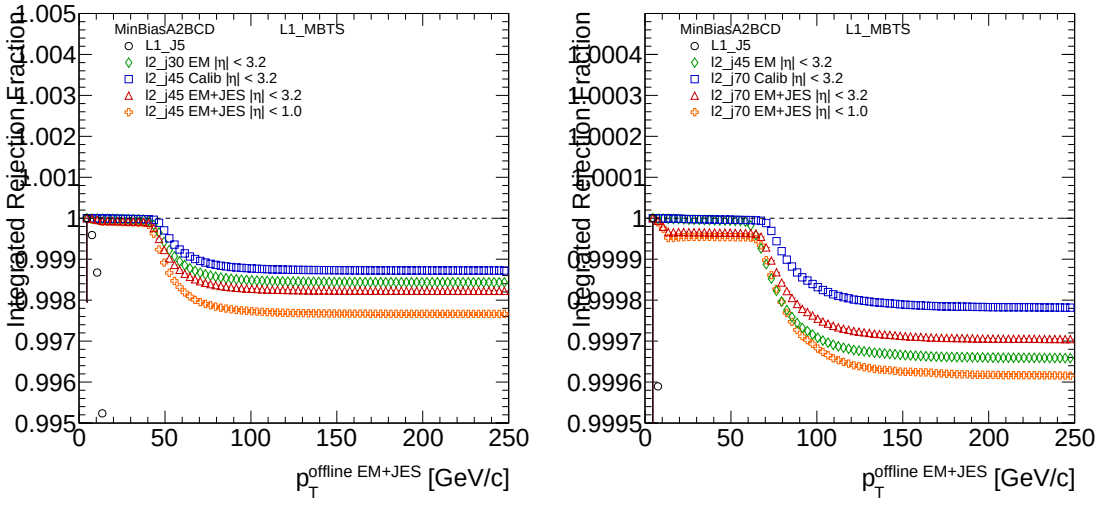

(a) (b)

FIGURE 3.33: Integrated rejection fractions for (a) `l2_j45`, and (b) `l2_j70` jet trigger signatures, for different L2 jet energy scales, as a function of the offline jet p_{T} at the EM+JES scale. The L2 thresholds at the EM scale were lowered to effectively match the calibrated thresholds.

3.2.4 Summary and conclusions

During 2010 and 2011 data-taking, the L2 jet trigger ran online at the so-called EM scale. The possibility of applying hadronic calibration to L2 trigger jets was studied,

with the goal of improving the efficiency of the jet trigger at L2, for selecting offline jets at the EM+JES scale. Two different energy calibration schemes for L2 jets were considered: the dedicated L2 jet calibration; and the offline EM+JES calibration. The studies used pp collision data collected by ATLAS in 2010.

First, the average p_{T} response ratio, between L2 and offline jets was evaluated, as a function of p_{T} and η. As anticipated, given the similarity between L2 and offline jets at the EM scale, the EM and EM+JES scales showed overall very similar behaviors. For the response ratios as function of offline p_{T}, all L2 jet energy scales exhibited approximately flat ratios in a large range, with deviations from unity smaller than 1%.

As a function of η, the EM and EM+JES L2 energy scales showed very uniform response ratios in the central region of the detector. The compatibility with 1 depended on the p_{T} range, but was generally better than $\pm 2\%$. On the other hand, the dedicated L2 calibration produced large variations on the response ratio, even in the central region of the detector.

The relative p_{T} resolution of L2 jets was also evaluated, with respect to offline jets. There was very little dependence with p_{T}. EM jets showed the best resolution, overall better than 2.5%. The relative p_{T} resolution for L2 jets calibrated at the EM+JES scale varied between $3-4\%$, and was found to be better than 4.5% for the dedicated L2 calibration.

Finally, the efficiency of the L2 jet trigger, using different energy scales, was evaluated with respect to offline jets at the EM+JES scale. It was found that once the threshold applied for L2 jets at EM scale was lowered, to effectively match the threshold of the calibrated L2 jets, all of the studied options performed in a similar way. In particular, all L2 jet energy scales provided comparable levels of rejection of low p_{T} offline jets.

It is, nonetheless, possible to slightly improve the 99% efficiency points of the L2 efficiency curves by calibrating the L2 jets. In this case, the offline JES calibration applied to L2 jets behaves better than the dedicated L2 calibration. The L2 efficiency can be further improved by developing an improved JES calibration for L2 jets, which produces a L2 response ratio with respect to offline that is flat and uniform in pseudorapidity.

For offline jets, the EM+JES energy scale is the one of interest for physics analyses. It is desirable that the jet trigger uses jets at a comparable jet energy scale, which allows for the trigger thresholds to be easily changed without dedicated studies, since the 99% efficiency points are closer to the trigger thresholds. This is true, even if the results of these studies show that the EM scale L2 jet trigger thresholds can be adjusted to reproduce the behavior of the calibrated thresholds. In this sense, applying the offline JES calibration to L2 jets produced overall better results than the dedicated L2 calibration.

Data-taking in 2011 started with the L2 jet trigger running at the EM scale. It was decided that the same conditions should remain throughout the year, in order to simplify the measurements of jet cross-sections. In 2012 data-taking, however, the L2 jet trigger finally ran with a hadronic calibration, based on the offline JES scheme, as supported by these studies.

3.3 Jet trigger efficiency with 2011 data

2011 data-taking in ATLAS began with all jet trigger levels actively rejecting events for the first time. The EM scale was used in the jet trigger throughout the whole year. Though the L2 had been extensively validated in 2010, as described in Section 3.1, it was essential to confirm that entire jet trigger chain, i.e. L1 $\rightarrow$ L2 $\rightarrow$ EF, was selecting data as expected. Thus, the efficiency of the jet trigger was studied in detail.

Furthermore, the data produced in 2010 was very different from the one produced in 2011, namely in what concerns pile-up (see Section 2.2.2). While no significant pile-up was observed in 2010, up to 20 interactions per bunch crossing occurred in 2011. At the jet trigger, resources were activated at L2 and at the EF to mitigate the impact of pile-up, and their effects on the efficiency were also assessed.

For L2, pile-up noise suppression consisted of requirement on the minimum signal-to-noise ratio of the cells included in the jet finding. For the EF, pile-up noise suppression entered through the formation of topo-clusters, described in Section 2.6.4.1. In 2010, the cell noise definition, which steers the topo-cluster formation, included only electronic noise. However, for 2011 operations, both offline and at the trigger level, the noise created by pile-up, determined from simulation for an average mean number of interactions per bunch crossing of 8, was also added to the cell noise definition.

3.3.1 Samples and event selection

The efficiency of the jet trigger was measured using $\sqrt{s} = 7$ TeV pp collision data from the LHC, collected by the ATLAS detector between April 14^{th} and June 18^{th} 2011. The data-taking periods referred to as D, E, F, G and H1 were analyzed. Starting from period G onwards, pile-up noise suppression was activated at the jet trigger for L2 and the EF. Thus, the efficiencies for periods D+E+F and G+H1 were evaluated separately.

Inclusive central jet trigger efficiencies were extracted using either the bootstrap method, or a pass-through trigger. It was no longer possible to use the orthogonal method of the analyses of Sections 3.1 and 3.2, because orthogonal triggers were too heavily prescaled and did not provide enough statistics. Thus, the data samples were collected from the `JetTauEtmiss` stream using different jet triggers, as will be explained in what follows.

A GRL was applied to all selected data samples, to ensure the quality of the data-taking for the chosen events. Collisions candidate events were selected by requiring at least one primary vertex, with $|z| < 10$ cm and at least 5 tracks pointing to it.

Offline jets with $p_{\text{T}} > 7$ GeV, $|\eta| < 2.8$, and calibrated at the EM+JES scale, were reconstructed from topo-clusters, using the anti-k_t jet algorithm with $R = 0.4$. Similar to what was described in Section 3.1.1, the reduced pseudorapidity range ensures that the entire jet is reconstructed in the central part of the detector, and avoids inefficiencies from the transition regions between different calorimeters. To guarantee the quality of the reconstructed jets, events containing *loose bad* jets (see Section 2.6.4.2) were removed

from the analysis, following the recommendations and selection criteria in Ref. [138]. Moreover, *ugly* jets were rejected from the remaining events, following the prescription in Section 3.1.1.

Standard L1, L2 and EF trigger jets, with $|\eta| < 2.8$, were retrieved from the selected events. At the EF, the studied jet trigger chains used the anti-k_t jet algorithm with $R = 0.4$, on topo-cluster inputs. The EF was running in full-scan mode, as explained in Section 2.6.4.5.

Trigger and offline jets were matched following a prescription similar to the one described in Section 3.1.3.1. Since the goal was to determine the efficiency of the whole trigger chain, the matching was performed for all the involved jets:

- when the efficiency for L1 triggers was being extracted, L1 jets were matched to offline jets using $\Delta R < 0.4$;
- for the efficiency of L1 $\rightarrow$ L2 chains, L2 jets were matched to offline jets using $\Delta R < 0.4$, and L2 and L1 jets were matched using the RoIWord (see Section 3.1.2);
- to determine the efficiency for the full L1 $\rightarrow$ L2 $\rightarrow$ EF jet trigger chain, EF jets were matched to offline jets, as well as L2 jets, using $\Delta R < 0.4$, and the matched L2 jets were matched to L1 jets using the RoIWord.

3.3.2 Efficiency of the jet trigger with pile-up suppression

The inclusive central jet trigger chains analyzed in these studies, with the corresponding L1, L2 and EF thresholds, are detailed in Table 3.5. The table also includes the trigger used to select the event sample for each of the efficiency measurements. The efficiencies are shown in Figures 3.34 and 3.36, as a function of offline p_{T}, at the EM+JES scale. L1 is shown by the red circular markers, L2 by the blue square markers, and EF by the green triangular markers. Data-taking periods D+E+F, where there was no pile-up noise suppression, are separated from periods G+H1, where pile-up noise suppression was activated for L2 and EF. For L1 all data-taking periods are shown together.

In these studies the *per jet* efficiencies were computed. Considering a generic `L1_JX` $\rightarrow$ `l2_jY` $\rightarrow$ `EF_jZ` trigger chain, they were determined using the definition in Equation 3.2, with the following modifications:

- for ε(`L1_JX`), the numerator was defined as the number of offline jets with a match to a L1 jet passing `L1_JX`;
- for ε(`L1_JX` $\rightarrow$ `l2_jY`), the numerator was defined as the number of offline jets with a match to a L2 jet passing `l2_jY`, matching a L1 jet passing `L1_JX`;
- for ε(`L1_JX` $\rightarrow$ `l2_jY` $\rightarrow$ `EF_jZ`), the numerator was defined as the number of offline jets with a match to a EF jet passing `EF_jZ`, matching a L2 jet passing `l2_jY`, matching a L1 jet passing `L1_JX`.

	Trigger chain	Thresholds [GeV]	Selecting trigger
Fig. 3.34a	L1_J10	10	EF_j10 pass
	l2_j25	25	l2_j25 pass-through
	EF_j30	30	
Fig. 3.34b	L1_J15	15	EF_j10 pass
	l2_j35	35	l2_j25 pass-through
	EF_j40	40	
Fig. 3.36a	L1_J30	30	
	l2_j50	50	EF_j30 pass
	EF_j55	55	
Fig. 3.36b	L1_J50	50	
	l2_j70	70	EF_j30 pass
	EF_j75	75	

TABLE 3.5: Inclusive central jet trigger chains relevant for the analysis, running in the trigger menu for early 2011 data taking. The efficiencies for each of the chains are shown in the indicated Figures. The trigger selection used to determine the efficiency is also shown.

The jet trigger efficiencies were extracted either using the bootstrap method, or a pass-through trigger. In the bootstrap method, events are selected using a lower threshold trigger, in a p_{T} range where it is fully efficient, so that its selection presents no bias to the efficiency under study. With a pass-through technique, the efficiencies are extracted using events obtained from a trigger running in pass-through mode. This means that a certain pass-through rate is established for the trigger, such that a fraction of the events is accepted, regardless of the trigger decision.

Figure 3.34 shows that the L1 efficiency curves have, in general, a slow turn-on compared to L2 or the EF. In Figure 3.34a, for example, one can see that the L1_J10 selection, i.e. the lowest L1 jet trigger threshold in the menu, only becomes fully efficient for offline jets with p_{T} above 55 GeV (at the EM+JES scale). For L1_J15, displayed in Figure 3.34b, the 99% efficiency point occurs around 65 GeV only. Already in Section 3.2.3 (see e.g. Figure 3.29a), the L1_J5 trigger showed a similar behavior. The slow turn-on of L1 jet triggers is related to the poor granularity of the jet elements and the sliding window algorithm used at L1 (see Section 2.6.4.5). This behavior causes the selection of the jet trigger to be very inefficient for low p_{T} jets, which were needed, for example, to determine the efficiencies of higher p_{T} jets (bootstrap method), or for jet energy scale studies.

The full scan approach introduced at the EF presents a solution to this problem. Starting from 2011, it was possible to run the EF jet trigger unseeded, i.e. over any event, whether it had been triggered by the L1/L2 jet trigger or not. In particular, the EF jet trigger could run directly over inelastic pp collision events triggered by the MBTS at L1. Three of these trigger chains were included in the 2011 menu: EF_j10, EF_j15 and EF_j20. Their efficiencies are presented in Figure 3.35 as a function of

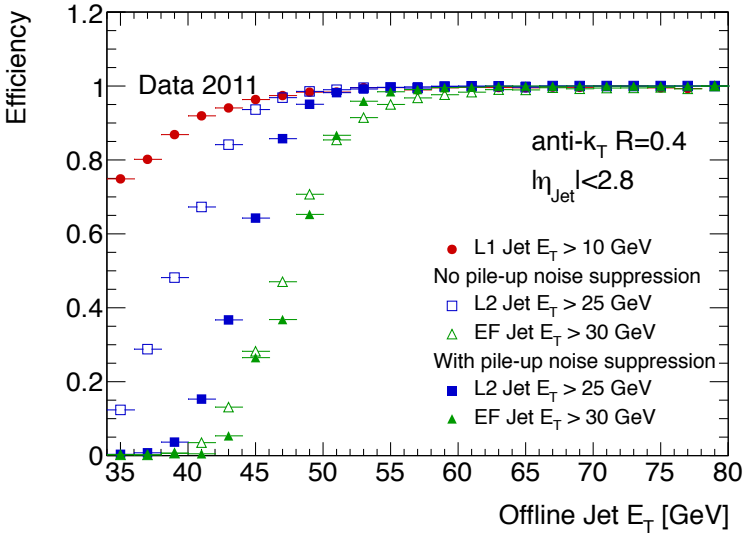

(a)

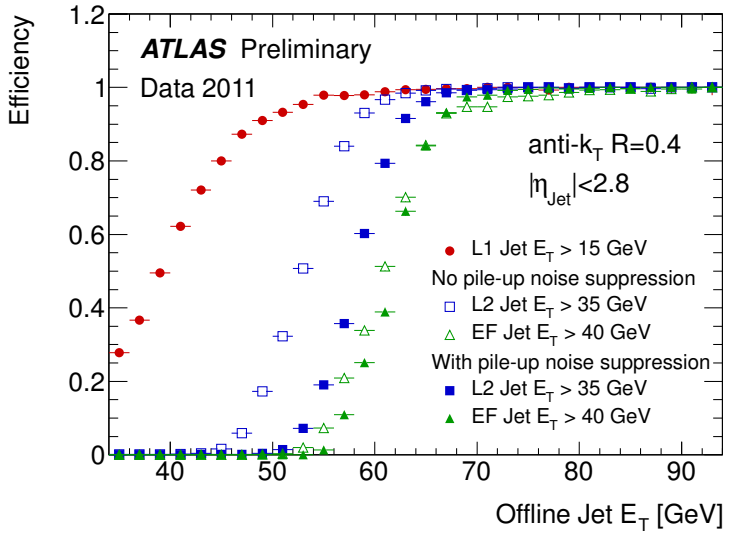

(b)

FIGURE 3.34: Inclusive central jet trigger efficiencies, as a function of the offline jet p_T at the EM+JES scale, for the: (a) `L1_J10` → `12_j25` → `EF_j30` chain; and (b) `L1_J15` → `12_j35` → `EF_j40` chain. Two different data-taking scenarios are shown: before (empty markers) and after (full markers) pile-up noise suppression was applied to both L2 and EF jets.

$p_{\mathrm{T}}^{\text{offline-EM+JES}}$, and show very sharp turn-on curves. This is a consequence of the use of the same granularity, same calibration and same anti-k_t jet algorithm, both offline and online. Furthermore, the introduction of pile-up suppression at the EF sharpens the curves even further, improving the 99% efficiency points by ~ 5 GeV. The `EF_j10` trigger, in particular, becomes fully efficient for $p_{\mathrm{T}} \gtrsim 35$ GeV, which represents a great improvement with respect to the lowest L1 jet trigger in the menu, shown in Figure 3.34a.

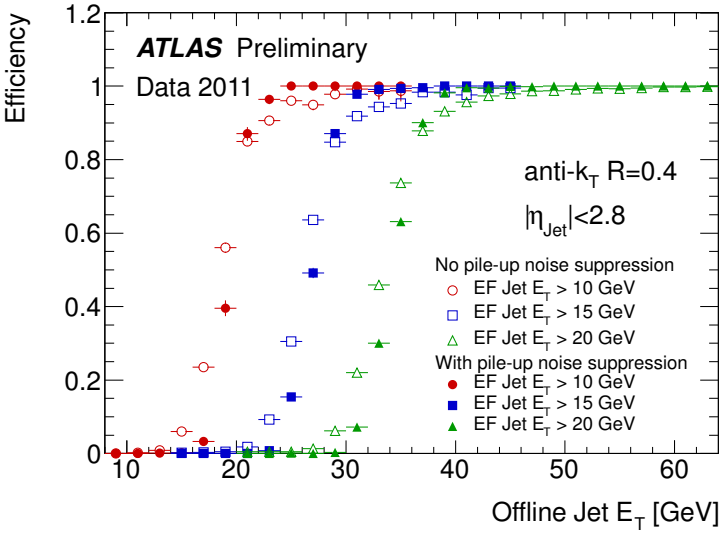

FIGURE 3.35: Inclusive central jet trigger efficiencies for the `EF_j10`, `EF_j15` and `EF_j20` chains, as a function of the offline jet p_{T} at the EM+JES scale. The EF selection is applied to inelastic pp collision candidates, triggered by the MBTS at L1. Two different data-taking scenarios are shown: before (empty markers) and after (full markers) pile-up noise suppression was applied to both L2 and EF jets.

Returning now to Figure 3.34, the `L1_J10` and `L1_J15` efficiencies, shown in Figures 3.34a and 3.34b respectively, were extracted using the bootstrap method, from events that passed the `EF_j10` trigger, as indicated in Table 3.5. As just described, this trigger becomes fully efficient for $p_{\mathrm{T}} \gtrsim 35$ GeV, which is why the distributions do not show the p_{T} range below that threshold, as it would be biased by the `EF_j10` selection.

The L2 and EF efficiency curves in Figure 3.34 were obtained from pass-through events at `l2_j25`, as indicated in Table 3.5. In other words, the efficiencies were extracted from events that were accepted regardless of the decision of the `l2_j25` $\rightarrow$ `EF_j30` chain. Using a pass-through trigger, rather than bootstraping from `EF_j10` as was done for L1, allowed for a larger data sample for the efficiency measurement.

The L2 and EF efficiencies of Figure 3.34 show sharper turn-on curves than L1, since the granularity and jet-finding algorithms are superior. Pile-up noise suppression at L2 causes some sharpening of the turn-on curve, as well as shift towards higher p_{T}. Thus, the 99% efficiency point is approximately kept, but the rejection is improved, with no impact on the EF efficiency. At the EF, the sharpening of the curve after pile-up noise suppression causes the overall 99% efficiency point to improve by ~ 5 GeV. The efficiencies of the `EF_j55` and `EF_j75` trigger chains, displayed in Figures 3.36a and 3.36b respectively, were extracted using the bootstrap method, in events triggered

by `EF_j30`, as indicated in Table 3.5. As shown in Figure 3.34a, this trigger is fully efficient for $p_{\mathrm{T}} \gtrsim 55 - 60$. Thus, events selected by `EF_j30` provide an unbiased sample with sufficient statistics, in the p_{T} range of interest.

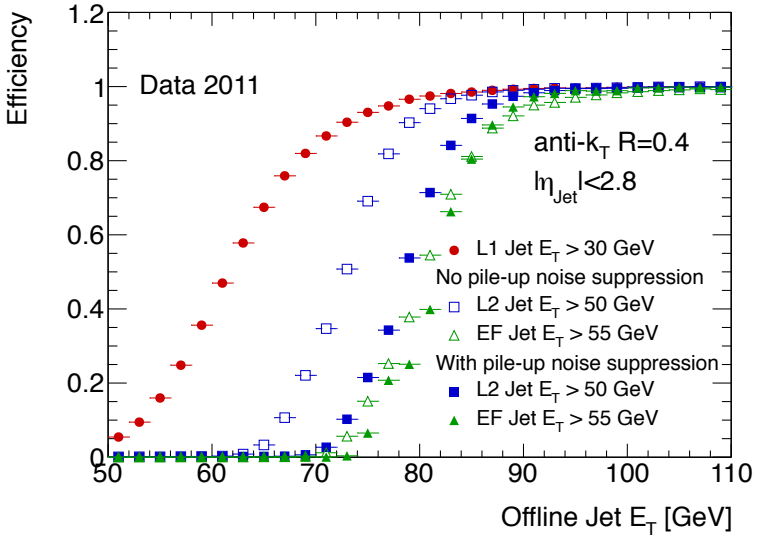

(a)

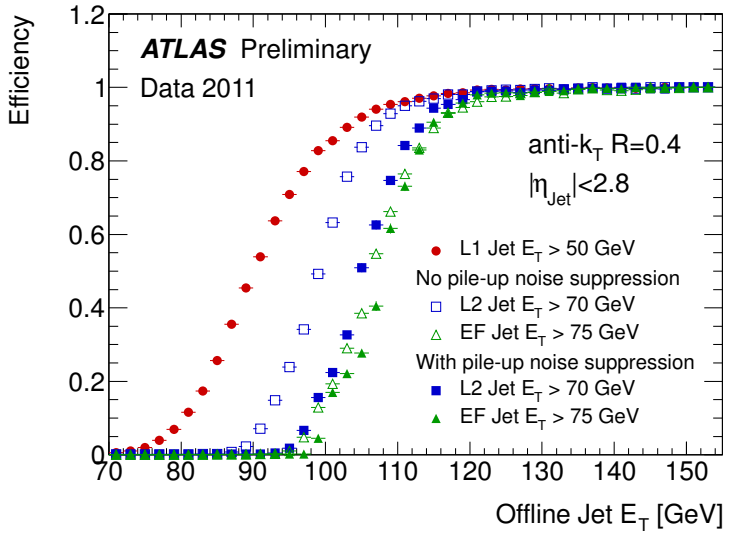

(b)

FIGURE 3.36: Inclusive central jet trigger efficiencies, as a function of the offline jet p_{T} at the EM+JES scale, for the: (a) `L1_J30` → `12_j50` → `EF_j55` chain; and (b) `L1_J50` → `12_j70` → `EF_j75` chain. Two different data-taking scenarios are shown: before (empty markers) and after (full markers) pile-up noise suppression was applied to both L2 and EF jets.

These efficiencies show overall similar behaviors to what was seen for the lower threshold chains in Figure 3.34: the turn-on for L1 is slower than for L2 or the EF, and pile-up noise suppression increases the rejection at L2 and improves the overall 99% efficiency point of the full chain by ~ 5 GeV.

3.3.3 Summary and conclusions

During 2011 data-taking, all jet trigger levels were used to actively reject events for the first. Pile-up increased with respect to 2010, and an average of 9 interactions per bunch crossing was observed. The efficiency of inclusive central jet trigger chains was evaluated in data, for two different data-taking scenarios: before and after pile-up noise suppression was activated for both L2 and EF jets.

Overall, results show the jet trigger was behaving well, and efficiently selecting events in a large E_{T} range. The use of pile-up noise suppression at L2 and the EF translated in sharper turn-on curves, with an improvement of the overall 99% efficiency point by ~ 5 GeV.

Chapter 4

Observation and measurement of the Higgs boson in the WW^* decay channel with ATLAS at the LHC

The Higgs mechanism spontaneously breaks EW symmetry, generating the observed masses of the W and Z bosons. The Higgs boson appears as a consequence of this mechanism, and the couplings between the Higgs and gauge bosons are predicted in the theory and precisely determined by their masses (see Section 1.1.8). This is reflected in the production and decay rates of this fundamental particle. Thus, observing and measuring the $H \to WW^*$ decay constitutes a fundamental test of the theory.

The $H \to WW^* \to \ell\nu\ell\nu$ channel was presented as one of the most sensitive channels at the LHC (see Section 1.2.3.3). Here, the Higgs boson is identified by its decay to two W bosons, which in turn decay leptonically, either to an electron or a muon and corresponding neutrino ($\ell = e, \mu$). This channel profits from the large $H \to WW^*$ branching ratio, that in fact dominates the total width for $m_H \gtrsim 130$ GeV (see Figure 1.17), as well as from the sizable leptonic decays of the W boson, which provide a clean experimental signature.

In the early days of Higgs searches at the LHC, before the actual discovery of the Higgs boson, the $H \to WW^* \to \ell\nu\ell\nu$ analysis provided most of the exclusion power in ATLAS [87, 169]. Later, this channel was used for the discovery of the Higgs boson at the LHC [35]. Although the two escaping neutrinos in the $H \to WW^* \to \ell\nu\ell\nu$ final state make it impossible to fully reconstruction of the Higgs resonance mass, the large rate of events provides the best measurements of total, ggF and VBF Higgs production rates in ATLAS [89, 155, 170]. Furthermore, results in the $H \to WW^* \to \ell\nu\ell\nu$ channel contribute significantly to the measurement of the couplings of the Higgs boson to fermions and vector bosons [155, 170]. Finally, this channel also offers sensitivity to study the spin nature of the Higgs boson [93, 171].

This chapter presents the $H \to WW^* \to \ell\nu\ell\nu$ analysis in ATLAS, using the full LHC Run I pp collision dataset. It focuses on a ggF-produced Higgs, and on the same flavour channels, where either two electrons or two muons are observed in the final state, accompanied by missing transverse energy, and 0 or 1 jet, i.e. $H \to WW^* \to e\nu e\nu/\mu\nu\mu\nu + 0/1$ jet. This analysis is particularly difficult, due to the large contamination of Drell-Yan background. Nevertheless, it contributes to the overall observation and measurements of the $H \to WW^*$ decays in ATLAS, reported in Ref. [172].

This chapter is organized as follows. First, an overview of the $H \to WW^* \to \ell\nu\ell\nu$ analysis is presented in Section 4.1, followed by some general considerations about the final states with two same flavor leptons in Section 4.2. The data samples and MC simulation used in the analysis are presented in Section 4.3. Sections 4.4 and 4.5 describe the physics objects and event selection used. They are followed by Sections 4.6 and 4.7, where a detailed description of the background estimation procedures is presented. The strategy to extract the Higgs signal is provided in Section 4.8, followed by a description of the different sources of systematic uncertainty in Section 4.9. Section 4.10 presents the statistical treatment employed to extract the results. Finally, the combined results of the $H \to WW^* \to \ell\nu\ell\nu$ analysis are included in Section 4.11.

4.1 Overview of the analysis

The Feynman diagram in Figure 4.1 depicts the $H \to WW^* \to \ell\nu\ell\nu$ decay chain for a Higgs boson produced via the gluon fusion mechanism. The goal of the $H \to WW^* \to \ell\nu\ell\nu$ analysis is to observe and measure the production of the Higgs boson by investigating the $H \to WW^*$ decay, and subsequent leptonic decays of the W bosons. The $H \to WW^*$ decay vertex, indicated in blue in Figure 4.1, provides access to the Higgs boson coupling to gauge bosons (the W boson in particular), while the ggF production vertex, signaled in red, indirectly probes the couplings between the Higgs boson and fermion sector (namely heavy quarks).

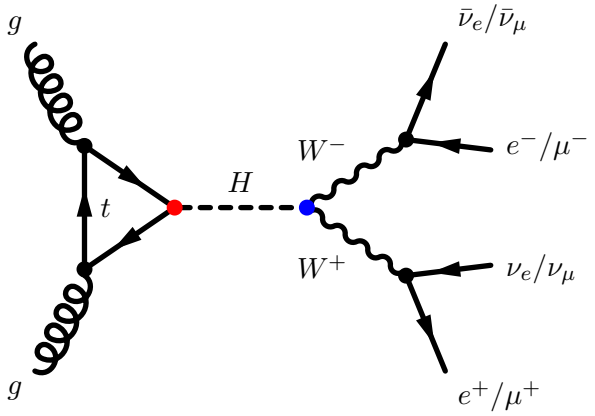

FIGURE 4.1: Feynman diagram for a Higgs boson produced via ggF, decaying to a W boson pair which in turn decays leptonically to either electrons or muons and corresponding neutrinos. The production vertex in red is sensitive to the coupling between the Higgs boson and heavy quarks, while the decay vertex in blue probes the coupling between the Higgs and W bosons.

The $H \to WW^* \to \ell\nu\ell\nu$ analysis is a challenging one, that relies on information from the entire ATLAS detector and on accurate and precise estimation of the contamination of different backgrounds. The key features of this analysis are presented in what follows.

4.1.1 Signal signature

The basic signal signature in the $H \to WW^* \to \ell\nu\ell\nu$ analysis consists of two isolated, opposite charge leptons, and large missing transverse energy originating from the two escaping neutrinos. Only final states with electrons and/or muons will be considered, as indicated in Figure 4.1. The largest signal contribution to this final state originates from direct $W \to e\nu$ and $W \to \mu\nu$ decays. The very small contribution that arises from a leptonic decay of an intermediate τ-lepton, i.e. $W \to \tau\bar{\nu}_\tau \to \ell\bar{\nu}_\ell\nu_\tau\bar{\nu}_\tau$, is implicitly included.

The presence of neutrinos in the final state does not allow for the full reconstruction of the Higgs boson mass. Instead, the so-called transverse mass m_{T} is used to provide the final discrimination between signal and background. m_{T} is computed using the kinematics of the two leptons and the missing transverse momentum. This variable is sensitive to the mass of the Higgs boson, but has a very poor resolution. The exact definition of m_{T} and the procedure used to extract the signal will be discussed in Section 4.8 ahead.

Further separation between signal and backgrounds is achieved by exploiting the spin properties of the SM Higgs boson and the V-A structure of the weak decays (see Sections 1.1.2 and 1.1.6). These features create an angular correlation between the charged leptons in the final state, as illustrated in Figure 4.2. In Figure 4.2, the direction of the spin is indicated by the double blue arrows, while the direction of the momentum is illustrated by the black and red arrows. The spin-0 SM Higgs boson decays to two spin-1 W bosons, which in turn decay to two spin-1/2 leptons. Conservation of the angular momentum requires that the spins of the W bosons are anti-parallel in the $H \to WW^*$ decay, and that the spins of each lepton pair are parallel in the $W \to \ell\nu$ decays. Since only left-handed (right-handed) fermions (antifermions) participate in the weak decay of the W bosons, the leptons (ℓ^- and ν_ℓ) will emerge in directions opposite to the spin. On the other hand, the anti-leptons (ℓ^+ and $\bar{\nu}_\ell$) will travel in the same direction of the spin. Thus, the two charged-leptons, represented in red in Figure 4.2, emerge approximately in the same direction, and the two neutrinos tend to travel in the opposite direction. As a result, the final state is characterized by a small opening angle between the leptons (low $\Delta\phi_{\ell\ell}$), small invariant mass of the dilepton system (low $m_{\ell\ell}$), and large missing transverse energy in the opposite direction of the lepton pair.

Yet another feature of the $H \to WW^* \to \ell\nu\ell\nu$ decays is the transverse momentum of the charged leptons. For a Higgs boson with a mass of ~ 125 GeV, one the of the W bosons decays off-shell. Consequently, the sub-leading lepton in the final state tends to be softer than in background processes where the two W bosons are produced on-shell.

Figure 4.3 shows an event display of a $H \to WW^* \to \ell\nu\ell\nu$ candidate event, recorded by the ATLAS detector in 2012. The final state contains one electron and one muon,

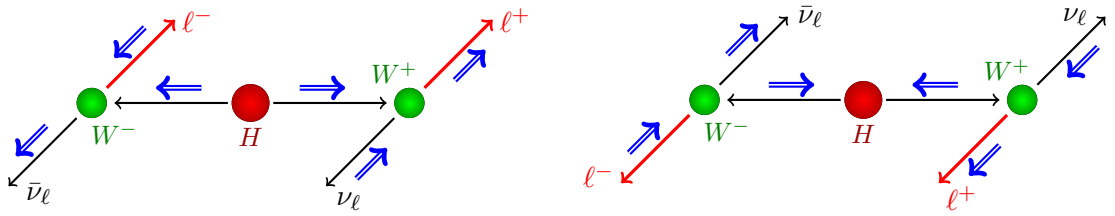

FIGURE 4.2: Schematic diagrams illustrating the $H \to WW^* \to \ell\nu\ell\nu$ decay and angular correlation between the final state leptons. The direction of the spin is represented by the double blue arrows and the direction of the momentum is illustrated by the black/red arrows. The spin-0 SM Higgs boson decays into two spin-1 W bosons with: (a) positive helicity; and (b) negative helicity. Each W boson decays into two spin-1/2 leptons and, given the V-A structure of the decay, the charged leptons (in red) emerge in the same direction.

separated by a small opening angle, and large missing transverse energy pointing in the opposite direction.

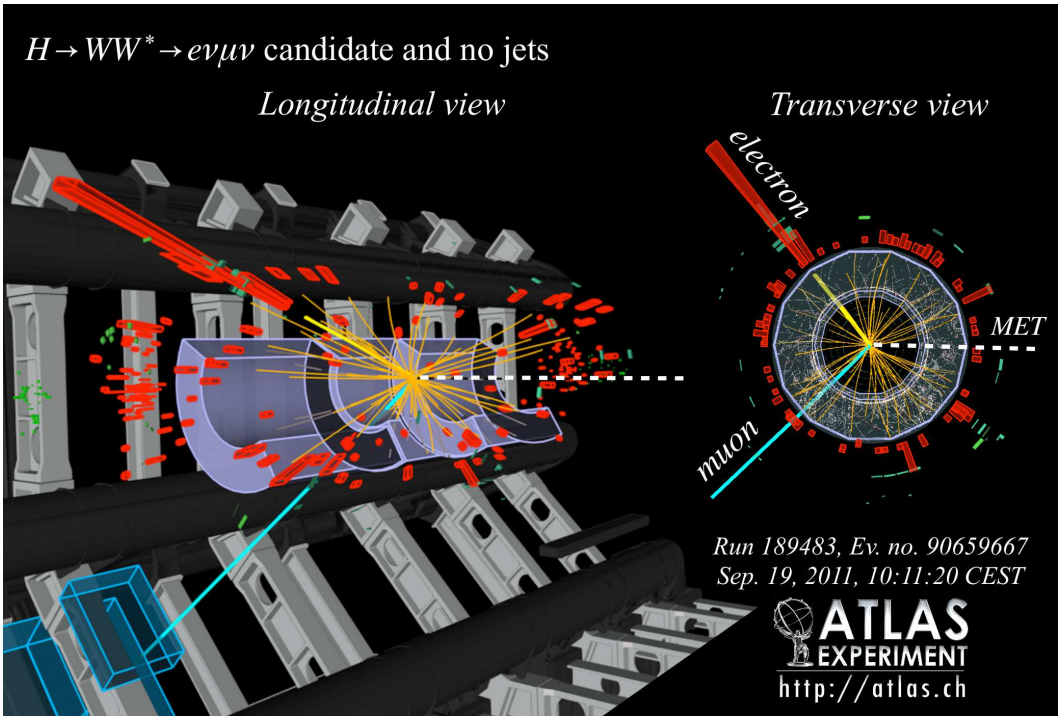

FIGURE 4.3: Event display of a $H \to WW^* \to \ell\nu\ell\nu$ candidate recorded in ATLAS, with one electron, one muon and large missing transverse energy in the final state.

4.1.2 Event categories

The $H \to WW^* \to \ell\nu\ell\nu$ analysis is performed considering several orthogonal event categories, also referred to as channels. The categorization is performed as illustrated in Figure 4.4. Different event selections are applied to each category and the individual results are then combined in a procedure detailed in Section 4.10. This improves the

sensitivity of the analysis, by exploiting different background compositions, signal purity and/or production mechanisms.

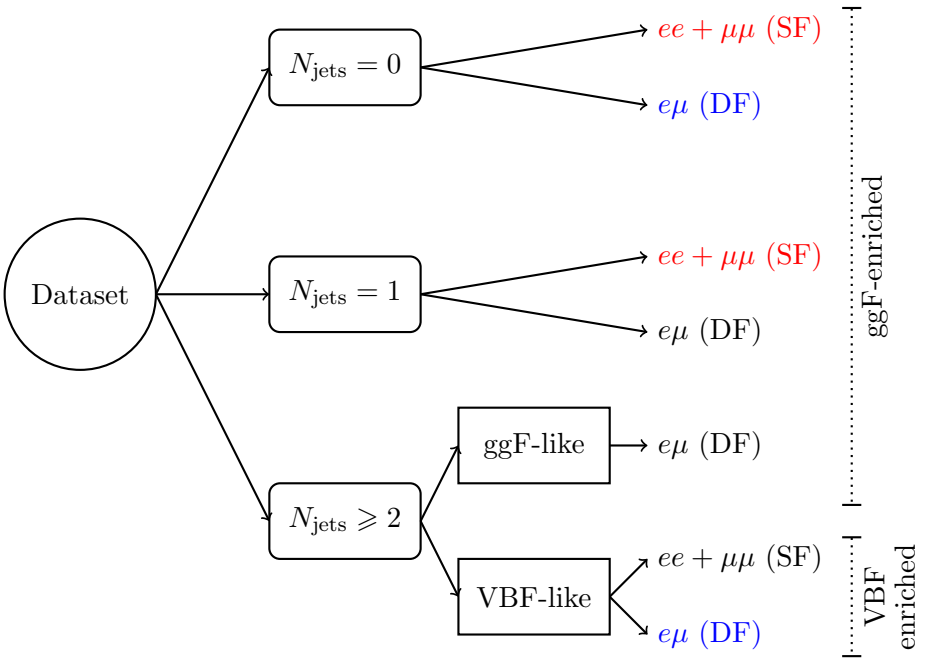

FIGURE 4.4: Orthogonal event categories created in the $H \to WW^* \to \ell\nu\ell\nu$ analysis, according to jet multiplicity and lepton flavor. The categorization results in ggF- and VBF-enriched samples as indicated. The channels marked in blue provide most of the sensitivity in each of the ggF- and VBF-enriched samples. The same flavor (SF = $ee + \mu\mu$) 0- and 1-jet channels, highlighted in red, are the focus of this thesis.

The first categorization consists in splitting the sample by the number of reconstructed jets that accompanies the 2 leptons + $E_{\text{T}}^{\text{miss}}$ final state: $N_{\text{jets}} = 0$, $N_{\text{jets}} = 1$ and $N_{\text{jets}} \geqslant 2$, are referred to as the 0-jet, 1-jet and 2-jet channels respectively.

The 2-jet channel is further split into two categories, that are sensitive to different production mechanisms. For the 2-jet-VBF category, the two leading jets in the events are required to be very forward and widely separated in pseudorapidity. This selection probes the typical VBF event topology (see Figure 1.15b and Section 1.2.3.1), and most of the signal in the resulting sample is produced via VBF. Thus, this category is used to measure VBF production. The 2-jet-ggF category contains events from the 2-jet channel that fail the VBF-like event selection.

The 0-jet, 1-jet and 2-jet-ggF channels produce samples enriched in the ggF production mode, illustrated in Figure 4.1. The requirements of 1 or 2 jets probe topologies where ISR led to jets being reconstructed in the final state. Even though all three categories are sensitive to the same production mechanism, it is important to keep them separate, given the different background compositions and signal purity in each. In particular, the 1-jet and 2-jet-ggF channels suffer from a larger contamination of $t\bar{t}$ events than the 0-jet channels (more on this in Section 4.1.3 ahead).

Further categorization is obtained by splitting each of the categories according to the flavor of the final state leptons. The same flavor (SF) categories, which include final

states with two electrons (ee) or two muons ($\mu\mu$), are separated from the different flavor (DF) categories, with one electron and one muon in the final state ($e\mu$), due to the higher contamination of Drell-Yan background.

The 0-jet channel is the most sensitive of all the jet categories. In each jet channel, the DF categories are purer in signal, and therefore more sensitive than the SF ones. The descriptions that follow will focus on the 0- and 1-jet channels only, and particularly in the SF final states, highlighted in red in Figure 4.4.

4.1.3 Backgrounds

Figure 1.22 shows the cross-sections of different SM processes measured in ATLAS. Nearly every process in this Figure represents a source of background for the $H \to WW^* \to \ell\nu\ell\nu$ analysis, either because it produces the same 2 leptons + $E_{\mathrm{T}}^{\mathrm{miss}}$ final state, or because it mimics this signature, due to misidentified objects or limited detector coverage/resolution. The contamination of each background in each category depends on the cross-section, which is generally several orders of magnitude higher than the signal production, as indicated in Figure 1.22, as well as on the resemblance of the process to the signal topology.

As already noted, since no mass peak can be seen above the background, the $H \to WW^* \to \ell\nu\ell\nu$ analysis relies on accurate and precise estimation of the contamination of the different backgrounds in signal region. The majority of the background processes are modeled using MC simulated samples. However, data is used to validate, normalize or even replace the MC prediction whenever possible, to provide a more reliable, and in general more precise, estimate. This subject will be further discussed in Sections 4.6 and 4.7 ahead. For now, the different sources of background to the $H \to WW^* \to \ell\nu\ell\nu$ analysis are presented.

4.1.3.1 Continuum WW

The main source of background in the $H \to WW^* \to \ell\nu\ell\nu$ analysis arises from SM continuum W^+W^- production, referred to as WW in the following, where both W bosons decay leptonically. Figures 4.5a and 4.5b show the LO Feynman diagrams for the dominant WW production mode at the LHC, mediated by quarks. The gluon fusion process, shown in Figure 4.5c, accounts for 3% of the total cross-section.

WW is considered an irreducible source of background, as it produces exactly the same 2 leptons + $E_{\mathrm{T}}^{\mathrm{miss}}$ final state as the signal. Separation between signal and WW is achieved my exploiting the features described in Section 4.1.1. Given the spin-0 nature of the SM Higgs boson, the angular separation between the charged leptons, and the invariant mass of the dilepton system, tend to be smaller for the signal than for the continuum WW process. Furthermore, in the $H \to WW^*$ decay, one of the W bosons is produced off-shell, while for SM WW both are produced on-shell, resulting in softer sub-leading leptons for the signal.

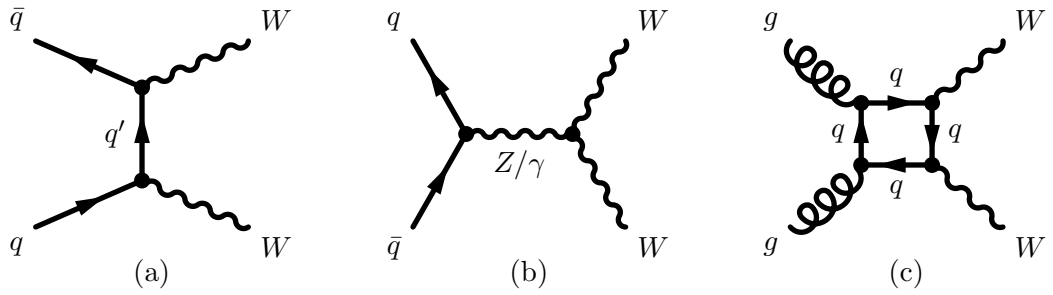

FIGURE 4.5: LO Feynman diagrams for SM continuum WW production at the LHC: (a) t-channel via $q\bar{q}$ initial state; (b) s-channel via $q\bar{q}$ initial state; and (c) gluon fusion.

4.1.3.2 Other VV

Other diboson (VV) processes, beyond non-resonant WW production, also contaminate the $H \to WW^* \to \ell\nu\ell\nu$ signal region, namely: $W\gamma$, $W\gamma^*$, WZ and ZZ. These processes generally lead to more than two charged leptons in the final state. Therefore, suppression from these backgrounds is achieved by placing a veto on a third lepton.

Background from $W\gamma$ arises when the W boson decays leptonically and the photon is misidentified as an electron. Therefore, it is particularly important in the DF and ee channels, where it can be of the same size as the signal. The misidentification of the photon usually occurs because of an asymmetric conversion into an electron-positron pair - $\gamma \to e^+e^-$ - with the highest p_{T} electron (or positron) being reconstructed as the electron in the final state, and the other electron failing to be reconstructed.

$W\gamma^*$ background occurs when the W boson decays leptonically and the photon converts internally to a pair of oppositely charged leptons. Unlike the external conversions, which occur in the detector, the internal conversions include any of the $\gamma^* \to ee$, $\gamma^* \to \mu\mu$ and $\gamma^* \to \tau\tau$ decays, though the latter is negligible. Thus, $W\gamma^*$ contaminates both the DF and SF channels. The same final state is achieved with the WZ process, when the Z boson decays to a charged lepton pair - $Z \to ee$, $Z \to \mu\mu$ and $Z \to \tau\tau$ - and one of these leptons is lost.

The ZZ process constitutes a very small source of background. It can arise from the $ZZ \to \ell\ell\ell\ell$ decay, when two leptons are unidentified, as well as via the $ZZ \to \ell\ell\nu\nu$ decay, in which case the same signature of the signal is reproduced. The latter represents a more significant background contribution for events with dilepton invariant mass at the Z pole, while signal events have lower $m_{\ell\ell}$.

4.1.3.3 Top

The dominant contribution to top backgrounds arises from $t\bar{t}$ production. LO Feynman diagrams for this process are shown in Figure 4.6. The top quark decays into a W boson and a b quark with $\sim 100\%$ branching ratio. If both W bosons decay leptonically, one obtains $t\bar{t} \to WWbb \to \ell\nu\ell\nu bb$, i.e. a 2 leptons + $E_{\mathrm{T}}^{\mathrm{miss}}$ final state with two additional b-jets.

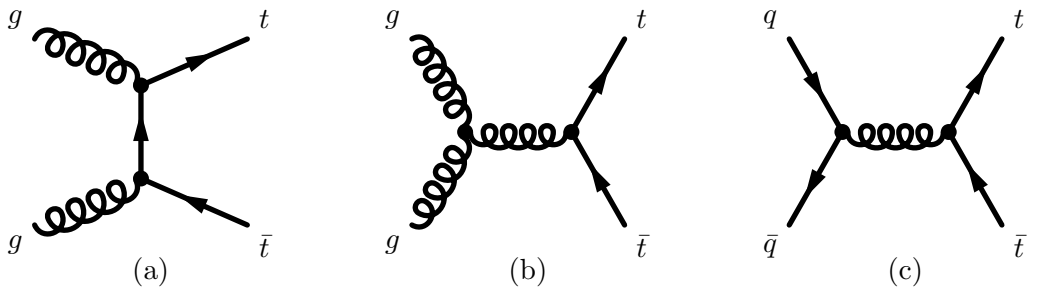

FIGURE 4.6: LO Feynman diagrams for $t\bar{t}$ production at the LHC: (a) t-channel via gg initial state; (b) s-channel via gg initial state; and (c) s-channel via $q\bar{q}$ initial state.

Categorization of the event samples according to the jet multiplicity exploits mostly the different top background contamination in each jet bin. The contamination of $t\bar{t}$ in the 0-jet channel is small, as both b-jets in the final state would have to be lost. It is, however, more significant in the 1 and 2-jet channels. Suppression of $t\bar{t}$ in these channels is achieved by requiring that the reconstructed jets are not identified as b-jets.

Single top production is also a source of top background. Examples of LO Feynman diagrams for single top production are shown in Figure 4.7. Though the t-channel (Figure 4.7a) has the highest cross-section, most of the contamination in the $H \to WW^* \to \ell\nu\ell\nu$ analysis arises from Wt production (Figure 4.7c), since it leads to two W bosons in the final state: $Wt \to WWb \to \ell\nu\ell\nu b$.

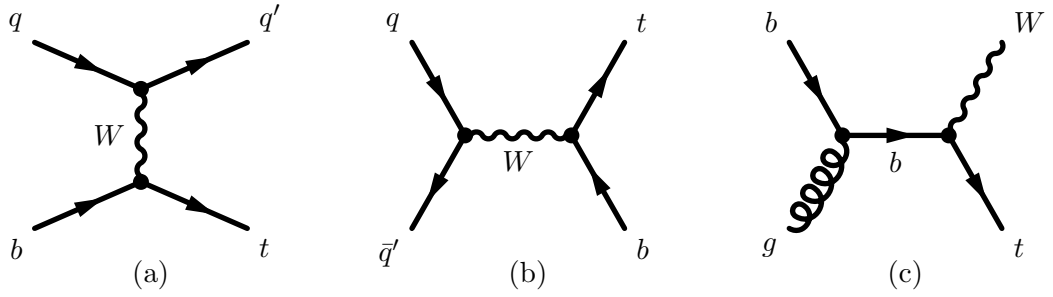

FIGURE 4.7: LO Feynman diagrams for single top production at the LHC: (a) t-channel; (b) s-channel; and (c) s-channel Wt production.

4.1.3.4 W + jets and QCD multijet

W + jets refers to processes where a W boson, which decays to leptons, is produced in association with one or more jets. These processes can contaminate the signal region if the jet is misidentified as a charged lepton. Such leptons are referred to as fake leptons. The probability of a jet faking a lepton is relatively small, and can be reduced by applying tight lepton isolation requirements. However, the W boson production is several orders of magnitude higher than the signal (see Figure 1.22). Thus, the W + jets process ends up having a similar contribution to that of the signal.

QCD multijet production is also a source of background to the $H \to WW^* \to \ell\nu\ell\nu$ analysis. In this case, two jets are misidentified as leptons. Again, the probability for the reconstruction of two fake leptons is small, but as already discussed jet production at

the LHC dominates the total cross-section. No neutrinos exists in the final state, but a significant imbalance of transverse momentum can arise from detector resolution effects or pile-up (see Section 2.6.6). This is referred to as fake $E_{\mathrm{T}}^{\mathrm{miss}}$. The QCD contamination can be neglected after tight $E_{\mathrm{T}}^{\mathrm{miss}}$ selections.

4.1.3.5 Drell-Yan

The Drell-Yan process refers to the quark-antiquark anihilation resulting in the production of a Z boson or a virtual photon, which decays into a pair of oppositely-charged same flavour leptons, as shown in Figure 4.8a: $q\bar{q} \to Z/\gamma^* \to \ell^+\ell^-$. It is also referred to as $Z+$jets, since it can be produced in association with jets (see Figure 4.8b), or Z/γ^*. At this point, it is important to distinguish $Z/\gamma^* \to ee/\mu\mu$ decays from $Z/\gamma^* \to \tau\tau$ decays.

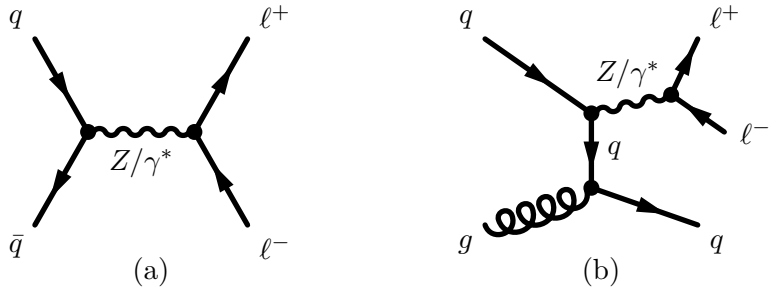

FIGURE 4.8: Feynman diagrams for Drell-Yan production at the LHC: (a) LO; and (b) with one accompanying jet.

$Z/\gamma^* \to \tau\tau$ events are a source of background both in the SF and DF analyses. The contribution of this background is small, as it arises from leptonic decays of the τ-leptons - $Z/\gamma^* \to \tau\tau \to \ell\nu\nu\ell\nu\nu$. These produce a signature identical to the signal, with 2 leptons and genuine $E_{\mathrm{T}}^{\mathrm{miss}}$ originating from the neutrinos.

$Z/\gamma^* \to ee/\mu\mu$ events contaminate mostly the SF channels. In fact, these decays are one of the main sources of background, as they produce a final state with two leptons of the same flavor, with a cross-section $\sim 10^4$ times higher than the signal (see Figure 1.22). Since no neutrinos are present in the final state, $Z/\gamma^* \to ee/\mu\mu$ is generally suppressed by applying a $E_{\mathrm{T}}^{\mathrm{miss}}$ cut. However, the degradation of the $E_{\mathrm{T}}^{\mathrm{miss}}$ resolution due to pile-up in the detector causes $Z/\gamma^* \to ee/\mu\mu$ to be reconstructed with significant $E_{\mathrm{T}}^{\mathrm{miss}}$, even if fake. Suppression of $Z/\gamma^* \to ee/\mu\mu$ in the SF channels was a major challenge and the focus of the work presented in this thesis.

In what follows, we will refer to $Z/\gamma^* \to ee/\mu\mu$ decays that contaminate the SF channels as DY. As just explained, $Z/\gamma^* \to \tau\tau$ decays contaminate both the SF and DF channels, but are different in nature, as they produce genuine missing transverse energy in the detector. We will keep the $Z/\gamma^* \to \tau\tau$ nomenclature for this background.

4.2 The same flavor channels

The work of this thesis focuses on the SF 0- and 1-jet channels. The categorization of the event samples into SF and DF is motivated mostly by the different DY contamination in each. In fact, the other sources of background in the analysis, which generate true missing transverse energy, as described in Section 4.1.3, are expected to be approximately the same for DF and SF events, due to flavor universality. Thus, the SF analysis in the 0- and 1-jet channels builds on the 0- and 1-jet DF analysis, with additional or tighter selection cuts to handle DY. The optimization of these selections will be discussed in Section 4.5 ahead. The added selection cuts end up suppressing other backgrounds besides DY, but at the cost of reducing the signal acceptance as well. As a result, the SF channels are less sensitive than the DF channels, but provide, nonetheless, important and valuable input to the overall analysis.

As discussed throughout Section 2.6, the extra activity in the detector caused by pile-up generally degrades the performance of physics objects reconstruction. Reconstruction of missing transverse energy is particularly affected. As the pile-up increased throughout data-taking, severe worsening of the $E_{\mathrm{T}}^{\mathrm{miss}}$ resolution was observed in ATLAS. Different $E_{\mathrm{T}}^{\mathrm{miss}}$ flavors were developed in an attempt to improve the performance. For the $H \to WW^* \to \ell\nu\ell\nu$ analysis, the worsening of the $E_{\mathrm{T}}^{\mathrm{miss}}$ resolution with pile-up translates in an increase of fake $E_{\mathrm{T}}^{\mathrm{miss}}$ in the detector. As a result, the DY contamination increased in the SF channels, making this analysis especially difficult.

Half-way through the 2011 data-taking, β^* was squeezed and the average mean number of interactions in ATLAS increased from 6 to more than 11, as shown in Figure 2.5a. Already at that time, the $E_{\mathrm{T}}^{\mathrm{miss}}$ selection in the SF channels was tightened to cope with the increase in DY contamination. However, neutrinos in the $H \to WW^* \to \ell\nu\ell\nu$ decay are produced with an average transverse momentum of $p_{\mathrm{T}}^{\nu\nu} \approx 40$ GeV. Thus, tightening of the $E_{\mathrm{T}}^{\mathrm{miss}}$ cuts beyond this threshold results in a substantial reduction of the signal efficiency. At that point, it became clear that a new strategy had to be used for the analysis of the SF channels with 2012 data, where an average of 20 interactions per bunch crossing were expected (see Figure 2.5b). The increase of the DY contamination by a factor of ~ 5 in 2012, with respect to 2011, led to the development of new kinematic variable, discussed in Section 4.4.3, that allowed the suppression of the DY background to a manageable level, while still maintaining a reasonable signal acceptance.

It is very hard to model fake $E_{\mathrm{T}}^{\mathrm{miss}}$ with MC simulation. As a result, MC cannot accurately predict the DY contamination in the SF channels. The challenge with DY is, therefore, not only to reduce its overwhelming contribution as a background, but also to accurately estimate it. Because of the unusual region of phase-space exploited in this analysis, the standard background estimation techniques used in physics analyses led either to inaccurate estimates of DY or to large associated systematic uncertainties, causing degradation of the sensitivity of the SF analysis. Thus, a new technique was developed to estimate the DY contamination in the SF $H \to WW^* \to \ell\nu\ell\nu$ analysis using data. The so-called Pacman method will be presented in detail in Section 4.7.

4.3 Data samples and MC simulation

The data used to perform the analysis, as well as the MC simulation samples used to model the Higgs signal and the different backgrounds processes are presented here.

4.3.1 Data samples

The $H \to WW^* \to \ell\nu\ell\nu$ analysis uses two different datasets of pp collision data from the LHC, collected by the ATLAS detector:

- 4.5 fb^{-1} of data taken at $\sqrt{s} = 7$ TeV in 2011;
- 20.3 fb^{-1} of data taken at $\sqrt{s} = 8$ TeV in 2012.

The datasets will be referred to by their center-of-mass energies.

The data was selected using a variety of lepton triggers. More details will be provided ahead. The selected datasets were required to pass Good Run Lists, that ensure the good quality of the event samples, namely that the detector was operating correctly when the data was recorded.

The data was blinded for the purpose of the analysis. The term "blinding" refers to excluding a part of the selected data, in a region of phase-space with high signal-to-background ratio, usually a strict subset of the final signal region. The exact blinding criteria applied is channel-dependent. Regions of the phase space that are kinematically similar to the signal region, but that are signal-free and therefore unblinded, are used as control and validation regions, to verify or correct the MC modeling of the data. The goal is, therefore, to prevent biases from any possible result shown by the data in the signal region.

The analyses of the 7 TeV and 8 TeV datasets were done separately, as two individual event categories, and the results were combined in the end. The 8 TeV data dominates the final result. The analysis of the 7 TeV data follows closely that of the 8 TeV data, with differences in event reconstruction, event selection or background estimation procedures being motivated by the different data-taking conditions between the two years (especially different pile-up). Apart from that and if not specified, the descriptions and material presented next will refer to the 8 TeV analysis only. We note, however, that since part of the work presented in this thesis was developed on 7 TeV data, some illustrative and auxiliary material referring to this dataset may also be shown.

4.3.2 MC simulation

In the $H \to WW^* \to \ell\nu\ell\nu$ analysis, signal and background processes are modeled using MC simulation. Information about the different MC samples used is summarized in Table 4.1. W + jets and multijet processes are not included, since these are modeled using data directly, as will be clarified in Section 4.6 ahead.

	Process	MC generator	$\sigma \times$ BR [pb]
Signal	ggF, $H \to WW^*$	Powheg + Pythia8	0.435
	VBF, $H \to WW^*$	Powheg + Pythia8	0.036
	VH, $H \to WW^*$	Pythia8	0.025
WW	$q\bar{q}/qg \to WW$	Powheg + Pythia6	5.68
	$gg \to WW$	gg2ww + Herwig	0.196
	WW MPI	Pythia8	0.480
Other VV	$W\gamma$	Alpgen + Herwig	369
	$W\gamma^*$ ($m_{\ell\ell} \leqslant 7$ GeV)	Sherpa	12.2
	WZ ($m_{\ell\ell} > 7$ GeV)	Powheg + Pythia8	12.7
	ZZ ($m_{\ell\ell} > 4$ GeV)	Powheg + Pythia8	0.73
	$ZZ \to \ell\ell\nu\nu$ ($m_{\ell\ell} > 4$ GeV)	Powheg + Pythia8	0.50
Top	$t\bar{t}$	Powheg + Pythia6	26.6
	t-channel single-t	AcerMC + Pythia6	28.4
	s-channel single-t	Powheg + Pythia6	1.82
	Wt	Powheg + Pythia6	2.35
Z/γ^*	Z/γ^* ($m_{\ell\ell} < 10$ GeV)	Alpgen + Herwig	16 500
	$Z\gamma$ ($p_{\mathrm{T}}^{\gamma} > 7$) GeV	Sherpa	163

Table 4.1: MC simulation samples used to model the different signal and background processes, and corresponding cross-sections times branching ratios at $\sqrt{s} = 8$ TeV. The branching ratios include the $t \to Wb$, $W \to \ell\nu$ and $Z \to \ell\ell$ decays (here $\ell = e, \mu, \tau$), unless noted otherwise.

Some processes in Table 4.1 are generated using Sherpa [173] and Pythia8 [174] MC programs, which provide full modeling of the high-energy pp collisions, including hard-scattering, parton shower, hadronization and underlying event (see Section 1.2.1.3). For the remaining processes, two different MC generators are used. A matrix-element-level program is used to generate the hard-scattering, which is then matched to models of parton shower, hadronization and underlying event, from generators such as Pythia6 [175], Pythia8 or Herwig [176], the latter being interfaced with the Jimmy [177] program for modeling of the underlying event.

For the hard-scatter, most processes use Powheg [178], since it includes NLO QCD corrections. When that is not possible, Alpgen [179] is used to provide LO calculations with up to several additional partons. The AcerMC [180] and gg2ww [181, 182] LO programs are used to generate the single-top t-channel (Figure 4.7) and $gg \to WW$ (Figure 4.5c) processes, respectively.

Generating the hard-scatter requires input from parton distribution functions (see Section 1.2.1.2). The CT10 [183] PDF set is used for the Powheg, Sherpa and gg2ww samples, while the Pythia8, Alpgen and AcerMC generators use the CTEQ6L1 [184] PDF set. However, the Alpgen + Herwig samples used to simulate the Z/γ^* process (see Table 4.1) are reweighted to the MRSTMCal [185] PDF set.

The samples in Table 4.1 include simulation of several pile-up interactions, done with the PYTHIA8 program. The generation of pile-up interactions is done before data-taking. Better pile-up description after data-taking is achieved by re-weighting the MC $\langle\mu\rangle$ distribution to the distribution in data. A rescaling factor of 0.9 is also applied to produce a flat data-to-MC ratio of the $\langle\mu\rangle$ distribution.

The full simulation of the ATLAS detector with GEANT4 is performed for all samples in Table 4.1, except for the top samples and the $Z \to \mu\mu$ decay of the $Z\gamma$ sample, where fast simulation is used. To allow for the generation of large samples of events in the desired phase-space, kinematic selections are applied at the generator level. These are indicated in parenthesis in Table 4.1. The $\sigma \times$ BR information for the different samples is also shown in Table 4.1, and includes the $t \to Wb$, $W \to \ell\nu$ and $Z \to \ell\ell$ decays, unless another decay is explicitly noted.

Details on the computation of cross-sections for the signal processes have been discussed in Section 1.2.3.1. The inclusive WW cross-section is computed at NLO with MCFM [186], except for $gg \to WW$, which is calculated and modeled at LO with GG2WW. Processes with two W bosons originating from double parton interaction are also included, modeled by PYTHIA8. The cross-section for $t\bar{t}$ is computed at NNLO+NNLL using TOP++2.0 [187]. Single-top processes are normalized to NNLL following the calculations from Refs. [188–190].

The $W\gamma^*$ process, modeled using SHERPA with up to one additional parton, is defined as $W + Z/\gamma^*$ with an opposite-charge same-flavor lepton pair with $m_{\ell\ell} \leqslant 7$ GeV. A K-factor corrects the SHERPA LO cross-section to the NLO prediction of MCFM. The remaining $m_{\ell\ell} > 7$ GeV range uses the POWHEG + PYTHIA8 cross-section and modeling. The ZZ process also uses the POWHEG + PYTHIA8 computation.

ALPGEN + HERWIG, with the MLM [191] matching scheme, is used to describe the $W\gamma$ and Z/γ^* processes, with up to five partons. The cross-section of $W\gamma$ is computed at NLO with MCFM. For Z/γ^* normalization, a NNLO calculation from DYNNLO [192] is used.

A SHERPA sample of $Z\gamma$ events is included in the Drell-Yan section of Table 4.1, because it produces the same dilepton final state (photons are not reconstructed in the $H \to WW^* \to \ell\nu\ell\nu$ analysis). In fact, the $Z\gamma$ process is partly generated by the ALPGEN + HERWIG Z/γ^* sample, which includes photon-FSR (performed by PHOTOS [193]) events: $Z/\gamma^* \to \ell\ell + \gamma$. SHERPA, however, performs the LO ME generation of the $Z\gamma$ process. The cross-section is normalized to the NLO MCFM prediction.

The MC samples presented in Table 4.1 constitute the so-called "nominal samples". Additional samples have been produced for the different processes, using different MC generators. These will be used for validation and derivation of systematic uncertainties ahead.

4.3.2.1 p_{T}^{Z} reweighting of Drell-Yan samples

Here we describe a reweighting procedure applied to the Drell-Yan ALPGEN + HERWIG samples.

Mismodelling Drell-Yan production is a significant source of background in the same flavor channels, where the $Z/\gamma^* \to ee/\mu\mu$ decays with mismeasured missing transverse energy dominate. It is also an important contribution in the different flavor channels, where it enters primarily through $Z/\gamma^* \to \tau\tau$ events decaying leptonically and generating true missing transverse energy. Thus, the modeling of the p_{T} of the Z/γ^* system affects both the SF and DF channels. Moreover, many kinematic variables used in the analysis, such as lepton p_{T}, $E_{\mathrm{T}}^{\mathrm{miss}}$, m_{T}, $\Delta\phi_{\ell\ell}$ and $m_{\ell\ell}$, are strongly correlated to p_{T}^{Z}, and can show mismodeling deriving from the p_{T}^{Z} description.

The modeling of p_{T}^{Z} in Drell-Yan was studied by analyzing the $p_{\mathrm{T}}^{\ell\ell}$ (magnitude of the vectorial sum of p_{T} of the two leptons) distribution of events with two opposite-charge same-flavour leptons, with an invariant mass near the Z boson mass. The range $|m_{ee/\mu\mu} - m_Z| < 15$ GeV was chosen and, in the following, it will be referred to as the Z-window or the Z-peak.

Different levels of $p_{\mathrm{T}}^{\ell\ell}$ mismodeling have been observed in the Z-peak. The inclusive $p_{\mathrm{T}}^{\ell\ell}$ spectrum for these events is shown in Figure 4.9. The data is shown by the black points, and the stacked colored histograms represent the contributions of the different background and signal processes, as predicted by the MC samples in Table 4.1. As noted in Section 4.3.2, W + jets and multijet QCD processes are modeled directly with data. The lower pad displays the data/MC ratio. Different MC generators are used to model Drell-Yan (shown in green) in the different distributions.

In Figure 4.9 one actually observes reasonable agreement at the level of $\sim 10\%$ between data and simulation, for the different MC generators. These results are compatible with, and show the same level of data-to-MC agreement as the ones presented in the latest ATLAS measurement of p_{T}^{Z} [194]. However, when selecting events in the Z-peak with exactly zero accompanying jets[1] - Figure 4.10 -, severe discrepancies between data and simulation are observed, particularly for $p_{\mathrm{T}}^{\ell\ell} \gtrsim 40$ GeV.

The modeling of p_{T}^{Z} in the 0-jet channel shows a strong dependence on the choice of MC, as shown by the different distributions in Figure 4.10. The distributions in Figure 4.11 show, however, that a similar level of disagreement is observed for ee and $\mu\mu$ events. In fact, the mismodelling of p_{T}^{Z} is related to the ability of the MC to correctly describe soft jets, rather than the modeling of the lepton properties themselves. Two-lepton events with significant $p_{\mathrm{T}}^{\ell\ell}$ and no reconstructed jets with $p_{\mathrm{T}} > 25$ (30) GeV, must have a hadronic recoil system of very soft jets, with p_{T} below the jet counting threshold, to balance the dilepton system. Indeed, when looking at the vectorial sum

[1] As will be clarified ahead, jets in the $H \to WW^* \to \ell\nu\ell\nu$ analysis are counted if above a threshold of $p_{\mathrm{T}} > 25(30)$ GeV, depending on the η range.

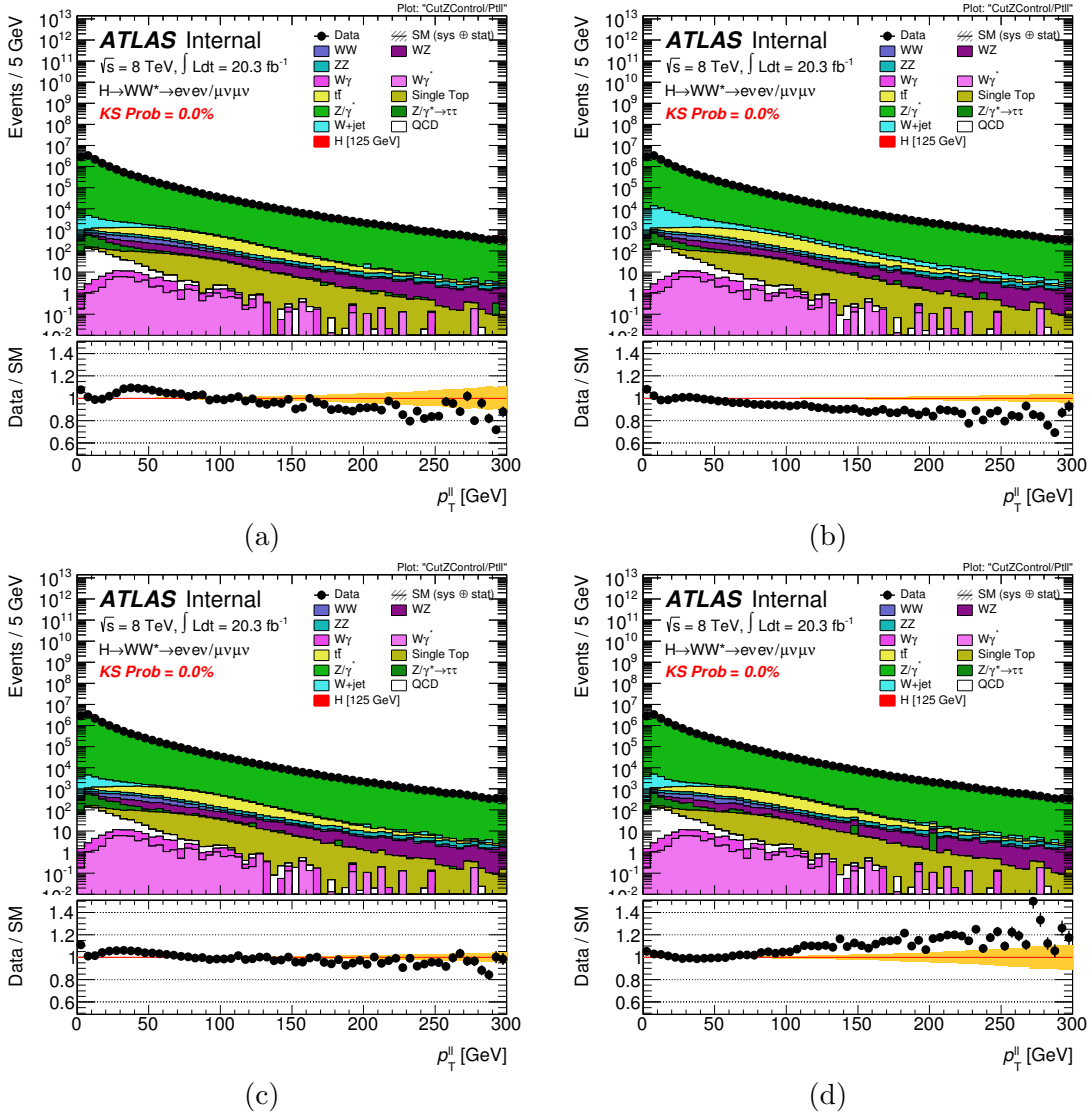

FIGURE 4.9: $p_T^{\ell\ell}$ distributions for same flavor events ($ee + \mu\mu$) in the inclusive Z-peak. Different MC generators are used to model Drell-Yan in each distribution: (a) ALPGEN + HERWIG; (b) ALPGEN + PYTHIA; (c) SHERPA; and (d) POWHEG + PYTHIA. The modeling is reasonably good.

of the transverse momentum of soft jets[2] for events with zero jets and $p_T^{\ell\ell} > 40$ GeV - Figure 4.12 -, one can observe the mismodelings are very similar to the ones seen in the $p_T^{\ell\ell}$ distributions.

For ALPGEN + HERWIG (Figure 4.10a) or ALPGEN + PYTHIA (Figure 4.10b) models, these very soft jets can be generated from either the ME, for jets with $p_T > 20$ GeV, or the PS, for jets with $p_T < 20$ GeV. Multiple soft jet events are enhanced with respect to events with harder jets. Thus, the prediction of the high $p_T^{\ell\ell}$ tail is very uncertain and subject to the PS modeling, as well as UE tuning. The ALPGEN + HERWIG model

[2]Soft jets are defined as jets with p_T below the analysis threshold for jet counting, and above the jet reconstruction threshold - $10 < p_T < 25$ (30) GeV.

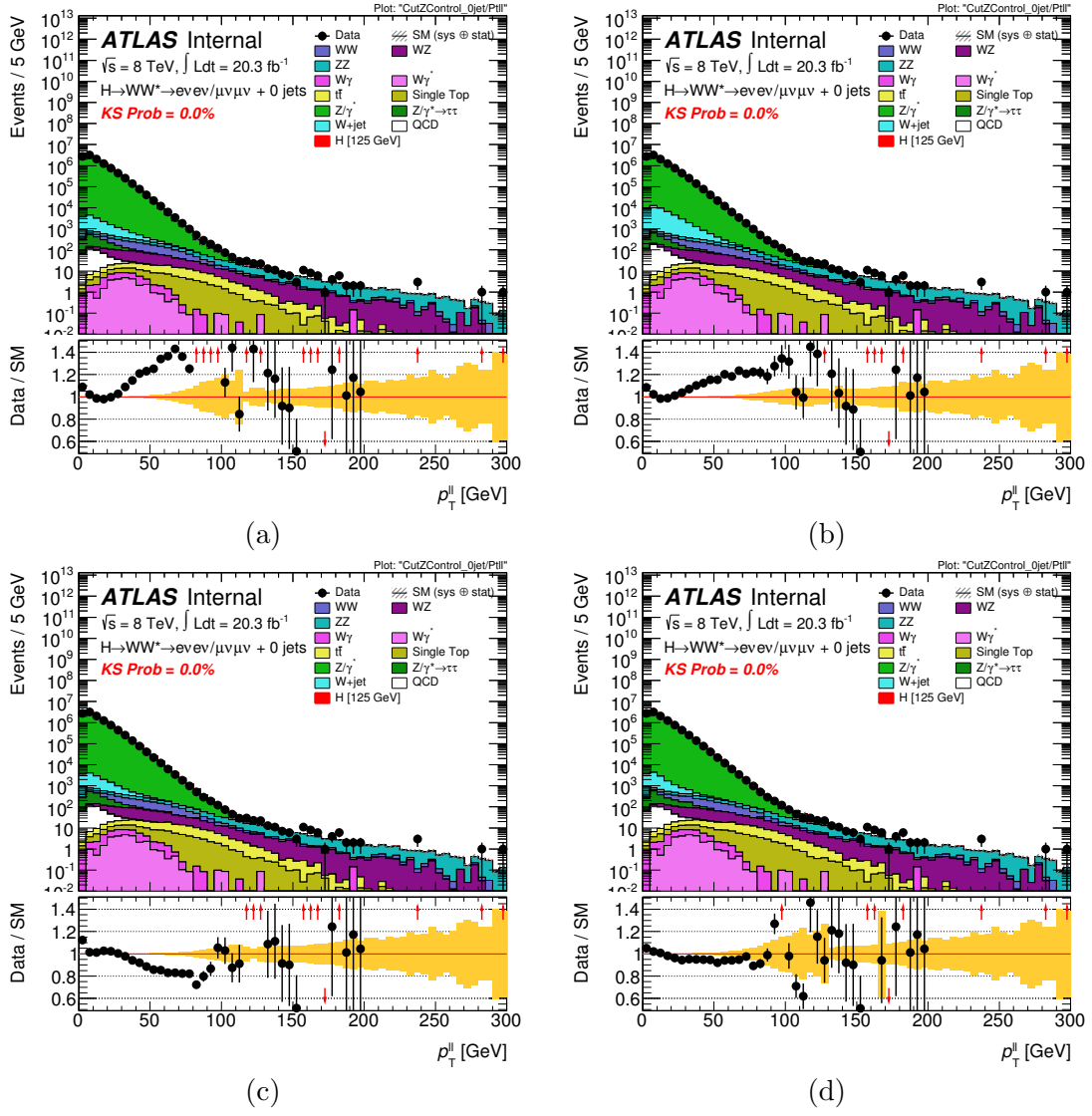

FIGURE 4.10: $p_{\mathrm{T}}^{\ell\ell}$ distributions for same flavor events in the 0-jet Z-peak. Different generators are used in each distribution to model Drell-Yan: (a) ALPGEN + HERWIG; (b) ALPGEN + PYTHIA; (c) SHERPA; and (d) POWHEG + PYTHIA. Severe discrepancies are observed, particularly at high values of $p_{\mathrm{T}}^{\ell\ell}$.

(the nominal one), in particular, produces a too soft hadronic recoil and we observe an under-prediction of the high $p_{\mathrm{T}}^{\ell\ell}$ tail in the comparison to data in Figure 4.10a.

Reweighting In order to correct for the observed mismodeling of p_{T}^{Z}, a procedure was set up to reweight the $p_{\mathrm{T}}^{\ell\ell}$ distribution in events of the 0-jet channel[3]. Because the mismodeling in 0-jet is related to the soft hadronic activity, we can compute its effect by looking at its recoil, using the di-muon system. The $\mu\mu$ p_{T} in the Z-peak is, thus, used as a probe of p_{T}^{Z}, because of the extremely good resolution of reconstructed muons in the p_{T} range of interest. Any effects due to the muon resolution will be neglected, since

[3]The modeling of the $p_{\mathrm{T}}^{\ell\ell}$ distribution of Drell-Yan events in the 1- and 2-jet channels is good, given the presence of hard-jets, and no reweighting procedure is needed.

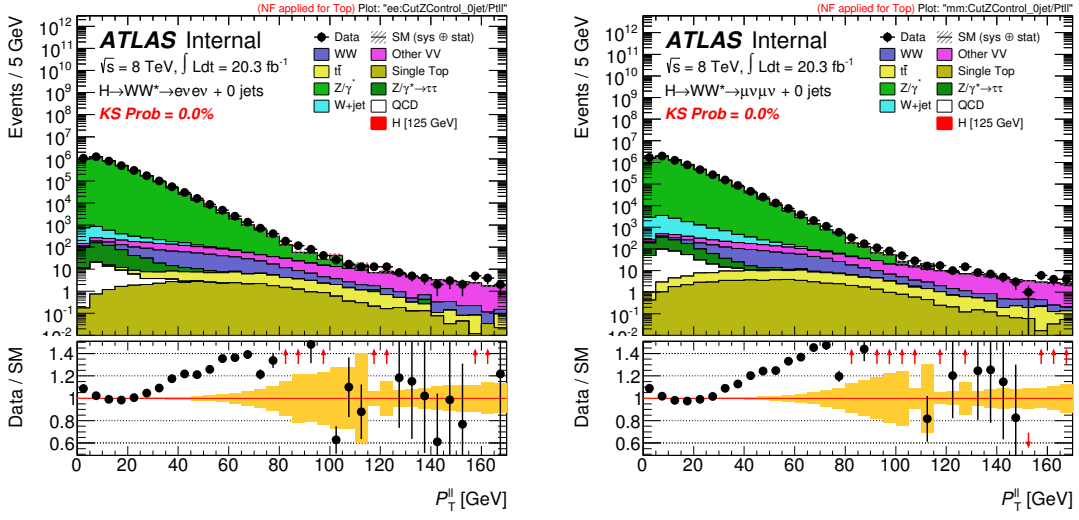

(a) (b)

FIGURE 4.11: $p_{\mathrm{T}}^{\ell\ell}$ distributions for events in the Z-peak: (a) $ee+0$-jet; and (b) $\mu\mu+0$-jet. The nominal ALPGEN + HERWIG generator is used to model Drell-Yan events. The same level of mismodelling is observed for the two final states.

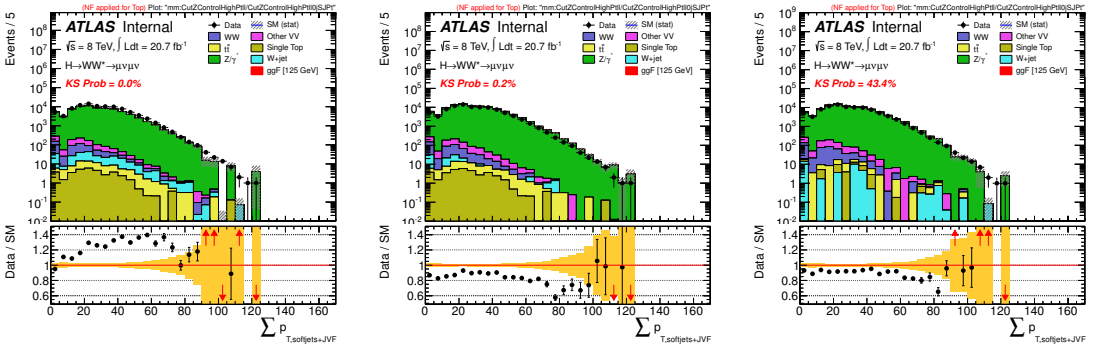

(a) (b) (c)

FIGURE 4.12: Distributions of the vectorial sum of the transverse momentum of soft jets for $\mu\mu+0$-jet events in the Z-peak passing a $p_{\mathrm{T}}^{\ell\ell} > 40$ GeV selection. Different generators are used in each distribution to model Drell-Yan: (a) ALPGEN + HERWIG; (b) SHERPA; and (c) POWHEG + PYTHIA. The level of discrepancy observed is similar to that of Figure 4.10.

it is well known from other analyses in ATLAS that the impact of smearing on muons has, at most, a percent level effect on the relevant differential distributions. The validity of this assumption will, nonetheless, be tested ahead. Final state radiation, where a photon is radiated by one of the muons, would also affect the transfer from $p_{\mathrm{T}}^{\mu\mu}$ to p_{T}^{Z}, but this is a small effect in the Z-window considered here.

The reweighting procedure consists of extracting weights directly from the data-to-Drell-Yan-MC ratio in $\mu\mu+0$-jet events in the Z-peak (contributions from non-DY processes are subtracted from data using simulation). The weights are extracted in bins of $p_{\mathrm{T}}^{\ell\ell}$. The binning is chosen to keep the Drell-Yan purity high, and an approximately constant statistical uncertainty on the ratios. The results are summarized in Table 4.2, for the reweighting of the nominal ALPGEN + HERWIG Drell-Yan sample to data. In

Figure 4.13, the weights for different generators are shown. The extracted weights are, then, applied to the truth-level p_{T}^{Z}, for all lepton decays - $Z/\gamma^* \to ee/\mu\mu/\tau\tau$ - and in the 0-jet channel only.

$p_{\mathrm{T}}^{\ell\ell}$ **range** [GeV]	**Weight (stat. unc.)**	**DY purity** [%]
0 - 2	1.14301 ± 0.00447	100
2 - 4	1.08608 ± 0.00279	100
4 - 6	1.04971 ± 0.00256	100
6 - 8	1.01794 ± 0.00260	100
8 - 10	1.00350 ± 0.00277	100
10 - 12	0.98864 ± 0.00298	100
12 - 14	0.98025 ± 0.00325	100
14 - 16	0.97700 ± 0.00356	100
16 - 18	0.97859 ± 0.00394	100
18 - 20	0.97144 ± 0.00430	100
20 - 25	0.99200 ± 0.00335	100
25 - 30	1.01691 ± 0.00455	100
30 - 35	1.08940 ± 0.00666	100
35 - 40	1.13003 ± 0.00950	99
40 - 50	1.22037 ± 0.01152	99
50 - 70	1.31238 ± 0.02144	97
70 -	1.55969 ± 0.09636	79

TABLE 4.2: Data-to-ALPGEN + HERWIG Drell-Yan MC ratio in bins of $p_{\mathrm{T}}^{\ell\ell}$, for $\mu\mu+0$-jet events in the Z-peak. Non-Drell-Yan backgrounds are subtracted from data using simulation. The ratios are used as weights in the p_{T}^{Z} reweighting procedure. The uncertainties quoted are statistical only. The Drell-Yan purity in each $p_{\mathrm{T}}^{\ell\ell}$ bin is also indicated.

Figure 4.14 shows the $p_{\mathrm{T}}^{\ell\ell}$ distribution in the Z-peak for $ee + 0$-jet and $\mu\mu + 0$-jet channels, after reweighting of p_{T}^{Z}. The agreement between data and MC is greatly improved, as expected, being now at percent level for both lepton flavors. We note that the agreement is not by construction, since the weights are derived from $\mu\mu$ at reconstruction-level and applied to all flavors at truth-level. Problems related to the unfolding of the spectrum between reconstructed muons and truth muons would show up in the $\mu\mu + 0$-jet distribution in Figure 4.14b. The very good agreement observed shows the validity of the assumption that these effect are negligible. On the other hand, problems related to statistical effects on the derived weights would appear on the $ee+0$-jet distribution in Figure 4.14a, since here the weights are applied to a different sample. Again, the very good agreement observed between data and MC rules out problems of this type.

As already mentioned, the reweighting procedure is also applied to the $Z/\gamma^* \to \tau\tau$ process and impacts, therefore, the different flavor channels as well. Figure 4.15 displays the $p_{\mathrm{T}}^{\ell\ell}$ distribution of events with two different flavor leptons and zero jets, before (Figure 4.15a) and after (Figure 4.15b) p_{T}^{Z} reweighting. The full $m_{\ell\ell}$ spectrum is shown, rather than selecting the Z-window, since the $m_{\ell\ell}$ distribution does not peak at the Z

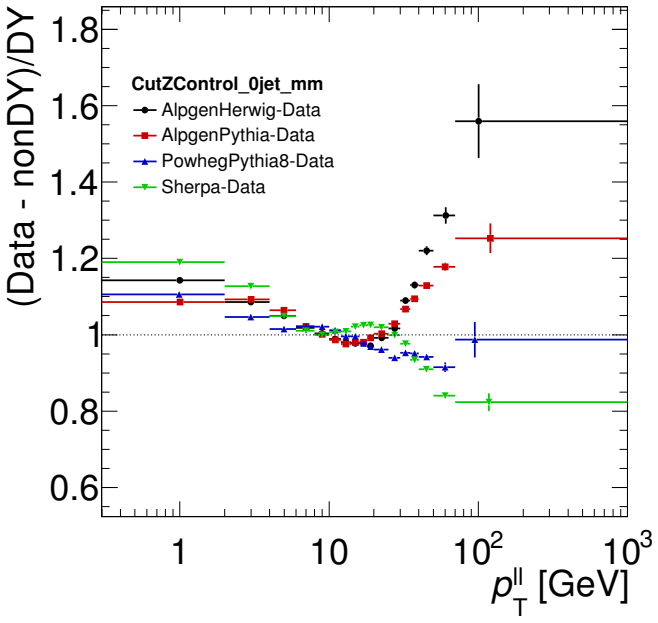

FIGURE 4.13: Data-to-Drell-Yan MC ratio in bins of $p_{\mathrm{T}}^{\ell\ell}$, for $\mu\mu + 0$-jet events in the Z peak. Non-DY backgrounds are subtracted from data using simulation. Different histograms use different generators to model Drell-Yan: ALPGEN + HERWIG (black circles), ALPGEN + PYTHIA (red squares), POWHEG + PYTHIA (blue triangles) and SHERPA (green triangles). The ratios are used as weights in the p_{T}^{Z} reweighting procedure.

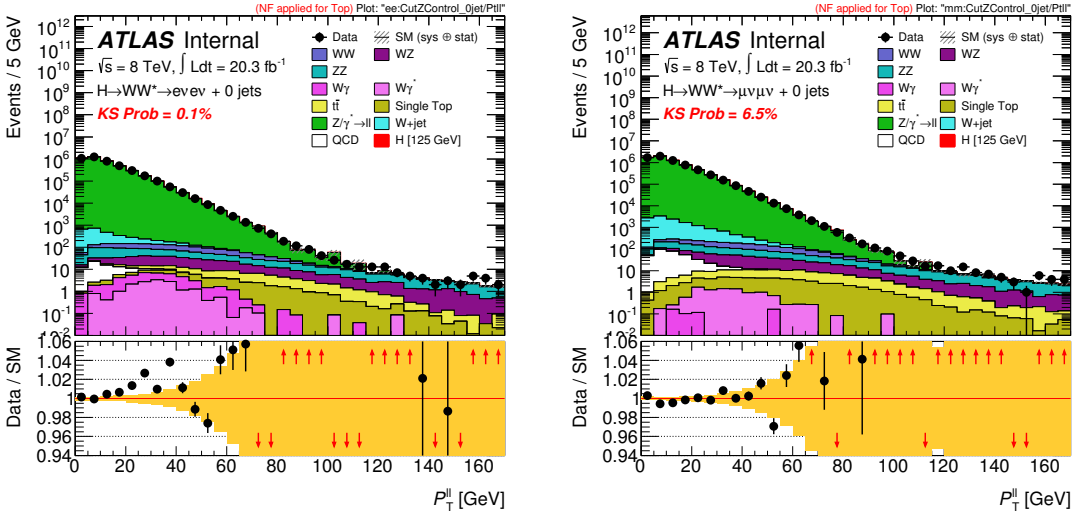

(a) (b)

FIGURE 4.14: $p_{\mathrm{T}}^{\ell\ell}$ distributions for events in the Z-peak: (a) $ee + 0$-jet; and (b) $\mu\mu + 0$-jet. The nominal ALPGEN + HERWIG generator is used to model Drell-Yan events. p_{T}^{Z} reweighting is applied and the modeling is improved (compare to Figure 4.11).

mass in the case of $Z \to \tau\tau$ decays. A large contribution from $Z \to \tau\tau$ events is seen in the low $p_{\mathrm{T}}^{\ell\ell}$ region. For the DF channels, the effect of p_{T}^{Z} reweighting is less pronounced than in the SF channels, since it is smoothed out by the moderate correlation between p_{T}^{Z} and $p_{\mathrm{T}}^{\ell\ell}$, due to the escaping neutrinos in τ decays.

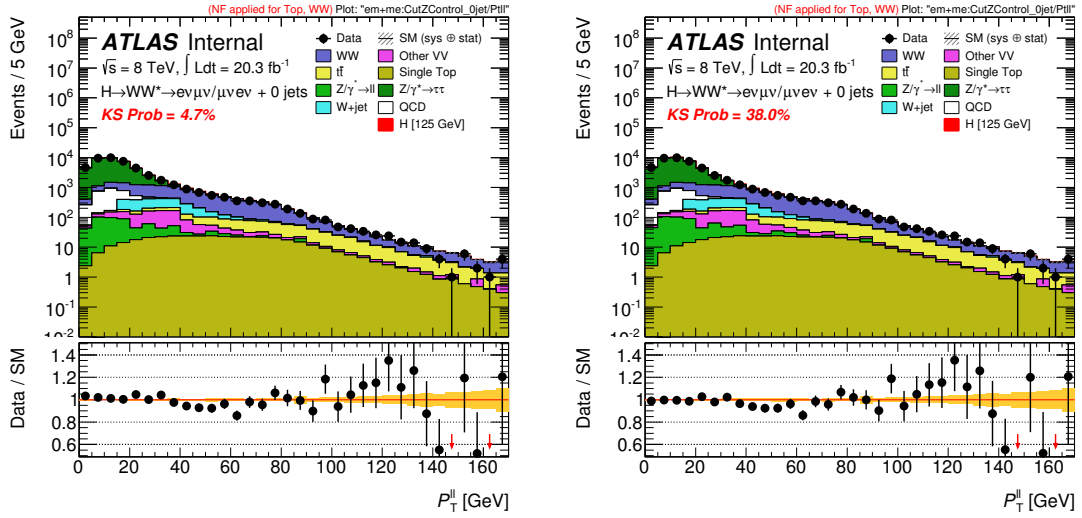

FIGURE 4.15: $p_{\mathrm{T}}^{\ell\ell}$ distributions for different flavor 0-jet events: (a) before; and (b) after p_{T}^{Z} reweighting is applied. The nominal Alpgen+Herwig generator is used to model Drell-Yan events. A slight improvement is observed at very low $p_{\mathrm{T}}^{\ell\ell}$, where the $Z \to \tau\tau$ contribution dominates.

As already mentioned, due to correlations with $p_{\mathrm{T}}^{\ell\ell}$, the description of other kinematic variables in the same flavor 0-jet Z-peak, such as lepton p_{T}, missing transverse energy, transverse mass and $\Delta\phi_{\ell\ell}$, is also greatly improved by the p_{T}^{Z} reweighting procedure. For different flavor events, the improvement is more moderate, but still present. More information can be found in Appendix B.

Uncertainties In this reweighting procedure, $p_{\mathrm{T}}^{\ell\ell}$ weights are extracted from $\mu\mu$+0-jet events in the Z-peak and applied to all lepton flavours in the final 0-jet signal regions. The signal region selections, namely low $m_{\ell\ell}$ and high missing transverse energy, can change the weights, due to correlations, but this cannot be verified directly in data.

To assess the impact of the $m_{\ell\ell}$ and missing transverse energy selection cuts on the reweighting procedure, new weights are computed directly from the SHERPA-to-ALPGEN + HERWIG Drell-Yan MC ratio. In other words, Drell-Yan SHERPA samples are used as if they were data, in the nominal procedure. The new weights are computed for $\mu\mu$+0-jet events passing the missing transverse energy selection of the different flavor channels - $p_{\mathrm{T}}^{\mathrm{miss,jetCorr}} > 20$ GeV -, and $\mu\mu + 0$-jet events with low invariant mass of the two leptons - $m_{\ell\ell} < 55$ GeV. They are then compared to the weights obtained with $\mu\mu + 0$-jet events in the Z-peak. This is shown in Figure 4.16a, which suggests that the dependence of the weights is small with $m_{\ell\ell}$ but large with $p_{\mathrm{T}}^{\mathrm{miss,jetCorr}}$.

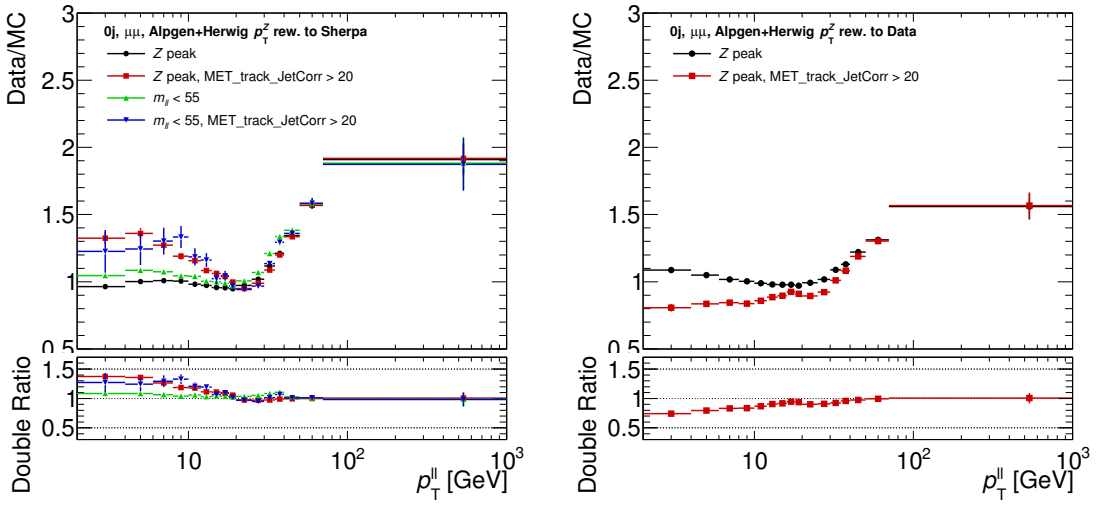

FIGURE 4.16: (a) Ratio between the SHERPA model and the nominal ALPGEN + HERWIG model of Drell-Yan, in bins of $p_{\mathrm{T}}^{\ell\ell}$, for $\mu\mu$+0-jet events; different histograms use different event selections: Z-peak (black circles); Z-peak with $p_{\mathrm{T}}^{\mathrm{miss,jetCorr}} > 20$ GeV (red squares); $m_{\ell\ell} < 55$ GeV (blue triangles); and $m_{\ell\ell} < 55$ GeV and $p_{\mathrm{T}}^{\mathrm{miss,jetCorr}} > 20$ GeV (green triangles). Right: Data-to-nominal ALPGEN + HERWIG Drell-Yan MC ratio, in bins of $p_{\mathrm{T}}^{\ell\ell}$, for $\mu\mu + 0$-jet events in the Z-peak; non-DY backgrounds are subtracted from data using simulation; different histograms use different event selections: Z-peak (black circles) and Z-peak with $p_{\mathrm{T}}^{\mathrm{miss,jetCorr}} > 20$ GeV (red squares). The double ratios shown below each plot are done with respect to the distribution in the Z-peak (black circles).

For this reason, a new set of weights is computed using, again, the data-to-ALPGEN + HERWIG Drell-Yan MC ratio for $\mu\mu$+0-jet events in the Z peak, and passing $p_{\mathrm{T}}^{\mathrm{miss,jetCorr}} > 20$ GeV. These new weights are compared to the nominal weights (computed in the Z peak without any missing transverse energy requirements, as described above) in Figure 4.16b. The nominal weights are used as the central value for the correction, and the difference between the two sets of weights is used as the systematic uncertainty on the p_{T}^{Z} reweighting procedure.

4.4 Event reconstruction

The subject of event reconstruction in ATLAS was discussed in Section 2.6. Here, we present the reconstruction strategy used in the $H \to WW^* \to \ell\nu\ell\nu$ analysis. The triggers used to select the events are presented first, followed by the requirements applied to the different physics objects. The approach used to measure the soft hadronic activity in the events is also presented.

4.4.1 Trigger

Events are selected using a logical `OR` between different single-lepton and di-lepton unprescaled triggers. The choices are summarized in Table 4.3. For the single-lepton

triggers, the OR between a lower and higher threshold trigger compensates for efficiency losses at high p_{T}. The use of di-lepton triggers allows for a selection of looser leptons, recovering the inefficiencies of the single-lepton triggers at lower p_{T}. This is fundamental to lower the p_{T} threshold of the leptons used in the analysis, increasing the signal acceptance.

	lepton	L1 p_{T} [GeV]	HLT p_{T} [GeV]	additional requirements
single-lepton	e	18	24	medium, isolated, had. leakage
		30	60	medium
	μ	15	24	isolated
		15	36	-
di-leptons	ee	10 AND 10	12 AND 12	loose, had. leakage
	$\mu\mu$	15 AND 0	12 AND 8	-
	$e\mu$	10 AND 6	12 AND 8	medium, had. leakage

TABLE 4.3: Trigger selection used in the $H \to WW^* \to \ell\nu\ell\nu$ analysis. A logical OR between the different single- and di-lepton triggers in each row is used. The L1 and HLT p_{T} thresholds of each trigger are indicated. Additional requirements, such as the identification criteria for electrons, hadronic leakage selection, or isolation, are also shown.

The efficiencies of the different triggers in data were computed using the tag-and-probe method on $Z \to ee/\mu\mu$ candidates. For leptons that satisfy the analysis selection criteria (described below), the efficiencies are approximately 70% (90%) for muons with $|\eta| < 1.05$ ($|\eta| > 1.05$), and 90% for electrons. Per-lepton scale factors correct the trigger efficiency in MC simulation to that measured in data. These are converted into per-event scale factors, since the events in the analysis have two leptons, and therefore a higher chance of passing the trigger.

4.4.2 Physics objects

Here we present the requirements applied to the different physics objects used in the analysis.

Primary vertex Collision candidates in the analysis are selected by requiring events with a hard-scatter primary vertex that has at least 3 tracks pointing to it.

Leptons Events are required to have exactly two leptons, either two electrons (ee), two muons ($\mu\mu$), or one electron and one muon ($e\mu$). The lepton with the highest transverse momentum is referred to as the leading lepton, and has $p_{\mathrm{T}}^{\mathrm{lead}} > 22$ GeV. The remaining lepton has $p_{\mathrm{T}}^{\mathrm{sub}} > 10$ GeV, and is referred to as the sub-leading lepton. A summary of all the requirements applied for the reconstruction of electrons and muons in the $H \to WW^* \to \ell\nu\ell\nu$ analysis is presented in Table 4.4.

Selections	**p_{T} range [GeV]**	**Muons**	**Electrons**
Transverse momentum	-	$p_{\mathrm{T}} > 10$	$p_{\mathrm{T}} > 10$
Pseudorapidity	-	$\lvert\eta\rvert < 2.5$	$\lvert\eta\rvert < 2.47$ crack excluded
Reconstruction & identification	$10-25$ $25-$	Staco Combined	*very tight* likelihood *medium++* cut-based w/ "CBL"
Transverse impact parameter	-	$d_0/\sigma_{d_0} < 3.0$	$d_0/\sigma_{d_0} < 3.0$
Longitudinal impact parameter	-	$z_0 \sin\theta < 1.0$ mm	$z_0 \sin\theta < 0.4$ mm
Calorimeter isolation	$10-15$ $15-20$ $20-25$ $25-$	$E_{\mathrm{T}}^{\text{cone-0.3}}/p_{\mathrm{T}}^{\mu} < 0.06$ $E_{\mathrm{T}}^{\text{cone-0.3}}/p_{\mathrm{T}}^{\mu} < 0.12$ $E_{\mathrm{T}}^{\text{cone-0.3}}/p_{\mathrm{T}}^{\mu} < 0.18$ $E_{\mathrm{T}}^{\text{cone-0.3}}/p_{\mathrm{T}}^{\mu} < 0.30$	$E_{\mathrm{T}}^{\text{cone-0.3}}/E_{\mathrm{T}}^{e} < 0.20$ $E_{\mathrm{T}}^{\text{cone-0.3}}/E_{\mathrm{T}}^{e} < 0.24$ $E_{\mathrm{T}}^{\text{cone-0.3}}/E_{\mathrm{T}}^{e} < 0.28$
Track isolation	$10-15$ $15-20$ $20-$	$p_{\mathrm{T}}^{\text{cone-0.4}}/p_{\mathrm{T}}^{\mu} < 0.06$ $p_{\mathrm{T}}^{\text{cone-0.3}}/p_{\mathrm{T}}^{\mu} < 0.08$ $p_{\mathrm{T}}^{\text{cone-0.3}}/p_{\mathrm{T}}^{\mu} < 0.12$	$p_{\mathrm{T}}^{\text{cone-0.4}}/E_{\mathrm{T}}^{e} < 0.06$ $p_{\mathrm{T}}^{\text{cone-0.3}}/E_{\mathrm{T}}^{e} < 0.08$ $p_{\mathrm{T}}^{\text{cone-0.3}}/E_{\mathrm{T}}^{e} < 0.10$

TABLE 4.4: Requirements applied for the reconstruction of electrons and muons used in the $H \to WW^* \to \ell\nu\ell\nu$ analysis.

The analysis uses Staco Combined muons with $p_{\mathrm{T}} > 10$ GeV and $|\eta| < 2.5$. The MS track is required to have a segment in all three layers of the MS. Quality requirements are applied to the ID track, namely on minimum number of hits and holes on the silicon sensors, as well as on the number of dead silicon sensors. A successful TRT extension of the ID track must be found.

Electrons are reconstructed with $p_{\mathrm{T}} > 10$ GeV and $|\eta| < 2.47$. Electrons falling in the crack-region, i.e. with $1.37 < |\eta| < 1.52$, are excluded. The identification of the electrons uses both the cut-based and the likelihood menu. For electrons with $E_{\mathrm{T}} < 25$ GeV the *very tight* selection of the likelihood menu is found to be optimal for the analysis. Compared to the tightest selection available in the cut-based menu, it provides better background rejection from non-prompt electrons, with the same signal efficiency. For electrons with $E_{\mathrm{T}} > 25$ GeV, where misidentification backgrounds are less important, the *medium++* cut-based identification is chosen, with two additional requirements: electrons with a track that is part of a conversion vertex are rejected; and the associated track must have a hit in the B-layer. These extra requirements, referred to as "CBL", suppress electrons from photon conversions and are applied in the entire η range (the *medium++* selection only applies them for $|\eta| < 2.37$.)

Further suppression of non-prompt lepton backgrounds is achieved by applying conditions to the transverse and longitudinal impact parameters of the lepton tracks, as well as by applying isolation requirements, as presented in Table 4.4. The latter were optimized as a function of lepton p_{T}: higher p_{T} leptons are less contaminated by backgrounds and looser isolation criteria can be used. The calorimeter isolation energy for both electrons and muons includes corrections for the inefficiencies caused by pile-up.

The efficiencies for reconstruction + identification and isolation + impact parameter selections, are determined using the Z tag-and-probe technique for the leptons used in

the analysis. Scale factors are used to correct the MC efficiencies to the ones measured in data.

Jets Jets are reconstructed from topo-clusters using the anti-k$_t$ algorithm with $R = 0.4$, in the $|\eta| < 4.5$ pseudorapidity range. Only jets with $p_{\mathrm{T}} > 25$ (30) GeV, for $|\eta| < 2.4$ ($|\eta| > 2.4$) are considered. As will be explained ahead, for the purpose of b-tagging, the threshold is changed to $p_{\mathrm{T}} > 20$ GeV. The LCW+JES calibration scheme is applied. For jets with $p_{\mathrm{T}} < 50$ GeV and $|\eta| < 2.4$, a |JVF| > 0.5 selection is used, aimed at reducing the contamination from pile-up jets. Finally, jets are required to pass the *looser* quality criteria. These jets are used for jet counting, i.e. for the event categorization based on the jet multiplicity, as explained in Section 4.1.2.

Overlap removal The same physical particle can produce more than one reconstructed object passing the analysis reconstruction criteria. Thus, a procedure referred to as overlap removal is applied to the reconstructed leptons and jets, to ensure an unambiguous identification. It considers the ΔR distances (in the $\eta - \phi$ space) between the identified objects, and rejects one of the objects if the distance is below a certain threshold, i.e. if the objects overlap, while retaining the other. The procedure is summarized in Table 4.5. Electron candidates that overlap with muon candidates are removed, as this is usually an indication that the muon has undergone bremsstrahlung in the ID or the calorimeter. Also due to bremsstrahlungh, a prompt electron can produce more than one electron candidate in its proximity, which is why the lowest E_{T} electron is removed in case of overlap between two candidates. High p_{T} electrons are always reconstructed as a jet, so in case of overlap between these two objects, only the electron is retained. On the other hand, if a jet and a muon overlap, only the jet is retained, under the assumption that the muon likely originates from a heavy-flavor decay.

Overlap	**Action**
$\Delta R(e, \mu) < 0.1$	remove electron
$\Delta R(e, e) < 0.1$	remove lowest E_{T} electron
$\Delta R(e, \mathrm{jet}) < 0.3$	remove jet
$\Delta R(\mu, \mathrm{jet}) < 0.3$	remove muon

TABLE 4.5: Overlap removal criteria applied to leptons and jets in the $H \to WW^* \to \ell\nu\ell\nu$ analysis.

***b*-tagging** The MV1 algorithm is chosen, with an 85% b-tagging efficiency working point. The efficiency is measured in data using a combinatorial likelihood approach, and scale factors correct for the differences between data and MC. For the purpose of b-tagging, a second class of jets is considered. They are defined and reconstructed as explained above, but the transverse momentum threshold is changed to $p_{\mathrm{T}} > 20$ GeV, and the pseudorapidity range is changed to $|\eta| < 2.4$, matching the ID acceptance. The lower p_{T} threshold allows for a more efficient rejection of top backgrounds.

Missing transverse energy Given the presence of two neutrinos in the final state, $E_{\mathrm{T}}^{\mathrm{miss}}$ is a very important observable in the $H \to WW^* \to \ell\nu\ell\nu$ analysis. Optimizations have shown that the choice of $E_{\mathrm{T}}^{\mathrm{miss}}$ flavor, as well as threshold, is highly dependent on the event category considered. All different flavors of $E_{\mathrm{T}}^{\mathrm{miss}}$ available in ATLAS, and discussed in Section 2.6.6, have been considered for this analysis. An additional computation of $E_{\mathrm{T}}^{\mathrm{miss}}$, referred to as relative-$E_{\mathrm{T}}^{\mathrm{miss}}$ or $E_{\mathrm{T,rel}}^{\mathrm{miss}}$, was also investigated. It is defined as:

$$E_{\mathrm{T,rel}}^{\mathrm{miss}} = \begin{cases} E_{\mathrm{T}}^{\mathrm{miss}} \times \sin\Delta\phi_{\mathrm{near}} \text{ , if } \Delta\phi_{\mathrm{near}} > \pi/2 \\ E_{\mathrm{T}}^{\mathrm{miss}} \text{ , otherwise} \end{cases} , \tag{4.1}$$

where $\Delta\phi_{\mathrm{near}}$ is the azimuthal separation between $E_{\mathrm{T}}^{\mathrm{miss}}$ and the nearest lepton or jet[4]. $E_{\mathrm{T,rel}}^{\mathrm{miss}}$ can be computed for any of the different flavors. It provides a better measure of the missing transverse energy in events with mismeasured leptons or jets. In these cases, $E_{\mathrm{T}}^{\mathrm{miss}}$ tends to point approximately in the same direction as the mismeasured object, and only the orthogonal component is kept. This is illustrated in Figure 4.17.

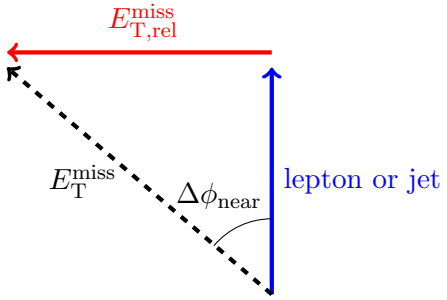

FIGURE 4.17: Schematic diagram illustrating the computation of $E_{\mathrm{T,rel}}^{\mathrm{miss}}$

The majority of backgrounds contaminating the DF channels have neutrinos in the final state, and produce true $E_{\mathrm{T}}^{\mathrm{miss}}$. As discussed in Section 2.6.6.2, $p_{\mathrm{T}}^{\mathrm{miss,jetCorr}}$ has the best resolution out of all the $E_{\mathrm{T}}^{\mathrm{miss}}$ flavors, and was shown to provide the best result for the DF channels. The SF channels, on the other hand, are completely dominated by DY, which produces fake $E_{\mathrm{T}}^{\mathrm{miss}}$. The $E_{\mathrm{T}}^{\mathrm{miss}}$ flavors and $E_{\mathrm{T}}^{\mathrm{miss}}$ thresholds were chosen to provide the best rejection power against this background. As will be clarified in Section 4.5 ahead, this means that a combination of cuts on $E_{\mathrm{T,rel}}^{\mathrm{miss,calo}}$ and $p_{\mathrm{T,rel}}^{\mathrm{miss,track}}$ is used for the SF channels.

4.4.3 Soft hadronic recoil

The contamination of DY events in the SF channels is large, even after tight $E_{\mathrm{T}}^{\mathrm{miss}}$ selections. As discussed in Section 4.2, a new kinematic variable was developed to suppress the DY background to a manageable level, while still maintaining a reasonable signal acceptance. This kinematic variable is a measure of the soft hadronic recoil of the dilepton system.

[4]Jets are defined as the ones used for counting, except the JVF selection is removed, improving the measurement of the missing transverse energy in events with mismeasured jets.

Let us start by considering the SF 0-jet channel. After all selections are applied, the most important being the requirements on high $E_{\mathrm{T}}^{\mathrm{miss}}$, low $m_{\ell\ell}$ and small $\Delta\phi_{\ell\ell}$ (or equivalently high $p_{\mathrm{T}}^{\ell\ell}$), only a special region of the total phase-space is available. DY events in this phase-space have two boosted, close-by leptons with low invariant mass. This configuration is very unnatural, since the missing transverse energy in the events is fake and no true neutrinos exist to balance the dilepton system. The two leptons must, therefore, be balanced by a hadronic recoil system. For the 0-jet channel, in particular, the jet veto requirement ensures this recoil is not reconstructed as a high p_{T} jet. Instead, the boosted dilepton system is balanced by a soft, non-collimated, hadronic recoil.

The distributions in Figure 4.18 illustrate that the constituents of this soft hadronic recoil of the dilepton system can be reconstructed as ID tracks and/or soft calorimeter jets. These plots are based on 7 TeV data, and are shown for illustrative purposes only. Figure 4.18a displays the azimuthal separation between soft jets[5] and the dilepton axis. The distribution for the different backgrounds with true $E_{\mathrm{T}}^{\mathrm{miss}}$, a well as for the signal, is approximately flat. For DY, however, the distribution peaks at $\Delta\phi \approx \pi$, indicating that for these events the soft jets are back-to-back with the two leptons. This is interpreted as the soft hadronic activity recoiling against the dilepton system. A similar behavior is seen in Figure 4.18b, this time for the azimuthal separation between ID tracks and the $\ell\ell$-axis. In this distribution, the shapes of three MC samples - WW, DY and signal - are directly compared. While signal and WW background show a flat distribution, DY events peak at $\Delta\phi \approx \pi$.

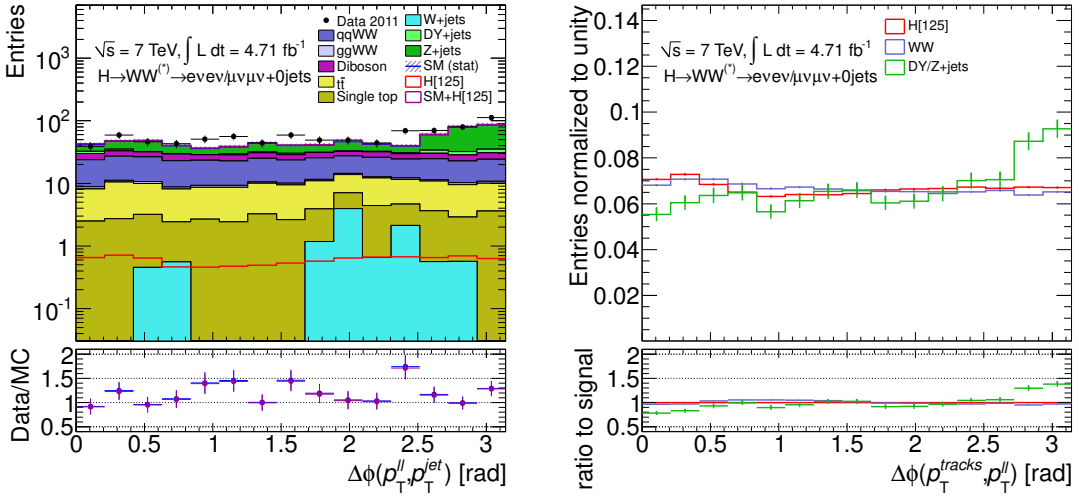

(a) (b)

FIGURE 4.18: Azimuthal separation between the dilepton system and: (a) soft jets, for data and different signal and background simulated process; and (b) ID tracks, for signal (red), WW (blue) and Z/γ^* (green) simulated processes. SF 0-jet events from the 7 TeV dataset are shown, for illustration purposes only.

Based on the distributions in Figure 4.18, two quadrants were defined in the transverse plane, with respect to the dilepton axis: the "opposite" and the "perpendicular".

[5] As before, soft jets are defined as jets with p_{T} below the analysis threshold for jet counting, and above the reconstruction threshold.

These regions are illustrated in Figure 4.19. The region opposite to the dilepton axis provides a measure of the recoil system, while the perpendicular regions serve as a control.

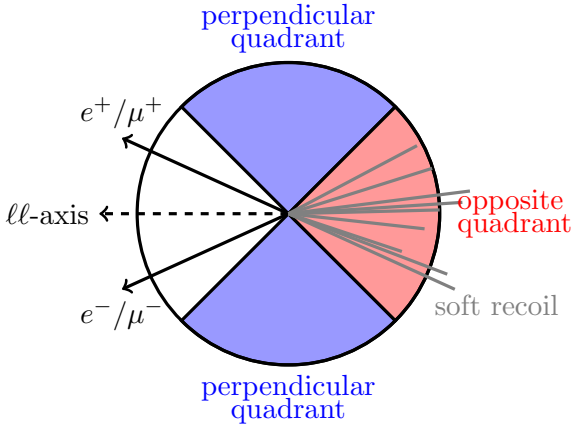

FIGURE 4.19: Schematic diagram illustrating the opposite and perpendicular quadrants in the transverse plane, defined with respect to the dilepton axis.

Several variables quantifying the soft hadronic recoil have been developed. These variables combine the multiplicity or momentum of jets and/or tracks, located in the quadrant opposite to the dilepton axis, into a single recoil variable. For illustrative purposes only, a ROC-curve from the 7 TeV dataset is shown in Figure 4.20a, indicating the relative performance of the different variables. The ROC-curve (Receiver Operating Characteristic curve) shows the efficiency on the signal, versus the rejection of DY background, measured using simulation. Each point on the ROC-curve corresponds to a different upper threshold on the recoil variable. In general, it appears that variables using only track information are less performing than variables based on soft jets (which have, themselves, some tracking information through JVF). However, the correlation matrix for DY events shown in Figure 4.20b shows that the correlations between some of the recoil variables is small, indicating that it is, in principle, possible to achieve higher rejection levels by combining several variables.

The ROC-curve in Figure 4.21a displays the relative performance of three of the recoil variables based on soft jets, this time for the 8 TeV dataset. All SF 0-jet channel selections are applied (see Table 4.6 ahead), apart from the cut on the recoil variable itself. Because simulation is not expected to correctly model these variables for DY events, the background rejection was measured directly in data, using events in the Z-peak (Section 4.7 ahead will detail the procedure used to measure the DY background rejection in data).

Soft-jets used for the variables in Figure 4.21a are reconstructed similar to the jets used for jet-counting, except the transverse momentum threshold is changed to $p_{\mathrm{T}} > 10$ GeV. In the 0-jet channel, this effectively means the soft jets have $10 < p_{\mathrm{T}} < 25$ (30) GeV, for $|\eta| < 2.4$ ($|\eta| > 2.4$). The requirement $\frac{3\pi}{4} < \Delta\phi(\ell\ell, \text{soft-jets}) < \frac{5\pi}{4}$ is imposed, such that the soft-jets are located in the quadrant opposite to the dilepton-axis. The variable plotted with blue triangles in Figure 4.21a is simply the multiplicity

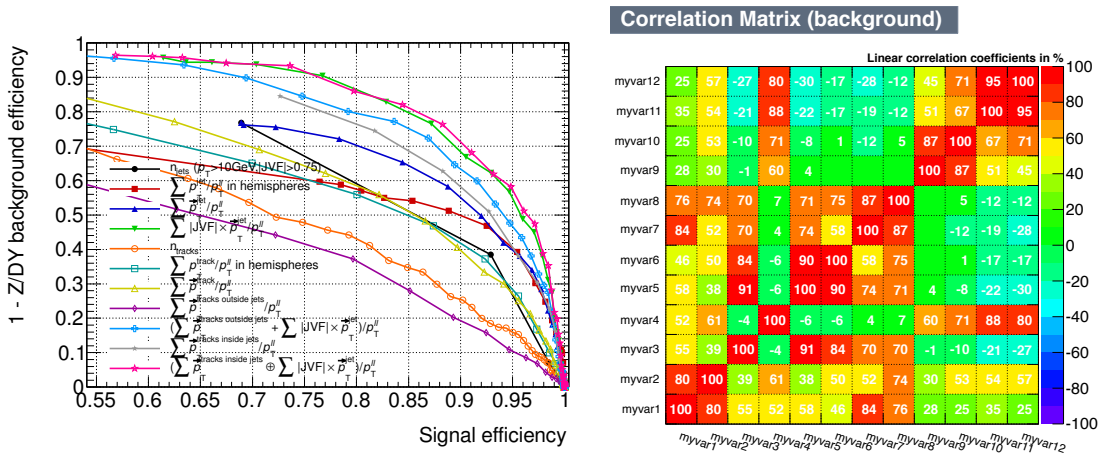

(a) (b)

FIGURE 4.20: (a) ROC curve showing the DY rejection vs. signal efficiency of an upper cut on different variables measuring the soft hadronic recoil of the dilepton system. (b) Correlation matrix for the different soft hadronic recoil variables for DY events. SF 0-jet events from the 7 TeV dataset are shown for illustration purposes only.

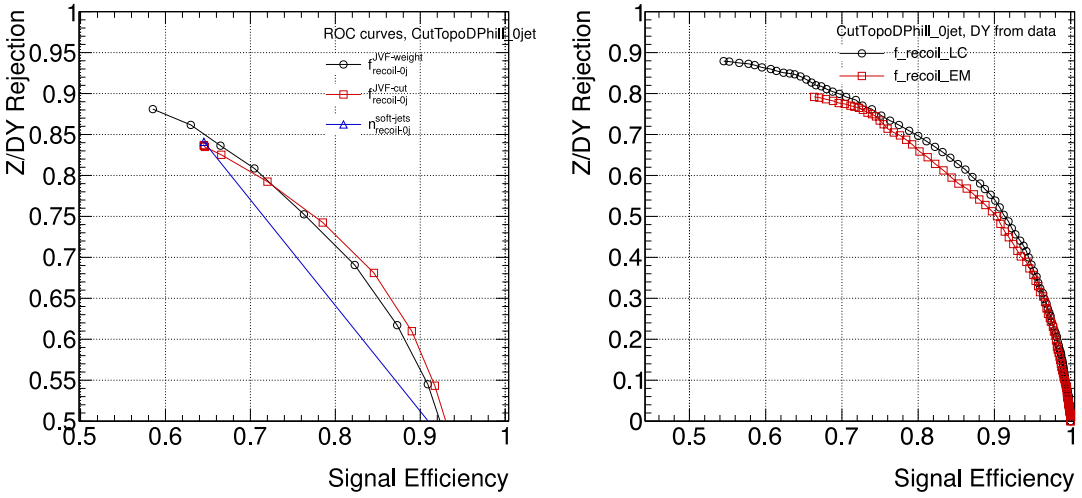

(a) (b)

FIGURE 4.21: ROC-curves showing the DY rejection vs. the signal efficiency for an upper selection cut on different variables measuring the soft hadronic recoil of the dilepton system. All variables use soft-jets and the details on the computation are described in the text. (a) The performance of different variables is compared. (b) The performance of the same variable, using soft-jets with different calibrations, is compared. Events pass the full SF 0-jet event selection, apart from the requirement on the soft hadronic recoil variable itself. DY rejection is measured using data events in Z-peak, while the signal efficiency is taken from simulation.

of these soft-jets. As for variable in the red squares, it is computed by doing a vectorial sum of the transverse momentum of these soft-jets, normalized to $p_{\mathrm{T}}^{\ell\ell}$. Finally, for the recoil variable shown by the black circles, the $|\mathrm{JVF}| > 0.5$ requirement is removed from the soft-jets, and applied as a weight in the vectorial sum:

$$\frac{|\sum_{\text{soft-jets}} |\mathrm{JVF}| \times \vec{p}_{\mathrm{T}}|}{p_{\mathrm{T}}^{\ell\ell}}. \tag{4.2}$$

This definition ensures that soft-jets that most likely originate from pile-up enter the sum with lower weights. On the other hand, soft-jets forming the dilepton recoil originate from the hard-scatter, and will enter the sum with higher weights. After the jet veto is applied, this variable will effectively use soft-jets with $10 < p_{\mathrm{T}} < 25$ (30) GeV, if they pass the $|\mathrm{JVF}| > 0.5$ criteria, and jets with $p_{\mathrm{T}} > 25$ (30) GeV if $|\mathrm{JVF}| < 0.5$. Therefore, jets with lower p_{T} enter the sum with higher weights. This definition is chosen to measure the soft hadronic recoil in the $H \to WW^* \to \ell\nu\ell\nu$ analysis, since it offers slightly more DY rejection, up to a signal efficiency of $\sim 70\%$. In what follows, this variable will be referred to as f_{recoil}.

The soft-jets used to build f_{recoil} are defined based on the nominal jet definition used for jet-counting. Therefore, they are calibrated using the LCW+JES scheme. The possibility of using the EM+JES calibration to calculate f_{recoil} was also investigated (while maintaining the LCW+JES jet binning of the analysis), since this calibration is known to provide better resolution for jets with low p_{T}. A ROC-curve comparing the f_{recoil} variable built with EM+JES (red squares) and LCW+JES (black circles) jets is shown in Figure 4.21b. Again, the rejection for the DY background is calculated directly from data in the Z-peak. The performance of the two variables is comparable, as the curves overlay in most of the range. However, the variable built with LCW+JES jets is able provide more DY rejection, and is kept as the default recoil variable.

Figure 4.22a shows the shapes of the f_{recoil} distributions for events in the SF 0-jet category (event selections up to $p_{\mathrm{T}}^{\ell\ell}$, in Table 4.6 ahead, are applied). The DY background is shown in green, the sum of non-DY backgrounds, i.e. top, W + jets, diboson and $Z/\gamma^* \to \tau\tau$, is shown in blue, and a 125 GeV Higgs signal is displayed in red (all simulated events). The soft hadronic recoil activity for the DY process is clearly visible, and peaks at approximately 50% of the $p_{\mathrm{T}}^{\ell\ell}$ value. Events with neutrinos in the final state, such as the remaining non-DY backgrounds and the signal, do not produce measurable hadronic recoil. Differences in the f_{recoil} shape between the signal and non-DY background are within $\sim 9\%$, and attributed to the higher probability for initial state QCD emission in gluon-gluon initiated processes.

The large difference in shapes visible in Figure 4.22a, between DY and non-DY processes, allows for a tight cut on f_{recoil}. A requirement of $f_{\mathrm{recoil}} < 0.1$ (the optimization of the selection is described in Section 4.5.1 ahead) has a large signal efficiency - $\sim$ 65% - and significant DY background rejection - $\sim 85\%$. The f_{recoil} variable is used further, in a data-driven technique for estimating the efficiency of the f_{recoil} cut and

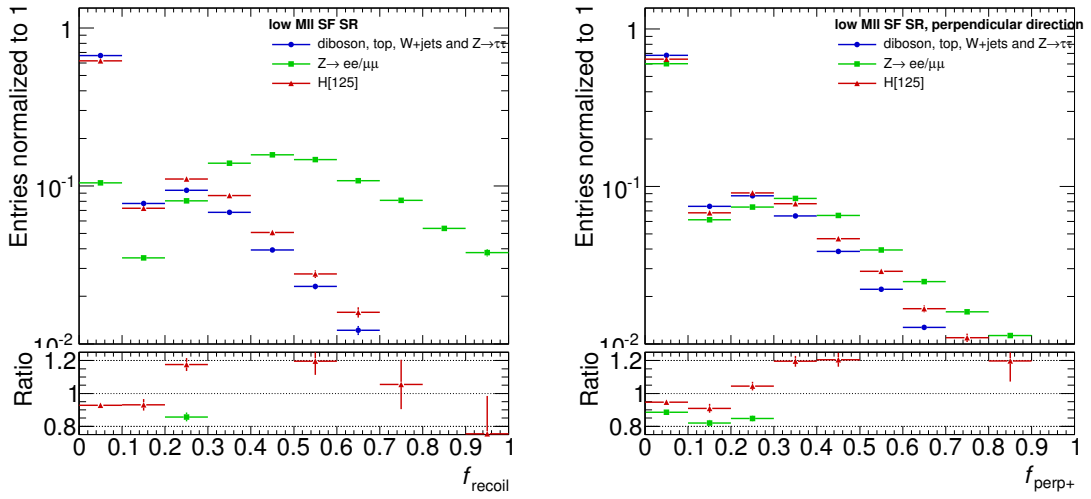

(a) (b)

FIGURE 4.22: Simulated shapes of (a) f_{recoil} and (b) f_{perp} for DY background (green squares), non-DY backgrounds (blue circles), i.e. top, W + jets, $Z/\gamma^* \to \tau\tau$, diboson, and m_H125 GeV Higgs signal (red triangles). $ee/\mu\mu$ + 0-jet events are shown passing all the SF 0-jet signal region selections shown in Table 4.6 ahead, apart from the requirements on $p_{\text{T,rel}}^{\text{miss,track}}$, $\Delta\phi_{\ell\ell}$ and f_{recoil}, to allow for more statistics. The $p_{\text{T}}^{\ell\ell}$ selection is applied and it is enough to boost the dilepton system, creating the shape difference between DY and other processes with true missing transverse energy, visible in (a).

the normalization of the remaining DY background in the signal region, which will be explained in Section 4.7 ahead.

In Figure 4.22b, the same MC samples are used to plot f_{perp}. This variable is computed using the same definition as the f_{recoil} variable, but the soft-jets are located in the two quadrants of the transverse plane perpendicular to the dilepton axis (see Figure 4.19). The quadrant opposite to the dilepton axis (used in f_{recoil}) probes the recoil of the dilepton system coming from momentum conservation, whereas the quadrants orthogonal to the $\ell\ell$-direction are sensitive to the underlying event and pile-up jets. This variable has, thus, similar shapes for the DY and non-DY processes, and will be used later as a validation region, to probe the modeling of the f_{recoil} shape for non-DY events directly in data.

The f_{recoil} variable described for events in the 0-jet channel can be extended to events in the 1-jet channel. In this case, DY is still the only background process without neutrinos in the final state. For this process, the $\ell\ell$ + jet system is balanced by a soft hadronic recoil. Thus, a natural extension of the f_{recoil} variable proposed above can be constructed with two differences: the sum is performed over the p_{T} of soft-jets in the quadrant opposite to the dilepton+jet axis, and it is normalized to $p_{\text{T}}^{\ell\ell j}$, i.e. the magnitude of the vectorial sum of p_{T} of the two leptons and the jet.

Figure 4.23a compares the performance of the nominal f_{recoil} variable (black circles), as well as the version where soft-jets have the JVF selection applied (blue triangles), with the corresponding extended definitions (shown in red squared and green diamonds), for events in the SF 1-jet signal region. The ROC-curves show that the extended definitions

of f_{recoil} reject approximately 25% more DY events in the 1-jet signal region, compared to the default f_{recoil} definition (this is true whether JVF is applied as a weight or as a cut). Furthermore, Figure 4.23a shows that the performance of the JVF-weight definition of $f_{\text{recoil}}^{\text{extended}}$ (red squares), is better than the JVF-cut version (green diamonds), up to a signal efficiency of $\sim 70\%$, also for the 1-jet channel of the analysis. In Figure 4.23b, the performances of $f_{\text{recoil}}^{\text{extended}}$ computed with LCW+JES and EM+JES jets are compared. Similar to what was seen for f_{recoil} in the 0-jet bin (Figure 4.21b), LCW+JES jets allow for higher DY background suppression in the 1-jet channel. In what follows, f_{recoil} will be used to refer to the extended definition for the 1-jet channel.

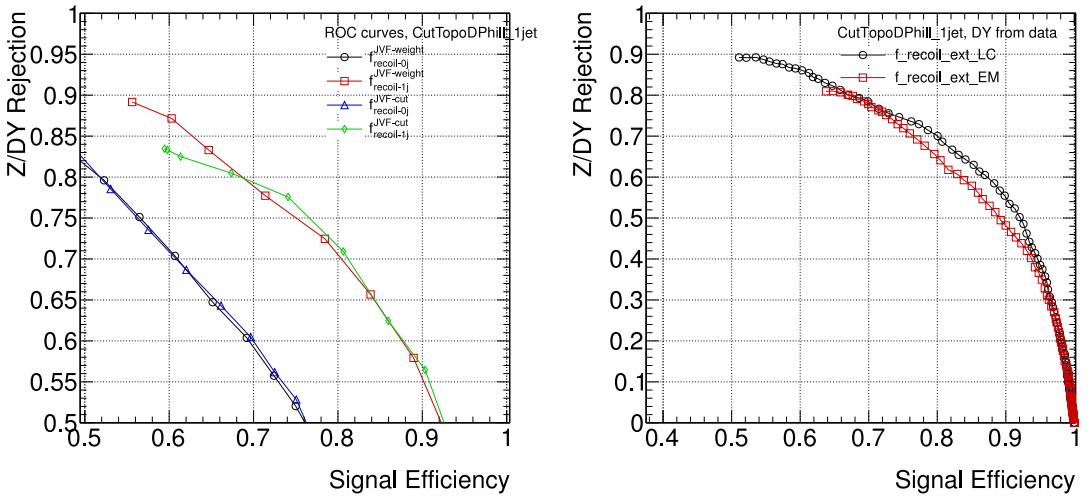

(a) (b)

FIGURE 4.23: ROC-curves showing the DY rejection vs. the signal efficiency for an upper selection cut on different variables measuring the soft hadronic recoil of the dilepton(+jet) system. All variables use soft-jets and the details on the computation are described in the text. (a) The performance of different variables is compared. (b) The performance of the same variable, using soft-jets with different calibrations, is compared. Events pass the full SF 1-jet event selection, apart from the requirement on the soft hadronic recoil variable itself. DY rejection is measured using data events in Z-peak, while the signal efficiency is taken from simulation.

In Figure 4.24 the shapes of f_{recoil} and f_{perp} are shown for the DY background in green, the sum of non-DY backgrounds in blue, and signal in red, for simulated events the SF 1-jet category. The hadronic recoil opposite the $\ell\ell + \text{jet}$ system is, again, clearly visible for DY events, whereas the perpendicular direction shows smaller shape differences between DY and non-DY processes. A selection on $f_{\text{recoil}} < 0.1$ was chosen for the 1-jet analysis, which provides a DY rejection of $\sim 85\%$, while maintaining a signal efficiency of $\sim 60\%$.

4.5 Event selection

A summary of the event selections applied in the 0- and 1-jet categories of the SF channels is presented in Table 4.6. For completeness, the event selections applied in the

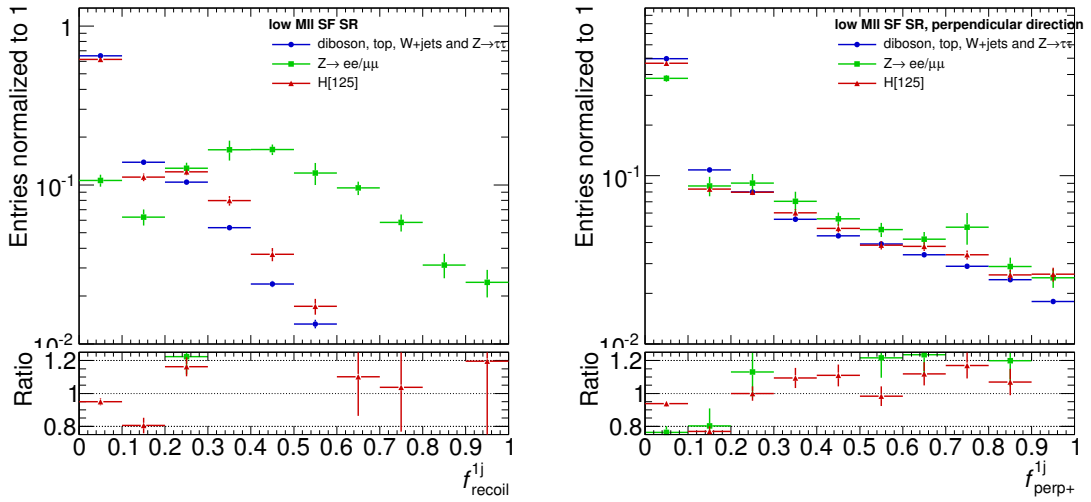

(a) (b)

FIGURE 4.24: Simulated shapes of (a) f_{recoil} and (b) f_{perp} for DY background (green squares), non-DY backgrounds (blue circles), i.e. top, W + jets, $Z/\gamma^* \to \tau\tau$, diboson, and m_H125 GeV Higgs signal (red triangles). $ee/\mu\mu$ + 0-jet events are shown passing all the SF 1-jet signal region selections shown in Table 4.6 ahead, apart from the requirements on $\Delta\phi_{\ell\ell}$ and f_{recoil}, to allow for more statistics. The $p_{\text{T,rel}}^{\text{miss,track}}$ selection is applied and it is enough to boost the dilepton+jet system, creating the shape difference between DY and other processes with true missing transverse energy, visible in (a).

DF 0- and 1-jet channels are included in Table 4.7. It is interesting to note that the SF selections mostly mimic the DF ones, apart from cuts relating to the suppression of DY. In particular, the $E_{\text{T}}^{\text{miss}}$ selections are looser in the DF channels, and no f_{recoil} cut is applied. On the other hand, the DF channels apply an explicit veto of $Z/\gamma^* \to \tau\tau$ decays. It is also required that at least one of the leptons passes a $m_{\text{T}}^W = \sqrt{2p_{\text{T}}^{\ell} \cdot E_{\text{T}}^{\text{miss}} \cdot (1 - \Delta\phi)}$ selection (where $\Delta\phi$ is the azimuthal separation between the lepton and the missing transverse momentum), to suppress multijet backgrounds. This selection is unnecessary in the SF 1-jet channel, as the multijet background is entirely rejected by the tight $E_{\text{T}}^{\text{miss}}$ requirements.

After the event reconstruction described in Section 4.4, a sample of two oppositely charged leptons is selected. The leading lepton is required to have $p_{\text{T}}^{\text{lead}} > 22$ GeV, and events with more than two leptons are rejected. No jet selection is applied at this stage, yet.

At this point, the SF sample has over 1.6×10^7 events, almost entirely composed of DY. The $m_{\ell\ell}$ lineshape of these events is shown in Figure 4.25a. Low mass resonances have been suppressed by requiring $m_{\ell\ell} > 12$ GeV. The description of the data by simulation is very good, apart from the $m_{\ell\ell} \lesssim 50$ GeV range, where a discrepancy between data and MC of up to 15% exists. Approximately 90% of the DY events in the SF channels lie in the Z-window, which is therefore rejected. The $m_{\ell\ell}$ distribution of DF events is shown in Figure 4.25b for completeness.

Further suppression of DY in the SF channels is achieved by requiring significant missing transverse energy in the events. The $E_{\text{T,rel}}^{\text{miss,calo}}$ distribution of SF events with 0

	$ee + \mu\mu$ event selection		
Pre-selection	two leptons, $p_{\mathrm{T}}^{\mathrm{lead}} > 22$ GeV, $p_{\mathrm{T}}^{\mathrm{sub}} > 10$ GeV		
	opposite charge leptons		
	$m_{\ell\ell} > 12$ GeV		(1)
	$\lvert m_{\ell\ell} - m_Z \rvert > 15$ GeV		
	$E_{\mathrm{T,rel}}^{\mathrm{miss,calo}} > 40$ GeV		
Jet	0-jet	1-jet	(2)
Bkg. rejection	-	zero b-jets	
	$\Delta\phi(\ell\ell, E_{\mathrm{T}}^{\mathrm{miss}}) > \pi/2$ rad	-	(3)
	$p_{\mathrm{T}}^{\ell\ell} > 30$ GeV	-	
	$p_{\mathrm{T,rel}}^{\mathrm{miss,track}} > 40$ GeV	$p_{\mathrm{T,rel}}^{\mathrm{miss,track}} > 35$ GeV	(5)
	$f_{\mathrm{recoil}} < 0.1$		(7)
Higgs	$m_{\ell\ell} < 55$ GeV		(4)
	$\Delta\phi_{\ell\ell} < 1.8$ rad		(6)

TABLE 4.6: Event selections applied for the same flavor 0- and 1-jet channels of the $H \to WW^* \to \ell\nu\ell\nu$ analysis. The event selections were grouped into: pre-selection, which is common to all jet categories; jet multiplicity categorization; background rejection, which depends on the jet category; and selection of Higgs candidates, which is also common to all jet categories, as well as to the different flavor channels. The order in which the event selection is applied in the analysis is indicated by the number is parenthesis on the right-hand side.

	$e\mu$ event selection	
Pre-select.	two leptons, $p_{\mathrm{T}}^{\mathrm{lead}} > 22$ GeV, $p_{\mathrm{T}}^{\mathrm{sub}} > 10$ GeV	
	opposite charge leptons	
	$m_{\ell\ell} > 10$ GeV	
	$p_{\mathrm{T}}^{\mathrm{miss,jetCorr}} > 20$ GeV	
Jet	0-jet	1-jet
Bkg. rej.	-	zero b-jets
	$\Delta\phi(\ell\ell, E_{\mathrm{T}}^{\mathrm{miss}}) > \pi/2$ rad	$m_{\mathrm{T}}^{W} > 50$ GeV
	$p_{\mathrm{T}}^{\ell\ell} > 30$ GeV	$m_{\tau\tau} < m_Z - 25$ GeV
Higgs	$m_{\ell\ell} < 55$ GeV	
	$\Delta\phi_{\ell\ell} < 1.8$ rad	

TABLE 4.7: Event selections applied for the different flavor 0- and 1-jet channels of the $H \to WW^* \to \ell\nu\ell\nu$ analysis. The event selections are divided into: pre-selection, which is common to all jet categories; jet multiplicity categorization; background rejection, which depends on the jet category; and selection of Higgs candidates, which is also common to all jet categories, as well as to the same flavor channels. The event selection is applied in the same order presented here.

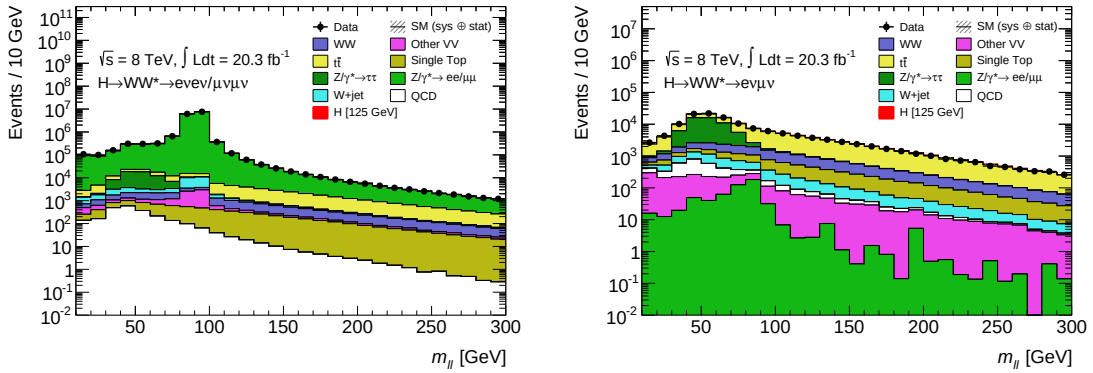

(a) (b)

FIGURE 4.25: $m_{\ell\ell}$ distributions of (a) SF and (b) DF opposite charge dilepton events, after the minimum invariant mass requirement.

or 1 accompanying jets is shown in Figure 4.26a. A selection of $E_{\mathrm{T,rel}}^{\mathrm{miss,calo}} > 40$ GeV is applied for these events, rejecting $\sim 98\%$ of the DY background. A looser selection on $p_{\mathrm{T}}^{\mathrm{miss,jetCorr}}$, shown in Figure 4.26b, is applied for the DF 0- and 1-jet events.

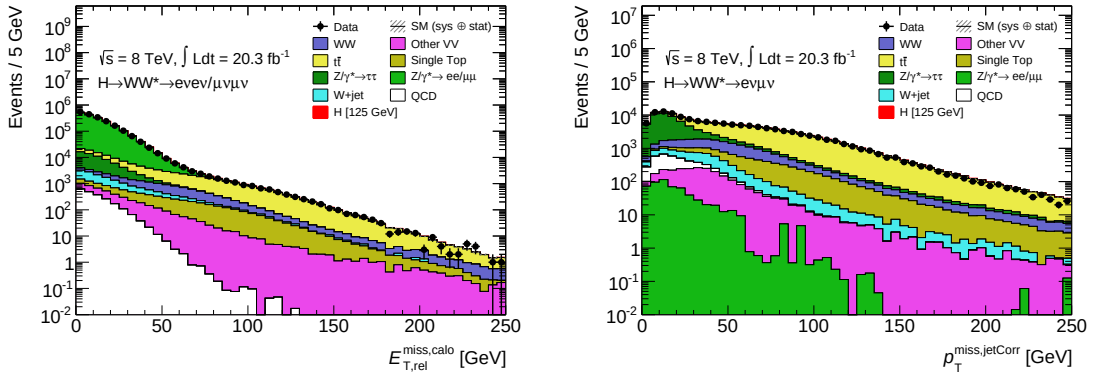

(a) (b)

FIGURE 4.26: Distributions of (a) $E_{\mathrm{T,rel}}^{\mathrm{miss,calo}}$ for SF events and (b) $p_{\mathrm{T}}^{\mathrm{miss,jetCorr}}$ for DF events, with 0 or 1 accompanying jets, after the veto on events in the Z-peak.

Figure 4.27a shows the jet multiplicity distribution of SF events passing the pre-selection. The distribution for DF events is shown in Figure 4.27b, for completeness. The background composition in each bin is clearly different, which motivates the categorization of events according to the number of jets. In the 0-jet bin, DY and WW are the main sources of background. As for the 1-jet bin, DY and top processes dominate.

A factor of ~ 5 rejection of top backgrounds is achieved in the SF 1-jet category, by requiring that no b-jets are found in the sample. This selection retains over 85% of the signal.

In the 0-jet category, potentially mismodeled events are suppressed by requiring that the $E_{\mathrm{T}}^{\mathrm{miss}}$ points away from the dilepton-axis: $\Delta\phi(\ell\ell, E_{\mathrm{T}}^{\mathrm{miss}}) > \pi/2$. This selection retains all signal events, rejecting almost 10% of DY in SF.

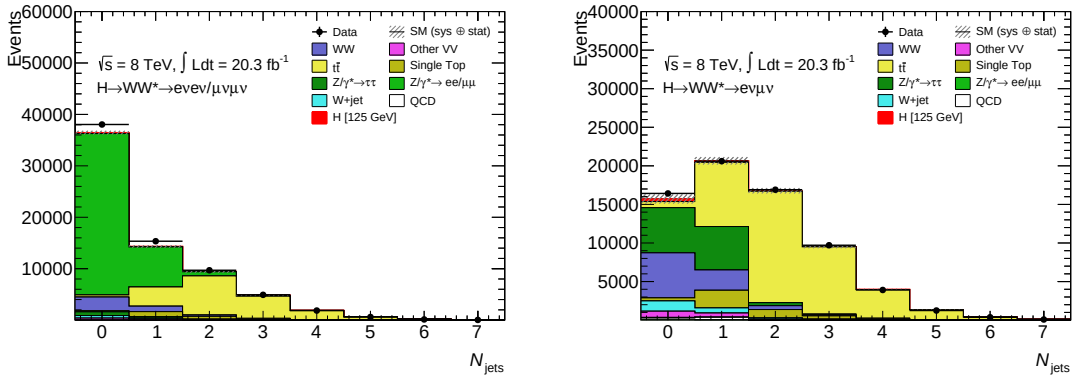

(a) (b)

FIGURE 4.27: Distributions of (a) $E_{\mathrm{T,rel}}^{\mathrm{miss}}$ for SF events and (b) $p_{\mathrm{T}}^{\mathrm{miss,jetCorr}}$ for DF events, with 0 or 1 accompanying jets, after the veto on events in the Z-peak.

As shown in Figure 4.28a, DY events with zero accompanying jets are mostly produced at rest, i.e. with low $p_{\mathrm{T}}^{\ell\ell}$ and the two leptons pointing in opposite directions. Thus, a $p_{\mathrm{T}}^{\ell\ell} > 30$ GeV requirement suppresses DY events in the SF 0-jet channel by a factor of ~ 4, while retaining $\sim 94\%$ of the signal events. Almost all the $Z/\gamma^* \to \tau\tau$ decays in the SF 0-jet channel are suppressed with this selection. The same selection is applied for DF 0-jet events, shown in Figure 4.28b.

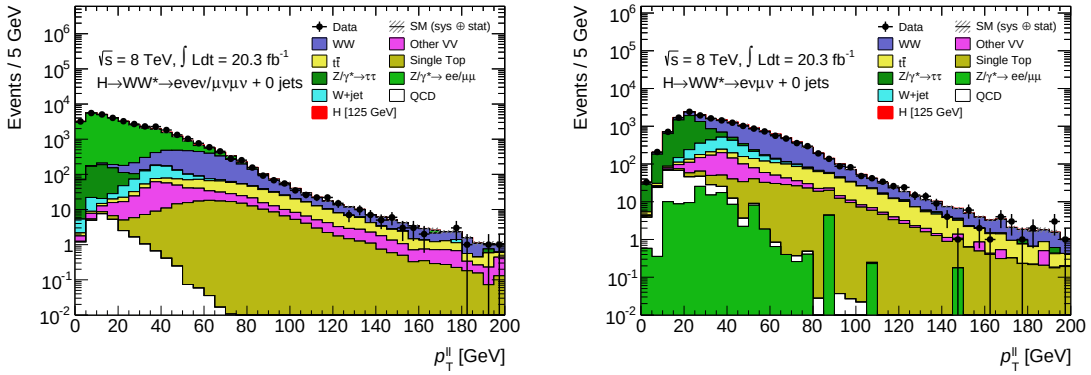

(a) (b)

FIGURE 4.28: $p_{\mathrm{T}}^{\ell\ell}$ distributions of (a) SF and (b) DF events in the 0-jet category, after the requirement on $\Delta\phi(\ell\ell, E_{\mathrm{T}}^{\mathrm{miss}})$.

After these selections, the features of the Higgs decay are exploited, as explained in Section 4.1.1. A selection of $m_{\ell\ell} < 55$ GeV retains $\sim 90\%$ of the signal, and rejects $\sim 60\%$ of the WW background.

The DY contamination at low $m_{\ell\ell}$ is still ~ 30 (60) times the size of the signal, in the 0-jet (1-jet) SF category. A requirement of high $p_{\mathrm{T,rel}}^{\mathrm{miss,track}}$ is, therefore, applied for both jet categories. The distributions of $p_{\mathrm{T,rel}}^{\mathrm{miss,track}}$ for 0- and 1-jet SF events are shown in Figure 4.29. The threshold applied on the $p_{\mathrm{T,rel}}^{\mathrm{miss,track}}$ variable is 40 GeV in the SF 0-jet channel, which suppresses DY events by a factor ~ 7, keeping over 80% of the Higgs signal. In the 1-jet channel, $p_{\mathrm{T,rel}}^{\mathrm{miss,track}}$ is more efficient in suppressing DY. Thus, a looser

selection at 35 GeV rejects $\sim 94\%$ of DY, while retaining more than 70% of the signal events.

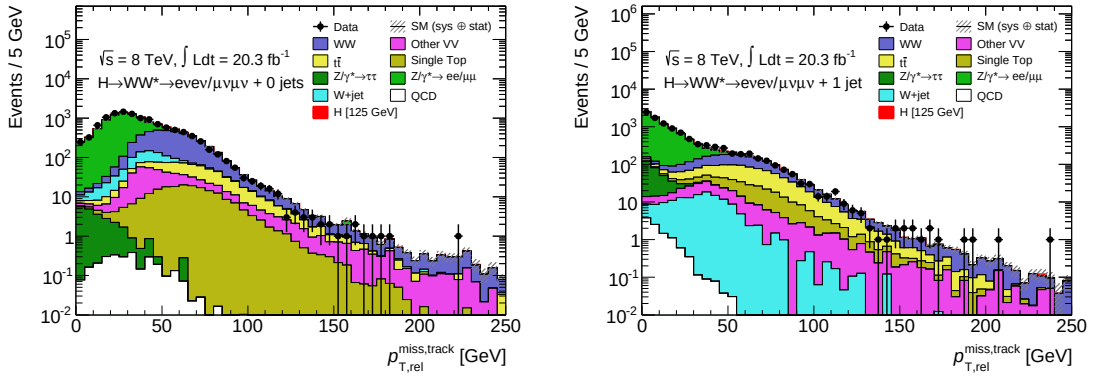

FIGURE 4.29: $p_{\mathrm{T,rel}}^{\mathrm{miss,track}}$ distributions of events in the SF (a) 0-jet and (b) 1-jet categories, after the $m_{\ell\ell} < 55$ GeV requirement.

At this stage, the angular correlations between the charged leptons are once again used, as detailed in Section 4.1.1. The $\Delta\phi_{\ell\ell}$ distribution of SF events in the 0- and 1-jet channels is shown in Figure 4.30. A $\Delta\phi_{\ell\ell} < 1.8$ rad selection is applied in both jet categories. This selection suppresses both WW and DY, and retains $\sim 97\%$ (90%) of the signal in the 0-jet (1-jet) bin.

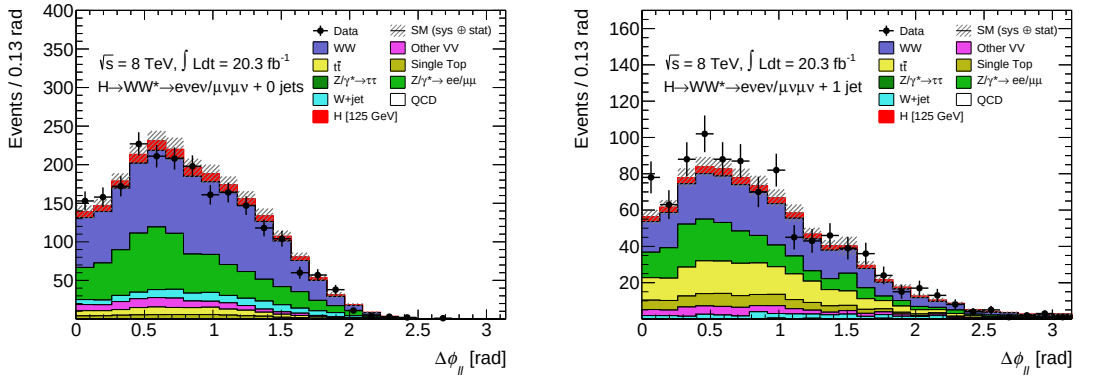

FIGURE 4.30: $\Delta\phi_{\ell\ell}$ distributions of events in the SF (a) 0-jet and (b) 1-jet categories, after the $p_{\mathrm{T,rel}}^{\mathrm{miss,track}}$ requirement.

Final suppression of DY is achieved by requiring $f_{\mathrm{recoil}} < 0.1$, for both 0- and 1-jet SF channels. The f_{recoil} distributions of SF events are shown in Figure 4.31. As discussed in Section 4.4.3, this cut suppresses 85% of the DY background, in both jet categories. After all the selections are applied, the DY yield is approximately the same as the signal.

Table 4.8 shows the cutflow for the SF 0- and 1-jet channels, i.e the evolution of the predicted signal and background yields, as well as of the observed number of events in data, throughout the sequential application of the different event selections. The transverse mass provides the final discrimination between signal and background events.

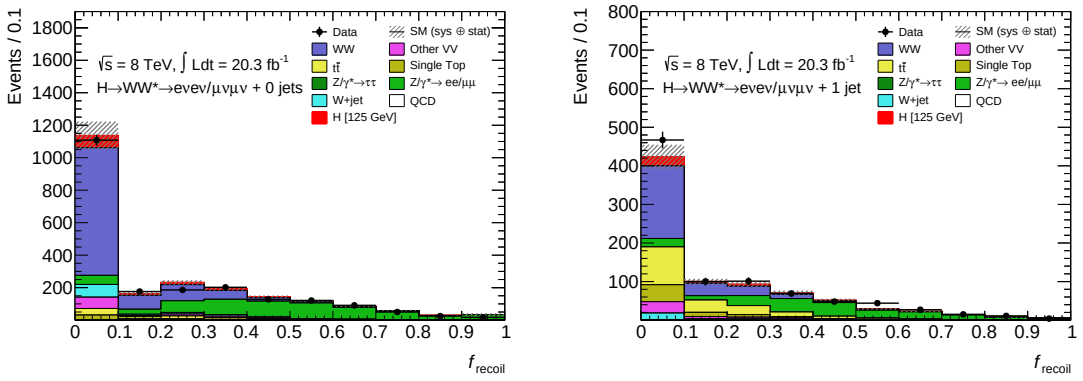

(a) (b)

FIGURE 4.31: f_{recoil} distributions of events in the SF (a) 0-jet and (b) 1-jet categories, after the $\Delta\phi_{\ell\ell}$ requirement.

Thus, the cutflow includes a m_{T}-window requirement in the final signal regions, that selects the transverse mass region where the signal purity is highest. The selected range is $\frac{3}{4}m_H < m_{\text{T}} < m_H$. The DF cutflow is also provided in Table 4.9, for completeness. For the cutflows and the different distributions shown throughout this Section, the backgrounds were estimated as discussed in Sections 4.6 and 4.7 ahead. The signal is predicted by MC for $m_H = 125$ GeV.

$ee + \mu\mu$	Obs./Bkg.	Obs.	Bkg.	H	WW	$t\bar{t}$	single top	$W+$ jets	multi jet	other VV	Z/γ^* $ee/\mu\mu$	Z/γ^* $\tau\tau$
0-jet	1.04 ± 0.01	38040	36520	170	3260	418	211	504	29	358	31060	685
$\Delta\phi(\ell\ell, E_{\text{T}}^{\text{miss}}) > \pi/2$ rad	1.05 ± 0.01	35445	33890	170	3250	416	211	493	26	355	28520	622
$p_{\text{T}}^{\ell\ell} > 30$ GeV	1.06 ± 0.01	11660	11040	161	3010	394	201	396	2.6	309	6700	21
$m_{\ell\ell} > 55$ GeV	1.01 ± 0.01	6786	6710	147	1260	109	64	251	2.0	179	4840	8.7
$p_{\text{T,rel}}^{\text{miss,track}} > 40$ GeV	1.02 ± 0.02	2197	2160	121	1097	99	59	133	0.5	106	660	0.3
$\Delta\phi_{\ell\ell} < 1.8$ rad	1.01 ± 0.02	2127	2100	117	1068	96	57	122	0.5	104	649	0.3
$f_{\text{recoil}} < 0.1$	1.01 ± 0.03	1108	1096	75	786	41	31	79	0.0	69	91	0.1
m_{T}-window	0.99 ± 0.05	510	517	58	349	11	8	53	0	31	64	0.1
1-jet	1.05 ± 0.01	15344	14640	76	1111	3770	999	178	13	192	8100	280
zero b-jets	1.08 ± 0.02	9897	9140	65	972	725	245	137	10	163	6640	241
$m_{\ell\ell} > 55$ GeV	1.16 ± 0.02	5127	4410	58	351	226	85	73	7.8	79	3420	168
$p_{\text{T,rel}}^{\text{miss,track}} > 40$ GeV	1.14 ± 0.04	960	842	43	292	193	73	38	0.2	49	194	2
$\Delta\phi_{\ell\ell} < 1.8$ rad	1.14 ± 0.04	889	783	38	265	179	68	30	0.2	44	194	2
$f_{\text{recoil}} < 0.1$	1.16 ± 0.05	467	404	24	188	98	44	17	0	29	26	1
m_{T}-window	1.11 ± 0.10	143	129	16	59	23	11	11	0	11	14	0

TABLE 4.8: Evolution of the observed and predicted yields throughout the events selection in the SF 0- and 1-jet channels. The uncertainties shown on the ratio comparing the observed and background expected number of events are statistical only. The yields quoted for the Higgs signal are for $m_H = 125$ GeV. The m_{T}-window is $\frac{3}{4}m_H < m_{\text{T}} < m_H$.

The cutflows in Tables 4.8 and 4.9 provide the ratio between the observed number of events in data and the predicted number of total background events. The uncertainties shown on these ratios are statistical only. For the SF 0-jet channel, the ratios are compatible with unity, suggesting no excess of events observed over the expected background prediction. The remaining analysis categories observe excesses above the background expectation.

$e\mu$	Obs./Bkg.	Obs.	Bkg.	H	WW	$t\bar{t}$	single top	W+ jets	multi jet	other VV	Z/γ^* $ee/\mu\mu$	Z/γ^* $\tau\tau$
0-jet	1.01 ± 0.01	16423	16330	302	7110	820	407	1330	237	739	115	5570
$\Delta\phi(\ell\ell, E_{\mathrm{T}}^{\mathrm{miss}}) > \pi/2$ rad	1.00 ± 0.01	16339	16270	302	7110	812	405	1330	230	736	114	5530
$p_{\mathrm{T}}^{\ell\ell} > 30$ GeV	1.00 ± 0.01	9339	9280	266	5690	730	363	1054	28	571	60	783
$m_{\ell\ell} > 55$ GeV	1.11 ± 0.02	3411	3060	230	1670	141	79	427	12	353	27	350
$\Delta\phi_{\ell\ell} < 1.8$ rad	1.12 ± 0.02	2642	2350	209	1500	132	75	278	9.2	324	19	12
m_{T}-window	1.20 ± 0.04	1129	940	133	660	40	21	133	0.8	78	4.3	2.3
1-jet	1.00 ± 0.01	20607	20700	163	2750	8410	2310	663	334	496	66	5660
zero b-jets	1.01 ± 0.01	10859	10790	140	2410	1610	554	535	268	423	56	4940
$m_{\mathrm{T}}^{W} > 50$ GeV	1.01 ± 0.01	7368	7280	126	2260	1540	530	477	62	366	43	1990
$m_{\tau\tau} < m_Z - 25$ GeV	1.02 ± 0.02	4574	4490	116	1670	1106	390	311	32	275	21	692
$m_{\ell\ell} > 55$ GeV	1.05 ± 0.02	1656	1570	99	486	297	111	129	19	139	6.4	383
$\Delta\phi_{\ell\ell} < 1.8$ rad	1.10 ± 0.03	1129	1030	87	418	269	102	88	6.1	119	5.0	22
m_{T}-window	1.21 ± 0.06	407	335	49	143	76	30	40	0.5	42	1.1	2

TABLE 4.9: Evolution of the observed and predicted yields throughout the events selection in the DF 0- and 1-jet channels. The uncertainties shown on the ratio comparing the observed and background expected number of events are statistical only. The yields quoted for the Higgs signal are for $m_H = 125$ GeV. The m_{T}-window is $\frac{3}{4}m_H < m_{\mathrm{T}} < m_H$.

Signal region (SR) is the term used to refer to the region of phase space that remains after all event selections are applied. The $m_{\ell\ell}$, $p_{\mathrm{T}}^{\mathrm{sub}}$ and m_{T} distributions of the events in the final SF and DF signal regions are shown in Figures 4.32 and 4.33, respectively. Overall the simulation appears to model these kinematic variables well.

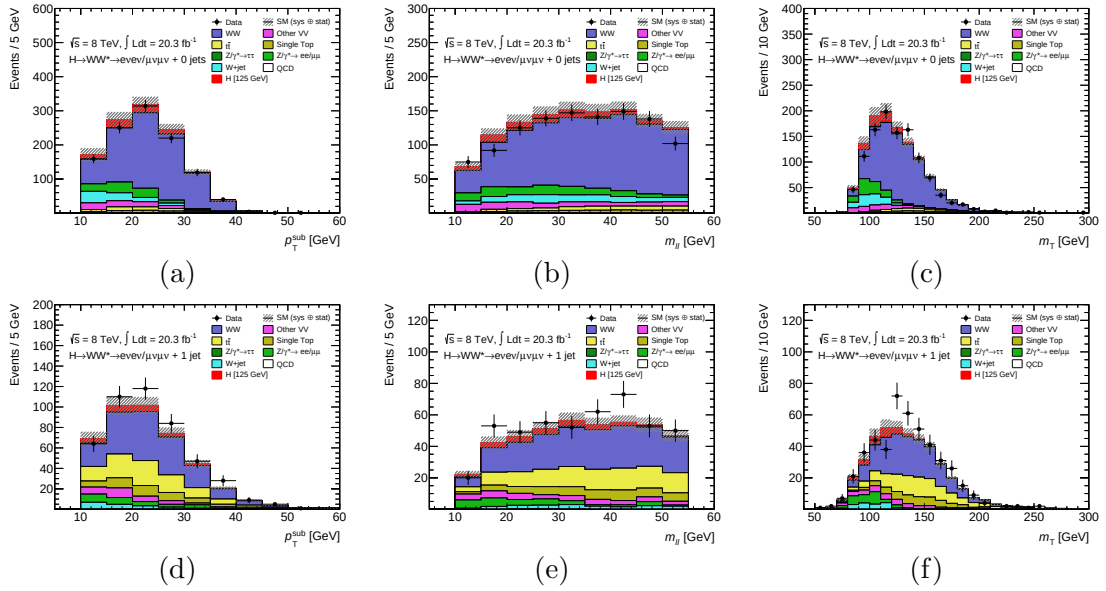

FIGURE 4.32: Distributions of (a) $p_{\mathrm{T}}^{\mathrm{sub}}$, (b) $m_{\ell\ell}$ and (c) m_{T} in the SF 0-jet signal region. (d)-(f) show the same kinematic variables in the SF 1-jet signal region.

4.5.1 Optimization of SF channels

As previously mentioned, the event selection chosen for the SF channels mostly mimics that of the DF channels, with added cuts to suppress DY, on $E_{\mathrm{T}}^{\mathrm{miss}}$ and f_{recoil} variables. The requirements applied to these variables, as well as the $E_{\mathrm{T}}^{\mathrm{miss}}$ flavors used, were

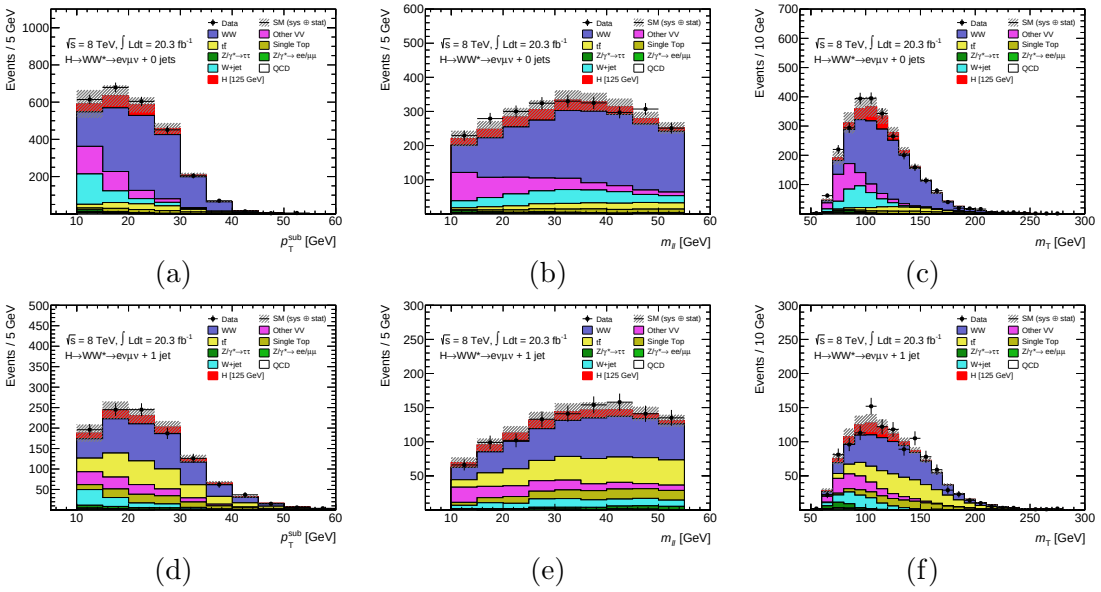

FIGURE 4.33: Distributions of (a) $p_{\mathrm{T}}^{\mathrm{sub}}$, (b) $m_{\ell\ell}$ and (c) m_{T} in the SF 0-jet signal region. (d)-(f) show the same kinematic variables in the DF 1-jet signal region.

optimized simultaneously. Selections on $p_{\mathrm{T}}^{\ell\ell}$ (for 0-jet) and $p_{\mathrm{T}}^{\ell\ell j}$ (for 1-jet) were also optimized at the same time, given their strong correlation to f_{recoil}: the soft hadronic recoil is observed for DY events with a high boost of the dilepton system; DY events with $p_{\mathrm{T}}^{\ell\ell} \approx 0$ have both leptons back-to-back and are balanced.

4.5.1.1 Choice of $E_{\mathrm{T}}^{\mathrm{miss}}$ flavors

All four $E_{\mathrm{T}}^{\mathrm{miss}}$ flavors discussed in Section 2.6.6, as well as their relative versions presented in Section 4.4.2, were considered for the SF channels. It was found that, regardless of the flavor, the relative quantities generally provided better rejection of DY events, since one is mostly dealing with fake $E_{\mathrm{T}}^{\mathrm{miss}}$ originating from mismeasured objects.

The track-based computations of $E_{\mathrm{T}}^{\mathrm{miss}}$ were considered first, since they showed better resolution and stability with pile-up (see Section 2.6.6). For the SF 1-jet category, that meant two flavors were available: $p_{\mathrm{T}}^{\mathrm{miss,jetCorr}}$ and $p_{\mathrm{T}}^{\mathrm{miss,track}}$ (these flavors are the same for events with no jets). Figure 4.34a shows in black circles the $p_{\mathrm{T}}^{\mathrm{miss,track}}$ and in red squares the $p_{\mathrm{T}}^{\mathrm{miss,jetCorr}}$ distributions of data events with 2 same flavor leptons and 1 jet. The invariant mass of the dilepton is required to be in the Z-peak, so that the events are dominated by DY. As expected, the distribution of $p_{\mathrm{T}}^{\mathrm{miss,jetCorr}}$ shows a smaller mean and RMS, indicating that, for the same cut, $p_{\mathrm{T}}^{\mathrm{miss,jetCorr}}$ rejects more DY than $p_{\mathrm{T}}^{\mathrm{miss,track}}$. Figure 4.34b shows the relative computations of the same quantities, i.e. $p_{\mathrm{T,rel}}^{\mathrm{miss,track}}$ and $p_{\mathrm{T,rel}}^{\mathrm{miss,jetCorr}}$. For the relative quantities, the situation is reversed, and the distribution of $p_{\mathrm{T,rel}}^{\mathrm{miss,track}}$ shows the lowest mean and RMS. So even though $p_{\mathrm{T}}^{\mathrm{miss,jetCorr}}$ shows better resolution than $p_{\mathrm{T}}^{\mathrm{miss,track}}$, $p_{\mathrm{T,rel}}^{\mathrm{miss,track}}$ provides better DY rejection than $p_{\mathrm{T,rel}}^{\mathrm{miss,jetCorr}}$. Thus, $p_{\mathrm{T,rel}}^{\mathrm{miss,track}}$ was chosen as one of the flavors.

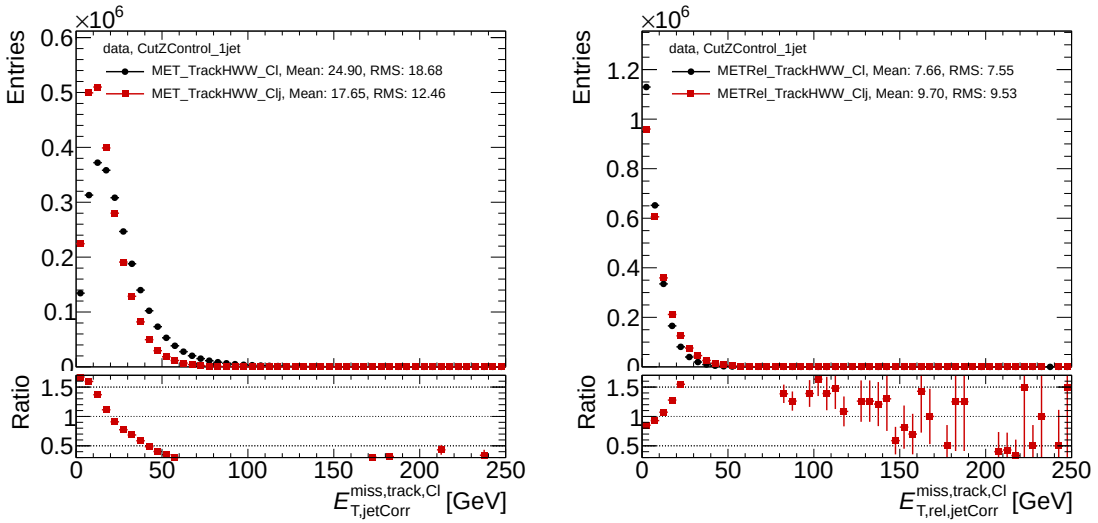

FIGURE 4.34: Comparison of shapes in the SF 1-jet Z-peak: (a) $p_{\mathrm{T}}^{\mathrm{miss,track}}$ (black circles) and $p_{\mathrm{T}}^{\mathrm{miss,jetCorr}}$ (red circles); and (b) $p_{\mathrm{T,rel}}^{\mathrm{miss,track}}$ (black circles) and $p_{\mathrm{T,rel}}^{\mathrm{miss,jetCorr}}$ (red circles).

DY events that contaminate the SF 1-jet category acquire significant $E_{\mathrm{T}}^{\mathrm{miss}}$ mostly through mismeasurements of the jet. Therefore, in these events, $p_{\mathrm{T}}^{\mathrm{miss,track}}$ tends to point in the same direction of the jet. This is illustrated in Figure 4.35a, where the azimuthal separation between $p_{\mathrm{T}}^{\mathrm{miss,track}}$ and the jet is shown, for SF 1-jet events in the Z-peak, displaying a peak around zero. The $p_{\mathrm{T}}^{\mathrm{miss,jetCorr}}$ flavor, on the other hand, tends to point away from the jet, as shown in Figure 4.35b, since the jet has been included in its computation. The azimuthal separations shown in Figure 4.35 correspond to the $\Delta\phi_{\mathrm{near}}$ used in the computation of $E_{\mathrm{T,rel}}^{\mathrm{miss}}$ in Equation 4.1, for events when the jet is the nearest object. Thus, it is clear that when computing the relative quantities $p_{\mathrm{T}}^{\mathrm{miss,track}}$ is more often corrected by $\sin\Delta\phi_{\mathrm{near}}$, than $p_{\mathrm{T}}^{\mathrm{miss,jetCorr}}$. As a result, the distribution of $p_{\mathrm{T,rel}}^{\mathrm{miss,track}}$ is narrower, allowing for more DY suppression.

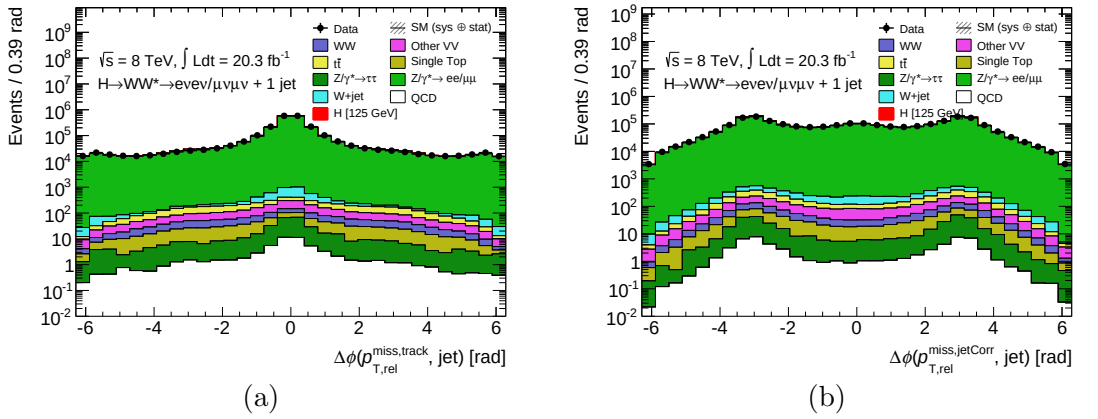

FIGURE 4.35: Azimuthal separation between the jet and (a) $p_{\mathrm{T}}^{\mathrm{miss,track}}$ or (b) $p_{\mathrm{T}}^{\mathrm{miss,jetCorr}}$, for SF 1-jet events in the Z-peak.

A single cut on $p_{\mathrm{T,rel}}^{\mathrm{miss,track}}$, together with f_{recoil}, does not provide sufficient rejection of DY. Thus, a second $E_{\mathrm{T}}^{\mathrm{miss}}$ flavor was chosen for the SF channels. The best result was achieved with the flavor that was less correlated with $p_{\mathrm{T}}^{\mathrm{miss,track}}$. The tails of $p_{\mathrm{T,rel}}^{\mathrm{miss,jetCorr}}$ were shown to be very correlated with the tails of $p_{\mathrm{T,rel}}^{\mathrm{miss,track}}$, dominated by mismeasured tracks. Between $E_{\mathrm{T,rel}}^{\mathrm{miss,calo}}$ and $E_{\mathrm{T,rel}}^{\mathrm{miss,STVF}}$, the former showed to have the least correlated tails, and was chosen for the SF channels.

4.5.1.2 Optimization of selection cuts

The optimization of selection cuts used the signal significance as a figure of merit, defined as:

$$\frac{S}{\sqrt{\sum_i B_i + \delta B_i{}^2}}. \tag{4.3}$$

S is the signal yield, B_i is the yield of background i, and δB_i is the estimated uncertainty on background i, with the sum running over all background processes. The estimates of the different background processes were obtained as explained in Sections 4.6 and 4.7 ahead. For the purpose of the optimization, the uncertainties on each background were taken from the previous iteration of the $H \to WW^* \to \ell\nu\ell\nu$ analysis [155, 170]. They are summarized in Table 4.10. This approach is conservative, as these uncertainties have now been reduced.

Background	**Uncertainty [%]**	
	0-jet	**1-jet**
W + jets	30	30
WW	7.4	37
top	13	30
$Z/\gamma^* \to \tau\tau$	14	40
other VV	16	22
$Z/\gamma^* \to ee/\mu\mu$	60	80

TABLE 4.10: Relative uncertainties on the yields of the different backgrounds considered for the optimization of the SF selections.

The optimal f_{recoil} and $p_{\mathrm{T}}^{\ell\ell(j)}$ cuts were determined by producing 2D significance grids of upper bound on f_{recoil} versus lower bound on $p_{\mathrm{T}}^{\ell\ell(j)}$, such as the ones in Figure 4.36. Events in these distributions were required to pass all selections in Table 4.6, apart from the cuts on f_{recoil} and $p_{\mathrm{T}}^{\ell\ell(j)}$. The grids were produced with different requirements on $p_{\mathrm{T,rel}}^{\mathrm{miss,track}}$ and $E_{\mathrm{T,rel}}^{\mathrm{miss,calo}}$, so that the selections on these variables were also optimized. The scans in Figure 4.36 require $p_{\mathrm{T,rel}}^{\mathrm{miss,track}} > 40$ (35) GeV and $E_{\mathrm{T,rel}}^{\mathrm{miss,calo}} > 40$ (40) GeV, for the 0-jet (1-jet) channel, which were the selections leading to the highest significance at the optimal point (signaled in the scans). ee and $\mu\mu$ final states were evaluated together.

The scan for SF 0-jet events in Figure 4.36a shows an optimal point for $p_{\mathrm{T}}^{\ell\ell} > 40$ GeV and $f_{\mathrm{recoil}} < 0.09$ requirements. The significance does not vary significantly in the horizontal direction of the scan, i.e. for different f_{recoil} thresholds around 0.1. For simplicity,

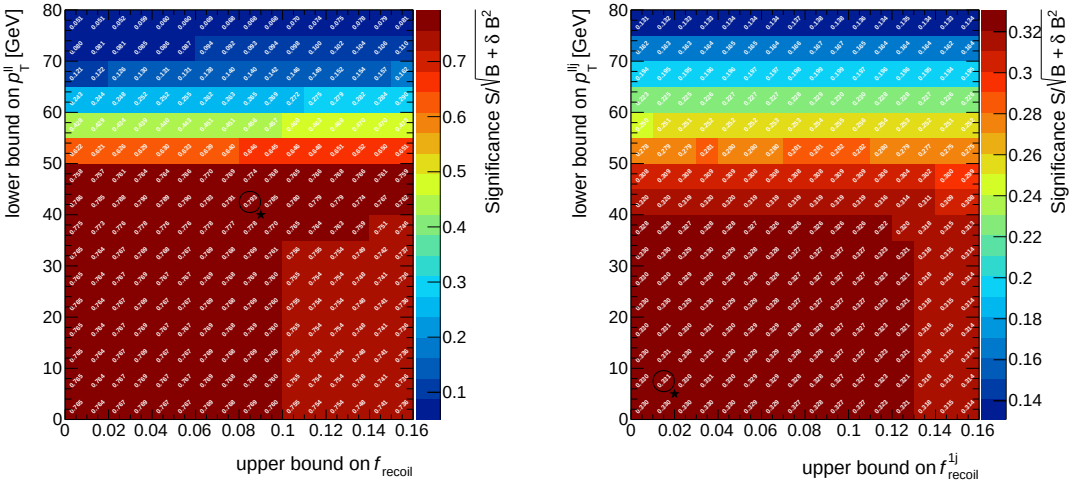

(a) (b)

FIGURE 4.36: 2D significance scans for the optimization of upper bounds on f_{recoil} and lower bounds on $p_{\text{T}}^{\ell\ell(j)}$. Events in the distribution pass the selections described in the text. Scan at the top are for the 0-jet channel and scans at the bottom are for the 1-jet channel. On the left the subleading lepton p_{T} threshold is 15 GeV, whereas on the right it is 10 GeV (i.e. the low-p_{T} events are included). The star indicates the optimal point in the grid and the circle highlights the significance for that optimal point.

$f_{\text{recoil}} < 0.1$ was chosen for the SF 0-jet channel, with only $\sim 1\%$ loss in significance with respect to the the optimal point.

For 1-jet events, shown in Figure 4.36b, a very loose cut on $p_{\text{T}}^{\ell\ell j} > 5$ GeV is preferred. However, the degradation in performance compared to not applying a $p_{\text{T}}^{\ell\ell j}$ selection is negligible. Therefore, no cut is applied in this variable. The reason for this is the strong correlation between $p_{\text{T}}^{\ell\ell j}$ and $p_{\text{T,rel}}^{\text{miss,track}}$. The optimal f_{recoil} threshold for 1-jet is 0.02. But similar to what was shown for the 0-jet bin, applying a $f_{\text{recoil}} < 0.1$ cut only impacts the significance marginally, by $\sim 1\%$. For harmonization reasons, the cut $f_{\text{recoil}} < 0.1$ was, thus, chosen for both the 0-jet and 1-jet channels.

The $p_{\text{T}}^{\ell\ell} > 40$ GeV selection, which was shown to be optimal for the 0-jet channel in Figure 4.36a, was revisited by computing the expected p_0-value (or equivalently the significance Z_0, as explained in Section 1.2.3.4), using the full statistical framework (see Section 4.10 ahead). The reason was that the significance dependence with $p_{\text{T}}^{\ell\ell}$ is, in fact, quite flat, and only $\sim 3\%$ degradation is seen between applying the 40 GeV cut or not applying a cut at all. For this test all selections were applied, including the $f_{\text{recoil}} < 0.1$ cut, and the expected Z_0 was computed for different $p_{\text{T}}^{\ell\ell}$ thresholds. The results are shown in Table 4.11, in terms of relative variations in Z_0 with respect to the $p_{\text{T}}^{\ell\ell} > 40$ GeV selection. Results show that a $p_{\text{T}}^{\ell\ell} > 30$ GeV is optimal for the SF 0-jet channel. Conveniently, this is the selection used for the different flavour channels as well.

Cut	ΔZ_0^{exp} [%]
no $p_{\text{T}}^{\ell\ell}$ cut	+3.5
$p_{\text{T}}^{\ell\ell} > 25$ GeV	+4.1
$p_{\text{T}}^{\ell\ell} > 30$ GeV	+4.1
$p_{\text{T}}^{\ell\ell} > 35$ GeV	+2.6
$p_{\text{T}}^{\ell\ell} > 40$ GeV	(ref.)
$p_{\text{T}}^{\ell\ell} > 45$ GeV	−6.2
$p_{\text{T}}^{\ell\ell} > 50$ GeV	−25

TABLE 4.11: Relative difference in expected Z_0, for $m_H = 125$ GeV, for the SF 0-jet category with different selections on $p_{\text{T}}^{\ell\ell}$. $p_{\text{T}}^{\ell\ell} > 40$ GeV is taken as the reference. A positive sign denotes an improvement and a negative sign denotes a degradation in the expected Z_0.

4.6 Non-DY backgrounds

Here we describe the strategies used to estimate the different non-DY backgrounds in the 0- and 1-jet SF channels. We use the term "non-DY" to refer to backgrounds with one or more neutrinos in the final state, that produce true missing transverse energy in the detector.

4.6.1 Fully data-driven

The W + jets contamination in the final SF signal regions amounts to $\sim 7\%$ in the 0-jet bin, and $\sim 4\%$ in the 1-jet bin, with respect to the total background. Both the normalization and shapes of this background are determined entirely from data, using the so-called "Fake Factor Method", which is briefly described in what follows. The same strategy is used to estimate the multijet QCD background (which is why it is adddressed here, even though it does not generate true missing transverse energy in the detector), although no contamination is predicted in the SF signal regions.

4.6.1.1 W + jets

A W + jets control sample of data events with two leptons is selected, where one of the leptons satisfies the criteria detailed in Table 4.4, and the other lepton satisfies a looser set of criteria, namely in what concerns identification, impact parameter cuts and isolation. These are referred to as the id and anti-id leptons, respectively, and are selected exclusively, i.e the anti-id lepton is required to fail the id selection. The anti-id selection enhances the probability of the lepton being a fake. Therefore, this id + anti-id control sample is primarily composed of W + jets events ($85 - 90\%$), in which a jet is identified as a lepton. Some contamination from QCD multijet and EW processes, such as Z/γ^* and other VV, exists in the W + jets control sample. Events in the W + jets control sample are otherwise required to pass nominal event selections.

The W + jets background prediction in the id + id sample that is the signal region - $N_{\text{id + id}}^{W+\text{jets}}$ - is obtained by scaling the W + jets control sample - $N_{\text{id + anti-id}}^{W+\text{jets}}$ - by an

extrapolation factor, referred to as the fake factor - f_{fake}. In other words:

$$N^{W+\text{jets}}_{\text{id + id}} = f_{\text{fake}} \times (N_{\text{id + anti-id}} - N^{\text{multijet}}_{\text{id + anti-id}} - N^{\text{EW bkg.}}_{\text{id + anti-id}}). \tag{4.4}$$

Contamination from QCD multijet background in the W + jets control sample is subtracted using data, as explained in Section 4.6.1.2 ahead. Other EW background processes are subtracted using MC simulation (see Table 4.1).

The fake factor is also measured in data, using a control sample of jets, produced in association with a Z boson. The Z bosons are identified by their $Z \to ee/\mu\mu$ decays, and the resulting sample is referred to as the Z + jets control sample. The fake factor is defined as the ratio between the number of jets passing the id selection and the number of jets passing the anti-id selection, in the Z + jets control sample:

$$f_{\text{fake}}(\eta, p_{\text{T}}) = \frac{N_{\text{id}}(\eta, p_{\text{T}})}{N_{\text{anti-id}}(\eta, p_{\text{T}})}. \tag{4.5}$$

The fake factor is computed separately for electrons and muons, and in bins of anti-id lepton p_{T} and η. It is important to note that the fake factor is not a fake rate, but rather a ratio of fake rates, and should not, therefore, be interpreted as a probability (N_{id} is not a subset of $N_{\text{anti-id}}$).

The jet compositions of the Z + jets and W + jets control samples can be different, namely in what concerns the fractions of jets originating from light quarks and gluons, and those originating from heavy quarks. Such differences can bias the fake factor measurement. To account for this effect, different fake factors were computed using several Z + jets and W + jets MC samples. The ratios between the W + jets and Z + jets MC fake factors were used to compute corrections, to be applied to the fake factors extracted from the Z + jets data control sample. The corrections are close to unity.

The systematic uncertainty on the estimated W + jets background in the signal region arises mainly from the uncertainties on the fake factor. These vary between $29 - 61\%$ for fake electrons, and $25 - 46\%$ for fake muons, depending on the anti-id lepton p_{T}. The sources of uncertainty on the fake factor are of theoretical and experimental nature. On the theoretical side there is the uncertainty on the MC-based corrections of the fake factors, which is assessed by comparing the corrections obtained from different MC samples. The experimental uncertainties originate from: the statistics of the id objects in the Z + jets control sample; and the subtraction of backgrounds contaminating the Z + jets control sample (namely WZ and ZZ), which is done using simulation.

4.6.1.2 Multijet

QCD multijet production in the signal region is also estimated using the fake factor method. For this background, a control sample is defined by selecting two anti-id leptons in data, and then applying all signal region requirements. This control sample is scaled by a fake factor twice (since there are two fake leptons) to obtain the prediction in the signal region. The fake factor is computed from data as in Equation 4.5, this time

using a sample of jets, identified at low missing transverse energy. This is referred to as the multijet sample. The multijet sample and the control sample of anti-id leptons are expected to have similar compositions. However, the composition of the multijet sample changes with the requirement of an id or anti-id lepton, biasing the fake factor. Corrections are applied to account for this bias.

4.6.2 Control regions

In the $H \to WW^* \to \ell\nu\ell\nu$ analysis, several control regions (CRs) are defined to normalize the different background sources in the signal regions. A CR for a given background process is built by inverting, or changing, one or more event selection requirements (see Table 4.7). The goal is to obtain an event sample that is kinematically similar to the signal region, but enriched in that particular background process.

The CR is then used to extract a so-called normalization factor (NF) for the relevant background process (generically labeled "bkg"). The NF is computed from the ratio between the observed data yield - $N^{\mathrm{CR}}_{\mathrm{data}}$ - and the MC predicted yield - $N^{\mathrm{CR}}_{\mathrm{bkg,MC}}$ - in the CR. Background processes other than the one in question - $N^{\mathrm{CR}}_{\mathrm{other}}$ - are subtracted for the NF computation. In summary:

$$\mathrm{NF}_{\mathrm{bkg}} = \frac{N^{\mathrm{CR}}_{\mathrm{data}} - N^{\mathrm{CR}}_{\mathrm{other}}}{N^{\mathrm{CR}}_{\mathrm{bkg,MC}}}. \tag{4.6}$$

Once the normalization factor is calculated, the estimated yield of the relevant background process in the signal region - $N^{\mathrm{bkg,est}}_{\mathrm{SR}}$, is obtained by multiplying the MC prediction of that process in the SR by the NF:

$$N^{\mathrm{SR}}_{\mathrm{bkg,est}} = \mathrm{NF}_{\mathrm{bkg}} \times N^{\mathrm{SR}}_{\mathrm{bkg,MC}}. \tag{4.7}$$

It is important to note that with this method, and unlike the backgrounds described in the Section 4.6.1, the shapes of the distributions are still the ones predicted by the simulated samples (see Table 4.1).

Systematic uncertainties on the normalization factors arise from: statistical uncertainties on the observed data and MC statistics in the CR; theoretical and experimental uncertainties on the absolute predicted event yields in the CR; and theoretical, experimental and statistical uncertainties related to the subtraction of other backgrounds in the CR. However, these are not the systematic uncertainties that impact the estimated background yields in the SR, as will be clarified in what follows.

Replacing Equation 4.6 in Equation 4.7, one obtains:

$$N^{\mathrm{SR}}_{\mathrm{bkg,est}} = \frac{N^{\mathrm{CR}}_{\mathrm{data}} - N^{\mathrm{CR}}_{\mathrm{other}}}{N^{\mathrm{CR}}_{\mathrm{bkg,MC}}} \times N^{\mathrm{SR}}_{\mathrm{bkg,MC}} = (N^{\mathrm{CR}}_{\mathrm{data}} - N^{\mathrm{CR}}_{\mathrm{other}}) \times \alpha^{\mathrm{bkg}}_{\mathrm{SR}}. \tag{4.8}$$

$\alpha^{\mathrm{bkg}}_{\mathrm{SR}} = N^{\mathrm{SR}}_{\mathrm{bkg,MC}}/N^{\mathrm{CR}}_{\mathrm{bkg,MC}}$ is the so-called CR-to-SR extrapolation factor, which relates the background estimate in the SR to the data in the CR. Because the extrapolation

factor α is a ratio between predicted MC yields in the SR and in the CR, the systematic uncertainties impacting the two yields largely cancel out. This verifies especially if the CR and SR are kinematically similar. Thus, the systematic uncertainties on α are generally small. Some theoretical uncertainties remain, and these are evaluated in detail, as will be clarified ahead. As a result of this procedure, the systematic uncertainties on the estimated background yields in the SR are greatly reduced, compared to the absolute MC predictions. This is one of the great advantages of using control regions.

The $H \to WW^* \to \ell\nu\ell\nu$ analysis uses control regions built from $e\mu$ final states only. In general, different flavour CRs have higher statistics and significantly higher purity than the corresponding $ee + \mu\mu$ samples, which suffer from DY contamination. These are, on the other hand, used as validation regions (VRs), i.e. additional regions of phase-space used to verify the MC modeling of the data. To summarize, DF CRs are used to normalize the backgrounds in the DF and SF signal regions. Different extrapolation uncertainties are computed for each case.

4.6.2.1 *WW*

Continuum WW production is the main source of background in the $H \to WW^* \to \ell\nu\ell\nu$ analysis. Two WW control regions are used, one for the 0-jet category and another for the 1-jet category, both using $e\mu$ events only. The extracted NF_{WW}^{0j} and NF_{WW}^{1j} normalization factors are used to normalize the this background (both the dominant $q\bar{q} \to WW$ contribution and $gg \to WW$) in the 0- and 1-jet signal regions respectively, for the SF and DF channels. As discussed in Section 4.1.1, the spin-0 SM Higgs boson, together with the V-A structure of the weak decays, cause the two charged leptons in the final state to emerge with a small opening angle and small invariant mass. These are also the main features that allow the separation between the $H \to WW^*$ signal and the irreducible non-resonant WW background. Thus, the WW control regions are defined by changing the $m_{\ell\ell}$ selection compared to the signal region.

Events in the WW control regions are selected by applying all the requirements presented in Table 4.7 for the $e\mu$ channels, up until the $p_{\mathrm{T}}^{\ell\ell} > 30$ GeV (0-jet) and $m_{\mathrm{T}}^{W} > 50$ GeV (1-jet) selections. These are included to provide suppression of Z/γ^* and multijet backgrounds, ensuring the purity of the control regions in WW. An additional requirement on $p_{\mathrm{T}}^{\mathrm{sub}} > 15$ GeV is applied for both 0- and 1-jet events, to reject $W+\mathrm{jets}$ background. $Z/\gamma^* \to \tau\tau$ contamination is reduced by requiring $\Delta\phi_{\ell\ell} < 2.6$ for 0-jet, and $|m_{\tau\tau} - m_Z| > 25$ GeV for 1-jet. Finally, the invariant mass ranges of $55 < m_{\ell\ell} < 110$ GeV and $m_{\ell\ell} > 80$ GeV, are chosen for the 0- and 1-jet CRs, respectively. The range chosen for the 0-jet CR maximizes the precision and accuracy of the background estimate in the SR, by balancing the effects of the statistical precision of the CR, and the systematic uncertainties on the extrapolation factor.

Figure 4.37 shows the m_{T} distribution of events in the WW control regions, and Table 4.12 provides the composition of each CR. As indicated, the 0-jet WW CR is $\sim 70\%$ pure in WW background, while the 1-jet CR has only a $\sim 45\%$ purity, suffering from a large contribution of top background. The simulation models the shape of the

data well. The computed WW normalization factors, together with their statistic and systematic uncertainties, are:

- $\mathrm{NF}_{WW}^{0j} = 1.22 \pm 0.03$ (stat.) ;
- $\mathrm{NF}_{WW}^{1j} = 1.05 \pm 0.05$ (stat.) .

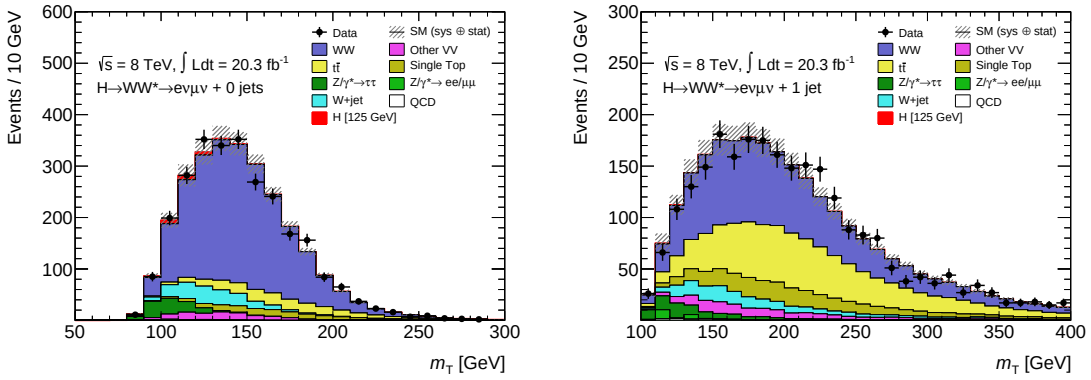

(a) (b)

FIGURE 4.37: m_{T} distribution in the WW (a) 0-jet and (b) 1-jet control regions.

***WW* CR**	**Obs.**	**Bkg.**	***H***	***WW***	**top**	**fakes**	**other *VV***	***Z*/γ* *ee*/*μμ***	***Z*/γ* *ττ***	**Purity [%]**
0-jet	2713	2680	28	1959	335	184	97	8.7	106	73
1-jet	2647	2640	4.3	1148	1114	165	127	17	81	43

TABLE 4.12: Composition of the WW 0- and 1-jet control regions.

For completeness, the m_{T} distributions in the SF WW validation regions are shown in Figure 4.38. These are built starting from the $ee + \mu\mu$ event selection in Table 4.6. Requirements up to f_{recoil} are applied and the $m_{\ell\ell} < 55$ GeV cut is replaced by $55 < m_{\ell\ell} < 110$ GeV in the 0-jet category, and $m_{\ell\ell} > 80$ GeV in the 1-jet category (we note that events in the Z-window are vetoed). In the 0-jet channel, the $\Delta\phi_{\ell\ell}$ selection in Table 4.6 is replaced by a $\Delta\phi_{\ell\ell} < 2.6$ rad. Finally $p_{\mathrm{T}}^{\mathrm{sub}}$ is raised to $p_{\mathrm{T}}^{\mathrm{sub}} > 15$ GeV. In general, good modeling is observed.

Theoretical uncertainties on the $\alpha_{WW}^{\mathrm{SR}}$ extrapolation factors arise from different sources. The effect of PDF modeling is assessed by comparing different PDFs, following the procedure detailed in Ref. [80]. The impact of missing higher orders in the perturbative calculation is determined by varying the factorization and renormalization scales (see Section 1.2.3.1). An uncertainty due to missing higher order EW corrections is included. Matching of the ME generator to the PS model is investigated by comparing α predicted by POWHEG + HERWIG and aMC@NLO + HERWIG models. Finally, the effect of the PS and UE modeling is studied by comparing α predicted by POWHEG + PYTHIA8, POWHEG + PYTHIA6 and POWHEG + HERWIG. The resulting uncertainties on the extrapolation factors to the SF 0- and 1-jet signal regions are

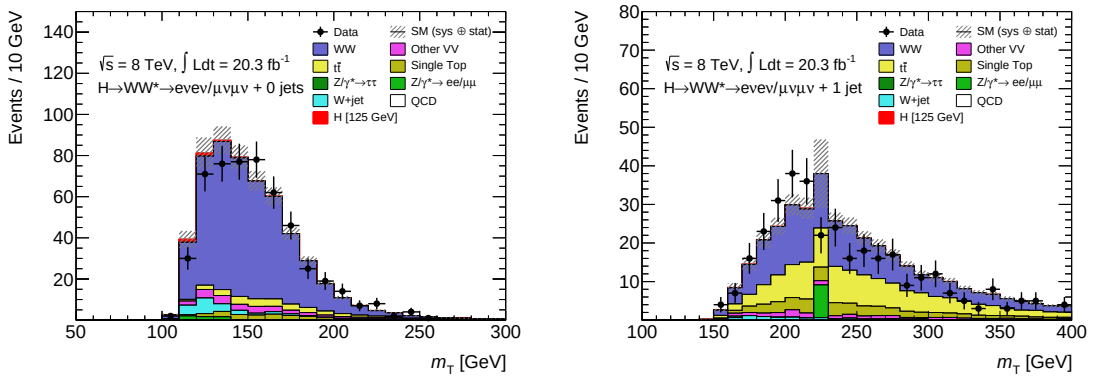

(a) (b)

FIGURE 4.38: m_{T} distribution in the WW (a) 0-jet and (b) 1-jet same flavor validation regions.

summarized in Table 4.13. For the DF signal regions, the uncertainties range between $2.0 - 4.8\%$ for 0-jet, and $3.9 - 7.1\%$ for 1-jet.

	PDF	**Scales**	**EW**	**Match.**	**UE/PS**	**Total**
0-jet	1.1	0.8	0.1	2.4	-1.2	2.9
1-jet	0.9	0.8	-2.1	3.8	-2.3	5.1

TABLE 4.13: Theoretical uncertainties on the α extrapolation factors from the WW control regions to the same flavor signal regions. Numbers are shown in [%] for the 0- and 1-jet categories. The negative sign indicates an anti-correlation with respect to the unsigned uncertainties.

As already discussed, the transverse mass m_{T} provides the final discrimination between signal and background. Since WW is the dominant background, an additional theoretical uncertainty is evaluated on the shape of the m_{T} distribution for this process. Three sources of uncertainty are considered, and evaluated similarly to the uncertainties on the extrapolations factors: higer-order QCD corrections, PS and UE modeling, and ME-PS matching. The measured variations in the WW m_{T} shape are minimal at $m_{\mathrm{T}} \sim 100 - 120$ GeV, and maximal in the tails, where they reach 5-10%.

4.6.2.2 $Z/\gamma^* \to \tau\tau$

The $Z/\gamma^* \to \tau\tau$ background prediction in the SF and DF signal regions is normalized using a $e\mu$ control regions, in a procedure identical to the WW background. Although the contamination $Z/\gamma^* \to \tau\tau$ in the SF signal regions is negligible, this background contributes significantly to the DF signal regions, as well as to the WW CRs.

The event selection used to build the $Z/\gamma^* \to \tau\tau$ CRs, starts from the requirements presented in Table 4.7 for the $e\mu$ channels, up until the jet veto (0-jet) and $m_{\mathrm{T}}^{W} > 50$ GeV (1-jet) selections. The 0-jet CR is then defined by requiring $\Delta\phi_{\ell\ell} > 2.8$ rad and $m_{\ell\ell} < 80$ GeV. For the 1-jet CR, events with $m_{\ell\ell} < 80$ GeV and $m_{\tau\tau} > m_Z - 25$ GeV

are selected. The resulting CRs have a purity of 90% and 75%, for the 0- and 1-jet categories respectively. The corresponding normalization factors are:

- $\mathrm{NF}^{0j}_{Z/\gamma^*\to\tau\tau} = 1.00 \pm 0.02$ (stat.) ;
- $\mathrm{NF}^{1j}_{Z/\gamma^*\to\tau\tau} = 1.05 \pm 0.04$ (stat.) .

Three sources of uncertainty are considered for the extrapolation of the $Z/\gamma^* \to \tau\tau$ background: QCD scale variations, PDFs and MC modeling. They are computed for both the CR-to-SR extrapolation (only DF signal regions are considered), as well as for the CR-to-CR extrapolation, given that this background contaminates the WW CR. The MC modeling uncertainties contain those related to the p_{T}^{Z} reweighting procedure, and a residual modeling uncertainty. The former are evaluated by comparing the α extrapolation factors predicted with the nominal and alternative sets of p_{T}^{Z} weights (see Figure 4.16b). The residual modeling uncertainties are obtained through the comparison of the Alpgen + Herwig and Alpgen + Pythia generators. The uncertainties are of the order of $\sim 20\%$ for 0-jet and $\sim 7\%$ for 1-jet.

4.6.2.3 Top in the 0-jet category

The estimation of top-backgrounds in the 0-jet channel is done by assessing the jet veto survival probability (JVSP) [195] for top events. A control region is defined using $e\mu$ events after the DF pre-selection requirement (see Table 4.7). $Z/\gamma^* \to \tau\tau$ contamination is suppressed by requiring $\Delta\phi_{\ell\ell} < 2.8$ rad. The resulting sample is 74% pure in top-quark processes. No jet selection is applied and the CR is inclusive in jet multiplicity. Thus, the CR is a superset of the 0-jet signal region.

The estimated number of top background events in the $e\mu + 0$-jet sample, at the jet veto cut level (see Table 4.7), can be written as:

$$N^{0j}_{\mathrm{top,est}} = (N^{\mathrm{CR}}_{\mathrm{data}} - N^{\mathrm{CR}}_{\mathrm{other}}) \times f^{0j}_{\mathrm{est}}, \tag{4.9}$$

where f^{0j}_{est} is a data-driven estimate of the JVSP, i.e. the fraction of top events passing the jet veto selection. This probability can be written as the same probability measured in MC, corrected by a factor using data:

$$f^{0j}_{\mathrm{est}} = f^{0j}_{\mathrm{MC}} \times \left(\frac{p^{b\text{-tag}}_{\mathrm{data}}}{p^{b\text{-tag}}_{\mathrm{MC}}} \right)^2 . \tag{4.10}$$

The terms $p^{b\text{-tag}}$ are computed for both data and MC, in a control sample defined as the CR above, but with at least one b-tagged jet. This selection ensures the control sample has a high purity in top background events. $p^{b\text{-tag}}$ is simply defined as the fraction of events in the b-tagged sample that have no jets, in addition to the one that is tagged.

The ratio between the estimated and predicted top yields in the $e\mu + 0$-jet SR results in a normalization factor that normalizes the predicted top yield in both SF and DF 0-jet events:

- $\mathrm{NF}_{\mathrm{top}}^{0j} = 1.08 \pm 0.02\ (\mathrm{stat.})$.

Systematic uncertainties on the predicted yield are assessed similar to the uncertainties on the α CR-to-SR extrapolation parameters described in Section 4.6.2. An uncertainty of 6.8% enters through the stability of the ratio $f_{\mathrm{MC}}^{0j}/p_{\mathrm{MC}}^{b\text{-tag}^2}$ with experimental and theoretical variations. An additional uncertainty of 4.5% arises from the extrapolation of the estimate from the jet veto cut level to the final signal region. The jet energy scale and resolution are the dominant sources of experimental uncertainty. The theoretical uncertainties include the usual PDF, QCD scale and MC modelling. The final systematic uncertainty on the predicted top yield in the 0-jet channel is $\sim 8\%$.

4.6.2.4 Top in 1-jet category

Top-quark processes are a significant source of background in the 1-jet category, both in the signal regions and in the WW control region, as discussed in Section 4.6.2.1. They are suppressed by applying a b-jet veto. A top control region for the 1-jet channel is built by inverting this selection in $e\mu$ events, and requiring at least one b-tagged jet in the sample. The requirement on m_{T}^{W} is also applied (see Table 4.7), to suppress the contamination of other backgrounds. The resulting CR has a purity of over 90%. The m_{T} distribution in this CR is shown in Figure 4.39a. For completeness, the m_{T} distribution in the equivalent same flavor validation region is shown in Figure 4.39b. This VR is obtained by applying all SF requirements in Table 4.6, except for $m_{\ell\ell}$ and $\Delta\phi_{\ell\ell}$, and requiring that the jet in the sample is identified as a b-jet.

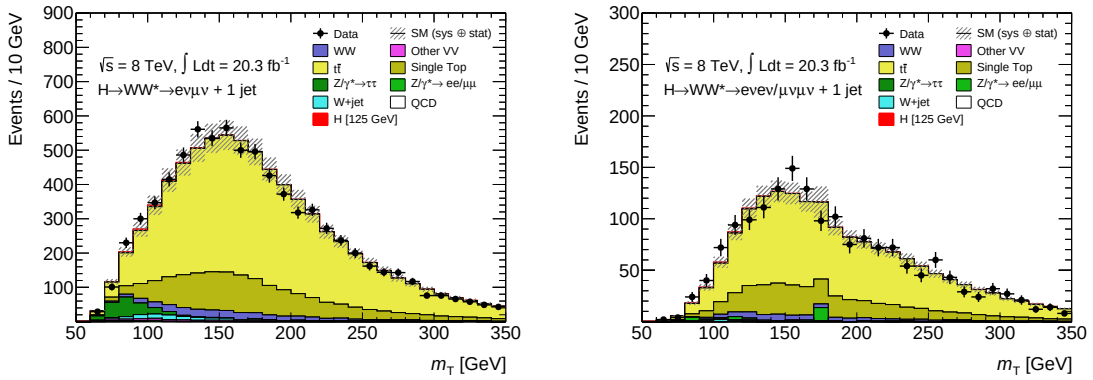

FIGURE 4.39: m_{T} distribution in top 1-jet (a) control region and (b) same flavor validation region.

The estimated number of top events in the 1-jet channel, at the m_{T}^{W} cut level (see Table 4.7), can be computed by normalizing the MC prediction by a factor extracted from the top CR (see Equations 4.6 and 4.7):

$$N_{\mathrm{top,est}}^{1j,\mathrm{SR}} = N_{\mathrm{top,MC}}^{1j,\mathrm{SR}} \times \frac{N_{\mathrm{data}}^{1j,\mathrm{CR}} - N_{\mathrm{other}}^{1j,\mathrm{CR}}}{N_{\mathrm{top,MC}}^{1j,\mathrm{CR}}}. \tag{4.11}$$

Considering that the signal region selection includes a b-veto, and that the CR includes a b-tag, Equation 4.11 can be written as:

$$N_{\text{top,est}}^{1j,\text{SR}} = \left(N_{\text{data}}^{1j,\text{CR}} - N_{\text{other}}^{1j,\text{CR}}\right) \times \frac{\left(1 - \varepsilon_{\text{MC}}^{1j,\text{CR}}\right)}{\varepsilon_{\text{MC}}^{1j,\text{CR}}}. \tag{4.12}$$

where $\varepsilon_{\text{MC}}^{1j,\text{CR}}$ is the MC probability for a jet to be b-tagged. It is important to note that this is not a b-tagging efficiency discussed in Section 2.6.5, which refers to the probability of a b-jet to be b-tagged.

The term $\left(1 - \varepsilon_{\text{MC}}^{1j,\text{CR}}\right)/\varepsilon_{\text{MC}}^{1j,\text{CR}}$ in Equation 4.12 is also the CR-to-SR extrapolation parameter α, which, as discussed earlier, represents the main source of uncertainty on the predicted background yield in the SR. From simple uncertainty propagation on this term, it is clear that the experimental uncertainties on the b-tagging efficiency have a large impact on the uncertainties on α. For example, an uncertainty of 5% on b-tagging induces a $\sim$ 20% uncertainty on the estimated top background yield in the SR. This effect is reduced by replacing $\varepsilon_{\text{MC}}^{1j,\text{CR}}$ by a data-driven measurement - $\varepsilon_{\text{est}}^{1j,\text{CR}}$.

An additional control region is, therefore, built by selecting $e\mu$ events in data with two jets, one of which is b-tagged. This sample is dominated by top-quark events, and any residual contamination from other background processes is subtracted. We use $\varepsilon_{\text{data}}^{2j,\text{CR}}$ to indicate the fraction of events in this sample in which the second jet is also b-tagged. $\varepsilon_{\text{est}}^{1j,\text{CR}}$ is simply equal to $\varepsilon_{\text{data}}^{2j,\text{CR}}$, with an additional MC correction factor to account for biases introduced by using a 2-jet sample for a 1-jet measurement. Thus, the estimate of the top background yield in the 1-jet SR is:

$$N_{\text{top,est}}^{1j,\text{SR}} = \left(N_{\text{data}}^{1j,\text{CR}} - N_{\text{other}}^{1j,\text{CR}}\right) \times \frac{\left(1 - \varepsilon_{\text{data}}^{2j,\text{CR}} \times f_{\text{corr}}\right)}{\varepsilon_{\text{data}}^{2j,\text{CR}} \times f_{\text{corr}}}, \tag{4.13}$$

with:

$$f_{\text{corr}} = \frac{\varepsilon_{\text{MC}}^{1j,\text{CR}}}{\varepsilon_{\text{MC}}^{2j,\text{CR}}}. \tag{4.14}$$

The ratio between the estimated and predicted top yields in the $e\mu$+1-jet SR results in a normalization factor that normalizes the predicted top yield in both SF and DF 1-jet events:

- $\text{NF}_{\text{top}}^{1j} = 1.06 \pm 0.03$ (stat.) .

Systematic uncertainties on the top background 1-jet estimate enter through the stability f_{corr} with experimental and theoretical variations. The similar kinematics of the 1-jet and 2-jet control regions, results in small uncertainties on the MC correction factor. The experimental systematic uncertainties amount to 1.4%, dominated by the uncertainties on the b-tagging efficiency. The theoretical uncertainties include PDFs, QCD scale, MC modeling, cross-section and interference effects between Wt and $t\bar{t}$ processes, totaling only 0.8%. In the 1-jet category, top processes are estimated with an uncertainty of $\sim$ 5%.

4.6.2.5 Other VV

The contamination of diboson processes other than WW in the $H \to WW^* \to \ell\nu\ell\nu$ analysis is of the same order of magnitude as the signal. For the SF channels, the shapes and normalizations of these processes are predicted using MC simulation only (see Section 4.3.2). Control regions (see Section 4.6.2) are used to normalize the sum of $W\gamma$, $W\gamma^*/Z$ and ZZ in the DF channels.

Out of all VV processes, $W\gamma$ and $W\gamma^*$ are the dominant contributing backgrounds. Special validation regions are selected to verify the modeling of these backgrounds in $e\mu$ events. Since $W\gamma$ and $W\gamma^*$ are equally likely to produce two same charge or two opposite charge leptons, a control sample of $e\mu$ events is selected by applying the same requirements of the DF signal region (see Table 4.7), except the leptons have the same charge. The resulting 0- and 1-jet CRs are $\sim 60\%$ pure in VV processes, with the remaining contribution being dominated by $W+$jets. The normalization factors computed from these regions are:

- $\mathrm{NF}_{VV}^{0j} = 0.92 \pm 0.07$ (stat.) ;
- $\mathrm{NF}_{VV}^{1j} = 0.96 \pm 0.12$ (stat.) .

No uncertainties are applied on the CR-to-SR extrapolation, as simulation shows these processes contribute to same-charge and opposite-charge events in equal amounts.

In the SF channels, where the MC prediction is used, the shapes and normalizations of other VV backgrounds, as well as of $W+$ jets, are validated with a sample of same flavor and same charge leptons, passing all the $ee + \mu\mu$ requirements listed in Table 4.6. The m_{T} distributions in these 0- and 1-jet validation regions are shown in Figure 4.40.

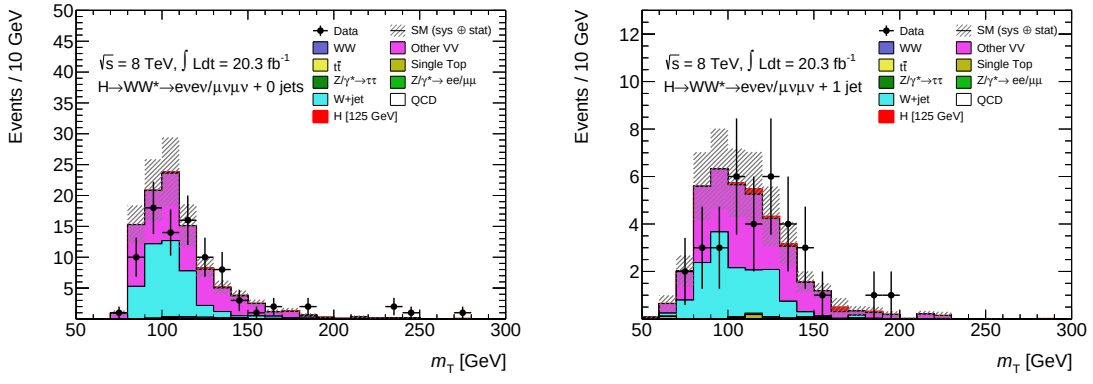

(a) (b)

FIGURE 4.40: m_{T} distribution in the same charge (a) 0-jet and (b) 1-jet validation regions.

Systematic uncertainties on the prediction of these VV backgrounds arise from uncertainties on the cross-sections of the individual processes (total and in each jet category). For the $W\gamma$ process, the total cross-section has an uncertainty of 6%, correlated across jet categories. The uncorrelated jet-bin uncertainties for this process are 9% and 53%

for 0- and 1-jet respectively. The same uncertainties for the $W\gamma^*$ process are 7% (total), 7% (0-jet) and 30% (1-jet).

4.7 DY background

Modeling of DY background in the same flavor channels is particularly challenging. Generally, the MC prediction cannot be trusted in the selected region of phase-space, which involves tight selections of fake missing transverse energy and very soft jets. A method was, therefore, developed to estimate the DY contamination entirely from data. The so-called Pacman method is presented in what follows.

4.7.1 Pacman method

The f_{recoil} variable shows a clear shape difference between DY and all other processes with true missing transverse energy in the final state, including the signal. Based on this feature, a data-driven technique has been developed – the Pacman method – that allows the measurement of the DY efficiency of a cut on f_{recoil} from data, and, consequently, the estimation of the remaining contribution of DY in the same flavor signal region, after such a cut.

The Pacman method is illustrated in Figure 4.41. It consists of a template fit of the f_{recoil} data distribution in the final same flavor signal region (low $m_{\ell\ell}$), represented by the red box. Two f_{recoil} templates are extracted from data, in control samples, and fitted to data in the signal region: a non-DY template, represented by the blue box, and a DY template, represented by the green box. The normalizations of the two templates, $N_{\text{non-DY}}$ and N_{DY}, are free parameters of the fit.

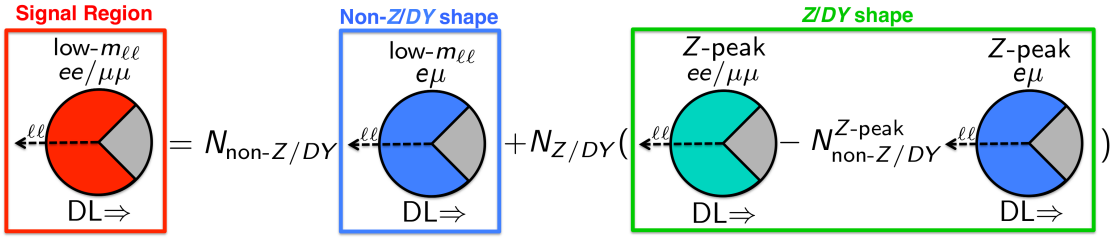

FIGURE 4.41: Schematic diagram of the Pacman method, used to estimate the DY background contamination.

The non-DY template is extracted from the f_{recoil} data distribution of different flavor events passing exactly the same selections as those applied to the SF signal region (see Table 4.6). This different flavor region[6] is $\sim 100\%$ pure in non-DY events. Moreover, the relative fractions of most non-DY processes in the signal region are expected to be the same in different flavor and same flavor events, due to flavor universality. For these

[6]Note that these are not the signal region events of the different flavour channels (i.e. resulting from the event selection in Table 4.7), but rather a subset of those, passing the tighter SF requirements of Table 4.6.

reasons, one can expect the f_{recoil} shape in different flavor events to describe the non-DY component of the same flavor distribution.

The DY template is extracted from the f_{recoil} data distribution of same flavor events in the the Z-peak. All same flavor signal regions selections included in Table 4.6 are applied, and the low $m_{\ell\ell}$ cut is simply replaced by the Z-window selection. The purity of this region in DY events is $\sim 50\%$, since all SF signal selections, such as high missing transverse energy, are applied. Thus, the non-DY contribution in the Z-peak needs to be subtracted. For this purpose, another non-DY template is built, similar to the one described in the previous paragraph, using different flavor data events in the Z-peak (also $\sim 100\%$ pure in non-DY). This non-DY template is subtracted to the SF Z-peak template, with a normalization $N_{\text{non-DY}}^{Z\text{-peak}}$ given by simulation.

For the $H \to WW^* \to \ell\nu\ell\nu$ analysis, a simplified implementation of the Pacman template fit was chosen, where the full f_{recoil} shape was replaced by two bins: pass and fail the f_{recoil} selection. Thus, instead of extracting templates for DY and non-DY, efficiencies of a cut on f_{recoil} are measured using the same samples described above. Moreover, instead of fitting the signal region, the extraction of a single analytical solution of the DY normalization becomes possible. This simplified implementation is described in the following.

4.7.2 Simplified implementation

Let us consider a control sample of different flavor events passing the same flavor signal selections shown in Table 4.6. The f_{recoil} distribution of events in this sample is plotted in Figure 4.42a for the 0-jet category, and in Figure 4.42c for the 1-jet category, before the requirement on f_{recoil} is applied. As shown, no DY contamination is predicted for these events. The shapes and normalizations of the different non-DY backgrounds are estimated as described in Section 4.6. If $N_{\text{data}}^{\text{DF,SR}}$ and $n_{\text{data}}^{\text{DF,SR}}$ are the number of data events in this sample before and after the final f_{recoil} selection, the efficiency of a cut on f_{recoil} for non-DY processes can be simply calculated as:

$$\varepsilon_{\text{non-DY}} = \frac{n_{\text{data}}^{\text{DF,SR}}}{N_{\text{data}}^{\text{DF,SR}}}. \tag{4.15}$$

Considering now a control sample of same flavor events passing the selections in Table 4.6, with the low $m_{\ell\ell}$ cut replaced by the Z-window requirement. The f_{recoil} distribution of this sample is shown in Figure 4.42b for the 0-jet category, and in Figure 4.42d for the 1-jet category. The efficiency of the f_{recoil} cut for DY can be simply calculated as the fraction of data events in the control sample passing the f_{recoil} selection. As previously explained, the non-DY contribution in this region is not negligible. The total yield that has to be subtracted - $N_{\text{non-DY}}^{\text{SF},Z\text{peak}}$ - is the one predicted using the techniques described in Section 4.6, and has an associated uncertainty of $\sim 10\%$. The f_{recoil} efficiency for this non-DY component is determined in a similar fashion to what

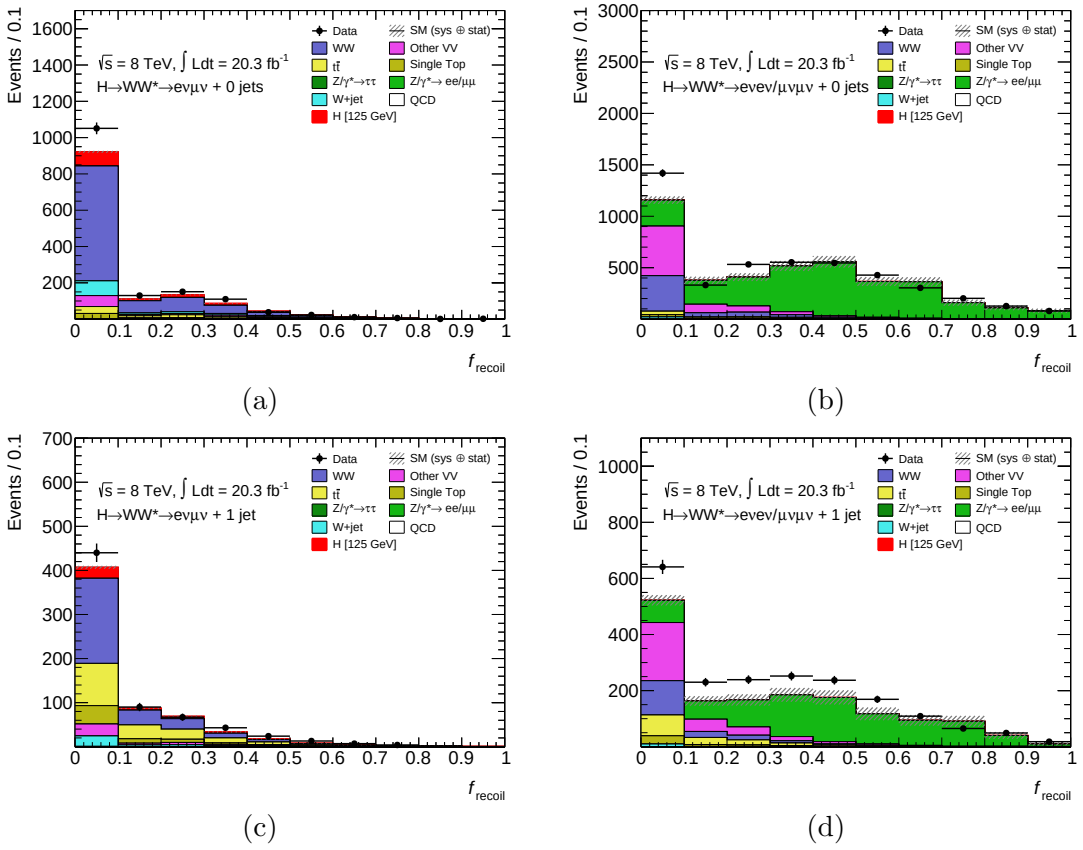

FIGURE 4.42: f_{recoil} distributions of events used to measure the (a) non-DY 0-jet, (b) DY 0-jet, (c) non-DY 1-jet and (d) DY 1-jet, efficiencies of the f_{recoil} selection in the SF channel.

was shown in Equation 4.15, using different flavor data events in the Z-window:

$$\varepsilon_{\text{non-DY}}^{Z\text{peak}} = \frac{n_{\text{data}}^{\text{DF},Z\text{peak}}}{N_{\text{data}}^{\text{DF},Z\text{peak}}}. \tag{4.16}$$

Note that this $\varepsilon_{\text{non-DY}}^{Z\text{peak}}$ is used only for subtraction of the non-DY contribution in the same flavor Z-peak. Elsewhere, the efficiency at low $m_{\ell\ell}$ (corresponding to the signal region) is used: $\varepsilon_{\text{non-DY}}$ from equation 4.15. The final f_{recoil} efficiency for DY is, therefore, given by:

$$\varepsilon_{\text{DY}} = \frac{n_{\text{data}}^{\text{SF},Z\text{peak}} - \varepsilon_{\text{non-DY}}^{Z\text{peak}} \times N_{\text{non-DY}}^{\text{SF},Z\text{peak}}}{N_{\text{data}}^{\text{SF},Z\text{peak}} - N_{\text{non-DY}}^{\text{SF},Z\text{peak}}}. \tag{4.17}$$

Knowing the DY and non-DY efficiencies of the f_{recoil} selection, measured using data samples as described above, the DY contamination in the signal region - $n_{\text{DY}}^{\text{SF,SR}}$ - can be analytically calculated to match the observed fraction of data events passing the f_{recoil} cut in the same flavour signal region. This is done as follows:

$$n_{\text{DY}}^{\text{SF,SR}} = \varepsilon_{\text{DY}} \times \frac{n_{\text{data}}^{\text{SF,SR}} - \varepsilon_{\text{non-DY}} \times N_{\text{data}}^{\text{SF,SR}}}{\varepsilon_{\text{DY}} - \varepsilon_{\text{non-DY}}}. \tag{4.18}$$

This is equivalent to inverting the matrix:

$$\begin{bmatrix} n_{\text{data}}^{\text{SF,SR}} \\ N_{\text{data}}^{\text{SF,SR}} \end{bmatrix} = \begin{bmatrix} 1 & 1 \\ 1/\varepsilon_{\text{DY}} & 1/\varepsilon_{\text{non-DY}} \end{bmatrix} \begin{bmatrix} n_{\text{DY}}^{\text{SF,SR}} \\ n_{\text{non-DY}}^{\text{SF,SR}} \end{bmatrix}, \tag{4.19}$$

in order to solve for $n_{\text{DY}}^{\text{SF,SR}}$.

As shown, the Pacman method uses data events directly in the same flavor signal region, to estimate the DY background contamination. However, the presence or strength of the signal has a negligible effect on this estimate, given that efficiencies are being measured, rather than absolute numbers. Figure 4.43 indicates that variations of signal strength μ in the range $0-10$ cause less than 10% change in the DY estimate provided by Pacman, which is well within the uncertainties of the Pacman procedure, which will be described next. The distributions were obtained applying the Pacman method on simulated events as if they were data, with different levels of signal injection.

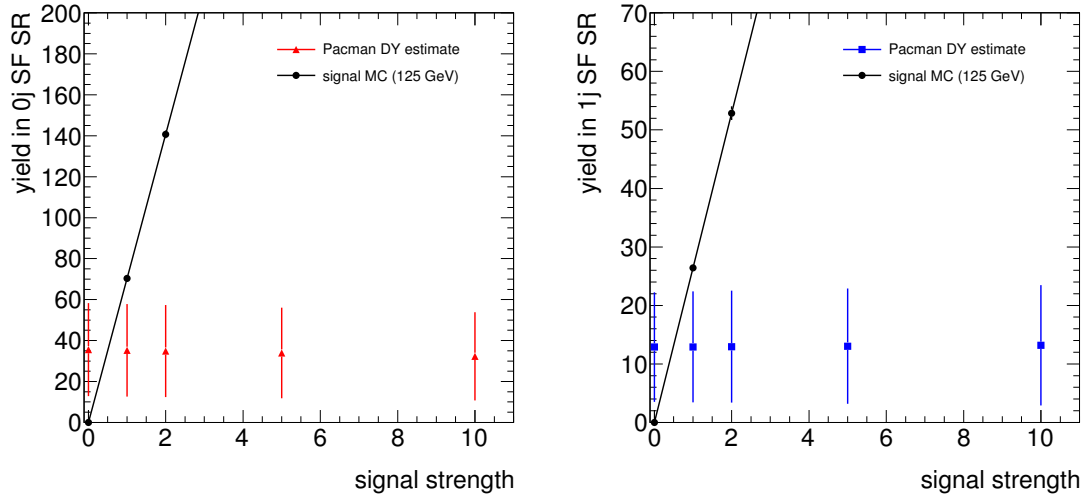

(a) (b)

FIGURE 4.43: Effect of the signal strength on the estimated DY yield in the signal region for: (a) 0-jet, and (b) 1-jet channels. Inject different amounts of signal (0, 1, 2, 5 and 10 times the SM prediction), the DY background estimate provided by Pacman is shown in color. The small variations in the background estimate, of less than 10% over a wide range of signal strength values, are well within the systematic uncertainties of the Pacman method.

4.7.3 Systematic uncertainties

The Pacman method uses control samples in data, as similar as possible to the SF signal region, to calculate the DY and non-DY efficiencies of a cut on f_{recoil}. The procedure used to evaluate the systematic uncertainties consists of assigning an uncertainty to each of the measured efficiencies. These are meant to cover the extrapolation, i.e. the relative difference between the measured efficiency and the actual efficiency in the SF signal region. The extrapolation is evaluated directly, using simulation, and validated, using alternative MC samples, as well as data.

Once computed, each extrapolation is added, as a systematic uncertainty, in quadrature to the statistical uncertainty of the measured DY and non-DY efficiencies. The final uncertainty on the DY estimate is then computed through uncertainty propagation on Equation 4.18, the data terms contributing with their statistical uncertainties, and the efficiency terms entering with statistical and systematic uncertainties.

4.7.3.1 Systematic uncertainties on the non-DY efficiencies

The efficiencies $\varepsilon_{\text{non-DY}}$ and $\varepsilon_{\text{non-DY}}^{Z\text{peak}}$ are measured using different flavor events and applied to same flavor events, in the same region of phase-space (either the low $m_{\ell\ell}$ signal region or the Z-window). The different flavor $\rightarrow$ same flavor extrapolation is, therefore, assigned as a systematic uncertainty to the non-DY efficiencies.

First, the relative difference between the f_{recoil} cut efficiency on DF and SF events, is evaluated for the individual non-DY backgrounds - WW, $t\bar{t}$, single top, $W+\text{jets}$ and other VV (i.e. the sum of WZ, ZZ, $W\gamma^*$ and $W\gamma$) - using different MC generators for these processes. For $W+\text{jets}$, the data-driven estimate is also considered. The distributions for $Z/\gamma^* \rightarrow \tau\tau$ are not shown as the statistics are poor, since the contamination in the signal region is negligible (see Table 4.8). This comparison is shown in Figures 4.44 and 4.45 for the 0-jet signal region (at low $m_{\ell\ell}$), and in Figures 4.46 and 4.47 for the 0-jet Z-peak. The corresponding Figures in the 1-jet category are 4.48, 4.49, 4.50 and 4.51. Each plot shows the shapes of the f_{recoil} distribution for DF and SF events, predicted by different MC generators, for a given non-DY background source. The distributions are made after the $p_{\text{T,rel}}^{\text{miss,track}}$ selection (see Table 4.6), which means that all requirements are applied, except for the ones on $\Delta\phi_{\ell\ell}$ and f_{recoil}. The ratio shown below each plot always compares the SF and the DF distributions for a given MC generator, so that the extrapolation can be read directly from the first bin (remember a cut of $f_{\text{recoil}} < 0.1$ is used). This extrapolation is also indicated in the legend, with its corresponding statistical uncertainty.

As expected, the differences in f_{recoil} efficiency for DF and SF, measured for the different background processes, are compatible with zero, within their statistical uncertainties. Moreover, the different samples used show compatible results.

In what follows, the DF $\rightarrow$ SF extrapolation is determined for the whole non-DY background component. For this purpose, the highest statistics sample is chosen for each individual background process, in order to have the most precise measurement possible. The samples chosen are, in fact, the nominal samples used in the analysis (see Table 4.1). The information provided by the remaining samples should be interpreted as a validation of the extrapolation measured from the nominal samples. No additional uncertainties will be considered form this validation, since the differences between different simulations are within the statistical uncertainty.

The nominal samples (data-driven in the case of $W+\text{jets}$, and MC for the rest) for the individual non-DY background processes are, thus, added to obtain the nominal f_{recoil} distributions for non-DY, shown in Figure 4.52 for DF and SF events. As before, distributions are plotted at the $p_{\text{T,rel}}^{\text{miss,track}}$ cut stage. Each process is normalized to its

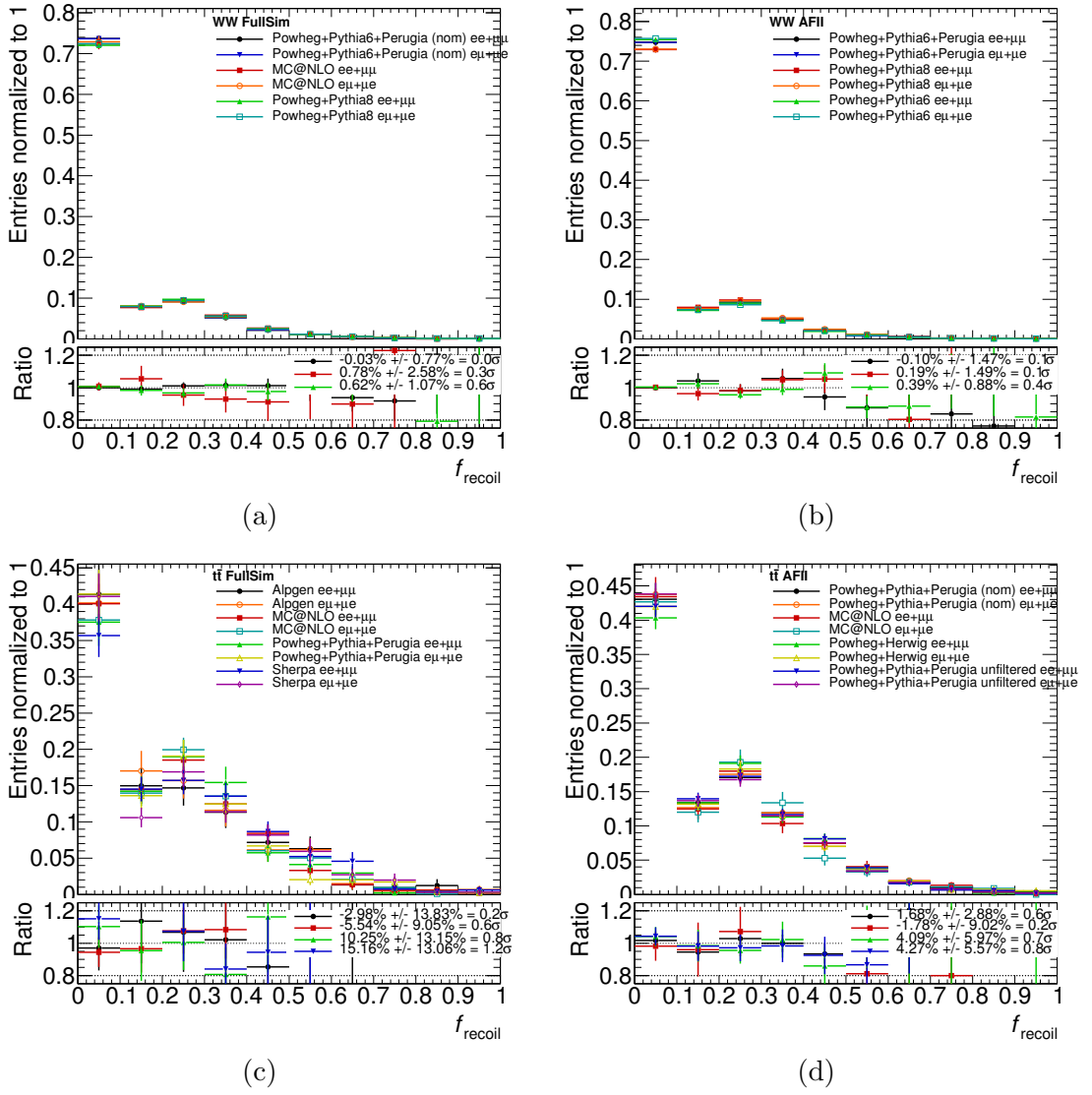

FIGURE 4.44: Comparison between SF and DF f_{recoil} shapes, in the low $m_{\ell\ell}$ 0-jet signal region, with different MC generators for (a-b) the WW background and (c-d) the $t\bar{t}$ background. (a) and (c) show FullSim samples, while (b) and (d) show ATLFAST-II samples. The ratios below the plots compare the SF and DF distributions for each generator and each process. The legend on the ratio plot indicates the relative difference in efficiency of the $f_{\text{recoil}} < 0.1$ cut, between the SF events and the DF events. The uncertainty shown is statistical.

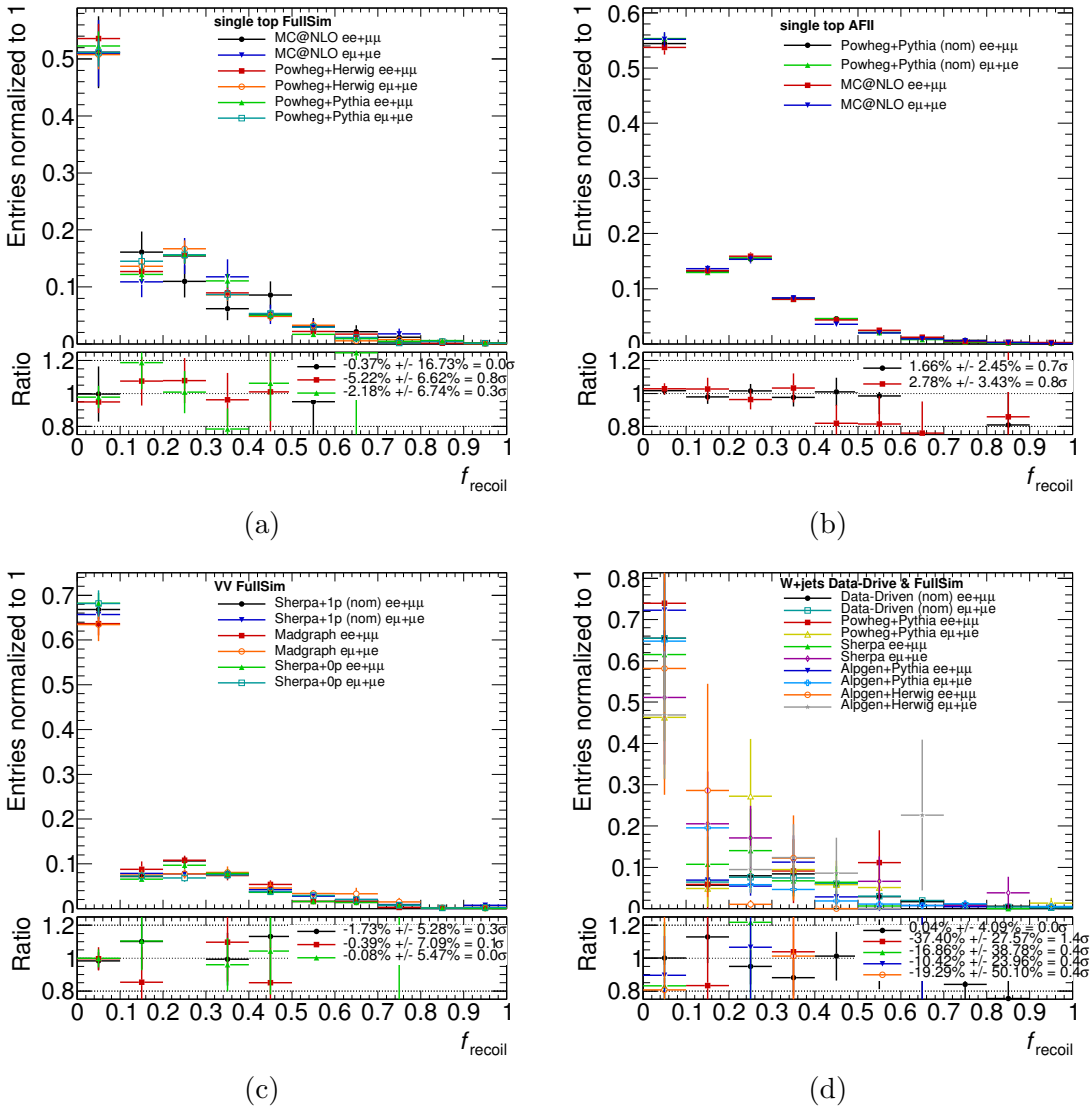

FIGURE 4.45: Comparison between SF and DF f_{recoil} shapes, in the low $m_{\ell\ell}$ 0-jet signal region, with different MC generators for (a-b) single-top, (c) other VV and (d) W+jets backgrounds. For single-top (a) shows FullSim samples, while (b) shows ATLFAST-II samples. More details in the legend of Figure 4.44.

cross-section, and the data normalizations described in Section 4.6 are also applied. As expected, no statistically significant difference is measured between the SF (red circles) and DF (blue squares) f_{recoil} efficiency.

The difference between the SF and DF f_{recoil} efficiencies for the non-DY background component consists of, basically, the weighted sum of the differences for each individual process, as assessed in Figures 4.44 through 4.51. The weight is the relative contribution of each individual background, with respect to all non-DY backgrounds. It follows from this that if the composition of the non-DY sample is changed, the DF $\rightarrow$ SF extrapolation also changes.

To determine the impact of the sample composition on the DF $\rightarrow$ SF extrapolation, the yield of each individual non-DY process was varied up and down by its uncertainty,

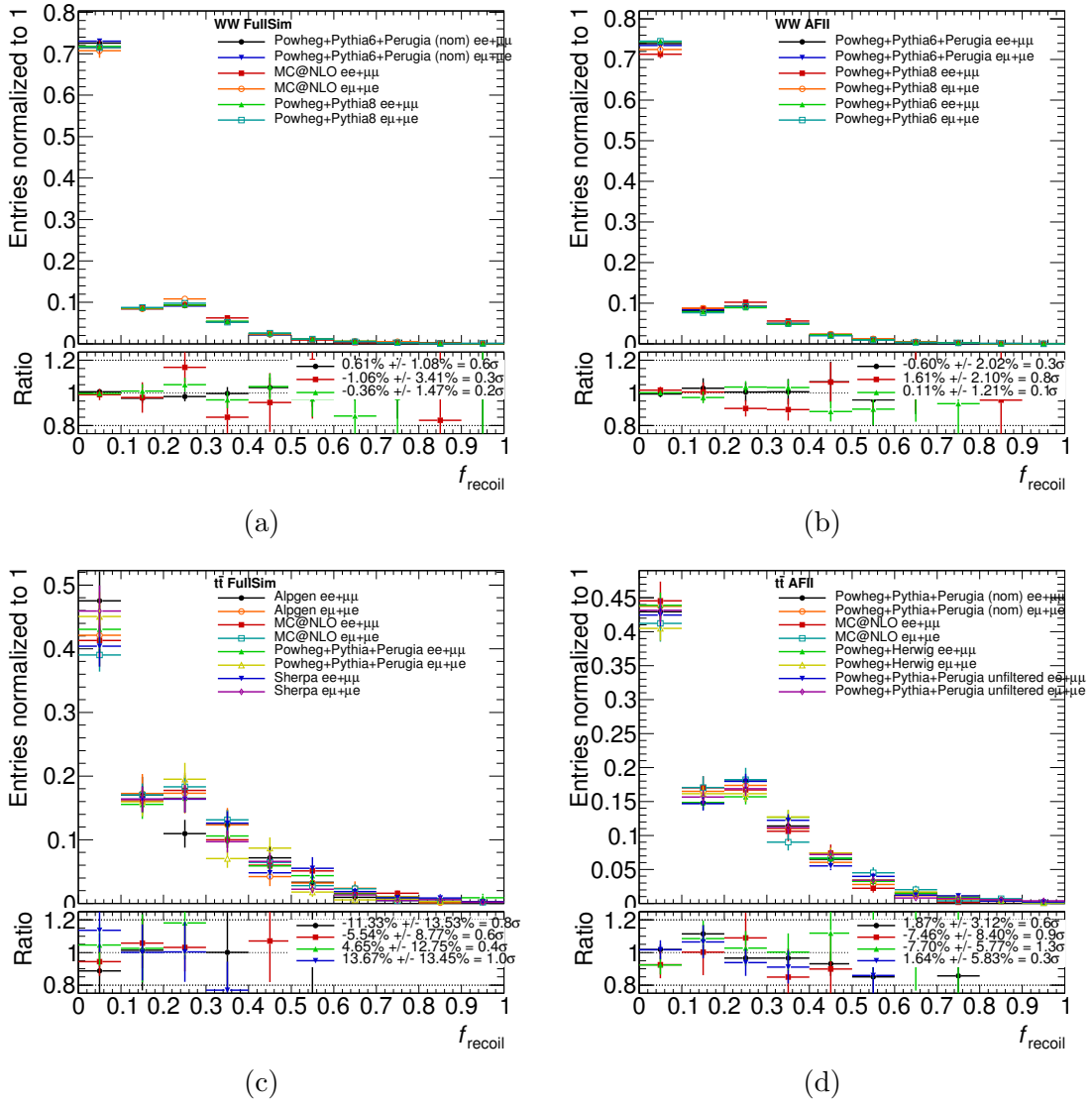

FIGURE 4.46: Comparison between SF and DF f_{recoil} shapes, in the 0-jet Z-peak, with different MC generators for (a-b) the WW background and (c-d) the $t\bar{t}$ background. (a) and (c) shown FullSim samples, while (b) and (d) show ATLFAST-II samples. More details in the legend of Figure 4.44.

thus changing its relative contribution to the sum of all non-DY backgrounds. For this purpose, the uncertainties quoted on the previous iteration of the $H \to WW^* \to \ell\nu\ell\nu$ analysis [155, 170] were used, an approach which is conservative, as they have now been reduced.

For each up and down background yield variation, the relative difference in f_{recoil} cut efficiency for SF and DF non-DY events is re-calculated. The results obtained are summarized in Table 4.14. The systematic uncertainties assigned to the non-DY efficiencies are highlighted and they are: the largest extrapolation measured in any of the background variations, if statistically significant; or the statistical uncertainty on the nominal extrapolation, if not statistically significant.

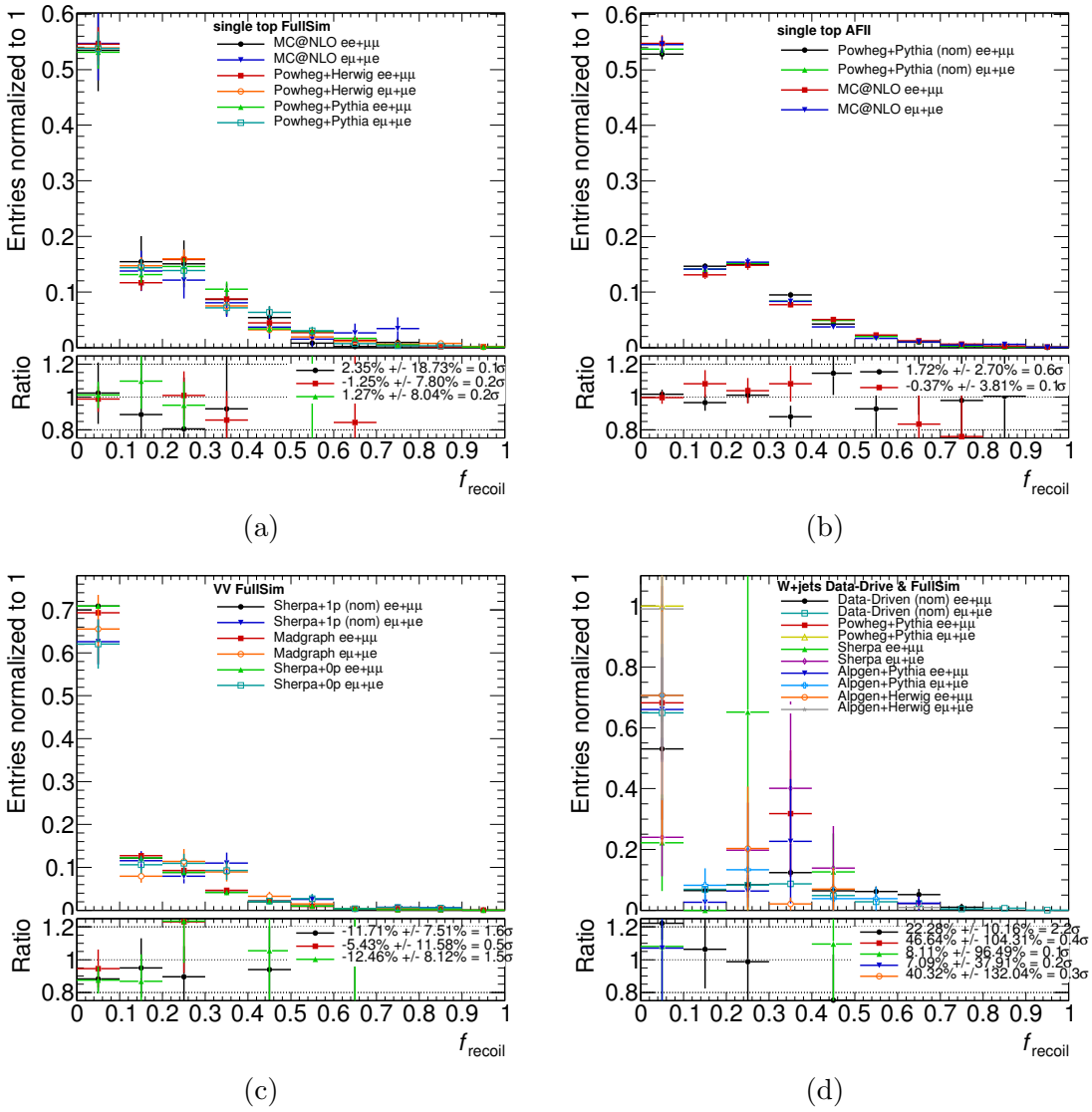

FIGURE 4.47: Comparison between SF and DF f_{recoil} shapes, in the 0-jet Z-peak, with different MC generators for (a-b) single-top, (c) other VV and (d) W+jets backgrounds. For single-top (a) shows FullSim samples, while (b) shows ATLFAST-II samples. More details in the legend of Figure 4.44.

The extrapolation measured for non-DY is further validated using simulation. The DF $\rightarrow$ SF extrapolation, computed using the nominal MC samples after the $p_{\text{T,rel}}^{\text{miss,track}}$ selection, is shown in bins of $E_{\text{T,rel}}^{\text{miss,calo}}$ (in Figure 4.53) and of $m_{\ell\ell}$ (in Figure 4.53). The assigned systematic uncertainty (see Table 4.14) is indicated by the gray bands and, as the plots show, cover most of the extrapolations in the different bins. The very low $E_{\text{T,rel}}^{\text{miss,calo}}$ bins in the 0-jet bin show differences between DF and SF larger than the assigned uncertainty. However, this region is considered far from the high $E_{\text{T,rel}}^{\text{miss,calo}}$ signal region, where the different bins show extrapolations well within the uncertainty.

Finally, one last validation step is performed by comparing the DF and SF f_{recoil} efficiencies for non-DY, directly using data events. The $m_{\ell\ell}$ regions between the low $m_{\ell\ell}$ signal region and the Z-window, and after the Z-window are used, i.e. $55 < m_{\ell\ell} <$

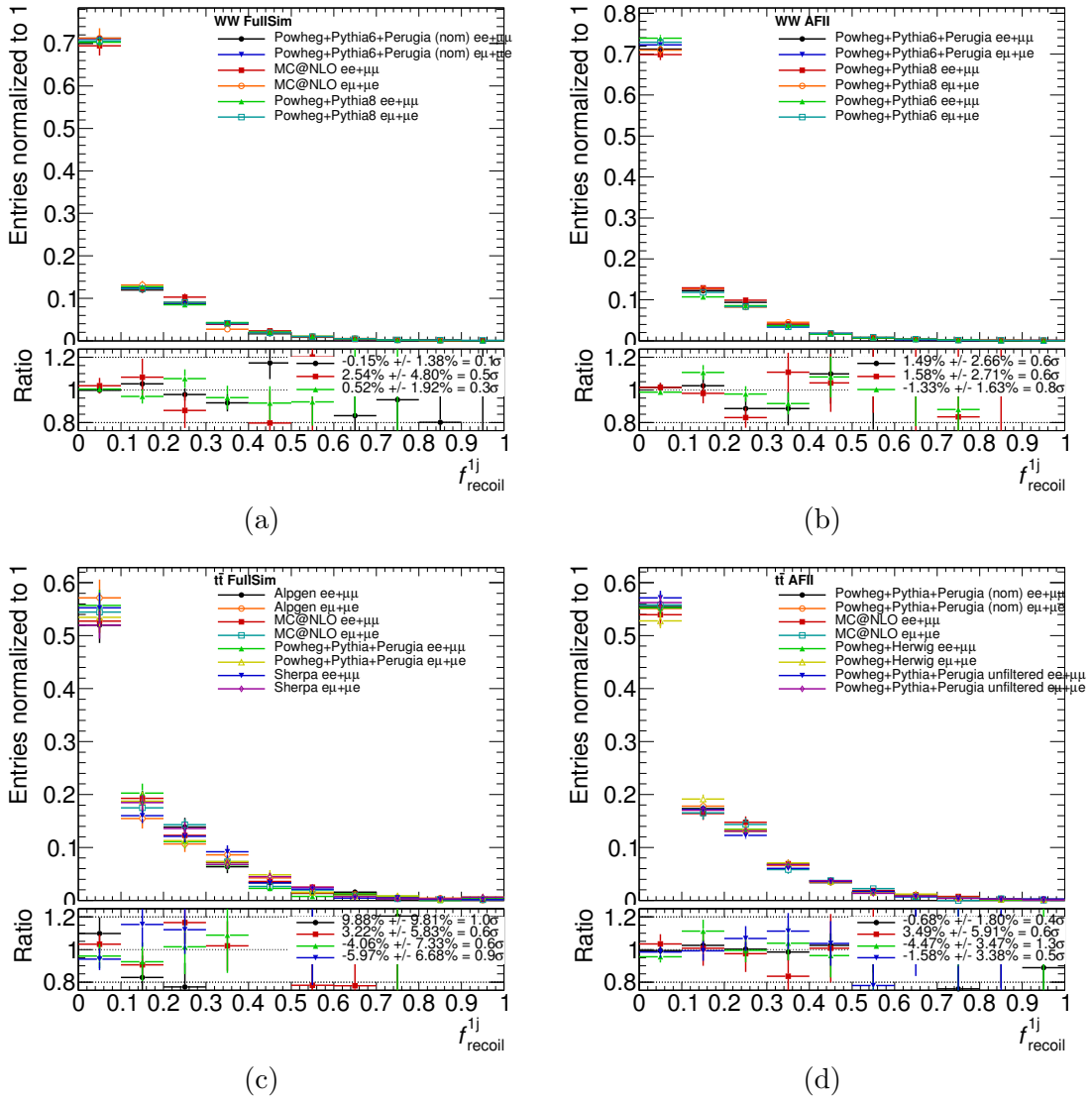

FIGURE 4.48: Comparison between SF and DF f_{recoil} shapes, in the low $m_{\ell\ell}$ 1-jet signal region, with different MC generators for (a-b) the WW background and (c-d) the $t\bar{t}$ background. (a) and (c) shown FullSim samples, while (b) and (d) show ATLFAST-II samples. More details in the legend of Figure 4.44.

$m_Z - 15$ GeV and $m_{\ell\ell} > m_Z + 15$ GeV. Events falling in the Z-peak are removed in order to reduce the DY contamination in data. The impact of any DY contamination in the f_{recoil} efficiencies is suppressed by looking at the f_{perp} distributions, instead of f_{recoil}. The contamination is, nonetheless, subtracted from data using simulation.

Thus, the f_{perp} distributions for SF and DF data events are compared, as shown in Figure 4.54. Again, the relative difference in efficiency of a cut on $f_{\text{perp}} < 0.1$, for SF (red circles) and DF (blue squares) events, is computed and shown in the distributions. The data does not seem to indicate that the extrapolation is larger than the one measured in simulation, which is assigned as a systematic uncertainty, as mentioned previously.

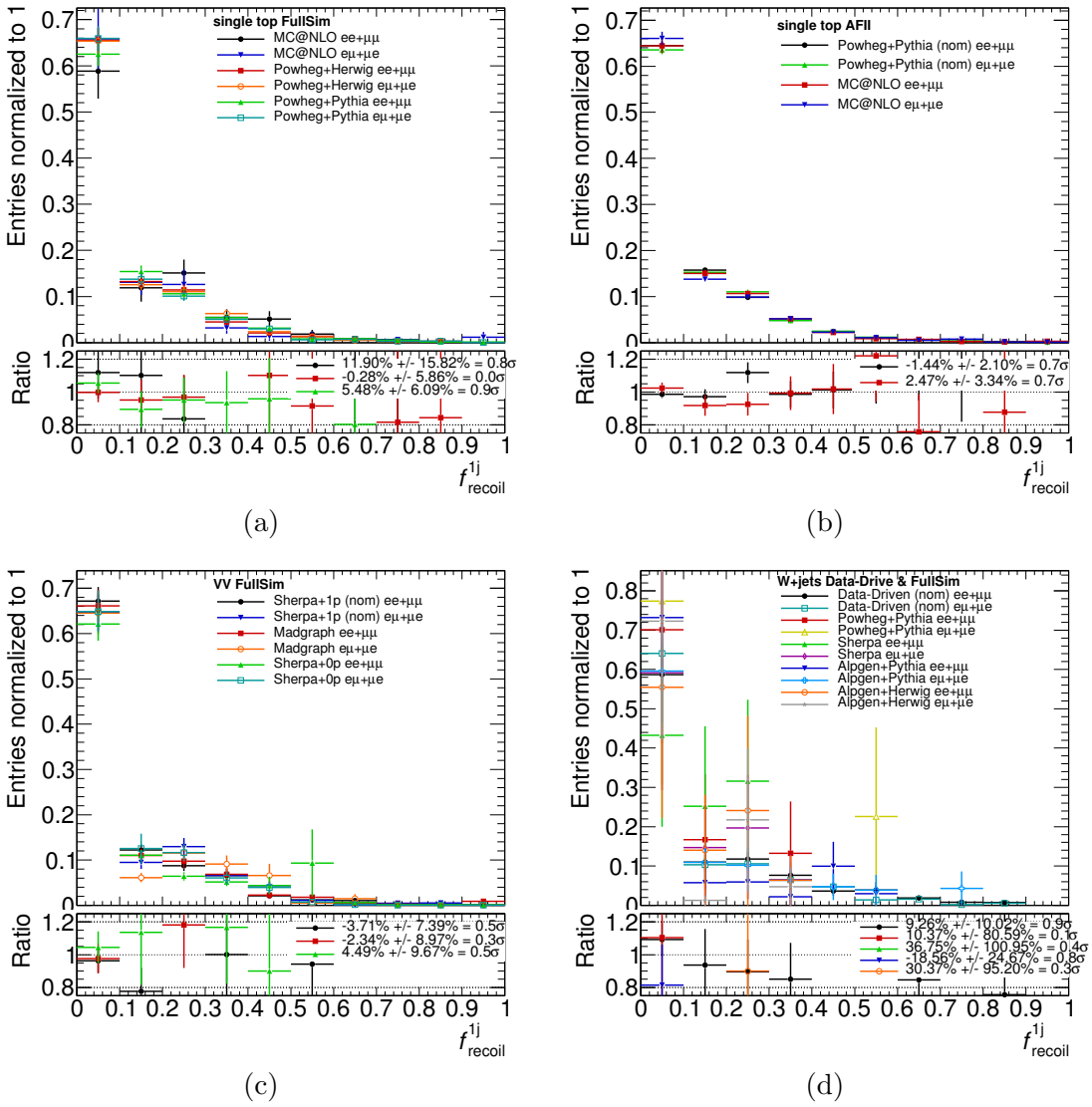

FIGURE 4.49: Comparison between SF and DF f_{recoil} shapes, in the low $m_{\ell\ell}$ 1-jet signal region, with different MC generators for (a-b) single-top, (c) other VV and (d) W+jets backgrounds. For single-top (a) shows FullSim samples, while (b) shows ATLFAST-II samples. More details in the legend of Figure 4.44.

Systematic uncertainties on the signal efficiency An additional uncertainty of 9% and 8% is assigned to the Higgs signal for the efficiency of the f_{recoil} selection, in the SF 0- and 1-jet channels respectively. This uncertainty is taken as the full difference between the f_{recoil} efficiency measured for non-DY and for the signal, in simulation (see Figure 4.22). The uncertainty is validated by comparing the f_{recoil} efficiency predicted by different signal samples, as shown in Figure 4.55. The several MC samples predict similar efficiencies within $\sim 5\%$, which is smaller than the assigned uncertainty.

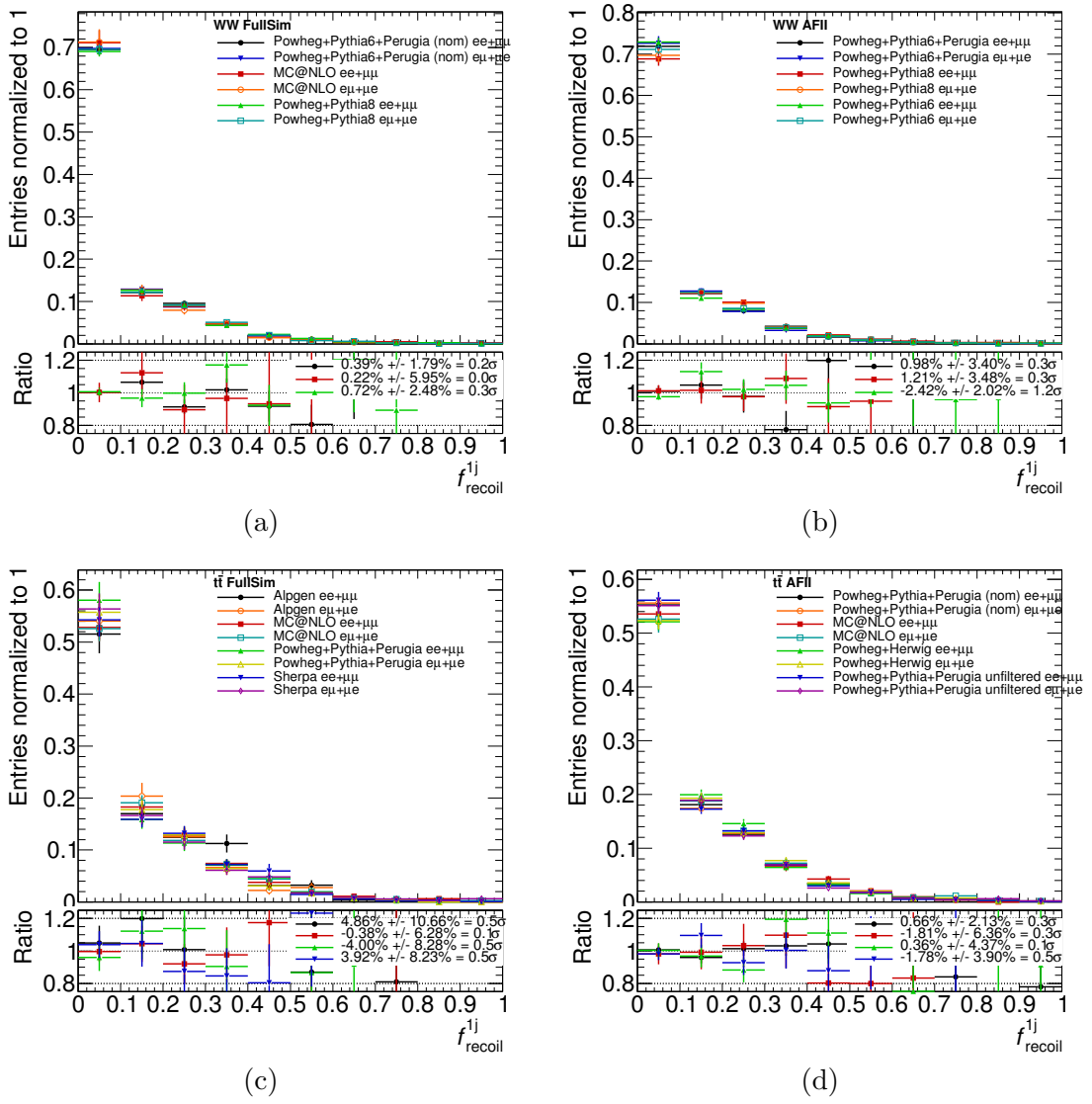

FIGURE 4.50: Comparison between SF and DF f_{recoil} shapes, in the 1-jet Z-peak, with different MC generators for (a-b) the WW background and (c-d) the $t\bar{t}$ background. (a) and (c) shown FullSim samples, while (b) and (d) show ATLFAST-II samples. More details in the legend of Figure 4.44.

4.7.3.2 Systematic uncertainties on the DY efficiency

The ε_{DY} efficiency is measured using same flavor events in the Z-peak and applied to same flavor events in the low $m_{\ell\ell}$ signal region (the phase-space is approximately the same, only the $m_{\ell\ell}$ selection is changed). The Z-peak $\rightarrow$ low $m_{\ell\ell}$ extrapolation is, therefore, assigned as a systematic uncertainty to the DY efficiency.

The extrapolation is measured by directly measuring the relative difference between the f_{recoil} cut efficiency for DY events at low $m_{\ell\ell}$ and in the Z-peak, using MC simulation. This is shown in Figure 4.56, where the f_{recoil} shapes for DY events in the low $m_{\ell\ell}$ signal region and in the Z-window, are compared for two different simulated samples. The distributions are plotted after the $p_{\text{T}}^{\ell\ell}$ cut in the 0-jet channel, and after the $p_{\text{T,rel}}^{\text{miss,track}}$

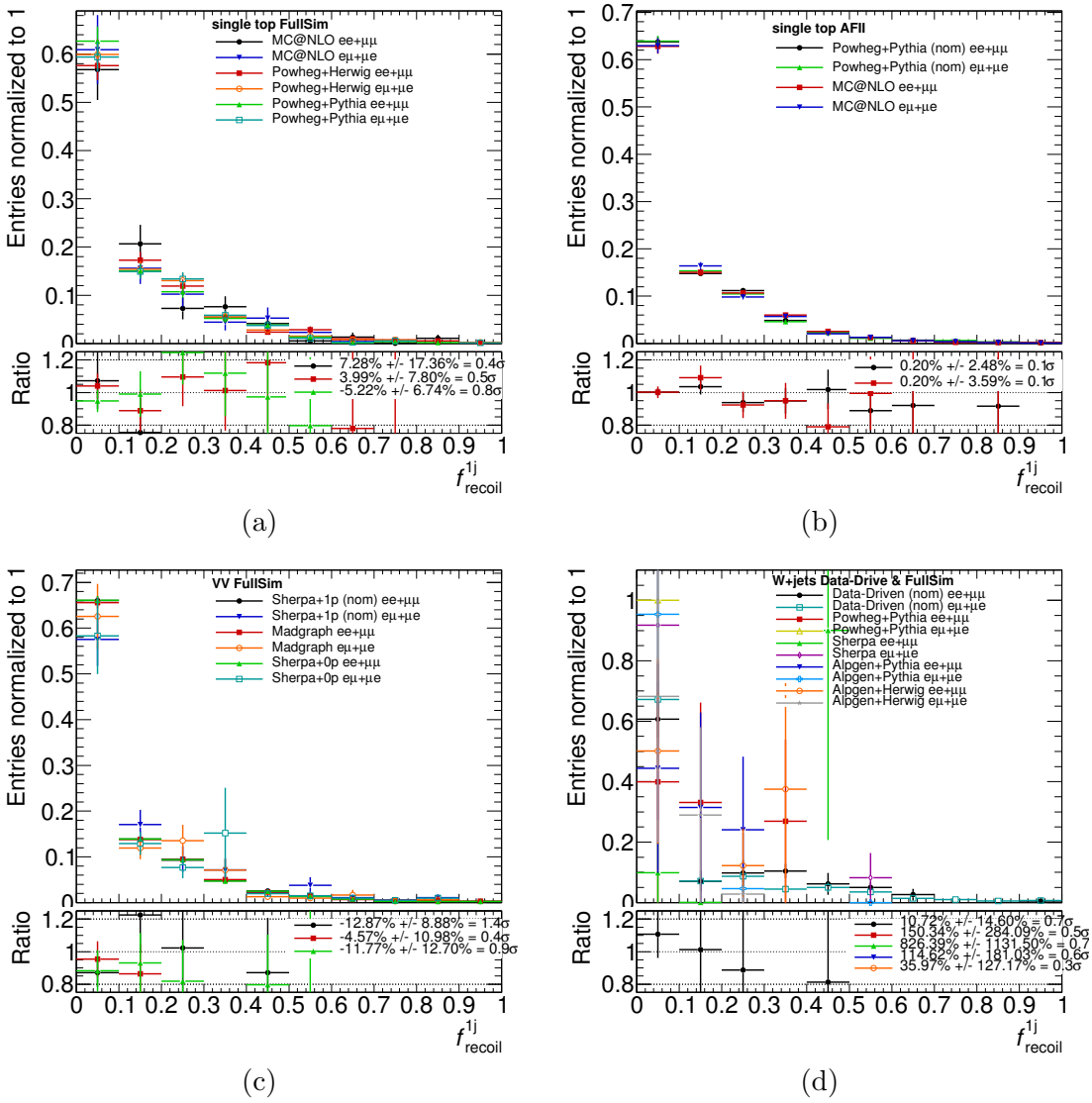

FIGURE 4.51: Comparison between SF and DF f_{recoil} shapes, in the 0-jet Z-peak, with different MC generators for (a-b) single-top, (c) other VV and (d) W+jets backgrounds. For single-top (a) shows FullSim samples, while (b) shows ATLFAST-II samples. More details in the legend of Figure 4.44.

cut for the 1-jet channel. These are the requirements that boost the dilepton (+ jet) system and shape the f_{recoil} distribution of DY events. The remaining signal region selections (see Table 4.6) are not applied, to increase the statistics available to measure this extrapolation[7].

The ratio shown below the plots in Figure 4.56 compares the low $m_{\ell\ell}$ distributions with the distributions in the Z peak. Since a cut of $f_{\text{recoil}} < 0.1$ was chosen, the extrapolation for each generator can be read directly in the first bin. This extrapolation is also indicated in the legend, with its corresponding statistical uncertainty. The largest

[7]This is done only for the evaluation of the systematic uncertainties (and unless stated otherwise). When estimating the DY yield in the same flavour signal region, the full selection is applied.

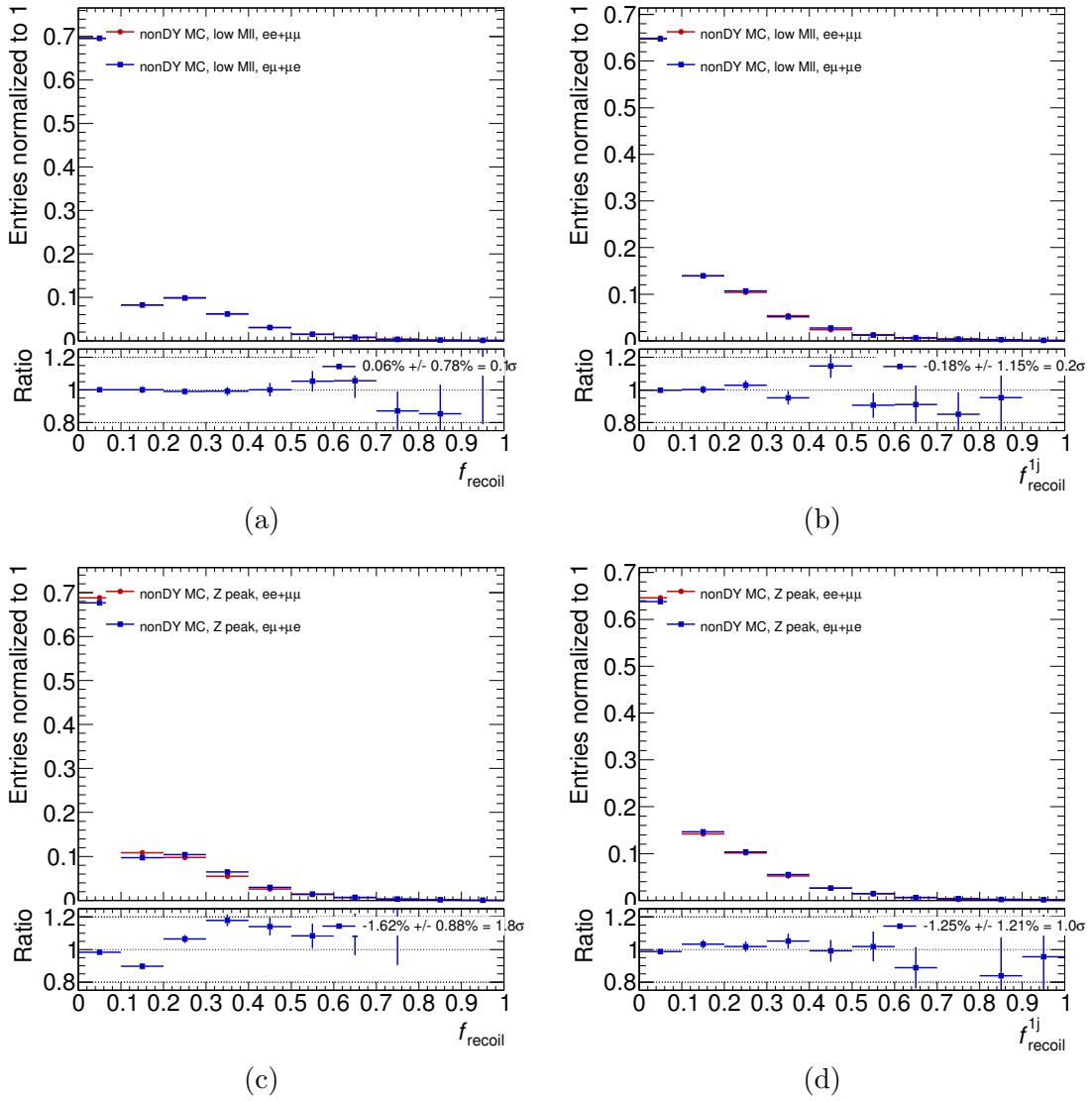

FIGURE 4.52: Comparison between SF and DF f_{recoil} shapes for non-DY backgrounds. Each distributions shows: (a) the 0-jet low $m_{\ell\ell}$ signal region; (b) the 1-jet low $m_{\ell\ell}$ signal region; (c) the 0-jet Z-peak; and (d) the 1-jet Z-peak. The composition of the non-DY sample is taken from the nominal simulated samples, with normalization factor from data where available. More details in the legend of Figure 4.44.

extrapolation predicted between the two different DY MC samples is assigned as systematic uncertainty on measured DY efficiency: 32% for the 0-jet bin and 16% for the 1-jet bin.

This Z-peak $\rightarrow$ low $m_{\ell\ell}$ extrapolation, evaluated with DY simulation, is validated using SF events in data at low $E_{\text{T,rel}}^{\text{miss,calo}}$, which have a high purity in DY. Contributions from non-DY processes are, nonetheless, subtracted from data using simulation. This validation is shown in Figure 4.57, where the extrapolation is plotted in bins of $E_{\text{T,rel}}^{\text{miss,calo}}$, for data and two DY simulated samples. The assigned systematic uncertainties, coming from the largest difference in f_{recoil} cut efficiency measured in MC, as described in the previous paragraph, are shown by the gray bands.

	Background	Variation [%]	DF → SF non-DY extrapolation [%] low $m_{\ell\ell}$	DF → SF non-DY extrapolation [%] Z-peak
0-jet	nominal	-	$0.06 \pm \mathbf{0.78}$	-1.62 ± 0.88
	WW	+7.4	0.06 ± 0.77	-1.37 ± 0.88
		−7.4	0.06 ± 0.79	-1.91 ± 0.88
	top	+13	0.07 ± 0.77	$\mathbf{-1.92} \pm 0.87$
		−13	0.05 ± 0.78	-1.30 ± 0.89
	$Z/\gamma^* \to \tau\tau$	+15	0.06 ± 0.78	-1.62 ± 0.88
		−15	0.06 ± 0.78	-1.62 ± 0.88
	W + jets	+34	0.06 ± 0.81	-1.47 ± 0.89
		−34	0.06 ± 0.75	-1.77 ± 0.87
	other VV	+16	0.05 ± 0.79	-1.86 ± 0.89
		−16	0.07 ± 0.76	-1.34 ± 0.87
1-jet	nominal	-	$-0.18 \pm \mathbf{1.15}$	-1.25 ± 1.21
	WW	+37	-0.16 ± 1.12	-0.55 ± 1.22
		−37	-0.24 ± 1.25	$\mathbf{-2.39} \pm 1.25$
	top	+28	-0.25 ± 1.11	-1.55 ± 1.18
		−28	-0.11 ± 1.22	-0.75 ± 1.28
	$Z \to \tau\tau$	+40	-0.21 ± 1.15	-1.25 ± 1.21
		−40	-0.16 ± 1.15	-1.24 ± 1.21
	W + jets	+25	-0.06 ± 1.19	-1.16 ± 1.24
		−25	-0.31 ± 1.11	-1.33 ± 1.19
	other VV	+22	-0.24 ± 1.19	-1.51 ± 1.24
		−22	-0.12 ± 1.12	-0.94 ± 1.19

TABLE 4.14: DF → SF extrapolation, measured in MC, for the non-DY f_{recoil} efficiencies in the low $m_{\ell\ell}$ signal region and in the Z-peak, after the $p_{\text{T,rel}}^{\text{miss,track}}$ selection, for events in the 0- and 1-jet categories. For each row, the nominal MC composition of the non-DY sample is changed, by varying the yield of each background source individually, up and down by its uncertainty. The uncertainty considered for each processes is indicated, in [%], under the column "Variation". The uncertainty shown on the extrapolation is statistical only. Numbers in bold correspond to the final systematic uncertainties assigned to $\varepsilon_{\text{non-DY}}$ and $\varepsilon_{\text{non-DY}}^{Z\text{peak}}$.

The 0-jet channel is shown in Figure 4.57a, after the $p_{\text{T}}^{\ell\ell}$ cut. The distribution suggests that the Z-peak → low $m_{\ell\ell}$ extrapolation is correlated to $E_{\text{T,rel}}^{\text{miss,calo}}$. The distribution in Figure 4.57c is similar, but uses events in the 0-jet channel, after the $p_{\text{T,rel}}^{\text{miss,track}}$ cut is also applied. The statistical uncertainties are larger, but the correlation of the extrapolation with $E_{\text{T,rel}}^{\text{miss,calo}}$ appears to be smaller. The 1-jet channel is shown in Figure 4.57b, after the $p_{\text{T,rel}}^{\text{miss,track}}$ cut, also with large statistical errors. For all cases, the data and MC points in the distributions are contained within the assigned systematic uncertainty band, thus validating the procedure. Variations of these plots are shown in Appendix C for completeness.

Further validation is performed by looking at the dependence of the extrapolation with $m_{\ell\ell}$, at high values of $E_{\text{T,rel}}^{\text{miss,calo}}$. Even though one is interested in the extrapolation from the Z-window to the low $m_{\ell\ell}$ signal region, other regions in $m_{\ell\ell}$ can provide useful information. For this purpose, the relative difference between the f_{recoil} cut efficiency in

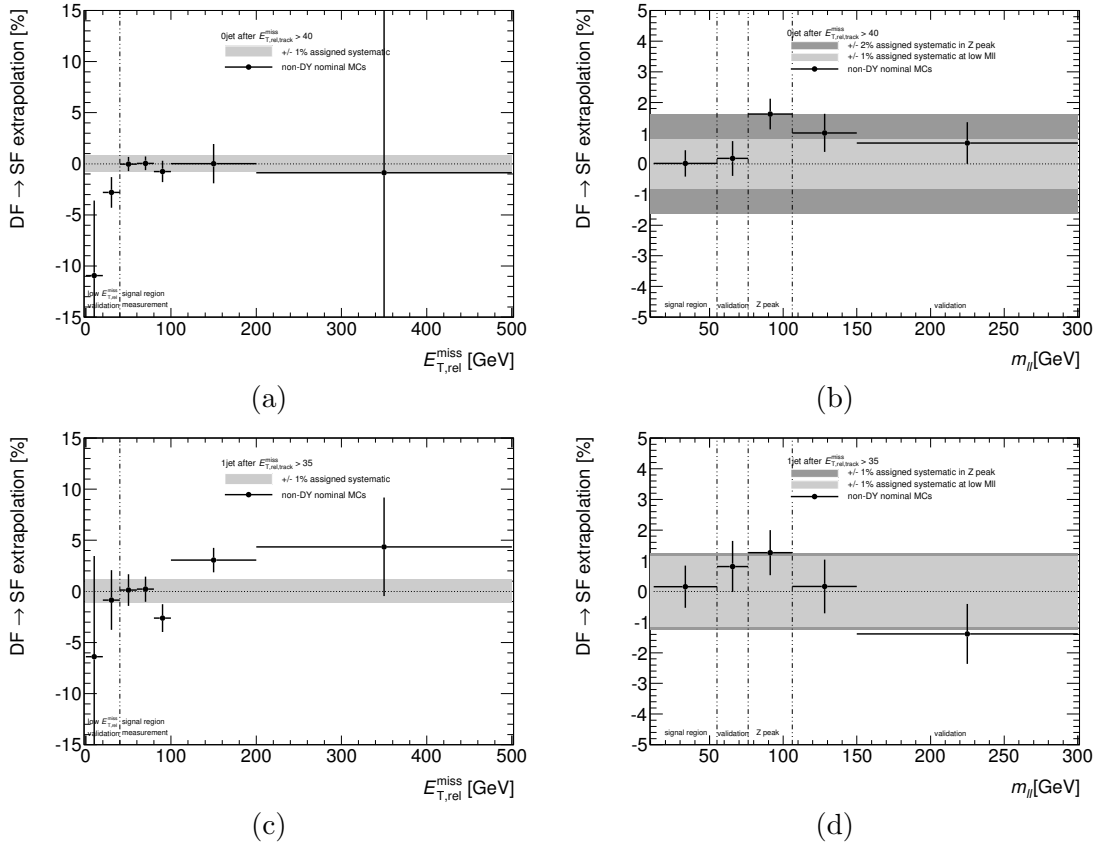

FIGURE 4.53: DF → SF extrapolation for the non-DY f_{recoil} efficiencies, measured in the nominal non-DY samples after the $p_{\text{T,rel}}^{\text{miss,track}}$ cut, for (a-b) 0-jet and (c-d) 1-jet. For (a) and (c), the extrapolation is plotted in bins of $E_{\text{T,rel}}^{\text{miss,calo}}$, for events with $m_{\ell\ell} < 55$ GeV. For (b) and (d), the extrapolation is plotted in bins of $m_{\ell\ell}$ for events with $E_{\text{T,rel}}^{\text{miss,calo}} > 40$ GeV. The gray bands show the assigned systematic uncertainty, computed as explained in the text.

the Z-peak and in a given $m_{\ell\ell}$ bin is plotted for that $m_{\ell\ell}$ bin, as shown in Figure 4.58, for data and the two available DY MC samples. Again, the assigned systematic uncertainty is indicated by the gray bands and covers the majority of the points in the plot. The exception is the very high $m_{\ell\ell}$ bin for the 1-jet channel, shown in Figure 4.58b, which is considered far from the low $m_{\ell\ell}$ region of interest here.

4.7.3.3 Summary of Pacman numbers

It is important to note that the procedure used to assign systematic uncertainties to the Pacman efficiencies measured in data, does not rely on MC to model the data f_{recoil} distributions. Even though simulation is used, only relative differences in MC-to-MC comparisons are considered and they are validated using data-to-data comparisons as well.

Table 4.15 summarizes the Pacman f_{recoil} efficiencies measured in data and the corresponding systematic and statistical uncertainties, for the 0- and 1-jet SF channels. The result of a closure test on the Pacman method is included, that was performed by

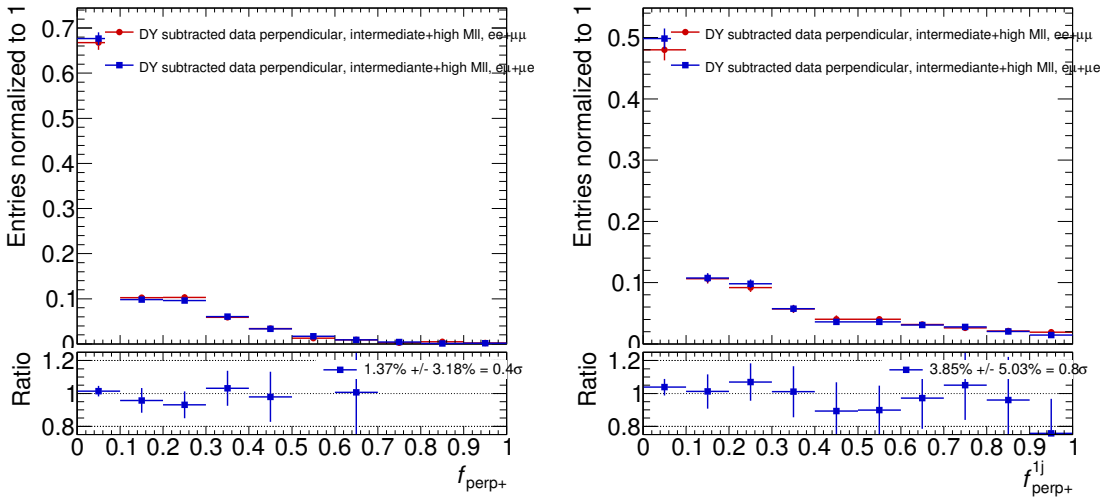

FIGURE 4.54: Comparison between SF and DF f_{perp} shapes in data, for (a) 0-jet and (b) 1-jet. Events have $55 < m_{\ell\ell} < m_Z - 15$ GeV or $m_{\ell\ell} > m_Z + 15$ GeV. The DY contamination has been subtracted, using simulation. The ratios below the plots compare the SF and DF distributions. More details in the legend of Figure 4.44.

applying the described procedure to MC simulated events as if they were data. The final estimate on DY was compared to the true DY content of the simulated events. As indicated in Table 4.15, the difference is compatible with zero, indicating closure of the Pacman method.

	0-jet	**1-jet**
$\varepsilon^{\textbf{non-DY}}$	0.69 ± 0.01	0.64 ± 0.02
DF $\rightarrow$ SF extrapolation	0.8%	1.2%
statistical uncertainty	1.8%	3.0%
total uncertainty	1.9%	3.2%
$\varepsilon^{\textbf{non-DY}}_{\boldsymbol{Z}\textbf{peak}}$	0.68 ± 0.02	0.66 ± 0.03
DF $\rightarrow$ SF extrapolation	1.9%	2.4%
statistical uncertainty	2.5%	3.9%
total uncertainty	3.1%	4.5%
$\varepsilon^{\textbf{DY}}$	0.14 ± 0.05	0.13 ± 0.04
Z peak $\rightarrow$ low $m_{\ell\ell}$ extrapolation	32%	16%
statistical uncertainty	9.4%	16%
total uncertainty	38%	32%
estimated DY yield in SF SR	88 ± 43	26 ± 12
statistical uncertainty	15%	29%
total uncertainty	49%	45%
MC closure	$1.2\% \pm 6.5\%$	$0.8\% \pm 11\%$

TABLE 4.15: Summary of Pacman f_{recoil} efficiencies and uncertainties.

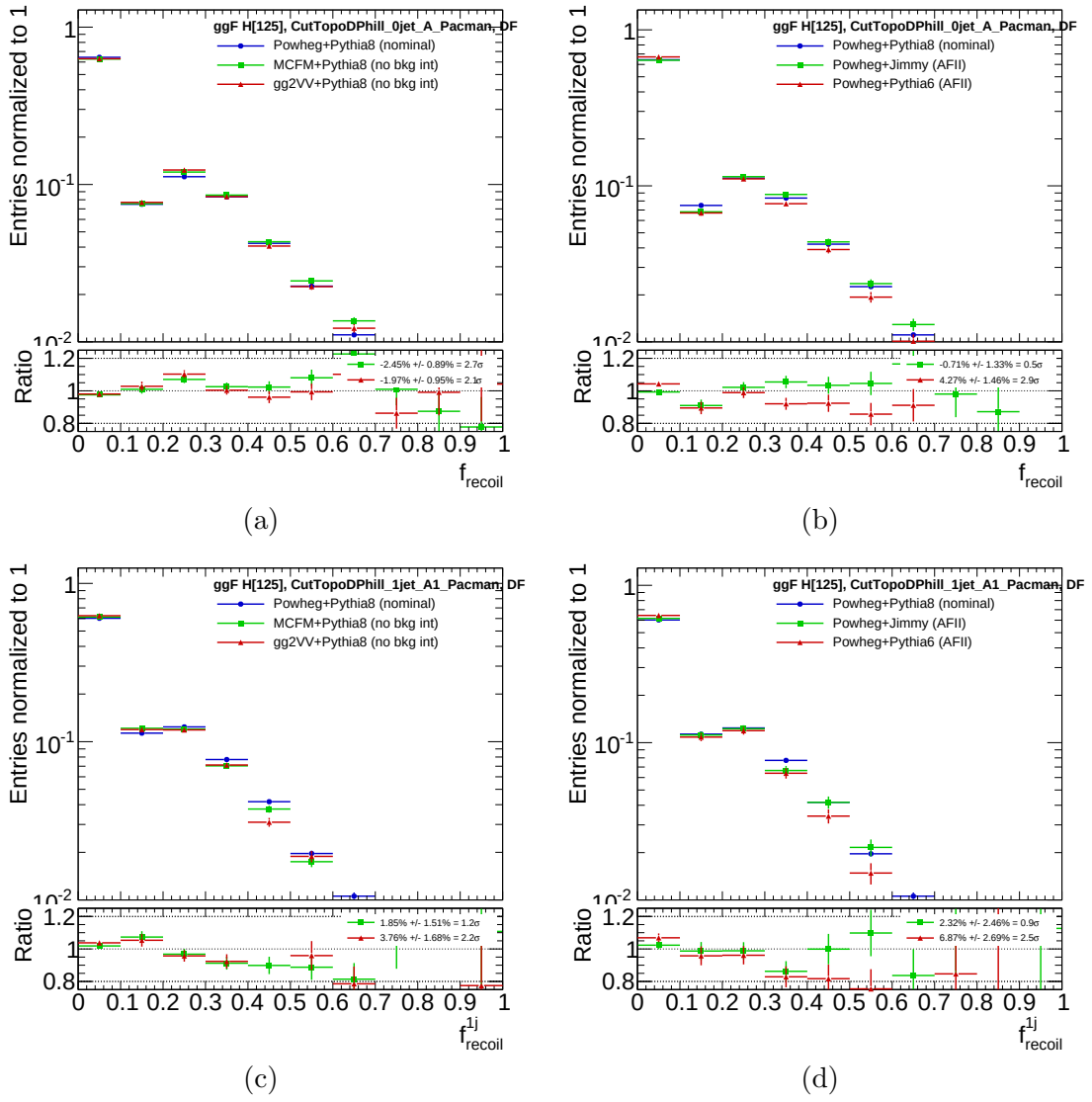

FIGURE 4.55: Comparison between f_{recoil} shapes of DF signal events, predicted by different MC generators, in the low $m_{\ell\ell}$ signal region ($m_H = 125$ GeV). (a-b) show events in the 0-jet category, and (c-d) show events in the 1-jet category. The ratios below the plots compare the shapes predicted by different generators with the shape predicted by the nominal generator for signal events. More details in the legend of Figure 4.44.

4.8 Signal extraction

As already discussed, the presence of two neutrinos in the final state does not allow for the full reconstruction of the Higgs resonance mass. Only the transverse component of the event kinematics is entirely accessible and, therefore, the transverse mass is used to provide the final discrimination between signal and background events.

At the truth particle level, the transverse mass is unambiguously defined using the final state leptons and neutrinos:

$$m_{\text{T}}^{\text{truth}} = \sqrt{\left(E_{\text{T}}^{\ell\ell} + E_{\text{T}}^{\nu\nu}\right)^2 - \left(\boldsymbol{p}_{\text{T}}^{\ell\ell} + \boldsymbol{p}_{\text{T}}^{\nu\nu}\right)^2}, \tag{4.20}$$

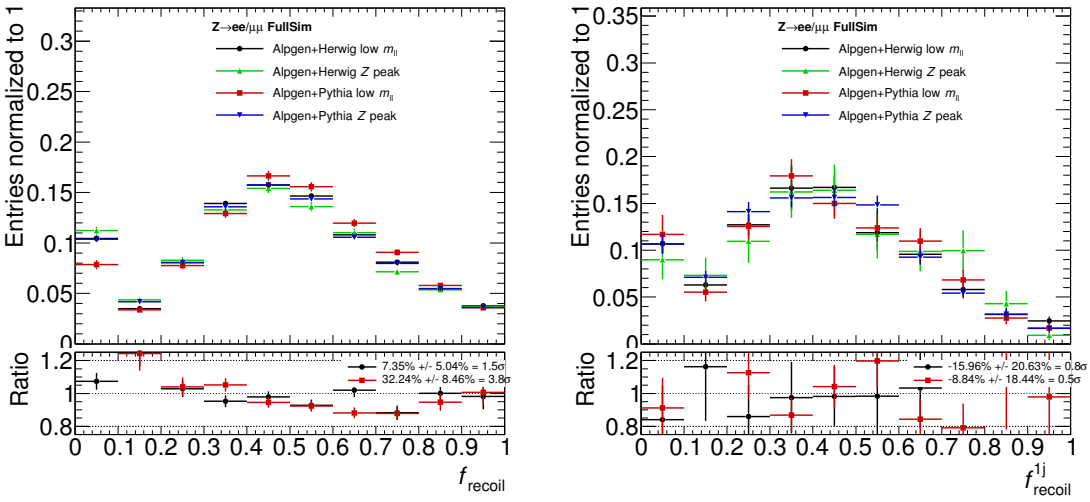

(a) (b)

FIGURE 4.56: Comparison between SF DY f_{recoil} shapes in the low $m_{\ell\ell}$ signal region and in the Z-peak, in the (a) 0-jet and (b) 1-jet categories, for two different MC generators. The ratios below the plots compare the low $m_{\ell\ell}$ and Z-peak distributions for each generator. The legend on the ratio plot indicates the relative difference in efficiency of the $f_{\text{recoil}} < 0.1$ cut, between the low $m_{\ell\ell}$ events and the Z-peak events. The uncertainty shown is statistical.

where:

$$E_{\text{T}}^{\ell\ell(\nu\nu)} = \sqrt{m^2_{\ell\ell(\nu\nu)} + \boldsymbol{p}_{\text{T}}^{\ell\ell(\nu\nu)^2}}, \tag{4.21}$$

with $m_{\ell\ell(\nu\nu)}$ denoting the invariant mass of the dilepton (dineutrino) system, and $\boldsymbol{p}_{\text{T}}^{\ell\ell(\nu\nu)}$ the vectorial sum of the transverse momentum of the two leptons (neutrinos). The distribution of $m_{\text{T}}^{\text{truth}}$ for $H \to WW^* \to \ell\nu\ell\nu$ events shows a Jacobian peak at the true Higgs boson mass. Therefore, the following is verified: $m_{\text{T}}^{\text{truth}} \leqslant m_H$.

At the reconstruction level, different transverse mass definitions can be considered, depending on how the information from the missing individual neutrino components is included. The definition most commonly used by the $H \to WW^* \to \ell\nu\ell\nu$ analysis in ATLAS consists simply of making the following substitutions in Equation 4.20:

$$\boldsymbol{p}_{\text{T}}^{\nu\nu} = \boldsymbol{p}_{\text{T}}^{\text{miss}} \quad \text{and} \quad E_{\text{T}}^{\nu\nu} = E_{\text{T}}^{\text{miss}} = |\boldsymbol{p}_{\text{T}}^{\text{miss}}|. \tag{4.22}$$

One therefore obtains:

$$m_{\text{T}} = \sqrt{\left(E_{\text{T}}^{\ell\ell} + E_{\text{T}}^{\text{miss}}\right)^2 - \left(\boldsymbol{p}_{\text{T}}^{\ell\ell} + \boldsymbol{p}_{\text{T}}^{\text{miss}}\right)^2}, \tag{4.23}$$

with $E_{\text{T}}^{\ell\ell}$ defined as in Equation 4.21.

Another transverse mass definition can be used, under the assumption that the W bosons decay at rest in the Higgs boson frame. In this case, the invariant mass of the dineutrino system will be equal to the invariant mass of the dilepton system,

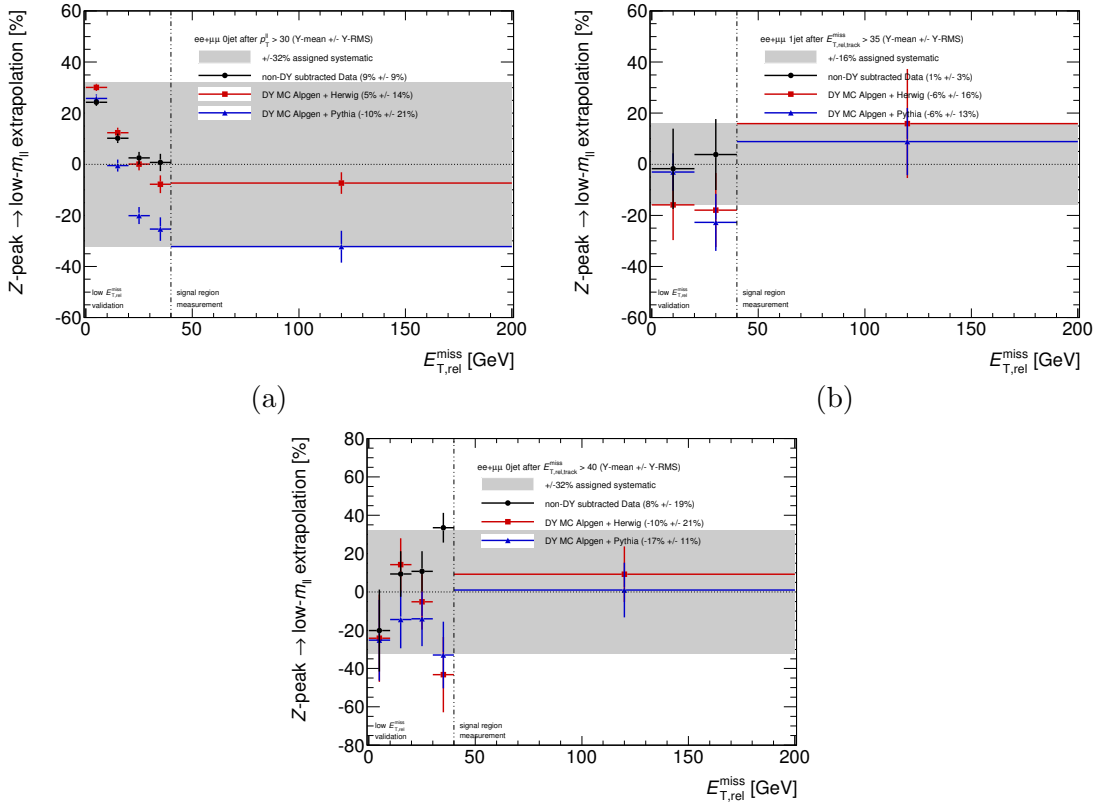

FIGURE 4.57: Z-peak → low $m_{\ell\ell}$ extrapolation as a function of $E^{\mathrm{miss,calo}}_{\mathrm{T,rel}}$, for events with: (a) 0-jets after the $p^{\ell\ell}_{\mathrm{T}}$ selection; (b) 1-jet after the $p^{\mathrm{miss,track}}_{\mathrm{T,rel}}$ selection; and (c) 0-jets after the $p^{\mathrm{miss,track}}_{\mathrm{T,rel}}$ selection. The black bullets show data, with the non-DY contribution subtracted using simulation; the red squares show the nominal DY MC sample; the blue triangles show an alternative DY MC sample. The gray bands display the assigned systematic uncertainties, taken from the largest extrapolation seen in MC at high $E^{\mathrm{miss,calo}}_{\mathrm{T,rel}}$. The numbers in the legend are informative only and show the mean ± RMS of the distributions over the y-axis.

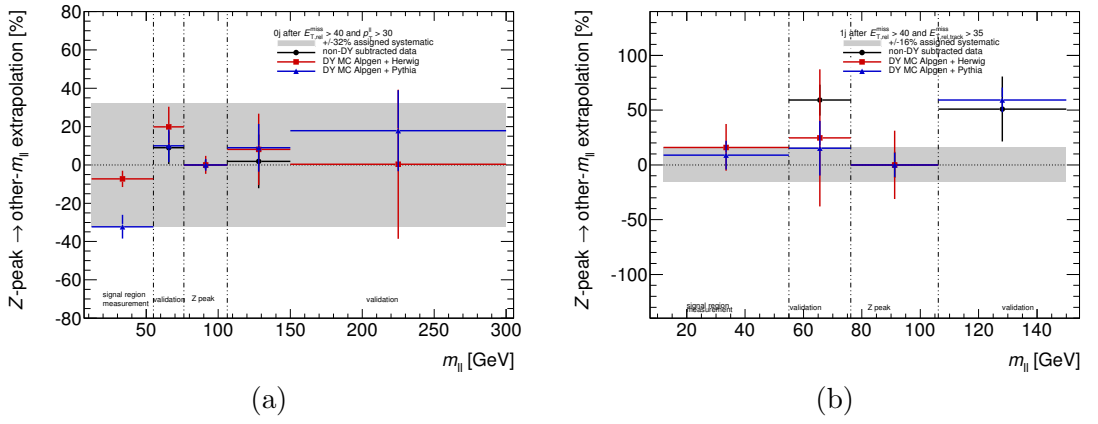

FIGURE 4.58: Z-peak → other $m_{\ell\ell}$ regions extrapolation, as a function of $m_{\ell\ell}$, for events in the (a) 0-jet and (b) 1-jet categories. Data and two different DY MC samples are shown, for events with $E^{\mathrm{miss,calo}}_{\mathrm{T,rel}} > 40$ GeV. The gray bands show the assigned systematic uncertainty, taken from the largest extrapolation seen in MC at high $E^{\mathrm{miss,calo}}_{\mathrm{T,rel}}$, between the Z peak and low $m_{\ell\ell}$ (first bin).

i.e. $m_{\nu\nu} = m_{\ell\ell}$. One can then write:

$$m_{\mathrm{T}}^{\mathrm{CSC}} = \sqrt{\left(E_{\mathrm{T}}^{\ell\ell} + E_{\mathrm{T}}^{\nu\nu,\mathrm{approx}}\right)^2 - \left(\boldsymbol{p}_{\mathrm{T}}^{\ell\ell} + \boldsymbol{p}_{\mathrm{T}}^{\mathrm{miss}}\right)^2}, \tag{4.24}$$

where $E_{\mathrm{T}}^{\ell\ell}$ is defined as in Equation 4.21 and:

$$E_{\mathrm{T}}^{\nu\nu,\mathrm{approx}} = \sqrt{m_{\ell\ell}^2 + \boldsymbol{p}_{\mathrm{T}}^{\mathrm{miss}\,2}}. \tag{4.25}$$

The $m_{\mathrm{T}}^{\mathrm{CSC}}$ definition exactly matches the true transverse mass for $m_H = 2 \times m_W$, where the $H \to WW$ decay occurs at threshold. Below threshold, the assumption of a decay at rest is still a very good approximation.

Yet another proposed transverse mass definition is:

$$m_{\mathrm{T}}^{\ell\ell\nu} = \sqrt{2 p_{\mathrm{T}}^{\ell\ell} E_{\mathrm{T}}^{\mathrm{miss}} \left(1 - \cos\Delta\phi\right)}, \tag{4.26}$$

in analogy to the transverse mass of the W boson m_{T}^{W} (see Section 4.5). $\Delta\phi$ refers to the azimuthal separation between $\boldsymbol{p}_{\mathrm{T}}^{\ell\ell}$ and $\boldsymbol{p}_{\mathrm{T}}^{\mathrm{miss}}$. This definition can be obtained from Equations 4.23 or 4.24, by taking $m_{\ell\ell} = 0$.

Despite the name, the transverse mass definitions proposed so far are not purely transverse kinematic quantities. Such a definition, labeled m_{Trans}, can be constructed by consistently replacing $m_{\ell\ell}$ by the transverse mass of the dilepton system in Equation 4.23. One thus obtains:

$$m_{\mathrm{Trans}} = \sqrt{\left(E_{\mathrm{Trans}}^{\ell\ell} + E_{\mathrm{T}}^{\mathrm{miss}}\right)^2 - \left(\boldsymbol{p}_{\mathrm{T}}^{\ell\ell} + \boldsymbol{p}_{\mathrm{T}}^{\mathrm{miss}}\right)^2}, \tag{4.27}$$

with:

$$E_{\mathrm{Trans}}^{\ell\ell} = \sqrt{m_{\mathrm{T}}^{\ell\ell\,2} + \boldsymbol{p}_{\mathrm{T}}^{\ell\ell\,2}} \quad \text{and} \quad m_{\mathrm{T}}^{\ell\ell} = \sqrt{m_{\ell\ell}^2 + p_{\mathrm{T}}^{\ell\ell\,2}}. \tag{4.28}$$

The transverse mass distributions for a Higgs signal with $m_H = 125$ GeV, at truth level and reconstructed level computed with different definitions, are shown in the top row of Figure 4.59. The bottom row of Figure 4.59 displays the corresponding difference between $m_{\mathrm{T}}^{\mathrm{truth}}$ and the different definitions at reconstructed level. $H \to WW^* \to \ell\nu\ell\nu$ events from both the SF and DF channels are shown. In Figure 4.59a, events have passed the selection up to the minimum dilepton invariant mass requirement (see Tables 4.6 and 4.7). In Figures 4.59b and 4.59c, events are required to pass the full event selection of the 0- and 1-jet categories, respectively.

For an event selection consisting only of two signal leptons with minimum requirements (Figure 4.59a), the shapes of the different transverse mass distributions differ significantly. m_{T} and m_{Trans} have the most similar shapes and appear to peak closer to the $m_{\mathrm{T}}^{\mathrm{truth}}$ peak, than the remaining definitions. However, the full event selection of the $H \to WW^* \to \ell\nu\ell\nu$ analysis shapes the transverse mass distributions, making them more similar among each other. After the full event selection, $m_{\mathrm{T}}^{\ell\ell\nu}$ has a mean closest to the mean of m_{Truth}, but also the worst RMS. Furthermore, the difference with respect

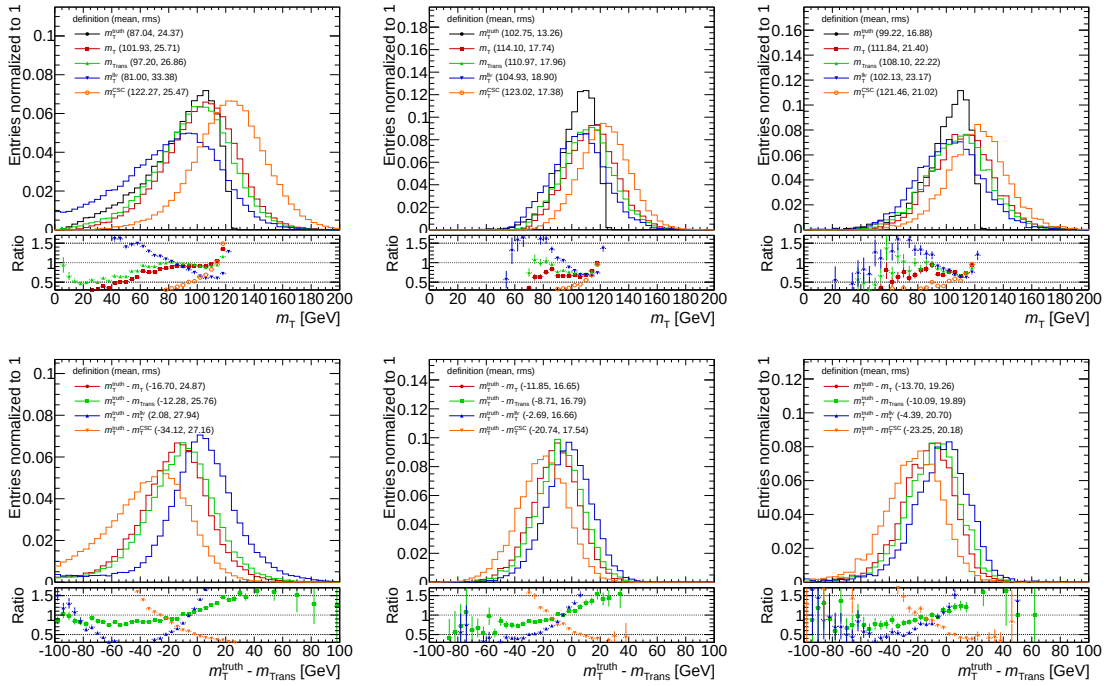

FIGURE 4.59: The distributions on top shown the transverse mass of simulated signal events. The true transverse mass - $m_{\mathrm{T}}^{\mathrm{truth}}$ is shown in black. The colored histograms show different reconstructions of the transverse mass: m_{T} in red, m_{Trans} in green, $m_{\mathrm{T}}^{\ell\ell\nu}$ in blue, and $m_{\mathrm{T}}^{\mathrm{CSC}}$ in orange. The distributions below show the difference between $m_{\mathrm{T}}^{\mathrm{truth}}$ and the different computations of the reconstructed transverse mass. The distributions are shown at different stages of the event selection: (a) up to minimum dilepton invariant mass; (b) full event selection of 0-jet category; (c) full event selection of 1-jet category. All leptons flavors are included.

to truth indicates that all transverse mass definitions produce similar results in terms of resolution, with each one giving different biases.

Since the transverse mass shows a broad distribution and the sensitivity to the Higgs mass is poor, it is more interesting to investigate which definition allows for a better separation between signal and background. For this purpose, the different definitions were compared to the nominal m_{T} computation, for signal and background processes, via the ratios shown in Figure 4.60. Figures 4.60a, 4.60b and 4.60c, show the distributions of $m_{\mathrm{T}}^{\ell\ell\nu}/m_{\mathrm{T}}$, $m_{\mathrm{T}}^{\mathrm{CSC}}/m_{\mathrm{T}}$ and $m_{\mathrm{Trans}}/m_{\mathrm{T}}$ respectively, for signal, WW, and all background events passing the full 0-jet category event selection. Figures 4.60d, 4.60e and 4.60f display the corresponding ratios in the 1-jet signal region.

The ratios in Figure 4.60 show that the different transverse mass definitions produce differently-shaped distributions for signal (as already seen in Figure 4.59) as well as background processes. However, the double ratios shown in the pads below each distribution compare directly the transverse mass ratios for signal and background processes. These double ratios are very close to unity in the range $0.75m_H < m_{\mathrm{T}} < m_H$, where the signal-to-background ratio is highest. This indicates that the shape difference introduced by the different definitions is similar for signal and background events in

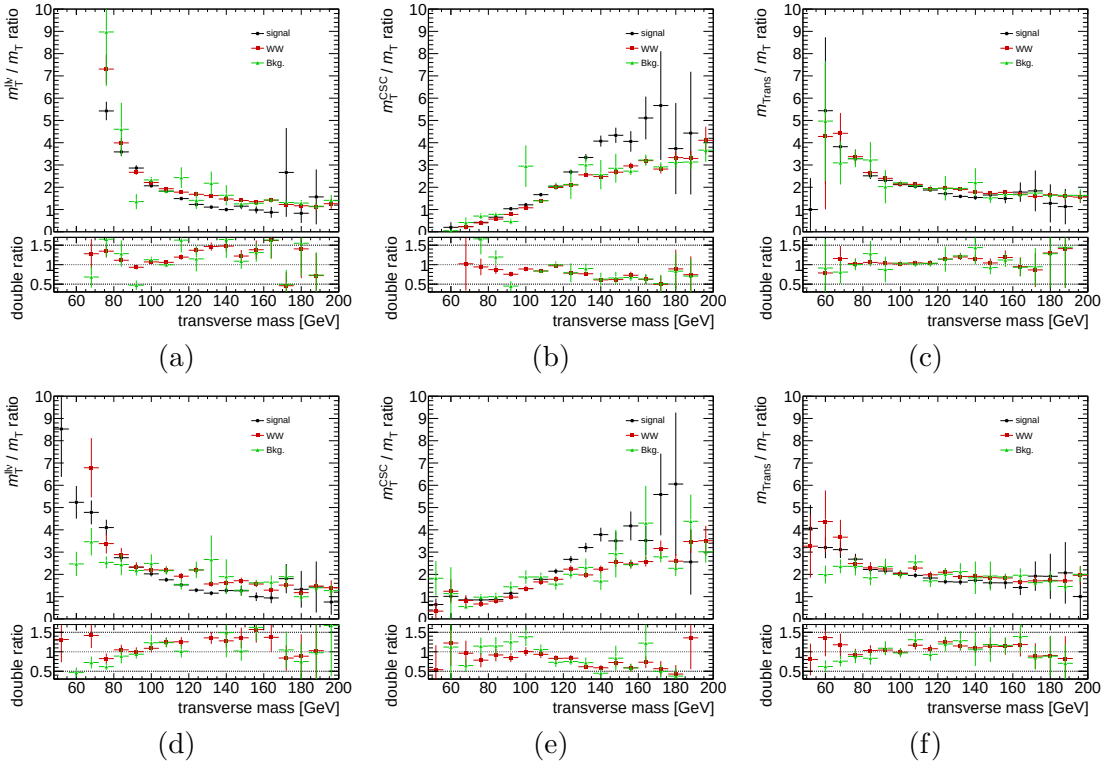

FIGURE 4.60: Ratios between the distributions of: (a) and (d) $m_{\mathrm{T}}^{\ell\ell\nu}/m_{\mathrm{T}}$; (b) and (e) $m_{\mathrm{T}}^{\mathrm{CSC}}/m_{\mathrm{T}}$; and (c) and (f) $m_{\mathrm{Trans}}/m_{\mathrm{T}}$, for signal (black), WW (red), and total background events (green). Events have passed the full selection of the (a-c) 0-jet and (d-f) 1-jet categories. All leptons flavors are included.

the most significant transverse mass window. As a result, no definition provides better signal-to-background discrimination compared to the nominal m_{T}.

The expected signal significance and expected precision on the signal strength (see Section 1.2.3.4 or 4.10 ahead) were computed for the full analysis, using the different transverse mass definitions. Variations of less than 1% were observed, supporting the conclusions drawn from the previous distributions. Thus, the nominally used m_{T} definition was kept.

These small differences in performance are interpreted as a consequence of the SM Higgs signal originating events with low invariant mass of the dilepton system. Given that each of the presented transverse mass definitions differs only in the $m_{\ell\ell}$ term, it is expected that low values of $m_{\ell\ell}$ will not induce large variations in transverse mass shapes, especially when the signal Higgs topology is selected.

Having chosen the way to define the transverse mass, the flavor of $E_{\mathrm{T}}^{\mathrm{miss}}$ to be used in the computation was also investigated. The m_{T} distributions for a Higgs signal with $m_H = 125$ GeV, at truth level and reconstructed level using different flavors of $E_{\mathrm{T}}^{\mathrm{miss}}$, are shown in the top row of Figure 4.61. The bottom row indicates the difference between the different m_{T} computations and $m_{\mathrm{T}}^{\mathrm{truth}}$. $H \to WW^* \to \ell\nu\ell\nu$ events from both the SF and DF channels are shown. In Figure 4.61a, events have passed the selection up to the minimum dilepton invariant mass requirement (see Tables 4.6 and 4.7). In

Figures 4.61b and 4.61c, events are required to pass the full event selection of the 0- and 1-jet categories, respectively.

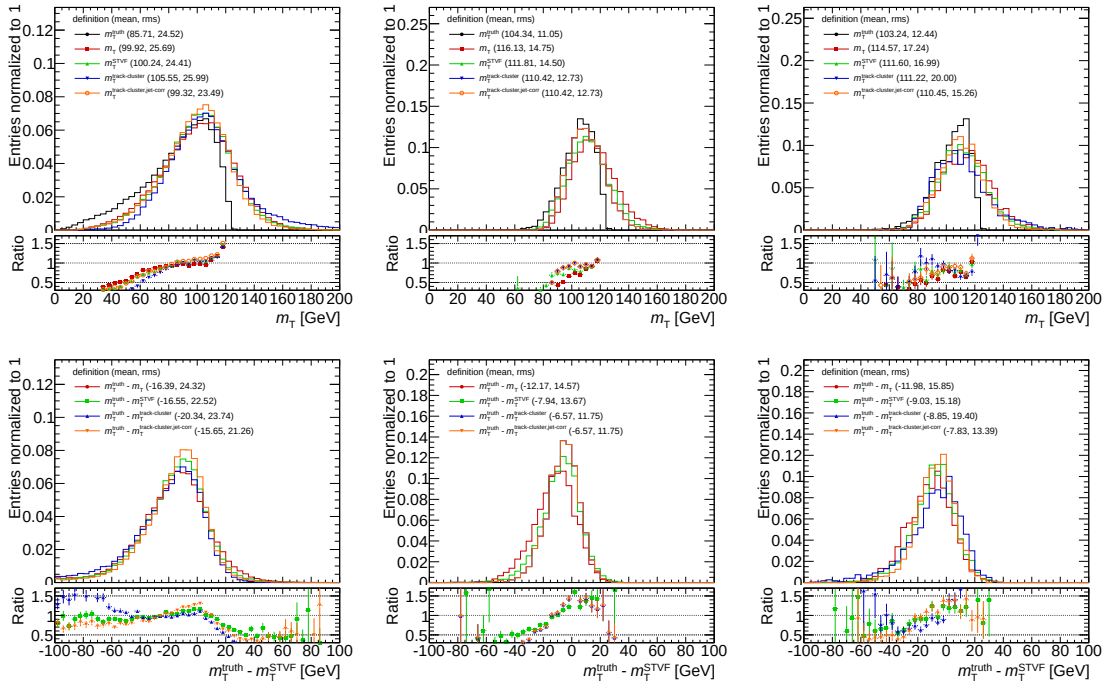

FIGURE 4.61: The distributions on top shown the transverse mass of simulated signal events. The true transverse mass - $m_{\mathrm{T}}^{\mathrm{truth}}$ is shown in black. The colored histograms show computations of m_{T} with different $E_{\mathrm{T}}^{\mathrm{miss}}$ flavors: $E_{\mathrm{T}}^{\mathrm{miss,calo}}$ in red, $E_{\mathrm{T}}^{\mathrm{miss,STVF}}$ in green, $p_{\mathrm{T}}^{\mathrm{miss,track}}$ in blue, and $p_{\mathrm{T}}^{\mathrm{miss,jetCorr}}$ in orange. The distributions below show the difference between $m_{\mathrm{T}}^{\mathrm{truth}}$ and the different computations of m_{T}. The distributions are shown at different stages of the event selection: (a) up to minimum dilepton invariant mass; (b) full event selection of 0-jet category; (c) full event selection of 1-jet category. All leptons flavors are included.

Figure 4.61 shows that using $p_{\mathrm{T}}^{\mathrm{miss,jetCorr}}$ to calculate the transverse mass leads to a better performance. In general, both the bias and the resolution of the Higgs m_{T} with respect to truth are improved compared to other flavors, and especially with the $E_{\mathrm{T}}^{\mathrm{miss,calo}}$ flavor used in previous iterations of the $H \to WW^* \to \ell\nu\ell\nu$ analysis. A more quantitative analysis was performed by computing the signal significance and expected precision on the signal strength. Improvements of up to $\sim 20\%$ were seen when using $p_{\mathrm{T}}^{\mathrm{miss,jetCorr}}$. Thus, this flavor was kept for the default computation of m_{T} in the $H \to WW^* \to \ell\nu\ell\nu$ analysis.

4.9 Systematic uncertainties

Two types of systematic uncertainties affecting the $H \to WW^* \to \ell\nu\ell\nu$ analysis can be considered. Theoretical uncertainties are specific to each process, and are related to the way the process is modeled. Experimental uncertainties are common to all signal and

background processes, and originate from the uncertainties on event reconstruction in the ATLAS detector, as described in Section 2.6.

4.9.1 Theoretical uncertainties

The Higgs signal process is modeled using simulation. The details about the computation of the total cross-sections, branching fractions, and corresponding uncertainties were discussed in detail in Section 1.2.3.1. Additional uncertainties are considered due to the jet binning categorization performed in the analysis. These were evaluated using the jet-veto efficiency method [54, 196] for the ggF categories and the Stewart-Tackmann method [197] for the VBF category. Finally, acceptance uncertainties are computed for each of the signal region categories in the analysis. These include PDF modeling and scale uncertainties, evaluated as described in Section 1.2.3.1. An uncertainty due to the ME and matching of the ME and the PS is computed by comparing the predictions of Powheg + Herwig and aMC@NLO + Herwig. Uncertainties due to UE and PS models are estimated through the comparison of Powheg + Herwig and Powheg + Pythia8. These uncertainties are summarized in Table 4.16.

Source		**0-jet**	**1-jet**
Total cross-section		10	10
Jet binning/veto		11	25
Acceptance	scale	1.4	1.9
	PDF	3.2	2.8
	matching ME-PS	2.5	1.4
	UE/PS model	6.4	2.1

Table 4.16: Different sources of uncertainty on the ggF signal yield for events in the SF 0- and 1-jet categories. Numbers are shown in [%].

As for the systematics impacting the different background yields, they have been discussed in detail in Sections 4.6 and 4.7.

4.9.2 Experimental uncertainties

The experimental sources of systematic uncertainty considered in the analysis are discussed next.

Jets The determination of the jet energy scale and resolution, and associated systematic uncertainties has been discussed in Section 2.6.4. JES and JER are one of the dominant sources of experimental uncertainty in the $H \to WW^* \to \ell\nu\ell\nu$ analysis. The uncertainties on the JES vary between $1-7\%$, depending on p_{T} and η of the jet. The relative uncertainty on the JER ranges from $2-40\%$.

***b*-tagging** Systematic uncertainties related to b-tagging, determined as described in Section 2.6.5, are also dominant in the $H \to WW^* \to \ell\nu\ell\nu$ analysis. The uncertainties on the b-tag efficiency range from $< 1-7.8\%$, depending on the jet p_{T}.

The uncertainties on the mistag and c-tag rate vary between $9-19\%$ and $6-14\%$, respectively.

Leptons Uncertainties on the reconstruction, identification, isolation and trigger efficiencies for electrons and muons, as well as their energy/momentum scale and resolution have been discussed in Sections 2.6.3 and 2.6.2. These are generally smaller than 1%, except for the uncertainty on the electron identification, which varies between $0.2-2.7\%$, and the uncertainty on the isolation efficiencies, which amount to 1.6% (2.7%) for electrons (muons) with $p_{\mathrm{T}} < 15$ GeV.

Missing transverse momentum The changes in the jet and leptons energy/momentum due to the systematic variations are propagated to the computation of the missing transverse momentum, discussed in Section 2.6.6. Thus, the uncertainties on $E_{\mathrm{T}}^{\mathrm{miss}}$ are fully correlated to the uncertainties on the high-p_{T} objects used in the analysis. Additional sources of uncertainty on the scale and resolution of $E_{\mathrm{T}}^{\mathrm{miss}}$ are considered, as also discussed in Section 2.6.6. For the calorimeter-based measurement of $E_{\mathrm{T}}^{\mathrm{miss}}$, these result in variations in the scale of $0.2-0.3$ GeV and variations in the resolution between $1-4\%$. For the track-based flavors of $E_{\mathrm{T}}^{\mathrm{miss}}$, the scale variations range from $0.3-1.4$ GeV, while the resolution varies between $1.5-3.3$ GeV.

Pile-up Systematic uncertainties on pile-up modeling are assessed by varying the 0.9 rescaling factor used to produce a flat data-to-MC ratio on the $\langle\mu\rangle$ distribution (see Section 4.3.2). 0.8 and 1.0 are taken as variations of the rescaling factor. These variations change the background (signal) yields by $\sim 4\%$ ($\sim 2\%$).

Luminosity The uncertainty on the integrated luminosity [198] of the 7 TeV and 8 TeV datasets is 1.8% and 2.8%, respectively.

4.10 Statistical treatment

A statistical treatment is employed to measure the Higgs signal in the $H \to WW^* \to \ell\nu\ell\nu$ analysis. It involves the definition of a likelihood function, that encodes the event yields of several different samples defined in the analysis, which are simultaneously fitted. These samples are the different signal regions defined by the categorization in Figure 4.4, and the control regions used to measure the different background sources, as described in Section 4.6.2. The sensitivity of the analysis is improved by further splitting the events in the DF 0- and 1-jet categories. The event selection remains unchanged with respect to what was presented in Table 4.7, but 12 orthogonal signal regions are created for each of these two categories:

- two according to the flavor of the leading lepton - electron and muon - exploiting the different contamination of backgrounds originating from fake leptons;
- two according to the invariant mass of the dilepton system - $10 < m_{\ell\ell} < 30$ GeV and $30 < m_{\ell\ell} < 55$ GeV - exploiting the distinct low $m_{\ell\ell}$ distribution of the signal;

- three according to the p_{T} of the subleading lepton - $10 < p_{\mathrm{T}}^{\mathrm{sub}} < 15$ GeV, $15 < p_{\mathrm{T}}^{\mathrm{sub}} < 20$ GeV and $p_{\mathrm{T}}^{\mathrm{sub}} > 20$ GeV - exploiting the low $p_{\mathrm{T}}^{\mathrm{sub}}$ distribution of the signal, as well as the rapidly falling $p_{\mathrm{T}}^{\mathrm{sub}}$ spectrum for background processes with a single W boson.

The remaining categories in the analysis (i.e. SF 0- and 1-jet, and 2-jet categories) are not split any further.

The m_{T} distributions (see Section 4.8) are fitted for all ggF-enriched signal regions. For the 0- and 1-jet categories in particular, the m_{T} distributions are binned using a variable binning scheme. It is defined to optimize the result in each of the signal regions, providing an approximately flat distribution for the signal. Ten bins are defined for the 0-jet categories, while the 1-jet signal regions use six bins in m_{T}. The analysis of the two VBF-enriched categories employs a boosted decision tree (BDT) MVA technique, and the output discriminant of this algorithm is fitted in this case.

The details of the likelihood and of the statistical procedure are described in what follows.

4.10.1 Likelihood function

The likelihood - $\mathcal{L}(\mu, \boldsymbol{\theta})$ - is a function of the signal strength μ and of set of nuisance parameters (NP) $\boldsymbol{\theta} = \{\theta_a, \theta_b, \ldots\}$, which represent the uncertainties. The signal strength μ is the parameter of interest (POI) that we wish to determine, and is a free parameter of the fit. It scales the signal yield relative to the SM prediction, which means $\mu = 0$ corresponds to a the background only hypothesis, while $\mu = 1$ refers to the SM signal expectation. Simply put, the likelihood is a probability, that expresses how likely the values of the POI and the NPs are. The true values of these parameters are unknown quantities, that one estimates by maximizing the likelihood in the fit.

The likelihood is written as a product of different probability distribution functions:

$$\begin{aligned}\mathcal{L}(\mu, \boldsymbol{\theta}) = &\prod_{c}^{\text{SRs}} \prod_{i}^{\text{bins}} \mathcal{P}\left(N_{ci} \,\middle|\, \mu \cdot S_{ci}(\boldsymbol{\theta}) + \sum_{b}^{\text{bkgs}} \mu_b \cdot B_{bci}(\boldsymbol{\theta})\right) \times \\ &\times \prod_{r}^{\text{CRs}} \mathcal{P}\left(N_r \,\middle|\, \sum_{b}^{\text{bkgs}} \mu_b \cdot B_{br}(\boldsymbol{\theta})\right) \times \\ &\times \prod_{k}^{\text{NPs}} \mathcal{F}_k\left(\tilde{\theta}_k \,\middle|\, \theta_k\right)\end{aligned} \tag{4.29}$$

The first term described the signal regions, the second term contains the control regions, and the third term provides constraints on the nuisance parameters. These terms are described in more detail in the following.

The first term in Equation 4.29 describes the signal regions using Poisson functions:

$$\mathcal{P}(N|\lambda) = \frac{e^{-\lambda}\lambda^N}{N!}, \tag{4.30}$$

for the probability of observing a N events in the data, given the signal plus background expectation λ. This term contains the product of different Poisson functions defined for each of the m_{T} bins in each of the signal regions. N_{ci}, S_{ci} and B_{bci} denote, respectively, the observed yield, the expected signal yield and the expected yield of background source b, in bin i of SR c. As will be clarified ahead, the expected yields are functions of the nuisance parameters ($\boldsymbol{\theta}$). As explained and noted in Equation 4.29, μ is the signal strength that scales the signal expectation. The parameters μ_b are also strength parameters and scale the different background expectations, so these represent the normalization factors described in Section 4.6, which are free parameters of the fit.

The second term in Equation 4.29 describes the control regions presented in Section 4.6.2. It is defined using Poisson functions, similar to the first term which contains the likelihood for the signal regions. One difference is that there is no product over the different m_{T} bins, since only the overall normalization is extracted from the CRs. Furthermore, the signal expectation in the CRs was not explicitly written out, as the control regions are designed to be free of signal. This second term of the likelihood is designed to constrain the normalization factors μ_b, that are also present in the first term of the likelihood. It is important to note that no CR terms of this type are included in the likelihood for top background in the 0-jet channel, W + jets and multijet backgrounds, which are estimated independently as described in Sections 4.6.1 and 4.6.2.3.

As mentioned, the signal and background expectations, written in the first two terms of Equation 4.29, are functions of the nuisance parameters, to account for the impact of the uncertainties on the expected yields. These functions are parametrized such that the response of S and B to each NP θ_k is factorized from the nominal value, S_0 and B_0, of the expected yields:

$$S(\boldsymbol{\theta}) = S_0 \times \prod_{k}^{\mathrm{NPs}} \nu(\theta_k) \quad \text{and} \quad B(\boldsymbol{\theta}) = B_0 \times \prod_{k}^{\mathrm{NPs}} \nu(\theta_k). \tag{4.31}$$

Different parameterizations $\nu(\theta)$ are considered depending on the systematic uncertainty represented by the NP θ, and will be described in what follows. It should be noted that not all NPs affect each expected yield. As clarified in Section 4.9, some uncertainties apply to the signal, to a particular source of background only, or to a certain signal regions only. Conversely, some uncertainties apply to all processes and, therefore, the corresponding θ will impact all yields in a correlated way.

The third term in Equation 4.29 describes the product of different auxiliary functions $\mathcal{F}_k$, designed to constrain the values of the nuisance parameters θ_k, by means of an auxiliary measurement $\tilde{\theta}_k$. As a consequence, the variations allowed on the expected signal and background yields (first and second terms of the likelihood), are also constrained through the parameterizations $\nu(\theta_k)$ in Equation 4.31. Two types of constraints are used in the analysis: unit Gaussian and Poisson.

Unit Gaussian constraints, defined as:

$$\mathcal{G}(\tilde{\theta}|\theta, 1) = \frac{1}{\sqrt{2\pi}} e^{(\tilde{\theta}-\theta)^2/2}, \tag{4.32}$$

are used for NPs θ representing the systematic uncertainties described in Section 4.9. If these uncertainties have no impact on the shape of the m_{T} distribution, and affect only the normalization on the individual backgrounds, the response function $\nu^{\mathrm{norm}}(\theta)$ is parametrized as:

$$\nu^{\mathrm{norm}}(\theta) = (1+\epsilon)^{\theta}, \tag{4.33}$$

where ϵ is evaluated by measuring $\nu^{\mathrm{norm}}(\theta)$ at $\theta = \pm 1$. For example, if $\epsilon = 3\%$, then the expected yield changes by $\pm 3\%$, when the quantity associated to θ (e.g. the JES) is varied by $\pm$ one standard deviation. Given that the constraint on θ is Gaussian, the expected number of events follows a log-normal distribution, centered at B_0 or S_0. This type of parametrization is considered for most sources of uncertainty. It is important to note that, since the systematics are applied to the individual sources of backgrounds, which are not distributed equally among the bins of m_{T}, the m_{T} shape of the total background will still vary under normalization systematics. In fact, the m_{T} shape of the total background is dominated by the individual normalizations of the different background sources, while the individual shapes are only a small effect. Nonetheless, in cases where the systematics affect the shape, a different response function is used for each bin i of m_{T}:

$$\nu_i^{\mathrm{shape}}(\theta) = 1 + \epsilon_i \cdot \theta. \tag{4.34}$$

In this case the expected yields are normally distributed.

Poisson constraints $\mathcal{P}(\tilde{\theta}|\zeta\theta)$, defined as in Equation 4.30, are used deal with statistical uncertainties, related to the finite size of the samples used in the analysis. If a particular background source has an expectation B_0, with an associated statistical uncertainty σ, then $\zeta = (B_0/\sigma)^2$ is the nominal value of $\tilde{\theta}$. The response function that multiplies the expected yields in this case is:

$$\nu^{\mathrm{stat}}(\theta) = \theta. \tag{4.35}$$

4.10.2 Pacman likelihood

As described in Section 4.7, the Pacman method uses data in specific regions of phase space, passing and failing the f_{recoil} selection, to determine the efficiency of the f_{recoil} cut for DY and non-DY processes, which include the Higgs signal. Data in the SF Z-peak is used to measure $\varepsilon_{\mathrm{DY}}$, while DF events are used to measure $\varepsilon_{\text{non-DY}}$ and $\varepsilon_{\text{non-DY}}^{Z\text{-peak}}$. Extrapolation uncertainties are assigned to each of the efficiencies. The Pacman method is implemented in the likelihood function. It involves defining separate Poisson functions for the data events that pass and fail the f_{recoil} requirement, in order to measure the efficiencies.

The following Poisson functions are defined similar to the control regions terms in Equation 4.29, for the different flavor regions used to extract the efficiency of the non-DY processes in the low $m_{\ell\ell}$ region:

$$\mathcal{P}_{e\mu}\left(N_{\mathrm{pass}} \,\middle|\, \varepsilon_{\text{non-DY}} \cdot B_{\text{non-DY}}\right) \times \mathcal{P}_{e\mu}\left(N_{\mathrm{fail}} \,\middle|\, (1-\varepsilon_{\text{non-DY}}) \cdot B_{\text{non-DY}}\right), \tag{4.36}$$

and in the Z peak:

$$\mathcal{P}_{e\mu}\left(N_{\text{pass}}^{Z\text{-peak}} \,\middle|\, \varepsilon_{\text{non-DY}}^{Z\text{-peak}} \cdot B_{\text{non-DY}}^{Z\text{-peak}}\right) \times \mathcal{P}_{e\mu}\left(N_{\text{fail}}^{Z\text{peak}} \,\middle|\, (1-\varepsilon_{\text{non-DY}}^{Z\text{-peak}}) \cdot B_{\text{non-DY}}^{Z\text{-peak}}\right). \quad (4.37)$$

N_{pass}, N_{fail}, $N_{\text{pass}}^{Z\text{-peak}}$ and $N_{\text{fail}}^{Z\text{-peak}}$ denote the observed number of $e\mu$ events that pass and fail the f_{recoil} selection (at low $m_{\ell\ell}$ and in the Z-window). The quantities $B_{\text{non-DY}}$ $B_{\text{non-DY}}^{Z\text{-peak}}$ denote the expected yields for the non-DY processes, without any f_{recoil} selection applied. The normalization factors (μ_b in Equation 4.29) of each individual non-DY background source are applied, though not explicitly written (they will be omitted in the following as well, for simplicity). No B_{DY} quantity is written for the expected DY yield, since $e\mu$ events are 100% pure in non-DY. These Poisson functions provide the constraints on $\varepsilon_{\text{non-DY}}$ and $\varepsilon_{\text{non-DY}}^{Z\text{-peak}}$, which will appear in the terms described ahead.

The same flavor Z-peak is included in the likelihood with the following function:

$$\begin{aligned}&\mathcal{P}_{ee+\mu\mu}\left(N_{\text{pass}}^{Z\text{-peak}} \,\middle|\, \varepsilon_{\text{DY}} \cdot \mu_{\text{DY}}^{Z\text{-peak}} \cdot B_{\text{DY}}^{Z\text{-peak}} + \varepsilon_{\text{non-DY}}^{Z\text{-peak}} \cdot B_{\text{non-DY}}^{Z\text{-peak}}\right) \times \\ &\times\mathcal{P}_{ee+\mu\mu}\left(N_{\text{fail}}^{Z\text{-peak}} \,\middle|\, (1-\varepsilon_{\text{DY}}) \cdot \mu_{\text{DY}}^{Z\text{-peak}} \cdot B_{\text{DY}}^{Z\text{-peak}} + (1-\varepsilon_{\text{non-DY}}^{Z\text{-peak}}) \cdot B_{\text{non-DY}}^{Z\text{-peak}}\right),\end{aligned} \quad (4.38)$$

which constrains ε_{DY}, according to $N_{\text{pass}}^{Z\text{-peak}}$ and $N_{\text{fail}}^{Z\text{-peak}}$, i.e. the observed number of $ee + \mu\mu$ events that pass and fail the f_{recoil} selection in the Z-peak. The expected non-DY contribution is now explicitly written, since it is not negligible, as discussed in Section 4.7. The term $\varepsilon_{\text{non-DY}}^{Z\text{-peak}}$ already appeared in Equation 4.37, where it is constrained. The normalization factor $\mu_{\text{DY}}^{Z\text{-peak}}$ normalizes the expected DY yield in the Z-peak to the data.

Finally, the following Poisson terms are written for the same flavor signal regions (the product over m_{T} bins is omitted for simplification):

$$\begin{aligned}&\mathcal{P}_{ee+\mu\mu}\left(N_{\text{pass}} \,\middle|\, \varepsilon_{\text{signal}} \cdot \mu \cdot S + \varepsilon_{\text{DY}} \cdot \mu_{\text{DY}} \cdot B_{\text{DY}} + \varepsilon_{\text{non-DY}} \cdot B_{\text{non-DY}}\right) \times \\ &\times\mathcal{P}_{ee+\mu\mu}\left(N_{\text{fail}} \,\middle|\, (1-\varepsilon_{\text{signal}}) \cdot \mu \cdot S + (1-\varepsilon_{\text{DY}}) \cdot \mu_{\text{DY}} \cdot B_{\text{DY}} + (1-\varepsilon_{\text{non-DY}}) \cdot B_{\text{non-DY}}\right).\end{aligned} \quad (4.39)$$

N_{pass} and N_{fail} are the observed events that pass and fail the f_{recoil} selection in the $ee + \mu\mu$ signal region. ε_{DY} and $\varepsilon_{\text{non-DY}}$ are constrained in Equations 4.38 and 4.36, respectively. μ_{DY} normalizes the expected DY yield and μ is the usual signal strength. S, B_{DY} and $B_{\text{non-DY}}$ are the expected signal, DY and non-DY yields, with no f_{recoil} selection.

The term $\varepsilon_{\text{signal}}$ in Equation 4.39 is the signal efficiency of the f_{recoil} selection. As discussed in Section 4.4.3, simulation indicates that the f_{recoil} efficiency for signal is generally lower than for non-DY backgrounds, as shown in Figures 4.22a and 4.24a. Thus, $\varepsilon_{\text{signal}}$ is parametrized as a function of $\varepsilon_{\text{non-DY}}$, so that the difference of efficiencies

is taken as a correction, as well as a systematic uncertainty:

$$\begin{aligned}\varepsilon_{\text{signal}}(\varepsilon_{\text{non-DY}}, \theta) = \varepsilon_{\text{non-DY}} \times \\ \times \left(1 - (1 - f_0)\frac{\varepsilon_{\text{non-DY}}(1 - \varepsilon_{\text{non-DY}})}{\varepsilon^0_{\text{non-DY}}(1 - \varepsilon^0_{\text{non-DY}})}\right) \times \\ \times \left(1 + \Delta\frac{\varepsilon_{\text{non-DY}}(1 - \varepsilon_{\text{non-DY}})}{\varepsilon^0_{\text{non-DY}}(1 - \varepsilon^0_{\text{non-DY}})}\right)^{\theta}.\end{aligned} \tag{4.40}$$

The second term in Equation 4.40 provides the correction, while the third term represents the uncertainty. $f_0 = \varepsilon^{\text{MC}}_{\text{signal}}/\varepsilon^{\text{MC}}_{\text{non-DY}}$, is the ratio between the signal and non-DY f_{recoil} efficiencies measured in simulation. $\varepsilon^0_{\text{non-DY}}$ is the nominal value of $\varepsilon_{\text{non-DY}}$, taken from data. The quadratic parameterization of the correction naturally satisfies the boundary conditions, while the ansatz $\varepsilon_{\text{signal}} \sim f_0\varepsilon_{\text{non-DY}}$ breaks. The uncertainty Δ, taken as $\Delta = 1 - f_0$, is introduced through modified log-normal response in the third term, similar to the one in Equation 4.33. Also here, the quadratic parametrization is applied to satisfy the boundary conditions.

As for the extrapolation uncertainties described in detail in Section 4.6, they are implemented in the Pacman likelihood as nuisance parameters, with Gaussian constraints defined as in Equation 4.32, and log-normal response terms applied to the expected yields of the relevant regions and processes, as in Equation 4.33.

4.10.3 Results of the likelihood fit

The likelihood fit allows for the simultaneous extraction of the signal strength μ, and of the nuisance parameters $\boldsymbol{\theta}$. $\hat{\mu}$ and $\hat{\boldsymbol{\theta}}$ are the unconditional maximum likelihood estimators, i.e. the values of these parameters that maximize the likelihood. It will also be useful to define $\hat{\hat{\boldsymbol{\theta}}}(\mu)$, which is the conditional maximum likelihood estimator of $\boldsymbol{\theta}$, for a fixed value of μ. The procedure by which one chooses specific values for $\boldsymbol{\theta}$ is referred to as profiling.

The uncertainty on the extracted POI, $\hat{\mu}$, arises from the uncertainties Δ_θ on the different θ parameters. The impact of a single NP θ on $\hat{\mu}$, labeled $\Delta_{\hat{\mu}}$, is assessed as follows:

$$\Delta_{\hat{\mu}} = \hat{\mu}(\hat{\theta} \pm \Delta_\theta) - \hat{\mu}(\hat{\theta}). \tag{4.41}$$

In the likelihood fit, the parameters are adjusted to fit the data, and the post-fit result may differ from the pre-fit estimation, for every parameter θ as well as its uncertainty Δ_θ. Even though the fit is designed to avoid them, over-constraints - when Δ_θ is smaller than the pre-fit value - and pulls - when θ is changed with respect to the pre-fit value - may occur. These will modify the predicted rates of the signal and background process, and affect the corresponding systematic uncertainties.

4.10.4 Hypothesis testing

The estimation of the parameter of interest μ provides no information on the level of agreement between the data and the background-only or background-plus-signal hypothesis. Hypothesis testing [199] in the $H \to WW^* \to \ell\nu\ell\nu$ analysis is based on the profiled likelihood ratio, $\tilde{\lambda}(\mu)$, defined as:

$$\tilde{\lambda}(\mu) = \begin{cases} \frac{\mathcal{L}\left(\mu, \hat{\hat{\boldsymbol{\theta}}}(\mu)\right)}{\mathcal{L}\left(\hat{\mu}, \hat{\boldsymbol{\theta}}\right)}, & \hat{\mu} \geqslant 0 \\ \frac{\mathcal{L}\left(\mu, \hat{\hat{\boldsymbol{\theta}}}(\mu)\right)}{\mathcal{L}\left(0, \hat{\hat{\boldsymbol{\theta}}}(0)\right)}, & \hat{\mu} < 0 \end{cases} . \tag{4.42}$$

For $\hat{\mu} \geqslant 0$, the numerator maximizes the likelihood for a specific value of μ, while the denominator is the unconditional maximized likelihood. The $\hat{\mu} < 0$ case is defined to avoid complications in the computations in the case of a deficit of signal-like events.

Different test statistics $\tilde{t}_\mu$ are defined to test a particular value of μ, depending on the tested hypothesis. For the observed data, the test statistic has a specific value - $\tilde{t}_\mu^{\text{obs}}$. The sampling distribution of the test statistic is denoted by $f\left(\tilde{t}_\mu \mid \mu, \hat{\hat{\boldsymbol{\theta}}}(\mu)\right)$. The p-value for a given observation, under a particular μ hypothesis, is the probability for an equal or more extreme outcome than the observed, under the assumed hypothesis:

$$p_\mu = \int_{\tilde{t}_\mu^{\text{obs}}}^{\infty} f\left(\tilde{t}_\mu \mid \mu, \hat{\hat{\boldsymbol{\theta}}}(\mu)\right) \mathrm{d}\tilde{t}_\mu. \tag{4.43}$$

Small p-values present evidence against the tested hypothesis. p-values are often converted into the equivalent normal significance Z.

In case of an excess in data, the test statistic $\tilde{q}_0$ is defined:

$$\tilde{q}_0 = \begin{cases} -2\ln\tilde{\lambda}(0), & \hat{\mu} > 0 \\ 0, & \hat{\mu} \leqslant 0 \end{cases} . \tag{4.44}$$

One wishes to test the compatibility of the data with the background-only hypothesis $\mu = 0$. The compatibility is tested by using the p_0-value, computed as:

$$p_0 = \int_{\tilde{q}_0^{\text{obs}}}^{\infty} f\left(\tilde{q}_0 \mid 0, \hat{\hat{\boldsymbol{\theta}}}(0)\right) \mathrm{d}\tilde{q}_0. \tag{4.45}$$

p_0 represents the probability that the background-only hypothesis leads to a test statistic equal to or larger than the observed, i.e. the probability that, in the absence of a Higgs boson, the background can produce a fluctuation greater than or equal to the excess observed in the data. A discovery is made if the background-only hypothesis is rejected at the 5σ level.

A test statistic, $\tilde{q}_\mu$, defined as:

$$\tilde{q}_\mu = \begin{cases} -2\ln\tilde{\lambda}(\mu), & \hat{\mu} \leqslant \mu \\ 0, & \hat{\mu} > \mu \end{cases} , \tag{4.46}$$

is used for setting upper limits on μ, i.e. to compare the hypothesis of the signal being produced at a rate μ or at a rate smaller than μ. The $\mathrm{CL_s}$ procedure [200] is adopted to set these limits. It involves computing the p-values p_μ and p_b from $\tilde{q}_\mu$:

$$p_\mu = \int_{\tilde{q}_\mu^{\mathrm{obs}}}^{\infty} f\left(\tilde{q}_\mu \mid \mu, \hat{\hat{\boldsymbol{\theta}}}(\mu)\right) \mathrm{d}\tilde{q}_\mu \quad \text{and} \quad p_b = \int_{\infty}^{\tilde{q}_\mu^{\mathrm{obs}}} f\left(\tilde{q}_\mu \mid 0, \hat{\hat{\boldsymbol{\theta}}}(0)\right) \mathrm{d}\tilde{q}_\mu. \tag{4.47}$$

We note that p_b is the p_μ under the background-only hypothesis. The 95% confidence level (CL) upper limits on μ are, thus, given for

$$\mathrm{CL_s}(\mu) = \frac{p_\mu}{1 - p_b} \leqslant 5\%. \tag{4.48}$$

4.11 Results

The final results of the $H \to WW^* \to \ell\nu\ell\nu$ analysis, obtained from a combined likelihood fit to all the signal categories (7 TeV and 8 TeV, ggF- and VBF-enriched), are presented in what follows.

4.11.1 Yields and distributions

Table 4.17 shows the final signal and background yields for the SF 0- and 1-jet categories in the 8 TeV dataset. Figure 4.62 displays the m_T distributions used as input to extract the Higgs signal. Post-fit results are shown in both Table 4.17 and Figure 4.62, so all processes are normalized to their post-fit predictions, including the signal. Furthermore, pulls and over-constraints of the nuisance parameters are taken into account in the rates of the different processes. The reported uncertainties include both statistical and systematic components. The different sources of these uncertainties are shown in Table 4.18.

$ee + \mu\mu$	Obs.	Bkg.	H	WW	$t\bar{t}$	single top	$W+$ jets	multi jet	other VV	Z/γ^*
0-jet	1108	1040 ± 40	79 ± 15	740 ± 40	39 ± 3	65 ± 5	82 ± 16	2 ± 0.5	68 ± 7	50 ± 21
1-jet	467	427 ± 21	26 ± 6	184 ± 15	46 ± 4	119 ± 10	19 ± 4	0.2 ± 0.1	31 ± 4	28 ± 12

TABLE 4.17: SF 0- and 1-jet signal region observed and predicted yields. The post-fit estimates are shown for all processes, including the signal, so pulls, constraints and correlations are accounted for. The quoted uncertainties include statistic and systematic sources.

As described in Section 4.10.3, the likelihood model is designed to avoid significant pulls and over-constraints of the NPs. In general, it is verified that these are indeed small, which is why the yields shown Table 4.17 do not differ significantly from the ones showed in Table 4.8. In the combined likelihood fit, the most significant over-constraint occurs in the uncertainty associated to the WW m_T shape (see Section 4.6.2.1). The over-constraint is at the level of $\sim 35\%$. It occurs due to events in the high tail of the m_T distribution in the DF 0- and 1-jet signal regions, where WW dominates. As for pulls

	Source	0-jet	1-jet
Uncertainty on signal yield	ggF, jet veto for 0-jet category	8.1	14
	ggF, jet veto for 1-jet category	-	12
	ggF acceptance	6.8	3.5
	ggF total cross-section	9.6	8.5
	VBF acceptance	-	0.3
	VBF total cross-section	-	0.4
	$H \to WW^*$ branching ratio	4.3	4.3
	Integrated luminosity	2.8	2.8
	JES and JER	6.2	4.0
	$E_{\mathrm{T}}^{\mathrm{miss}}$ scale and resolution	1.1	2.9
	f_{recoil} efficiency	9.8	9.8
	Trigger efficiency	1.3	1.3
	Electrons id., iso. and reco. efficiency	1.2	2.1
	Muons id., iso. and reco. efficiency	1.3	2.6
	Pile-up model	2.1	1.5
	Total	20	25
Uncertainty on total background yield	WW theoretical model	1.6	1.6
	top theoretical model	0.1	0.9
	VV theoretical model	0.2	1.0
	$Z/\gamma^* \to \tau\tau$ estimate	0.6	0.2
	W + jets estimate	0.8	0.7
	Multijet estimate	-	0.1
	JES and JER	0.9	0.7
	$E_{\mathrm{T}}^{\mathrm{miss}}$ scale and resolution	0.2	0.1
	b-tag efficiency	-	0.3
	mistag rate	-	0.3
	f_{recoil} efficiency	1.8	1.6
	Trigger efficiency	0.6	0.6
	Electrons id., iso. and reco. efficiency	0.2	0.3
	Muons id., iso. and reco. efficiency	0.3	0.3
	Pile-up model	0.9	1.2
	Total	3.8	5.0

TABLE 4.18: Sources of uncertainty (in %) in the post-fit predicted signal and total background yields in the SF 0- and 1-jet signal regions.

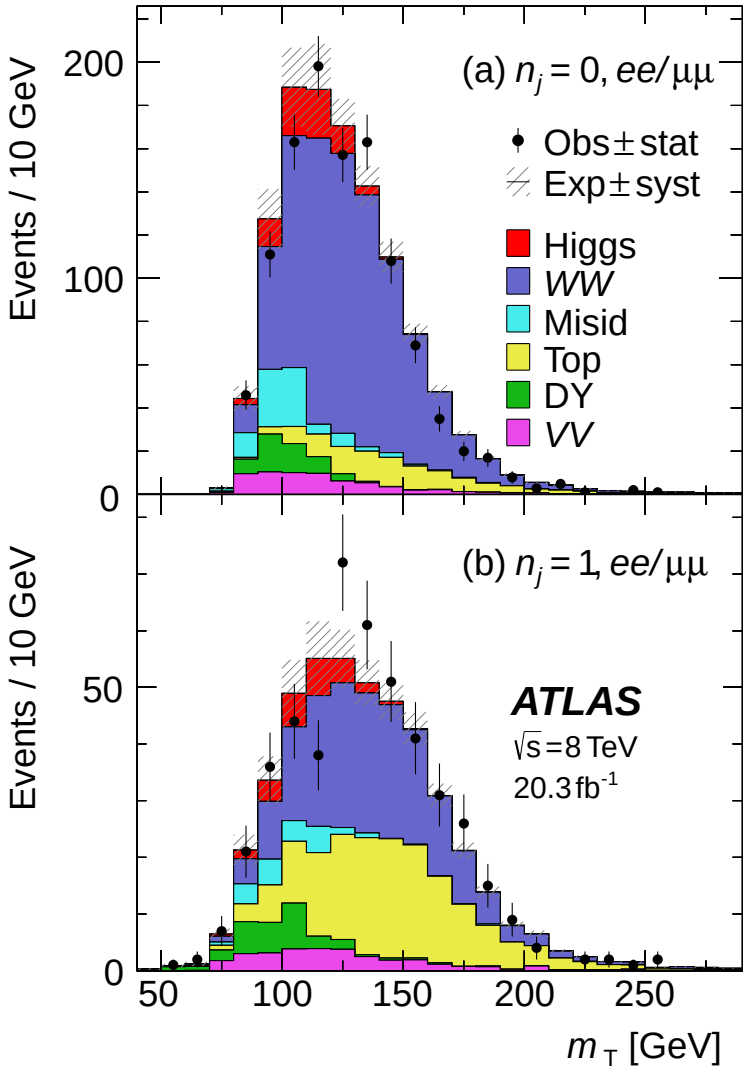

FIGURE 4.62: m_T distributions of events in the SF (a) 0-jet and (b) 1-jet signal regions. All processes are normalized to the post-fit predictions, including the signal.

of the NPs, these are generally smaller than 1σ. The most significant one is at the level of 1.6σ, and occurs for the NP associated to the uncertainty on the DY f_{recoil} efficiency, in the SF 0-jet category. As a result, the DY yield in this category is reduced post-fit by $\sim 40\%$. It is important to note that the pull of this NP increases when considering the combined likelihood of all categories in the analysis. This behavior is interpreted as an attempt of the fit to compensate for an apparently lower observed signal rate in the SF 0-jet channel, compared to the DF 0- and 1-jet channels (see Tables 4.8 and 4.9).

Figure 4.63 a shows the combined m_T distribution of the SF and DF, 0- and 1-jet samples. Both 7 TeV and 8 TeV datasets are included. As before, signal and background processes are scaled to the post-fit predictions. An excess of observed events over the background-only prediction is clearly visible. Figure 4.63 b displays the background subtracted m_T distribution of the observed events. Here, a direct comparison can be done between the m_T shape of the excess and the one predicted for a Higgs signal with

$m_H = 125$ GeV. Very good agreement is observed, strongly suggesting the need for the inclusion of the Higgs signal to explain the observed excess of events.

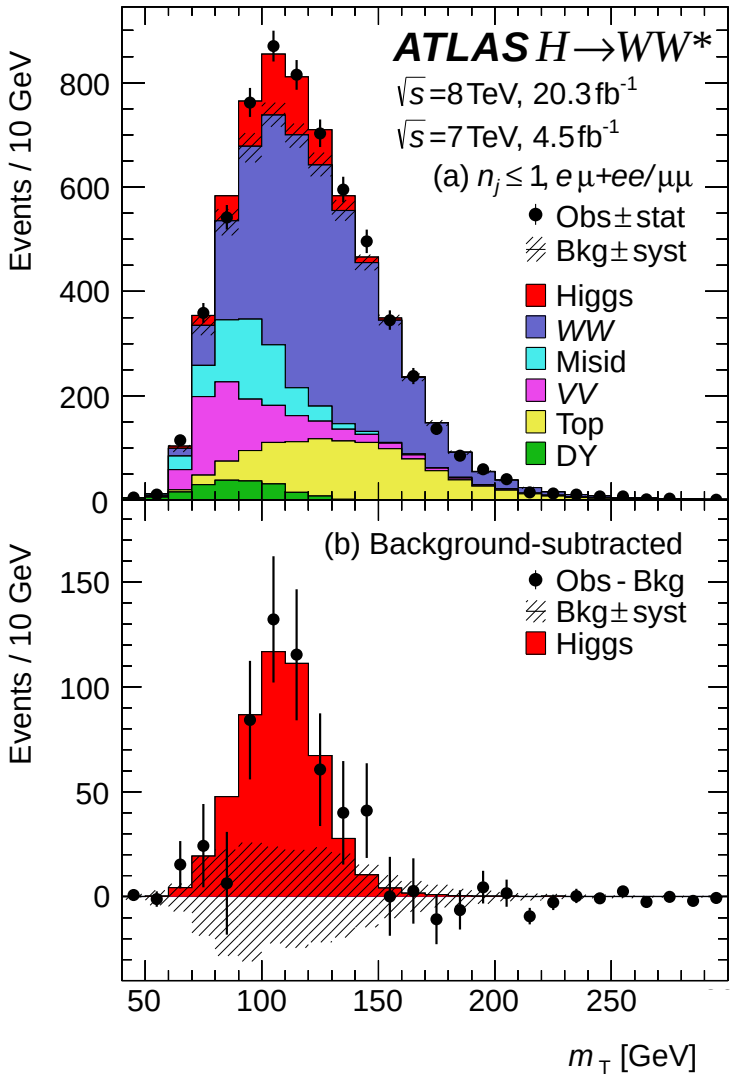

FIGURE 4.63: (a) m_{T} distribution of events in the SF and DF, 0- and 1-jet signal region, for the 7 TeV and 8 TeV dataset. (b) shows the residuals of the data with respect to the total estimated background, compared to the signal prediction. All processes in both distributions are normalized to the post-fit predictions, including the signal.

4.11.2 Observation of the $H \to WW^*$ decay

As explained in Section 4.10.4, the observed excess of events can be quantified by computing the p_0-value, which is shown in Figure 4.64 as a function of m_H, as extracted from the combined likelihood fit of all signal categories. Three curves are displayed in Figure 4.64: the observed result; the expected result considering the background-only hypothesis; and the expected result considering the background-plus-signal hypothesis, with $m_H = 125.36$ GeV (see Section 1.2.3.4). The observed curve and the expected curve including the Higgs signal agree well. A broad minimum is seen for the observed p_0-value, around $m_H \approx 125$ GeV. The minimum value is achieved at $m_H = 130$ GeV,

and corresponds to an observed significance of 6.1σ. For $m_H = 125.36$ GeV, the observed significance is 6.1σ, while the expectation is 5.8σ. This result conclusively establishes the discovery of the Higgs boson in the $H \to WW^* \to \ell\nu\ell\nu$ channel.

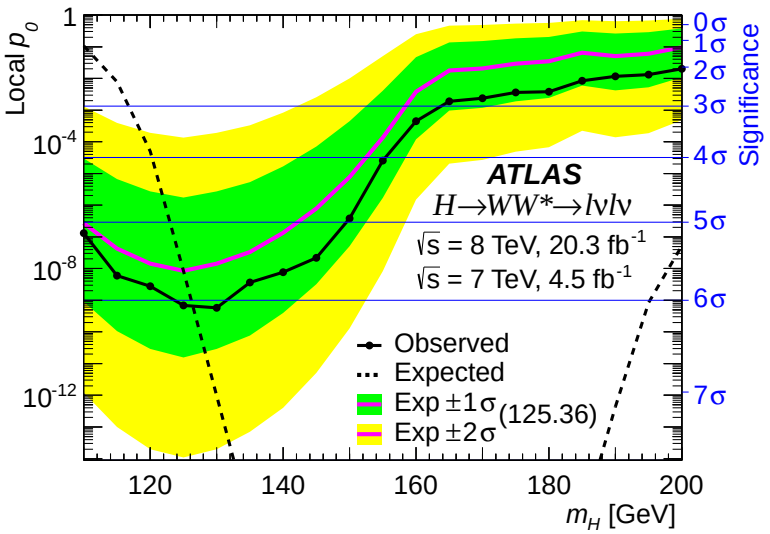

FIGURE 4.64: Local p_0 as a function of m_H. The observed values are shown as a solid black line. The dashed black curve shows the expectation given the presence of a signal at each mass hypothesis m_H. The dashed blue curve shows the expectation given the presence of a signal with $m_H = 125.36$ GeV.

The expected and observed significance measured for the different signal categories of the analysis, for $m_H = 125.36$ GeV, are summarized in Table 4.19. The SF 0- and 1-jet channels observe lower significances than expected, as anticipated from the small excess of events already reported for these channels.

Category	**Exp. Z_0**	**Obs. Z_0**
0-jet	3.71	4.09
$e\mu$ (leading e)	2.92	3.08
$e\mu$ (leading μ)	2.33	3.12
$ee + \mu\mu$	1.44	0.70
1-jet	2.61	2.49
$e\mu$	2.51	2.83
$ee + \mu\mu$	1.04	0.21
2-jet-ggF	1.20	1.44
2-jet-VBF	3.38	3.84
$e\mu$	3.01	3.02
$ee + \mu\mu$	1.58	2.96
Total	5.76	6.07

TABLE 4.19: Expected and observed significances in the different categories of the analysis for $m_H = 125.36$ GeV.

4.11.3 Measuring the signal strength

The signal strength measured as a result of the combined fit, for a Higgs mass of $m_H = 125.36$ GeV is:

$$\begin{aligned}\hat{\mu}^{\text{obs}} &= 1.08\ ^{+0.16}_{-0.15}\ (\text{stat.})\ ^{+0.08}_{-0.07}\ (\text{expt.})\ ^{+0.13}_{-0.11}\ (\text{theo.})\ \pm 0.03\ (\text{lumi.})\ = \\ &= 1.08\ ^{+0.16}_{-0.15}\ (\text{stat.})\ ^{+0.16}_{-0.13}\ (\text{syst.})\ = \\ &= 1.08\ ^{+0.22}_{-0.20}.\end{aligned} \tag{4.49}$$

As shown, μ is measured with a $\sim 20\%$ precision in the $H \to WW^* \to \ell\nu\ell\nu$ analysis. Both statistical and systematic uncertainties contribute at the level of $\sim 15\%$ each. The breakdown of the sources of uncertainty impacting the error on μ is shown in Table 4.20.

Source	**Error**	
	+	−
Data statistics	0.16	0.15
Signal regions	0.12	0.12
Control regions	0.10	0.10
MC statistics	0.04	0.04
Theoretical systematics	0.13	0.11
Signal $H \to WW^*$ BR	0.05	0.04
Signal ggF normalization	0.06	0.05
Signal ggF acceptance	0.05	0.04
Signal VBF normalization	0.01	0.01
Signal VBF acceptance	0.02	0.01
Background WW	0.06	0.06
Background top	0.03	0.03
Background W + jets	0.05	0.05
Others	0.02	0.02
Experimental systematics	0.07	0.06
Background W + jets	0.03	0.03
Background DY (Pacman)	0.02	0.02
Muons and electrons	0.04	0.04
Missing transverse momentum	0.02	0.02
Jets and b-tagging	0.03	0.02
Others	0.03	0.02
Integrated luminosity	0.03	0.03
Total	0.22	0.20

TABLE 4.20: Summary of the uncertainties on the observed signal strength $\hat{\mu}^{\text{obs}}$ measured from the combined fit for $m_H = 125.36$ GeV.

The signal strength measured in a SF 0- and 1-jet fit only, for the 8 TeV dataset, is:

$$\begin{aligned}\hat{\mu}^{\text{obs}}_{\text{SF01}j} &= 0.38\ ^{+0.44}_{-0.43}\ (\text{stat.})\ ^{+0.39}_{-0.40}\ (\text{expt.})\ ^{+0.22}_{-0.20}\ (\text{theo.})\ \pm 0.03\ (\text{lumi.})\ = \\ &= 0.38\ ^{+0.44}_{-0.43}\ (\text{stat.})\ ^{+0.43}_{-0.42}\ (\text{syst.})\ = \\ &= 0.38\ ^{+0.62}_{-0.60}.\end{aligned} \tag{4.50}$$

As already discussed, a smaller data excess is visible in the SF channels, resulting in a lower measured signal strength. Within the quoted uncertainty, the result is, however, compatible with the presence of the SM Higgs signal. Also for these categories, statistical and systematic uncertainties contribute at a similar level to a measured precision of $\sim 60\%$. The different sources of uncertainty impacting this measurement are shown in Table 4.21. Here we note that, on the experimental systematics side, the uncertainties on the f_{recoil} efficiencies and statistics of the MC samples, dominate.

Source	**Error**	
	+	−
Data statistics	0.44	0.43
Signal regions	0.28	0.28
Control regions	0.34	0.32
MC statistics	0.29	0.32
Theoretical systematics	0.22	0.20
Signal $H \to WW^*$ BR	0.03	0.00
Signal ggF normalization	0.08	0.01
Signal ggF acceptance	0.05	0.01
Signal VBF normalization	0.00	0.00
Signal VBF acceptance	0.00	0.00
Background WW	0.16	0.16
Background top	0.03	0.03
Background W + jets	0.09	0.10
Others	0.03	0.04
Experimental systematics	0.26	0.24
Background W + jets	0.07	0.08
Background DY (Pacman)	0.20	0.21
Muons and electrons	0.06	0.04
Missing transverse momentum	0.02	0.02
Jets and b-tagging	0.09	0.05
Others	0.09	0.07
Integrated luminosity	0.02	0.02
Total	0.62	0.60

TABLE 4.21: Summary of the uncertainties on the observed signal strength $\hat{\mu}^{\text{obs}}_{\text{SF01}j}$ measured from the combined fit for $m_H = 125.36$ GeV.

For completeness, a summary of the expected and observed signal strength measured in the different analysis categories is presented in Table 4.22.

Category	Expected		Observed						
	Tot. Error		Tot. Error		Stat. Error		Syst. Error		$\hat{\mu}$
	+	−	+	−	+	−	+	−	
0-jet	0.32	0.29	0.34	0.30	0.22	0.22	0.26	0.21	1.14
$e\mu$ (leading e)	0.40	0.36	0.40	0.36	0.30	0.29	0.27	0.22	1.07
$e\mu$ (leading μ)	0.48	0.44	0.53	0.47	0.38	0.36	0.37	0.30	1.40
$ee + \mu\mu$	0.73	0.69	0.68	0.66	0.45	0.44	0.50	0.50	0.47
1-jet	0.44	0.40	0.45	0.40	0.33	0.32	0.30	0.24	0.96
$e\mu$	0.46	0.41	0.49	0.43	0.35	0.35	0.33	0.27	1.16
$ee + \mu\mu$	1.04	0.96	1.00	0.96	0.80	0.76	0.60	0.59	0.20
2-jet-ggF	0.90	0.84	0.91	0.84	0.70	0.68	0.58	0.48	1.20
2-jet-VBF	0.42	0.36	0.45	0.38	0.36	0.33	0.27	0.19	1.20
$e\mu$	0.48	0.40	0.47	0.39	0.40	0.35	0.24	0.16	0.98
$ee + \mu\mu$	0.84	0.67	0.97	0.78	0.83	0.71	0.51	0.33	1.98
Total	0.22	0.21	0.22	0.20	0.16	0.15	0.16	0.13	1.08

TABLE 4.22: Expected and observed signal strength in the different categories of the analysis for $m_H = 125.36$ GeV.

Figure 4.65 shows the observed and expected signal strength, as a function of m_H, for the combined analysis. The observed $\hat{\mu}$ is compatible with zero for $m_H > 160$ GeV. However, the signal strength shows a strong dependence with m_H, increasing as the Higgs boson mass decreases. Nonetheless, the observed curve is in very good agreement with the expected curve for $m_H = 125.36$ GeV. The reason for this behavior is the low mass mass resolution of the $H \to WW^* \to \ell\nu\ell\nu$ channel, and the dependence of the $H \to WW^*$ branching fraction with the Higgs boson mass (see Figure 1.17). As a result, a Higgs boson with $m_H = 125.36$ GeV produced with a rate similar to the SM prediction, generates a signal very similar to a Higgs boson with a lower mass, being predicted at a much higher rate.

Given the strong dependence of μ with m_H, it is useful to check the consistency of the observed excess with the mass measured by the high resolution channels ($m_H = 125.36$ GeV). This is shown in Figure 4.66, where a 2D scan of the likelihood is shown in the (m_H, μ) plane. The best fit value is shown for values that maximize the likelihood, or equivalently for values at which the plotted quantity - $-2\ln\tilde{\lambda}$ (see Equation 4.45) - is zero. $m_H = 125.36$ GeV is well within the 1σ uncertainty bands.

4.11.4 Probing different production mechanisms

In the combined fit, which includes ggF- and VBF-sensitive categories, the ggF and VBF production mechanisms can be probed separately. For this purpose, separate signal strength parameters - μ_{ggF} and μ_{VBF} - are defined to scale the expected ggF and VBF[8] contributions to the signal, respectively. The two parameters can be measured

[8]The small expected VH contribution is scaled together with VBF.

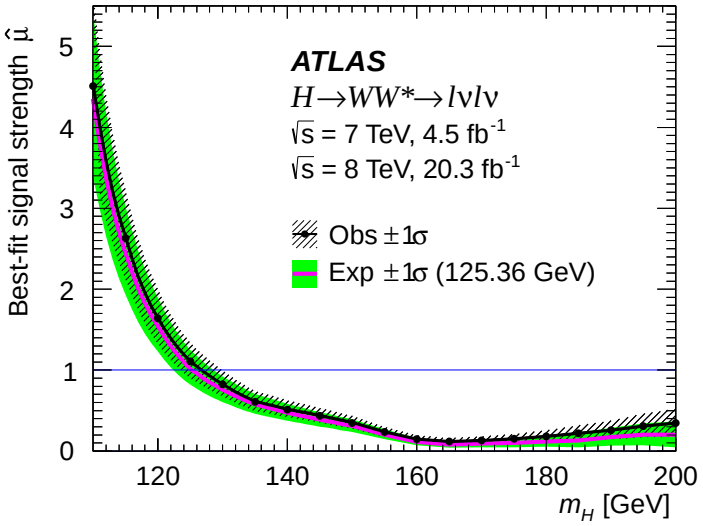

FIGURE 4.65: Best-fit signal strength μ as a function of m_H. The observed values are shown as a solid black line. The dashed red horizontal curve ($\hat{\mu} = 1$)shows the expectation given the presence of a signal at each mass hypothesis m_H. The solid red curve shows the expectation given the presence of a signal with $m_H = 125.36$ GeV.

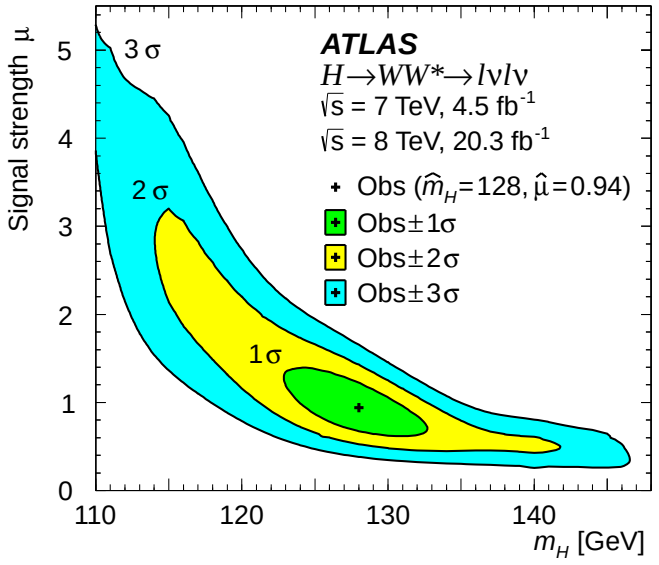

FIGURE 4.66: Scan of the negative log-likelihood in the (m_H, μ) plane.

simultaneously in the combined fit. The result is shown in the 2D likelihood scan displayed in Figure 4.67. The individual measurements are:

$$\mu_{\text{ggF}} = 1.01 \pm 0.19 \text{ (stat.)} \, ^{+0.20}_{-0.17} \text{ (syst.)} \, = 1.01^{+0.27}_{-0.25}, \tag{4.51}$$

and:

$$\mu_{\text{VBF}} = 1.27 \, ^{+0.44}_{-0.40} \text{ (stat.)} \, ^{+0.29}_{-0.21} \text{ (syst.)} \, = 1.27^{+0.53}_{-0.45}, \tag{4.52}$$

well in agreement with the SM expectation.

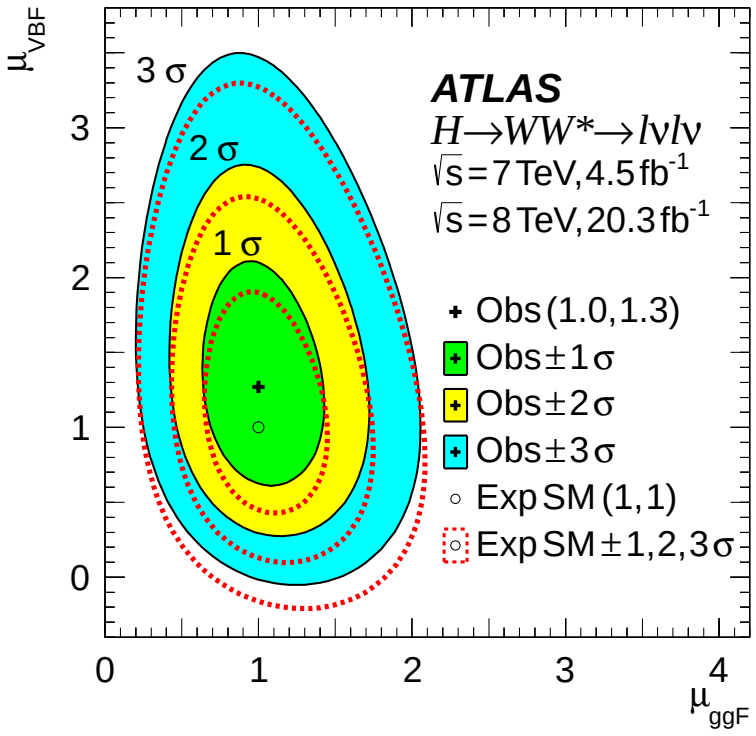

FIGURE 4.67: Scan of the negative log-likelihood in the $(\mu_{\text{ggF}}, \mu_{\text{VBF}})$ plane.

A combined likelihood fit was performed using $\mu_{(VBF)}/\mu_{\text{ggF}}$ as the parameter of interest. The scan of this likelihood is shown in Figure 4.68, indicating that the best-fit value, for $m_H = 125.36$, is:

$$\frac{\mu_{\text{VBF}}}{\mu_{\text{ggF}}} = 1.25^{+0.79}_{-0.52}. \tag{4.53}$$

The p_0-value determined with this POI, i.e. testing the $\mu_{\text{VBF}}/\mu_{\text{ggF}} = 0$ hypothesis, corresponds to an observed significance of 3.2σ, for an expectation of 2.7σ. This result establishes evidence for VBF production in the $H \to WW^* \to \ell\nu\ell\nu$ channel.

4.11.5 Higgs couplings

As described in Section 1.2.3.4, the measurement of the signal strengths μ_{ggF} and μ_{VBF} can be converted into a measurement of the factors κ_{F} and κ_{V}, which scale the strength of the couplings of the Higgs boson to fermions and vector bosons, respectively. This

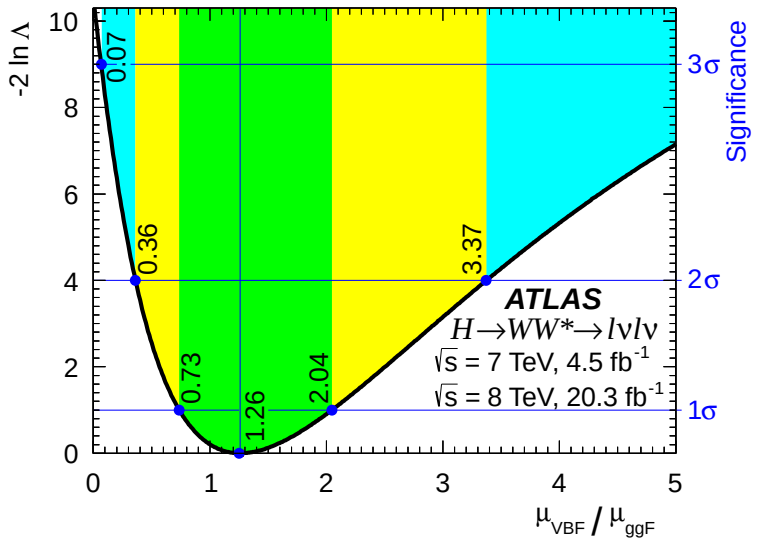

FIGURE 4.68: Scan of the negative log-likelihood as a function of $\mu_{\mathrm{VBF}}/\mu_{\mathrm{ggF}}$ plane.

is particularly important since these Higgs couplings are exactly determined in the SM (see Section 1.1.8). Thus, any deviation from $\kappa_{\mathrm{V}} = 1$ or $\kappa_{\mathrm{F}} = 1$, which are the SM expectations, represent a clear sign of new physics.

Following the procedure detailed in Ref. [55], the ggF production cross-section, which probes the fermionic coupling, is proportional to κ_{F}^2. On the other hand, the VBF production cross-section scales with κ_{V}^2, since it probes the coupling of the Higgs boson to vector bosons. The $H \to WW^*$ partial width also scales with κ_{V}^2. Finally, the Higgs total width scales with $0.25\kappa_{\mathrm{V}}^2 + 0.75\kappa_{\mathrm{F}}^2$, assuming only SM contributions (see Table 1.6). In summary:

$$\sigma_{\mathrm{ggF}} \times \mathrm{BR}(H \to WW^*) \propto \mu_{\mathrm{ggF}} \propto \frac{\kappa_{\mathrm{F}}^2 \times \kappa_{\mathrm{V}}^2}{0.25\kappa_{\mathrm{V}}^2 + 0.75\kappa_{\mathrm{F}}^2}, \tag{4.54}$$

and:

$$\sigma_{\mathrm{VBF}} \times \mathrm{BR}(H \to WW^*) \propto \mu_{\mathrm{VBF}} \propto \frac{\kappa_{\mathrm{V}}^4}{0.25\kappa_{\mathrm{V}}^2 + 0.75\kappa_{\mathrm{F}}^2}. \tag{4.55}$$

The 2D scan of the likelihood in the $(\kappa_{\mathrm{V}}, \kappa_{\mathrm{F}})$ plane is shown in Figure 4.69. Given the parameterizations in Equations 4.54 and 4.55, high values of κ_{F} are mostly constrained by μ_{VBF}, hence the relatively low discrimination in this case. The best fit values of the coupling strength parameters are:

$$\kappa_{\mathrm{F}} = 0.92^{+0.31}_{-0.23}, \tag{4.56}$$

and:

$$\kappa_{\mathrm{V}} = 1.04^{+0.10}_{-0.11}, \tag{4.57}$$

compatible with the SM expectation.

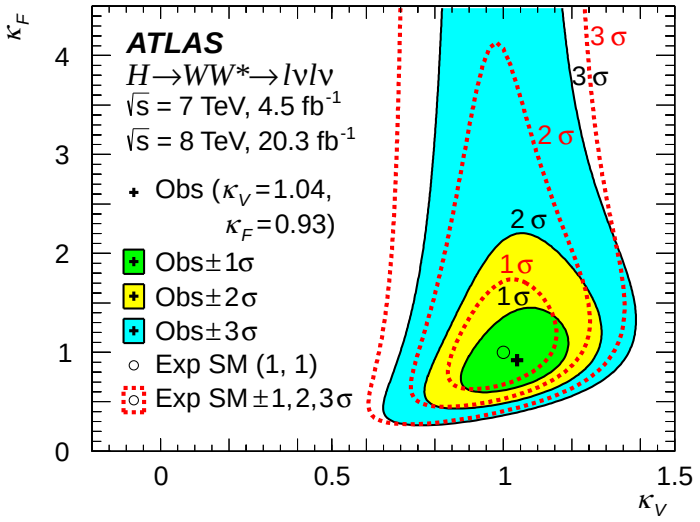

FIGURE 4.69: Scan of the negative log-likelihood in the (κ_V, κ_V) plane.

4.11.6 Exclusion limits

Limits on μ, computed as detailed in Section 4.10.4, are shown in Figure 4.70, as a function of m_H. Values of the Higgs boson mass falling below the line at $\mu = 1$ are excluded at 95% CL. The $H \to WW^* \to \ell\nu\ell\nu$ analysis is expected to exclude a SM Higgs boson in the $114 < m_H < 200$ GeV range. Given the observed excess of events, compatible with the SM Higgs boson at $m_H = 125.36$ GeV, the observed exclusion range is $132 < m_H < 200$ GeV.

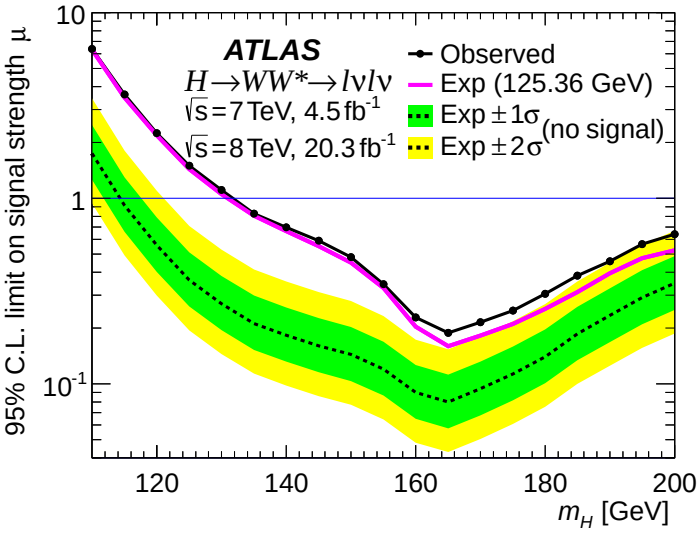

FIGURE 4.70: CL_s exclusion as a function of m_H at 95% CL. The observed limits are indicated by the solid black line. The dashed black line shows the expected limit assuming the background-only hypothesis. The solid red line indicates the expectation under the signal-plus-background hypothesis.

4.11.7 Inclusive cross-sections

The measurements of the signal strengths μ_{ggF} and μ_{VBF} can be used to compute the products $\sigma \times \text{BR}$ for a $m_H = 125.36$ GeV Higgs boson decaying to $H \to WW^*$. These are obtained simply by multiplying μ by the prediction used to define it:

$$(\sigma \times \text{BR}_{H\to WW^*})_{\text{obs}} = \hat{\mu} \cdot (\sigma \times \text{BR}_{H\to WW^*})_{\text{exp}}. \tag{4.58}$$

The uncertainties that impact the $\hat{\mu}$ measurement scale similarly, apart from the theoretical uncertainties on the absolute yield prediction, i.e on the total signal cross-section and branching ratio (see Section 1.2.3.1), which do not apply.

The relevant signal strengths are:

$$\begin{aligned}
\hat{\mu}^{7\text{TeV}}_{\text{ggF}} &= 0.57 \pm 0.52\ (\text{stat.})\ ^{+0.35}_{-0.33}\ (\text{syst.})\ ^{+0.13}_{-0.01}\ (\text{abs. sig.}) \\
\hat{\mu}^{8\text{TeV}}_{\text{ggF}} &= 1.09 \pm 0.20\ (\text{stat.})\ ^{+0.18}_{-0.16}\ (\text{syst.})\ ^{+0.13}_{-0.08}\ (\text{abs. sig.}) \\
\hat{\mu}^{8\text{TeV}}_{\text{VBF}} &= 1.45\ ^{+\ 0.48}_{-\ 0.43}\ (\text{stat.})\ ^{+0.37}_{-0.22}\ (\text{syst.})\ ^{+0.11}_{-0.06}\ (\text{abs. sig.}),
\end{aligned} \tag{4.59}$$

where (abs. sig.) denotes the uncertainties on the absolute signal prediction. No VBF signal is observed with the 7 TeV dataset and, therefore, the cross-section is not computed. The measured cross sections times branching ratios are:

$$\begin{aligned}
\sigma^{7\text{TeV}}_{\text{ggF}} \times \text{BR}_{H\to WW^*} &= 1.9 \pm 1.7\ (\text{stat.})\ ^{+1.2}_{-1.1}\ (\text{syst.})\ = 1.9\ ^{+2.1}_{-2.0}\ \text{pb} \\
\sigma^{8\text{TeV}}_{\text{ggF}} \times \text{BR}_{H\to WW^*} &= 4.6 \pm 0.9\ (\text{stat.})\ ^{+0.8}_{-0.7}\ (\text{syst.})\ = 4.6 \pm 1.1\ \text{pb} \\
\sigma^{8\text{TeV}}_{\text{VBF}} \times \text{BR}_{H\to WW^*} &= 0.51^{+0.17}_{-0.15}\ (\text{stat.})\ ^{+0.13}_{-0.08}\ (\text{syst.})\ = 0.51^{+0.22}_{-0.17}\ \text{pb},
\end{aligned} \tag{4.60}$$

which agree with the predictions of 3.3 ± 0.4 pb, 4.2 ± 0.5 pb, and 0.35 ± 0.02 pb, respectively.

4.12 Summary and conclusions

The $H \to WW^* \to \ell\nu\ell\nu$ decay channel offers a very sensitive experimental signature to probe the Higgs boson. Events with two leptons and missing transverse momentum were analyzed, using 25 fb^{-1} of proton collision data from the LHC at $\sqrt{s} = 7$ TeV and $\sqrt{s} = 8$ TeV, collected by the ATLAS detector in 2011 and 2012.

Event categories are created in the analysis, to increase the sensitivity and probe the ggF and VBF production mechanisms separately. The full Higgs resonance cannot be reconstructed, given the two neutrinos in the final state. The transverse mass is used to discriminate signal from background, but no narrow peak can be seen above the background. Thus, precise and accurate background estimation is fundamental. Data is used to validate, normalize or even replace the MC prediction whenever possible.

The categories with two leptons of the same flavor in the final state are particularly challenging, due to the overwhelming contamination of Drell-Yan background. A new kinematic variable, measuring the soft hadronic recoil of the dilepton system, was created

with the purpose of suppressing this background to a manageable level. Furthermore, given the difficulty in modeling the Drell-Yan background in the signal region with simulation, a data-driven technique was developed to estimate the residual Drell-Yan contamination in these categories.

An excess of events is observed over the background prediction, with a significance of 6.1σ, establishing the observation of the Higgs boson in the $H \to WW^* \to \ell\nu\ell\nu$ decay channel. The analysis also presents evidence of VBF production at the 3.2σ level. The observation is compatible with the SM Higgs boson with $m_H = 125.36$ GeV, as shown by the ratio between the measured and predicted rates: $\mu = 1.08^{+0.22}_{-0.20}$. The couplings strengths of the Higgs boson to fermions and vector bosons are also measured and compatible with the SM expectation. SM Higgs bosons in the $132 < m_H < 200$ GeV mass range are excluded at the 95% CL.

Conclusions

The hunt for the Higgs boson was the centerpiece of the physics programs for the experiments at the Large Hadron Collider, during Run-I of data-taking. The discovery of this particle, announced on July 4^{th} 2012 by the ATLAS and CMS collaborations, represented a milestone in clarifying the mechanism of electroweak symmetry breaking, by which fundamental particles acquire mass. It is now essential that the Higgs boson is extensively studied. Precise measurements of its properties will confirm its nature, and any deviations from the Standard Model prediction will represent a clear sign of new physics.

The work presented in this thesis focuses on the observation and measurement of the Higgs boson production in the $H \to WW^* \to \ell\nu\ell\nu$ channel and, in addition, presents studies of the ATLAS jet trigger performance with early collision data. Since jets are very complex objects and the most commonly produced at the LHC, and the jet trigger is the primary mean of selecting these objects, the performance of this system has implications on a variety of physics analyses in ATLAS, including $H \to WW^* \to \ell\nu\ell\nu$.

At the start of Run I, it was important to validate the behavior of the ATLAS jet trigger using data. Thus, the performance at L2 was examined using the first $\sqrt{s} = 7$ TeV pp collisions recorded in 2010. Results were overall satisfactory: the η, ϕ and E_{T} residuals of L2 jets with respect to offline were better than 5%; L2 efficiency curves showed sharp turn-ons; and simulation was generally able to model the distributions of L2 jets, at the level of $1-2\%$. As a consequence, the L2 jet trigger was declared validated to run online in rejection mode.

As more data was collected in 2010, an improvement of the performance of the jet trigger was sought out, by studying different hadronic calibrations for trigger jets. Due to the similarities between L2 and offline jets at the EM-scale, applying an offline-based calibration to L2 jets, resulted in flat p_{T} response ratios with respect to offline, within 1% (2%) as a function of p_{T} (η). The offline-based calibration was able to improve the 99% efficiency points of L2 efficiency curves, and was, therefore, chosen as the default L2 calibration during 2012 data-taking.

Finally, the overall efficiency of the ATLAS jet trigger was evaluated using $\sqrt{s} =$ 7 TeV data collected in 2011, with and without the application of a pile-up noise suppression technique. Results showed the jet trigger was behaving well, and efficiently selecting events in a large transverse energy range. Moreover, the use of pile-up noise

suppression led to sharper turn-on curves, with an improvement of the overall 99% efficiency point by ~ 5 GeV.

Measurements of the Higgs boson production were performed using 25 fb^{-1} of pp collision data from the LHC at center-of-mass energies of 7 TeV and 8 TeV, collected by the ATLAS detector in 2011 and 2012. The $H \to WW^* \to \ell\nu\ell\nu$ decay channel was chosen for its large branching ratios and clean signature, of events with two leptons and large missing transverse momentum.

Drell-Yan is a major source of background in the $H \to WW^* \to \ell\nu\ell\nu$ analysis, especially for final states with two same flavor leptons. The degradation of the missing transverse energy resolution with pile-up makes it difficult to suppress this background, without significant loss of signal, particularly during 2012 data-taking, with an average number of interactions per bunch crossing of ~ 20. Therefore, a new kinematic variable - f_{recoil} - measuring the soft hadronic recoil of the dilepton system, was defined. A tight cut on f_{recoil} suppresses Drell-Yan by more than a factor of 7, even after tight $E_{\text{T}}^{\text{miss}}$ selections, while keeping $\sim 65\%$ of the signal.

Drell-Yan in the same flavor final states is very hard to accurately predict from simulation, as it depends on the modeling of fake $E_{\text{T}}^{\text{miss}}$ and soft jets. Therefore, a new data-driven technique - Pacman - was developed to estimate this background. In this technique, f_{recoil} distributions in data are used to measure the efficiency of the f_{recoil} selection for different processes, and to provide an estimate of the Drell-Yan contamination in the signal region that is insensitive to the presence of signal. Systematic uncertainties on Pacman were evaluated in detail using MC, and validated extensively in data. After all event selections are applied, the Drell-Yan yield is reduced to the same level of the signal, and estimated with a precision better than 50%.

The f_{recoil} variable and the Pacman technique were essential in reviving the $H \to WW^* \to \ell\nu\ell\nu$ analysis in same flavor final states, in 2012. With respect to the different flavor channels only, the same flavor analysis represents a $\sim 5\%$ improvement in sensitivity for $H \to WW^* \to \ell\nu\ell\nu$. An additional $10 - 20\%$ improvement in sensitivity was obtained by using a combined tracking and calorimeter measurement of the missing transverse energy in the computation of the transverse mass, which allowed for an improvement of the signal resolution and better separation between signal and background processes.

An excess of events over the background prediction, with a significance of 6.1σ, is observed in the combined (i.e. all final states and categories) analysis of the $H \to WW^* \to \ell\nu\ell\nu$ decay channel . This result establishes the first-ever observation of the Higgs boson in this channel. The signal strength - $1.08\ ^{+0.16}_{-0.15}$ (stat.) $^{+0.08}_{-0.07}$ (expt.) $^{+0.13}_{-0.11}$ (theo.) $\pm$ 0.03 (lumi.) $= 1.08\ ^{+0.22}_{-0.20}$ - is measured with a precision of $\sim 20\%$ and compatible with unity, indicating the observed rate is consistent with the Standard Model expectation for a Higgs boson with $m_H = 125.36$ GeV. This is the most precise measurement of the Higgs boson signal strength in ATLAS, and puts important constraints on measurements of the couplings of this particle to fermions and vector bosons. The statistical and systematic uncertainties on the measured signal strength are approximately of the

same size. The systematic uncertainty will be difficult to reduce, as the largest component arises from theoretical predictions. However, the precision on this measurement is expected to improve during Run II of the LHC, as more data is collected and the statistical uncertainty decreases.

Appendix A

Additional plots for studies in Section 3.2.2

The average p_{T} ratio between L2 and offline jets was evaluated for samples collected in 2010 with different L1 triggers. This is shown in Figures A.1 through A.6, as a function of of offline jet p_{T}, and offline jet η. For the former, the vertical line indicates the offline p_{T} threshold above which the L1 trigger selection is fully efficient. For the latter, only jets with p_{T} above this threshold are considered. Different data-taking periods are shown in each distribution. Figures A.1 and A.2 use L2 and offline jets and the EM scale. Figures A.3 and A.4 show the dedicated L2 calibration compared to the offline EM+JES scale. Finally, Figures A.5 and A.6 use the EM+JES calibration scheme for both L2 and offline jets.

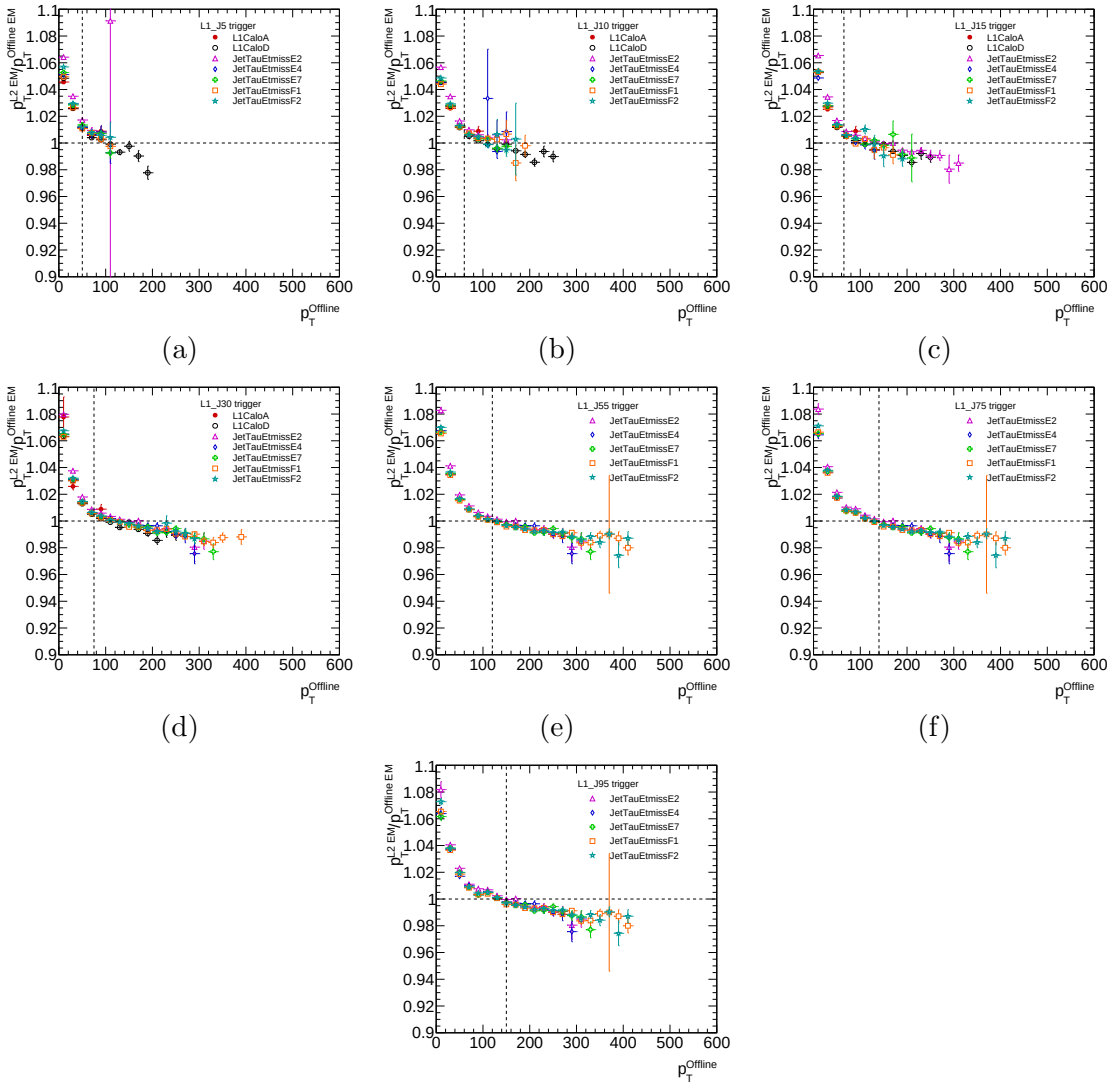

FIGURE A.1: Average L2 jet transverse momentum response ratio at the EM scale, with respect to the offline reconstructed jet p_T at the EM scale, for different data-taking periods. The datasets were collected with the following triggers: (a) `L1_J5`, (b) `L1_J10`, (c) `L1_J15`, (d) `L1_J30`, (e) `L1_J55`, (f) `L1_J75` and (g) `L1_J95`. The vertical lines indicate the offline thresholds for which the L1 trigger selection is selection is fully efficient.

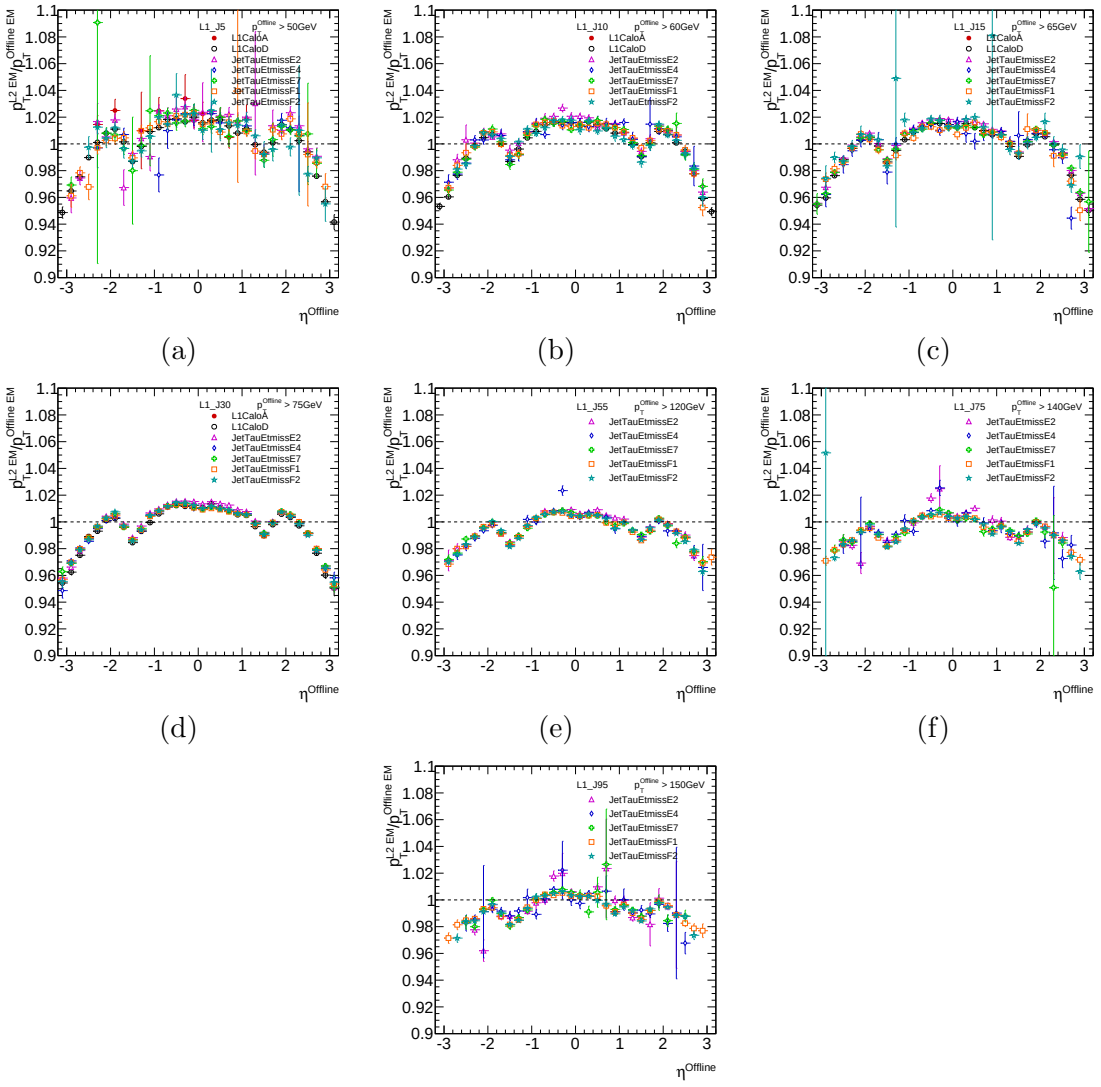

FIGURE A.2: Average L2 jet transverse momentum response ratio at the EM scale, with respect to offline η, for different data-taking periods. Only offline jets above the L1 bias threshold are included. The datasets were collected with the following triggers: (a) L1_J5, (b) L1_J10, (c) L1_J15, (d) L1_J30, (e) L1_J55, (f) L1_J75 and (g) L1_J95.

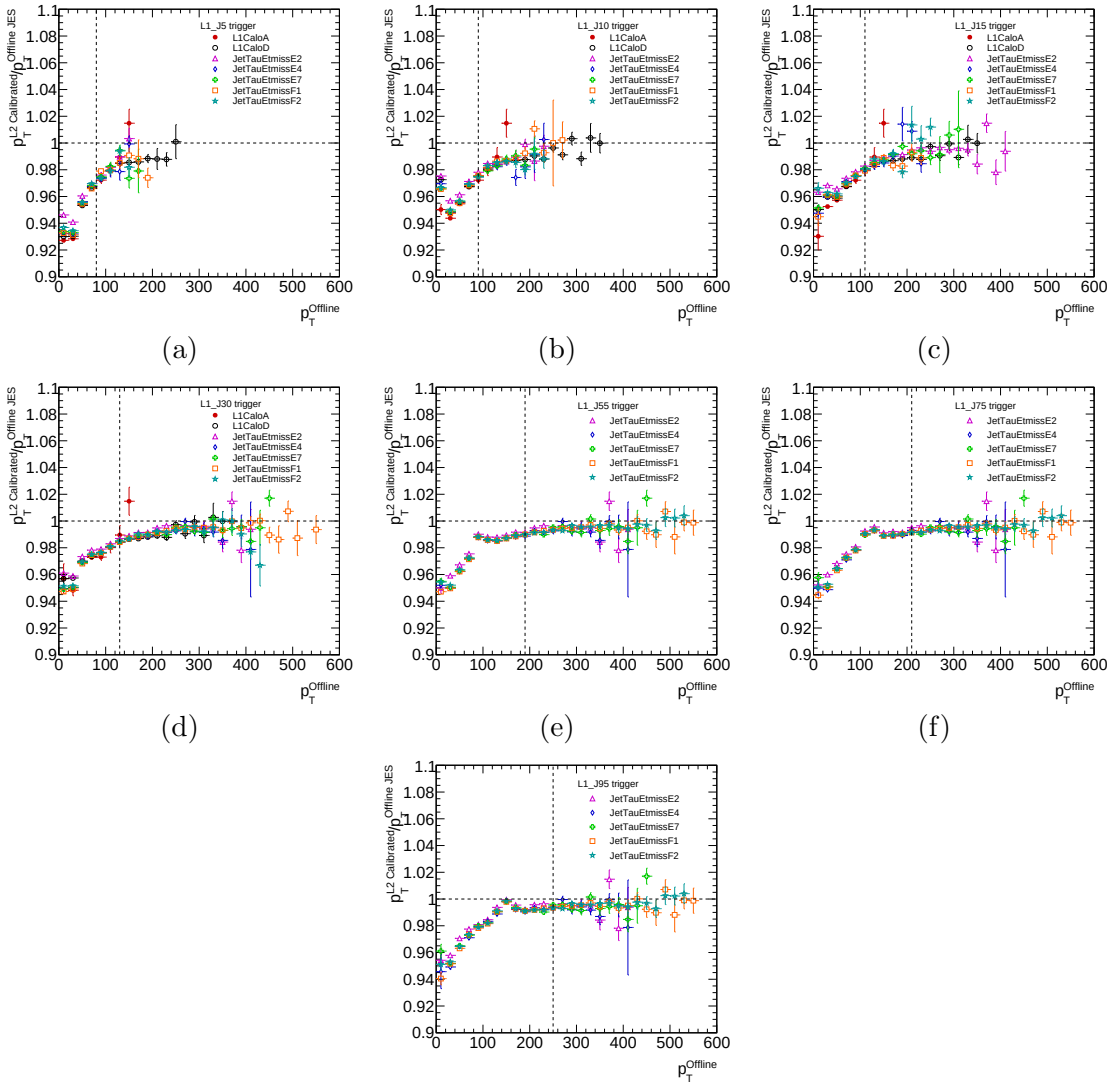

FIGURE A.3: Average L2 jet transverse momentum response ratio at the default calibrated scale, with respect to the offline reconstructed jet p_T at the EM+JES scale, for different data-taking periods. The datasets were collected with the following triggers: (a) L1_J5, (b) L1_J10, (c) L1_J15, (d) L1_J30, (e) L1_J55, (f) L1_J75 and (g) L1_J95. The vertical lines indicate the offline thresholds for which the L1 trigger selection is selection is fully efficient.

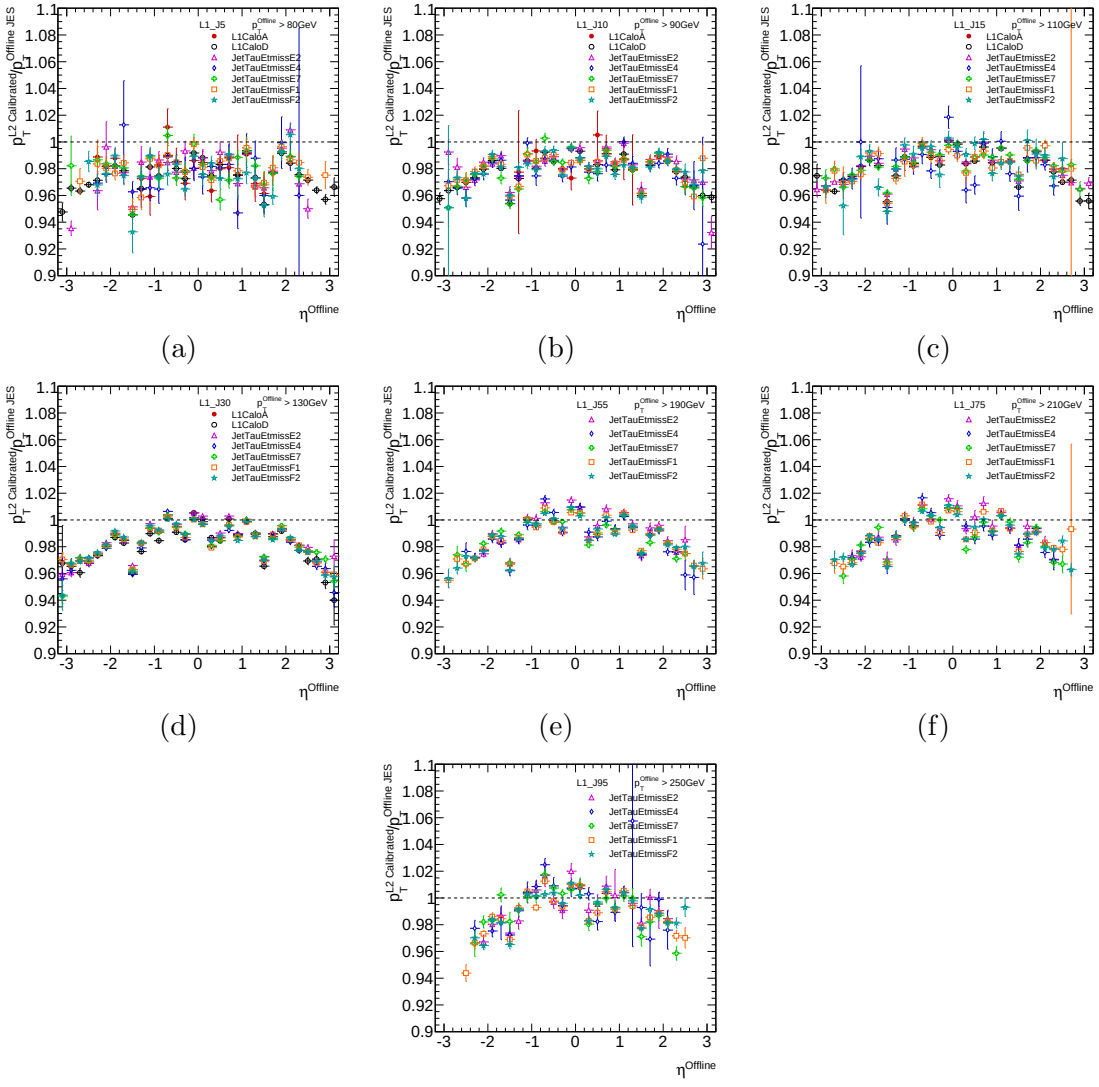

FIGURE A.4: Average L2 jet transverse momentum response ratio at the default calibrated scale, with respect to offline η, for different data-taking periods. Only offline jets above the L1 bias threshold are included. The datasets were collected with the following triggers: (a) L1_J5, (b) L1_J10, (c) L1_J15, (d) L1_J30, (e) L1_J55, (f) L1_J75 and (g) L1_J95.

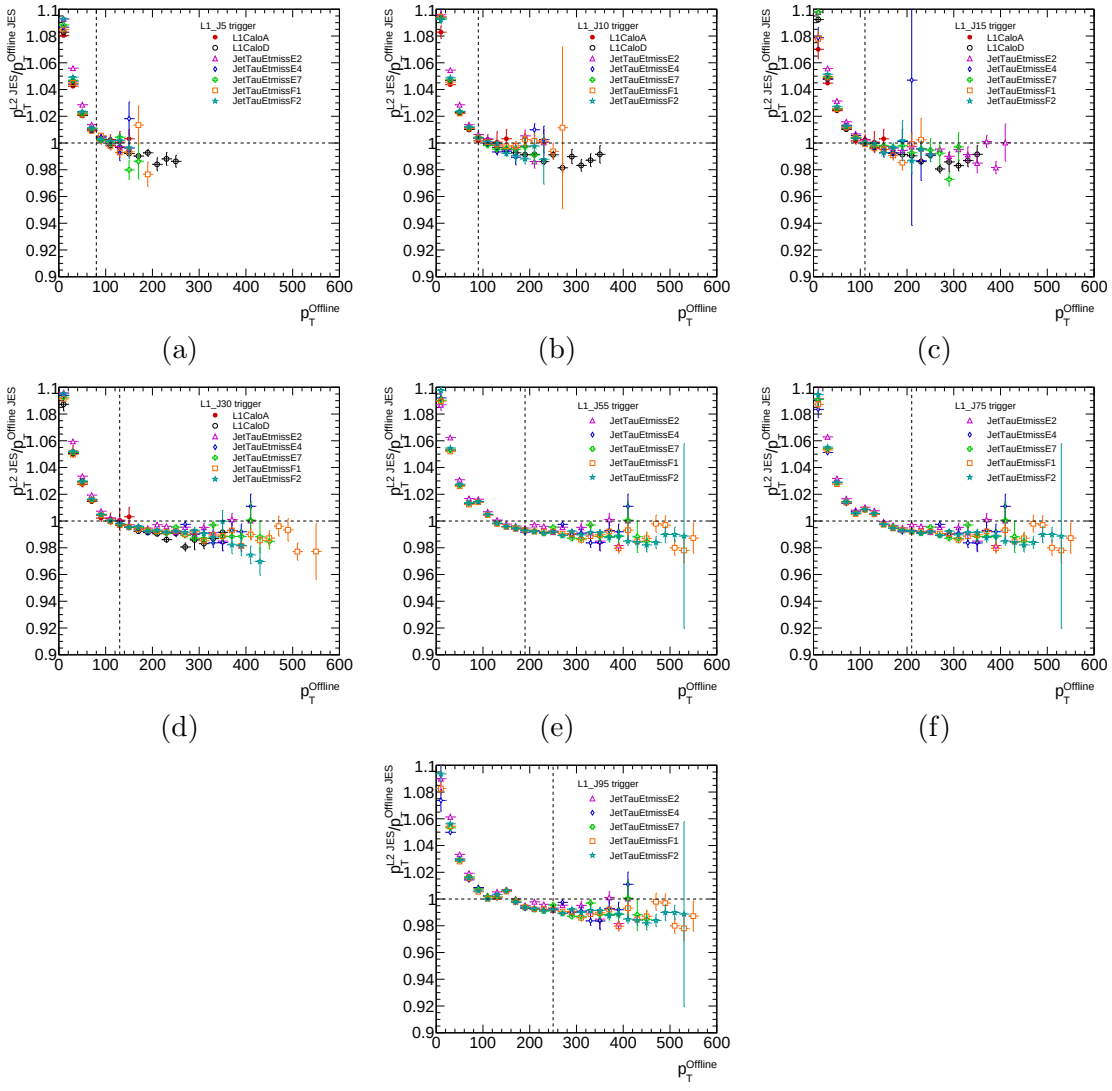

FIGURE A.5: Average L2 jet transverse momentum response ratio at the EM+JES scale, with respect to the offline reconstructed jet p_T at the EM+JES scale, for different data-taking periods. The datasets were collected with the following triggers: (a) `L1_J5`, (b) `L1_J10`, (c) `L1_J15`, (d) `L1_J30`, (e) `L1_J55`, (f) `L1_J75` and (g) `L1_J95`. The vertical lines indicate the offline thresholds for which the L1 trigger selection is selection is fully efficient.

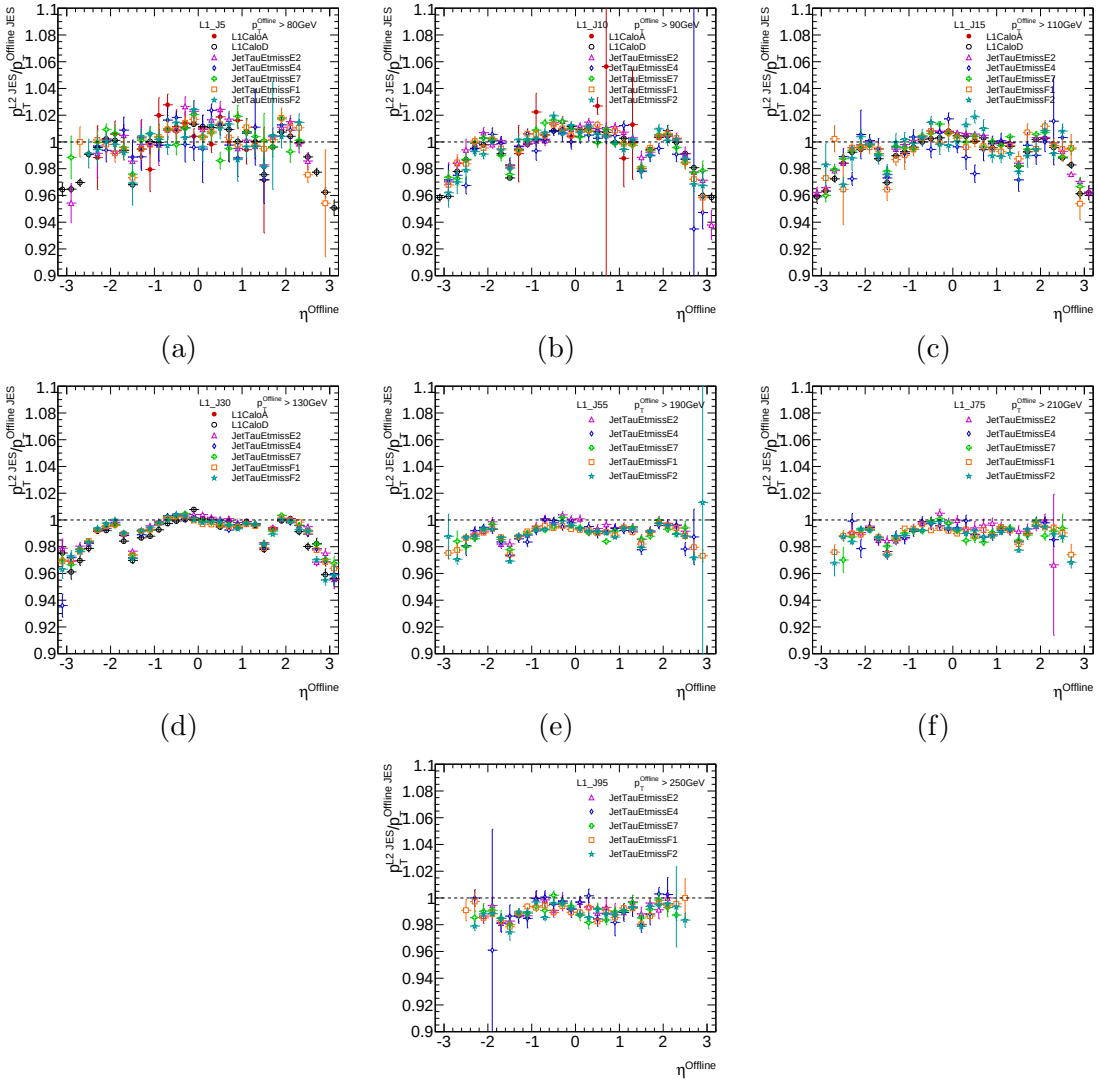

FIGURE A.6: Average L2 jet transverse momentum response ratio at the EM+JES scale, with respect to offline η, for different data-taking periods. Only offline jets above the L1 bias threshold are included. The datasets were collected with the following triggers: (a) L1_J5, (b) L1_J10, (c) L1_J15, (d) L1_J30, (e) L1_J55, (f) L1_J75 and (g) L1_J95.

Appendix B

Additional plots for p_{T}^{Z} reweighting

Due to correlations with $p_{\mathrm{T}}^{\ell\ell}$, the description of other kinematic variables in the same flavor 0-jet Z-peak, such as lepton p_{T}, missing transverse energy, transverse mass and $\Delta\phi_{\ell\ell}$, is also greatly improved by the p_{T}^{Z} reweighting procedure. This is shown in Figures B.1 and B.2, where the left-hand side shows the distributions before the reweighting and the right-hand side shows the distributions after the reweighting.

The improvement is not as noticeable in the different flavor channels, where the dilepton system is less correlated with the Z boson. The distributions in Figures B.3 and B.4 show already a good modeling of different kinematic variables, that slightly improves after p_{T}^{Z} reweighting, as indicated by the KS probabilities which tend to increase.

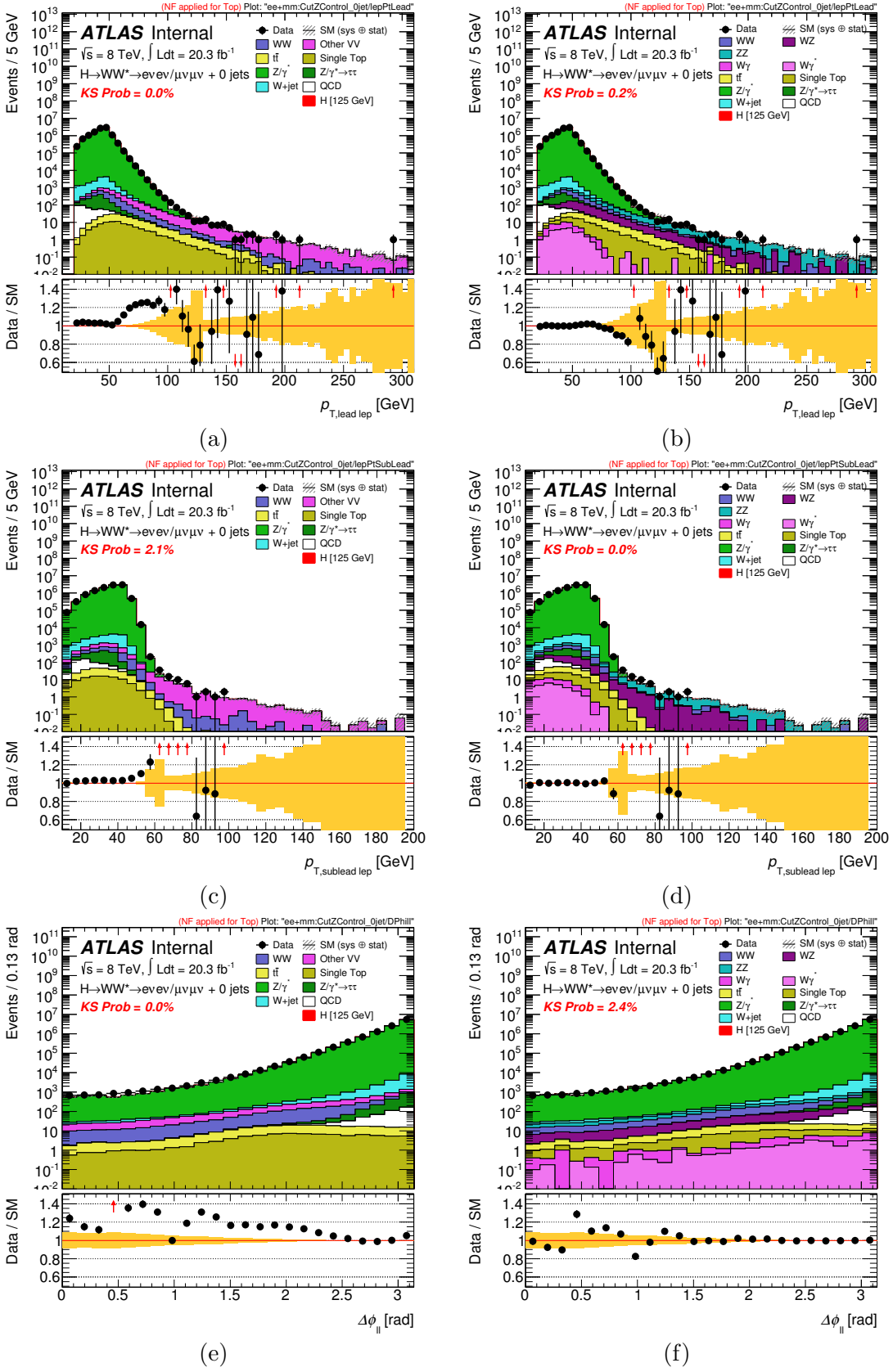

FIGURE B.1: Distributions for $ee + \mu\mu + 0$-jet events in the Z-peak of: (a-b) leading lepton p_{T}; (c-d) subleading lepton p_{T}; and (e-f) $\Delta\phi_{\ell\ell}$. The nominal ALPGEN + HERWIG generator is used to model Drell-Yan events. (a), (c) and (e) are shown before p_{T}^Z reweighting. (b), (d) and (f) are shown after p_{T}^Z reweighting is applied. The modelling of the distributions improves in general after the p_{T}^Z reweighting.

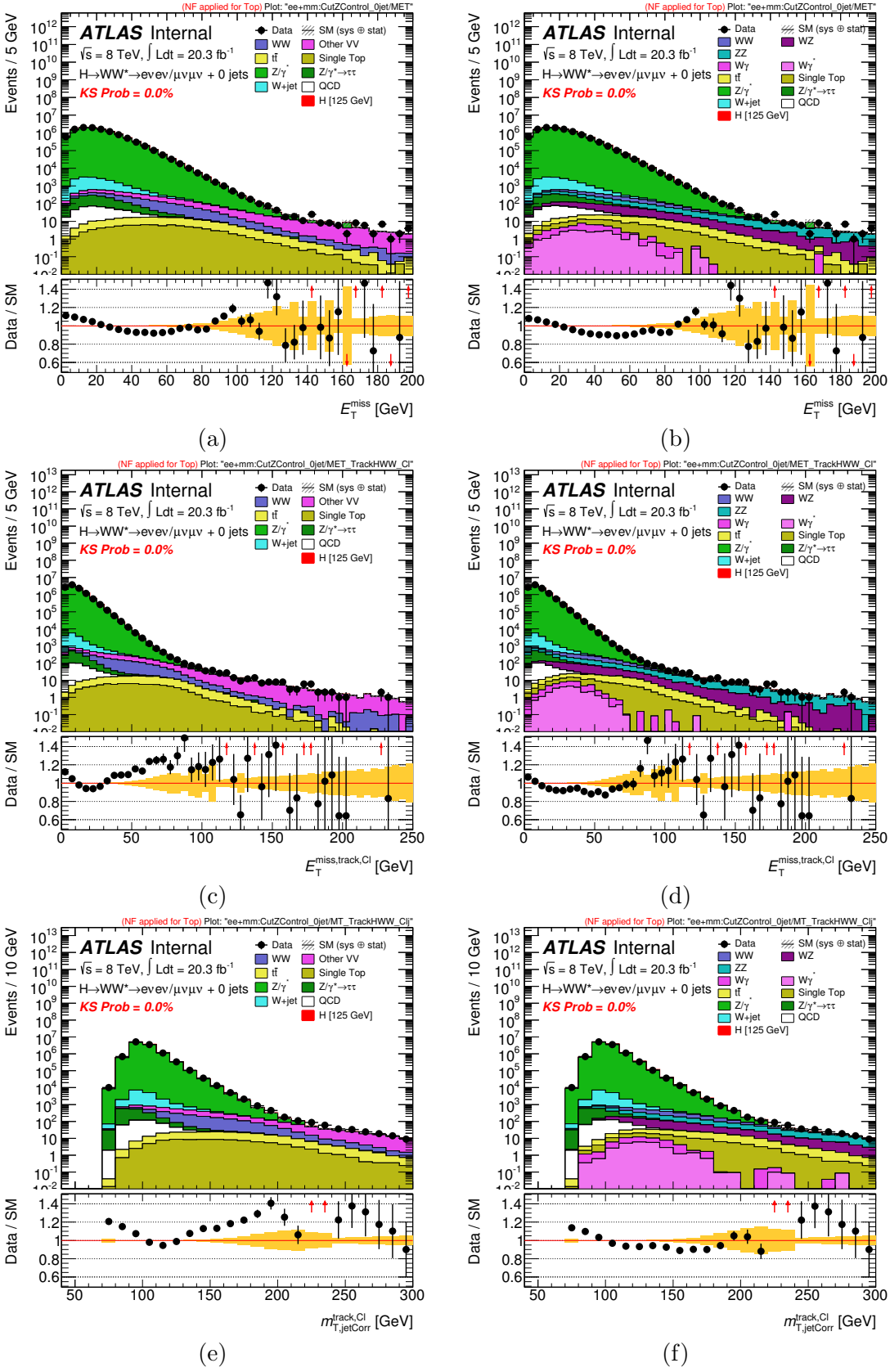

FIGURE B.2: Distributions for $ee+\mu\mu+0$-jet events in the Z-peak of: (a-b) $E_{\mathrm{T}}^{\mathrm{miss,calo}}$; (c-d) $p_{\mathrm{T}}^{\mathrm{miss,track}}$; and (e-f) m_{T}. The nominal ALPGEN + HERWIG generator is used to model Drell-Yan events. (a), (c) and (e) are shown before p_{T}^{Z} reweighting. (b), (d) and (f) are shown after p_{T}^{Z} reweighting is applied. The modelling of the distributions improves in general after the p_{T}^{Z} reweighting.

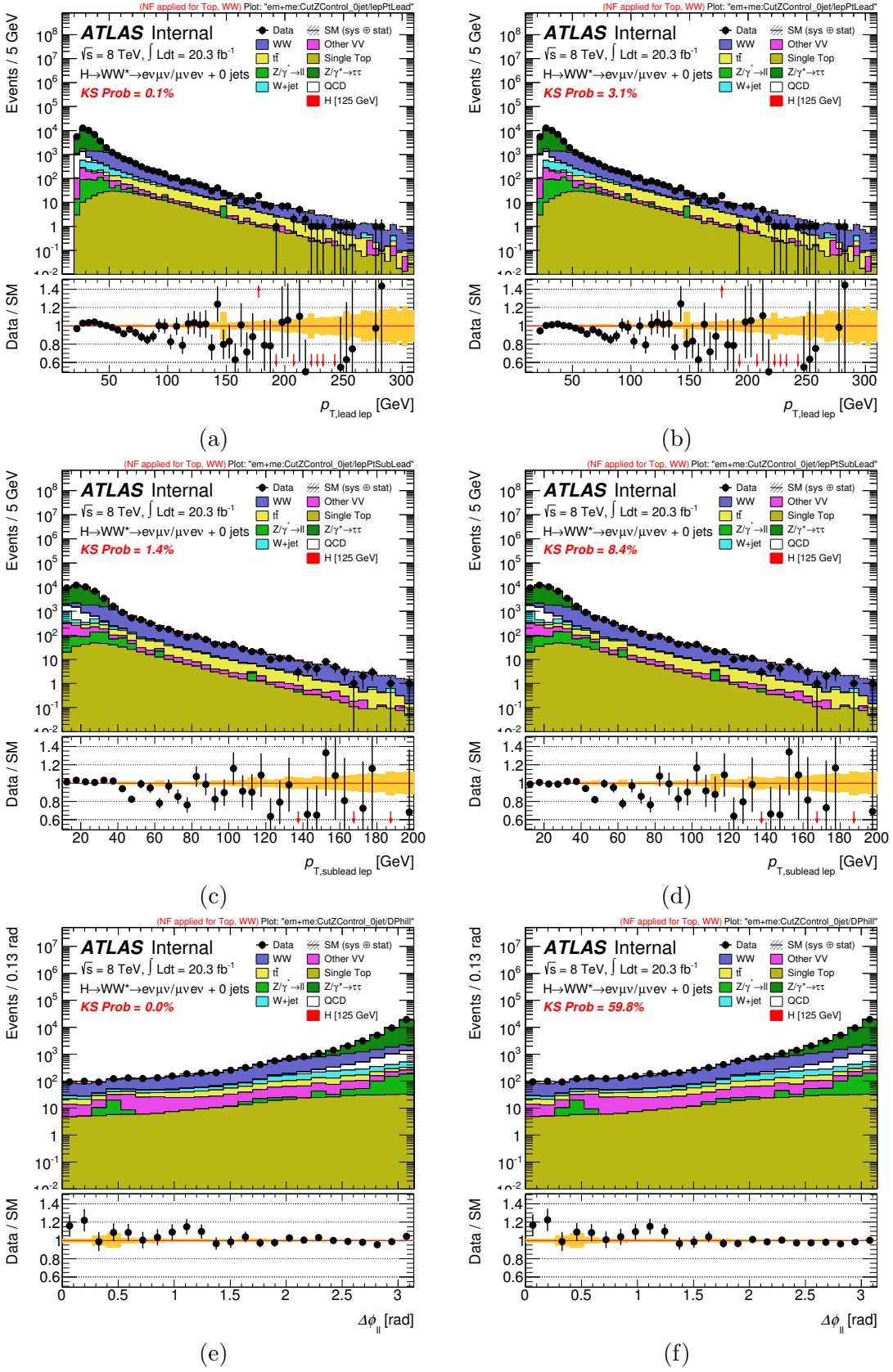

FIGURE B.3: Distributions for $e\mu + \mu e + 0$-jet events of: (a-b) leading lepton p_{T}; (c-d) subleading lepton p_{T}; and (e-f) $\Delta\phi_{\ell\ell}$. The nominal ALPGEN + HERWIG generator is used to model Drell-Yan events. (a), (c) and (e) are shown before p_{T}^Z reweighting. (b), (d) and (f) are shown after p_{T}^Z reweighting is applied. The modelling of the distributions improves in general after the p_{T}^Z reweighting.

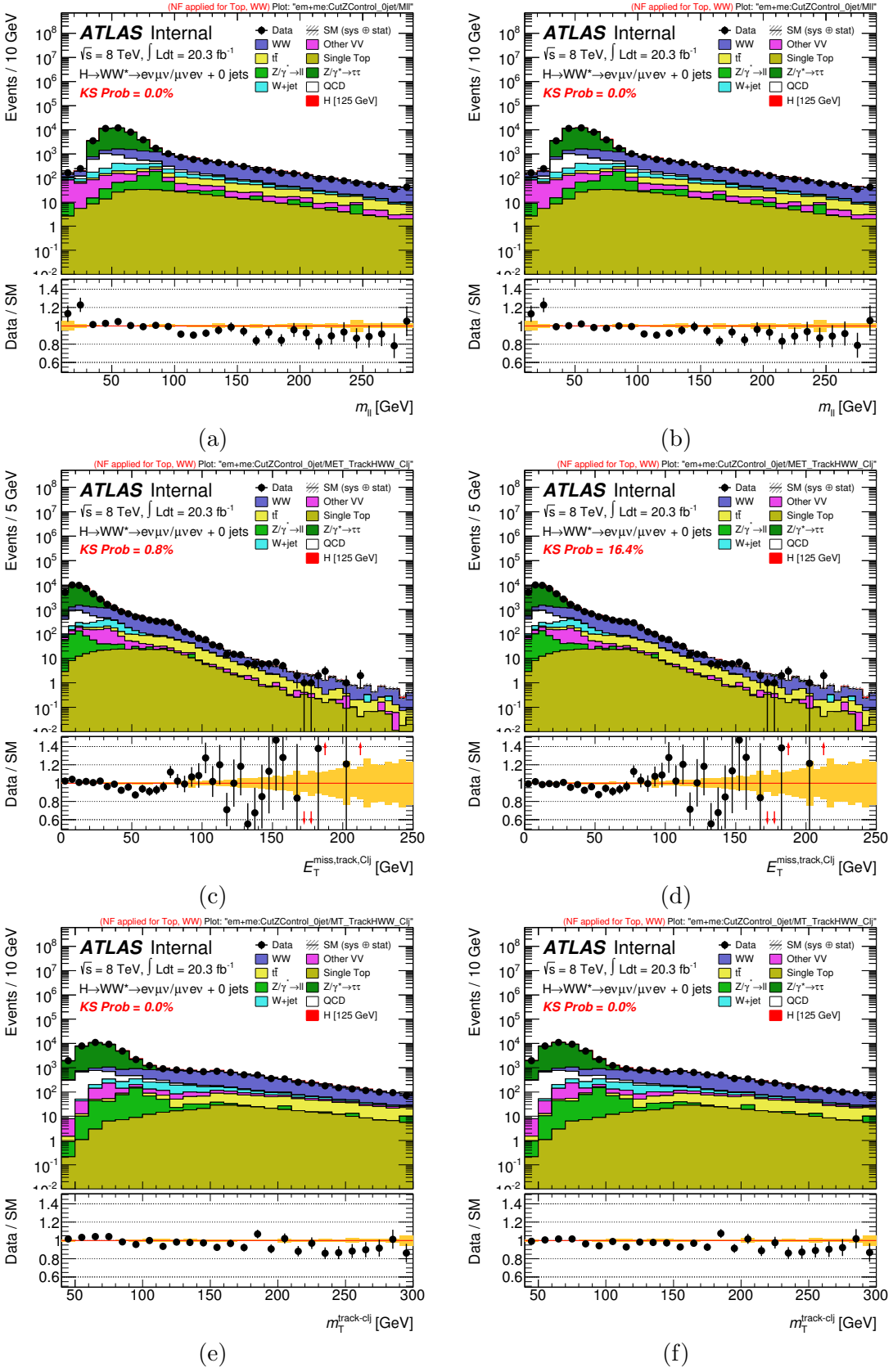

FIGURE B.4: Distributions for different flavor 0-jet events of: (a-b) $E_{\mathrm{T}}^{\mathrm{miss,calo}}$; (c-d) $p_{\mathrm{T}}^{\mathrm{miss,track}}$; and (e-f) m_{T}. The nominal ALPGEN + HERWIG generator is used to model Drell-Yan events. (a), (c) and (e) are shown before p_{T}^Z reweighting. (b), (d) and (f) are shown after p_{T}^Z reweighting is applied. The modelling of the distributions improves in general after the p_{T}^Z reweighting.

Appendix C

Additional plots for studies in Section 4.7.3.2

The systematic uncertainties assigned to the DY f_{recoil} efficiencies measured for the Pacman method were validated by checking the dependence of the Z-peak $\rightarrow$ low $m_{\ell\ell}$ extrapolation with $E_{\text{T,rel}}^{\text{miss,calo}}$, for same flavor data and MC DY events. This was shown in Figure 4.57. Here, variations of these distributions are shown. In Figure C.1 (Figure C.2) only ee ($\mu\mu$) events are considered. Figure C.3 shows the impact of the p_{T}^{Z} reweighting procedure on the Z peak $\rightarrow$ low $m_{\ell\ell}$ extrapolation. Figure C.4 shows the extrapolation for the 0-jet channel with different selections on $p_{\text{T,rel}}^{\text{miss,track}}$. These distributions further validate the systematic uncertainties assigned in the Pacman method.

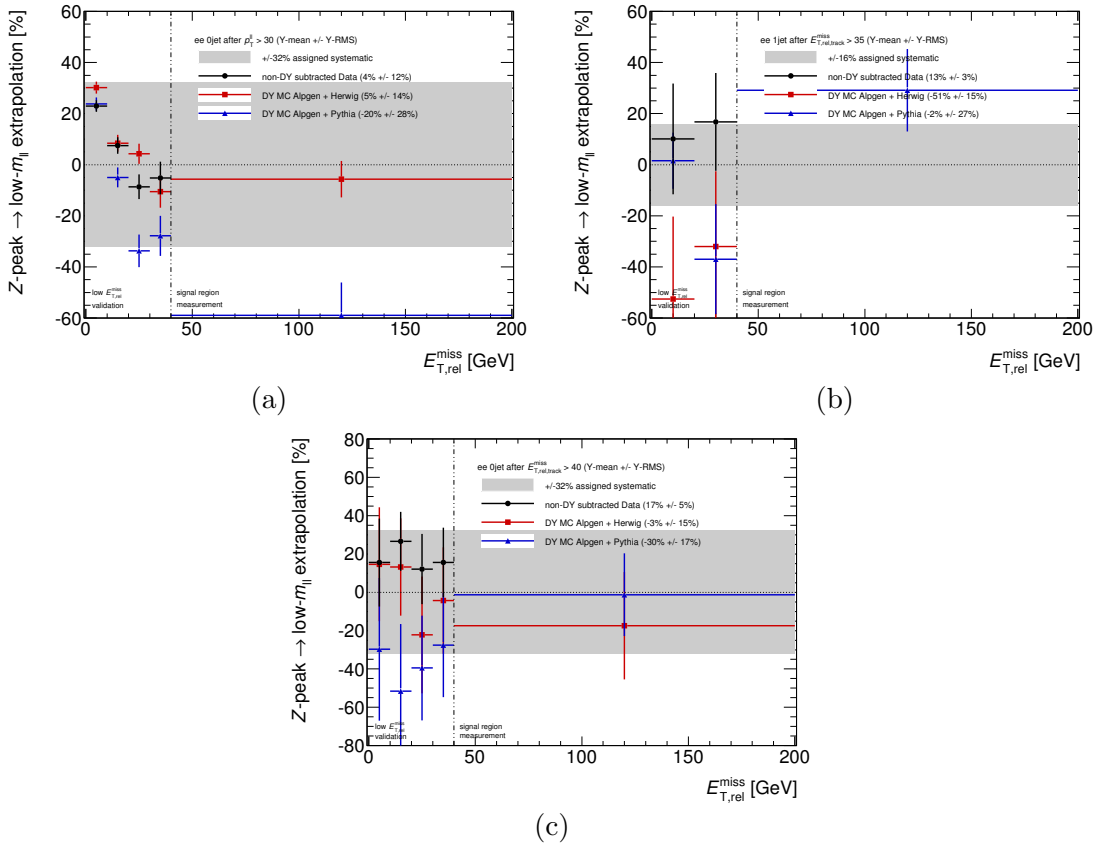

FIGURE C.1: Z-peak → low $m_{\ell\ell}$ extrapolation as a function of $E^{\mathrm{miss,calo}}_{\mathrm{T,rel}}$, for ee events with: (a) 0-jets after the $p^{\ell\ell}_{\mathrm{T}}$ selection; (b) 1-jet after the $p^{\mathrm{miss,track}}_{\mathrm{T,rel}}$ selection; and (c) 0-jets after the $p^{\mathrm{miss,track}}_{\mathrm{T,rel}}$ selection. The black bullets show data, with the non-DY contribution subtracted using simulation; the red squares show the nominal DY MC sample; the blue triangles show an alternative DY MC sample. The gray bands display the assigned systematic uncertainties. The numbers in the legend are informative only and show the mean ± RMS of the distributions over the y-axis.

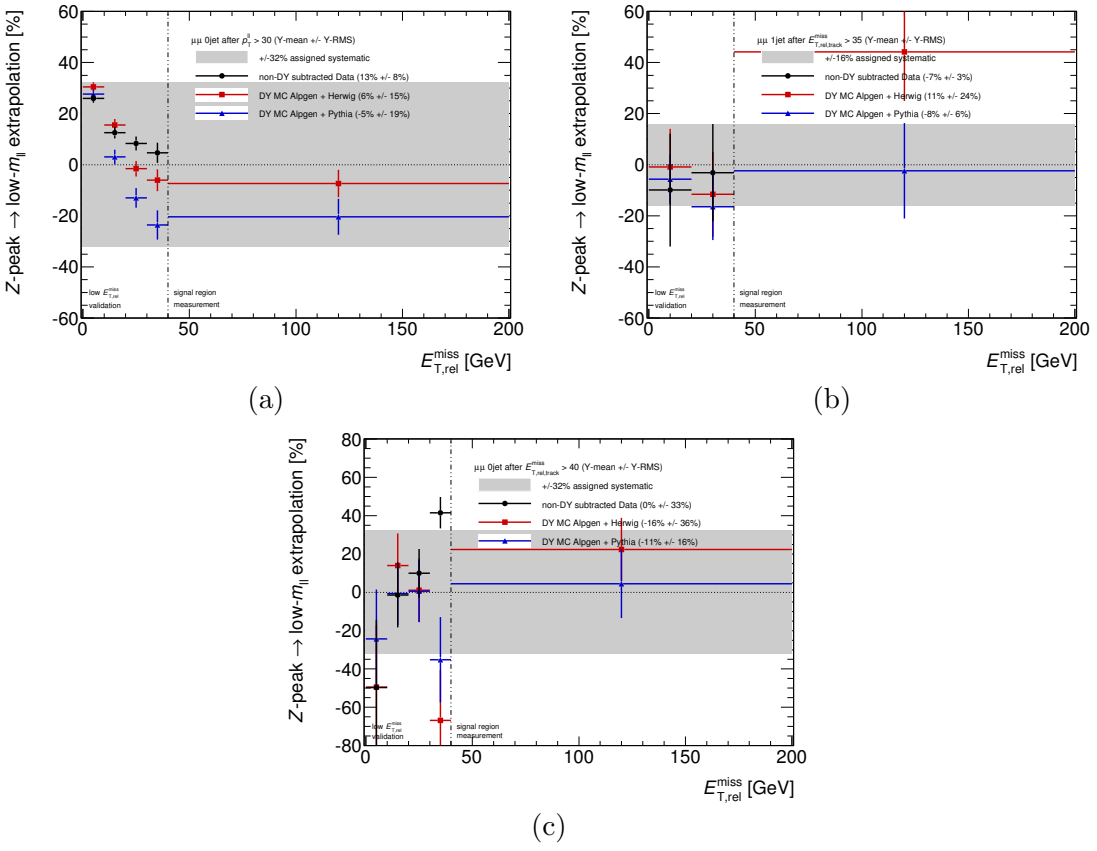

FIGURE C.2: Z-peak → low $m_{\ell\ell}$ extrapolation as a function of $E_{\mathrm{T,rel}}^{\mathrm{miss,calo}}$, for $\mu\mu$ events with: (a) 0-jets after the $p_{\mathrm{T}}^{\ell\ell}$ selection; (b) 1-jet after the $p_{\mathrm{T,rel}}^{\mathrm{miss,track}}$ selection; and (c) 0-jets after the $p_{\mathrm{T,rel}}^{\mathrm{miss,track}}$ selection. The black bullets show data, with the non-DY contribution subtracted using simulation; the red squares show the nominal DY MC sample; the blue triangles show an alternative DY MC sample. The gray bands display the assigned systematic uncertainties. The numbers in the legend are informative only and show the mean ± RMS of the distributions over the y-axis.

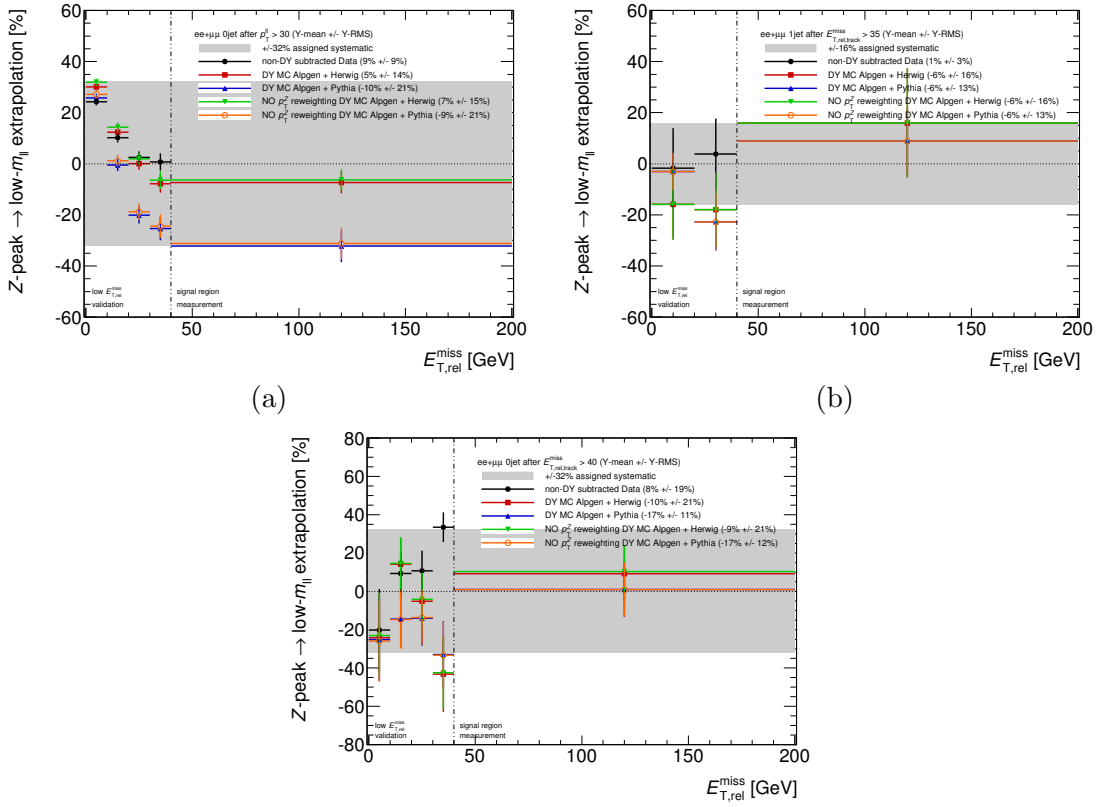

FIGURE C.3: Z-peak → low $m_{\ell\ell}$ extrapolation as a function of $E^{\mathrm{miss,calo}}_{\mathrm{T,rel}}$, for events with: (a) 0-jets after the $p^{\ell\ell}_{\mathrm{T}}$ selection; (b) 1-jet after the $p^{\mathrm{miss,track}}_{\mathrm{T,rel}}$ selection; and (c) 0-jets after the $p^{\mathrm{miss,track}}_{\mathrm{T,rel}}$ selection. The black bullets show data, with the non-DY contribution subtracted using simulation; the red squares (green triangles) show the nominal DY MC sample, after (before) p^Z_{T} reweighting; the blue triangles (orange circles) show an alternative DY MC sample, after (before) p^Z_{T} reweighting. The gray bands display the assigned systematic uncertainties. The numbers in the legend are informative only and show the mean ± RMS of the distributions over the y-axis.

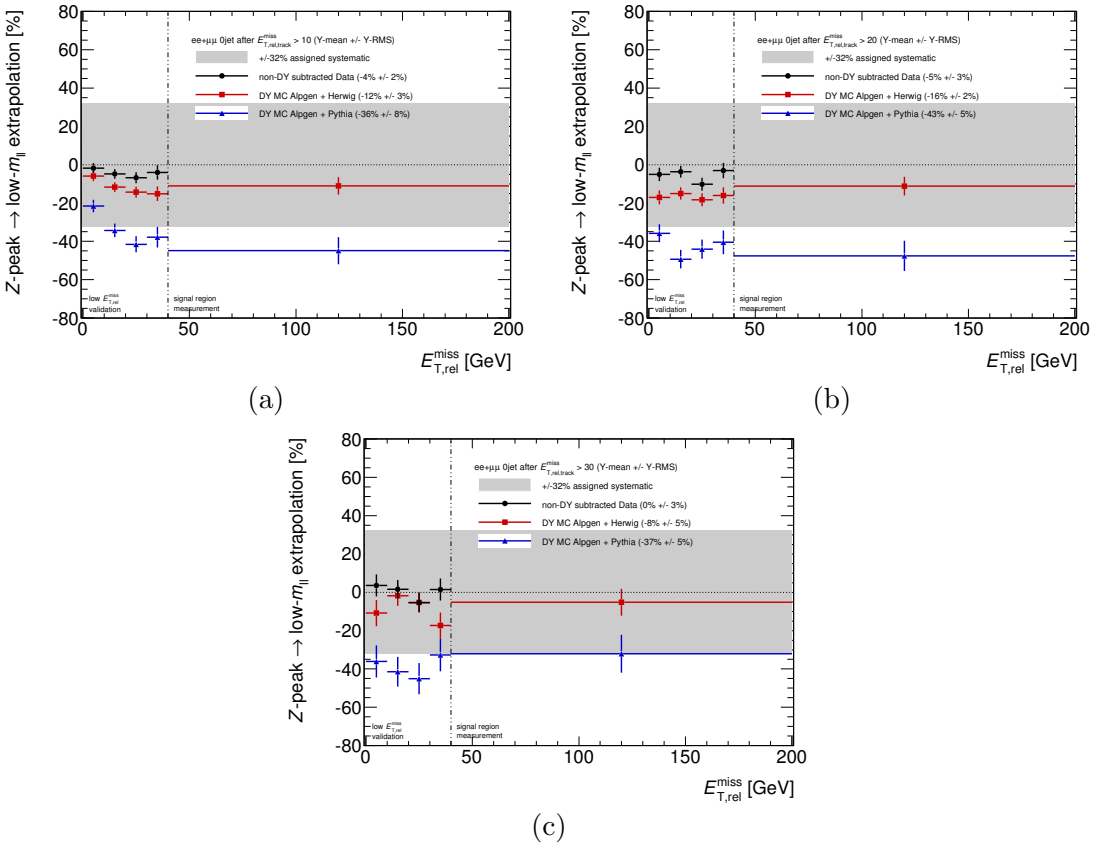

FIGURE C.4: Z-peak → low $m_{\ell\ell}$ extrapolation as a function of $E^{\mathrm{miss,calo}}_{\mathrm{T,rel}}$, for events with 0-jets after different $p^{\mathrm{miss,track}}_{\mathrm{T,rel}}$ selections: (a) $p^{\mathrm{miss,track}}_{\mathrm{T,rel}} > 10$ GeV; (b) $p^{\mathrm{miss,track}}_{\mathrm{T,rel}} > 20$ GeV; and (c) $p^{\mathrm{miss,track}}_{\mathrm{T,rel}} > 30$ GeV. The black bullets show data, with the non-DY contribution subtracted using simulation; the red squares show the nominal DY MC sample; the blue triangles show an alternative DY MC sample. The gray bands display the assigned systematic uncertainties. The numbers in the legend are informative only and show the mean ± RMS of the distributions over the y-axis.

Bibliography

[1] J. Ellis, *Higgs Physics*, `arXiv:1312.5672 [hep-ph]`.

[2] A. Pich, *The Standard Model of Electroweak Interactions*, `arXiv:1201.0537 [hep-ph]`.

[3] A. Djouadi, *The anatomy of electroweak symmetry breaking*, Physics Reports **457** no. 1-4, (2008) 1–216, `arXiv:hep-ph/0503172 [hep-ph]`.

[4] D. Griffiths, *Introduction to Elementary Particles*. John Wiley & Sons, 1987.

[5] F. Halzen and A. D. Martin, *Quarks & Leptons: An Introductory Course in Modern Particle Physics*. John Wiley & Sons, 1984.

[6] S. L. Glashow, *Partial-symmetries of weak interactions*, Nuclear Physics **22** no. 4, (1961) 579–588.

[7] F. Englert and R. Brout, *Broken Symmetry and the Mass of Gauge Vector Mesons*, Phys. Rev. Lett. **13** no. 9, (1964) 321–323.

[8] P. W. Higgs, *Broken symmetries, massless particles and gauge fields*, Physics Letters **12** no. 2, (1964) 132–133.

[9] G. S. Guralnik, C. R. Hagen, and T. W. B. Kibble, *Global Conservation Laws and Massless Particles*, Phys. Rev. Lett. **13** no. 20, (1964) 585–587.

[10] Y. Nambu, *Axial Vector Current Conservation in Weak Interactions*, Phys. Rev. Lett. **4** no. 7, (1960) 380–382.

[11] J. Goldstone, *Field Theories with Superconductor Solution*, Il Nuovo Cimento **19** no. 1, (1961) 154–164.

[12] J. Goldstone, A. Salam, and S. Weinberg, *Broken Symmetries*, Physical Review **127** no. 3, (1962) 965–970.

[13] P. W. Higgs, *Broken Symmetries and the Masses of Gauge Bosons*, Phys. Rev. Lett. **13** no. 16, (1964) 508–509.

[14] S. Weinberg, *A Model of Leptons*, Phys. Rev. Lett. **19** no. 21, (1967) 1264–1266.

[15] A. Salam, *Weak and electromagnetic interactions*, Proceedings of the 8th Nobel Symposium (1968) 367–377.

[16] M. Gell-Mann, *A schematic model of baryons and mesons*, Physics Letters **8** no. 3, (1964) 214–215.

[17] G. Zweig, *An SU(3) Model for Strong Interaction Symmetry and its Breaking*, CERN-8419-TH-412 (1964).

[18] O. W. Greenberg, *Spin and Unitary-Spin Independence in a Paraquark Model of Baryons and Mesons*, Phys. Rev. Lett. **13** no. 20, (1964) 598–602.

[19] H. Fritzsch, M. Gell-Mann, and H. Leutwyler, *Advantages of the color octet gluon picture*, Physics Letters B **47** no. 4, (1973) 365–368.

[20] D. Gross and F. Wilczek, *Ultraviolet Behavior of Non-Abelian Gauge Theories*, Physical Review Letters **30** no. 26, (1973) 1343–1346.

[21] H. Politzer, *Reliable Perturbative Results for Strong Interactions?*, Physical Review Letters **30** no. 26, (1973) 1346–1349.

[22] G. 't Hooft and M. Veltman, *Regularization and renormalization of gauge fields*, Nuclear Physics B **44** no. 1, (1972) 189–213.

[23] F. Hasert, S. Kabe, W. Krenz, et al., *Observation of neutrino-like interactions without muon or electron in the gargamelle neutrino experiment*, Physics Letters B **46** no. 1, (1973) 138–140.

[24] M. Banner, R. Battiston, P. Bloch, et al., *Observation of single isolated electrons of high transverse momentum in events with missing transverse energy at the CERN p collider*, Physics Letters B **122** no. 5-6, (1983) 476–485.

[25] G. Arnison, A. Astbury, B. Aubert, et al., *Experimental observation of isolated large transverse energy electrons with associated missing energy at*, Physics Letters B **122** no. 1, (1983) 103–116.

[26] E. D. Bloom, D. H. Coward, H. DeStaebler, et al., *High-Energy Inelastic e-p Scattering at 6^o and 10^o*, Phys. Rev. Lett. **23** no. 16, (1969) 930–934.

[27] M. Breidenbach, J. I. Friedman, H. W. Kendall, et al., *Observed Behavior of Highly Inelastic Electron-Proton Scattering*, Phys. Rev. Lett. **23** no. 16, (1969) 935–939.

[28] J. E. Augustin, A. M. Boyarski, M. Breidenbach, et al., *Discovery of a narrow resonance in e+e- annihilation*, Physical Review Letters **33** no. 23, (1974) 1406–1408.

[29] J. J. Aubert, U. Becker, P. J. Biggs, et al., *Experimental observation of a heavy particle J*, Physical Review Letters **33** no. 23, (1974) 1404–1406.

[30] R. Brandelik, W. Braunschweig, K. Gather, et al., *Evidence for planar events in $e + e-$ annihilation at high energies*, Physics Letters B **86** no. 2, (1979) 243–249.

[31] M. Perl, *Evidence for Anomalous Lepton Production in $e^+ - e^-$ Annihilation*, Phys. Rev. Lett. **35** (1975) 1489.

[32] S. W. Herb, D. C. Hom, L. M. Lederman, et al., *Observation of a Dimuon Resonance at 9.5 GeV in 400-GeV Proton-Nucleus Collisions*, Phys. Rev. Lett. **39** (1977) 252.

[33] CDF Collaboration, *Observation of Top Quark Production in $p\bar{p}$ Collisions with the Collider Detector at Fermilab*, Physical Review Letters **74** no. 14, (1995) 2626–2631, arXiv:hep-ex/9503002 [hep-ex].

[34] D0 Collaboration, *Observation of the Top Quark*, Physical Review Letters **74** no. 14, (1995) 2632–2637, arXiv:hep-ex/9503003 [hep-ex].

[35] ATLAS Collaboration, *Observation of a new particle in the search for the Standard Model Higgs boson with the ATLAS detector at the LHC*, Physics Letters B **716** no. 1, (2012) 1–29, arXiv:1207.7214 [hep-ex].

[36] CMS Collaboration, *Observation of a new boson at a mass of 125 GeV with the CMS experiment at the LHC*, Physics Letters B **716** no. 1, (2012) 30–61, arXiv:1207.7235 [hep-ex].

[37] Particle Data Group, *The Review of Particle Physics*, Phys. Rev. D **86** no. 010001, (2013).

[38] S. Bethke, *World Summary of α_s (2012)*, Nuclear Physics B - Proceedings Supplements **234** (2013) 229–234, arXiv:1210.0325v1 [hep-ex].

[39] The Gfitter Group, "A Generic Fitter Project for HEP Model Testing." http://www.cern.ch/Gfitter.

[40] G. P. Salam, *Elements of QCD for hadron colliders*, arXiv:1011.5131 [hep-ph].

[41] T. Sjostrand, *Monte Carlo Generators*, arXiv:hep-ph/0611247 [hep-ph].

[42] J. M. Campbell, J. Huston, and W. J. Stirling, *Hard interactions of quarks and gluons: a primer for LHC physics*, Reports on Progress in Physics **70** no. 1, (2007) 89–193, arXiv:hep-ph/0611148 [hep-ph].

[43] W. J. Stirling, "Parton Luminosity and Cross Section Plots." http://www.hep.ph.ic.ac.uk/$\sim$wstirlin/plots/plots.html.

[44] G. Altarelli and G. Parisi, *Asymptotic freedom in parton language*, Nuclear Physics B **126** no. 2, (1977) 298–318.

[45] G. P. Salam, *Towards Jetography*, arXiv:0906.1833 [hep-ph].

[46] S. D. Ellis, J. Huston, K. Hatakeyama, P. Loch, and M. Tönnesmann, *Jets in hadron–hadron collisions*, Progress in Particle and Nuclear Physics **60** no. 2, (2008) 484–551, arXiv:0712.2447.

[47] G. C. Blazey, J. R. Dittmann, S. D. Ellis, et al., *Run II Jet Physics: Proceedings of the Run II QCD and Weak Boson Physics Workshop*, `arXiv:hep-ex/0005012v2 [hep-ex]`.

[48] M. Cacciari, G. P. Salam, and G. Soyez, *The anti-k_t jet clustering algorithm*, Journal of High Energy Physics **2008** no. 04, (2008) 063–063, `arXiv:0802.1189 [hep-ph]`.

[49] Y. Dokshitzer, G. Leder, S. Moretti, and B. Webber, *Better jet clustering algorithms*, Journal of High Energy Physics **1997** no. 08, (1997) 001–001, `arXiv:hep-ph/9707323 [hep-ph]`.

[50] M. Wobisch and T. Wengler, *Hadronization Corrections to Jet Cross Sections in Deep-Inelastic Scattering*, `arXiv:hep-ph/9907280 [hep-ph]`.

[51] S. Catani, Y. Dokshitzer, M. Seymour, and B. Webber, *Longitudinally-invariant k_t-clustering algorithms for hadron-hadron collisions*, Nuclear Physics B **406** no. 1-2, (1993) 187–224.

[52] S. D. Ellis, *Successive combination jet algorithm for hadron collisions*, Physical Review D **48** no. 7, (1993) 3160–3166, `arXiv:hep-ph/9305266 [hep-ph]`.

[53] The LHC Higgs Cross Section Working Group, *Handbook of LHC Higgs Cross Sections: 1. Inclusive Observables*, `arXiv:1101.0593 [hep-ph]`.

[54] The LHC Higgs Cross Section Working Group, *Handbook of LHC Higgs Cross Sections: 2. Differential Distributions*, `arXiv:1201.3084 [hep-ph]`.

[55] The LHC Higgs Cross Section Working Group, *Handbook of LHC Higgs Cross Sections: 3. Higgs Properties*, `arXiv:1307.1347 [hep-ph]`.

[56] The LHC Higgs Cross Section Working Group, "LHC Higgs Cross Section Working Group." `https://twiki.cern.ch/twiki/bin/view/LHCPhysics/LHCHXSWG`.

[57] H. M. Georgi, S. L. Glashow, M. E. Machacek, and D. V. Nanopoulos, *Higgs Bosons from Two-Gluon Annihilation in Proton-Proton Collisions*, Phys. Rev. Lett. **40** no. 11, (1978) 692—-694.

[58] D. de Florian and M. Grazzini, *Higgs production at the LHC: Updated cross sections at $\sqrt{s} = 8 \sim TeV$*, Physics Letters B **718** no. 1, (2012) 117–120.

[59] C. Anastasiou and K. Melnikov, *Higgs boson production at hadron colliders in NNLO QCD*, Nuclear Physics B **646** no. 1-2, (2002) 220–256.

[60] M. Spira, A. Djouadi, D. Graudenz, and R. Zerwas, *Higgs boson production at the LHC*, Nuclear Physics B **453** no. 1-2, (1995) 17–82.

[61] A. Djouadi, M. Spira, and P. Zerwas, *Production of Higgs bosons in proton colliders. QCD corrections*, Physics Letters B **264** no. 3-4, (1991) 440–446.

[62] V. Ravindran, J. Smith, and W. van Neerven, *NNLO corrections to the total cross section for Higgs boson production in hadron–hadron collisions*, Nuclear Physics B **665** (2003) 325–366.

[63] R. Harlander and W. Kilgore, *Next-to-Next-to-Leading Order Higgs Production at Hadron Colliders*, Physical Review Letters **88** no. 20, (2002) 201801, arXiv:hep-ph/0201206 [hep-ph].

[64] S. Dawson, *Radiative corrections to Higgs boson production*, Nuclear Physics B **359** no. 2-3, (1991) 283–300.

[65] S. Catani, D. de Florian, M. Grazzini, and P. Nason, *Soft-gluon resummation for Higgs boson production at hadron colliders*, Journal of High Energy Physics **2003** no. 07, (2003) 028–028, arXiv:hep-ph/0306211 [hep-ph].

[66] U. Aglietti, R. Bonciani, G. Degrassi, and A. Vicini, *Master integrals for the two-loop light fermion contributions to $gg \to H$ and $H \to \gamma\gamma$*, Physics Letters B **600** no. 1-2, (2004) 57–64.

[67] S. Actis, G. Passarino, C. Sturm, and S. Uccirati, *NLO electroweak corrections to Higgs boson production at hadron colliders*, Physics Letters B **670** no. 1, (2008) 12–17, arXiv:0809.1301 [hep-ph].

[68] P. Bolzoni, F. Maltoni, S.-O. Moch, and M. Zaro, *Higgs Boson Production via Vector-Boson Fusion at Next-to-Next-to-Leading Order in QCD*, Physical Review Letters **600** no. 1, (2010) 011801, arXiv:1003.4451 [hep-ph].

[69] M. Ciccolini, D. A., and D. S., *Electroweak and QCD corrections to Higgs production via vector-boson fusion at the CERN LHC*, Physical Review D **77** no. 1, (2008) 013002, arXiv:0710.4749 [hep-ph].

[70] M. Ciccolini, A. Denner, and S. Dittmaier, *Strong and Electroweak Corrections to the Production of a Higgs Boson+2 Jets via Weak Interactions at the Large Hadron Collider*, Physical Review Letters **99** no. 16, (2007) 161803, arXiv:0707.0381 [hep-ph].

[71] K. Arnold, M. Bähr, G. Bozzi, et al., *Vbfnlo: A parton level Monte Carlo for processes with electroweak bosons*, Computer Physics Communications **180** no. 9, (2009) 1661–1670, arXiv:0811.4559 [hep-ph].

[72] S. L. Glashow, D. V. Nanopoulos, and A. Yildiz, *Associated production of Higgs bosons and Z particles*, Phys. Rev. D **18** no. 5, (1978) 1724—-1727.

[73] O. Brein, A. Djouadi, and R. Harlander, *NNLO QCD corrections to the Higgs-strahlung processes at hadron colliders*, Physics Letters B **579** no. 1-2, (2004) 149–156.

[74] M. Ciccolini, S. Dittmaier, and M. Krämer, *Electroweak radiative corrections to associated WH and ZH production at hadron colliders*, Physical Review D **68** no. 7, (2003) 073003, arXiv:hep-ph/0306211 [hep-ph].

[75] W. Beenakker, S. Dittmaier, M. Krämer, et al., *NLO QCD corrections to production in hadron collisions*, Nuclear Physics B **653** no. 1-2, (2003) 151–203, arXiv:hep-ph/0211352 [hep-ph].

[76] S. Dawson, C. Jackson, L. Orr, L. Reina, and D. Wackeroth, *Associated Higgs boson production with top quarks at the CERN Large Hadron Collider: NLO QCD corrections*, Physical Review D **68** no. 3, (2003) 034022, arXiv:hep-ph/0106293 [hep-ph].

[77] W. Beenakker, S. Dittmaier, M. Krämer, et al., *Higgs Radiation Off Top Quarks at the Tevatron and the LHC*, Physical Review Letters **87** no. 20, (2001) 201805, arXiv:hep-ph/0107081 [hep-ph].

[78] S. Dawson, L. Orr, L. Reina, and D. Wackeroth, *Next-to-leading order QCD corrections to* $pp \to t\bar{t}H$ *at the CERN Large Hadron Collider*, Physical Review D **67** no. 7, (2003) 071503, arXiv:hep-ph/0211438 [hep-ph].

[79] A. D. Martin, W. J. Stirling, R. S. Thorne, and G. Watt, *Parton distributions for the LHC*, The European Physical Journal C **63** no. 2, (2009) 189–285, arXiv:0901.0002 [hep-ph].

[80] M. Botje, J. Butterworth, A. Cooper-Sarkar, et al., *The PDF4LHC Working Group Interim Recommendations*, arXiv:1101.0538 [hep-ph].

[81] A. Djouadi, J. Kalinowski, and M. Spira, *HDECAY: a program for Higgs boson decays in the Standard Model and its supersymmetric extension*, Computer Physics Communications **108** no. 1, (1998) 56–74, arXiv:hep-ph/9704448 [hep-ph].

[82] J. M. Butterworth, F. Maltoni, F. Moortgat, et al., *THE TOOLS AND MONTE CARLO WORKING GROUP Summary Report from the Les Houches 2009 Workshop on TeV Colliders*, arXiv:1003.1643 [hep-ph].

[83] M. Spira, *QCD Effects in Higgs Physics*, arXiv:hep-ph/9705337 [hep-ph].

[84] A. Bredenstein, A. Denner, S. Dittmaier, and M. Weber, *Precise predictions for the Higgs-boson decay* $H \to WW/ZZ \to 4$ *leptons*, Physical Review D **74** no. 1, (2006) 013004, arXiv:hep-ph/0604011 [hep-ph].

[85] A. Bredenstein, A. Denner, S. Dittmaier, and M. Weber, *Precision calculations for the Higgs decays* $H \to ZZ/WW \to 4$ *leptons*, Nuclear Physics B - Proceedings Supplements **160** (2006) 131–135, arXiv:hep-ph/0607060 [hep-ph].

[86] A. Bredenstein, A. Denner, S. Dittmaier, and M. M. Weber, *Radiative corrections to the semileptonic and hadronic Higgs-boson decays* $H \to WW/ZZ \to 4$ *fermions*, Journal of High Energy Physics **2007** no. 02, (2007) 080–080, arXiv:hep-ph/0611234 [hep-ph].

[87] ATLAS Collaboration, *Combined search for the Standard Model Higgs boson in pp collisions at sqrt[s]=7 TeV with the ATLAS detector*, Physical Review D **86** no. 3, (2012) 032003, arXiv:1207.0319 [hep-ph].

[88] CMS Collaboration, *Combined results of searches for the standard model Higgs boson in pp collisions at*, Physics Letters B **710** no. 1, (2012) 26–48, arXiv:1202.1488 [hep-ex].

[89] ATLAS Collaboration, *Updated coupling measurements of the Higgs boson with the ATLAS detector using up to 25 fb^{-1} of proton-proton collision data*, ATLAS-CONF-2014-009 (2014). https://cds.cern.ch/record/1670012.

[90] CMS Collaboration, *Precise determination of the mass of the Higgs boson and studies of the compatibility of its couplings with the standard model*, CMS-PAS-HIG-14-009 (2014). https://cds.cern.ch/record/1728249.

[91] CMS Collaboration, *Evidence for the direct decay of the 125 GeV Higgs boson to fermions*, Nature Physics **10** (2014) 557–560, arXiv:1401.6527 [hep-ex].

[92] ATLAS Collaboration, *Measurement of the Higgs boson mass from the $H \to \gamma\gamma$ and $H \to ZZ^* \to 4\ell$ channels with the ATLAS detector using 25 fb^{-1} of pp collision data*, Phys. Rev. D **90** (2014) 052004, arXiv:1406.3827 [hep-ex].

[93] ATLAS Collaboration, *Evidence for the spin-0 nature of the Higgs boson using ATLAS data*, Physics Letters B **726** no. 1-3, (2013) 120–144, arXiv:1307.1432 [hep-ex].

[94] CMS Collaboration, *Measurement of the properties of a Higgs boson in the four-lepton final state*, Physical Review D **89** no. 9, (2014) 092007, arXiv:1312.5353 [hep-ex].

[95] CMS Collaboration, *Measurement of Higgs boson production and properties in the WW decay channel with leptonic final states*, Journal of High Energy Physics **2014** no. 1, (2014) 96, arXiv:1312.1129 [hep-ph].

[96] ATLAS Collaboration, "Summary plots from the ATLAS Standard Model physics group." https://atlas.web.cern.ch/Atlas/GROUPS/PHYSICS/CombinedSummaryPlots/SM/index.html.

[97] L. Evans and P. Bryant, *LHC Machine*, Journal of Instrumentation **3** no. 08, (2008) S08001.

[98] C. Lefevre, *LHC: the guide*,. http://cds.cern.ch/record/1165534.

[99] M. Lamont, *The first years of LHC operation for luminosity production*, Proceedings of IPAC2013, Shanghai, China (2013).

[100] P. Lebrun, *Interim summary report on the analysis of the 19 September 2008 incident at the LHC*,. https://edms.cern.ch/document/973073/1.

[101] ATLAS Collaboration, *The ATLAS Experiment at the CERN Large Hadron Collider*, Journal of Instrumentation **3** no. 08, (2008) S08003.

[102] ATLAS Collaboration, *Expected Performance of the ATLAS Experiment - Detector, Trigger and Physics*, arXiv:0901.0512 [hep-ex].

[103] ATLAS Collaboration, "ATLAS Photos." http://www.atlas.ch/photos/index.html.

[104] ATLAS Collaboration, "Luminosity Public Plots." https://twiki.cern.ch/twiki/bin/view/AtlasPublic/LuminosityPublicResults.

[105] ATLAS Collaboration, "Data Quality Information for 2010 and 2011 Data." http://twiki.cern.ch/twiki/bin/view/AtlasPublic/RunStatsPublicResults2010.

[106] ATLAS Collaboration, *Luminosity determination in pp collisions at $\sqrt{s} = 7$ TeV using the ATLAS detector at the LHC*, The European Physical Journal C **71** no. 4, (2011) 1630, arXiv:1101.2185 [hep-ex].

[107] ATLAS Collaboration, "Public Liquid-Argon Calorimeter Plots on Detector Status." https://twiki.cern.ch/twiki/bin/view/AtlasPublic/LArCaloPublicResultsDetStatus.

[108] ATLAS Collaboration, *Performance of the ATLAS Trigger System in 2010*, The European Physical Journal C **72** no. 1, (2012) 1849, arXiv:1110.1530 [hep-ex].

[109] ATLAS Collaboration, *ATLAS detector and physics performance: Technical Design Report, 1*, ATLAS-TDR-14; CERN-LHCC-99-014 (1999). https://cds.cern.ch/record/391176.

[110] R. Achenbach, P. Adragna, V. Andrei, et al., *The ATLAS Level-1 Calorimeter Trigger*, Journal of Instrumentation **3** no. 03, (2008) P03001.

[111] ATLAS Collaboration, *ATLAS Computing: technical design report*, ATLAS-TDR-17; CERN-LHCC-2005-022 (2005). https://cds.cern.ch/record/837738.

[112] ATLAS Collaboration, *The ATLAS Simulation Infrastructure*, The European Physical Journal C **70** no. 3, (2010) 823–874, arXiv:1005.4568 [physics.ins-det].

[113] S. Agostinelli, J. Allison, K. Amako, et al., *Geant4—a simulation toolkit*, Nuclear Instruments and Methods in Physics Research Section A: Accelerators, Spectrometers, Detectors and Associated Equipment **506** no. 3, (2003) 250–303.

[114] "ROOT Data Analysis Framework." http://root.cern.ch.

[115] T. Cornelissen, M. Elsing, S. Fleischmann, et al., *Concepts, Design and Implementation of the ATLAS New Tracking (NEWT)*, ATL-SOFT-PUB-2007-007; ATL-COM-SOFT-2007-002 (2007). https://cds.cern.ch/record/1020106.

[116] T. Cornelissen, M. Elsing, I. Gavrilenko, W. Liebig, and A. Salzburger, *Single Track Performance of the Inner Detector New Track Reconstruction (NEWT)*, ATL-INDET-PUB-2008-002; ATL-COM-INDET-2008-004 (2008). https://cds.cern.ch/record/1092934.

[117] R. Frühwirth, *Application of Kalman filtering to track and vertex fitting*, Nuclear Instruments and Methods in Physics Research Section A: Accelerators, Spectrometers, Detectors and Associated Equipment **262** no. 2-3, (1987) 444–450.

[118] ATLAS Collaboration, *Performance of the ATLAS Inner Detector Track and Vertex Reconstruction in the High Pile-Up LHC Environment*, ATLAS-CONF-2012-042 (2012). https://cds.cern.ch/record/1435196.

[119] ATLAS Collaboration, *Performance of the ATLAS Silicon Pattern Recognition Algorithm in Data and Simulation at* $\sqrt{s} = 7$ *TeV*, ATLAS-CONF-2010-072 (2010). https://cds.cern.ch/record/1281363.

[120] ATLAS Collaboration, *Performance of primary vertex reconstruction in proton-proton collisions at* $\sqrt{s} = 7 \sim$ *TeV in the ATLAS experiment*, ATLAS-CONF-2010-069 (2010). https://cds.cern.ch/record/1281344.

[121] W. Waltenberger, R. Frühwirth, and P. Vanlaer, *Adaptive vertex fitting*, Journal of Physics G: Nuclear and Particle Physics **34** no. 12, (2007) N343.

[122] ATLAS Collaboration, *Muon reconstruction efficiency and momentum resolution of the ATLAS experiment in proton-proton collisions at* $\sqrt{s}$*=7 TeV in 2010*, Eur. Phys. J. C **74** (2014) 3034, arXiv:1404.4562 [hep-ex].

[123] ATLAS Collaboration, *Preliminary results on the muon reconstruction efficiency, momentum resolution, and momentum scale in ATLAS 2012 pp collision data*, ATLAS-CONF-2013-088 (2013). https://cds.cern.ch/record/1580207.

[124] ATLAS Collaboration, *Pile-up Depedence of the ATLAS Muon Performance*, ATL-COM-PHYS-2011-1640 (2011). https://atlas.web.cern.ch/Atlas/GROUPS/PHYSICS/MUON/PublicPlots/2011/Dec/index.html.

[125] ATLAS Collaboration, *Performance of the ATLAS muon trigger in 2011*, ATLAS-CONF-2012-099 (2012). https://cds.cern.ch/record/1462601.

[126] ATLAS Collaboration, "Muon Trigger Public Results." https://twiki.cern.ch/twiki/bin/view/AtlasPublic/MuonTriggerPublicResults.

[127] ATLAS Collaboration, *Electron performance measurements with the ATLAS detector using the 2010 LHC proton-proton collision data*, The European Physical Journal C **72** no. 3, (2012) 1909, arXiv:1110.3174 [hep-ex].

[128] ATLAS Collaboration, *Electron reconstruction and identification efficiency measurements with the ATLAS detector using the 2011 LHC proton-proton collision data*, arXiv:1404.2240 [hep-ex].

[129] ATLAS Collaboration, *Electron efficiency measurements with the ATLAS detector using the 2012 LHC proton-proton collision data*, ATLAS-CONF-2014-032 (2014). https://cds.cern.ch/record/1706245.

[130] ATLAS Collaboration, *Improved electron reconstruction in ATLAS using the Gaussian Sum Filter-based model for bremsstrahlung*, ATLAS-CONF-2012-047 (2012). https://cds.cern.ch/record/1449796.

[131] ATLAS Collaboration, *Electron and photon energy calibration with the ATLAS detector using LHC Run 1 data*, ATL-COM-PHYS-2013-1652 (2013). https://cds.cern.ch/record/1637529.

[132] ATLAS Collaboration, *Expected electron performance in the ATLAS experiment*, ATL-PHYS-PUB-2011-006 (2011). https://cds.cern.ch/record/1345327.

[133] ATLAS Collaboration, *Performance of the ATLAS Electron and Photon Trigger in p-p Collisions at* $\sqrt{s} = 7\,TeV$ *in 2011*, ATLAS-CONF-2012-048 (2012). https://cds.cern.ch/record/1450089.

[134] ATLAS Collaboration, *Jet energy measurement and its systematic uncertainty in proton–proton collisions at* $\sqrt{s} = 7{\sim}TeV$ *with the ATLAS detector*, CERN-PH-EP-2013-222 (2014) 88, arXiv:1406.0076 [hep-ex].

[135] M. Cacciari, G. P. Salam, and G. Soyez, "FastJet." http://fastjet.fr.

[136] W. Lampl, S. Laplace, D. Lelas, et al., *Calorimeter Clustering Algorithms: Description and Performance*, ATL-LARG-PUB-2008-002; ATL-COM-LARG-2008-003 (2008). https://cds.cern.ch/record/1099735.

[137] ATLAS Collaboration, *Jet energy measurement with the ATLAS detector in proton-proton collisions at* $\sqrt{s} = 7$ TeV, The European Physical Journal C **73** no. 3, (2013) 2304, arXiv:1112.6426 [hep-ex].

[138] ATLAS Collaboration, *Selection of jets produced in proton-proton collisions with the ATLAS detector using 2011 data*, ATLAS-CONF-2012-020 (2012). https://cds.cern.ch/record/1430034.

[139] ATLAS Collaboration, *Pile-up subtraction and suppression for jets in ATLAS*, ATLAS-CONF-2013-083 (2013). https://cds.cern.ch/record/1570994.

[140] M. Cacciari and G. P. Salam, *Pileup subtraction using jet areas*, Physics Letters B **659** no. 1-2, (2008) 119–126, arXiv:0707.1378 [hep-ph].

[141] ATLAS Collaboration, "Jet/Etmiss Approved 2013 JES Uncertainty." https://twiki.cern.ch/twiki/bin/view/AtlasPublic/JetEtmissApproved2013JESUncertainty.

[142] ATLAS Collaboration, *Jet energy resolution in proton-proton collisions at* $\sqrt{s} = 7$ *TeV recorded in 2010 with the ATLAS detector*, The European Physical Journal C **73** no. 3, (2013) 2306, arXiv:1210.6210 [hep-ex].

[143] ATLAS Collaboration, "Jet/Etmiss Approved 2013 JER 2011." https://twiki.cern.ch/twiki/bin/view/AtlasPublic/JetEtmissApproved2013Jer2011.

[144] L. Ancu, M. Begel, M. Campanelli, et al., *The Design and Performance of the ATLAS Jet Trigger for the Event Filter*, ATL-COM-DAQ-2011-048 (2011). https://cds.cern.ch/record/1357014.

[145] ATLAS Collaboration, *Commissioning of the ATLAS high-performance b-tagging algorithms in the 7 TeV collision data*, ATLAS-CONF-2011-102 (2011). https://cds.cern.ch/record/1369219.

[146] ATLAS Collaboration, *Calibration of the performance of b-tagging for c and light-flavour jets in the 2012 ATLAS data*, ATLAS-CONF-2014-046 (2014). https://cds.cern.ch/record/1741020.

[147] ATLAS Collaboration, *Calibration of b-tagging using dileptonic top pair events in a combinatorial likelihood approach with the ATLAS experiment*, ATLAS-CONF-2014-004 (2014). https://cds.cern.ch/record/1664335.

[148] ATLAS Collaboration, *Measurement of the b-tag Efficiency in a Sample of Jets Containing Muons with 5*$\sim fb^{-1}$ *of Data from the ATLAS Detector*, ATLAS-CONF-2012-043 (2012). https://cds.cern.ch/record/1435197.

[149] ATLAS Collaboration, *Measuring the b-tag efficiency in a top-pair sample with 4.7*$\sim fb^{-1}$ *of data from the ATLAS detector*, ATLAS-CONF-2012-097 (2012). https://cds.cern.ch/record/1460443.

[150] ATLAS Collaboration, *Performance of missing transverse momentum reconstruction in proton-proton collisions at* $\sqrt{s} = 7 \sim$ *TeV with ATLAS*, The European Physical Journal C **72** no. 1, (2012) 1844, arXiv:1108.5602. http://arxiv.org/abs/1108.5602.

[151] ATLAS Collaboration, *Performance of Missing Transverse Momentum Reconstruction in ATLAS studied in Proton-Proton Collisions recorded in 2012 at 8 TeV*, ATLAS-CONF-2013-082 (2013). https://cds.cern.ch/record/1570993.

[152] ATLAS Collaboration, *Performance of Missing Transverse Momentum Reconstruction in ATLAS with 2011 Proton-Proton Collisions at* $\sqrt{s} = 7 TeV$, ATLAS-CONF-2012-101 (2012). https://cds.cern.ch/record/1463915.

[153] ATLAS Collaboration, *Analysis of $H \to WW^* \to \ell\nu\ell\nu$ in the same-flavour channels*, ATL-COM-PHYS-2012-1445 (internal) (2012). https://cds.cern.ch/record/1482155.

[154] ATLAS Collaboration, *Object selection for the $H \to WW$ search with the ATLAS detector at $\sqrt{(s)} = 8 \sim TeV$, 13 fb^{-1} update*, ATL-COM-PHYS-2012-1517 (internal) (2012). https://cds.cern.ch/record/1485533.

[155] ATLAS Collaboration, *Measurements of Higgs boson production and couplings in diboson final states with the ATLAS detector at the LHC*, Physics Letters B **726** no. 1-3, (2013) 88–119, arXiv:1307.1427 [hep-ex].

[156] ATLAS Collaboration, *Object selection for the $H \to WW$ search with the ATLAS detector at sqrts=$8 \sim TeV$*, ATL-COM-PHYS-2013-147 (internal) (2013). https://cds.cern.ch/record/1514336.

[157] ATLAS Collaboration, *Object Selections in the $H \to WW$ analysis with 20.3 fb-1 of data collected with the ATLAS detector at $\sqrt{s} = 8 \sim TeV$*, ATL-COM-PHYS-2013-1504 (internal). https://cds.cern.ch/record/1624408.

[158] ATLAS Collaboration, *Performance of the ATLAS Jet Trigger in the Early $\sqrt{s} = 7 \sim TeV$ Data*, ATLAS-CONF-2010-094. https://cds.cern.ch/record/1299109.

[159] J. Machado Miguéns, *Performance and Calibration of the ATLAS Jet Trigger*, ATL-DAQ-PROC-2011-034 (2011). http://cds.cern.ch/record/1397028.

[160] ATLAS Collaboration, *Jet Trigger Performance with 2011 Data*, ATL-COM-DAQ-2011-063. https://cds.cern.ch/record/1374159.

[161] ATLAS Collaboration, *Inclusive Jet Trigger Efficiencies for the Early 2011 Data*, ATL-COM-DAQ-2011-031 (2011). https://cds.cern.ch/record/1351823.

[162] ATLAS Collaboration, *Performance of the Minimum Bias Trigger in p-p Collisions at $\sqrt{s} = 7$ TeV*, ATLAS-CONF-2010-068 (2010). http://cds.cern.ch/record/1281343.

[163] ATLAS Collaboration, *Data-Quality Requirements and Event Cleaning for Jets and Missing Transverse Energy Reconstruction with the ATLAS Detector in Proton-Proton Collisions at a Center-of-Mass Energy of $\sqrt{s} = 7 \sim TeV$*, ATLAS-CONF-2010-038 (2010). https://cds.cern.ch/record/1277678.

[164] T. Sjostrand, S. Mrenna, and P. Skands, *PYTHIA 6.4 physics and manual*, Journal of High Energy Physics **2006** no. 05, (2006) 026–026, arXiv:0603175 [hep-ph].

[165] ATLAS Collaboration, *ATLAS Monte Carlo tunes for MC09*, ATL-PHYS-PUB-2010-002 (2010). https://cds.cern.ch/record/1247375.

[166] ATLAS Collaboration, "TrigDecisionTool." `https://twiki.cern.ch/twiki/bin/viewauth/Atlas/TrigDecisionTool`.

[167] ATLAS Collaboration, *Measurement of jet production in proton-proton collisions at 7 TeV centre-of-mass energy with the ATLAS Detector*, ATLAS-CONF-2010-050 (2010). `http://cds.cern.ch/record/1281305`.

[168] J. Machado Miguéns, *ATLAS Jet Trigger Performance and in-situ Calibration Studies*. Master thesis, Faculdade de Ciências da Universidade de Lisboa, 2009.

[169] ATLAS Collaboration, *Search for the Standard Model Higgs boson in the $H \to WW^* \to \ell\nu\ell\nu$ decay mode with 4.7 fb^{-1} of ATLAS data at $\sqrt{s} = 7{\sim}TeV$*, Physics Letters B **716** no. 1, (2012) 62–81.

[170] ATLAS Collaboration, *Measurements of the properties of the Higgs-like boson in the $WW^{(*)} \to \ell\nu\ell\nu$ decay channel with the ATLAS detector using 25$\sim$ fb^{-1} of proton-proton collision data*, ATLAS-CONF-2013-030 (2013). `https://cds.cern.ch/record/1527126`.

[171] ATLAS Collaboration, *Study of the spin properties of the Higgs-like particle in the $H \to WW^* \to e\nu\mu\nu$ channel with 21 fb^{-1} of $\sqrt{s} = 8$ TeV data collected with the ATLAS detector*, ATLAS-CONF-2013-031 (2013). `https://cds.cern.ch/record/1527127`.

[172] ATLAS Collaboration, *Observation and measurement of Higgs boson decays to WW^* with the ATLAS detector*, Phys. Rev. D (submitted) (2014), `arXiv:1412.2641 [hep-ex]`.

[173] T. Gleisberg, S. Höche, F. Krauss, et al., *Event generation with SHERPA 1.1*, Journal of High Energy Physics **2009** no. 02, (2009) 007–007, `arXiv:0811.4622 [hep-ph]`.

[174] T. Sjöstrand, S. Mrenna, and P. Skands, *A brief introduction to PYTHIA 8.1*, Computer Physics Communications **178** no. 11, (2008) 852–867, `arXiv:0710.3820 [hep-ph]`.

[175] T. Sjöstrand, S. Mrenna, and P. Skands, *PYTHIA 6.4 physics and manual*, Journal of High Energy Physics **2006** no. 05, (2006) 026–026, `arXiv:hep-ph/0603175 [hep-ph]`.

[176] G. Corcella, I. G. Knowles, G. Marchesini, et al., *HERWIG 6: an event generator for hadron emission reactions with interfering gluons (including supersymmetric processes)*, Journal of High Energy Physics **2001** no. 01, (2001) 010–010, `arXiv:hep-ph/0011363 [hep-ph]`.

[177] J. M. Butterworth, J. R. Forshaw, and M. H. Seymour, *Multiparton interactions in photoproduction at HERA*, Zeitschrift für Physik C: Particles and Fields **72** no. 4, (1996) 637–646, `arXiv:hep-ph9601371 [hep-ph]`.

[178] P. Nason and C. Oleari, *NLO Higgs boson production via vector-boson fusion matched with shower in POWHEG*, Journal of High Energy Physics **2010** no. 2, (2010) 37, arXiv:0911.5299 [hep-ph].

[179] M. L. Mangano, F. Piccinini, A. D. Polosa, M. Moretti, and R. Pittau, *ALPGEN, a generator for hard multiparton processes in hadronic collisions*, Journal of High Energy Physics **2003** no. 07, (2003) 001–001, arXiv:hep-ph/0206293 [hep-ph].

[180] B. P. Kersevan and R.-W. Elzbieta, *The Monte Carlo event generator AcerMC versions 2.0 to 3.8 with interfaces to PYTHIA 6.4, HERWIG 6.5 and ARIADNE 4.1*, Computer Physics Communications **184** no. 3, (2013) 919–985, arXiv:hep-ph/0405247 [hep-ph].

[181] N. Kauer and G. Passarino, *Inadequacy of zero-width approximation for a light Higgs boson signal*, arXiv:1206.4803 [hep-ph].

[182] T. Binoth, M. Ciccolini, N. Kauer, and M. Krämer, *Gluon-induced W -boson pair production at the LHC*, Journal of High Energy Physics **2006** no. 12, (2006) 046–046, arXiv:hep-ph/0611170 [hep-ph].

[183] H.-L. Lai, M. Guzzi, J. Huston, et al., *New parton distributions for collider physics*, Physical Review D **82** no. 7, (2010) 074024, arXiv:1007.2241 [hep-ph].

[184] P. Nadolsky, H.-L. Lai, Q.-H. Cao, et al., *Implications of CTEQ global analysis for collider observables*, Physical Review D **78** no. 1, (2008) 013004, arXiv:0802.0007 [hep-ph].

[185] A. Sherstnev and R. Thorne, *Parton distributions for LO generators*, The European Physical Journal C **55** no. 4, (2008) 553–575, arXiv:0711.2473 [hep-ph].

[186] J. M. Campbell and R. K. Ellis, *Update on vector boson pair production at hadron colliders*, Physical Review D **60** no. 11, (1999) 113006, arXiv:9905386 [hep-ph].

[187] M. Czakon and A. Mitov, *Top++: A program for the calculation of the top-pair cross-section at hadron colliders*, Computer Physics Communications **185** no. 11, (2014) 2930–2938.

[188] N. Kidonakis, *NNLL resummation for s-channel single top quark production*, arXiv:1001.5034 [hep-ph].

[189] N. Kidonakis, *Next-to-next-to-leading-order collinear and soft gluon corrections for t-channel single top quark production*, arXiv:1103.2792 [hep-ph].

[190] N. Kidonakis, *Two-loop soft anomalous dimensions for single top quark associated production with a W- or H-*, arXiv:1005.4451 [hep-ph].

[191] J. Alwall, S. Höche, F. Krauss, et al., *Comparative study of various algorithms for the merging of parton showers and matrix elements in hadronic collisions*, The European Physical Journal C **53** no. 3, (2007) 473–500, arXiv:0706.2569 [hep-ph].

[192] S. Catani, L. Cieri, G. Ferrera, D. de Florian, and M. Grazzini, *Vector boson production at hadron colliders: a fully exclusive QCD calculation at NNLO*, arXiv:0903.2120 [hep-ph].

[193] E. Barberio and Z. Was, *PHOTOS - a universal Monte Carlo for QED radiative corrections: version 2.0*, Computer Physics Communications **79** no. 2, (1994) 291–308.

[194] ATLAS Collaboration, *Measurement of the Z/γ^* boson transverse momentum distribution in pp collisions at $\sqrt{s}$ = 7 TeV with the ATLAS detector*, arXiv:1406.3660 [hep-ex].

[195] B. Mellado, X. Ruan, and Z. Zhang, *Extraction of Top Backgrounds in the Higgs Boson Search with the $H \to WW^\star \to \ell\ell + E_T^{miss}$ Decay with a Full-Jet Veto at the LHC*, arXiv:1101.1383 [hep-ph].

[196] J. Butterworth, G. Dissertori, S. Dittmaier, et al., *Les Houches 2013: Physics at TeV Colliders: Standard Model Working Group Report*, arXiv:1405.1067 [hep-ph].

[197] I. W. Stewart and F. J. Tackmann, *Theory Uncertainties for Higgs and Other Searches Using Jet Bins*, arXiv:1107.2117 [hep-ph].

[198] ATLAS Collaboration, *Improved luminosity determination in pp collisions at $\sqrt{s} = 7$ TeV using the ATLAS detector at the LHC*, arXiv:1302.4393 [hep-ph].

[199] G. Cowan, K. Cranmer, E. Gross, and O. Vitells, *Asymptotic formulae for likelihood-based tests of new physics*, The European Physical Journal C **71** (2011) 1554, arXiv:1007.1727.

[200] A. L. Read, *Presentation of search results: the CLs technique*, Journal of Physics G: Nuclear and Particle Physics **28** no. 10, (2002) 2693.